Calibrated Probes of Jet-Medium Interactions in Hot and Cold Nuclear Matter

by

Jeffrey C. Ouellette

B.A., Cornell University, 2017

M.S., University of Colorado, 2020

A thesis submitted to the

Faculty of the Graduate School of the

University of Colorado in partial fulfillment

of the requirements for the degree of

Doctor of Philosophy

Department of Physics

2022

Committee Members:

Dennis V. Perepelitsa, Chair

James L. Nagle

Alysia Marino

Paul Romatschke

François Georges Meyer

CERN-THESIS-2022-212
//2022



Ouellette, Jeffrey C. (Ph.D., Physics)

Calibrated Probes of Jet-Medium Interactions in Hot and Cold Nuclear Matter

Thesis directed by Prof. Dennis V. Perepelitsa

Ultrarelativistic collisions of large nuclei are understood to produce droplets of quark-gluon plasma (QGP), a deconfined phase of QCD matter that exists at high temperatures $\gtrsim 155$ MeV. *Jet quenching* is one of the key signatures of this phase, and is attributed to energy loss via collisional and radiative interactions between high-energy, strongly interacting probes and the plasma. Quenching model predict the lost energy to reemerge at low momentum scales, however data in this regime is limited by the background of low-momentum hadrons produced by the expanding and cooling medium. At the LHC, Z^0 + jet scattering events offer new insights to a more complete picture of the quenching phenomenon. Simultaneously, collisions of smaller nuclei consistently exhibit momentum anisotropies and other signatures traditionally associated with a QGP phase. Within current uncertainties, jet-quenching scenarios have neither been detected nor ruled out, particularly in central p+Pb collisions. To fully map out the minimal formation conditions for QGP droplets, a deeper understanding of small system dynamics is required.

This dissertation presents two new measurements of jet quenching in Pb+Pb and p+Pb collisions utilizing calibrated probes to tag hard-scattering events. The first is a measurement of Z^0-tagged charged hadron yields in Pb+Pb collisions. The color-neutral Z^0 boson tags the initial hard scattering, and a significant depletion of high-momentum hadrons is strongly sensitive to parton energy loss. At the very lowest momenta, a modest enhancement of hadrons is also observed, suggesting a redistribution of energy to the medium. Comparisons to theoretical expectations help build a more complete picture of the jet-medium interaction. The second study builds this analysis technology further by measuring jet-tagged hadron yields in central p+Pb collisions. The hadron yield in this system is found to be unmodified across a broad kinematic range to within a few percent, providing strong further constraints on potential energy loss phenomena in small systems.

Dedication

To my friends and family

Acknowledgements

The CU Heavy Ion Lab is a special place, which is certainly a reflection of the people who inhabit it. As I wrap up this dissertation, there are numerous people that have made my experience what it is, for which I am sincerely grateful, and deserve recognition. Foremost is my advisor, Prof. Dennis Perepelitsa, who took a risk hiring a newly-admitted graduate student with little to no formal background in heavy-ion physics four and a half years ago, and has imparted so much to me through his spirited curiosity and technical prowess. This gratitude also extends to Prof. Jamie Nagle for his fierce dedication to both students and the experimental process. The values I have built in this group are your product and will be invaluable as I move forward.

Many of my technical story-telling abilities were imparted to me by Kurt Hill and Javier Orjuela-Koop early in my graduate school years; these skills have guided my writing and plot-making process throughout multiple analyses and myriad technical presentations over the years. I am particularly indebted to Qipeng Hu and Sanghoon Lim for kick-starting my ATLAS endeavors, answering numerous questions as I became an independent worker, and instilling in me the virtues of patience and dedication. I need to thank Chris McGinn for his wit, and more importantly his continuous obscure movie references that bring an essential element of humanity to the problem-solving process. I am glad to have been accompanied by Daniel Lis, Berenice Garcia, and Sruthy Jyothi Das at Brookhaven, and will miss our lunch caravans to Taco Bell. In particular, I am grateful to Berenice Garcia for being an excellent running buddy and exemplifying the virtue of determination for the rest of us.

This is all in conjunction to the many other members who have made the lab an enjoyable

and productive place for me over the years: Ran Bi, Yeonju Go, Ron Belmont, Corben Browne, Morgan Kneusel, Spencer Griffith, Ross Snyder, Ahmed Alenezi, Megan Byres, Francesco Vassalli, Chase Smith, and Erin Bossard. Thank you to all.

A special thank you goes to Blair Seidlitz, who has been with me through my entire graduate school adventure. I am grateful for your ability to continually challenge me and force me to think more critically, while somehow introducing an element of humor along the way. Thank you for a constant friend through our ATLAS adventure; without a doubt I will miss working with you.

Beyond the CU group, I need to thank my collaborators and mentors in ATLAS for building an inspiring and engaged environment that enables students like myself to succeed: Aaron Angerami, Zvi Citron, Dominik Derendarz, Iwona Grabowska-Bold, Sasha Milov, Petr Balek, Timothy Rinn, Anne Sickles, Peter Steinberg, and Sebastian Tapia Araya. I am especially grateful to Martin Rybar for continually prioritizing student success with his guidance and support, often far beyond what is necessary.

I must also thank members of the sPHENIX community who guided me at Brookhaven during a global pandemic (particularly those who delivered groceries when I had Covid!): Stefan Bathe, John Haggerty, Eric Mannel, Dave Morrison, Rosi Reed, Daniel Richford, Veronica Canoa Roman, Sean Stoll, and Craig Woody.

Finally, I need to thank my friends and family for companionship, support, and just generally bearing with me sometimes. To Caitlin, Daniel, Ariel, Paul, Gwyn: thank you. To Mikki, thank you for being a tireless source of enthusiasm and a beacon of inspiration. To Nancy, thank you for your support and convivial hospitality these last few years. To Charlotte, thank you for your unwavering support and being the punchline of many of my jokes for the past $\sim$ 25 years; I feel that we understand each other better than many other people. Lastly, I am grateful to my parents for their generosity, love, and support for as long as I have been alive; know that I would not be here without you.

Contents

Chapter

Preface **1**

1 Introduction **6**

1.1 QCD Matter 11

1.2 Probing QCD via Scattering Experiments 16

1.3 Ultra-Relativistic Heavy-Ion Collisions 30

2 Jet Quenching **47**

2.1 Phenomenological Aspects of Quenching 49

2.2 Medium-Induced Energy Loss in pQCD 61

2.3 Strong-Coupling Calculations 74

2.4 Linear Boltzmann Transport 76

2.5 Energy Loss in Small Systems 79

3 The ATLAS Experiment at the LHC **85**

3.1 The Large Hadron Collider 85

3.2 The ATLAS detector 90

3.3 Triggering and Data Acquisition 110

3.4 Reconstruction of Collisions 114

4 $\boldsymbol{Z^0}$–Hadron Correlations in Pb+Pb Collisions **129**

4.1 Per-Trigger Yields . . . 132

4.2 The Basics: Data Sets & Event Selection . . . 138

4.3 Muon Channel . . . 147

4.4 Electron Channel . . . 156

4.5 Characterizing the Event Sample . . . 162

4.6 Tracking Considerations . . . 177

4.7 Underlying Event . . . 189

4.8 Discussion of Uncertainties . . . 203

5 Results of the $\boldsymbol{Z^0}$-Hadron Correlations Measurement **210**

5.1 Nuclear Modification . . . 213

5.2 Comparisons to γ-tagged Data . . . 216

5.3 Implications for Jet-Quenching Models . . . 218

5.4 Key Messages . . . 221

6 Constraining Final-State Energy Loss in $\boldsymbol{p}$+Pb **223**

6.1 The Basics: Data Sets & Event Selection . . . 226

6.2 Centrality . . . 233

6.3 The p+Pb Jet Calibration Sequence . . . 240

6.4 Tracking Considerations . . . 256

6.5 Underlying Event . . . 269

6.6 Deconvolving the Detector Response . . . 275

6.7 Discussion of Uncertainties . . . 290

7 Results of the Jet-Hadron Correlations Measurement **296**

7.1 Comparison to Fragmentation Function Measurements . . . 302

7.2 Small System Model Predictions . . . 304

7.3 Key Messages 308

8 Conclusions & Outlook **310**

Bibliography **315**

Appendix

A Auxiliary Material for the Z^0–Hadron Correlations Measurement **359**

A.1 Characterizing the Z boson Sample 359

A.2 Channel Dependence Checks 367

A.3 Monte Carlo Closure Studies 371

A.4 Decomposition of All Systematic Uncertainties 381

A.5 Impact of Z-based Acceptance Corrections 387

B Auxiliary Material for the Jet–Hadron Correlations Measurement **392**

B.1 Electromagnetic Backgrounds 392

B.2 Response Matrices 395

B.3 Unfolding Termination on the Near-side 398

B.4 Monte Carlo Closure Studies 403

B.5 Decomposition of All Systematic Uncertainties 415

C Auxiliary Results Figures **423**

Tables

Table

3.1 Overview of beam configuration parameters for LHC Run 2 heavy-ion and reference data sets . . . 88

3.2 Detailed schematics of the calorimeter systems . . . 98

3.3 Criteria for meeting a few different track working points . . . 116

4.1 List of good runs lists for 2018 Pb+Pb and 2017 pp data sets at 5.02 TeV . . . 137

4.2 Percentile $\Sigma E_{\mathrm{T}}^{\mathrm{FCal}}$ cuts in Pb+Pb collisions . . . 142

4.3 MC samples used in the Z-hadron correlations measurement . . . 146

4.4 Residual electron energy scale correction factors for Pb+Pb data and MC . . . 161

4.5 Detailed yield of Z bosons per centrality and p_{T}^{Z} bin . . . 165

4.6 Backgrounds contributions to the Z boson yield . . . 168

4.7 Run categorization for run-matching in the Pb+Pb mixed event . . . 191

4.8 $\Sigma E_{\mathrm{T}}^{\mathrm{FCal}}$ bin edges for the Pb+Pb mixed event . . . 192

4.9 Summary of systematic uncertainties in the Z-hadron correlations measurement . . . 207

6.1 Overview of the data sets used in the jet-hadron correlations measurement . . . 226

6.2 Peak pile-up rates $\langle\mu\rangle$ throughout the p+Pb and pp runs . . . 227

6.3 MC samples used in the jet-hadron correlations measurement . . . 230

6.4 Truth jet p_{T} ranges sampled by each `JZ` slice . . . 233

6.5 $\Sigma E^{\mathrm{ZDC,Pb}}$ centile cuts in p+Pb and corresponding $\langle N_{\mathrm{coll}}\rangle$ values from ALICE . . . 236

6.6 The numbers of jets in pp and each p+Pb centrality bin 242

6.7 $\Sigma E_{\mathrm{T}}^{\mathrm{FCal}}$ centiles used for the p+Pb and pp event matching 271

7.1 Average jet p_{T} after unfolding in pp and p+Pb 298

Figures

Figure

P.1 Cosmological expansion model of the universe 2

1.1 Fundamental particles described in the Standard Model 7

1.2 Allowed Feynman vertices in QCD 8

1.3 **(a)** A gluon flux tube from lattice QCD and **(b)** the QCD running coupling 10

1.4 Illustration of Gell-Manns' Eightfold Way 12

1.5 Parameters of the QCD equation of state from lattice calculations 15

1.6 Phase diagram of QCD matter 15

1.7 Feynman diagram of the DIS process 17

1.8 Structure function $F_2(x, Q^2)$ of the proton 18

1.9 Schematic illustration of data sets used in PDF fits 20

1.10 CT18 PDF fits at 2 GeV and 100 GeV 21

1.11 Lowest order parton splitting functions 22

1.12 Examples of fitted parton$\to \pi^+$ fragmentation functions at $Q^2 = M_Z^2$ 24

1.13 Visualization of anti-k_t jets in data and simulation 25

1.14 Nuclear modification of PDFs in Pb from the EPPS16 and nCTEQ15 global fits at $Q^2 = 10$ GeV^2 29

1.15 The Standard Model of Heavy-Ion Collisions 31

1.16 A simulated Au+Au collision in the Glauber model 35

1.17 Total forward energy measured by ATLAS fitted to a Glauber model 36

1.18 Rapidity dependence of charged-particle production in Pb+Pb collisions 39
1.19 Comparison between anisotropy coefficients in viscous hydrodynamics simulations and Pb+Pb data 40
1.20 Examination of collectivity in small collision systems 42
1.21 Formation lengths of a 0.8 GeV parton in an AMPT event 44

2.1 Illustration of jet quenching in a heavy-ion collision 48
2.2 Examination of the dijet asymmetry measured by ATLAS 50
2.3 N_{coll} distributions in Pb+Pb determined with MC Glauber 51
2.4 Nuclear modification factor R_{AA} of jets in 5.02 TeV Pb+Pb collisions 52
2.5 Per-trigger associated particle yields measured by PHENIX in 0–20% Au+Au and pp 53
2.6 Illustration of differential energy loss within an elliptical QGP droplet 54
2.7 Examples of medium-induced flavor-changing Feynman diagrams 56
2.8 Nuclear modification factors for hadron states in 5.02 TeV Pb+Pb collisions 57
2.9 Ratios of charged-hadron fragmentation functions between 0–10% Pb+Pb and pp . . 59
2.10 Ratio of photon-tagged jet-fragmentation functions in 0–10% Pb+Pb to pp 60
2.11 A Feynman diagram for medium-induced gluon bremsstrahlung in the MSSA limit . 64
2.12 The spectrum of medium-induced gluon radiations in the opacity expansion 66
2.13 Charged-hadron R_{AA} in central Pb+Pb compared to JEWEL and $\mathrm{SCET_G}$ predictions 71
2.14 Comparison of the photon-jet momentum balance between data and models 72
2.15 Overview of the Hybrid model approach to partonic energy loss 74
2.16 Snapshots of parton-medium coevolution in a $Z+$jet Pb+Pb event with the CoLBT-hydro model 78
2.17 Role of medium backreaction in jet-fragmentation modification within the Hybrid model 79
2.18 Angular dependence of two-particle correlations at high-p_{T} in p+Pb collisions 81
2.19 Nuclear modification factor $Q_{p\mathrm{Pb}}$ for charged hadrons in p+Pb measured by ALICE 82

2.20 Predictions for the charged-particle $R_{p\mathrm{Pb}}$ under various energy-loss scenarios 83

3.1 Overview of the CERN accelerator complex 86

3.2 Illustration of the ATLAS detector 90

3.3 Illustration of how different types of particles interact with the ATLAS detector . . . 91

3.4 Illustration of how the ATLAS inner detector observes charged-particle trajectories . 93

3.5 Schematics of the ATLAS pixel detector 94

3.6 The total material budget of the ID versus particle pseudorapidity 95

3.7 Schematic overview of the ATLAS liquid argon calorimeter system 96

3.8 Diagram showing the ATLAS calorimeters systems, including their coverage in $|\eta|$. 97

3.9 Detailed schematics of the ATLAS EMB 101

3.10 Illustration of a hadronic cascade from a neutron 102

3.11 Schematics of the forward LAr calorimeters (FCal) 103

3.12 Illustration of a tile drawer in the barrel segment of the tile calorimeter 104

3.13 Cross-sectional view of the tile calorimeter drawer layout in the rz-plane 105

3.14 Total material budget of the ATLAS calorimeter system 106

3.15 Cross-sectional view of the toroid magnets and the MS near mid-rapidity 107

3.16 Schematic illustrations of the ATLAS ZDC 110

3.17 Overview of the Run 2 trigger system, including the L1 and HLT triggers 111

3.18 Illustration of an MBTS wheel from Run 1 112

3.19 Illustrations of cluster merging techniques in the ID reconstruction 115

3.20 Flowchart of the heavy-ion jet reconstruction procedure 121

3.21 Illustration of the jet underlying event subtraction procedure 122

3.22 Average subtracted transverse energy for jets in Pb+Pb collisions 123

3.23 The heavy-ion jet calibration sequence 125

3.24 Schematic overview of the e/γ supercluster reconstruction 127

4.1 Tree-level Feynman diagrams for γ^*/Z^0 production at the LHC 129

4.2 High-level overview of the Z-hadron correlations measurement 131
4.3 Cartoon of *correlated* and *uncorrelated* background surrounding a jet 134
4.4 Truth Pb+Pb impact parameter distribution in minimum bias HIJING samples . . . 139
4.5 Distribution of $\Sigma E_{\mathrm{T}}^{\mathrm{FCal}}$ values in minimum bias Pb+Pb collisions at 5.02 TeV 141
4.6 Centrality distributions of the PC and CC minimum bias Pb+Pb data streams . . . 144
4.7 p_{T} distributions of Z decay leptons in pp and Pb+Pb collisions 148
4.8 Overview of the single muon trigger efficiency in 2018 Pb+Pb data 149
4.9 Summary of muon trigger efficiency corrections in 2018 Pb+Pb data 151
4.10 Overview of the single muon identification efficiency in 2018 Pb+Pb data 152
4.11 Dimuon invariant masses in Pb+Pb collisions with combined ID+MS kinematics . . 153
4.12 Dimuon invariant masses using ID versus MS kinematics 154
4.13 Dimuon invariant masses in Pb+Pb collisions with MS-only kinematics 155
4.14 Overview of the electron trigger efficiency studies in 2018 Pb+Pb data 158
4.15 Overview of the electron identification efficiency studies in 2018 Pb+Pb data 160
4.16 Dielectron invariant masses in pp and Pb+Pb data after residual ES corrections . . 162
4.17 Run-dependent Z yields per unit luminosity in the 2018 Pb+Pb data 164
4.18 Z p_{T} distributions in pp and 0–10% Pb+Pb collisions 166
4.19 Z rapidity distributions in pp and 0–10% Pb+Pb collisions 167
4.20 QCD multijet background contributions to Z mass distributions in Pb+Pb data . . 170
4.21 2D correlations between true and reco. Z boson p_{T} 173
4.22 Comparison of hadron yields at reco. versus truth-level Z selection versus $p_{\mathrm{T}}^{\mathrm{ch}}$ 175
4.23 Comparison of hadron yields at reco. versus truth-level Z selection versus x_{hZ} . . . 176
4.24 Truth matching probability distribution of tracks in pp and Pb+Pb MC 179
4.25 Projections of primary track fraction in pp and Pb+Pb 180
4.26 2D (p_{T}, η) maps of the primary track fraction in pp and Pb+Pb 181
4.27 Overview of the track reconstruction efficiency in pp and Pb+Pb 183
4.28 Track reconstruction efficiency in pp dijets versus particle species type 183

4.29 Distributions of ΔR between tracks and the closer Z decay lepton . . . 185
4.30 Track momentum resolution in pp and Pb+Pb MC . . . 187
4.31 Truth-level hadron yields in pp MC with and without resolution smearing . . . 188
4.32 Number of Z events versus minimum bias events in Pb+Pb . . . 190
4.33 $\Sigma E_{\mathrm{T}}^{\mathrm{FCal}}$ distributions in Z and mixed minimum bias events . . . 193
4.34 Azimuthal distribution of Z bosons relative to the event plane . . . 194
4.35 Illustration of the event plane angle matching procedure in Pb+Pb . . . 195
4.36 Impact of event plane angle matching on I_{AA} . . . 196
4.37 Illustration of the Z transverse plane . . . 197
4.38 Impact of pp event matching variations on I_{AA} . . . 199
4.39 Overview of the background subtraction on the charged-hadron yields . . . 202
4.40 Signal-to-background ratios in pp and Pb+Pb . . . 203
4.41 Relative uncertainties on the charged-hadron yield versus $p_{\mathrm{T}}^{\mathrm{ch}}$ . . . 208
4.42 Relative uncertainties on the charged-hadron I_{AA} versus $p_{\mathrm{T}}^{\mathrm{ch}}$ . . . 209

5.1 Azimuthal dependence of Z-tagged hadron yields in pp and 0–30% central Pb+Pb . 211
5.2 Mean per-Z yield of charged hadrons versus $p_{\mathrm{T}}^{\mathrm{ch}}$ and x_{hZ} . . . 212
5.3 Nuclear modification ratio of Z-tagged charged-hadron yields I_{AA} . . . 214
5.4 Z-tagged charged-hadron I_{AA} compared across p_{T}^{Z} bins . . . 215
5.5 Comparison of Z-tagged I_{AA} to RHIC and CMS γ-tagged data . . . 217
5.6 Comparison of Z-tagged I_{AA} in data and jet-quenching models . . . 219
5.7 Comparison of Z-tagged I_{AA} in data and the CoLBT-hydro model . . . 220

6.1 Jet trigger efficiency in the 2016 p+Pb data at 5.02 TeV . . . 228
6.2 Jet p_{T} spectrum from different JZ slices . . . 232
6.3 Distributions of $\Sigma E_{\mathrm{T}}^{\mathrm{FCal,Pb}}$ and $\Sigma E^{\mathrm{ZDC,Pb}}$ in p+Pb . . . 235
6.4 2D correlation between $\Sigma E_{\mathrm{T}}^{\mathrm{FCal,Pb}}$ and $\Sigma E^{\mathrm{ZDC,Pb}}$ in p+Pb . . . 236
6.5 Normalized projections of $\Sigma E_{\mathrm{T}}^{\mathrm{FCal,Pb}}$ at 5 $\Sigma E^{\mathrm{ZDC,Pb}}$ centile ranges . . . 238

6.6 $R_{p\mathrm{Pb}}$ of jets versus $\langle N_{\mathrm{coll}} \rangle$ in ZDC centile bins 239

6.7 (η, ϕ) distributions of accepted jets in pp and p+Pb 241

6.8 Examples of jet energy response distributions in p+Pb collisions 243

6.9 Examples of normalized fits to the mode jet energy response 245

6.10 $\hat{E}_{\mathrm{truth}}$ versus $p_{\mathrm{T}}^{\mathrm{truth}}$ in simulated pp and p+Pb events 246

6.11 Jet energy scale and resolution in pp and p+Pb 248

6.12 Mode differences between origin-corrected and truth-level jet η in pp and p+Pb . . . 249

6.13 Modal x_{ref}^{j} values in p+Pb data and MC from $\gamma+$jet and $Z+$jet studies 252

6.14 Flavor-fraction and flavor-response uncertainties in p+Pb as compared to pp 254

6.15 JES-related systematic uncertainties on the charged-particle yield 255

6.16 Truth-matching probability distributions for tracks in pp and p+Pb MC 257

6.17 2D scatterplots of reconstructed versus truth track p_{T} in p+Pb 258

6.18 Track momentum response distributions in pp and p+Pb with fits 259

6.19 Extracted track momentum resolution versus truth p_{T} in pp and p+Pb 260

6.20 Projections of track reconstruction efficiency at different $|\eta|$ bins 261

6.21 Multiplicity dependence of the track reconstruction efficiency 262

6.22 Overview of primary track fraction studies in pp and p+Pb 264

6.23 Primary track fraction versus distance to the nearest jet 265

6.24 Best estimates for the primary track fraction in p+Pb with uncertainties 266

6.25 Tracking-related systematic uncertainties on the charged-particle yield 268

6.26 Signal-to-background ratios in pp and each p+Pb centrality 273

6.27 Flow chart of the iterative Bayesian-inspired unfolding procedure 276

6.28 Examples of 1D response matrices for jets in pp and p+Pb 277

6.29 Jet-by-jet weights used to evaluate the response matrices in MC 279

6.30 Optimization of N_{iter} for the away-side of $p_{\mathrm{T}}^{\mathrm{jet}} > 30$ GeV events 281

6.31 Optimization of N_{iter} for the away-side of $p_{\mathrm{T}}^{\mathrm{jet}} > 60$ GeV events 282

6.32 Unfolding convergence of the away-side measurement 284

6.33 Effect of an additional iteration at $N_{\text{iter}}^{\text{opt.}}$ for the away-side 286

6.34 Optimization of N_{iter} for the 1D normalization of $p_{\text{T}}^{\text{jet}} > 30$ GeV events 287

6.35 Optimization of N_{iter} for the 1D normalization of $p_{\text{T}}^{\text{jet}} > 60$ GeV events 288

6.36 Unfolding convergence of the per-jet normalization 289

6.37 Refolded distributions of away-side charged particles 291

6.38 Numbers of jets above the $p_{\text{T}}^{\text{jet}}$ thresholds calculated from the refolded jet spectrum . 292

6.39 Total systematic uncertainties on the per-jet yield for $p_{\text{T}}^{\text{jet}} > 60$ GeV 294

7.1 Azimuthal dependence of jet-tagged hadron yields in pp and 0–20% p+Pb 297

7.2 Away-side $I_{p\text{Pb}}$ of jet-tagged hadrons in each p+Pb centrality 299

7.3 Near-side $I_{p\text{Pb}}$ of jet-tagged hadrons in each p+Pb centrality 300

7.4 Comparison between the near-side $I_{p\text{Pb}}$ and jet fragmentation functions from ATLAS 303

7.5 Comparison between the near-side $I_{p\text{Pb}}$ and ANGANTYR 305

7.6 Comparison between $I_{p\text{Pb}}$ in 0–20% p+Pb and ANGANTYR 306

7.7 Comparison between jet-tagged $I_{p\text{Pb}}$ in 0–20% p+Pb and AMPT 307

8.1 Comparison of nuclear modification ratios from the Z-h and jet-h measurements. . . 311

8.2 Time series of a hydrodynamically evolving O+O collision in SONIC. 312

8.3 sPHENIX calorimeters being instrumented & physics projections. 313

A.1 $Z \to \mu\mu$ mass distribution using the combined muon track 360

A.2 $Z \to \mu\mu$ mass distribution using the muon spectrometer track 361

A.3 $Z \to ee$ mass distribution before residual energy scale corrections 362

A.4 $Z \to ee$ mass distribution after residual energy scale corrections 363

A.5 Z boson p_{T} distributions in pp and Pb+Pb 364

A.6 Z boson rapidity and azimuthal angle heatmaps 364

A.7 Z boson pseudorapidity distributions in pp and Pb+Pb 365

A.8 Z boson rapidity distributions in pp and Pb+Pb 366

A.9 I_{AA} versus $p_{\mathrm{T}}^{\mathrm{ch}}$ and x_{hZ} broken into $Z \to ee$ and $Z \to \mu\mu$ channels 367

A.10 Pulls between the $Z \to ee$ and $Z \to \mu\mu$ channels 368

A.12 $\Sigma E_{\mathrm{T}}^{\mathrm{FCal}}$ study in Z-tagged, minimum bias, and data overlay MC events 373

A.13 $\Sigma E_{\mathrm{T}}^{\mathrm{FCal}}$ study in Z-tagged and data overlay and Hijing MC events 374

A.14 $N_{\mathrm{ch}}^{\mathrm{rec}}$ and $\Sigma E_{\mathrm{T}}^{\mathrm{FCal}}$ versus impact parameter in Hijing MC 375

A.15 Exact-event-matching closure test in Hijing MC events 377

A.16 Mixed-event closure test in Hijing MC events 378

A.17 Closure of hadron yields in Hijing versus signal-to-background ratio 379

A.18 Background normalization uncertainty versus signal-to-background ratio 379

A.19 Absolute systematic uncertainties on Y versus $\Delta\phi_{hZ}$ in pp 381

A.20 Absolute systematic uncertainties on Y versus $\Delta\phi_{hZ}$ in 0–30% Pb+Pb 382

A.21 Relative systematic uncertainties on Y versus $p_{\mathrm{T}}^{\mathrm{ch}}$ 383

A.22 Relative systematic uncertainties on Y versus x_{hZ} 384

A.23 Relative systematic uncertainties on I_{AA} versus $p_{\mathrm{T}}^{\mathrm{ch}}$ 385

A.24 Relative systematic uncertainties on I_{AA} versus x_{hZ} 386

A.25 Effect of reconstruction efficiency corrections in MC versus $p_{\mathrm{T}}^{\mathrm{ch}}$ 388

A.26 Effect of reconstruction efficiency corrections in MC versus x_{hZ} 389

A.27 Effect of trigger and reconstruction efficiency corrections in data versus $p_{\mathrm{T}}^{\mathrm{ch}}$ 391

B.1 Sum-of-gaps distributions in p+Pb to quantify UPC backgrounds 393

B.2 1D response matrices for jet response in pp and p+Pb 395

B.3 2D response matrices for near-side track and jet response in pp and p+Pb 396

B.4 2D response matrices for away-side track and jet response in pp and p+Pb 397

B.5 Optimization of N_{iter} for the near-side of $p_{\mathrm{T}}^{\mathrm{jet}} > 30$ GeV events 398

B.6 Optimization of N_{iter} for the near-side of $p_{\mathrm{T}}^{\mathrm{jet}} > 60$ GeV events 399

B.7 Unfolding convergence of the near-side measurement 400

B.8 Effect of an additional iteration at $N_{\mathrm{iter}}^{\mathrm{opt.}}$ for the near-side 401

B.9 Refolded distributions of near-side charged particles 402

B.10 Closure tests of the jet spectra 404

B.11 Summary of the full MC closure tests 406

B.12 Primary-only closure tests for particles in the away-side to jets between 30–300 GeV 407

B.13 Closure tests for particles in the away-side to jets between 60–300 GeV 408

B.14 Primary-only closure tests for particles in the near-side to jets between 30–300 GeV . 410

B.15 Closure tests for particles in the near-side to jets between 60–300 GeV 411

B.16 Closure tests for particles in the away-side to jets between 30–300 GeV 412

B.17 Closure tests for particles in the near-side to jets between 30–300 GeV 413

B.18 Additional summaries of full MC closure tests 414

B.19 JES-related systematic uncertainties on the per-jet yield for $p_{\mathrm{T}}^{\mathrm{jet}} > 60$ GeV 416

B.20 Tracking-related systematic uncertainties on the per-jet yield for $p_{\mathrm{T}}^{\mathrm{jet}} > 60$ GeV . . . 417

B.21 Signal-related systematic uncertainties on the per-jet yield for $p_{\mathrm{T}}^{\mathrm{jet}} > 60$ GeV 418

B.22 Total systematic uncertainties on the per-jet yield for $p_{\mathrm{T}}^{\mathrm{jet}} > 30$ GeV 419

B.23 JES-related systematic uncertainties on the per-jet yield for $p_{\mathrm{T}}^{\mathrm{jet}} > 30$ GeV 420

B.24 Tracking-related systematic uncertainties on the per-jet yield for $p_{\mathrm{T}}^{\mathrm{jet}} > 30$ GeV . . . 421

B.25 Signal-related systematic uncertainties on the per-jet yield for $p_{\mathrm{T}}^{\mathrm{jet}} > 30$ GeV 422

C.1 Comparison of Z-tagged I_{AA} in data and jet quenching models versus x_{hZ} 423

C.2 Comparison of Z-tagged I_{AA} in data and jet quenching models versus $p_{\mathrm{T}}^{\mathrm{ch}}$ 424

C.3 Away-side per-jet charged-particle yields in pp and p+Pb 425

C.4 Near-side per-jet charged-particle yields in pp and p+Pb 426

C.5 Comparison between the near-side $I_{p\mathrm{Pb}}$ and preliminary jet fragmentation functions from CMS 427

Preface

Since prehistory, the desire to understand the behavior of the cosmos has been a cornerstone of human existence. The ancient Greeks would explain the apparent motion of the Sun across the sky through stories of Helios' journey carrying it with his chariot. Children in schools are taught that Columbus' "great achievement" was proving the Earth is round, and that Copernicus' proposal for a heliocentric solar system – despite his great reverence for the church – was a resolute departure from conventional wisdom. While often we associate monetary value with scientific achievement, an anthropological perspective strongly suggests that the product of our pursuit to understand the world we live in is inherently priceless.

Following the development of formal scientific reasoning, we have built a far more detailed understanding of the universe and its contents. Our best models indicate that at the earliest times, our universe was in a highly compressed, low entropy state. As time progressed, the universe expanded and cooled, first decoupling the electroweak forces, then allowing baryonic matter to form atomic nuclei, free electromagnetic radiation, and finally the first stars and galaxies which we can see in the farthest reaches of space today. During this time, the types of matter varied widely. Building a full understanding of our modern universe necessitates understanding the phases that have occupied it in the past.

Basic dimensional analysis suggests that the temperature of a system of non-interacting, massless particles follows

$$\text{Temperature} \propto (\text{Energy Density})^{1/4} \tag{1}$$

which can be applied to generic physical systems in this limit. In the inflationary model, energy

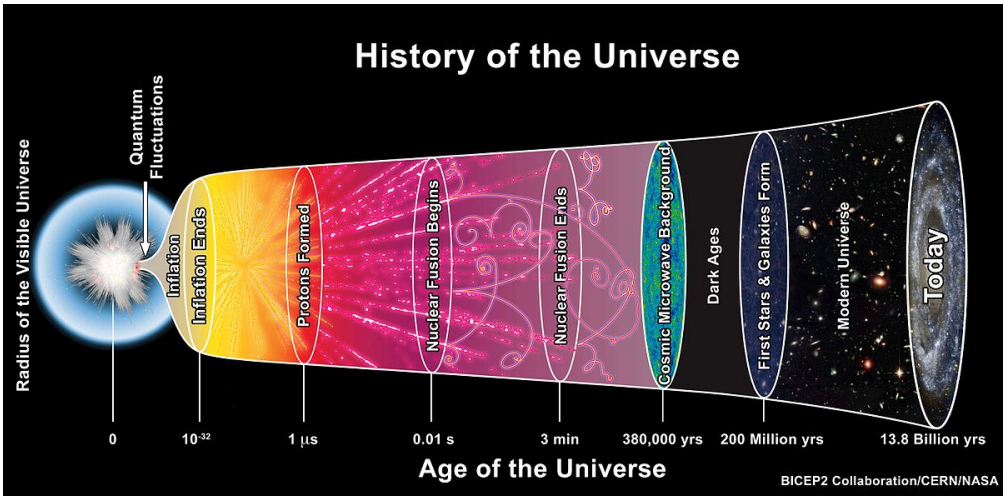


Figure P.1: Cosmological expansion model of the universe. Figure reproduced from Ref. [1].

density is – at least thus far – a monotonically decreasing function in time, so instead of *temporal* evolution of the universe, we can consider its *thermal* evolution. At the highest temperatures $T \gg \mathcal{O}(10^2 \text{ GeV})$, the electromagnetic and weak forces are united into the electroweak force and symmetry is restored.[1] Except for the Higgs, all particles are massless but scarcely roam freely due to high particle densities. Below the electroweak scale, the Higgs field acquires a nontrivial vacuum expectation value and symmetry is spontaneously broken, ceasing free propagation of the W bosons. As temperature decreases further, asymptotic freedom of the strong interaction begins to fade, and the quarks and gluons start interacting more and more frequently. This phase is known as the *weakly coupled* quark-gluon plasma (QGP).

The subject of this thesis concerns the *strongly coupled* quark-gluon plasma, described by the theory of quantum chromodynamics (QCD). One of the core features of QCD is that the coupling between particles is stronger at lower temperatures. A good conceptual picture for what occurs is that the underlying quarks and gluons interact more and more frequently with decreasing temperature, until they reach a point where they are *continuously* interacting. This is counterintuitive to, for example, the kinetic theory of gases, where the gas temperature and pressure are linearly related due to the increasing frequency of scatterings. More formally, the mean free time in kinetic

[1] This thesis uses temperature units where $k_B = 1$. For reference, 1 GeV $\approx 1.16 \times 10^{12}$ K or $^\circ$C.

theory scales as

$$\tau_{\mathrm{MFP}} \sim \frac{\lambda_{\mathrm{MFP}}}{\langle v \rangle} \propto \frac{\sqrt{T}}{P}, \tag{2}$$

and therefore the frequency of scatterings scales with $f \sim 1/\tau_{\mathrm{MFP}} \sim \sqrt{T}$.[2] In the QGP, the reverse happens: interactions occur more and more frequently as the temperature is lowered (at least until the crossover temperature).

Theories of strongly coupled quantum fields are inherently nonperturbative, and consequently progress has been much slower in their development as compared with weakly coupled theories, such as electrodynamics or the weak interaction. Perturbative QCD (pQCD) works well at high energies, but the strong coupling constant α_{S} is not particularly small and thus very high-order diagrams are necessary to make reasonably accurate calculations. Meanwhile, lattice calculations have recently been successful in describing hadron mass spectra and QCD thermodyanmics [2, 3], but are computationally very expensive, and moreover lack the succinct conceptual picture of the underlying physics that is present in pQCD.

In 1997, Juan Maldacena famously conjectured that conformal quantum field theories (CFT) in d dimensions are dual (i.e., equivalent) to $d+1$ quantum gravity theories in anti-de Sitter space (AdS) [4]. This is known as the AdS/CFT conjecture, and was originally proposed in the context of a particular equivalence between $N = 4$ Super Yang-Mills (SYM) and Type-IIB string theory on $\mathrm{AdS}_5 \times \mathrm{S}^5$. While not rigorously proven, the conjecture has notably not been disproven despite many extensive checks. Although no dual to QCD is known because it is not a CFT, models based on $N = 4$ SYM were proposed to grasp its nonperturbative aspects. Without diving into too many details, the fact that general relativity in a $4+1$ dimensional hyperbolic geometry is more calculable than its dual quantum field theory is a testament to the monumental difficulty of making tractable predictions in QCD.

The quark-gluon plasma that permeated the universe, however, froze out about 13.6 billion years ago, or roughly $1\,\mu$s after the Big Bang. Besides these early universe conditions, there are

[2] This relation can be easily calculated with a minimal set of ingredients: (1) a fixed particle-particle scattering cross-section σ that fixes λ_{MFP}, (2) the ideal gas law, to relate λ_{MFP} with T, and (3) the equipartition theorem to obtain the RMS velocity.

only two known places where quark-gluon plasma can exist: the first is in rare high-energy cosmic ray collisions in the upper atmosphere, and the second is in the confines of particle collisions at Brookhaven National Laboratory (BNL) in Upton, New York, and the European Organization for Nuclear Research (CERN) in Geneva, Switzerland. These droplets of QGP are created from the ultrarelativistic collisions of fully ionized heavy elements, such as gold (Au) or lead (Pb). Their scale is astronomically tiny. Because they are created from individual nuclei, their transverse radius is on the order of 4–8 fm. This nets a temperature gradient of roughly $dT/dx \sim 30$–$60\,\mathrm{MeV/fm}$ between the core of the droplet and the vacuum in its immediate surroundings.[3] It is easy to see then that the droplet will rip itself apart violently and rapidly. The timescale for this to occur is $\sim 3 \times 10^{-23}\,\mathrm{s}$, or 10 fm in natural units. The objective of the QGP experimental program is thus not to directly observe the plasma – this is much too impractical. Rather, the central goal is to observe the decay products that come out from the collision and classify their properties. Equipped with the law of large numbers, we can then begin to make statistical statements about the plasma properties.

The majority of this thesis will be dedicated to understanding and measuring the jet-quenching phenomenon in heavy-ion collisions. If you imagine firing a projectile into water, then the water will slow down the projectile via drag forces, and eventually stop it after some distance. Equivalently, the projectile loses energy over time to the water, and the two become equilibrated. This is known as an energy loss process, and essentially the same situation occurs in the QGP. Internally generated high momentum quarks and gluons – meaning quarks and gluons created simulatenously via pQCD processes in the same nuclear collision – will traverse the plasma, and will suffer from medium-induced interactions as a consequence of their color charges. Generically, if the energy loss effect is weak, then we should expect to see the partons come out of the medium unscathed. However, if the effect is strong, then we will not see these high-energy partons at all. This phenomenon is well known in heavy-ion physics, and is referred to as *jet quenching*. Therefore, measuring high-energy

[3] To put this number in perspective, if this temperature gradient were recreated across the width of a human hair, then one side would be at absolute zero and the other would be at roughly 10^{22}°C. (Avogadro's number is only a factor ~ 60 larger than this number.)

particle production allows us to quantify the energy loss, presenting an avenue for developing a deeper understanding of the strong interaction and other strongly coupled gauge theories.

The focus of this thesis is divided into two similarly structured measurements of jet quenching via calibrated probes. The first – presented in Chapter 4 – describes a measurement of hadron yields opposite a Z boson in ultrarelativistic lead-lead collisions. The premise is that the Z is colorless and, at sufficiently high transverse momenta, is produced opposite a high-energy parton during the initial stages of the collision. By measuring the yield of hadrons subsequent to energy loss, we are provided with a full before-and-after picture of the jet-quenching process. The results of this study are presented in Chapter 5.

The second is presented in Chapter 6 and details a measurement of hadron yields opposite a particle jet in proton-lead collisions. Contrary to large nuclear collisions, small systems are not traditionally expected to form a QGP phase. However, consistent experimental indicators associated with the QGP phase have been unambiguously observed in these systems, prompting the question of how they should be best described. If the QGP is indeed formed, then jet quenching may also be occurring. Therefore, by studying hadron yields in active proton-lead collisions, we can gain insight into the minimal formation conditions of the QGP phase. Similarly, the results of this study are presented in Chapter 7.

The thesis is laid out in the following way. First, Chapter 1 will review the theory of quantum chromodynamics and provide an overview of heavy-ion collisions. Chapter 2 will review experimental findings pertinent to jet quenching, as well as the theoretical background. Chapter 3 will introduce the LHC and the ATLAS experiment, and review how these machines can be used to make measurements at the subatomic level. Chapter 4 and Chapter 6 present technical details of the measurements described above. Chapter 5 and Chapter 7 present the main findings. Finally, Chapter 8 summarizes the thesis and provides an outlook.

Chapter 1

Introduction

At the microscopic level, the Standard Model (SM) is our best description of physical reality. It is built from an $\mathcal{SU}(3) \times \mathcal{SU}(2)_{\mathrm{L}} \times \mathcal{U}(1)$ gauge theory. Macroscopically, it can be described by effective theories of dramatically different forms, as the relevant degrees of freedom change with the length scale. If I am traveling in a car at 25 mph, then I would not need to describe the vibrations of atoms in my body to obtain a physical description of the system, but maybe I would be interested in the position of my foot as it controls the acceleration of the vehicle. The process by which we build up effective theories of the macroscopic world is not trivial; frequently, physicists work in the reverse direction by building microscopic theories that encapsulate macroscopic phenomena. For example, quantum electrodynamics – the $\mathcal{U}(1)$ part of the gauge theory above – was developed as the microscopic theory of electromagnetism. Simultaneously, it is responsible for everything from the propagation of radio waves to our phones to providing a balancing force that keeps planets like Earth from collapsing inwards.

The subject of this thesis, however, concerns the emergent properties of strong interactions. QCD – a more nuanced sibling to QED – was developed as a microscopic theory describing the strong nuclear interaction that binds nucleons together. The QCD Lagrangian constitutes the $\mathcal{SU}(3)$ part of the SM gauge theory, and can be written in the succinct form

$$\mathcal{L}_{\mathrm{QCD}} = -\frac{1}{4} F^{a}_{\mu\nu} F^{\mu\nu a} + \sum_{q} \bar{\Psi}_{q} \left(i \not{D} - m_{q} \right) \Psi_{q}. \tag{1.1}$$

with the $\mathcal{SU}(3)$ structure of QCD fully defined via the group generators λ_a and their structure

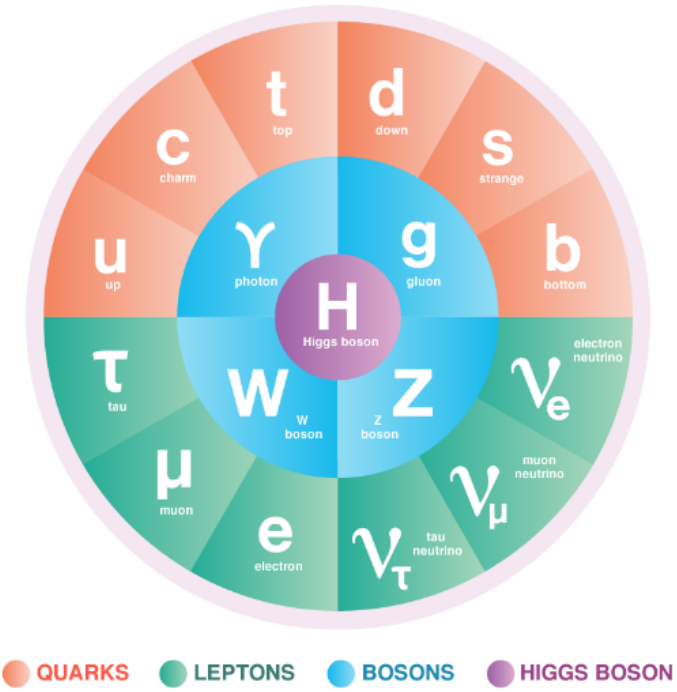


Figure 1.1: Fundamental particles described in the Standard Model. The outer ring shows the fermions with quarks on top and leptons below; the inner rings show the gauge and Higgs bosons. Figure reproduced from Ref. [5].

constants f_{abc}

$$[\lambda_a, \lambda_b] = 2i f_{abc} \lambda_c. \tag{1.2}$$

The gauge-covariant derivative is defined via

$$D^\mu = \partial^\mu - i\frac{g_s}{2} G^{\mu a} \lambda^a, \tag{1.3}$$

where $G^{\mu a}$ is the gauge field.

Quarks are the fermions Ψ_q in the fundamental representation of the QCD $\mathcal{SU}(3)$ gauge symmetry; therefore, there are three colors of quarks: red, green, and blue.[1] There are six quark flavors, each with a different mass, as shown in Fig. 1.1. From lightest to heaviest, they are the up, down, strange, charm, bottom, and top, each denoted by the first letter of its name. All but the u and d quarks are weakly unstable, and decay rates between different flavor states are governed

[1] Occasionally, red, white, and blue are used, for example in Ref. [6]. Beyond being unnecessarily Amerocentric, the choice of a white color is poor because of the necessary distinction between white and colorless states. In fact, Feynman publicly disapproved of the choice of the word "color" to define the gauge transformations in the fundamental representation, since quarks do not really have a visible color [7].

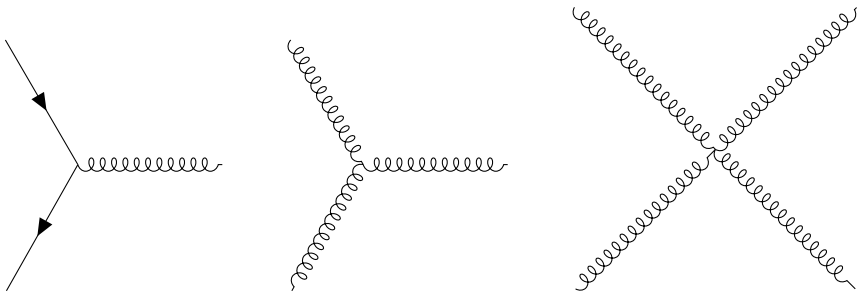


Figure 1.2: Allowed Feynman vertices in QCD: the **(a)** quark-quark-gluon, **(b)** 3-gluon, and **(c)** 4-gluon vertices.

by the CKM matrix. The *gluons* are the force-mediating bosons $G^{\mu a}$ in the adjoint representation, with field tensor

$$F^{\mu\nu a} = \partial^\mu G^{\nu a} - \partial^\nu G^{\mu a} + g_s f^{abc} G^{\mu b} G^{\nu c}. \tag{1.4}$$

Accordingly, there are $3^2 - 1 = 8$ gluons. Together, quarks and gluons are referred to as *partons*. There are three basic parton interactions described by the Lagrangian. These are the quark-quark-gluon, 3-gluon, and 4-gluon vertices shown in Fig. 1.2. By dimensional analysis, the 3-gluon vertex is unique in that it is accompanied by a derivative operator acting on the gauge field, and thus a gluon momentum appears in the vertex factor.

Broadly speaking, these constructions are simple, and in principle fully describe exotic emergent phenomena when sources, boundary conditions, etc. are provided. However there is a nontrivial disconnect between the Lagrangian and the emergent physics it attempts to describe. Therefore we must look beyond the microscopic theory to attempt to build new physical intuition.

QCD exhibits two defining properties which guide its macroscopic manifestation:

- **Confinement**. Historically, the primary reason that the quark theory was difficult to confirm experimentally was that physicists could not manage to free quarks from the grasp of their parent hadrons. This is due to the principle of *confinement*. Contrary to QED, where the potential energy between two like-sign charges decreases as they are separated, in QCD the total energy V stored in a $q\bar{q}$ system (the *quarkonia* states) actually *increases*

boundlessly with inter-quark separation r,

$$V(r) \simeq -\frac{\alpha_{\mathrm{S}}}{r} + \kappa r. \tag{1.5}$$

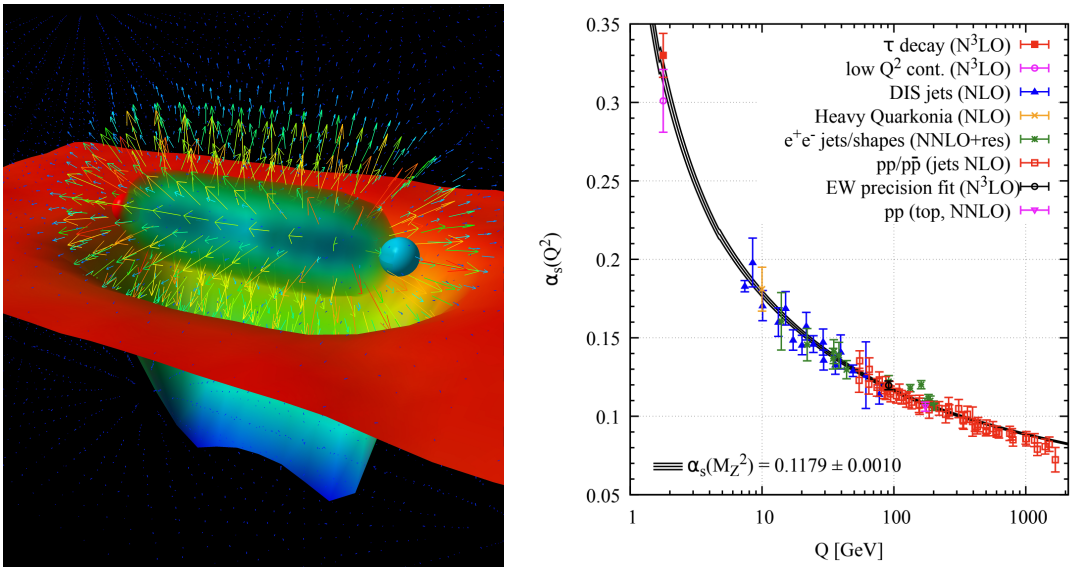
In the literature, this parametrization is referred to as the Cornell potential [8], which interpolates between the single gluon exchange (the Coulomb $1/r$ term) and the nonperturbative aspects of QCD bundled in the linear term. This latter component is the effect of self-interactions in the gluon field forming a region of roughly constant field strength inside a cylindrical region (sometimes referred to as a flux tube) between the two quarks, as illustrated in Fig. 1.3. As you pull the quarks apart further and further, the amount of energy grows without bound, and eventually it is energetically favorable to produce a quark-antiquark pair in the gap. The final product is two color neutral hadrons rather than individual quarks. Therefore, quarks can never be isolated in this way.

- **Asymptotic freedom.** The $SU(3)$ Yang-Mills β function, which describes how the coupling varies with the length scale used to probe QCD matter (or alternatively, the energy scale of the probe), decreases at smaller lengths to zero in the limit of infinitely short length scales. This is juxtaposed with QED, where at smaller length scales, fewer and fewer virtual electron pairs pop in and out of the vacuum and increase the probability of an interaction – i.e., the coupling becomes stronger. In QCD, virtual quark pairs indeed increase the coupling similarly, but their effects are negated by a myriad of gluon interactions, providing an anti-screening effect. Consequently, the renormalization group (RG) evolution equation for α_{S} – the aforementioned β function – is negative [9, 10]:

$$\beta(\alpha_{\mathrm{S}}) = \frac{\partial \alpha_{\mathrm{S}}}{\partial \log Q^2} = -\frac{\alpha_{\mathrm{S}}^2}{2\pi^2}\beta_0. \tag{1.6}$$

where $\beta_0 = 11 - \frac{2}{3}n_f$ is the 1-loop correction and n_f is the number of quark flavors. Introducing the QCD energy scale $\Lambda_{\mathrm{QCD}}^2 = Q^2 \exp\left(-2\pi^2/\beta_0 \alpha_{\mathrm{S}}(Q^2)\right)$, the solution is

$$\alpha_{\mathrm{S}}\left(Q^2\right) = \frac{1}{\alpha_{\mathrm{S}}\left(Q_0^2\right) \log\left(Q^2/\Lambda_{\mathrm{QCD}}^2\right)} \tag{1.7}$$



(a) A gluon flux tube in lattice QCD **(b)** The QCD running-coupling $\alpha_S(Q^2)$

Figure 1.3: **(a)** Illustration of a gluon flux tube between a quark-antiquark pair as they are pulled apart. The inter-quark force is approximately constant with distance. **(b)** The QCD running coupling calculated in perturbation theory compared with experimental data. Due to asymptotic freedom, the coupling decreases with energy. Figures reproduced from Refs. [11] and [12], respectively.

and therefore the coupling α_S decreases with increasing energy, as shown in Fig. 1.3. With decreasing energy, the coupling becomes stronger, surpassing unity and rendering perturbative calculations intractable.

The emergence of an energy scale $\Lambda_{QCD} \approx 220$ MeV where $\alpha_S(\Lambda_{QCD}) = 1$ breaks conformal symmetry. Far above this energy scale, QCD can be described perturbatively in powers of α_S (pQCD). Below, the physics is inherently nonperturbative[2] and dominated by confinement. However, even in the regime $Q \gg \Lambda_{QCD}$, $\alpha_S > \alpha_{EM}$ generally speaking, so pQCD calculations are more sensitive to higher-order diagrams than in QED. Both confinement and a relatively large α_S directly illustrate the complexity to making tractable predictions in QCD.

[2] By nonperturbative, we mean there is no finite diagrammatic picture for describing the strong interaction in this limit.

1.1 QCD Matter

Hadronic Matter

Due to confinement, quarks are bound within hadrons in everyday nuclear matter, which are the QCD color-neutral states with well-defined quantum numbers such as isospin/flavor, spin, and electric charge. To achieve this objective, they are made of groups of quarks, usually in quark-antiquark pairs (*mesons*) or quark triplets (*baryons*).

When studying hadron states, it is useful to exploit an emergent symmetry in QCD. The bare masses of the quarks appear as free parameters and ultimately are attributed to the ABEGHHK'tH (Higgs) mechanism in electroweak theory. It so happens that the up, down, and strange quarks have small masses $m_q \ll \Lambda_{\mathrm{QCD}}$ and therefore exhibit an approximate $\mathcal{SU}(3)_{\mathrm{F}}$ global flavor symmetry, which plays a cornerstone role in the relations between hadronic states. Ignoring heavy quarks for the moment, we can build a set of light hadronic states from the u, d, and s. The light mesons are $q\bar{q}$ states and therefore transform in the $3 \otimes \bar{3} = 8 \oplus 1$ representation of $\mathcal{SU}(3)_{\mathrm{F}}$. There are consequently eight light meson flavor states (ignoring spin). This was the premise of the "Eightfold Way" pioneered by Gell-Mann and Ne'eman [13, 14], which offered an insight to the hadronic structure by organizing the light meson and baryon states in terms of a novel symmetry group. This visual aid is shown in Fig. 1.4. Along the diagonal axis, states are organized by electrical charge; along the vertical, they are organized by strangeness content. The vertical axis denotes the isospin symmetry, so for example, the π^+ and π^- mesons are isospin partners; thus they have the same mass. Combined with the neutral π^0, the three comprise a trio of isospin states with quantum numbers -1, 0, and 1.

Analogously, the light baryons transform in the $3 \otimes 3 \otimes 3 = 10 \oplus 8 \oplus 8 \oplus 1$ representation of $\mathcal{SU}(3)_{\mathrm{F}}$. The octet and decuplet are shown in Fig. 1.4 along with the meson octet. Perhaps the most notable baryons are the neutron and proton, which are isospin partners. In turn, these combine to form more complicated nuclear states. Others include the Σ, Ξ and Δ baryons, which

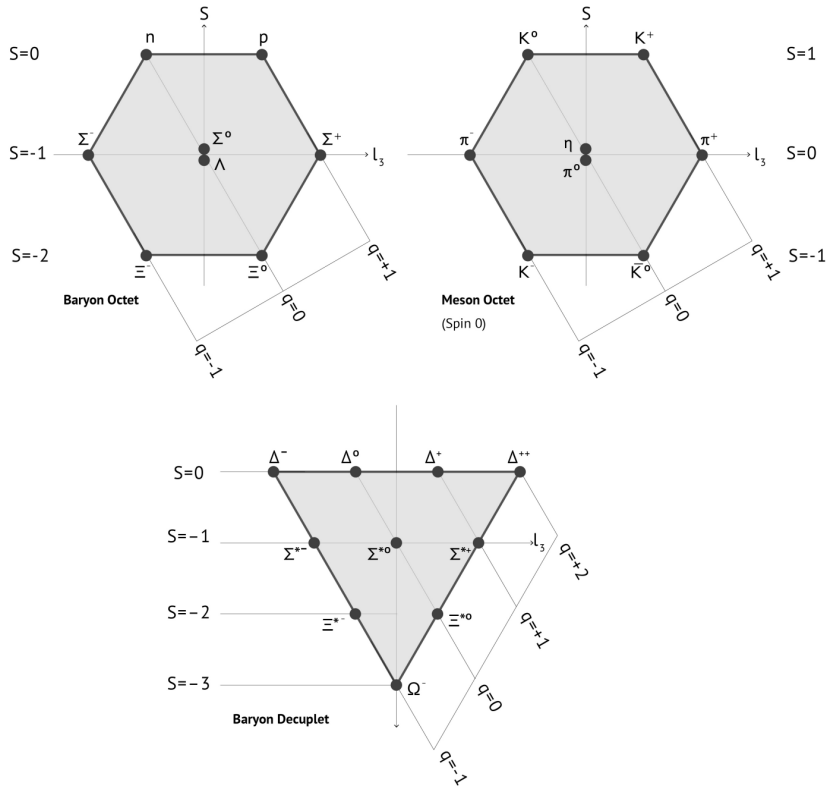


Figure 1.4: Illustration of Gell-Mann's Eightfold Way to organize the light mesons and baryons in $\mathcal{SU}(3)_{\mathrm{F}}$. On top, baryons (left) and mesons (right) in the octet representation; below, baryons in the decuplet representation. The horizontal and vertical axes indicate isospin and strangeness; the diagonal axis indicates electric charge. Figure reproduced from Ref. [15].

possess varying amounts of strangeness.[3] The success of the "Eightfold Way" was most notable in the prediction of the Ω triply-strange baryon to complete the baryon decuplet. A matching particle was observed shortly thereafter, with mass and quantum numbers nicely matching their predicted values [16].

Heavy quarks also form hadronic states, though they do not exhibit the $\mathcal{SU}(3)_{\mathrm{F}}$ symmetry due to their much larger masses $m_c \approx 1.4$ GeV and $m_b \approx 4.6$ GeV. The top quark is significantly more massive than electroweak bosons, $m_t \approx 170$ GeV. Therefore, it decays on a very short timescale $\tau_t \sim 5 \times 10^{-25}\,\mathrm{s} < 1/\Lambda_{\mathrm{QCD}}$ and does not live long enough to form hadrons.

[3] The Σ, Ξ, and Ω are also known as the *hyperons*.

Nonhadronic Phases

Due to confinement, QCD matter in the universe is dominated by hadronic particles. From a conceptual perspective, confinement should not hold, however, at large energy scales. As temperature increases, more and more color charge screening occurs inside hadrons, and the confining potential transitions to a Yukawa one. Eventually at sufficiently high temperatures, the partons bound within hadrons will be imparted sufficient energy to break the confining potential and can wander freely from their parents [6]. The hadronic gas will effectively melt away, leaving partonic degrees of freedom instead of hadronic ones.

This was first noticed by Hagedorn, who calculated the density of hadronic resonance states $\rho(m)$ from a statistical bootstrap model, asserting that fireballs of hadrons consist of fireballs of hadrons, which consist of fireballs of hadrons, ...*ad infinitum* [17]:

$$\rho(m) \simeq \frac{c}{m^a} e^{m/T_0}, \tag{1.8}$$

where $a \sim 2.5$–3, and c and T_0 are free parameters. Fits to data indeed reveal an exponentially rising number of hadronic resonance states with $T_0 \approx 160$ MeV (modern calculations put it at 154 ± 9 MeV [18]). In the limit $T \to T_0$, the partition function for the hadronic gas *diverges*, suggesting a phase transition in the vicinity of this temperature. Hagedorn's conclusion was that – if the model were to be believed – hadronic matter cannot exist above T_0. The physical intuition is that the number of degrees of freedom rises exponentially, and therefore the system can accommodate *any* amount of additional energy but remain at the same temperature. The system would simply allocate the extra energy to the exponentially increasing number of hadronic resonances. In this sense, T_0 was thought of as an absolute "hot" temperature for hadronic matter.

This ignores the possible existence of a phase transition at T_0, however. As an analogy, liquid water boils at 100° C and "cannot" exist above this temperature. However, as we know, it merely converts into a gas. The matter is still present and the temperature can continue increasing, it is just in a different phase. Ref. [19] notes that the Gibbs free energy experiences a singularity in this regime, and thus the boiling of hadronic matter would likely be second order. The authors

further connected the hypothesized transition with the theory of QCD to predict that it is in fact *confinement* which breaks down in this regime. In other words, the degrees of freedom switch from hadronic ones to partonic ones as quarks are liberated from hadrons, which "melt" into a plasma [20].

This forms a conceptual basis of what is known as the *quark-gluon plasma* (QGP). As the temperature of hadronic matter is raised to temperatures $T \sim T_0$, called the *critical temperature* (despite a smooth crossover), new partonic degrees of freedom emerge. Lattice QCD calculations, which operate by evaluating the action directly, have confirmed the QCD equation of state (EoS) shifts away from the predictions by Hagedorn for the resonance gas, and approach behavior that more closely resembles the noninteracting gas (i.e., Blackbody radiation) as T grows beyond T_0. This is shown in Fig. 1.5. The y-axis curve for the blue curve (ε/T^4) is particularly sensitive to the number of massless degrees of freedom in the system, and can be used to build a qualitative picture for what occurs above the transition temperature. At temperatures above T_0 (T_C in the diagram), the number of degrees of freedom stops rising exponentially, and starts to follow a curve more closely resembling a logistic, which approaches the horizontal dashed line for a non-interacting system. This is the Stefan-Boltzmann limit describing the blackbody radiation of 8×2 gluon states and $3 \times 3 \times 2 \times 2 \times 2 \times \frac{7}{8}$ massless quark states. Clearly, the system approaches this regime at high temperatures. In the ultra-hot limit $T \gg T_0 \sim \Lambda_\mathrm{QCD}$, asymptotic freedom kicks in and makes the coupling weak. Thus as the QGP is heated, it becomes more and more weakly interacting. However, as long as $T \sim \Lambda_\mathrm{QCD}$, the physics of the QGP is strongly coupled and nonperturbative.

A broader picture of QCD phenomena can be obtained by studying the phase diagram, shown in Fig. 1.6. Along the horizontal axis is the quark chemical potential, or equivalently baryon density μ_B (since the mesons are $q\bar{q}$ and have no net baryon number). Along the vertical axis is system temperature. Ordinary atomic nuclei are located at the point labeled "nuclear matter" and the vacuum at the origin; both have temperature ≈ 0. At low μ_B, when QCD matter is heated, it smoothly crosses over into the QGP phase, which dominates at high temperature [3]. At moderate baryon densities, the phase transition is hypothesized to become first order, suggesting a latent heat

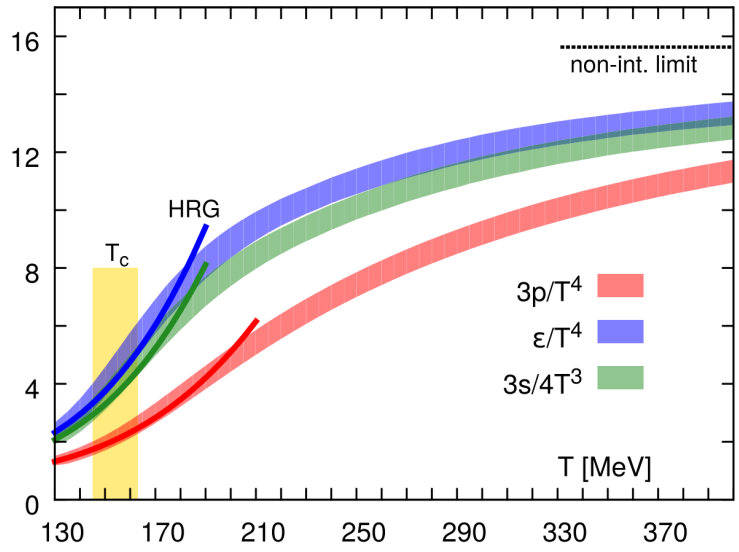


Figure 1.5: Parameters of the QCD equation of state, including temperature dependence of energy, pressure, and entropy densities, are shown. Shaded bands show lattice calculations; these are compared with the noninteracting limit and Hagedorn's hadronic resonance gas (HRG). Figure reproduced from Ref. [21].

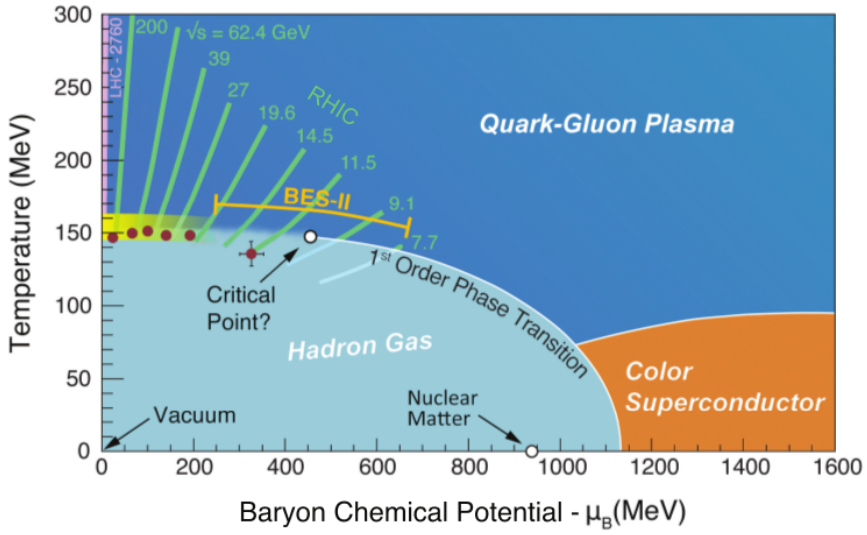


Figure 1.6: Phase diagram of QCD matter. Figure reproduced from Ref. [22].

is associated with making the phase transition in this region. Finding indications of a first-order transition is a primary goal of the beam energy scan currently underway at RHIC [23, 24].[4]

[4] As collision energy decreases, participant nucleons can be stopped in a shorter distance, increasing the baryon density, pushing the phase space trajectory away from the temperature axis (as well as from equilibrium) in Fig. 1.6 [25]

The more exotic color superconducting phase occurs at high μ_B, where hadrons are packed together into tight volumes [26]. At sufficiently high densities, quarks are hypothesized to form Cooper pairs. This can be loosely understood by calculating the t-channel gluon exchange between two quarks near the Fermi surface perturbatively in $\mu_B \gg \Lambda_{\rm QCD}$. The result is an attractive potential between quarks of different color. With $N_f = 3$ quark flavors, a color-flavor locked (CFL) phase of quark matter forms, spontaneously breaking the color-flavor symmetry group [27][5]

$$\mathcal{SU}(3)_{\rm C} \times \mathcal{SU}(3)_{\rm L} \times \mathcal{SU}(3)_{\rm R} \to \mathcal{SU}(3)_{\rm C+R+L}. \tag{1.9}$$

Such phases of matter are currently hypothesized to exist in the cores of neutron stars, where nuclei are packed densely together under their own gravity. With the advent of successful detection of neutron star mergers with gravitational waves [28], we may be on the cusp of experimental probes of highly dense quark matter [29].

1.2 Probing QCD via Scattering Experiments

The development of the Standard Model has an intimate relationship with scattering experiments at particle colliders. Cross sections for QED processes are perturbatively calculable, and predict experimentally measured scattering rates remarkably accurately [7]. By colliding particles at extreme rates, generating millions or billions of collisions, all but the rarest processes will occur. Individual collisions are stochastic, but equipped with the law of large numbers, we can begin to make deductions about what processes occur, collision time-evolution, couplings between various particles, decay rates, and so on.

QCD Factorization

Theoretically, the composite nature of hadrons was already beginning to emerge in the early 1960s due to Regge theory. The proportionality between spin and mass $J \propto m^2$ for states with increasing spin suggested that meson states could be modeled as a rotating string, and therefore

[5] Note that the approximate $\mathcal{SU}(3)_{\rm L} \times \mathcal{SU}(3)_{\rm R}$ chiral symmetry in the limit $m_f \to 0$ is also broken to $SU(3)_{\rm F}$ in vacuum QCD. The 8 Goldstone bosons are the light mesons.

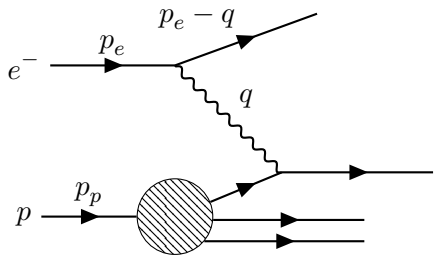


Figure 1.7: Feynman diagram of the DIS process.

hadrons were composite objects [30]. However it was high-energy deep-inelastic scattering (DIS) experiments that provided crucial evidence in favor of the parton model. These experiments collided high-energy electrons on protons to tease out the inner structure of the proton. The general form of the elastic DIS cross section is known as the Rosenbluth formula [31]:

$$\frac{d^2\sigma}{dxdQ^2} = \frac{4\pi\alpha^2}{Q^4}\left[\left(1 - y - \frac{m_p^2 y^2}{Q^2}\right)\frac{F_2(x,Q^2)}{x} + y^2 F_1(x,Q^2)\right]. \tag{1.10}$$

Here we have introduced the DIS process characteristics Bjorken x and inelasticity y

$$x = \frac{Q^2}{2p\cdot q} \qquad \text{and} \qquad y = \frac{p_p\cdot q}{p_p\cdot p_e} \qquad \text{where} \qquad q = -\Delta p_e \qquad \text{and} \qquad Q^2 = -q^2, \tag{1.11}$$

as well as the structure functions of the proton $F_{1,2}(x,Q^2)$, shown in Fig. 1.8. In the elastic scattering limit, the structure functions describe the electric and magnetic moments of the proton.[6] For inelastic scattering, which dominates the total cross section for $Q^2 \gtrsim 2$–3 GeV^2, the interpretation of structure is nonobvious, but can be in fact related to proton substructure using the parton model.

This is because the parton model implies a different, equivalent form of the $e+p$ cross section. One of the most successful aspects of QCD pertains to its ability to make perturbative predictions at high energy scales $\mu \gg \Lambda_{\rm QCD}$. As long as relevant degrees of freedom remain in this regime, then perturbative calculations are tractable due to asymptotic freedom. This provides a foothold with which to calculate scattering cross sections at high energies. Despite this, the result will depend on the exact value of renormalization scale μ because either ratios Q/μ or μ/m will inevitably appear. For hard scatterings, where $Q \gg m$, at least one of these is guaranteed to be large. This

[6] In fact, a less well-known Nobel Prize was awarded in 1961 for experimentally demonstrating internal electromagnetic structure of the proton.

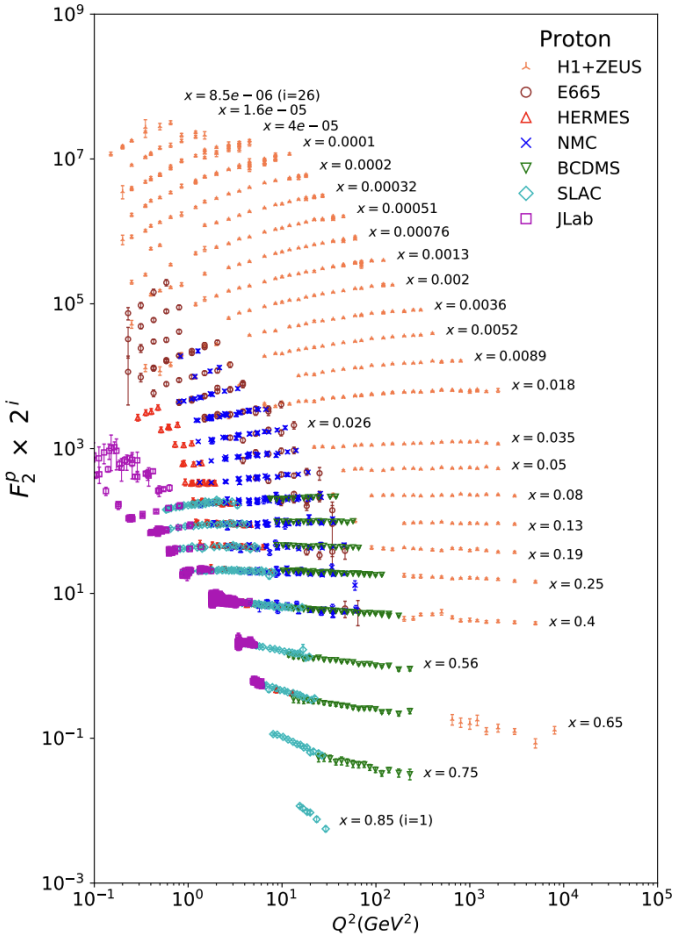


Figure 1.8: Structure function $F_2(x, Q^2)$ of the proton from a wide variety of experimental data. Constant x projections are offset by factors of 2. Bjorken scaling is the observation that each F_2 projection is approximately flat. Figure reproduced from Ref. [12].

represents the effect of long-wavelength modes in the perturbation which will *not* be perturbatively tractable. (The exception to this rule is initial states without hadrons – for example e^+e^- or $\mu^+\mu^-$ collisions [32].)

To resolve the conflict between multiple energy scales, QCD factorization theorems have been formulated. Effectively, these theorems contextualize cross sections for hadron scatterings within the parton model of hadronic structure. Consider a scattering event between an arbitrary particle X and a hadron h in the center of mass frame (perhaps an $e + p$ collision). h is a spatially extended object of (transverse) radius $R \sim 1\,\text{fm}$ composed of virtual partons. Due to time dilation,

the parton virtualities are reduced, enabling them to survive for longer times $\sim 1/q_{\text{parton}}$, while due to length contraction the hadron is flattened and X takes a short period of time to traverse the hadron $\sim R/\gamma$. For sufficiently high energies $1/\gamma \ll Rq_{\text{parton}}$, the hadron can be viewed as a collection of quasi-free partons with collinear momenta. During the scattering event, X picks out a single parton in h to scatter from, as long as the parton density is not too large. The momentum of this parton is xp_h, and thus x can be identified as the momentum fraction carried by the parton $p \in h$. The kinematics of the $p + X$ scattering are determined based on the momentum fraction $0 \lesssim x \lesssim 1$ carried by parton $p \in h$, and can be calculated according to the allowed QCD perturbative interactions. The total cross section for $h + X$ can then be calculated by directly summing over partons p with momentum fraction x:

$$\sigma_{h+X}(x, Q^2) = \sum_p \int_x^1 dx' f_{p/h}(x') \sigma_{p+X}(x/x', Q^2) = \sum_p f_{p/h} \otimes \sigma_{p+X}(x/x', Q^2). \tag{1.12}$$

This statement is essentially semiclassical due to the lack of interference effects from other partons in the $p + X$ scattering process. Here we have introduced the *parton distribution function* (PDF) $f_{p/h}(x)$ which represents the probability density of drawing a parton p of momentum fraction x in hadron h. This prescription applies to a wide variety of potential scattering events. For example consider the Drell-Yan process in pp collisions, $p + p \to \mu^+ + \mu^- + X$; its cross section can be written as a convolution

$$\sigma_{pp\to\mu^+\mu^- X}(y, Q^2) = \sum_a \int_{x_1}^1 dx_1' \int_{x_2}^1 dx_2' f_{a/p}(x_1') f_{\bar{a}/p}(x_2') \sigma_{a\bar{a}\to\mu^+\mu^- X}(y, Q^2) \tag{1.13}$$

$$= \sum_a f_{a/p} \otimes f_{\bar{a}/p} \otimes \sigma_{a\bar{a}\to\mu^+\mu^- X}(y, Q^2). \tag{1.14}$$

From this last line, we can see the total scattering mechanism is separated into multiple components by factorization:

- random selection of partons from incident hadrons according to the PDFs,
- calculation of the parton-level cross sections,
- vacuum evolution of any final-state partons, and

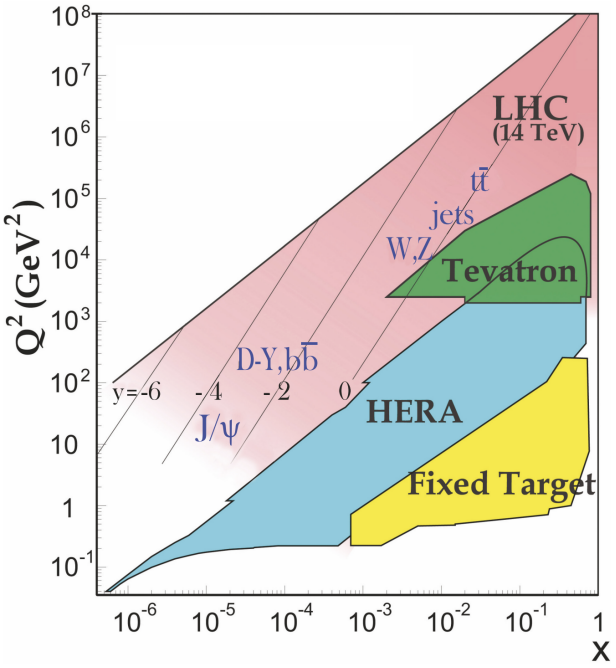


Figure 1.9: Schematic illustration of data sets used in PDF fits, and their coverage in the (x, Q^2) plane. Figure reproduced from Ref. [12].

- convolution of the above over intermediate degrees of freedom.

We see here that one of the main objectives of pQCD is therefore to provide the parton-level cross sections in the intermediate steps.

Finally, we can write down the $e + p$ cross section in terms of the parton model as

$$\sigma_{e+p\to X}(x, Q^2) = \sum_a \int_x^1 dx' f_{a/p}(x')\sigma_{e+a\to X}(x/x', Q^2). \tag{1.15}$$

Bjorken noticed a particular scaling in DIS experiments: the structure functions seemed to be (nearly) independent of the hardness Q^2, $F_{1,2}(x, Q^2) \simeq F_{1,2}(x)$ [33]. This observation can be satisfied if the scattering partons are spin-1/2 fermions, and thus directly motivated the parton model. If this is assumed, we arrive at the Callan-Gross relation $2xF_1(x) = F_2(x)$. Simplifying Eq. (1.10) for this case yields (we also take the inelastic scattering limit $m_p^2 y^2 \ll Q^2$)

$$\frac{d^2\sigma}{dxdQ^2} \simeq \frac{2\pi\alpha}{Q^4}\left(1 - y + \frac{y^2}{2}\right) F_1(x). \tag{1.16}$$

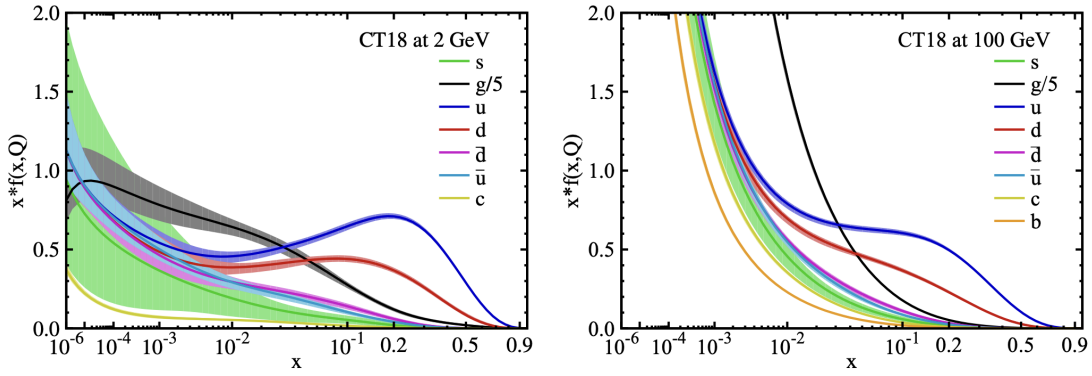


Figure 1.10: CT18 PDF fits at 2 GeV (left) and 100 GeV (right). Different colors show different particle types. Gluons are scaled down by 5 for visibility. HERA and LHC data are included, as well as data used in the CT14 fit. Figure reproduced from Ref. [34].

The system Eqs. (1.15) and (1.16) is solved when $F_{1,2}$ are a convolution over PDFs [12]

$$F_i \simeq \sum_a C_i^a \otimes f_{a/p} + \mathcal{O}(Q^{-2}), \tag{1.17}$$

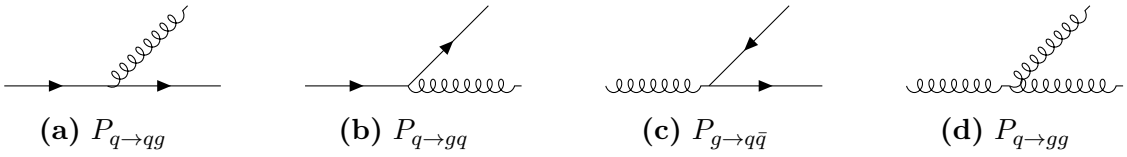
with C_i^a some calculable expansion in α_S. The leading term in Eq. (1.17) is known as the *leading-twist* contribution; higher-order effects dropped in this approximation are referred to as *higher-twist* corrections and are suppressed by powers of the momentum transfer $1/Q^2$. Thus, under a parton model with two quarks (u and d),

$$F_2(x) = x\left(\frac{4}{9}f_{u/p}(x) + \frac{1}{9}f_{d/p}(x)\right). \tag{1.18}$$

The factors 4/9 and 1/9 refer to the non-integer electric charges of quarks (recall that the structure functions are a measure of the electromagnetic moments). From this relation, a rather direct relationship between parton distribution functions and high-energy cross sections is found, and we are provided a straightforward methodology for determining PDFs from data.

In practice, PDFs are determined from a wide variety of data sets. For example, DIS is only sensitive to quark PDFs at leading order, as shown in Eq. (1.18) above. Gluons are electrically neutral and so do not directly couple to the exchanged photon. So, gluon distributions cannot be probed this way.[7] Multiple experimental data sets provide insight to PDFs at different kinematic

[7] The momentum constraint $\sum_i \int dx x f_{i/h}(x) = 1$ can however be used to extract the gluon PDF.



(a) $P_{q\to qg}$ **(b)** $P_{q\to gq}$ **(c)** $P_{g\to q\bar{q}}$ **(d)** $P_{q\to gg}$

Figure 1.11: Lowest order parton splitting functions, as described in the text. The final-state, horizontally-traveling parton carries the larger horizontal momentum fraction x of the initial parton.

scales and parton species, as shown in Fig. 1.9. Global fitting procedures combine all of the data into a single PDF fit. DIS data from HERA at DESY probed PDFs up to $Q^2 \sim 10^4$ GeV^2 and down to $x \sim 10^{-4}$. Tevatron $p\bar{p}$ collision data covered up to $Q^2 \sim 10^5$ GeV^2, but a smaller range in x. Modern fits, such as one by the CTEQ collaboration [34] shown in Fig. 1.10, are therefore able to cover a broad range in (x, Q^2) space. At high-x, PDFs are dominated by valence quarks contributing to the electric charge of the hadron. Meanwhile gluons and sea quarks dominate at low-x.

Parton Evolution, Fragmentation, and Jets

Ab initio calculations of parton distribution functions are immensely difficult, as no perturbative approach exists. However Bjorken scaling is approximate; it is valid only in the high-Q^2 limit and moderate to high-x. Such events are referred to as *hard scatterings* because of the large impulse. At lower values of Q^2, scaling violations are observed in experiment. Thus, in this regime, the PDFs implicitly depend on the energy scale. To understand how this arises in QCD, consider the Drell-Yan process as an example. The factorization statement lumps nonperturbative physics into initial-state parton distribution functions while all α_S perturbative physics is described by the parton-level cross section. This separation implies a renormalization scale μ which must vanish in any physical cross section. If the scale for perturbative calculations is modified, then there must be a corresponding shift in the nonperturbative physics that cancels the scale dependence. Consequently, the PDFs must depend on the scale μ. Although there is no ground-up approach to determine PDFs, there *is* a perturbative framework for understanding their scale dependence.

This is the role of the DGLAP (Dokshitzer–Gribov–Lipatov–Altarelli–Parisi) evolution equations.[8] These are defined in terms of the kernel or *parton splitting function* $P_{p\to p_1p_2}$, which perturbatively describes the probability of the parton p splitting $p \to p_1p_2$ (with momentum fraction x and transverse kick $k_\perp$ allocated to parton p_1). The lowest order diagrams in α_S are shown in Fig. 1.11. The results are [12, 35]

$$\begin{cases} P_{q\to qg}(x) &= \frac{4}{3}\left(\frac{1+x^2}{1-x}\right) \\ P_{q\to gq}(x) &= \frac{4}{3}\left(\frac{1+(1-x)^2}{x}\right) \\ P_{g\to q\bar{q}}(x) &= \frac{1}{2}\left(x^2+(1-x)^2\right) \\ P_{g\to gg}(x) &= 6\left(\frac{x}{1-x}+\frac{1-x}{x}+x(1-x)\right). \end{cases} \tag{1.19}$$

Often, $P_{p\to p_1p_2} \equiv P_{p_1p} \equiv P_{p\to p_1}$ are written exchangeably, since the trio is uniquely determined in each case. This reinterprets P as a the probability p undergoes a particular splitting. The DGLAP equations are derived by asserting $\log \mu^2$ dependence is nonphysical, and read [36–38]

$$\frac{\partial}{\partial \log \mu^2} f_{i/h}(x) = \frac{\alpha_S(\mu)}{2\pi} \sum_j \int_x^1 \frac{dx'}{x'} P_{j\to i}\left(x';\alpha_S\right) f_{j/h}\left(x'/x;\mu\right). \tag{1.20}$$

Therefore if the PDFs are obtained at *one* energy scale μ_1 (e.g. HERA energies), they can be predicted at *another* scale μ_2 (e.g. LHC energies).

What DIS essentially tells us is that in high-energy e+h collisions, where $\sqrt{s} \gg \Lambda_{\rm QCD}$, partons are struck from the hadron by a large momentum kick from the electron. Due to a combination of time dilation and asymptotic freedom, the parton can travel effectively freely for some time before it rehadronizes. Recall that the confinement potential grows as the parton escapes the hadron. Eventually, the color flux tube breaks, forming new partons in a cascading process. This is known as *fragmentation*, because collectively the new hadron "fragments" carry the energy and momentum of the single initial parton. Their momenta tend to be collinear, forming a collective spray of hadrons called a *jet*. The fragmentation pattern is encapsulated by the nonperturbative fragmentation function $D_{i\to h}(z)$, which describes the probability of parton i fragmenting into hadron h with longitudinal momentum fraction z. Although there is no ground-up approach to calculating $D_{i\to h}$,

[8] These are also occasionally referred to as the Altarelli-Parisi evolution equations in the literature.

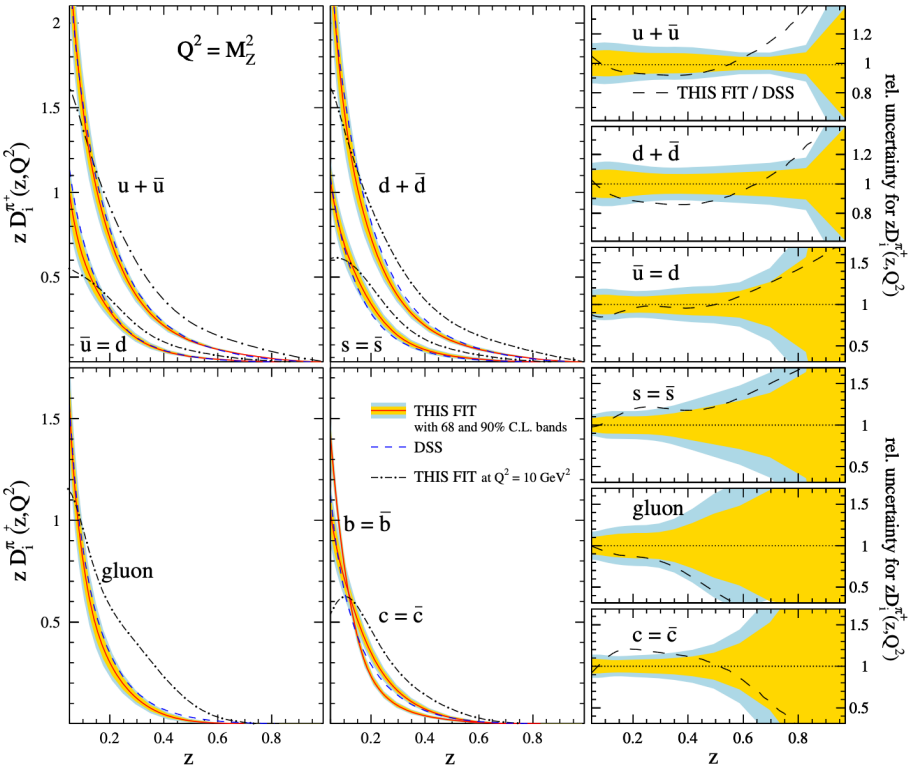


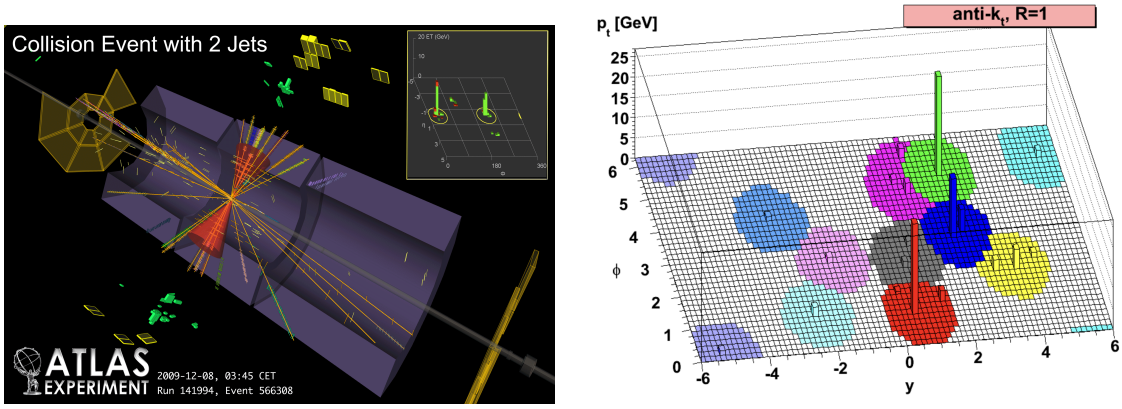
Figure 1.12: Examples of fitted parton→ π^+ fragmentation functions at the Z pole $Q^2 = M_Z^2$. Each panel shows different parton types. Figure reproduced from Ref. [39].

DGLAP also pertains to the evolution of the final-state parton shower, so we can describe how it evolves with energy scale. Thus,

$$\frac{\partial}{\partial \log \mu^2} D_{i\to h}(z,\mu) = \frac{\alpha_S(\mu)}{2\pi} \sum_j \int_z^1 \frac{dz'}{z'} P_{j\to i}(z',\alpha_S) D_{j\to h}(z'/z,\mu). \tag{1.21}$$

Typically, the scattering hardness $Q^2 \gg {\Lambda_{\rm QCD}}^2$ is used as the RG scale μ^2. In this sense, they can be conceptualized as an inverse of the parton distribution function: the PDF tells you the probability of selecting a parton i from hadron h, and the fragmentation function tells you the probability of obtaining a hadron h from the shower of parton i. A few examples of parton fragmentation function $D_{i\to\pi^+}(z)$ global fits are shown in Fig. 1.12.

Thus, jets represent our best tool for understanding parton dynamics in the asymptotically free limit. Although the jet is essentially a proxy for the kinematics of the parton due to momentum conservation, a better understanding for what a jet is comes from studying the energy flow of an



(a) Dijet event recorded by ATLAS **(b)** Anti-k_t jets in simulation

Figure 1.13: **(a)** Visual representation of a dijet event in 900 GeV pp collisions recorded by the ATLAS detector, including a map of transverse energy depositions. **(b)** Momentum density in (y, ϕ) space in a simulated HERWIG event. Anti-k_t $R = 1.0$ jets are indicated by the shaded regions. Figures reproduced from [40] and [41], respectively.

event. High-p_{T} partons carry a significant fraction of the collision energy in a direction far from the beam axis. A jet can therefore be defined instead as a collimated flow of energy. For example, $Z \to q\bar{q}$ decays have an inherently nonpartonic origin, yet this process easily forms jets. We see from this qualitative discussion that defining what a jet is can be tricky. In order to properly define the energy flow, we are faced with the issues of infrared and collinear safety ("IRC" safety). *Infrared (IR)* safety refers to the stability of the jet definition with respect to production of zero-momentum particles. Under production of additional particles with vanishingly small momenta, one would expect the energy flow of the event to remain constant and therefore the jet definition should remain invariant. On the other hand, when two particles have nearly collinear momenta, a *collinear safe* algorithm would return the same jets if the two collinear particles were merged into one. This is a particularly important property for jet algorithms with purely calorimetric inputs where only the total deposited energy is measured, because there is no way to determine how many particles passed through the material.

There are a variety of jet algorithms in use, such as Cambridge/Aachen [42, 43], k_t [44, 45], or SISCone [46] though the most commonly used one is the anti-k_t algorithm [41]. This algorithm is IRC safe and can be performed quickly under certain implementations, and thus most modern

jet definitions feature the anti-k_t algorithm. It takes a dimensionless radius parameter R which governs the angular extent of jets. Thus, a related benefit is that the jet shape is nearly circular in the (y, ϕ) plane. Typically, R ranges from 0.2 for a somewhat narrow, collimated jet cone, up to 1.0 for a wide, fat cone. Beyond IRC safety, algorithmic time complexity is also important in defining the algorithm. Of course, this plays no role phenomenologically, but must be considered experimentally, for example when a trigger needs to decide whether to keep an event. The anti-k_t algorithm offers a good compromise on speed, with limiting behavior scaling with the number of particles N as $\mathcal{O}\left(N^{3/2}\right)$ (as opposed to $N \log N$ from the k_t algorithm) [41].

Lund String Model & Event Generators

Because scattering events are naturally discrete occurrences, Monte Carlo models offer a clean methodology to make predictive inferences and are frequently used to simulate data. While PDFs can be determined from, for example, DIS data, this does not work for fragmentation fucntions. There is first a trivial effect from the parton selection: in $e + p$ collisions, it is far more likely that the electron kicks out a quark than a gluon. Therefore, DIS fragmentation functions are representative of the quark fragmentation, and less is known about gluons. In pp collisions, gluon-gluon interactions are far more common. Moreover, the beam remnants can be color connected to the event, allowing jets to have fragments over a much broader range in solid angle. To make quantitative predictions, phenomenological fragmentation models are necessary.

Foremost of these is the *Lund String Model* [47]. The basis for the model is that mesons are built from a $q\bar{q}$ pair connected by a massless string. The pair oscillates back and forth, and the oscillation energy is related to the mass of the state, as determined from the approximate string and orbital angular momentum Hamiltonians[9]

$$H_{\text{total}} = H_{\text{string}} + H_{\text{orbital}} = \underbrace{\left|\vec{p}_q\right| + \left|\vec{p}_{\bar{q}}\right| + \kappa \left|\vec{x}_q - \vec{x}_{\bar{q}}\right|}_{H_{\text{string}}} + \underbrace{\frac{1}{2} I J^2}_{H_{\text{orbital}}} . \tag{1.22}$$

where $\kappa \sim 1\,\text{GeV/fm}$. In the center-of-mass frame, the momenta are equal and opposite, $\vec{p}_q =$

[9] Here, we take the massless quark limit $m_q = m_{\bar{q}} \to 0$.

$-\vec{p}_{\bar{q}} = \vec{p}$. If $H_{\text{string}} \gg H_{\text{orbital}}$, then we can say at separation $\vec{x}_q - \vec{x}_{\bar{q}} = 0$ the invariant mass of the system is

$$M^2_{J=0} = \frac{1}{4} |\vec{p}|^2 . \tag{1.23}$$

When the pair has nonzero orbital angular momentum, there is a centripetal force on each quark

$$F_q = \frac{p}{R} = \kappa. \tag{1.24}$$

where $R = p/\kappa$ is half of the maximum separation. Therefore the angular momentum is

$$J \propto 2pR = \frac{M^2}{2\kappa} \Longrightarrow J \propto M^2. \tag{1.25}$$

The linear relations between J and M^2 are the Regge trajectories for meson scattering amplitudes.

The model is therefore phenomenological, as it is not based on *ab initio* calculations, and inherently designed to match onto observation. In order to produce hadrons from partons, the model identifies color connected partons and provides a string matching them together. It then breaks apart the string into hadrons. The probability distribution of a hadron carrying momentum fraction z is set by an empirical form

$$f(z) = N \frac{(1-z)^a}{z} \exp\left(\frac{-bE_\perp^2}{z}\right), \tag{1.26}$$

where a, b are fitted parameters and $E_\perp = m \oplus p_\perp$ is the transverse energy of the string.[10]

The Lund String Model is most commonly used as the fragmentation model in the Pythia event generator [48]. This model is frequently used in modern collider experiments to provide "good-enough" simulations of QCD processes. Beyond implementing the string fragmentation model, parton shower models were also key to the development of Pythia, particularly for the initial state. Given the probability of a parton splitting from above, the probability element of a particular emission at hardness scale $q_\perp^2$ is

$$d\mathcal{P}_{\text{emission}}(q_\perp^2) = \frac{\alpha_S}{2\pi} \frac{dq_\perp^2}{q_\perp^2} \int_z^{1-z} dz' P_{ji}(z'). \tag{1.27}$$

[10] In this thesis, we use the notation $a \oplus b$ to denote the Pythagorean sum $\sqrt{a^2 + b^2}$ as a shorthand.

The corresponding probability of *no* emission between scales $q^2_{\perp,1}$, $q^2_{\perp,2}$ can be written as an exponential[11]

$$\mathcal{P}_{\text{no emission}}\left(q^2_{\perp,1}, q^2_{\perp,2}\right) = \exp\left[-\int_{q^2_{\perp,1}}^{q^2_{\perp,2}} \frac{dq^2_\perp}{q^2_\perp}\frac{\alpha_S}{2\pi}\int_z^{1-z} dz' P_{ji}(z')\right] \equiv \Delta_i\left(q^2_{\perp,1}, q^2_{\perp,2}\right). \tag{1.28}$$

This probability is known as a *Sudakov form factor* Δ_i, and as we have seen, can be calculated in pQCD using the perturbative splitting functions. Its purpose is to regulate the rapid parton showering as highly virtual partons escape (or go into) the hard parton-level vertex. For example, the final-state parton begins evolution with a high virtuality $\sim Q^2$, and the parton shower is evolved recursively until the parton and each emission reaches virtuality Q^2_0, a free parameter. At this point, the shower is fed to the fragmentation model and a set of final-state hadrons is obtained. Other Monte Carlo event generators also apply similar parton shower formalisms, such as Herwig [49] and Sherpa [50].

Nuclear Modification

It is understood that PDFs in nuclei (nPDFs) are different from those in protons, although the mechanisms are less well-understood [52]. Such modifications are quantified via the ratio

$$R^A_{F_2}(x, Q^2) = \frac{F_2^A(x, Q^2)}{AF_2^p(x, Q^2)} \tag{1.29}$$

where A is nuclear mass number and F_2^A is the nucleon structure function in the nucleus. $R^A_{F_2}$ can be directly measured for example in nuclear DIS. There are four main parts to the modification curve:

- **Shadowing**, or the suppression of F_2^A in the range $x \lesssim 0.05$,
- **Fermi motion**, which enhances the nuclear structure function at very high $x \gtrsim 0.8$ due to fluctuations in nucleon center-of-mass energies,

[11] This can be derived by expanding $\mathcal{P}_{\text{no emission}}$ in the differential probability element $d\mathcal{P}_{\text{emission}} \ll 1$ and casting the sum to an exponential.

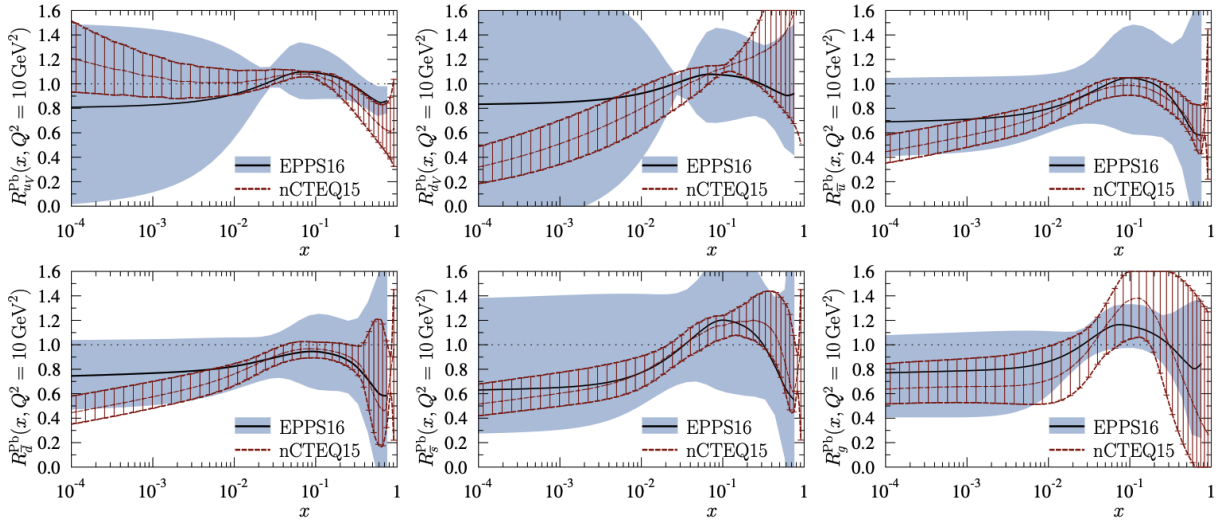


Figure 1.14: Nuclear modification of PDFs in Pb from the EPPS16 and nCTEQ15 global fits at $Q^2 = 10$ GeV^2. Each panel shows as different type of parton, including $u, \bar{u}, d, \bar{d}, \bar{s}$, and g. The shadowing, anti-shadowing, EMC effect, and Fermi motion regions can be seen with increasing x. Figure reproduced from Ref. [51].

- **The EMC effect**, which is the observation of a suppressed nuclear structure function in moderate-high Bjorken $0.3 \lesssim x \lesssim 0.8$, named after the European Muon Collaboration which discovered it, and

- **Anti-shadowing**, which enhances the nuclear structure function in the intermediatary range $0.05 \lesssim x \lesssim 0.3$ due to the overall normalization of F_2^A counteracting shadowing effects.

Shadowing is particularly evident in LHC data due to the high collision energies counterbalancing low-x partons, pushing the energies of products into tangible GeV ranges. This explains, as one example, the suppression of J/ψ states at backwards rapidity[12] in p+Pb collisions [53]. Fits from nPDF collaborations such as EPPS16 [51] or nCTEQ15 [54] have reproduced these qualitative features. Both fits are illustrated in Fig. 1.14. Direct measurement of nPDFs and building a stronger understanding of these effects is one of the motivations for building the Electron-Ion

[12] *Rapidity* (y) in hadronic collisions is defined as the boost along the z-axis of a particle: $y = \frac{1}{2}\log\frac{E+p_z}{E-p_z}$. A particle with $y = 0$ has a z-axis momentum $p_z = 0$. Thus, the rapidity encodes the Lorentz transformation to the reference frame where the particle has no z-axis momentum.

Collider at BNL in the coming decade [22].

1.3 Ultra-Relativistic Heavy-Ion Collisions

While ultra-relativistic pp collisions can be understood in the context of the parton model in the hard sector, and Regge trajectories in the soft sector, it is generally understood that the ultra-relativistic collisions of heavy ions produce droplets of quark-gluon plasma.[13] Thus, nuclear collisions present the foremost mechanism to study this phase of nuclear matter experimentally [22]. The mechanism allowing these droplets to form can be understood as the onset of deconfinement at extreme energy densities, allowing partons to roam outside of hadrons. The droplets quickly "evaporate" (*hadronize*) into an interacting gas of hadrons within tens of yoctoseconds (10^{-24} seconds) of their creation.[14] During their incredibly brief lifetime, they witness intense pressures and rapidly expand, cooling and decreasing their energy density until partons are reconfined. The products of the hadronization are then observed by particle detectors. Thus, the central objective of heavy-ion physics is to infer the physical properties of the plasma by studying these final-state hadrons.

Currently, these collisions are created at both the Relativistic Heavy Ion Collider (RHIC) at Brookhaven National Laboratory in Upton, NY, and the Large Hadron Collider (LHC) at CERN in Geneva, Switzerland. Both colliders are circular and can collide a variety of hadronic systems. RHIC, which turned on in the year 2000, typically collides gold ions at a center-of-mass energy $200A$ GeV, but offers versatility in both collision energy and system variety. The LHC turned on in 2008 and typically collides proton beams to create and study ultra-rare particles, such as the Higgs, though also operates a large heavy-ion program by colliding primarily lead ions. Compared with RHIC, there is a less diverse set of systems and the per-nucleon-nucleon-pair collision energy is substantially higher (by a factor of ~ 25). Thus the two colliders provide complementary yet distinct measurements.

[13] Also referred to as QGP *fireballs*.

[14] In this thesis, we use $c = 1$ units. For reference, $1\,\mathrm{fm}/c \sim 3 \times 10^{-24}\,\mathrm{s}$.

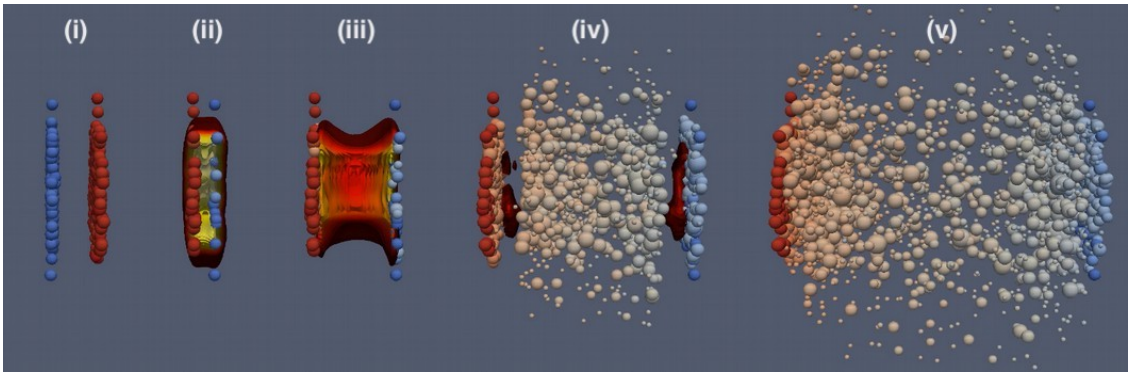


Figure 1.15: The Standard Model of Heavy-Ion Collisions, including (i) the initial state, (ii) onset of hydrodynamics, (iii) hadronization at freeze-out, (iv) hadronic rescattering, and (v) free streaming. Figure produced by Jonah Bernhard.

To identify and understand the quark-gluon plasma droplets created in heavy-ion collisions, there are a variety of signatures experiments search for. These include chemical equilibration of strangeness, collectivity of final-state particles, jet quenching, sequential suppression of quarkonia (in particular the $\Upsilon(nS), n \geq 2$ states), among others. Ultimately, each signature is sensitive to a variety of aspects of the collision. Key to contextualization of such studies is a standard model for the evolution of the fireball, which we explore in this section.

The Standard Model of Heavy-Ion Collisions

As a play on words, heavy-ion physicists work not only with the Standard Model of *particle* physics, but also the so-called Standard Model of *heavy-ion* physics. This model is illustrated by Fig. 1.15. It asserts that heavy-ion collisions proceed in a well-defined sequence of stages:

(1) **Initial collision & hard scatterings.** The timescale for large momentum exchanges is extremely small. Simple uncertainty principle arguments suggest $\tau \sim 1/Q$. As an example, near the Z-pole ($Q \sim 90$ GeV), $\tau \sim 10^{-3}$ fm. In contrast, soft strong interactions have timescales $\tau_{\mathrm{S}} \sim 1/\Lambda_{\mathrm{QCD}} \sim 1$ fm. Therefore, the production of very high-energy particles must occur near immediately. The initial geometry of each nucleus can be viewed as a quasi-free, spatially concentrated collection of nucleons within a *Glauber model*, which we

detail shortly. However, evolution of the nuclei between this timescale and the next is not fully understood, and is an active field of research.

(2) **Onset of hydrodynamics.** After approximately $0.5-1$ fm, the QGP fireball has formed. It can be well-modeled hydrodynamically, even though the underlying degrees of freedom are quarks and gluons ripping themselves apart at $\mathcal{O}\,(50\text{–}60\%)$ of the speed of light.[15] This behavior can be observed experimentally via the consequence of pressure gradients. Due to elliptical asymmetry in the initial state, a pressure gradient forms along the short axis spanning between the center of each nucleus. This pushes the quarks and gluons along that axis with a greater force, resulting in global momentum anisotropies in the final state. Higher-order moments such as triangularity or quadrupolarity, represent the effect of fluctuations in the initial state. Hydrodynamics persists as long as the fireball is dominated by the QGP phase, typically for timescales $\tau_{\text{hydro}} \sim 10\text{–}15$ fm in voluminous AA collisions.

(3) **Recombination.** Once the fireball expands sufficiently, the temperature (recall this scales with $T \sim \varepsilon^{1/4}$ according to the number of massless degrees of freedom) reaches the transition temperature, at which point the fireball recombines into hadrons. This is described statistically by the Cooper-Frye hypersurface integral [55]

$$E_h \frac{dN_h}{dp^3} = \int_\Sigma p^\mu d^3\sigma_\mu f_h\left(\vec{x},\vec{p}\right). \tag{1.30}$$

In equilibrium, f_h is the quantum statistics function for hadron h. Out of equilibrium, it depends on pressure, energy density, fluid velocity, and so on. Equivalently, it depends implicitly on the position $\vec{x}$. In the MUSIC hydrodynamic package [56, 57], this $\vec{x}$ dependence is factored into a "small" correction δf, which encapsulates the properties of the medium only. Systematic uncertainties on δf are currently very large, though matching to hadron spectra in data might offer insights in the future [58]. As a comment, because the transition is continuous between the two phases, recombination does not actually occur

[15] Explaining the emergence of hydrodynamic behavior in this far-from-equilibrium system is one of the ongoing great challenges in heavy-ion physics [22].

on a hypersurface (rather, there is coexistance between the two phases across a temperature range), though models often treat the transition as first order with no latent heat for computational simplicity.

(4) **Hadronic rescattering.** Following recombination, the fireball is in the hadronic gas phase. The constituent hadron density is still high, so hadrons can undergo successive rescatterings. Two freeze-out processes occur during the rescattering phase: (1) chemical equilibration, and then (2) kinetic equilibration. After approximately 50–100 fm, the hadrons free-stream away from the collision and are picked up by particle detectors.

The Initial State & Glauber Modeling

The initial state is naturally modeled in Monte Carlo with Glauber models [59–61]. These models are conceptually very appealing and rely primarily on knowledge of cold nuclear structure. On short timescales, each nucleus consists of quasi-free nucleons with well-defined positions and momenta. The position of each nucleon is distributed with a Woods-Saxon distribution

$$\rho(r) = \frac{1 + w\left(\frac{r}{R}\right)^2}{1 + e^{\frac{r-R}{a}}}, \tag{1.31}$$

where w, R, a are constructed via measurements of each nucleus.[16] For nucleus A, the inverse area density function $\hat{T}_A(\vec{s}, z)$ represents the probability of finding a nucleon at position $(\vec{s}, z)$ in A. At an impact parameter $\vec{b}$ between two nuclei A and B, the thickness function is defined via an integral over $\vec{s}$

$$\hat{T}_{AB}(\vec{b}) = \int d^2s \hat{T}_A(\vec{s})\hat{T}_B(\vec{s} - \vec{b}). \tag{1.32}$$

As the nuclei are roughly spherical objects, collisions with small impact parameters produce a large overlap region between the nuclei. These are referred to as *central* collisions. Inversely, collisions with large impact parameters produce a smaller overlap region, and are referred to as *peripheral* collisions. Typically, the centrality is classified with a parameter such as the number of binary

[16] Deformed nuclei such as uranium can be included via spherical harmonics [60].

nucleon-nucleon collisions N_{coll}, or the number of collided or *participant* nucleons N_{part} in each nucleus. In the optical limit, the number of binary nucleon-nucleon collisions N_{coll} is binomial distributed, with probability

$$\mathcal{P}(N_{\text{coll}}, \vec{b}) = \binom{AB}{n} \left(\hat{T}_{AB}(\vec{b})\sigma_{\text{inel.}}^{\text{NN}}\right)^{N_{\text{coll}}} \left(1 - \hat{T}_{AB}(\vec{b})\sigma_{\text{inel.}}^{\text{NN}}\right)^{AB-N_{\text{coll}}}, \tag{1.33}$$

where $\sigma_{\text{inel.}}^{\text{NN}}$ is the inelastic nucleon-nucleon cross section. At 5.02 TeV, $\sigma_{\text{inel.}}^{\text{NN}} = 67.6\,\text{mb}^{-1}$ [61]. The expected number of collisions is therefore

$$\langle N_{\text{coll}} \rangle (\vec{b})\Big|_{\text{MB}} = \sum_{n=1}^{AB} \mathcal{P}(N_{\text{coll}}, \vec{b}) = AB\hat{T}_{AB}(\vec{b})\sigma_{\text{inel.}}^{\text{NN}}. \tag{1.34}$$

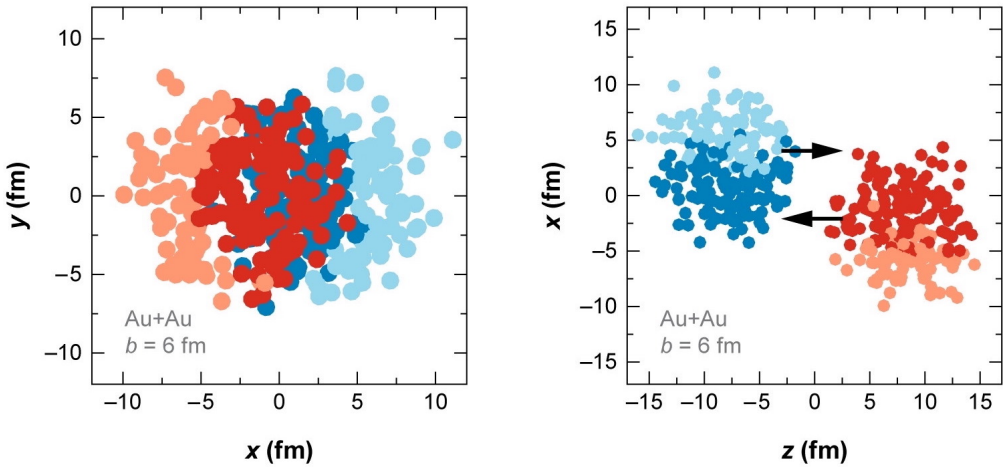
The optical approximation provides an analytical approach to centrality studies, and is valid in the limit of large nuclei, where the relevant degrees of freedom are primarily hadronic. Collisions involving small nuclei $A \gtrsim 1$ are more susceptible to the partonic substructure of constituent nucleons affecting the overall geometry, affecting estimates for $\langle N_{\text{coll}} \rangle$.

However, N_{coll} is more naturally defined outside of the optical approximation in the Monte Carlo approach, whereby the positions of nucleons can be directly simulated. Two nucleons are said to have collided if their relative distance d is shorter than the cross-sectional radius; that is,

$$d \leq \sqrt{\frac{\sigma_{\text{inel.}}^{\text{NN}}}{\pi}} \approx 1.47\,\text{fm at 5.02 TeV}. \tag{1.35}$$

N_{coll} can then be directly evaluated by counting the number of overlapping nucleons. The number of participants N_{part} is also defined as the number of nucleons undergoing at least one collision. Nucleons with no collision are called *spectators* and are assumed to continue traveling quasi-free. They do not contribute to the formation of a QGP fireball.

There is myriad experimental evidence in support of the Glauber model. By the original quasi-free assumption, the formation of hard probes (jets, Z bosons, photons, and so on) is understood to occur in single nucleon-nucleon collisions. Therefore the frequency of large momentum transfers and the creation of hard probes is expected to be maximal in head-on or *central* collisions. Such probes are expected to be much rarer in glancing or *peripheral* collisions. This is known as



(a) xy-plane cross-sectional view **(b)** xz-plane cross-sectional view

Figure 1.16: A simulated Au+Au collision in the Glauber model. **(a)** View of participant and spectator neutrons in the transverse xy-plane. **(b)** View along the beam axis. Figure reproduced from Ref. [59].

N_{coll}-scaling of hard processes, and has been confirmed on numerous occasions both at RHIC and the LHC with electroweak probes [62–64].

Another success is found in the soft sector. The distribution of forward rapidity energy deposition has been successfully described by the Glauber model:

$$\left.\frac{dN_{\text{evt}}}{dE_{\text{T}}^{\text{total}}}\right|_{3\lesssim|y|\lesssim5} = \sum N_{\text{part}} \frac{dN_{\text{evt}}}{dN_{\text{part}}} \mathcal{P}\left(E_{\text{T}}^{\text{total}} \middle| N_{\text{part}}\right), \tag{1.36}$$

where the probability mass function is frequently taken to be a gamma distribution via the ansatz

$$\mathcal{P}\left(E_{\text{T}}^{\text{total}} \middle| N_{\text{part}}\right) = \Gamma\left(E_{\text{T}}^{\text{total}}; k(N_{\text{part}}), \theta(N_{\text{part}})\right). \tag{1.37}$$

Conceptually, this is simply asserting that the total energy (as well as its variance) at forward rapidities scales with N_{part}. This distribution of forward energy deposition can thus be fitted to data. The use of a gamma distribution is merely a model to link Glauber variables N_{coll} and N_{part} with experimental observables $N_{\text{ch}}^{\text{rec}}$ or ΣE_{T}. Other distributions (negative binomials, Gaussians, and so on) have also generated similar results. A result from ATLAS is shown in Fig. 1.17 and shows remarkably good data-model agreement.

Beyond providing a computationally straightforward methodology to simulate initial-state

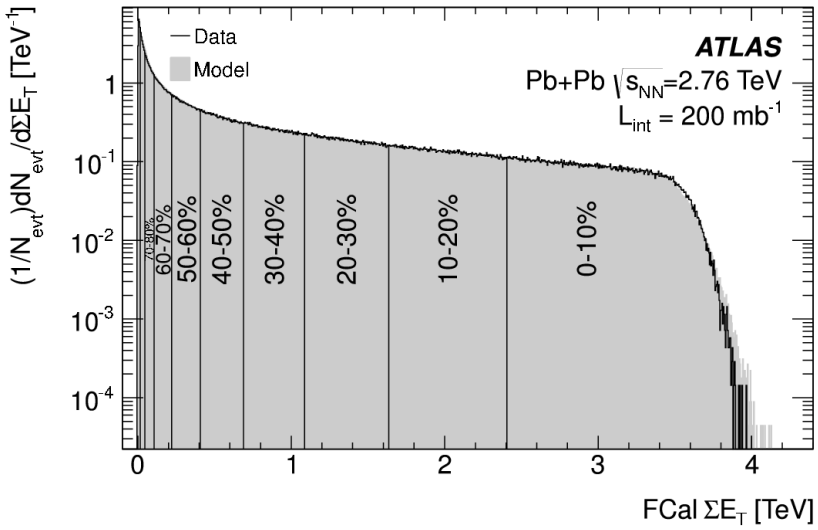


Figure 1.17: Total forward energy measured by ATLAS fitted to a Glauber model. Percentiles of the distribution are denoted and are separated by vertical lines. Figure reproduced from Ref. [65].

geometries, Monte Carlo Glauber also can be extended to small systems. Some model extensions including subnucleon fluctuations exist, but these are smeared away in large AA collisions [66]. In smaller target-on-projectile systems like p+Pb or d+Au, the notion of centrality purely defined via impact parameter is washed away, but a notion of N_{coll} still remains. Extensions of the Glauber model to these systems have also proven useful. Fluctuations in nucleon interaction strength become more apparent when there are fewer interactions, and Glauber-Gribov models have seen success as well [67]. These sample the *total* cross section σ_{total} from

$$\mathcal{P}(\sigma) \propto \frac{\sigma}{\sigma + \sigma_0} \exp\left(-\frac{(\sigma/\sigma_0 - 1)^2}{\Omega^2}\right) \tag{1.38}$$

and assume a nucleon-nucleon cross section $\sigma_{\text{inel.}}^{\text{NN}} = \sigma_{\text{total}}\lambda$ for some λ such that $\left\langle \sigma_{\text{inel.}}^{\text{NN}} \right\rangle \simeq 70$ mb (at LHC energies).

Hydrodynamics

One of the surprising findings from the initial RHIC experiments is that the QGP droplet, for the majority of its lifetime, behaves hydrodynamically. Traditionally one arrives at hydrodynamic

description for kinetic systems by asserting that the mean free path is much smaller than the system size and relating the degrees of freedom up to first order in gradients. Any higher order modes are assumed to damp out quickly and the system becomes dominated by long-range behavior.

Fundamental to basic hydrodynamic theory is the stress-energy tensor $T^{\mu\nu}$ in a local rest frame where the system has achieved thermal equilibrium. It is defined as [68]

$$T^{\mu\nu} = T^{\mu\nu}_{(0)} + T^{\mu\nu}_{(1)} + \dots \tag{1.39}$$

$$T^{\mu\nu}_{(0)} = \varepsilon u^\mu u^\nu + P(\varepsilon)\left(g^{\mu\nu} + u^\mu u^\nu\right) = \varepsilon u^\mu u^\nu + p(\varepsilon)\Delta^{\mu\nu}. \tag{1.40}$$

Here, $\varepsilon(x)$ is the energy density, $u^\mu(x)$ is the fluid velocity, and $p(\varepsilon)$ is the pressure determined from the QCD EoS (perhaps from the lattice, for example). $\Delta^{\mu\nu}(x) = g^{\mu\nu} + u^\mu u^\nu$ is a projection operator. Since hydrodynamics is a long-wavelength theory, $T^{\mu\nu}$ is frequently decomposed into terms based on the number of derivative operators $T^{\mu\nu}_{(0)}$, $T^{\mu\nu}_{(1)}$, and so on. (Thus the subindex indicates the number of derivatives.) Because derivatives indicate momentum operators, short-wavelength phenomena are contained in the higher-order terms, so a long-wavelength theory can be built from only a few terms. The simplest theory we can build is

$$\nabla_\mu T^{\mu\nu}_{(0)} = 0. \tag{1.41}$$

Here, ∇_μ is the geometric covariant derivative. In flat spacetime ($g^{\mu\nu} = \eta^{\mu\nu}$), $\nabla_\mu \to \partial_\mu$. This is known as *ideal* hydrodynamics. Such models of fireball expansion are frequently used due to their computational simplicity as a first order differential equation. However, from both theory and experimental perspectives we know that the fluid must be somewhat viscous. This requires the use of the higher order *viscous* hydrodynamic expansion. We introduce

$$T^{\mu\nu}_{(1)} = \pi^{\mu\nu} + \Delta^{\mu\nu}\Pi, \tag{1.42}$$

where

$$\sigma^{\mu\nu} = \Delta^{\mu\lambda}\nabla_\lambda u^\nu + \Delta^{\nu\lambda}\nabla_\lambda u^\nu - \frac{2}{3}\Delta^{\mu\nu}\nabla_\lambda u^\lambda, \tag{1.43}$$

$$\pi^{\mu\nu} = -\eta\sigma^{\mu\nu}, \text{ and} \tag{1.44}$$

$$\Pi = -\zeta\nabla_\lambda u^\lambda. \tag{1.45}$$

The shear and bulk stress tensors $\pi^{\mu\nu}$ and Π represent the traceless and trace parts of $T^{\mu\nu}_{(1)}$. These embed microscopic properties of QCD in the macroscopic dynamics. The bulk viscosity ζ concerns the radial expansion of the fluid and is understood to have both a nontrivial temperature dependence and an impact on a broad range of observables [58]. Famously, the ratio between shear viscosity η and entropy density s has been hypothesized to obey the bound

$$\frac{\eta}{s}\Big|_{\text{infinite}-\text{coupling}} \geq \frac{1}{4\pi} \sim 0.08. \tag{1.46}$$

in a wide class of strongly interacting gauge theories [69]. This prediction can be obtained explicitly via the AdS/CFT conjecture. In the weak-coupling limit, however, qualitative arguments suggest

$$\frac{\eta}{s}\Big|_{\text{weak}-\text{coupling}} \to \infty. \tag{1.47}$$

This is the case in ordinary QED plasmas [70]. In QCD however, the strong coupling means that hydrodynamic models match data best with small values $\sim$ 0.1–0.2 near the conjectured bound. For this reason, the strongly coupled QGP is sometimes called *the perfect fluid*.

The equation of motion for viscous hydrodynamics,

$$\nabla_\mu \left(T^{\mu\nu}_{(0)} + T^{\mu\nu}_{(1)}\right) = 0, \tag{1.48}$$

is known as the *Navier-Stokes* equation. In the nonrelativistic limit, this equation describes the behavior of liquid water, air currents, and so on. A frequent approximation is that particles obtain their velocity at the initial collision, so the fluid 4-velocity can be written in Milne coordinates as[17]

$$u^\mu(x) = (u_\tau, u_\xi, \vec{u}_\perp) = (1, 0, \vec{0}). \tag{1.49}$$

[17] The Milne coordinate system uses proper time $\tau = \sqrt{t^2 - z^2}$ and rapidity $\xi = \text{arctanh}(z/t)$ coordinates. The metric is $ds^2 = -d\tau^2 + d\vec{x}^2 + \tau^2 d\xi^2$.

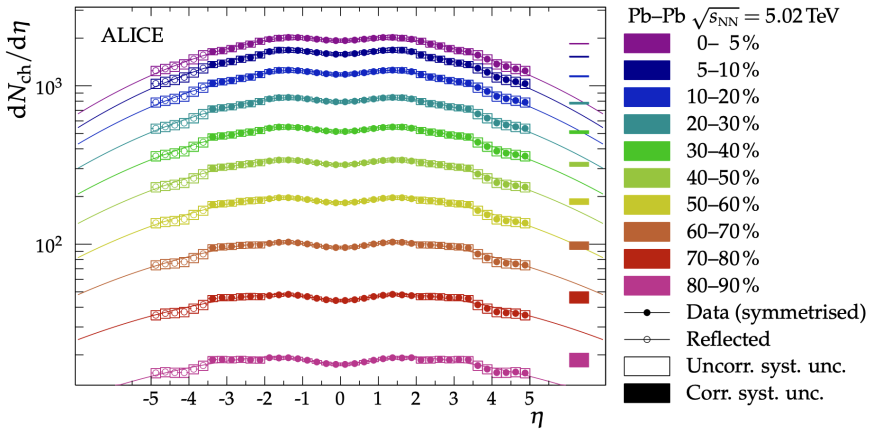


Figure 1.18: Rapidity dependence of charged-particle production in Pb+Pb collisions in bins of centrality as measured by ALICE. Figure reproduced from Ref. [71].

This is known as Bjorken expansion. Thus, this approximation asserts that $T^{\mu\nu}(\vec{x}_\perp, \xi, \tau) = T^{\mu\nu}(\tau)$. The system is constant in the transverse plane (at least within the region of overlap) and has infinite extent in z. In this case, Navier-Stokes reduces to $\partial_\tau T^{\tau\tau} = 0$ and thus

$$\partial_\tau \varepsilon = -\frac{\varepsilon + p(\varepsilon)}{\tau} + \frac{4\eta}{3\tau^2}. \tag{1.50}$$

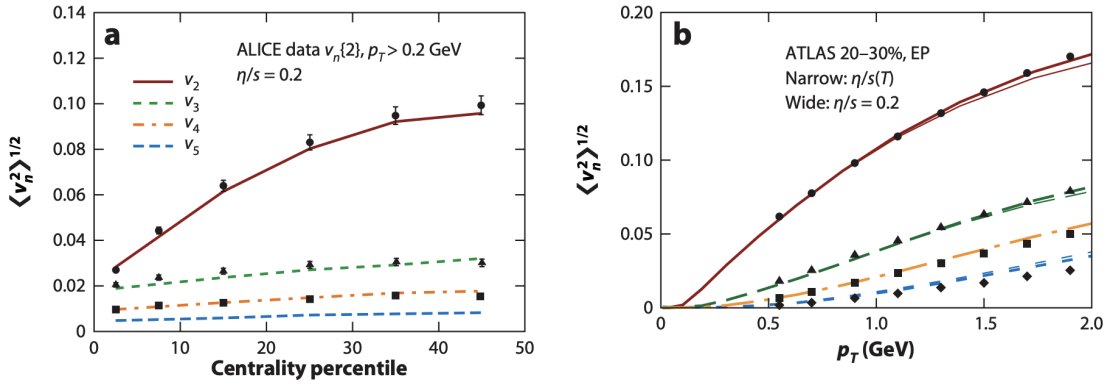
Note that the bulk viscosity ζ necessarily disappears. Mathematically, this is due to the fixed 4-velocity of the fluid in Eq. (1.49). Conceptually, it is due to the fact that Bjorken "expansion" doesn't expand the fluid volumetrically. In the ideal limit, and approximating $p(\varepsilon) = c_s^2 \varepsilon$ where $c_s = \sqrt{p'(\varepsilon)}$ is the speed of sound, the Bjorken flow is solved if

$$\varepsilon(\tau) = \varepsilon(\tau_0) \left(\frac{\tau_0}{\tau}\right)^{1+c_s^2}. \tag{1.51}$$

Further approximation of the EoS $T \propto \varepsilon^{1/4}$ then reveals the temperature evolution:

$$T(\tau) = T(\tau_0) \left(\frac{\tau_0}{\tau}\right)^{\frac{1+c_s^2}{4}}. \tag{1.52}$$

This equation is accurate for a chemically equilibrated hadronic gas, though applicability to the QGP is questionable. An implicit assumption of this model is that the entropy density does not vary with rapidity $\partial s/\partial y \approx 0$, and therefore the number of charged particles should be loosely independent of y. (Since N_{ch} is related to the entropy.) Experimental measurements of the charged-particle rapidity distribution do suggest rapidity invariance $dN_{\mathrm{ch}}/dy \approx$ const. for $|y| \lesssim 2$–3, or



(a) v_2 versus centrality **(b)** v_2 versus p_{T}

Figure 1.19: Comparison between anisotropy coefficients in viscous hydrodynamics simulations and Pb+Pb data. Coefficients v_2 through v_5 are shown versus collision **(a)** centrality and **(b)** p_{T}, and extracted from two-particle correlations. Figure reproduced from Ref. [72].

thereabouts. This can be seen for example in Fig. 1.18. Though, the symmetry assumed by Bjorken expansion is somewhat oversimplified, making it little more than a rough approximation. However the Bjorken expansion is useful for its simplicity, and can be easily implemented to describe the fireball evolution in jet-quenching models, as we will see in Chapter 2.

Global momentum anisotropies are frequently cited as strong evidence for hydrodynamic expansion of the QGP fireball. Hadron spectra in heavy-ion collisions can be best described via a Fourier series in the transverse plane

$$\left\langle \frac{dN}{dp^3} \right\rangle = \left\langle \frac{dN}{dp_{\mathrm{T}}^2} \right\rangle \left[1 + 2 \sum_{n=1}^{\infty} v_n \cos\left(n(\phi - \Psi_n)\right) \right]. \tag{1.53}$$

The elliptic flow coefficient v_2 is sensitive to pressure gradients in the plasma. As the fireball expands, fluid cells along the short axis experience a larger boost than the long axis. The net consequence is that particles within a fixed momentum range are more likely to be produced in one direction than 90° away. The p_{T} and centrality dependence of the v_n parameters is examined in Fig. 1.19. These calculations are performed by feeding hydrodynamic solvers with initial conditions from, for example Monte Carlo Glauber, and subsequently evaluating the freeze-out with a hadronic cascade that applies Cooper-Frye and evolves the hadronic rescattering. From Fig. 1.19, the anisotropy coefficients are clearly well-matched in data. Some tension is seen for v_5, though

such high orders are more susceptible to smaller fluctuations in the initial state not accounted for in the particular Glauber model.

Despite its success, an ongoing challenge in heavy-ion physics is to fully explain the emergence of hydrodynamic degrees of freedom. It is well understood that the perturbative series

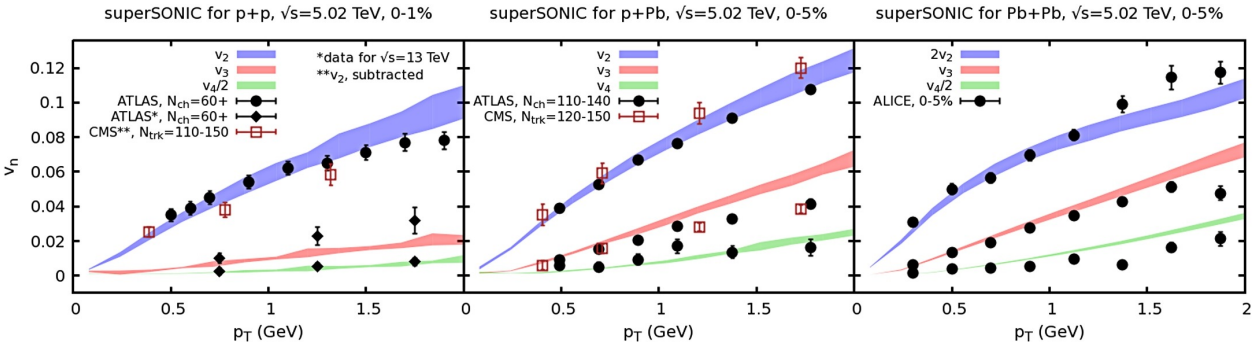
$$T^{\mu\nu}_{(0)} + T^{\mu\nu}_{(1)} + T^{\mu\nu}_{(2)} + \dots \tag{1.54}$$

diverges in out-of-equilibrium systems. This is because the number of terms in $T^{\mu\nu}_{(n)}$ grows factorially in n, but each derivative has a comparable magnitude as the last. As derivatives essentially represent factors of momentum, this means that high-momentum modes have significant impact on the theory. Borel resummation techniques have proven useful for assigning values to the stress-energy tensor in such scenarios, and suggest the existence of hydrodynamic attractors [73, 74].

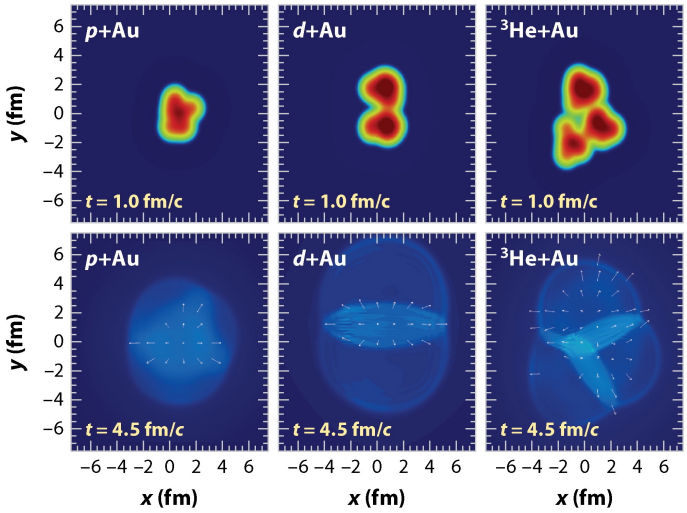
These insights are particularly interesting in the context of small nuclear collision systems, notably p+Pb, p+Au, d+Au, ^{3}He+Au and pp.[18] Conventional wisdom is that these systems are not voluminous enough to form a QGP phase. Historically, they were studied to build understanding of cold nuclear matter effects, such as shadowing and partonic rescattering. However, consistent indications of global momentum anisotropies in these systems have challenged our understanding. This is examined in Fig. 1.20, where hydrodynamic predictions for a few systems are compared with experimental data. The superSONIC model is used to make the fits to LHC data [75] while the pre-equilibrium flow (the "super" part of superSONIC) is not used in the RHIC predictions. In all cases, the unified hydrodynamic approach with a common set of parameters (QCD EoS, viscosity parametrizations, etc.) matches the data remarkably well. If, in fact, out-of-equilibrium hydrodynamics is a good model for these kinds of systems, then our understanding of QGP formation should be upended.

Thus, while viscous hydrodynamics has been identified as the best description of a wide variety of heavy-ion collisions for nearly twenty years, a full understanding of its emergence remains elusive. As the question of QGP formation in small systems remains forefront, either finding or

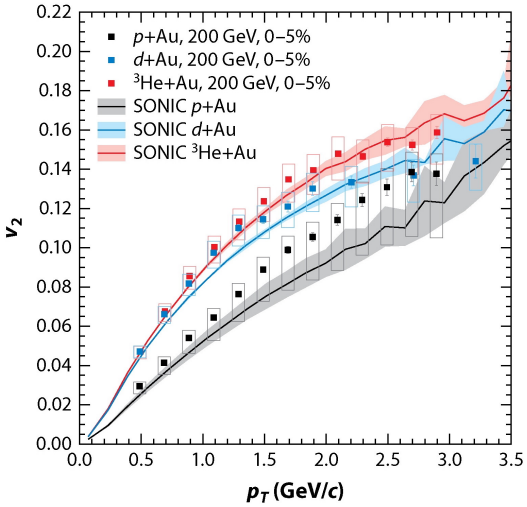
[18] We remind the reader that pp collisions can also be treated as a nuclear system in addition to a hadronic one.



(a) pp **(b)** p+Pb **(c)** Pb+Pb



(d) Hydrodynamic expansion in p+Au, d+Au, and ^{3}He+Au



(e) v_2 coefficients

Figure 1.20: Examination of collectivity in small collision systems. **(a–c)** Comparison of anisotropy components in LHC data within a unified hydrodynamic framework. **(d)** Time evolution of QGP droplet energy densities in 200 GeV p+Au, d+Au, and ^{3}He+Au collisions at $t = 1.0$ fm and 4.5 fm. **(e)** Anisotropy component v_2 versus particle p_{T} for each collision system in data and the hydrodynamic model. All hydrodynamic calculations are performed in the (super)SONIC model. Figures reproduced from Refs. [75] and [76], respectively.

ruling out additional indicators of the QGP phase in small systems can offer new insight to the dynamics of hadronic collisions and possibly allow a major step forward in this field.

Kinetic Approaches

Hydrodynamics has been a successful theory in describing large systems; but, this success poses an important question. How could a violent, far-from-equilibrated fireball possibly reach thermal equilibrium, let alone within a timescale $\tau \lesssim 1$ fm [77]? The obvious answer is that it cannot. This inspired alternative frameworks to model heavy-ion collisions based on semiclassical kinetic theory, which is a standard tool in physics for addressing out-of-equilibrium statistical physics. These approaches have also shown notable success, particularly where hydrodynamics was historically expected to fail. The foremost model is A Multi-Phase Transport Model (AMPT) [78], a general purpose heavy-ion event generator. Conceptually, AMPT can be viewed as a fully contained model describing the entire heavy-ion collision. Therefore, there are four main stages to each event:

(1) Initial state of excited strings and minijet partons from HIJING,

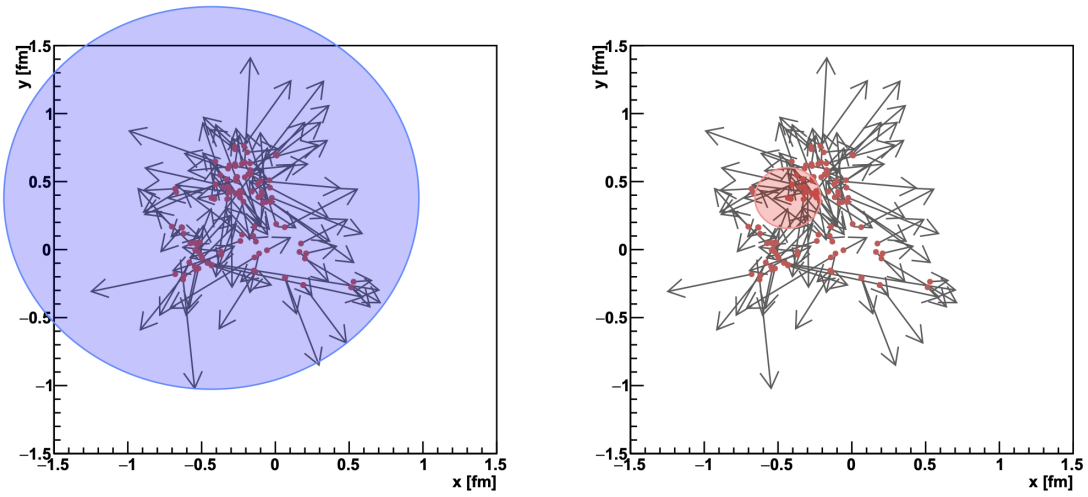
(2) Time-evolution of the fireball via Zhang's Parton Cascade (ZPC),

(3) Recombination of hadrons,

(4) A Relativistic Transport model for the expanding hadron gas (ART).

There are two main variations of AMPT. The default version feeds only the minijet partons to the cascade, which are then recombined with the excited strings at freeze-out and fed to a Lund string model for fragmentation. The string melting version attempts to introduce partonic degrees of freedom and also fragments the excited strings into partons, which are then fed to the cascade alongside the minijet partons. Finally, a coalescence model is used to rehadronize the partons instead of the Lund model.

The core feature of AMPT is the parton cascade, which assumes a coupled set of Boltzmann equations for each parton type. In the Monte Carlo, partons free stream in between scattering



(a) Formation length via the de Broglie wavelength

(e) Formation length via the uncertainty principle

Figure 1.21: Formation lengths of a 0.8 GeV parton in an AMPT event calculated via **(a)** the de Broglie wavelength and **(b)** the uncertainty principle. The formation length is shown as the colored circle. In each case, many additional partons are found within the formation length. Arrows indicate the initial parton momenta. Figure reproduced from Ref. [80].

events, which occur if partons pass within a distance $d \leq \sqrt{\sigma/\pi}$. The parton-parton cross sections σ are determined from pQCD by default, though the effect of Debye color-charge screening can also be considered. At freeze-out, partons are recombined into hadrons via coalescence, forming baryons and mesons by simply pairing up nearby partons. Since hadronization in vacuum is well-described by Lund string fragmentation, this can be viewed as an oversimplified but convenient model of recombination suitable for large heavy-ion systems where the typical parton energy is $\sim \mathcal{O}(T_0)$.

Counterintuitively, AMPT has been able to reproduce experimental data of momentum anisotropies even with small parton-parton cross sections $\sigma \sim 3$ mb. AMPT simulations were key in deducing that higher order anisotropy coefficients $v_{n\geq 3}$ were driven by fluctuations in the initial state of the heavy-ion collision [79]. Historically, alternative *Mach cone* theories supposed that wide angle gluon bremsstrahlung could induce higher order flows, but were ruled out by this finding. It therefore presents itself as a compelling, competing framework to treat the evolution of the QGP fireball.

There are some inconsistencies within AMPT, however. Namely, the mean free path in kinetic theory should be much longer than the formation time to ensure that on-shell parton formation

does not suffer from interference effects. This is not the case, as illustrated by Fig. 1.21. Based on either de Broglie wavelength or uncertainty principle arguments[19] , the formation length is clearly longer than the interparticle spacing. Numerically, it has been shown that the interparticle spacing is smaller than the mean free path in AMPT [80]. Therefore the $2 \to 2$ picture of parton-level scatterings in AMPT must be incomplete.

Cold Nuclear Models

What we have seen is that there is a distinction in approaches between Monte Carlo event generators in high-energy physics and heavy-ion physics. In high-energy physics, the main issues that generators like PYTHIA must solve pertain to description of the parton-parton construction, parton virtuality evolution, fragmentation, and so on. In heavy-ion physics, the event generator must inherit parameters for the high-energy generators and model the overall nucleus-nucleus collision. To bridge these gaps, other models like HIJING [81] and ANGANTYR [82] attempt to describe the heavy-ion event as a scaled-up hadronic collision. These models include phenomenological aspects to describe soft particle production (both perform final-state fragmentation using the Lund String Model) as well as hard-scattering processes as implemented in PYTHIA. These models are useful for providing a "good-enough" description of heavy-ion events.

HIJING has been publicly available for nearly 30 years, so we will focus on the somewhat newer ANGANTYR model as an example. In the context of small system flow observations, particularly in pp, it is clear that bare PYTHIA is an incomplete model of pp collisions. To incorporate nuclear structure effects, the PYTHIA authors extended the event generator to include the ANGANTYR model of heavy-ion collisions. Although fully built in the PYTHIA framework, ANGANTYR is a functionally distinct model of nuclear collisions.[20] On one hand, ANGANTYR can be viewed as an extrapolation of pp dynamics to p+A and A+A collisions. There are four main distinctions to vanilla PYTHIA:

[19] These approximations only differ by a factor of 2π.

[20] Notably, ANGANTYR predictions for some observables in pp differ from the baseline PYTHIA predictions, even using the same version.

(1) nPDF simulation. This is configurable and by default uses the EPS09 parametrization [83].

(2) Modeling the nuclear initial state via Glauber models. ANGANTYR uses the Glauber-Gribov color fluctuation model to generate initial nucleon positions.

(3) Understanding contribution to nucleon-nucleon collisions to the final state. ANGANTYR uses a model where soft particle production scales with N_{part} (rather than N_{coll}) [84].

(4) Implementation of hard-scattering processes in binary nucleon-nucleon collisions.

As an extension to PYTHIA, ANGANTYR makes minimal assumptions regarding possible QGP crossovers. It is therefore a useful theoretical tool for casting the heavy-ion collision into the context of more familiar models, and small systems in particular. While hydrodynamic, kinetic transport, and cold nuclear descriptions of the heavy-ion collision are interesting in their own right, for the purposes of this thesis they are useful tools for building a framework to describe jet quenching. The next Chapter will explore this phenomenon, plus current efforts to understand it, in detail.

Chapter 2

Jet Quenching

The evolution of the bulk medium with its hydrodynamic degrees of freedom can be starkly contrasted with that of partons emerging from a hard-scatter vertex into the violent QGP fireball. As these partons barrel through the hot, dense plasma, they strongly couple with the plethora of partons in their immediate environment and are subjected to energy-loss processes, a phenomenon referred to as *jet quenching*. Prior to interaction, the production of high-energy particles in hadronic collisions – typically $\mathcal{O}(10^1$–10^3 GeV) at the LHC – can be initially described by a power law tail at high momenta as predicted by pQCD. Medium-induced processes such as gluon bremsstrahlung divert the energy of the parton elsewhere, causing the parton to lose energy as it propagates. This leads to, for example, modification of final-state hadron spectra.

The possibility of energy-loss processes was first suggested by Bjorken in the 1980s [85]. He considered whether a hot nuclear environment created in a hadronic collision can induce asymmetry between initially balanced dijet pairs due to elastic scatterings between the emerging parton and resolved partons from the medium. Bjorken calculated the elastic scattering rate between hard-scattered partons in a gas of medium partons with fixed density. Averaging over successive scatterings, the energy lost per unit distance can be shown to be

$$-\left.\frac{dE}{dx}\right|_{\text{parton}} = \pi C_R \alpha_{\text{S}}^2 T^2 \left(1 + \frac{n_f}{6}\right) \log\left(\frac{q_{\text{max}}}{q_{\text{min}}}\right) \tag{2.1}$$

where C_R is the Casimir factor ($C_A = 3$ for gluons and $C_F = 4/3$ for quarks), n_f is the number of flavors in the QGP (i.e. ~ 3)[1] , $q_{\text{max}} \backsimeq 4ET$, and $q_{\text{min}} \backsimeq m_D^2 = 4\pi\alpha_{\text{S}}\left(1 + \frac{n_f}{6}\right) T^2$ – the Debye

[1] Although there are 6 quark flavors in QCD, the charm, bottom, and top quark masses are much larger than the

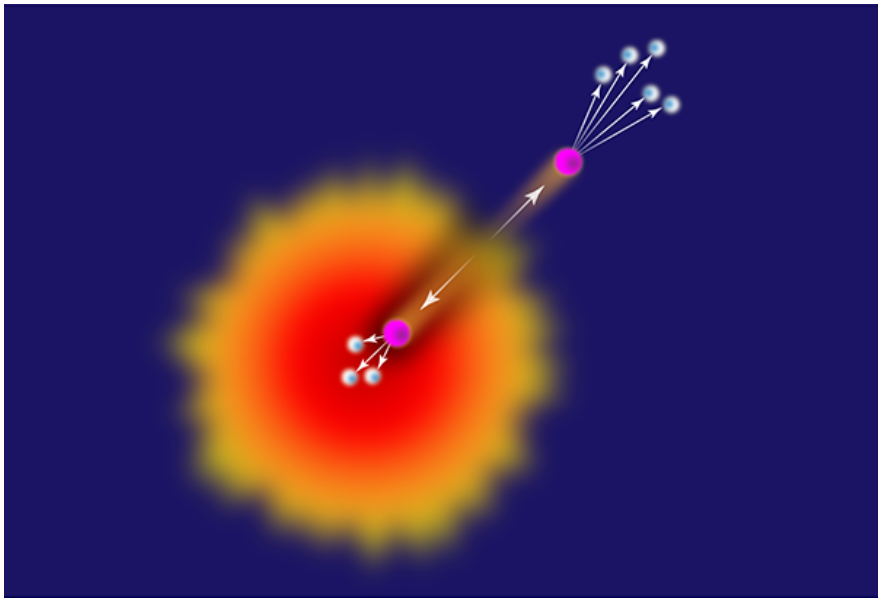


Figure 2.1: Illustration of jet quenching in a heavy-ion collision. One jet escapes into the vacuum, while its partner is forced to traverse the hot QGP. Figure reproduced from Ref. [88].

mass in a QCD plasma – are (ambiguous) UV and infrared cutoffs, respectively [85–87]. Bjorken originally predicted from this calculation that a $\sim$ 20 GeV parton could lose well over 50% of its momentum by this mechanism.[2] Consequently scatterings between partons was expected to lead to a strong signature on the production rate of jets in heavy-ion collisions, and dubbed "jet quenching". In modern parlance, jet quenching typically refers to any plasma-induced modification to jet properties, rather than just the manifestation of partonic energy loss.

In this chapter, we review experimental signatures of these modifications. There is a rich history of theoretical approaches to quenching rates and effects from the ground-up in QCD; we will explore some of these here. The primary goal here is to cover the main aspects of quenching that are relevant to the measurements presented in this thesis. Topics such as the quenching of charm and bottom quarks or quenching at very large-Q^2 are not discussed in detail.

medium temperature and therefore they do not reach chemical equilibrium in the plasma.

[2] An unpublished erratum revealed the energy loss was actually at the level of $\lesssim 1$ GeV/fm. The original calculation is important however for a more complete historical context of jet quenching.

2.1 Phenomenological Aspects of Quenching

Predictions for jet quenching from theory differ substantially in their methodology, with a variety of expansions, approximate theories, and medium couplings utilized. There are a number of common denominators, however, the majority of which are based in experimental findings. In this section, we outline the critical phenomenology of jet quenching that must be incorporated in theory. These are numerous; here we examine some of the main ones, including geometrical effects, flavor dependence, and structure modification.

Geometrical Effects

Quintessential to jet quenching is the dependence of energy loss on collision geometry. The geometry of heavy-ion collisions is well understood to determine the size and orientation of the fireball, and coupled to hydrodynamics, the two have been successful at explaining collective behavior of particles at low to moderate momenta [89]. Geometry has also been identified in experiment as a critical phenomenological component to partonic energy loss. The degree of jet quenching can depend on geometry in a few ways, including via total transverse area of the fireball, the initial positions and orientations of hard scatterings, and medium evolution effects. Here we highlight each of these dependencies as inferred from experimental measurements.

One of the first signals of jet quenching in LHC collisions was from the observation of momentum asymmetry in dijet pairs by the ATLAS and CMS experiments [90–92]. Typically this is quantified by the distribution of either A_J or x_J for dijet pairs:

$$A_J \equiv \frac{p_{\mathrm{T}1} - p_{\mathrm{T}2}}{p_{\mathrm{T}1} + p_{\mathrm{T}2}} \geq 0 \quad \text{or} \quad x_J \equiv \frac{p_{\mathrm{T}2}}{p_{\mathrm{T}1}} \leq 1. \tag{2.2}$$

where $p_{\mathrm{T}1,2}$ are the p_{T} of the leading and subleading jets, respectively. An illustration of an event with a large asymmetry measured by ATLAS can be seen in Fig. 2.2. The asymmetry distributions are directly compared for dijets in vacuum (pp collisions) versus medium (Pb+Pb collisions). The distribution in peripheral Pb+Pb is found to roughly match the vacuum baseline strongly favoring little to no quenching effect. In central collisions however, the observables become substantially

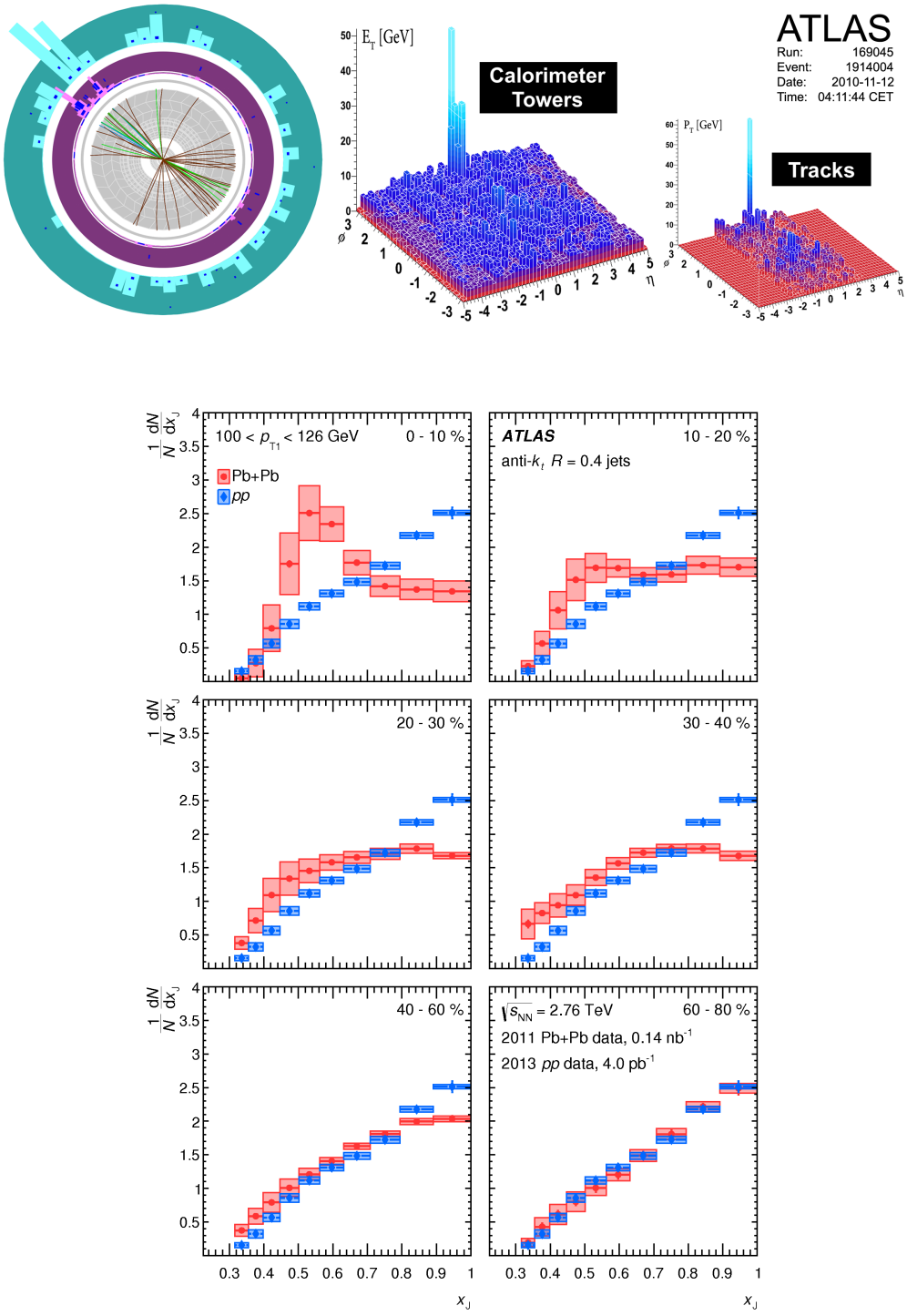
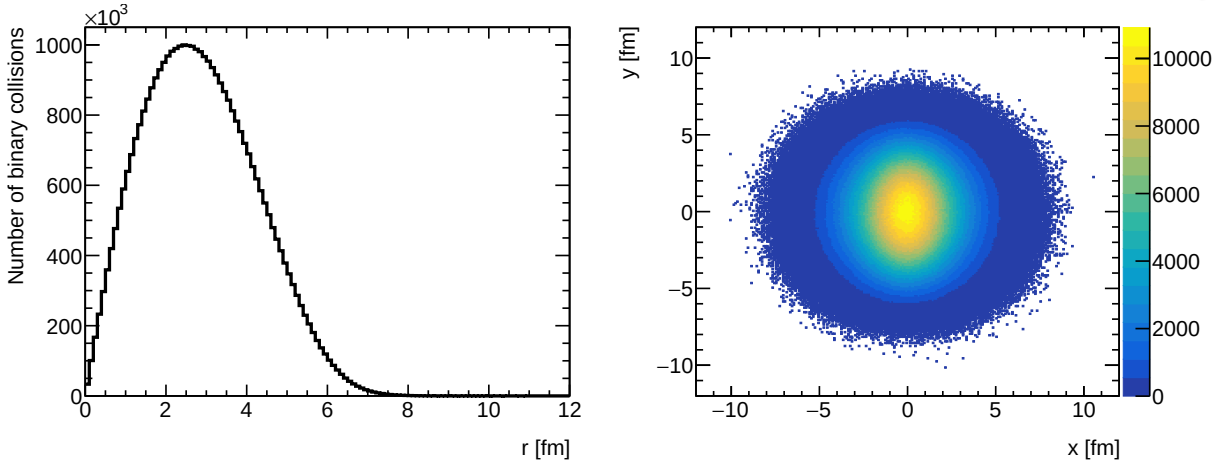


Figure 2.2: Top: Event display of a highly asymmetric dijet pair measured by ATLAS. A single jet is observed with $E_{\mathrm{T}} > 100\,\mathrm{GeV}$ with no recoil jet partner. Bottom: Distributions of the dijet asymmetry in pp and various centralities of Pb+Pb collisions for events with leading jet $100 < p_{\mathrm{T}}^{1} < 126$ GeV. Figures reproduced from Refs. [90] and [93], respectively.



(a) Binary collisions versus radial coordinate **(b)** Binary collisions in the xy-plane

Figure 2.3: Distribution of binary collisions in **(a)** radius and **(b)** the transverse plane in Pb+Pb collisions as calculated in Monte Carlo Glauber.

shifted to more asymmetric event topologies; this corresponds to the peak at lower values of x_J in the figure. This not only indicates a quenching effect, it shows that one dijet partner experiences a much more substantial quenching than the other.

There is a satisfyingly simple explanation, which invokes the geometry of the collision. The Glauber model asserts that jet-producing processes occur in hard scatters between colliding nucleons. Therefore the creation point of the jet partons is distributed according the positions of binary nucleon-nucleon collisions. Consider a central collision with impact parameter $b = 0$, and therefore a circular geometry, such as the collision illustrated in Fig. 2.1. For a distance, the transverse positions of nucleons will scale with r, out to the edge of the Woods-Saxon distribution of the nuclei. Consequently most binary collisions will occur further away from the core of the plasma, as illustrated in Fig. 2.3. Likewise, most of the jets are produced in this region. As the scattering occurs near immediately, the azimuthal angle can be assumed to be uniformly distributed within the nuclear collision.[3] This leads to variety of event topologies, including ones where one jet is directed at the plasma and its partner is pointed outside of it. In this situation, one jet escapes the plasma nearly unimpeded while the partner is forced to traverse the plasma, losing energy.

[3] By causality, other regions in the nuclear collision cannot affect the hard scattering due to the short timescale.

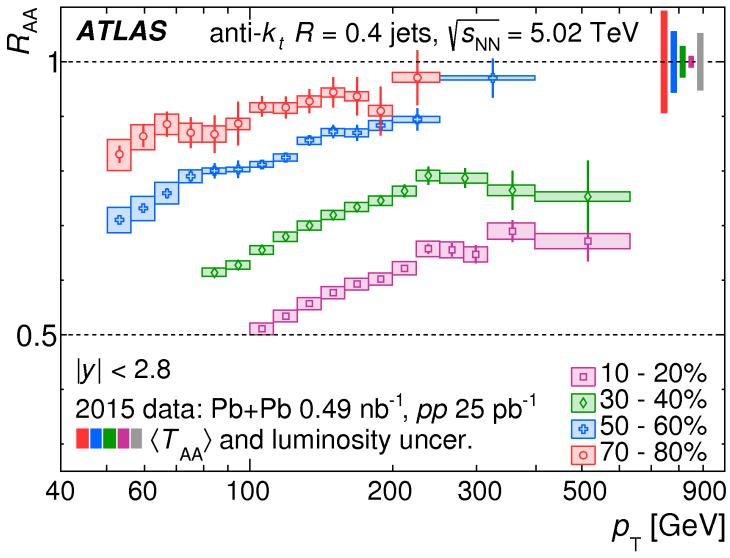


Figure 2.4: The nuclear modification factor R_{AA} of jets in 5.02 TeV Pb+Pb collisions of various centralities, as measured by ATLAS. Figure reproduced from Ref. [94].

Prior to energy loss, both jets have similar p_{T} simply due to conservation of transverse momentum, $p_{\mathrm{T}1} \approx p_{\mathrm{T}2}$. After energy loss, $p_{\mathrm{T}1} > p_{\mathrm{T}2}$, thus explaining the observed asymmetry. The quintessential lesson from these measurements is not that energy loss occurs (though it does), rather that the initial position and orientation of the parton within the fireball plays a significant role in how much energy is lost.

The most common *absolute* metric of quenching is the nuclear modification factor R_{AA}, which quantifies the suppression of the invariant yield relative to vacuum

$$R_{\mathrm{AA}} = \frac{1}{\langle N_{\mathrm{coll}} \rangle} \frac{d^2 N_{\mathrm{medium}}/dp_{\mathrm{T}}dy}{d^2 N_{\mathrm{vacuum}}/dp_{\mathrm{T}}dy}. \tag{2.3}$$

Jets in vacuum are produced according to a power law in p_{T}; consequently any change in momentum Δp_{T} is magnified in the spectrum due to the exponent. Consequently R_{AA} is highly sensitive to jet quenching, and measures the *absolute* quenching rather than the *relative* quenching, which the dijet asymmetry is sensitive to. Both ATLAS and CMS have measured R_{AA} for inclusive jets [94–96]; CMS has also now measured R_{AA} for jets of large radii [97]. The latest measurement of the jet R_{AA} in Pb+Pb collisions by ATLAS [94] is shown in Fig. 2.4. The p_{T} dependence of R_{AA}

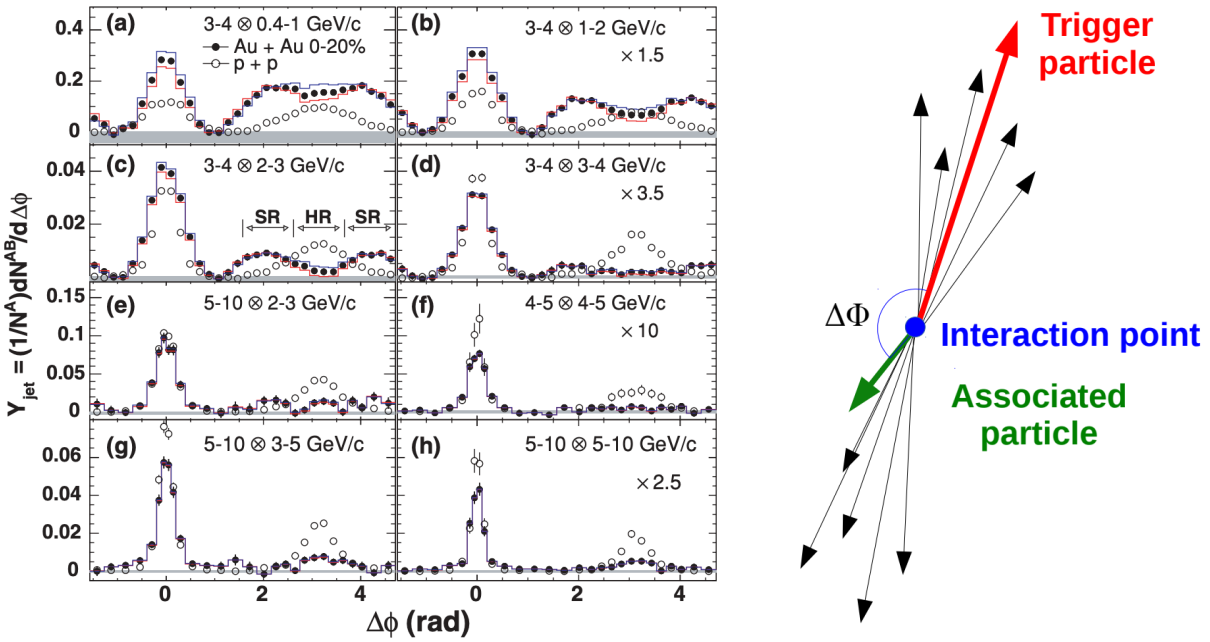


Figure 2.5: Left: Per-trigger associated particle yields measured by PHENIX in 0–20% Au+Au and pp. Each panel shows a different trigger particle ⊗ associated particle p_{T} combination. Solid histograms indicate background normalization uncertainties. Right: Schematic illustration of the per-trigger associated yield measurement in a dijet system. Figures reproduced from Refs. [98] and [99], respectively.

is similar between the different Pb+Pb centralities. However the magnitude of the suppression grows with centrality – jets tend to be more suppressed in collisions with larger nuclear overlap. This demonstrates that the initial transverse area of the fireball also impacts the amount of jet quenching. In other words, larger collision overlap areas translate to longer path lengths for partons in the medium, resulting in a larger quenching effect.

Although this thesis focuses on LHC measurements, jet quenching has a rich history starting with the RHIC program in the 2000's. Full reconstructed jet measurements have only recently been made with the LHC experiments, however measurements of hadron yields are similarly sensitive to jet quenching physics and can be made with more limited detectors. Conditional hadron yields – such as the per-trigger charged-particle yield Y_{ab} shown in Fig. 2.5 – are particularly sensitive to a convolution between quenching and fragmentation. These measurements typically have strong

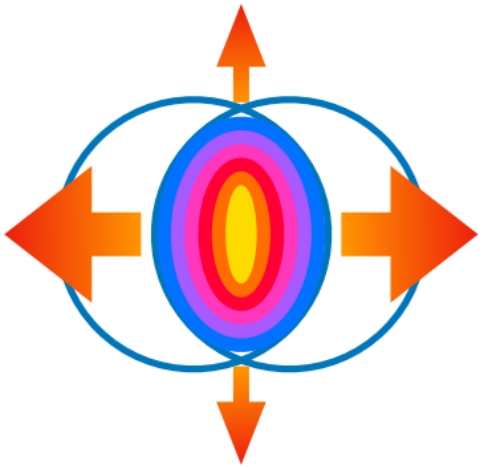


Figure 2.6: Illustration of differential energy loss within an elliptical QGP droplet. In this figure, jet quenching is greater along the semi-major axis of the ellipse. Figure reproduced from Ref. [100].

peaks at $\Delta\phi = 0$ and π as the most frequent trigger-associated pairings occur between particles in the same jet or a dijet system. However in central Au+Au collisions we observe that the away-side peak at π is depressed relative to the pp baseline. This is particularly noticeable in the bottom panels (g) and (h), where the particles have relatively high p_{T} values > 3 GeV, and therefore are much more likely to be the fragments of a parton traversing the plasma.

Lastly, the dynamics of the medium can also affect the degree of quenching. Though typically referred to as a plasma, in reality the hot nuclear matter created in heavy-ion collisions is ripping itself apart at $\sim$ 10–60% of the speed of light. Immense pressure gradients in different directions translate position-space anisotropies to momentum-space anisotropies in the final state. Such anisotropies have also been observed for jet production [101–103]. Hydrodynamic models describe correlations in long-wavelength modes; but high-energy, jet-producing partons have too short of a wavelength to truly be in a regime where hydrodynamics applies. For large heavy-ion systems, this effect can be explained by differential energy loss.

Consider, for simplicity, a heavy-ion collision with a perfectly elliptical geometry, and a dijet produced at the center of the plasma, such as in Fig. 2.6. Supposing that jets traveling along the semi-major and semi-minor axes of the ellipse lose different amounts of energy, then jet

production will be enhanced relative to the ϕ-averaged rate along one direction, and reduced along the perpendicular direction. In other words, the jet suppression would become correlated with the relative angle between the ellipse orientation (the *event plane*) and the jet direction. There are a variety of mechanisms for differential energy-loss phenomena: path-length differences along the semi-major and semi-minor axes, differential pressure gradients which could even apply a slight boost the jet energies, or differences in integrals of quantities such as energy density along the parton trajectory. For differential energy loss to occur in theory, models must take into account the spatial evolution of the medium.

Flavor Dependence

Quenched jets can arise from the fragmentation of three primary types of partons: light quarks (u, d, s), gluons, and heavy quarks (c, b). Quarks are typically considered separately from gluons due to differences in color charge – quarks only carry one color while gluons, in the adjoint representation, carry two. Therefore we expect the jet-quenching phenomenon to manifest differently for quarks versus gluons via the Casimir factor. The further distinction between heavy quarks and light quarks is important for two reasons. The first is that heavy quarks – defined by $m_{\mathrm{q}} \gtrsim T$ – cannot be chemically equilibrated. A simple argument is that their Boltzmann factor is small: $e^{-m_{\mathrm{q}}/T} \ll 1$. Heavy quark modes are therefore not found in the plasma, and consequently there is no medium-related strong interaction that alters heavy flavor quantum numbers. For sufficiently short periods of time $\tau \lesssim 100\,\mu$m (the weak decay timescale), the number of heavy flavor quarks is conserved. This can be contrasted with light quarks, which due to their near-zero masses are produced ubiquitously in the fireball. This enables effective flavor-changing processes for hard partons, such as ones seen in Fig. 2.7. In these diagrams, the identity of the parton carrying the highest momentum changes. For example a light quark can annihilate with an antiquark parton donated by the medium; after the collision, the momentum of the quark is carried by gluons. Because the medium cannot contribute heavy quarks, the flavor identity of heavy quarks cannot be easily altered.

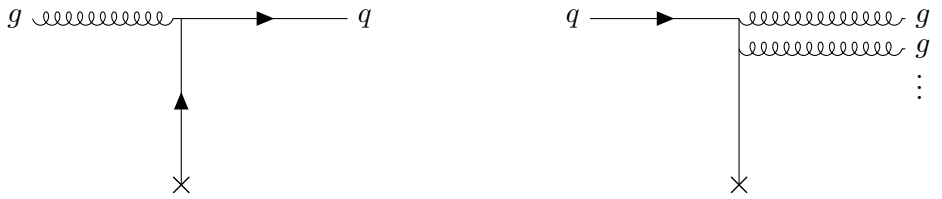


Figure 2.7: Examples of medium-induced flavor-changing Feynman diagrams. On the left, a gluon gives a hard kick to a medium-resolved quark. On the right, a light quark annihilates with another same-flavor quark, radiating gluon(s). Heavy quarks do not generally partake in such processes.

Second is that energy-loss mechanisms for light quarks operate in the regime $m \ll p_{\mathrm{T}}$. Effects that scale with m/p_{T} are more prevalent for heavy quarks. Notably this includes the dead-cone effect, which predicts a suppression of the gluon spectrum within a cone parameterized by angle $\theta \sim m/E$ around the quark direction of motion in vacuum QCD [104]. This has been a longstanding prediction by QCD which was only recently directly detected by the ALICE collaboration, who used iterative declustering methods to study the structure of charm-induced jets [105]. Medium effects could also, in principle, depend on the quark mass at p_{T} scales $p_{\mathrm{T}} \ll m$.

Extracting flavor dependence to yields is typically difficult in experiment due to the parent parton identity becoming smeared or even lost within the jet. b quark-initiated jets can be tagged by identifying a displaced vertex, but this requires high vertex resolution within the core of a jet. c-initiated jets can also be identified this way, but are more difficult due to the shorter path length of c quarks before their decay. Recently, advances have been made by exploiting non-hadronic probes which are less sensitive to detector resolution effects. For example, studies of heavy flavor mesons and their semileptonic decays have offered insight to the mass dependence of quenching effects in the QGP. In particular, we note that heavy flavor suppression rates have been observed to differ between charm and bottom at low-p_{T} where $p_{\mathrm{T}} \gtrsim m$ [106]. At high-p_{T}, the nuclear modification factors converge onto a common curve, possibly due to mass-dependent effects becoming suppressed by powers of m/p_{T}. This indicates at least that some role is played by the parton mass during interactions with the medium.

Scatterings off of color-neutral bosons are also frequently used to offer complementary insight

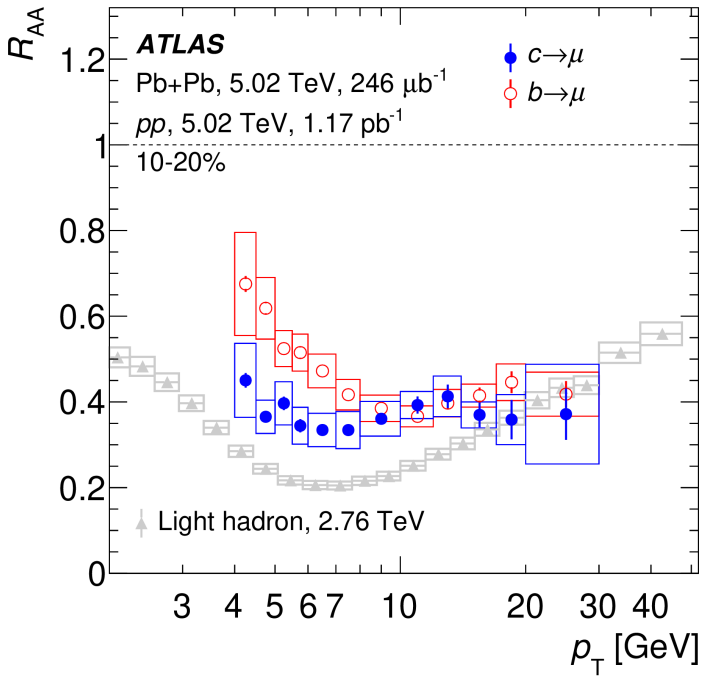


Figure 2.8: Comparison of nuclear modification factors for inclusive (light-dominated), charm, and bottom hadrons. Figure reproduced from Ref. [106].

to the differences in quenching between light quarks and gluons. In events tagged by a photon or a Z boson, the flavor of the emergent high-energy parton is still smeared by the subsequent jet, but the probability that a jet was created by the shower of any given flavor is different. By measuring the average quenching over an ensemble of scattering events with versus without a boson tag, separate quark and gluon energy-loss components can be parametrically extracted. Although no direct evidence of a difference between quark and gluon energy loss has yet been observed, current efforts are focusing on identifying this flavor dependence to jet quenching [107, 108], and theoretically driven models of quenching already account for this by feeding different admixtures of hard-scattering processes to their energy-loss calculations.

Modification to Jet Structure

The last manifestation of jet quenching we will discuss is the modification to jet structure. In experiment, the fragmentation function $D_{i\to h}(z)$ for hadron h in a jet initiated by parton i is defined via the probability to observe a hadron in a jet carrying momentum fraction $z = p_{\mathrm{T}}^{h}/p_{\mathrm{T}}^{\mathrm{jet}}$.[4] Explicitly it is given as

$$D_{\mathrm{jet}\to h}(z) = \frac{1}{N_{\mathrm{jet}}}\frac{dN_h}{dz}. \tag{2.4}$$

Studies of the fragmentation function thus provide a multi-scale probe of jet evolution. Production of low-p_{T} hadrons is dominated by nonperturbative, soft QCD processes, while high-p_{T} hadrons are sensitive to the early, highly virtual parton shower and can be described perturbatively in powers of α_{S}, with infrared cutoffs imposed at a scale μ.[5]

Historically the fragmentation function – particularly quark fragmentation functions – were studied extensively in e^+e^- collisions [109]. This is because the $e^+e^- \to hX$ cross section at lowest order is completely independent of parton distribution functions; it only depends on the fragmentation:

$$\frac{d\sigma_{e^+e^-\to hX}}{dx} = \sum_q D_{\mathrm{q}\to\mathrm{h}}(x/z)\otimes C_{\mathrm{q}}(z) + \mathrm{h.o.}, \tag{2.5}$$

where C_{q} encapsulates the microscopic cross section for $e^+e^- \to q\bar{q}$.

In heavy-ion collisions, jet-fragmentation functions are known to be modified relative to the vacuum. This is exemplified by Fig. 2.9, which shows the ratio of the fragmentation functions in central Pb+Pb to pp collisions, as measured by ATLAS, for fragments of jets at a particular p_{T} in the final state. We see that, typically, jets of a given total momentum are composed of hadrons with softer p_{T} in heavy ions. Hadrons with modest z are heavily suppressed and must be replaced by low p_{T} particles (since they are constrained by $\sum_h z_h = 1$). This is colloquially referred to as the feed-down or low-p_{T} migration effect. Finally, hadrons with high z values are observed to be

[4] Some measurements project the momentum onto the jet axis, $z_{\parallel} = |\vec{p}_h \cdot \vec{p}_{\mathrm{jet}}|/|\vec{p}_{\mathrm{jet}}|^2$, but for simplicity we focus on the non-projective variable. Other times, the fragmentation function is defined as a function of the particle p_{T}^{h} for a given type of jet.

[5] Recall from Chapter 1 that typically μ is chosen as the scattering hardness scale, $\mu^2 = Q^2$.

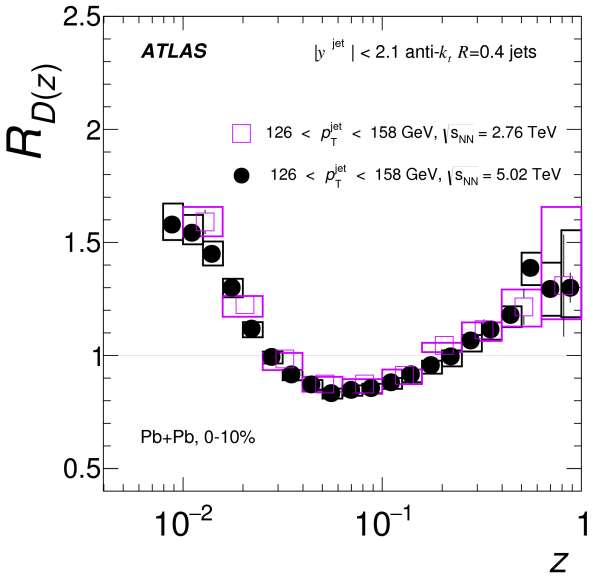


Figure 2.9: Ratio of jet to charged-hadron fragmentation functions $R_{D(z)}$ between 0–10% central Pb+Pb and pp collisions as measured by ATLAS at both 2.76 TeV [110] and 5.02 TeV [111], for jets with $p_{\mathrm{T}} = 126$–158 GeV. Figure reproduced from Ref. [111].

enhanced in Pb+Pb.

Previous measurements provide no satisfying explanation for the high-z enhancement. One possibility is that it represents an anti-selection effect whereby triggering on the presence of a jet biases the observed quenching effect. Essentially, this argument states that the high-z enhancement is also consequence of the $\sum z_h = 1$ constraint, which renormalizes the entire spectrum. Because the hadron spectrum is approximately a power law, only a small absolute increase in high-z particles is needed to enforce the constraint, while still appearing as a large relative effect. Considering that jets experiencing a substantial quenching effect will have a different momentum in the final state than what they started with, the momentum fraction variable can be misinterpreted because it does not correspond to the momentum imparted onto the hadron from the initial hard scattering. In vacuum, $\vec{p}_{\mathrm{jet}} \approx \vec{p}_{\mathrm{parton}}$ and thus the observed z refers to the fraction of the hadron carried by the initial parton.[6] In medium, typically $|\vec{p}_{\mathrm{jet}}| < |\vec{p}_{\mathrm{parton}}|$ due to quenching, and so the observed z solely refers to the fraction of the momentum after quenching. This disconnect can lead

[6] For sufficiently large jet radii $R \sim 1.0$, this is true, though out-of-cone radiation even in vacuum all-but-guarantees $|\vec{p}_{\mathrm{jet}}| \lesssim |\vec{p}_{\mathrm{parton}}|$. However, the jet is still our best proxy for its initial parton.

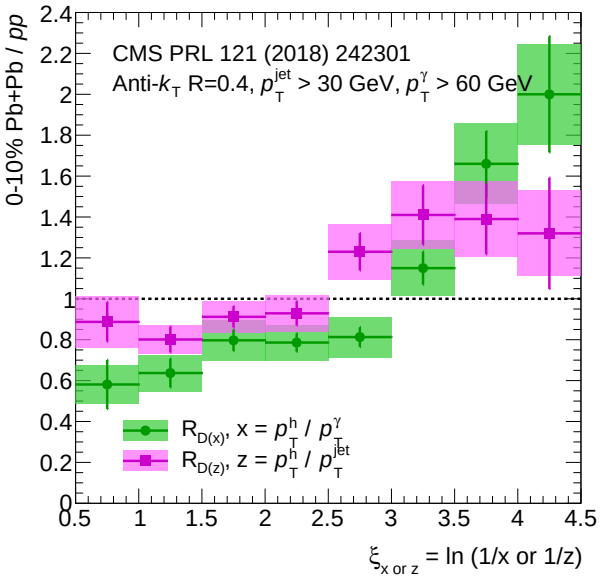


Figure 2.10: The ratio of jet-fragmentation patterns in 0–10% Pb+Pb divided by that in pp collisions in events tagged by the presence of a high-p_{T} photon as measured by CMS is shown [112]. The x-axis represents either the momentum balance between a charged hadron and the photon ($x = p_{\mathrm{T}}^{h}/p_{\mathrm{T}}^{\gamma}$) or the hadron and its associated jet ($z = p_{\mathrm{T}}^{h}/p_{\mathrm{T}}^{\mathrm{jet}}$).

to results where modification to the vacuum fragmentation is convolved with energy-loss effects, causing ambiguous interpretation. For this reason, the fragmentation is often studied as a function of parton p_{T} as well, though, jet-selection bias persists.

In addition to their usefulness in extracting flavor dependencies, electroweak probes can offer insight to selection biases as well. Both ATLAS and CMS have explored the fragmentation of jets in events triggered by high-p_{T} photons correlated with hard-parton production [112, 113]. In particular, CMS has studied the fragmentation as a function of the hadron-photon balance $x = p_{\mathrm{T}}^{h}/p_{\mathrm{T}}^{\gamma}$. In the leading order picture that high-p_{T} photon production is dominantly produced in conjunction with a single high-p_{T} parton (no hard-gluon splitting, multiple scattering, etc., occurs), then $x \approx p_{\mathrm{T}}^{h}/p_{\mathrm{T}}^{\mathrm{parton}}$ because $p_{\mathrm{T}}^{\gamma} \approx p_{\mathrm{T}}^{\mathrm{parton}}$ and so the medium-vacuum comparison between $D_{\gamma+\mathrm{jet}\to h}(x)$ distributions avoids convolution with the quenching effect. Compare for example the central Pb+Pb-to-pp ratio of fragmentation functions $D_{\gamma+\mathrm{jet}\to h}(z)$ and $D_{\gamma+\mathrm{jet}\to h}(x)$, as shown in Fig. 2.10. At the highest reported values $x \sim 0.35$–0.6 (the left side of the figure) a substantial

suppression of charged particles is observed, rather than an excess as seen for z values in the same range (see Fig. 2.9 or Refs. [111, 113]). At the lowest values $x \sim 0.01$–0.02 (the right side of the figure), an even greater excess is observed than for similar z values as well. There is a clearer dependence of the fragmentation modification on x rather than z, illustrating this effect. However, the measurements by CMS [112] and ATLAS [113] are still limited by requiring that hadrons fall within the cone of a reconstructed jet meeting selection cuts. This is expected to maintain some degree of bias on the observed fragmentation pattern by imposing the constraint $\sum_h p_{\mathrm{T}}^h > p_{\mathrm{T}}^{\mathrm{min}}$ for some $p_{\mathrm{T}}^{\mathrm{min}}$. One of the goals of this thesis is to explore this selection effect by relaxing the explicit jet requirement.

In summary there are several aspects to jet quenching that have been observed or are hypothesized and currently being tested. This includes

(1) dependence on the parton initial position and momentum within the plasma, as well as properties of the hard scattering and the dynamical medium evolution,

(2) differences in the amount of quenching for different parton species, due to differences in color charges and masses governing interactions with the medium, and

(3) modification to parton showering, observed as fragmentation function modification.

In the following section, we will investigate how these effects manifest in theoretical frameworks.

2.2 Medium-Induced Energy Loss in pQCD

Equipped with an understanding of how jet quenching looks in experiment, next we turn to the current theoretical understanding. In a perturbative picture, there are two microscopic mechanisms for partons to lose energy in the plasma. The first is by elastic $n \to n$ partonic scatterings, where high-momentum incident partons scatter off other resolved medium partons. Such partons typically have energies of $\mathcal{O}(T)$, and so at high energies the incident parton redistributes its energy to the medium parton, thereby losing energy in the collision. Typically this mechanism is called

collisional energy loss, and the lost energy is dominated by soft scatterings due to the low energy of the medium parton. The second is inelastic $n \to m$ scatterings. The key inelastic process is the generalization of bremsstrahlung to the QGP, whereby the hard parton is induced by color charges within the medium to emit gluons at an enhanced rate over the vacuum. Unlike QED, where photons cannot radiate at tree-level, gluons self-interact and therefore radiation is not restricted to the fermions. In the hot medium, the probability of a gluon emission is enhanced over the vacuum, causing a hard parton to gradually lose energy due to this "braking radiation". For this reason, these are typically known as *radiative* energy-loss processes. The goal of this section is to study the spectrum of induced gluon radiations in the plasma from formal calculations in pQCD.

First let us recap what happens in a similar QED scenario. For sufficiently high energies, it is understood that bremsstrahlung dominates electron energy loss in matter. Electrons in the regime $E \gg \alpha Z^{-1/3} m_e$ lose energy to bremsstrahlung following the Bethe-Heitler (BH) formula [114]

$$-\left.\frac{dE}{dx}\right|_{\rm BH} \sim \frac{E}{L}, \tag{2.6}$$

where $L \propto 1/N$ is the length scale, and is inversely proportional to the matter number density (e.g. number of atoms per cm^3). The total lost energy ΔE at a single scattering point can be classically computed from the induced-radiation spectrum $I(q_\perp)$,

$$-\Delta E_{\rm rad} = \int \omega \frac{dI}{d\omega dq_\perp^2} d\omega d^2 q_\perp. \tag{2.7}$$

The Opacity Expansion

The QCD analog was first analytically studied in the BDMPS-Z formalism [115–121] for the regime $T \ll \omega \ll E_{\rm parton}$. The gluon bremsstrahlung spectrum per unit distance for soft radiations ($\omega \ll E_{\rm parton}$) can be derived as in [119]; the limiting behavior is given by [122] (dropping $\mathcal{O}(1)$ numerical factors)

$$\left.\omega \frac{dI}{d\omega dz}\right|_{\rm BDMPS-Z} \sim \alpha_{\rm S} \times \begin{cases} \frac{1}{\lambda} & \omega \lesssim \omega_{\rm BH} \\ \frac{1}{\lambda}\sqrt{\frac{\omega_{\rm BH}}{\omega}} & \omega_{\rm BH} \lesssim \omega \lesssim \omega_{\rm c} \\ \frac{1}{L}\left(\frac{\omega_{\rm c}}{\omega}\right)^2 & \omega_{\rm c} \lesssim \omega \ll E_{\rm parton} \end{cases} \tag{2.8}$$

where $L = N\lambda$ relates the mean free path λ and the number of scatterings N (also known as the opacity) to the medium size L, $\omega_{\rm BH} \sim \lambda m_D^2$ represents the frequency scale for the BH regime and $\omega_{\rm c}$ the hard factorization scale. In the BH regime, the radiation is essentially viewed as a sequence of independent, incoherent scatterings. These scatterings can thus only constructively interfere to produce more radiation. In the high densities of the QGP, successive scatterings eventually begin to destructively interfere at sufficiently high frequencies, with a net effect that the hard radiation gluon spectrum becomes suppressed relative to the BH prediction by a factor $\sqrt{\omega_{\rm BH}/\omega}$. This is the Landau-Pomeranchuk-Migdal (LPM) regime, which also occurs in QED but in the soft part of the spectrum ($\omega dI/d\omega \sim \sqrt{\omega}$) [123]. In QCD, the suppression occurs above a critical frequency $\omega_{\rm c}$ where the gluons can pick up a phase $\Delta\phi \sim \mathcal{O}(1)$ between successive scatterings,

$$\Delta\phi = \left\langle \frac{\lambda}{t_{\rm coh}} \right\rangle = \left\langle \frac{\lambda}{k^2}\omega \right\rangle \equiv \frac{\hat{q}L^2}{2\omega_{\rm c}} \sim 1. \tag{2.9}$$

This relation generates a characteristic scale $\hat{q} = 2\omega_c/L^2 \sim m_D^2/\lambda$ known as the *transport coefficient* of the medium. Conceptually, $\hat{q} = d\left\langle q_\perp^2 \right\rangle/dt$ describes the tranverse momentum imparted upon the parton per unit time (length) by this mechanism [124]. It can be simply imagined as a model parameter that encapsulates the microscopic properties of the medium, and could be fitted to data. Finally at the highest frequencies, the radiation formation time is maximal and the spectrum becomes even more suppressed by $(\omega_{\rm c}/\omega)^2$ [122]. The BDMPS-Z spectrum can be plugged back into Eq. 2.7 to obtain the lost energy; we do not dive into these details here, but the calculation ends with the remarkable result

$$-\Delta E_{\rm BDMPS-Z} \propto L^2, \tag{2.10}$$

the implication being that the energy loss scales with the plasma size, squared. Numerically, the authors found that the radiation emitted by a high-energy parton in a $T = 250\,\text{MeV}$ plasma is $\mathcal{O}\,(10\,\text{GeV})$, indicating that in addition to collisional losses, induced radiations should also cause a substantial energy-loss effect [119].

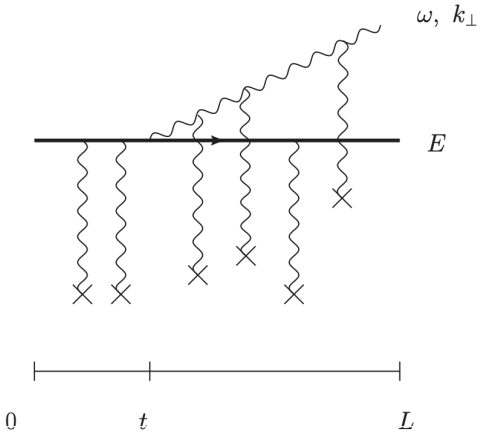


Figure 2.11: A Feynman diagram for medium-induced gluon bremsstrahlung in the multiple soft scattering approximation (MSSA) limit. The propagating parton (illustrated here as a quark) has energy $E \gg \omega \gg k_\perp$. Figure reproduced from Ref. [124].

The BDMPS-Z approach belongs to a broader set of calculations known as opacity expansions which assume very different numbers of scatterings (induced-gluon radiations) [125, 126]. The BDMPS-Z description corresponds to the *multiple soft-scattering approximation* (MSSA), which is illustrated in Fig. 2.11. In this limit, the medium is assumed to be highly dense, $\lambda \ll L$ or equivalently $N \gg 1$, though it breaks down for hard gluon radiation $\omega \lesssim E_{\text{parton}}$. In this case, the medium is essentially opaque to strongly interacting partons. There is also a reverse approximation known as the *single hard-scattering approximation* (SHSA), where the medium is assumed to be dilute or transparent, $\lambda \sim L$ or $N \sim 1$. Similar to how the BDMPS-Z approach examines the MSSA side of the spectrum, other approaches such as that by Gyulassy, Levai, and Vitev [127] and Djordjevic and Gyulassy [128] (DGLV) investigate the SHSA regime.

In the DGLV treatment, there are at most a few (generally ~ 1) emissions which occur and therefore $\lambda \sim L$. The interpretation is that all of the radiation occurs in a single scattering event, similar to how the hardest scatterings in the entire collision occur altogether at $t \sim 0$ (rather than dispersed over the entire medium evolution). The limiting behavior is obtained for $N = 1$ (again

dropping $\mathcal{O}(1)$ numerical factors)

$$\omega \frac{dI}{d\omega}\Big|_{\mathrm{DGLV}} \sim \alpha_{\mathrm{S}} \times \begin{cases} \frac{\omega_{\mathrm{c}}}{\omega} & \omega \gg \omega_{\mathrm{c}} \\ \log \frac{\omega_{\mathrm{c}}}{\omega} & \omega \ll \omega_{\mathrm{c}} \end{cases} . \tag{2.11}$$

Energy loss is dominated by the $\omega \gg \omega_c$ component and leads to the same result from the BDMPS-Z approach, i.e. $-\Delta E \propto L^2$. That these approaches find the same system size dependence to the radiative energy loss is rather remarkable, and strongly suggests that collisional energy loss – which scales with L – is subdominant in large systems, for light quarks and gluons.

There has also been work to obtain predictions in the intermediate regime between the MSSA and SHSA limits. Work by Armesto, Salgado, and Wiedemann (ASW) generalizes the opacity expansion within a path integral formalism which can describe both the MSSA and SHSA limits [125, 129, 130]. The BDMPS-Z and DGLV results are recovered in each case, respectively. Moreover, the ASW calculations can be numerically applied with so-called "quenching weights" that simulate the probability of a parton losing additional energy dE. These weights are applied for example in the JEWEL event generator, which we will discuss shortly.

Notably missing from these predictions, however, are thermodynamic elements. The temperature only enters indirectly through the Debye mass m_D and presumably the mean free path λ. Naïvely, the temperature or energy density should relate to the rate of collisions as well as induced radiations. The Arnold-Moore-Yaffe (AMY) approach to energy loss [70, 131–134] encapsulates this by providing a full thermal field theory (TQFT) description of the quark and gluon fields in the plasma. While the previous calculations correctly address bremsstrahlung radiation at gluon frequencies $T \ll \omega \ll E_{\mathrm{parton}}$, this calculation extends to all frequencies $\omega > T$ [133]. Studies on the impact to hadron spectra applying the AMY gluon spectrum (which can be found in Eq. 5 in Ref. [133]) also explicitly allow for collisional losses. The elastic collisions are taken to be soft with leading-order cross section

$$\frac{d\sigma_{\mathrm{soft}}}{dq_\perp^2} = \frac{C_{\mathrm{R}}\alpha_{\mathrm{S}}}{\pi} \frac{m_D^2}{q_\perp^2\left(q_\perp^2 + m_D^2\right)} \tag{2.12}$$

which can be combined with the mean free path to establish a mean scattering rate $d\Gamma/dtdq_\perp^2$. The

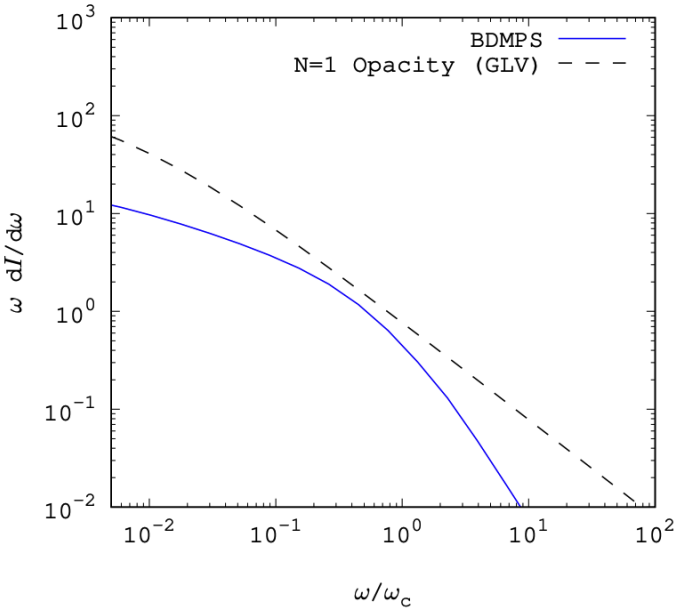


Figure 2.12: The spectrum of medium-induced gluon radiations is calculated in the BDMPS-Z and DGLV limits of the opacity expansion. Figure reproduced from Ref. [124].

clear advantages with this approach are the inclusion of both collisional and radiative processes, which are both expected to contribute to energy loss, as well as the thermal equilibrium treatment of the plasma [135]. Though, there is significant debate over how close the QGP fireballs formed at the LHC and RHIC are to full thermalization, as the droplets' rapid expansion should indicate they are in fact not equilibrated. Thus the applicability of TQFT calculations is not clear.

The higher-twist formalism also offers a theoretical grasp on the pQCD calculations. These calculations essentially expand in the parameter $\alpha_S \hat{q} L/Q^2$ rather than purely α_S. Initial HT calculations [136, 137] were performed in the SHSA limit $N \sim 1$, though there are now HT-MSSA calculations as well [138]. Higher-twist operates by incorporating the properties of the medium by introducing modified gauge field matrix operators in the pQCD formalism. The HT-SHSA calculations differ from the DGLV spectrum in that only the leading transferred momentum is considered rather than the full differential cross section for the single scattering center. So in short, the HT-SHSA calculations apply a further approximation to the DGLV spectrum. All of the medium dependence is compressed into the parameter $\hat{q}$, which is used in the expansion parameter.

Despite differences in the opacity limits used by each formalism, there are some common assumptions to these pQCD models. First, there is a consensus that there is a separation in timescales between the production of high-p_{T} partons and induced energy-loss effects. A naïve explanation for this is that dE/dx is modest, and therefore the parton must have sufficient time to traverse a reasonable distance $\sim 1\,\mathrm{fm}$ before a noticeable amount of energy is lost, while parton formation time scales roughly with $\sim 1/Q \ll 0.1\,\mathrm{fm}$. Therefore the initial hard-scatter process is assumed to decouple from the subsequent medium evolution, parton shower, and hadronization. This is similar to QCD factorization which has not been rigorously proven, but is theoretically appealing and generally accepted.[7] By decoupling parton *production* from parton *evolution* in the QGP fireball, medium-induced energy-loss phenomena can be studied separately from any cold nuclear matter effects.

These ground-up pQCD calculations of the energy loss also share some common assumptions. Parton trajectories are always taken to be eikonal relative to the medium effects, $E_{\mathrm{parton}} \gg \hat{q}$. In layman's terms, the direction of the parton is not modified. In a circular plasma, no net deflection might be expected on average from symmetry arguments, but this is not necessarily the case event-to-event. Thus this assumption is meant to be simplifying and could be revisited in the context of jet-broadening studies. Beyond the parton itself, sometimes the radiated (hard) gluon is also taken to be in the limit, $\omega \gg \hat{q}$, though all assume the gluon is collinear with the parton $\omega \gg q_{\perp}$. All of the formalisms also take $\omega \ll E_{\mathrm{parton}}$ (except in the AMY case). Lastly, the scatterings occur locally at discrete scattering points (which can be either static or dynamic, depending on the formulation). This requires the mean free path be larger than the Debye screening length: $\lambda \gg 1/m_D$.

However, they also share some common pitfalls. One of the most significant limitations comes from the aforementioned collinear approximation $\omega \gg q_{\perp}$. It is understood that even with this approximation, wide angle radiation constitutes a substantial effect to the total spectrum. Indeed, in the BDMPS-Z formalism, for example, the spectrum receives the majority of its contributions

[7] Recall from Chapter 1 that QCD factorization has been theoretically proven for some processes but not others.

from gluons with $q_\perp \sim \omega$ [139]. This translates to model uncertainties when compared with experiment; jet yield measurements are sensitive to this in particular. In-cone or collinear radiation will remain within the jet cone and no medium-induced effect can be observed without out-of-cone radiation. Measurements of jet structure, such as jet-fragmentation functions, are more sensitive to the momentum distribution of partons immediately preceeding hadronization, and are required to discern in-cone vs. out-of-cone radiation effects.

The effects of multiple emissions in medium can also be problematic. Most approaches neglect any interference between emissions as a simplification. Rather, multiple splitting kernels are applied according to the number of splittings. A frequent solution is to make a Poisson ansatz, whereby the number of splittings is taken to be Poisson distributed and therefore can be easily simulated. However the accumulated energy loss between scatterings is not accounted for and thus this ansatz can lead to unphysical scenarios where a parton loses more than its total energy. AMY and other modern approaches use transport models instead. The transport equations for the AMY formalism encapsulate the rate of emissions and can be found in Ref. [140]. Linear Boltzmann Transport (LBT) has been more recently explored which evolves partonic phase space densities within the medium evolution [141–143]. These prescriptions simulate a splitting probability at each timestep and therefore are best defined numerically, but are more physical than the Poisson ansatz. We will explore the LBT approach shortly. Though, we note that the HT-MSSA formalism explicitly re-solves the DGLAP equations for parton splittings in the medium, so this issue is avoided.

Model Implementations

Full descriptions of the parton evolution are best studied within Monte Carlo simulations. The advantage of the Monte Carlo approach is substantial: baseline predictions for hard-scattering cross sections and PDFs can be decoupled, and analytic calculations can be greatly simplified. The hard scatter can be decoupled and modeled in phenomenological generators such as Pythia, so the model only needs to implement the in-medium evolution. Event generators such as `PYQUEN`, `CUJET`, `PQM`, and Jewel are some common implementations (among others) using these pQCD radiation

calculations; here we explore a few of these. Beyond radiative energy loss, *post-hoc* parton-parton collision cross sections and rates can be added to implement collisional losses, but these must be separately formulated within each Monte Carlo implementation. These generators usually follow a basic recipe:

(1) generate partons in the hard-scatter vertex,

(2) using a model for medium evolution, evaluate the lost energy (either analytically or stochastically),

(3) simulate hadronization via fragmentation, coalescence, or other methods.

There is an element of creative freedom to this approach, and so the exact recipe differs model-to-model. For example, some calculations encapsulate the energy loss into a set of modified fragmentation functions while no energy-loss calculation is performed.[8] Others apply a stochastic lost energy to each parton, depending on a suite of variables such as the trajectory through the plasma, evolution of the medium, and so on, but apply vacuum fragmentation at freeze-out.

The Pythia Quenched (`PYQUEN`) model [144], for example, combines the BDMPS-Z gluon spectrum with the leading-order collision cross section from Refs. [87, 145],

$$\frac{d\sigma}{dq} = C_{\mathrm{R}} \frac{2\pi\alpha_{\mathrm{S}}^2(q)}{q^2} \frac{E_{\mathrm{parton}}^2}{E_{\mathrm{parton}}^2 - m_{\mathrm{parton}}^2} \tag{2.13}$$

to simulate the collisional losses. In this model $\alpha_{\mathrm{S}}(q)$ is taken to be the coupling at one-loop in pQCD where q represents the momentum transfer in the scattering. This cross section is used to determine the mean free path λ, which is related to $\hat{q}$ and thus defines the BDMPS-Z spectrum. First, hard scatterings are generated via Pythia with fragmentation disabled. The jet-forming partons are placed in position-space at binary nucleon-nucleon collisions to allow for geometry dependence. The generator then evolves the parton through a series of timesteps with the differential collisional

[8] There is a conceptual disconnect between modifying a fragmentation *function* and the fragmentation *hadronization* process. The fragmentation *function* appears in the cross section, for example see Eq. 2.5, and therefore is sensitive to *all* post-partonic scattering physics. However, you can imagine implementing a model where parton evolution in the plasma is modified relative to vacuum, but the vacuum fragmentation model operates on all final-state partons (post-energy loss). In this case, the fragmentation *process* is unchanged, but the fragmentation *function* is modified.

and radiative energy losses subtracted at each step. The time evolution is terminated when the parton leaves the medium, or reaches the thermal energy of the medium, at which point vacuum fragmentation is applied.

The Parton Quenching Model (PQM) also assumes the MSSA limit but applies the AWS quenching weights [146]. No collisional processes are included. Hard-scatter partons are generated from PYTHIA and placed within a Glauber geometry which determines the medium size parameter R and a critical frequency ω_c. The total energy loss is sampled according to the quenching weights, with effective cross section for hadron h modified from the vacuum by the energy-loss probability distribution $\mathcal{P}$; schematically it can be written as

$$\left.\frac{d^2\sigma^{\mathrm{h}}_{\mathrm{quenched}}}{dp_{\mathrm{T}}dy}\right|_{y=0} = f_a(x_a) \otimes f_b(x_b) \otimes \left.\frac{d^2\sigma^{ab\to jX}_{\mathrm{vacuum}}}{dp_{\mathrm{T},j}dy_j}\right|_{y_j=0} \otimes \mathcal{P}\left(\Delta E_j; R_j, \omega_{c,j}\right) \otimes \frac{D_{j\to h}\left(z_j^2\right)}{z_j^2}. \quad (2.14)$$

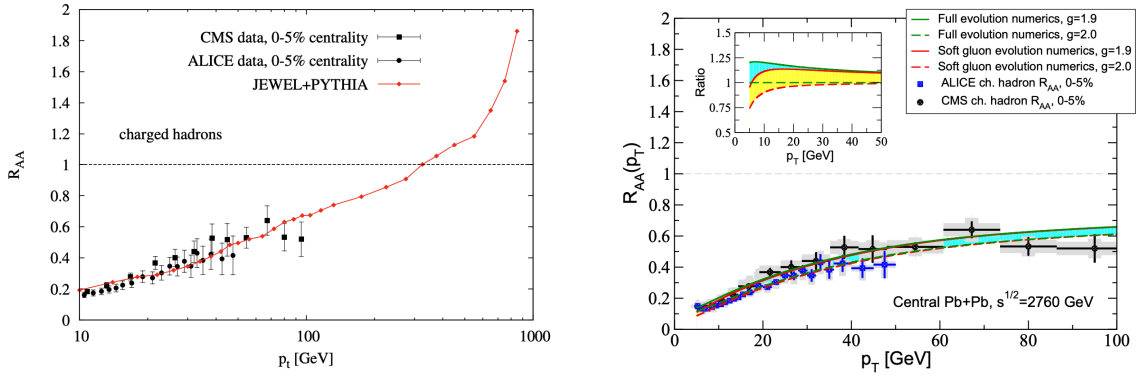
which is the factorization ansatz. Like PYQUEN, fragmentation proceeds independently using vacuum fragmentation functions.

CUJET [147] is a generator developed at Columbia University within the JET collaboration. It applies the DGLV gluon spectrum at dynamic scattering centers with quark-gluon cross section

$$\frac{d\sigma}{dq_\perp^2} = \frac{\alpha_{\mathrm{S}}^2(q_\perp^2)}{\left(q_\perp^2 + f_E^2 m_D^2\right)\left(q_\perp^2 + f_M^2 m_D^2\right)} \quad (2.15)$$

which is qualitatively similar to the AMY cross section. f_E, f_M are parameters describing the electric and magnetic screening and are set to 1 and 0 by default. The energy-loss distribution for each production vertex $\vec{r}$ and direction of propagation $\hat{n}$ is evaluated; simulations convolve this distribution $\mathcal{P}_{\mathrm{rad}}\left(\Delta E; \hat{n}, \vec{r}\right)$ with vacuum PDFs, cross sections, and fragmentation functions identically to Eq. (2.14) to obtain final cross sections. In both the CUJET and PQM generators, the effects of multiple gluon emissions are incorporated by Poisson ansatz.

JEWEL (jet evolution with energy loss) in particular is a successful, publicly available Monte Carlo event generator that uses the ASW formalism [148]. The generator was developed around the philosophy of providing a predictive tool that matches analytical pQCD results in all known limits, while making minimal simplifying assumptions [149]. Similar to PQM and CUJET, JEWEL simulates



(a) R_{AA} in JEWEL **(b)** R_{AA} in $\mathrm{SCET_G}$

Figure 2.13: The charged-hadron R_{AA} in 0–5% central Pb+Pb collisions is compared between **(a)** JEWEL or **(b)** $\mathrm{SCET_G}$ (right) and CMS [150] and ALICE [151] data. Figures reproduced from Refs. [148, 152], respectively.

a medium-modified parton shower including elastic and inelastic interactions, as well as the LPM effect. This allows JEWEL to account for collisional and radiational energy loss in a unified pQCD framework. JEWEL operates under the following assumptions [148]:

(1) the medium as seen by the evolving parton is a collection of partons,

(2) soft scatterings can be described by infrared continuation of perturbative matrix elements,

(3) multiple radiations are governed by their formation times (i.e., their hardness), and

(4) the LPM effect derived with eikonal kinematics $\omega \gg q_\perp$ also applies in non-eikonal kinematics.

The underlying physics of JEWEL avoids making assumptions of the medium and can in principle be coupled with any medium model, though by default the publicly available version applies a Bjorken model of medium evolution [153] with energy density $\varepsilon \propto T^4$ and initial conditions supplied by a Glauber model. The medium time evolution can be simply written as

$$\varepsilon(\tau) = \varepsilon(\tau_0)\left(\frac{\tau}{\tau_0}\right)^{-4/3} \quad \text{and} \quad T(\tau) = T(\tau_0)\left(\frac{\tau}{\tau_0}\right)^{-1/3}. \tag{2.16}$$

Both the initial conditions for the hard scatter and parton hadronization following freezeout are

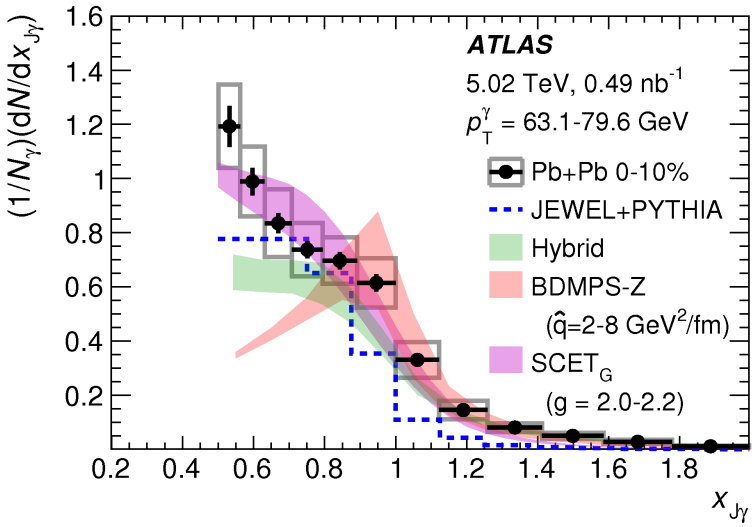


Figure 2.14: A comparison of the photon-jet momentum balance $x_{\mathrm{J}\gamma}$ between data from ATLAS [158] and a variety of model calculations is shown. Figure reproduced from Ref. [158].

handled by Pythia 6 [154]. Thus hadronization is performed using the Lund string fragmentation model.

Jewel has seen success in both reproducing experimental results and predicting new observables. As an example, the charged-hadron R_{AA} predicted by Jewel is consistent with Run 1 data from CMS [150] and ALICE [151], as shown in Fig. 2.13. Recent work has improved the base (v2.0) model [155] by incorporating first electroweak processes (v2.1) [156] and subsequently the effect of medium response (v2.2) [157]. The incorporation of vector boson + jet processes enabled predictions for photon-jet observables such as the momentum balance $x_{\mathrm{J}\gamma} = p_{\mathrm{T}}^{\mathrm{jet}}/p_{\mathrm{T}}^{\gamma}$, which was recently studied by ATLAS [158]. In Fig. 2.14, the comparison between data and theory for the $x_{\mathrm{J}\gamma}$ observable is shown for photons with transverse momenta $p_{\mathrm{T}}^{\gamma} = 63.1$–$79.6$ GeV in central Pb+Pb. Several models, including Jewel, are able to reproduce the qualitative features of the data. Notably, the BDMPS-Z prediction fails; the uncertainties correspond to variations in the transport coefficient $\hat{q}$, though the significant difference in shape from the data indicates modifications to the calculation beyond changing $\hat{q}$ are needed. The other two approaches – SCET$_{\mathrm{G}}$ and the Hybrid model – are more modern and we will discuss these next.

Soft Collinear Effective Theory

Effective field theory has historically proven useful in describing quantum field theories with multiple emergent energy scales $\Lambda_{\rm hard} \gg \Lambda_{\rm soft}$. Unimportant degrees of freedom can be integrated out of the action, leaving only the degrees meant for study. The main idea introduced by soft collinear effective theory (SCET) is that jet-forming partons with large virtuality Q emerging from a hard scatter have an emergent jet mass scale $m_{\rm J} \ll Q$ that describes the collinearity of their emissions as they rapidly become on-shell. Based on the use of $m_{\rm J}$, it is easy to see why SCET was originally developed to understand decays of heavy B meson states. Unnecessary degrees of freedom, namely the very soft quarks and gluons in the plasma, as well as the evolution of the hard-scatter parton, are integrated out of QCD to form an effective theory of collinear partons in an intermediate regime. In one picture, SCET can be viewed as essentially a boosted version of QCD, and thus the medium interactions are fully contained in a set of modified DGLAP evolution equations, similar to higher-twist. In another, SCET can be viewed as a factorization of the collinear radiation from the hard and soft physics; the cross section as a function of observable $\mathcal{O}$ (perhaps $p_{\rm T}$ or rapidity y) is schematically given by [159]

$$\frac{d\sigma_{ab\to N\text{jets}}}{d\mathcal{O}} \simeq H(Q) \times \prod_{i}^{N} J_i \otimes S_{ab\to 1\ldots N} \otimes \delta\left(\mathcal{O} - \mathcal{O}\left(p_c, p_s\right)\right) + \text{h.o.}, \tag{2.17}$$

where $H(Q)$ is hard function, J_i is a universal jet function akin to fragmentation functions or PDFs (and therefore comes equipped with RG evolution equations), and $S_{ab\to 1\ldots N}$ encapsulates the soft physics.

SCET is therefore a general-purpose framework for tackling pQCD calculations with infrared, collinear divergences. Over the past decade, the SCET with Glauber gluons ($\text{SCET}_{\rm G}$) model of partonic energy loss has been developed by extending the splitting functions provided in the vacuum theory to modified ones including the effect of induced radiations [152, 160]. By using the medium-modified splitting functions, $\text{SCET}_{\rm G}$ has been successful in reproducing the charged-hadron $R_{\rm AA}$, similar to JEWEL, as in Fig. 2.13. It has also successfully predicted the photon-jet balance in Pb+Pb collisions as shown in Fig. 2.14.

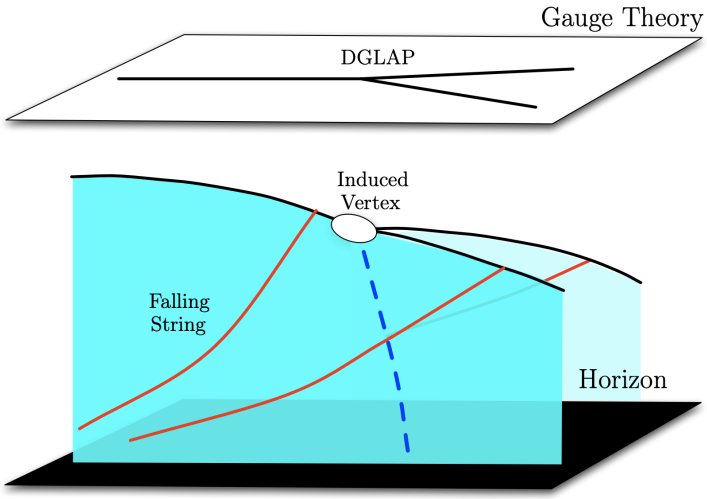


Figure 2.15: Overview of the Hybrid Strong/Weak Coupling model approach to partonic energy loss. There is no full perturbative picture for how partons evolve along trajectories where the coupling is strong. Likewise, there is no gravitational picture for how splittings occur at vertices, where the coupling is weak. The hybrid model uses a combination of strong and weak coupling calculations to fully describe parton evolution in each regime. Figure reproduced from Ref. [163].

2.3 Strong-Coupling Calculations

Dual gauge-gravity theories have proven useful models of QCD physics and avoid the growing low-energy coupling that plagues pQCD calculations. No gravitational dual to QCD in particular is known, but the strongly coupled plasma in $\mathcal{N} = 4$ SYM theory is often used as a model for the QGP due to similarities between the two phases: both feature non-Abelian and Debye-screened plasmas with finite correlation lengths and long-distance hydrodynamic modes [161]. Despite notable differences[9] , this model has been successful in describing the shear viscosity for the hydrodynamic behavior, with the famous prediction for the shear viscosity to entropy density ratio $\eta/s \geq 1/4\pi$ which seems to be obeyed by the QGP created in experiment, as well as all other forms of matter.

Initially the AdS/CFT duality was used to describe the phenomenology of the QGP bulk, but it was quickly realized that energy-loss calculations could be made as well. An approach that has seen success recently is the Hybrid Strong/Weak Coupling model, which takes advantage of

[9] $N = 4$ SYM is conformal field theory. However, QCD definitively breaks conformal symmetry because of the dimensional transmutation that gives rise $\Lambda_{\rm QCD}$ [162]. This is on top of obvious differences: SYM is a supersymmetric theory, whereas QCD is not.

calculations for the energy loss of a propagating parton in $N = 4$ SYM with $N_c \gg 1$ colors [163]. In this model, the parton is sent propagating through a slab or "brick" of plasma, and via its gravitational dual (Type IIB string theory on $\mathrm{AdS}_5 \times S^5$), the differential energy loss can be written in terms of the stopping distance x_{stop} and initial parton energy E_0 [161, 164]

$$-\left.\frac{dE}{dx}\right|_{\mathrm{strongly-coupled}} = \frac{4}{\pi}\frac{x^2}{x_{\mathrm{stop}}^2}\frac{E_0}{\sqrt{x_{\mathrm{stop}}^2 - x^2}}, \qquad \text{where} \qquad x_{\mathrm{stop}} = \frac{1}{\kappa_{sc}}\frac{E_0^{1/3}}{T^{4/3}}, \tag{2.18}$$

which features a similar x^2 dependence to the one found in the pQCD approaches. Nominally $\kappa_{sc} = 1.05\lambda'^{1/6}_{\mathrm{t\,Hooft}}$, but it is treated as a free parameter in the model. It is worthy to mention that no microscopic picture of this drag exists: the drag is caused not purely by collisional or radiative energy loss as these are perturbative processes (meaning they can be described diagrammatically). Rather, all types of processes contribute to obtain this final energy-loss rate. The energy loss of the parton between hard splittings (at a scale $Q_0 \gtrsim 1\,\mathrm{GeV}$) is continuously simulated with the strongly coupled energy-loss prediction, while the hard splittings are governed by weakly coupled DGLAP evolution via Pythia (hence the "Hybrid" title). Partons are evolved through a hydrodynamic simulation of the plasma until the local temperature drops below $T_c \sim 145$–170 MeV. An illustration of parton evolution is governed by weak coupling at splittings but strong coupling along its trajectory is shown in Fig. 2.15. It is worth mentioning, however, that because the Hybrid model is not actually based on QCD, it is most useful in the low-virtuality regime where the physics is soft and nonperturbative. pQCD-based models are theoretically more appealing in the high-Q^2 limit.

In the original formulation, the redistribution of energy to the medium was ignored. However, the advent of experimental measurements sensitive to medium response motivated this to be revisited within the model. Based on the relatively small energy lost by the jet compared to the overall medium energy, a perturbative, hydrodynamic expansion was later added to address the rapid transfer of energy from hard, jet modes to softer, long-range hydrodynamic modes [165].

Analytically, the impact of the backreaction or "wake" on the particle spectra is found to be

$$E\frac{d^3\Delta N_{\rm h}}{dp^3}(y,\phi) = \frac{1}{32\pi}\frac{m_{\rm T}}{T^5}\cosh(y-y_{\rm jet})\exp\left[-\frac{m_{\rm T}}{T}\cosh(y-y_{\rm jet})\right] \tag{2.19}$$

$$\times\left[p_{\rm T}\Delta P_{\rm T}\cos(\phi-\phi_{\rm jet}) + \frac{1}{3}m_{\rm T}\Delta M_{\rm T}\cosh(y-y_{\rm jet})\right], \tag{2.20}$$

where $m_{\rm T} = m \oplus p_{\rm T}$ is the transverse mass of the hadron h.[10] $\Delta P_{\rm T}$ and $\Delta M_{\rm T} = \Delta E/\cosh y$ describe the total transverse momentum and mass lost by the jet to the wake. Notably, this perturbation can be negative, implying destructive interference between the bulk medium and the wake. This is expected to occur, for example, at large angles relative to the jet, due to the parton wake de-exciting momentum modes antiparallel to its direction of motion. The Monte Carlo implementation of this spectrum is complicated due to the energy-momentum conservation constraint, though investigations show this approach typically overpredicts soft particle production $p_{\rm T} \lesssim 2$ GeV and underpredicts moderately hard particles $p_{\rm T} \sim 2$–4 GeV, which is attributed to the assumption that the wake is fully thermalized.

2.4 Linear Boltzmann Transport

The Linear Boltzmann Transport (LBT) approach to parton evolution is a semiclassical method for addressing the evolution of the parton in the medium [141, 142, 166, 167]. The motivation for this approach is that hard splittings will rapidly reduce parton virtualities and so virtuality-ordered parton showering models in medium should not be applicable. The LBT model prescribes, for a parton p with momentum p^μ, the following Boltzmann evolution equation

$$p^\mu\partial_\mu\left\{(2\pi)^3\delta^3(p-p_p)\delta^3(x-x_p)\right\} = E_p\left(C_p^{\rm el} + C_p^{\rm inel}\right). \tag{2.21}$$

The parton trajectory through phase space can be numerically evaluated by integrating Eq. (2.21). $C_p^{\rm el}$ and $C_p^{\rm inel}$ are the collision integrals for elastic and inelastic processes, respectively, and encapsulate the effects of the medium. The elastic energy-loss rate is taken from pQCD calculations of the $2 \to 2$ scattering rate (details can be found in [167]). The inelastic term corresponds to the gluon

[10] Experimentalists often write $m_{\rm T}$ as a transverse energy $E_{\rm T}$ rather than a mass, since this quantity grows with $p_{\rm T}$, and is exactly the total energy at midrapidity.

bremsstrahlung rate $\Gamma_p^{\rm inel}$ previously discussed; in the LBT model, this is taken from higher-twist calculations:

$$\Gamma_p^{\rm inel} = \frac{1}{1+\delta_{pg}} \int dz dk_\perp^2 \frac{2C_A \alpha_{\rm S} P_p^{vac}(z) k_\perp^4}{\pi C_R \left(k_\perp^2 + x^2 m_p^2\right)^4} \hat{q}_p \sin\left(\frac{t-t_i}{2\tau_f}\right). \tag{2.22}$$

The first term corrects for double counting the $g \to gg$ process, P_p^{vac} is the vacuum splitting probability, t_i is the production time of the parton (which can be after any hard-scattering timescales, if the parton under consideration is produced from the medium evolution of the initial parton) and τ_f is the gluon formation time. The effects of multiple gluon emissions are taken by the Poisson ansatz with the assertion that the emission probability is small. The medium parameters, as in the Hybrid model, are taken from a hydrodynamic simulation. VISHNU [168–170], CLVISC [171, 172], and superSONIC [75, 173–175] have all been used with the LBT model. Typically the initial conditions are taken from Monte Carlo Glauber or AMPT.

The LBT model has recently been extended to include parton-medium coevolution [176]. In most models incorporating a dynamic QGP fireball, the medium is simulated first and then treated as a background for the jet evolution. The coupled LBT-hydrodynamics (CoLBT-hydro) model differs in that the two are evolved together. The pitfall to this approach is that the 3+1D hydrodynamics is not usually feasibly computable – GPU clusters must be used for this purpose. The equation of motion for the medium (ideal hydrodynamics) is modified to include a source j^μ

$$\partial_\mu T^{\mu\nu} = j^\nu, \tag{2.23}$$

where

$$j^\mu = \sum_i \frac{\theta(p_{\rm cut}^0 - p_i \cdot u)}{(2\pi)^{3/2} \tau \sigma_r^2 \sigma_{\eta_s}} \frac{dp_i^\mu}{d\tau} \times \exp\left[-\frac{\left(\vec{x}_\perp - \vec{x}_\perp^{\,i}\right)^2}{2\sigma_r^2} - \frac{\left(\eta_s - \eta_s^i\right)^2}{2\sigma_{\eta_s}^2}\right] \tag{2.24}$$

describes a Gaussian source at the position of each emitted soft parton i meeting $p_i \cdot u < p_{\rm cut}^0$. At each timestep, jet partons (those above $p_{\rm cut}^0$) are updated according to LBT, and low-energy partons are transferred to the medium via an additional summand in j^μ. These are referred to in the literature as *jet-induced medium excitations* (or j.i.m.e.). Both the jet and medium are then updated according to Eq. (2.21) and Eq. (2.23). $p_{\rm cut}^0$ values between 1–4 GeV are typically chosen,

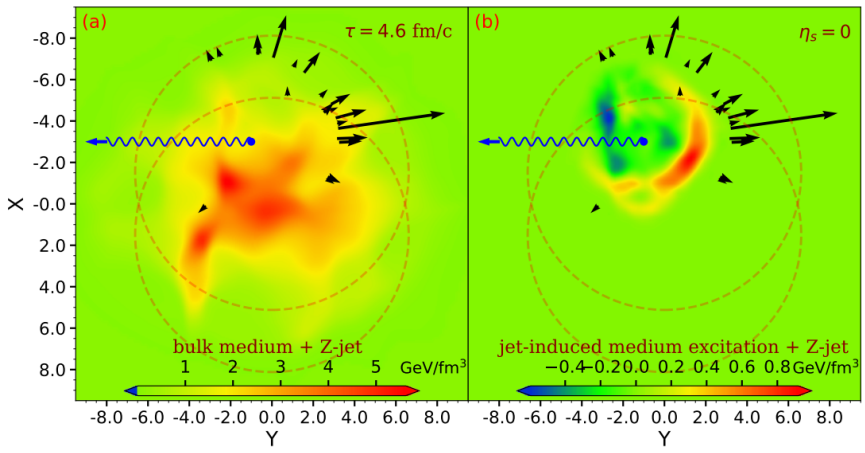


Figure 2.16: Snapshots of parton-medium coevolution in a $Z+$jet Pb+Pb event with the CoLBT-hydro model at proper time $\tau = 4.6\,\text{fm}$. Jet-induced medium excitations (j.i.m.e.) can be seen in the right panel, where the pure medium evolution is subtracted from the total as a background. Figure reproduced from Ref. [178].

and observables have been shown to be insensitive to choices within this range. At the end of the evolution, hadronization is performed with the parton recombination model [177].

Though perturbative calculations are employed, the advantage to this approach is the simultaneous, interactive evolution between the parton and the medium. For the implementation in [179], this is enabled by parallelizing the 3+1D hydrodynamic computation on a GPU cluster. Though, like the Hybrid treatment of the wake, CoLBT-hydro also assumes instantenous (within the timestep of the integration) thermalization of the j.i.m.e. partons. An illustration of the j.i.m.e. effect on the event topology is given in Fig. 2.16 for a $Z+$jet hard scatter in a Pb+Pb collision at RHIC. The left panel shows the total hydrodynamic+parton coevolution, while the right panel shows the net effect of the parton within the medium after the medium evolution is subtracted. The Z – traveling leftwards – is accompanied by a small depletion in energy density from the medium (indicated in blue). This is a consequence of the jet "wake" phenomenon.

The importance of the jet wake at low-p_{T} is a common thread among modern theoretical predictions. While the Hybrid model and JEWEL both must implement *post-hoc* medium backreaction effects to incorporate this (and therefore lose some of their "ground-up" theoretical appeal), it

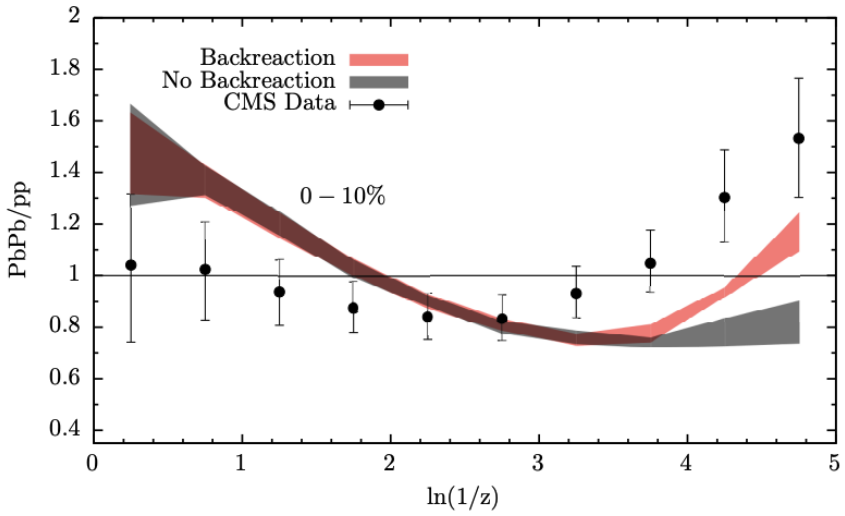


Figure 2.17: The role of the backreaction in jet-fragmentation modification within the Hybrid model; a comparison to CMS data is provided [180]. Figure reproduced from Ref. [181].

is an intrinsic feature to CoLBT-hydro. So although the approach is semiclassical, it is interesting to see how the models differ at low-p_{T} and wide angles. The Hybrid model, for example, shows an enhancement of low-p_{T} particles in jets when medium backreaction is considered, as seen in Fig. 2.17. Similar behavior is observed in JEWEL when hadrons associated with medium back-scatters or recoils are included in the simulation output. The away-side structure of the jet shower has been difficult to measure experimentally due to large background contributions over a modest signal. Very recently, multiparton interactions were even suggested to leave a visible signature on the wide-angle distribution of the wake [178]. Thus obtaining a full characterization of the medium backreaction is an important aspect of current jet quenching studies in large systems.

2.5 Energy Loss in Small Systems

The vast majority of theoretical predictions for jet quenching are performed in large systems, namely central Au+Au and Pb+Pb collisions, where there is all-but-universal consensus of QGP formation. In order to fully characterize this QGP fireball, it is important not only build an understanding of its behavior, but attempt to break that understanding by finding where it

does not apply. One avenue to pursue is by limiting where quenching phenomena occur. Small system collisions like pp, p+Pb, d+Au, and others are not traditionally expected to cross-over into the QGP phase. However, some key characteristics of QGP formation are consistently observed in these systems. This includes momentum-space anisotropies from two-particle correlation measurements (for a review see for example Ref. [76]), as well as evidence for strangeness enhancement in high-multiplicity pp and p+Pb collisions [182, 183]. Coupled with a consistent hydrodynamically driven picture of medium evolution, these observations challenge the accepted wisdom, and offer qualitatively novel insights to the dynamics of hadronic collisions.

A recent measurement of high-p_{T} two-particle correlations by ATLAS with 2016 p+Pb collision data at 8.16 TeV is particularly relevant to the discussion here. Essentially, it was found that charged particles with relatively high–p_{T} also exhibit momentum-space anisotropies characteristic of low-p_{T} hadrons. This is exemplified in Fig. 2.18, which shows the two-particle correlation function between particles where one of the particles has relatively high-p_{T} in the range 11–16 GeV. Dashed lines indicate the elliptical (blue) and triangular (yellow) components extracted from the template fit method (see Ref. [184] for a succinct review). The bottom panel shows the result after subtracting the non-flow component, which includes the trivial jet- and resonance-induced correlations.

While hydrodynamics is consistent with the collective behavior of the low-p_{T} hadrons [75], the persistence of anisotropy to high-p_{T} was surprising to find in this system. The current understanding is that these particles – because they carry significant momenta – are the fragments of high-energy partons created at the earliest stages of the collision. This leaves the possibility of a "trivial" initial-state correlation. However the two-particle correlation methodology considers only long-range correlations: all particles must be separated in pseudorapidity by $|\Delta\eta| > 2$. By causality, it is unlikely that particles with a significant rapidity gap can exhibit momentum-space correlations due to vacuum QCD processes alone (the nonflow components). This suggests there is yet-unresolved physics in these collisions; an ingredient to our physical picture is missing.

Meanwhile, observables sensitive to energy-loss effects have resulted in essentially a null signal

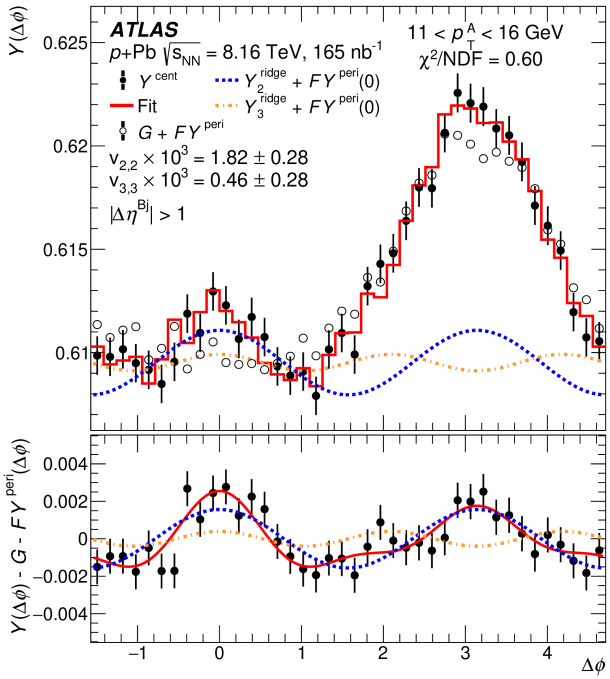


Figure 2.18: Angular dependence of the two-particle correlation function $Y(\Delta\phi)$ triggered by high-p_{T} (11–16 GeV) charged particles in 8.16 TeV p+Pb collisions, with pair rapidity gap $|\Delta\eta| > 2$. Figure reproduced from Ref. [185].

of quenching in, for example, p+Pb collisions. As an example, the nuclear modification factor $Q_{p\mathrm{Pb}}$ of charged hadrons is shown in Fig. 2.19, as measured by ALICE [186] in p+Pb collisions at 5.02 TeV.[11] Recall that the nuclear modification factor is strongly sensitive to energy redistribution due to the power law nature of the spectrum, so if a quenching effect can be observed, it should manifest here. But above $p_{\mathrm{T}} \sim 10$ GeV, it was found that $Q_{p\mathrm{Pb}}$ is consistent with unity to within a few percent near 10 GeV or 15–20% around 20–30 GeV. Moreover, the trend is remarkably flat in this regime, providing a strong signal that no final-state energy-loss occurs in this system. This finding has been corroborated by similar measurements by ATLAS [187] and CMS [188], as well as measurements of jet production [189, 190].

In the low-p_{T} regime, a few effects can be directly seen. Unlike Pb+Pb, these are not

[11] The ALICE publication introduces a centrality-differential nuclear modification factor $Q_{p\mathrm{Pb}}$ which is only distinguished from $R_{p\mathrm{Pb}}$ in the sense that a centrality-differential nuclear modification is susceptible to the jet autocorrelation bias. Thus, in a centrality-inclusive measurement, $R_{p\mathrm{Pb}}$ and $Q_{p\mathrm{Pb}}$ are mathematically equivalent.

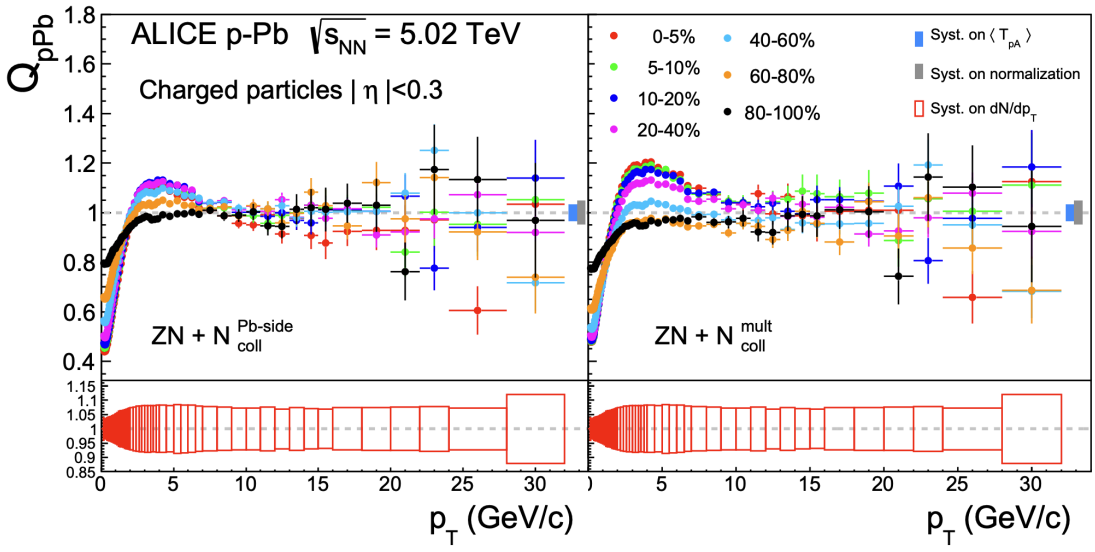


Figure 2.19: Nuclear modification factor $Q_{p\mathrm{Pb}}$ for charged hadrons in 5.02 TeV p+Pb collisions as measured by ALICE. The two panels use different estimates for the average number of binary collisions $\langle N_{\mathrm{coll}} \rangle$. Figure reproduced from Ref. [186].

attributed to any quenching backreaction effect; rather they are usually understood in the context of cold nuclear matter effects [191, 192]. The peak in $Q_{p\mathrm{Pb}}$ around 4 GeV for example is referred to as the *Cronin effect* throughout the literature, and was originally observed in fixed target p+W collisions at Fermilab [193]. Traditional explanations invoke momentum broadening due to partonic rescattering in the nucleus [194]; essentially, the parton from the hard-scatter vertex can undergo successive parton-nucleon collisions in the cold nuclear environment (analogous to "parton-QGP collisions" in QGP fireballs).[12] Partons with low tranverse momentum pick up kicks of order $Q_s \sim 0.2$–2 GeV that push them to slightly higher p_{T}, causing the spectrum to become slightly less steep [195]. Very high momentum partons can also scatter, but the relative effects of the kicks are drowned out by a much harder initial p_{T}. On the flipside, the production of very low p_{T} hadrons is slightly reduced due to a combination of soft QCD dynamics and their being pushed to slightly higher p_{T} from the rescattering. Because a rescattering effect represents a violation of QCD factorization, it cannot be simply absorbed as a modification to the nuclear PDF. Rather, it

[12] We note that gluon radiations are also possible, but require color charge in the immediate environment from a pQCD perspective.

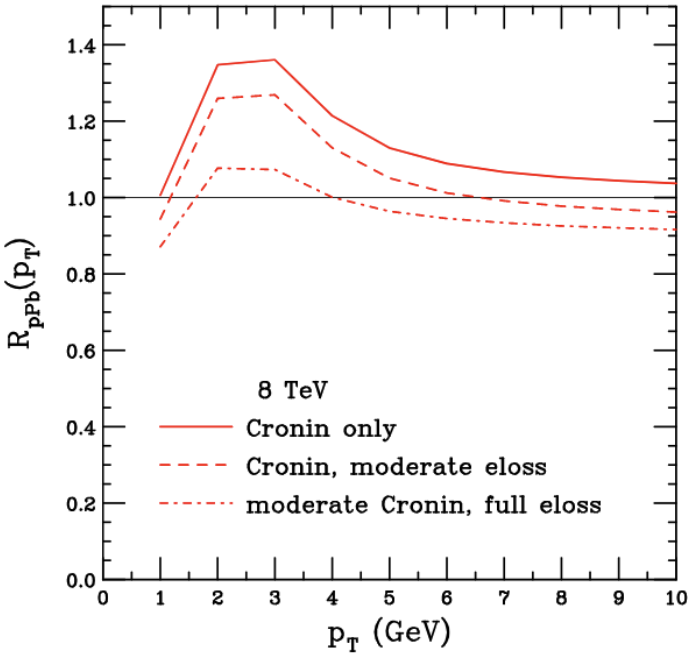


Figure 2.20: Predictions for the charged-particle $R_{p\mathrm{Pb}}$ in 8.16 TeV minimum bias collisions under (1) no energy loss, (2) moderate energy loss, and (3) full energy loss but reduced Cronin effect scenarios. Figure reproduced from Ref. [192].

is an example of a *cold nuclear matter* (CNM) effect. Others include isospin, initial & final-state energy-loss effects, and shadowing/antishadowing of nPDFs.

In summary,

(1) Both high-p_{T} and low-p_{T} particles exhibit momentum-space anisotropies indicative of collectivity; the low-p_{T} physics is consistent with hydrodynamics.

(2) No energy redistribution of high-p_{T} particles is observed at roughly the 10% level.

This is known as the $R_{\mathrm{AA}} + v_2$ puzzle [196] because it presents seemingly contradictory evidence regarding QGP formation in small system collisions.[13]

Energy-loss effects in p+Pb are a prime target for explaining the high-p_{T} anisotropy due to previous experience with differential energy loss in Pb+Pb collisions. In large systems it is

[13] As a historical note, the $R_{\mathrm{AA}} + v_2$ puzzle refers to the simultaneous description of energy-loss phenomena and high-p_{T} collective flow [89] in A+A collisions. In small systems, the apparent *lack* of energy loss invalidates explanations based on knowledge of A+A collisions.

the final-state energy loss from medium interactions that is primarily responsible for elliptic flow-like signatures of jets [89]. However, recall from Sec. 2.2 that $\Delta E \propto L$ for small system sizes L, implying path-length dependence even in p+Pb. Extending this explanation to small systems is natural because of the success of hydrodynamic models; however, this would imply there are measurable changes to jet structure, as compared with vacuum QCD.

Final-state energy-loss calculations suggest such effects – if they exist – are subtle. An example calculation is shown in Fig. 2.20 from Ref. [192]. The effect in the 5–10 GeV regime is modest, and the suppression when energy loss is included is only at the level of 10–15% at most. Moreover, the few percent enhancement due to the Cronin effect works against the energy-loss suppression. This implies that most experimental data up until now offers little discrimination as to whether any energy-loss effect really is occurring, as the current uncertainties are relatively large. In other words, the data is still consistent with all energy-loss scenarios.

Thus further investigation of jet quenching directly motivates higher precision measurements of charged-particle spectra. This would directly aid our understanding of energy-loss mechanisms in hadronic collisions, offer new insights to differential energy-loss scenarios and aid resolution of the $R_{\mathrm{AA}} + v_2$ puzzle.

Chapter 3

The ATLAS Experiment at the LHC

3.1 The Large Hadron Collider

The Large Hadron Collider or *LHC* is a set of corotating particle accelerators located at the European Organization for Nuclear Research (CERN) outside of Geneva, Switzerland. Straddling the Swiss-French border, the LHC is located approximately 100 m below ground, inhabiting the same tunnel as its parent, LEP (the Large Electron-Positron collider, [197]). The accelerators themselves are nearly circular and are designed to accelerate charged-particle beams of mass $m \geq m_p$, compared with the electron beams used in LEP. Typically proton beams are accelerated copiously for precision studies of the Standard Model and searches for potential violations. However circulation of heavy-ion beams is routinely a part of the scheduled LHC operations and several large heavy-ion data sets now exist following Run 2 between 2015 and 2018.

The LHC has a circumference of 26.7 km, delivering beam-beam collisions at four interaction points (IPs), where there are four different experiments situated: IP-1 (ATLAS), IP-2 (ALICE), IP-5 (CMS), and IP-8 (LHCb). The beam optics are designed for a maximum energy of 7 TeV $\times Z/A$, corresponding to a proton-proton (pp) collision energy of $\sqrt{s}_{\text{max}} = 14$ TeV. Maintenance of this energy is obtained by using superconducting dipole magnets with field strength 8.3 T, corresponding to a current of $\sim 12\,\text{kA}$. The magnets are made from a NbTi alloy with critical temperature $T_c \sim 10\,\text{K}$. To keep the magnets below this temperature, 130 tons of superfluid ^{4}He is circulated along the beamline to cool the 37 thousand tons of superconducting material. To cool the ^{4}He, 8 cyrostats are located along each beam, about 2.7 km apart. Consequently the system is the world's

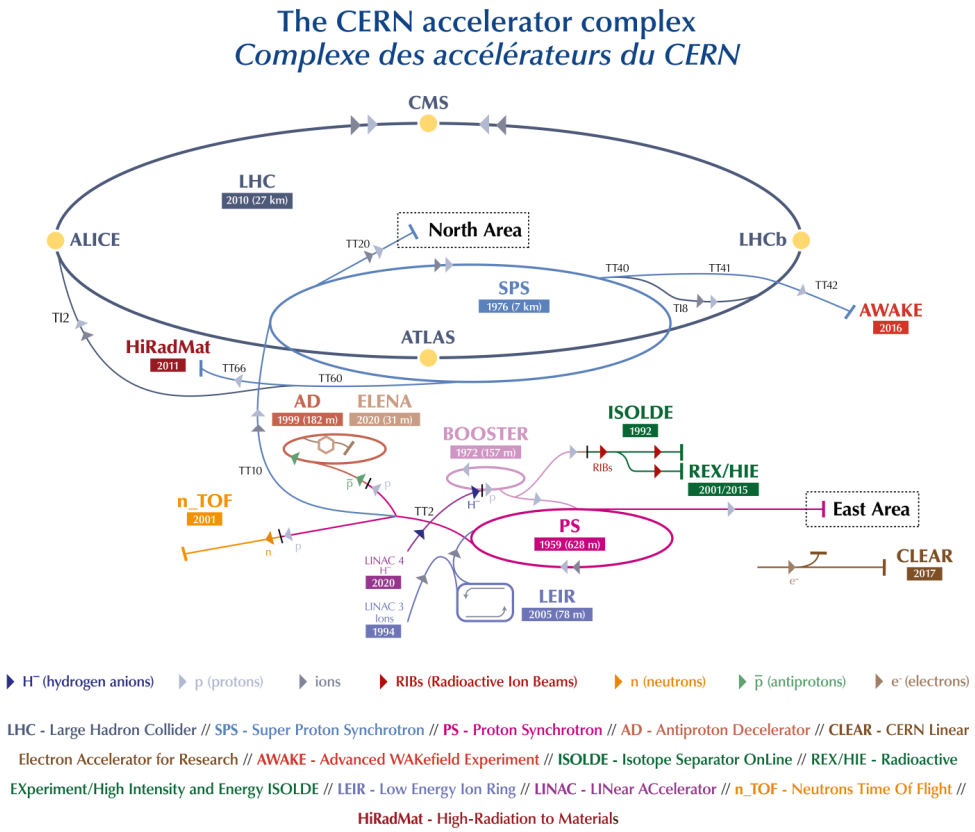


Figure 3.1: Overview of the CERN accelerator complex. Heavy-ion beams are injected to the LHC following the sequence LINAC3 → LEIR → PS → SPS → LHC. Figure reproduced from Ref. [198].

largest refrigerator [199]. Current is supplied to the magnets via 1600 parallelized power converters. In case of a quench (where the magnets quickly become thermally unstable and transition from the superconducting phase to the resistive or normal phase, converting the stored magnetic energy to heat), the current is rapidly diverted to large absorber resistors to disperse the stored magnetic energy, which is of order 1 GJ.

The beams themselves are formed by accelerating charged atoms through a series of injectors that serve to both increase the beam energy and strip away electrons, leaving only the nuclear core. A diagram of the LHC injector chain within the CERN accelerator complex is shown in Fig. 3.1. To illustrate how the injection sequence proceeds, consider the acceleration of corotating $^{208}\mathrm{Pb}^{82+}$

ion beams. First, pure ^{208}Pb is heated in an oven and partially ionized to $^{208}Pb^{29+}$ before injection to the LINAC 3, which then accelerates them to 4.2 MeV $\times$ A. At this stage the lead is further ionized to $^{208}Pb^{54+}$ by the Radio Frequency Quadrupole. Ions are accumulated in the Low-Energy Ion Ring (LEIR) over the course of several pulses, forming two dense groups. LEIR brings the ions up to 72 MeV $\times$ A, at which point they are injected to the proton synchrotron (PS). There they are further accelerated to 5.9 GeV $\times$ A before being transferred to the super proton synchrotron (SPS). This injection finishes the ionization process such that fully ionized $^{208}Pb^{82+}$ enters the SPS. They are then brought up to 450 GeV $\times$ A before being injected to the LHC, where they can be stored and brought up to full collision energies. Finally, beams are brought into collision by crossing them at the IPs.

At several points in this process, beams are temporarily held in injector accelerators to build structure. Localized *bunches* of particles are formed early in the sequence and form the fundamental unit for beam structure. The longitudinal size of the bunch is determined by the size of the RF bucket: one bunch fills one bucket. Due to the particle speed of essentially $\sim c$, separation between bunches is typically described in time units, usually nanoseconds. Groups of bunches are sometimes referred to as *batches* during the injection sequence, though in the LHC the most common grouping is a *train*, where a relatively long sequence of bunches is formed with constant spacing. The full LHC beam then comprises many bunch trains. Nominal heavy-ion operations fill the LHC with 592 bunches with a separation of 100 ns between bunches in a train [200]. For the 2018 Pb+Pb run however, a new configuration with a separation of 75 ns and 733 bunches was successfully implemented [201]. A summary of beam parameters for the heavy-ion data sets in Run 2, which took place between 2015 and 2018, can be found in Table 3.1.

The longitudinal behavior of the beam, including the beam energy, is moderated by 8 RF cavities per beam located around the ring. In these cavities, electric fields $\sim$ 5 MV/m parallel to the beam are rapidly oscillated at a frequency of 400 MHz. Particles perfectly synchronous with the center of the bunch see no electric field as they pass through. However the cavity is 180° out of phase with the bunch such that particles at the back of passing bunches see an acceleration while

LHC Run 2 Heavy-Ion and Low-μ pp Collision Systems					
Year	Beam 1+2	Energy / A	Max. N_b	Min. spacing	β^*
2015	p+p	2.51 TeV	1813	25 ns	4 m
	Pb+Pb	2.51 TeV	492	100 ns	0.8 m
2016	p+Pb	4 / 1.38 TeV	81	100 ns	11 m
	p+Pb	6.5 / 2.51 TeV	474	100 ns	0.6 m
	Pb+p	2.51 / 6.5 TeV	513	100 ns	0.6 m
2017	Xe+Xe	2.72 TeV	8	–	0.3 m
	p+p	2.51 TeV	1828	25 ns	3.1 m
2018	Pb+Pb	2.51 TeV	733	75 ns	1 m

Table 3.1: Overview of beam configuration parameters for LHC Run 2 heavy-ion and reference data sets. For asymmetric collision systems, the energy per nucleon of both beams is reported. Data from [201–205].

those at the front are decelerated instead. This traps particles within the bunch by providing a restoring force, and subjects them to synchrotron oscillations which vary their longitudinal momenta. Particles which stray too far away from the bunch become trapped in subsequent satellite bunches 2.5 ns behind the main bunch (particles cannot fall into the bunch ahead due to the laws of special relativity).

As a machine, the performance of the LHC is determined by its throughput. The purpose of the LHC is to deliver high-energy collisions at interaction points, and thus the collision rate per cross-sectional area or *luminosity* describes the performance. A higher luminosity generally implies more data can be taken. The luminosity delivered per unit time – which is defined as the cross-section-scaled collision rate – is determined via

$$\mathcal{L} = \frac{1}{\sigma}\frac{dN}{dt} = N_b f \frac{n_1 n_2}{4\pi\sigma_x\sigma_y}. \tag{3.1}$$

The parameters N_b, n_1, and n_2 describe the beam structure; N_b is the number of colliding bunches while n_1 and n_2 describe the particle densities within a given bunch in each beam. σ_x and σ_y describe the transverse profile of the beam and are tuned using quadrupole magnets in the LHC beam optics.[1]

Focusing magnets concentrate the beam immediately prior to arrival at an interaction point to

[1] Notice the product $\pi\sigma_x\sigma_y$ reflects the area of an elliptical beam cross section in the xy-plane.

maximize the delivered luminosity and reduce the particle density away from the IPs. Typical values are $\sigma_{x,y} \sim \mathcal{O}(20\ \mu\text{m})$. Lastly $f = 11.24\,\text{kHz}$ is the revolution frequency at the LHC.

The beam spread parameters $\sigma_{x,y}$ can be described in terms of the beam emittances $\varepsilon_{x,y}$. The transverse motion of a beam particle in direction i can be parameterized in terms of its longitudinal position within the beam s,

$$x_i(s) = A_i \sqrt{\beta(s)} \cos\left(\psi_i(s) + \delta_i\right). \tag{3.2}$$

This motion describes an elliptical trajectory ("Bevatron Oscillations") in phase space for the particle [12, 206]. The frequency of the oscillations is fixed via $d\psi_i/ds = \beta^{-1}$. Therefore, over an ensemble of non-interacting particles that comprise the beam, an ellipse with area $\varepsilon_i \equiv \pi\sigma_i^2/\beta^2$ is marked out in (x_i, x_i') phase space, and is an invariant if no energy-loss processes occur. This constraint on the emittance couples x_i and its time derivative inversely, and so the beam can only be focused over a short distance. The value of β at the IP (β^*) is particularly noteworthy as it determines the delivered luminosity to the experiment. Away from the IP, the beam spread increases approximately quadratically in s,

$$\sigma_i(s) \simeq \sigma_i(0) \left(1 + \frac{s^2}{\left(\beta^*\right)^2}\right). \tag{3.3}$$

The LHC has operated with a variety of β^* values to produce data sets with luminosities ranging from very low to very high. Experiments often refer to the instantaneous luminosity in terms of the collision rate, determined from the number of interactions per bunch crossing μ. Multiple collisions produced in the same beam crossing are colloquially referred to as *in-time pileup*. During nominal Run 2 pp data-taking, $\langle\mu\rangle \sim 37$ at IP-1. For heavy ions, pileup is disfavored from a detector perspective because the particularly violent head-on collisions already can lead to a high detector occupancy. Machine considerations also limit the number of ion bunches that can be collided. Consequently μ is typically very low, with values $\mu \sim 10^{-3} - 10^{-2}$ during ion operations. For comparison to heavy-ion data sets, special pp "low-μ" reference data sets were taken in 2015 and 2017, with μ values peaking only around $\sim 3 - 4$.

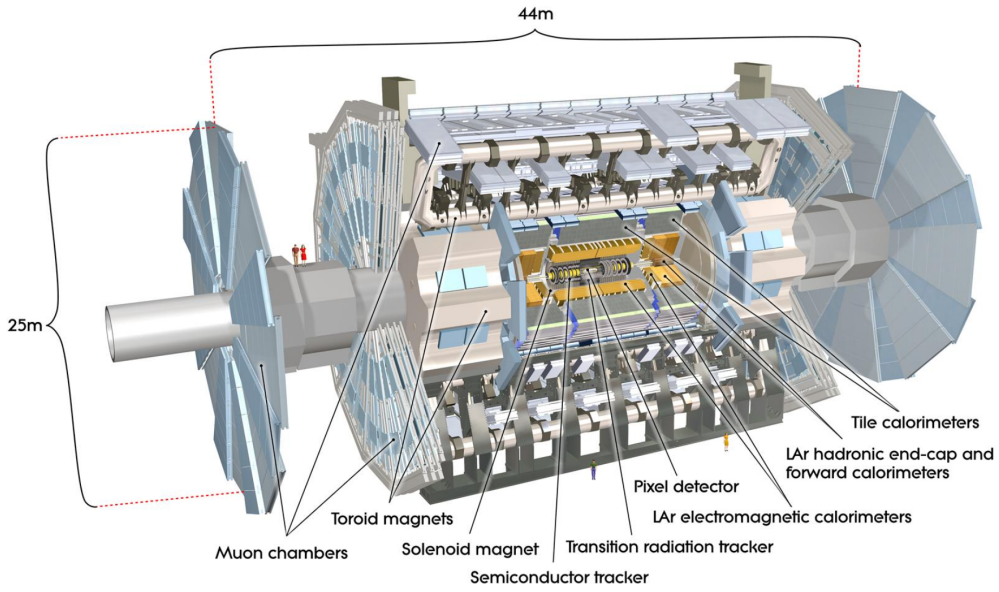


Figure 3.2: Illustration of the ATLAS detector, with a cross-sectional cutout to show its different layers [207].

3.2 The ATLAS detector

IP 1 is the closest LHC IP to the CERN main site, located directly across the street from the core campus. It is the home of the ATLAS detector (A Toroidal LHC Apparatus) [208, 209]. ATLAS is a general purpose particle detector and contains sophisticated instrumentation for a wide variety of particle and nuclear physics measurements. The detector is built around the LHC beamline with the beam spot at the core. A cylindrical coordinate system is used to describe the detector as well as particle objects found within it, with the origin set to the beam spot. The x-axis points from the beam spot to the center of the LHC ring, and the y-axis points vertically upwards. The z-axis points along the beam pipe with orientation as dictated by the right-hand rule. Colloquially, the "A-side" of the detector refers to the half with $+z$ coordinates and the "C-side" to the half with $-z$ coordinates. The transverse xy-plane defines the cylindrical coordinates (r, ϕ). The polar angle θ is defined relative to the $+z$-axis and is often expressed in terms of pseudorapidity

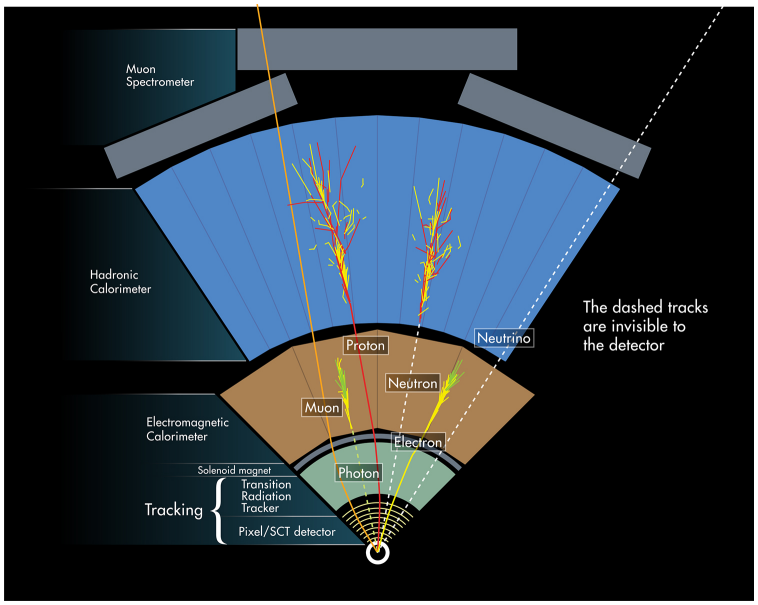


Figure 3.3: Illustration of how different types of particles interact with the ATLAS detector. Figure reproduced from Ref. [210].

η,

$$\eta = -\ln \tan \frac{\theta}{2}. \tag{3.4}$$

For massless particles, pseudorapidity is equivalent to their rapidity along the z-axis. For massive particles, the two are not equivalent, but $\eta \approx y + \mathcal{O}(m/p)^2$, providing a reasonable approximation near midrapidity. The center-of-mass rapidity for parton-parton scatterings is not uniquely determined within the parent hadron-hadron collision, so momentum conservation is only directly observable within the transverse plane. Therefore momenta are typically expressed in terms of the *transverse momentum* p_{T} in the xy-plane, as well as the angular coordinates η, ϕ.

An illustration of the ATLAS detector and its layers is shown in Fig. 3.2. The detector is ϕ-symmetric and has nearly 4π coverage in solid angle. It is equipped with multiple subdetectors, each with a different purpose:

- a highly segmented inner detector (ID) for high precision momentum determination of charged particles,
- multiple calorimeter systems for precise photon, electron, hadronic and missing E_{T} mea-

surements across a wide region of phase space,

- a muon spectrometer (MS) outside the detector core for high purity muon measurements,
- multiple strong electromagnets to control and understand charged-particle trajectories, and
- high-speed, multilevel event triggering that can sample high collision rates.

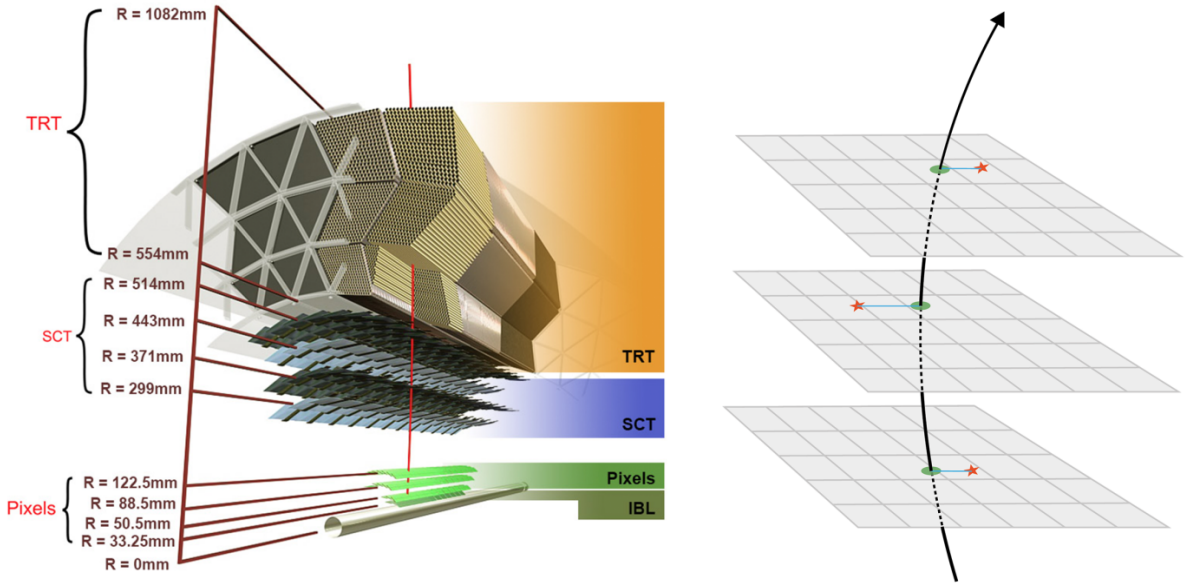
Fig. 3.3 illustrates how different types particles interact with the different subdetectors. The measurements presented in this dissertation use the majority of the ATLAS detector in some manner. This includes

- determining charged-particle trajectories in the ID,
- using calorimeter and MS measurements to recover Z^0 bosons and cluster jets, and
- classifying and selecting events based on total forward rapidity energy deposits.

In the following sections, we will discuss the design of the detector and how these types of measurements are enabled, working radially outwards from the interaction point.

Inner Detector

Aside from the beam pipe, the inner detector (ID) is the closest material to the actual collision point. Non-destructive measurements of particle trajectories – defined as measurements that don't significantly alter the trajectory – must occur as soon as possible after the collision; otherwise the kinematics in outer layers of the detector will be biased by energy-loss effects in the detector material. The purpose of the ID systems is thus to provide information on these trajectories without inducing particle showers prematurely. The design of the ID systems must therefore meet stringent requirements; it must be extremely finely segmented for high angular precision in dense collision environments, be able to perform consistently in a high-radiation environment, fit in as small of a space as possible, and extend over a wide range in z for broad pseudorapidity coverage. A versatile



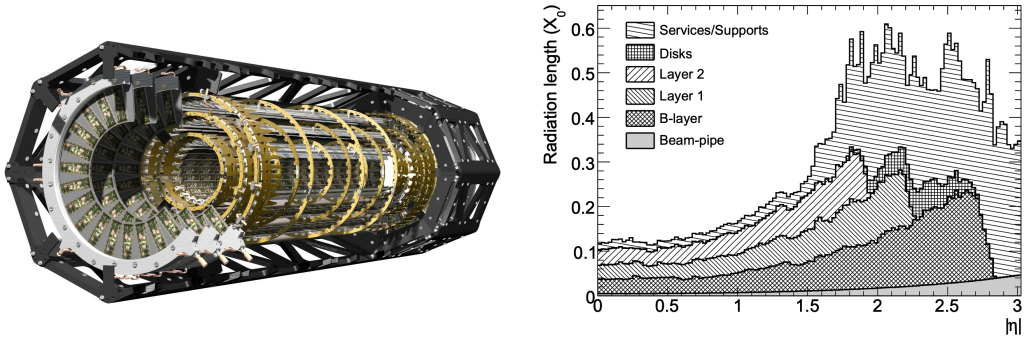
(a) Cross section of the inner detector **(b)** Illustration of the trajectory fitting

Figure 3.4: **(a)** A cross section of the ATLAS inner detector is shown, with each layer labeled. **(b)** A charged particle curves in the static magnetic field, leaving an ionized trail in detector modules. The particle momentum and charge are reconstructed by fitting the modules struck by the particle ("hits") to a curved trajectory [211].

ID is especially required for heavy flavor studies whereby reconstructed decay vertices displaced by $\sim 200 - 1000\,\mu$m play an essential role.

There are three main components to the ID system, illustrated in Fig. 3.4. In order of increasing radius, they are the pixel detectors (including the B-layers), the semiconductor trackers (SCT), and the transition radiation tracker (TRT). Directly outside the tracking system is a strong solenoid magnet with static field strength $B \simeq 2$ T which curves the trajectories of charged particles out to high momentum according to the Lorentz force law. The tracking cavity has radius 115 cm and length 7 m, enabling trajectories to be measured out to $|\eta| = 2.5$. Charged particles traversing the ID modules ionize trails of electrons on silicon sensors. The pattern of sensor hits are used to fit the curved trajectories. Particle charge sign and momentum are determined by the direction and radius of curvature, respectively.

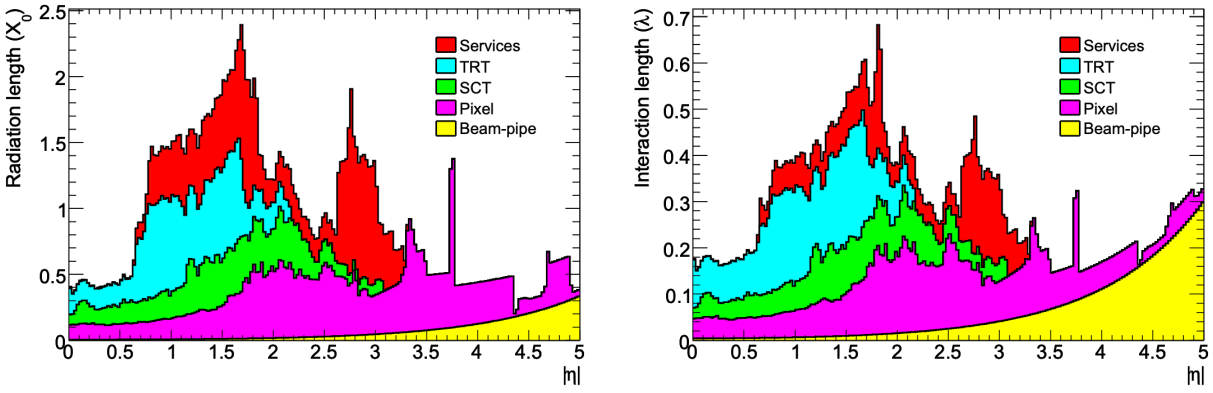
The pixel detector at the center comprises barrel and end-cap components [213, 214]. There



(a) Rendering of the pixel detector **(b)** Path-length in units of X_0

Figure 3.5: Left: A rendering of the Run 1 ATLAS pixel detector. Right: The path-length of particles in units of electromagnetic radiation lengths X_0 from the origin to the $\phi-$averaged outer radius of the Run 1 pixel detector is shown as a function of pseudorapidity. Figures from [212, 213], respectively.

are 4 barrels of pixels with radii $\sim 33\,\text{mm}, 50.5\,\text{mm}, 88.5\,\text{mm}$, and $122.5\,\text{mm}$. Three end-cap disks per side are located at $|z| \sim 495\,\text{mm}, 580\,\text{mm}$, and $650\,\text{mm}$. The innermost two barrel layers are commonly referred to as the insertable B-layer (IBL) and the B-layer due to their significant impact on b-tagging (analytical procedures which recognize jets formed by the fragmentation of bottom quarks). Due to the high expected Run 2 instantaneous luminosities $\sim 2 \times 10^{34}\,\text{cm}^{-2}\,\text{Hz}$ in pp operations, and an interest in an additional layer for more robust trajectory pattern recognition, the IBL was installed in 2014 as an upgrade while radiation damaged pixel sensors were repaired. For the IBL to fit, a new, smaller beampipe was simultaneously installed. Each layer and disk consists of sets of modules which are the basic building block for the pixel detector. A single module comprises a silicon sensor coupled to front end electronics, all mounted on a flexible printed circuitboard. The sensor on each module contains 46,080 pixel channels each with area $50\,\mu\text{m} \times 400\,\mu\text{m}$ in the $R\phi \times z$ directions. For the IBL, the dimensions are smaller, with pixel area $50\,\mu\text{m} \times 250\,\mu\text{m}$ and only 26,880 channels per module. The pixel electronics measure the integrated charge buildup in each channel with the time-over-threshold, which is dependent on the deposited energy. In each barrel layer, modules are mounted on staves in the turbine layout, with relative angle to the barrel of 20°. In order of increasing radius, each layer has 224, 286, 494, and 676 modules. The end-caps have 48 modules each, bringing the total number of readout channels to 92.4 million. The combined



(a) ID length in units of X_0 **(b)** ID length in units of λ

Figure 3.6: The total material budget of the ID in units of **(a)** radiation lengths X_0 and **(b)** hadronic interaction lengths λ is plotted as a function of particle pseudorapidity $|\eta|$. Figure reproduced from Ref. [208].

material budget is modest; the entire pixel detector only possesses $\sim$ 12% of a radiation length near midrapidity [213]. The addition of the IBL only increased this to 14% [215, 216].

Outside the pixel layers is the SCT, which is the single most expensive subsystem of ATLAS [217–220]. The overall design of the SCT is similar to the pixel detector; individual modules with two layers of 768 silicon strips with dimension $80\,\mu$m $\times$ 126 mm in $\phi \times z$ observe particle positions via a binary (on/off) signal. Unlike the pixel detector, no information on collected charge is provided by the readout. Four consecutive barrel layers contain 384, 480, 576, and 672 modules, respectively, at radii 299 mm, 371 mm, 443 mm, and 514 mm. A hit in the SCT is defined as a single strip reporting an observed signal; a particle moving radially outward at mid-rapidity can therefore leave a theoretical maximum of 8 hits in the SCT, assuming it does not hit multiple strips in the same layer (as opposed to a hit in each layer, corresponding to only four hits). Each barrel is 1492 mm long along the beam axis. Along with the barrels, nine end-caps are placed on both sides, each with between 52 and 132 modules of various geometries, are located between $|z| = 853.8 - 2720.2$ mm to provide coverage for high rapidity particles. In total there are 4088 modules providing $\sim$ 6.27 million readout channels. Even with $\mathcal{O}(10)$ fewer channels than the pixel detector, the SCT is designed for total occupancy of $\lesssim 0.5\%$ at the nominal LHC luminosity and

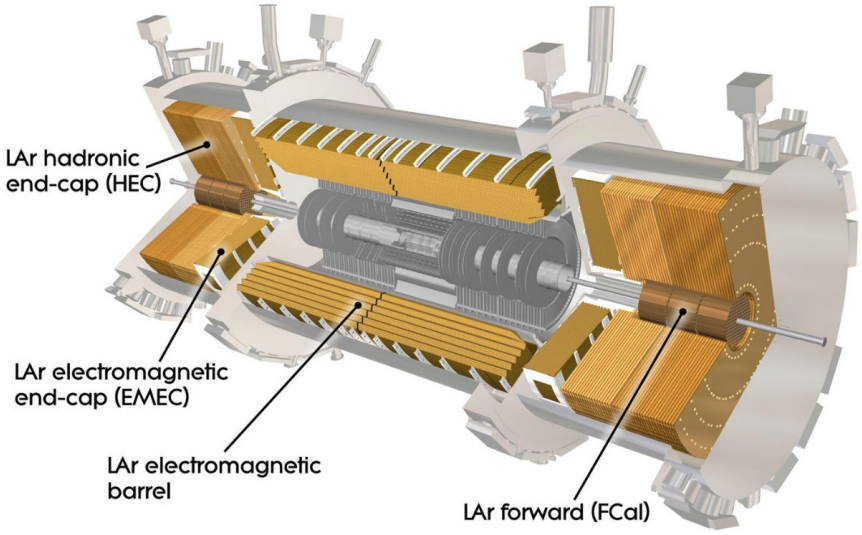


Figure 3.7: Schematic overview of the ATLAS liquid argon calorimeter system. Figure reproduced from Ref. [221].

$\mu \lesssim 23$. Heat generation – which depends on the leakage current during operation – is strongly dependent on temperature, as the leakage current roughly doubles with every 7° C. The SCT was therefore designed not only to minimize the material budget, but also the thermal expansion coefficient, as well as be able to efficiently conduct and disperse heat in case a thermal run-away situation occurs due to an exponentially increasing leakage current inducing higher temperatures via electrical resistance.

The last major component of the ID is the TRT outside of the SCT, which is a type of drift chamber, unlike the pixel and SCT detectors [222]. The TRT is composed of concentric layers of strawtubes interleaved with radiator layers. Each straw has radius 2 mm with intrinsic accuracy 130 μm. The inner coating of the straws contains a 0.2 μm layer of aluminum which serves as a cathode; a tungsten wire down the nominal core is the anode. Ionization electrons are collected across the potential as well as transition radiation (TR), its namesake. Ultra-relativistic charged particles with $\gamma \gtrsim 10^3$ emit TR X-rays as they pass through the radiator layers. These photons then pass through a gas mixture of 70% Xe, 27% CO_2, and 3% O_2 in each straw. The xenon – being a heavy element – is highly efficient at absorbing the X-ray TR photons. In this configuration,

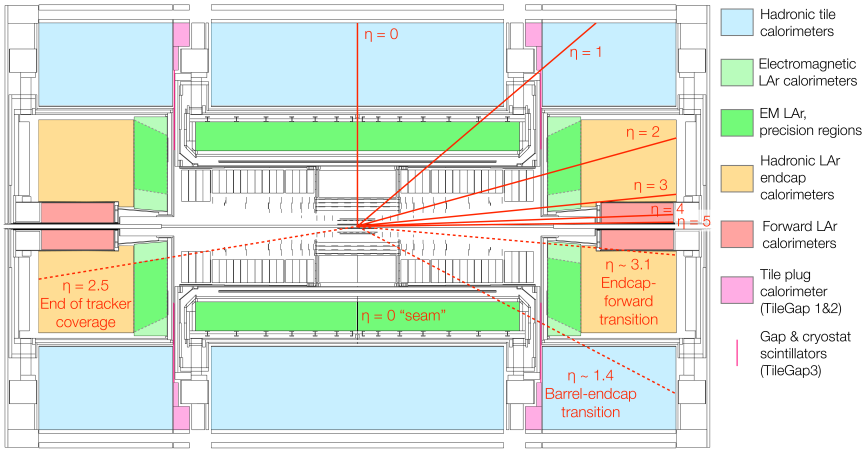


Figure 3.8: Diagram showing the ATLAS calorimeters systems, including their coverage in $|\eta|$. Figure reproduced from Ref. [226].

TR photons create about 5-6 ionization clusters per millimeter, which leaves a much stronger signal in the detector than ionizing radiation. Subsequent high and low-level filters can be used to discriminate TR photons. This is especially useful for separating charged pions and electrons, since only the latter are traveling at $\gamma \gtrsim 1000$ for momenta $\lesssim 100\,\text{GeV}$. This discriminator was not fully realized during Run 2 even in pp collisions as irreparable gas leaks required replacement of the expensive xenon with cheaper argon in some strawtubes [223, 224].

The 52,544 straws of length 144 cm are in the barrel section, oriented along the detector cylinder, while 122,880 of length 37 cm are in the end-caps oriented perpendicular to the beam axis, per side. The barrel extends tracking coverage from $554 - 1082\,\text{mm}$ in radius, and the end-caps extend from $848 - 2710\,\text{mm}$ in $|z|$. In total there are over 350,000 readout channels, with kinematic coverage for particles out to $|\eta| < 2$. This design ensures each particle travels through 35-40 straws in the TRT, aiding the tracking from the pixel and SCT layers. In environments with high pileup rates up to $\mu \sim 70$, the occupancy of the TRT is less than $\sim 35\%$. However, in central Pb+Pb collisions, the TRT occupancy can reach 90%, which makes track fitting difficult [225]. For this reason the TRT is not typically used in the heavy-ion reconstruction.

LAr Subdetector	EM Barrel		EM End-caps	
Total Coverage	$\|\eta\| < 1.475$		$1.375 < \|\eta\| < 3.2$	
Absorber Material	Lead		Lead	
Presampler Channels	$2 \times 3,904$		2×768	
Calorimeter Channels	$2 \times 50,880$		$2 \times 62,208$	
		$\|\eta\|$ interval		$\|\eta\|$ interval
Layers	Presampler	$0 - 1.52$	Presampler	$1.5 - 1.8$
	3	$0 - 1.35$	2	$1.375 - 1.5$
	2	$1.35 - 1.475$	3	$1.5 - 2.5$
			2	$2.5 - 3.2$
Presampler $\Delta\eta \times \Delta\phi$	0.025×0.1	$0 - 1.52$	0.025×0.1	$1.5 - 1.8$
Layer 1 $\Delta\eta \times \Delta\phi$	$0.025/8 \times 0.1$	$0 - 1.40$	0.050×0.1	$1.375 - 1.425$
	0.025×0.025	$1.40 - 1.475$	0.025×0.1	$1.425 - 1.5$
			$0.025/8 \times 0.1$	$1.5 - 1.8$
			$0.025/6 \times 0.1$	$1.8 - 2.0$
			$0.025/4 \times 0.1$	$2.0 - 2.4$
			0.025×0.1	$2.4 - 2.5$
			0.1×0.1	$2.5 - 3.2$
Layer 2 $\Delta\eta \times \Delta\phi$	0.025×0.025	$0 - 1.40$	0.050×0.025	$1.375 - 1.425$
	0.075×0.025	$1.40 - 1.475$	0.025×0.025	$1.425 - 2.5$
			0.1×0.1	$2.5 - 3.5$
Layer 3 $\Delta\eta \times \Delta\phi$	0.050×0.025	$0 - 1.35$	0.050×0.025	$1.5 - 2.5$

LAr Subdetector	Hadronic end-caps		Forward calorimeters	
Total Coverage	$1.5 < \|\eta\| < 3.2$		$3.1 < \|\eta\| < 4.9$	
Absorber Material	Copper		Copper, Tungsten	
Calorimeter Channels	$2 \times 2,816$		$2 \times 1,762$	
		$\|\eta\|$ interval		Module
Layers	4	$1.5 - 3.2$	3	$3.1 - 4.9$
$\Delta\eta \times \Delta\phi$ or	0.1×0.1	$1.5 - 2.5$	$\leq 3.0 \times 2.6\,\mathrm{cm}^2$	FCal1
$\Delta x \times \Delta y$	0.2×0.2	$2.5 - 3.2$	$\leq 3.3 \times 4.2\,\mathrm{cm}^2$	FCal2
			$\leq 5.4 \times 4.7\,\mathrm{cm}^2$	FCal3

Tile Segment	Barrel		Extension	
Total Coverage	$\|\eta\| < 1.0$		$0.8 < \|\eta\| < 1.7$	
Absorber Material	Steel		Steel	
Calorimeter Channels	$5,760$		$2 \times 2,046$	
Layers	3	$0 - 1.0$	3	$0.8 - 1.7$
		Layers		Layers
$\Delta\eta \times \Delta\phi$	0.1×0.1	1 and 2	0.1×0.1	1 and 2
	0.2×0.1	3	0.2×0.1	3

Table 3.2: Detailed schematics of the liquid argon and tile calorimeters, including the absorber material, total number of channel readouts, cell area dimensions, and pseudorapidity coverage [208].

Electromagnetic Calorimeters

Outside the solenoid is the first liquid argon calorimeter (LAr) barrel, which comprises both the entire electromagnetic calorimeter (EMCal) and parts of the hadronic (HCal) calorimeter systems. Unlike the ID, calorimetry stops particles by inducing energy loss; for this reason it is called a *destructive* measurement. The LAr is a sampling calorimeter system with coverage over the entire range $|\eta| < 4.9$. Where the coverage overlaps with the tracker ($|\eta| < 2.5$) the LAr is very finely segmented and optimized for precision measurements of electrons and photons. The remainder is less finely segmented and exists primarily for jet reconstruction. The argon is kept in the liquid phase at 88.5 K via liquid nitrogen refrigeration. Four separate calorimeters are built from the basic LAr design: the electromagnetic barrel (EMB) and end-caps (EMEC), the hadronic end-caps (HEC), and forward calorimeters (FCal).

The EMCals are designed to detect radiation from *electromagnetic (EM) showers*. Electrons and photons, as well as other charged particles, are well-understood to lose energy in dense media [12]. At high energies, bremmstrahlung dominates the loss of energy for electrons while pair production dominates for photons. These emissions build on each other, with electrons emitting photons that subsequently pair produce, emitting more photons, which pair produce, and so on. This creates a cascade of particles with decreasing energy – an EM shower – which eventually ceases when photons no longer meet the energy requirement to pair produce, and bremmstrahlung becomes a subdominant energy-loss mechanism for the electrons. The cascading process is inherently exponential in nature and so the length X of the cascade can be related to the initial energy of the particle E by

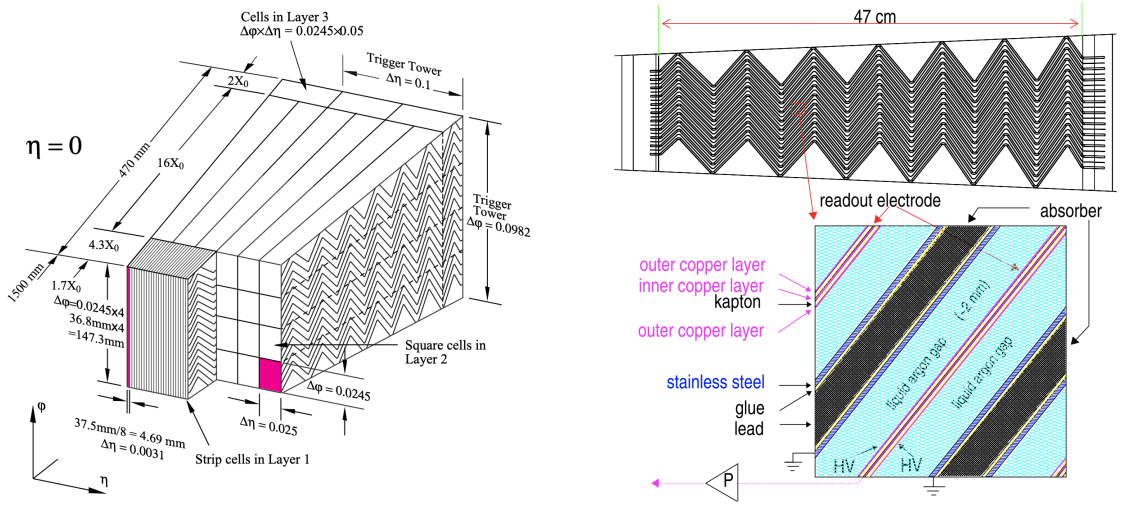
$$\frac{X}{X_0} = \frac{\ln E/E_0}{\ln 2}. \tag{3.5}$$

In this relation, X_0 is the *radiation length* and E_0 is the critical energy at which bremmstrahlung and ionization energy losses are equal. Conceptually, after a distance X_0 an electromagnetic particle is expected to lose all but a factor of $1/e \approx 37\%$ of its energy. The radiation length depends on the properties of the material, but typically $X_0 \propto AZ^{-2}$ where A and Z are the atomic mass

and number of the absorber material, which induces the EM shower. Eq. 3.5 shows that particles with more energy will produce larger EM showers which contain more final-state electrons. By measuring the number of electrons created in the shower, the initial energy can be determined.

Thin lead plates serve as the absorber material for the ATLAS LAr detectors. The plates are 1.53 mm and 1.13 mm thick in the EMB for $|\eta| < 0.8$ and $|\eta| > 0.8$, respectively. The EMB is built in two halves for both the A- and C-sides. Each half barrel has four concentric layers to it, and extends out to $|\eta| < 1.475$. First, a pure liquid argon presampler with thickness 11 mm with no absorber material is used to sample showers beginning closer to the IP. Next, layers 1, 2, and 3 each contain absorber material interleaved with electrodes to pick up ionization electrons in the liquid argon, which fills the gaps. The interleaving geometry is referred to as an accordian as illustrated by Fig. 3.9 due to the alternating orientation of the plates. Each layer contains segmented *cell* structures where the total electrode charge is integrated and recorded by the DAQ electronics. In layer 1, the cells have a strip shape with the narrow dimension along η and the long dimension along ϕ. Layers 2 and 3 have a more complex pattern in η and ϕ, as shown in Fig. 3.9. The electrodes are made of three copper plates separated by insulating polyimide layers. The outer layers are kept at a high voltage $\approx +2$ kV, and the inner layer, coupled capacitively, is read out. The drift time for electrons to accumulate on the electrodes is about 450 ns. The electrodes in layer 1 are read out on the front-end while layers 2 and 3 are read out on the back-end.

The electromagnetic end-caps (EMEC) are built similarly to the barrel, and provide coverage between $1.375 < |\eta| < 3.2$. Unlike the barrel which has the accordian ridges oriented along z, the ridges are oriented in the radial direction for the end-caps. This is sometimes referred to as the "Spanish fan" configuration. The EMEC is divided into two coaxial wheels. The outer wheel, which covers up to $|\eta| = 2.5$, is finely segmented into cells with dimensions similar to the barrel. The inner wheel goes out to $|\eta| = 3.2$ and is more coarsely segmented with $\Delta\eta \times \Delta\phi = 0.1 \times 0.1$ for use in jet reconstruction. Details on the cell segmentation can be found in Table 3.2. The lead plate absorbers have thicknesses 1.7 mm and 2.2 mm for the outer and inner wheels, respectively. Both the EMB and EMEC have been designed to have minimal punch-through: the total path



(a) Overview of an EMB module **(b)** Close-up view of the accordian structure

Figure 3.9: **(a)** Cross-sectional sketch of an EMB module near $\eta = 0$. The accordian structure of the middle layer can be seen from the side view. In layer 1, cells have a strip shape, while in layers 2 and 3 they have a square shape. **(b)** Close-up view of the gap and electrode within the accordian geometry. Figures reproduced from Refs. [208, 227].

length of the EMCal is at least $22X_0$ everywhere in η, nearly guaranteeing that EM showers for electrons and photons will begin in the EMCal. This allows the integrated charge in each cell to serve as a proxy for the size of the shower, and thus a total cell energy can be determined after a calibration procedure. Each cell is read out as a separate channel and provides a signal amplutide associated with an angular position, which can be later converted to a four-momentum input to the reconstruction. In total, there are 9,344 presampler and 163,968 calorimeter channels across the EMCals.

Hadronic Calorimeters

The LAr technology is also used as the active material in the forward hadronic calorimetry at $|\eta| > 1.5$. These calorimeters are designed to be sensitive to the energy deposited by *hadronic showers* in addition to EM showers. When hadrons enter a dense material, they may begin to interact electromagnetically if they are charged, leaving an ionized wake of electrons. But, eventually they will strike a nucleus in the absorber, generating new hadrons. This allows additional,

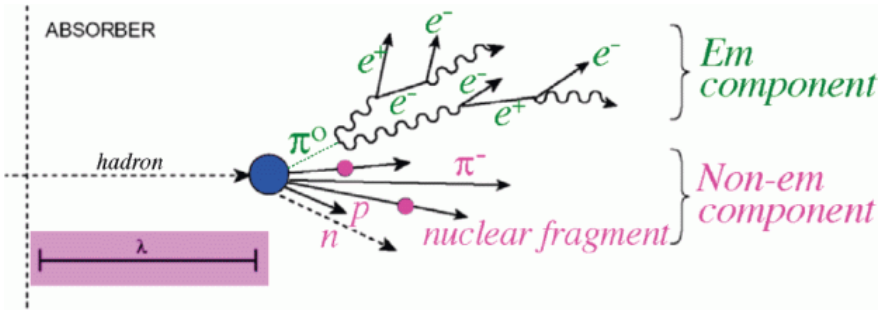


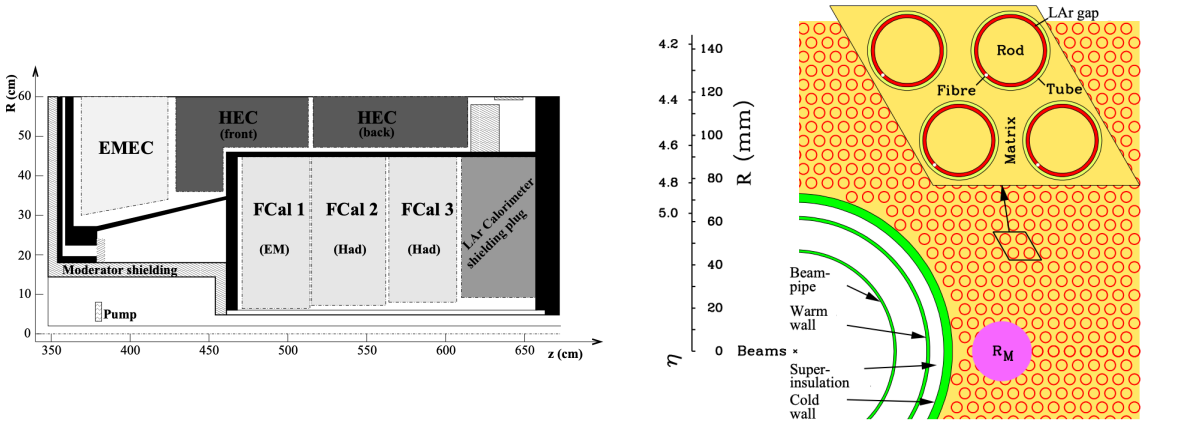
Figure 3.10: Illustration of a hadronic cascade formed by a neutron after entering an absorber material. Multiple components to the shower develop, including an EM component from a π^0 decay (top) and a hadronic component (bottom). Figure reproduced from Ref. [228].

followup measurements of charged hadrons, and in particular, is the only way to measure neutral hadrons. Similar to the radiation length, the mean free path or *interaction length* for a hadron to strike a nucleus is defined in terms of the nuclear cross section $\lambda = 1/n\sigma_{\text{tot}}$. In typical materials, the interaction length is much larger than the radiation length; i.e., the probability of a nuclear interaction grows more slowly with distance than an electromagnetic one. Therefore a hadronic cascade has a much larger size than an EM shower. The exact value of λ depends on the material, but generally $\lambda \propto A^{1/3}$, so $\lambda/X_0 \propto A^{4/3}$. Thus heavier materials are generally preferable for hadronic calorimetry.

In particular, π^0 and η hadrons created during the cascade will essentially immediately decay into photons, generating an irreversible EM shower component that can be measured. This is illustrated in Fig. 3.10 for a neutron-induced cascade. The energy deposited by induced EM showers is a key part of the *EM scale* in hadronic calibration, which correctly measures the deposited energy from EM particles[2] [229, 230]. The remaining hadronic component can then interact again, possibly producing another EM shower or inducing "invisible losses", such as recoil of the struck nucleus in the absorber. In short, the complexity of the strong interaction and the large number of final states make hadronic cascades much more stochastic in shape, depth, and integrated signal.

Because the ATLAS EMCal is expected to fully contain the showers of electrons and photons,

[2] Note the difference between the EM *fraction* and EM *scale*: the EM *fraction* denotes the pure EM shower components, while the EM *scale* includes the EM fraction as well as energy deposits from (e.g.) ionization losses by charged pions.



(a) rz-plane cross-sectional view **(b)** xy-plane cross-sectional view

Figure 3.11: **(a)** A cross-sectional view in the rz-plane of the forward LAr calorimeters. **(b)** Cross-sectional view of the FCal1 absorber matrix in the xy-plane. Electrodes are drilled into the copper plate along the $z-$direction and contain liquid argon as a sampling material. The beam pipe is shown in the bottom left corner. Figures reproduced from Ref. [208].

the hadronic calorimeters contain large absorbers to maximize the number of interaction lengths and force cascades of any remaining particles. Hadrons at intermediate-forward pseudorapidities $1.5 < |\eta| < 3.2$ pass through the hadronic end-caps (HEC) with a similar wheel shape to the EMEC. The two HEC wheels are located past the EMEC in z but at slightly higher radii to match the EMEC pseudorapidity range, as shown in Fig. 3.11. The absorber material is a series of flat thick copper plates of varying thickness, each oriented perpendicular to the beam. HEC1 is built with 24 plates with thickness 25 mm plus a thinner 12.5 mm front plate. HEC2 has 16 layers of plates at 50 mm and a 25 mm front plate. Gaps between layers are all 8.5 mm and filled with liquid argon. Three electrodes inserted in each gap create four drift zones in the fluid to collect drifting electrons. A high voltage ~ 1.8 kV is applied to the outer layers, and the inner layer is read out to the TDAQ, similar to the EM calorimeters. Cells at $|\eta| < 2.5$ have angular size $\Delta\eta \times \Delta\phi = 0.1 \times 0.1$; for $2.5 < |\eta| < 3.2$ they have size 0.2×0.2.

The final LAr-based calorimeter is the forward calorimeter (FCal), which functions as both an EMCal and an HCal at high pseudorapidities $3.1 < |\eta| < 4.9$. Due to its situation in η, the FCal is subject to high particle fluxes and so the liquid argon only fills a very tight volume. There are

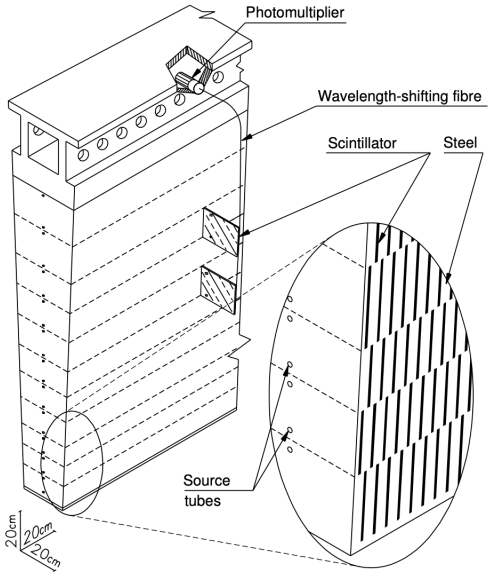


Figure 3.12: Illustration of a tile drawer in the barrel segment of the tile calorimeter. Figure reproduced from Ref. [208].

three consecutive segments to the FCal; the first FCal1 has fewer interaction lengths $L_1 \sim 2.7\lambda$ but many radiation lengths $L_1 \sim 27.6X_0$, while the second and third, FCal2 and FCal3, are thicker to hadrons $L_{2,3} \sim 3.6 - 3.7\lambda$. Thus EM showers will be concentrated in FCal1, while FCal2 and FCal3 pick up hadronic showers. Each segment is 45 cm long in z. FCal1 contains layers of copper plates as absorbers with electrode tubes inserted in holes parallel to the beam line. This orientation is chosen because particles will traverse the electrodes at very shallow angles. The dense pattern of electrodes within the absorber plates is sometimes called the "absorber matrix" due to its appearance, shown on the right in Fig. 3.11. Liquid argon fills the 0.27 mm gap between the grounded outer wall and the inner core of each electrode at 250 V. FCal2 and FCal3 use denser tungsten slugs instead which surround the electrodes in a hexagonal pattern instead of copper plates. These segments also feature modestly larger liquid argon gaps 38 mm and 51 mm in the electrodes. Readout is performed in the front-end of FCal1 but on the back-end of FCal2 and FCal3 to minimize cabling between FCal1 and FCal2, where the highest radiation levels are expected.

In the central region $|\eta| < 1.7$, outside the EMB, hadronic calorimetry is performed with the tile calorimeter system, which operates differently from the LAr. The tile calorimeter is also a

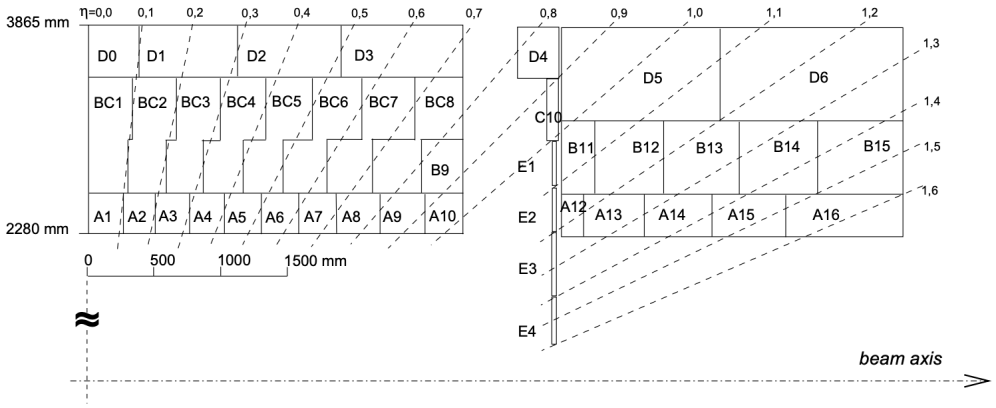
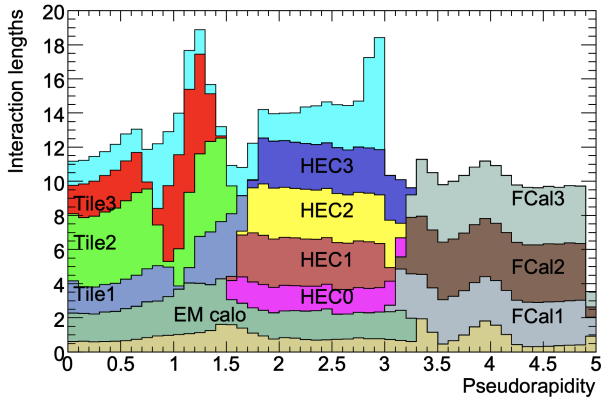


Figure 3.13: Cross-sectional view of the tile calorimeter drawer layout in the rz-plane. The origin is in the bottom left corner. Figure reproduced from Ref. [208].

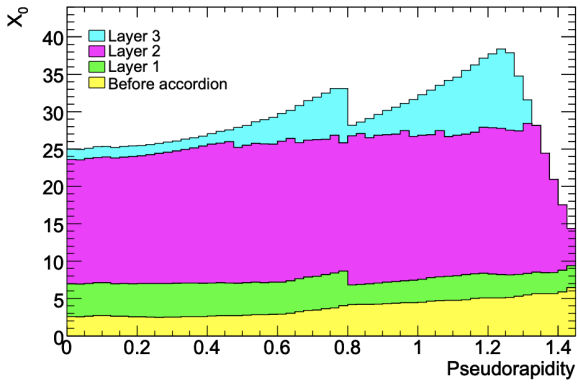
sampling calorimeter with steel serving as the absorber material, but tile scintillators as the active material. Scintillators are inserted into slots within a steel module; an example "drawer" module is shown in Fig. 3.12. Light in each scintillator is collected at the surface of the drawer and coupled to a photomultiplier by a wavelength-shifting fiber. Thus, the tile calorimeter is sensitive to the *photons* created in an EM shower, rather than the electrons. Similar to how the electrode total charge indicates the number of electrons collected and thus the shower size, the scintillator will pick up more photons in a larger shower and so the incident energy can be measured by the intensity of the light signal. EM shower photons are typically in the UV, but are shifted to the optical range by the fibers.

The tile calorimeter is divided into three segments, each with three concentric layers, as shown in Fig. 3.13. In the center is the 5.8 m long barrel with coverage $|\eta| < 1.0$, while the 2.6 m tile extensions cover $0.8 < |\eta| < 1.7$. Each has an inner radius 2.28 m and extends out to 4.25 m. At $\eta = 0$, the barrel has radial depth 7.4λ. By volume, the steel-to-scintillator material ratio is about 4.7. In both the barrels and the extensions, the first and second layers are built from drawers with angular granularity $\Delta\eta \times \Delta\phi = 0.1 \times 0.1$. Hadronic showers are expected to be very wide by the third layer, so the granularity is reduced to 0.2×0.1.

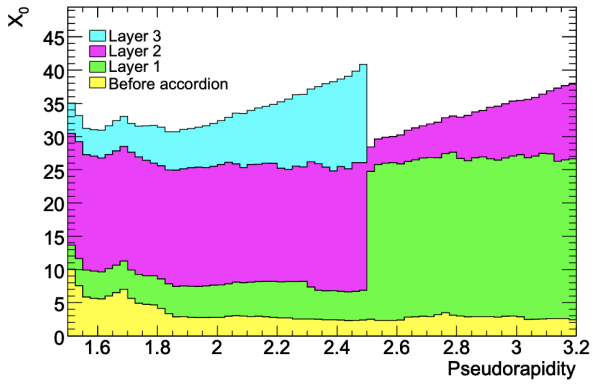
Fig. 3.14 shows the total depth ("material budget") of the calorimeter systems in units of



(a) Total material budget in units of λ



(b) Material budget for the barrel



(c) Material budget for the end-caps

Figure 3.14: **(a)** Total material budget of the ATLAS calorimeter system in units of interaction lengths λ, decomposed by layer. Non-calorimeter contributions (ID, magnets, services, etc.) are shown in **cyan** and **beige**. The material budget of the EMCal in units of radiation lengths X_0 is shown for the **(b)** barrel and **(c)** end-caps, including material in front of the calorimeter in **yellow**. Figures reproduced from Ref. [208].

interaction lengths and radiation lengths (EMCal only). Across the entire pseudorapidity range $-4.9 < \eta < 4.9$, the material budget is at least 10λ with $\lesssim 4\lambda$ before the HCal. The EMCal itself is extremely thick to electrons and photons. This assures that EM showering particles are extremely likely to be fully contained within the calorimeter, making it resilient against punch-through.

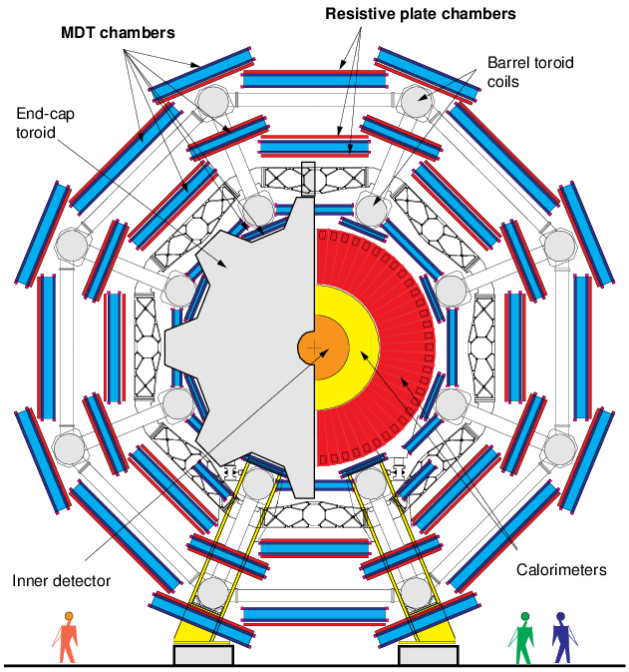


Figure 3.15: Cross-sectional view of the toroid magnets and the MS near mid-rapidity. Figure reproduced from Ref. [231].

Muon Spectrometer

Outside the ATLAS calorimeter is the muon spectrometer (MS) system, which is a dedicated tracking system for measuring the trajectories of muons. The MS operates under similar principles as the ID, with charged particles leaving hits in discrete sensors that can then be recombined in software to estimate a trajectory. The MS operates under the knowledge that all particles aside from muons and neutrinos have a very high probability of being stopped in the calorimeter. Muons largely pass through the calorimeter system without depositing significant energy, aside from ionization and δ-ray emissions, which amount to perhaps $1 - 2\,\mathrm{MeV g^{-1} cm^{-2}}$ until they are ultrarelativistic with $E \gtrsim 10^2\mathrm{GeV}$. Therefore they do not shower in the calorimeter like electrons and photons and can escape. The high probability that a given MS track is a muon leads to the operational assumption that *any* particle observed in the MS is a candidate muon. Offline identification criteria help increase the purity of the candidates.

By volume, the MS comprises the vast majority of the detector. A set of superconducting

toroids, arranged around the periphery of the calorimeter system, provide a $\sim 4\,\mathrm{T}$ magnetic field in the ϕ-direction to curve muon trajectories along the z-axis. For $|\eta| < 1.6$, muons are curved mostly by the barrel toroid field, while for $1.4 < |\eta| < 2.7$ they are affected mostly by the end-cap field. The ATLAS toroid magnet itself is iconic and weighs about 830 tons – combined with the muon chambers, the cylindrical shape of the outer detector sags by about $\sim 3\,\mathrm{cm}$ under its own weight. Large internal Lorentz forces caused by the magnetic field with stored energy $\sim 1.5\,\mathrm{GJ}$, as well as the ultra-low operating temperature of $4.6\,\mathrm{K}$, limit the number of power cycles over the lifetime of the toroid. During the end of the 2018 Pb+Pb data taking, the toroid slow dump was commenced prior to long shutdown 2 and it was not successfully reactivated, thus only $1.4\,\mathrm{nb}^{-1}$ of the integrated luminosity out of the total $1.7\,\mathrm{nb}^{-1}$ that was recorded is used for muon studies.

A large fraction of the muon-tracking system is built from monitoring drift tube (MDT) chambers. Each MDT is built from a set of drift tubes with diameter $\approx 3\,\mathrm{cm}$ filled with an $\mathrm{Ar}/\mathrm{CO}_2$ admixture in a 93:7 ratio. Ionization electrons are collected on a tungsten-rhenium wire down the nominal core, held at $3.08\,\mathrm{kV}$. Each wire is oriented along the ϕ-direction so to provide precision information on the z-coordinate of the hit. The MDTs themselves are rectangular in the barrel, with their broad face tangential to the cylindrical geometry, while MDTs in the end-caps are trapezoidal and perpendicular instead. In total there are 354,384 channels that are read out, divided amongst three concentric layers of MDT chambers.

Though situated well away from the IP, the MS is not impervious to signals from particles other than muons. Low-energy photon and neutron backgrounds for example are expected to exceed an acceptable rate for MDT modules at high pseudorapidities $|\eta| \gtrsim 2$. Thus, beyond this point in z a different design is used. Cathode strip chambers (CSCs), which are multiwire proportional chambers, cover $2.0 < |\eta| < 2.7$. The CSC modules are oriented so that the wires point radially outward. Cathode strips on one side are perpendicular to the wires and, like the MDTs, run in the ϕ-direction. Cathode strips on the other side of the wires are oriented parallel to the wires to provide the transverse coordinate of the hit. Unlike a traditional wire chamber where the wire signals are read out, for the CSC modulesm it is instead the induced charge on the cathodes that

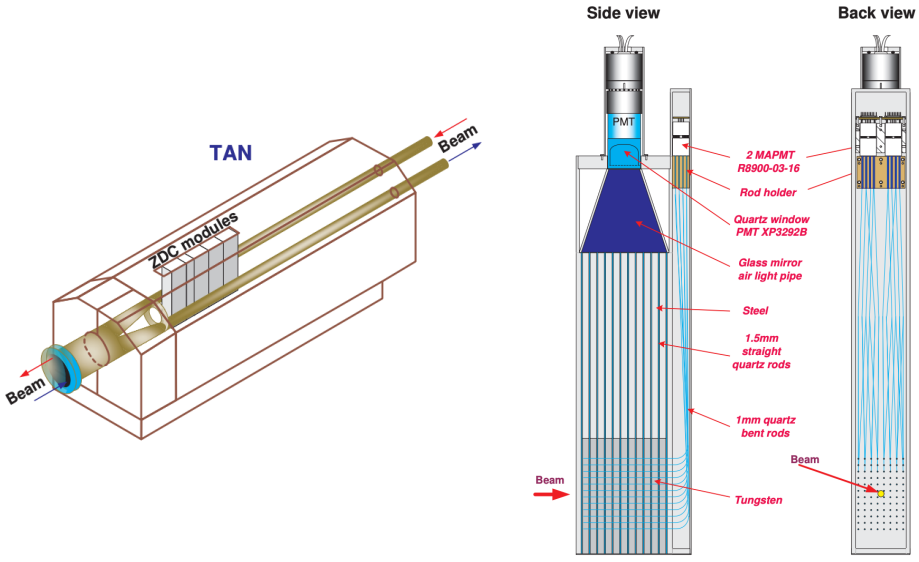
is read out. In total, there are 30,720 CSC readout channels.

In addition to the precision-oriented MDTs and CSCs, there are chambers that provide quick, reliable information to the trigger on the presence of muon tracks. These are the resistive plate chambers (RPCs) and the thin gap chambers in the barrel and end-cap regions, respectively. These components are designed to provide fast, coarse tracking information with adequate n/γ background rejection to enable muon triggering with kinematic filters. The trigger chambers cover a slightly smaller region $|\eta| < 2.4$, as compared with the full muon detector which covers out to $|\eta| = 2.7$. A more complete overview of the trigger chambers can be found in [208].

Zero-Degree Calorimeters

The ATLAS zero-degree calorimeters (ZDCs) are ultra-forward calorimeters covering the pseudorapidity range $|\eta| > 8.3$, which corresponds to polar angles $\theta \lesssim 0.025^{\circ}$ [208, 232, 233]. To situate at this forward position, the ZDC modules are located approximately 140 m down stream of the IP. The beam pipe is split around the modules to accommodate them, thus sweeping away any charged particles, as illustrated on the left of Fig. 3.16. This makes the ZDC particularly sensitive to deposits from neutrals. In heavy-ion collisions, this nominally includes fragmentation or *spectator* neutrons freed from a struck nucleus. Photons can also be detected by the ZDC, but typically have much lower energies than the spectator neutrons, which each carry a few TeV, depending on the beam energies.

One ZDC lives on each side of the IP and is made with four modules placed along the z-direction. The first module is the EM module, with length $29X_0$, and is designed to pick up energy by EM showers and commence the hadronic cascade. The EM module is built from 11 tungsten absorber plates facing perpendicular to the beam direction. Quartz rods run vertically between the plates and detect Čerenkov radiation emitted by shower products. Multi-anode phototubes atop the modules combine light from the rods and produce an electrical signal that is forwarded to the TDAQ. The next three modules are hadronic modules each with thickness 1.14λ (for a total arm depth of 4.6λ). These are built largely the same way as the EM module, but with only 24 rods



(a) **(b)**

Figure 3.16: **(a)** Positioning of the four ZDC modules on one side of the detector (one arm) within the neutral particle absorber (TAN). **(b)** Schematic illustration of a ZDC hadronic module with positional readout from the side and the rear. Figure reproduced from Ref. [232].

compared to 96, and only one phototube per module. Some of the modules also feature longitudinal quartz rods which can provide positional information, but this aspect of the calorimeter is not used here. A hadronic ZDC module with positional readout is illustrated on the right in Fig. 3.16.

The energy exposure of the ZDC is thus on the scale of 10^2 TeV per heavy-ion event and is subject to the highest radiation intensities of the entire detector. It is therefore ineffective at the high instantaneous luminosities delivered in nominal operations; to increase its lifetime it is designed to be removable and is only installed for heavy-ion operations.

3.3 Triggering and Data Acquisition

During pp collisions, the LHC delivers collisions in bunch crossings every 25 ns or at a frequency of 40 MHz. If each collision – with an average data size of 1 MB – were to be recorded by the data acquisition (DAQ) system, multiple TB of data would be written each second, which is infeasible for multiple reasons. Thus on-the-fly decisions must be made about which events to keep.

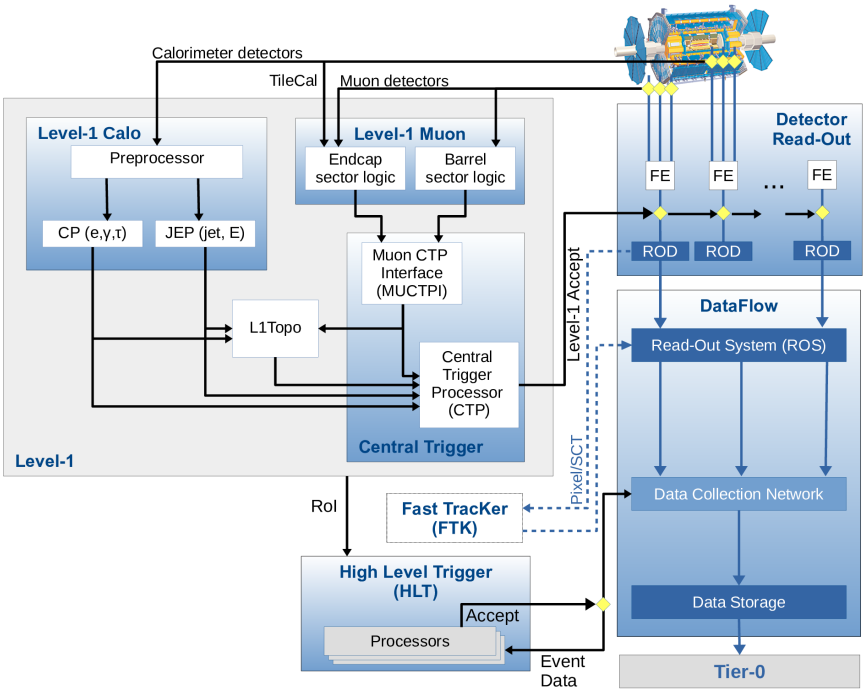


Figure 3.17: Overview of the Run 2 trigger system, including the L1 and HLT triggers. Figure reproduced from Ref. [234].

This is the purpose of the trigger system [208, 234].[3] There are two main levels to the Run 2 ATLAS trigger, illustrated in Fig. 3.17. First is the level-1 (L1) trigger which analyzes the full collision rate and accepts events at a maximum rate of 100 kHz. The L1 trigger is a hardware-based trigger system which searches for coarse, generic indicators of leptons, photons, calorimeter clusters, or high event activity. Inputs from minimum-bias trigger scintillators, ZDCs, calorimeters, and the MS are all considered at this stage. The input from each subsystem is processed by a separate piece of L1 hardware, e.g. the L1Calo or L1Muon. A Central Trigger Processor subsequently combines the output from each into a final acceptance decision. The total time-of-flight through the detector plus the signal travel time to the L1 is much longer than the bunch crossing time; therefore the L1 must also be able to synchronize detector signals and have the front-end electronics temporarily store the entire readout. With this accounted for, the total decision latency of the L1 is 2.5 μs. The

[3] The occasionally-used acronym TDAQ refers to the combined trigger-DAQ system.

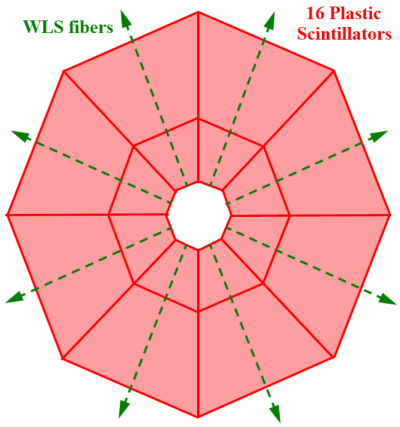


Figure 3.18: Illustration of an MBTS wheel from Run 1. Figure reproduced from Ref. [238].

L1 hardware also identifies topological regions-of-interest (RoIs) associated with the event which should be further studied at the software-level, as detailed next.

This additional software-level analysis is performed by the high-level trigger (HLT). The input rate to the HLT is greatly reduced by the L1 and therefore the HLT can spend more time analyzing each event. The HLT is a highly configurable software-based trigger based on the ATLAS software framework ATHENA. The level-2 (L2) trigger within the HLT first performs a fast, simplified reconstruction surrounding each RoI to provide as much discriminating power as possible. This procedure is parallelized across a computing farm of 40,000 processing units. Each processing unit can take hundreds of microseconds to study a given event. If the L2 trigger decides to accept the event, it is sent to the event filter, which determines the exact trigger firings and the output stream for the event depending on the trigger logic that was fired. If the event is accepted, it is passed to permanent storage at Tier-0 and offline reconstruction commences. The HLT typically accepts events at a rate of $\sim 1.2\,\text{kHz}$, corresponding to a data-recording rate of $1.2\,\text{GB/s}$. A full list of the triggers used to record the data sets in this dissertation can be found in [235–237].

Minimum-Bias Trigger Scintillators

The ATLAS triggers are assisted at the hardware level by the minimum-bias trigger scintillator (MBTS) system [238, 239]. The MBTS can be viewed as a minor extension to the tile calorimeter. Each MBTS – one on each side – consists of two concentric rings of scintillators at $|z| = 3.6\,\text{m}$, directly in front of the tile extension but at a slightly small radial position, as shown in Fig. 3.18. The outer ring covers pseudorapidities 2.08 to 2.76 and the inner ring from 2.76 to 3.86. This configuration was updated when the Run 1 MBTS was replaced prior to Run 2. The inner ring contains eight scintillator panels with a trapezoidal geometry, each covering an azimuthal angle $\Delta\phi = 45^\circ$. The outer ring has four panels covering angle $\Delta\phi = 90^\circ$, a reduction from Run 1 [240]. In total, there are 24 MBTS channels divided amongst the inner and outer rings on either side. Each panel is read out with wavelength-shifting fibers coupled to photomultiplier tubes that converts scintillation light in the panels to an electrical signal that is forwarded to the Central Trigger Processor. If the integrated charge meets a discriminator threshold, then the MBTS is said to have a hit. The number of hits on either side of the detector is frequently used to make L1 trigger decisions. For example, the `L1_MBTS_1_1` trigger requirement looks for at least one hit in both the A- and C-side MBTS disks at the L1-level.

ZDC Trigger

During heavy-ion data taking, the ZDC is frequently used as a minimum-bias trigger-level input due to the sensitivity to spectator neutron production. This is heavily exploited for example in the high-purity detection of ultra-peripheral collisions where the nuclei do not necessarily disassociate by vetoing events with a ZDC signal on either or both sides of the detector. In particular, the level-1 ZDC trigger `L1ZDC_A_C` requires a signal to be present in both the A- and C- side ZDCs and was partially used to trigger on peripheral Pb+Pb collisions during the 2018 data-taking. Spectator neutrons become rare in central collisions where most constituent nucleons participate, so the ZDC cannot be used to trigger on this class of collisions.

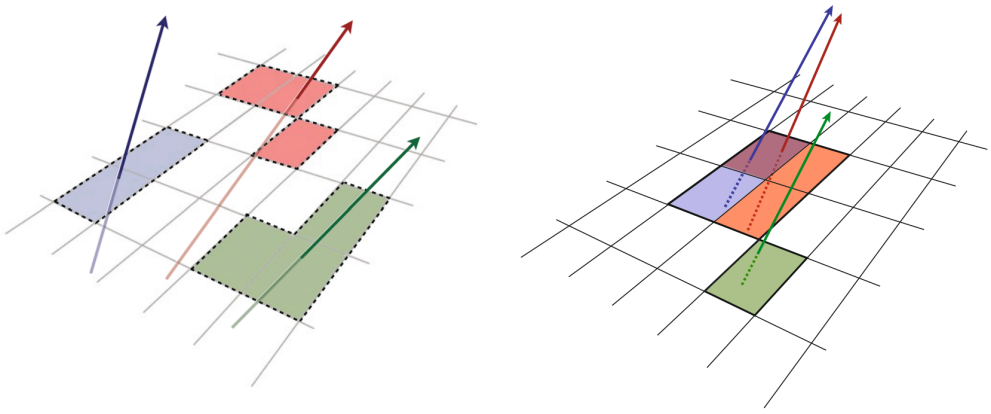
3.4 Reconstruction of Collisions

The ATLAS reconstruction procedure combines all of the detector signals to produce a well-calibrated set of physics objects that can be further studied at the analysis level. It can be loosely decomposed into the reconstruction of tracks using hit patterns in the ID and MS, and subsequently the identification of photons, electrons and jets from calorimeter signals. This section provides a high-level overview of how the ATLAS reconstruction algorithms take the raw detector signals and convert them into these more tangible objects.

Charged-Particle Spectroscopy

The basic function of the ID and MS is to separate charged particles based on their radius of curvature, and use that metric to deduce their momentum. This is performed by the track reconstruction algorithm which takes the ID hits pattern as input [225]. First a preprocessing step produces clusters of hits referred to as *space points*, which essentially are hits coupled to a 3-dimensional position (e.g., the location of the pixel that was hit). Often, multiple pixels can be merged into a cluster due to charge accumulating on adjacent pixels from a single charged particle, necessitating this step, as illustrated in Fig. 3.19. Hits on both layers of an SCT module correspond to the same space point. Groups of three space points in the SCT are seeded to a combinatorial Kalman filter [241] which chooses additional compatible hits in other layers to build track candidates while maintaining a high purity. Seeds from the pixel detectors are also considered but have lower priority due to their lower purity. The use of three space points uniquely specifies a helical trajectory. If a seed is compatible with multiple trajectories, then multiple track candidates are created. These combinatorial tracks are suppressed by the algorithm to maintain lower time complexity, and maintain a high purity.

Once a set of track candidates is obtained, it must be refined. An ambiguity-resolving stage ranks track candidates by a score value determined from the quality of the track. For example, observed hits raise the score, while missing hits ("holes") or shared hits reduce the score, as well as



(a) Single-particle clusters **(b)** Multi-particle merged clusters

Figure 3.19: (a) Single-particle clusters are formed from three separate particles exciting adjacent pixels in a single layer. **(b)** Multiple-particle *merged* clusters are formed from a collimated group of charged particles. Figure reproduced from Ref. [225].

large fit χ^2 values. High momentum tracks are favored by considering $\log \frac{p_{\mathrm{T}}}{1\,\mathrm{GeV}}$ in the score evaluation. The ambiguity solver is particularly sensitive to clusters used by multiple track candidates. This is important in highly collimated or high occupancy environments, such as in the cores of high-p_{T} jets or in central heavy-ion collisions. Such clusters are exclusively labeled either *merged* or *shared*. Merged clusters meet a set of criteria to indicate that they are likely associated with multiple tracks. Shared clusters fail these criteria, and must be suppressed as they indicate poor track candidates. A neural network is used to facilitate this assignment procedure. Shared clusters must not be associated with more than two tracks; if they are then track candidates are dropped in order of track score such that only two are kept. Finally, a high precision fit is performed on each track candidate to obtain high-resolution kinematic information. Because cluster shapes can vary track-by-track, the input position of each space point and its uncertainty (a nontrivial quantity if the cluster is composed of multiple hits) are provided to the fit by another neural network. The final outputs of the ID reconstruction are a set of tracks with highly precise kinematic and impact parameter measurements (d_0 in the transverse plane and z_0 in the longitudinal direction) relative to the beam spot. These are subsequently used to fit for collision and secondary vertices.

In the offline analysis, the properties of the reconstructed track are further considered to

	`TightPrimary`	`HILoose`	`HITight`
$\lvert\eta\rvert$	< 2.5		
Pixel + SCT hits	≥ 9 if $\lvert\eta\rvert < 1.65$ ≥ 11 otherwise	–	
Pixel hits	–	≥ 1	≥ 2
SCT hits	–	≥ 6 if $p_{\mathrm{T}} > 0.4$ GeV, or ≥ 4 if $p_{\mathrm{T}} > 0.3$ GeV, or ≥ 2 otherwise	≥ 8 if $p_{\mathrm{T}} > 0.4$ GeV, or ≥ 6 if $p_{\mathrm{T}} > 0.3$ GeV, or ≥ 4 otherwise
Holes	≤ 2 SCT holes, and No Pixel holes	–	
Shared hits	≤ 1 shared Pixel hit ≤ 2 shared SCT hits (But not both)	–	
B-layer hits	≥ 1 IBL or BL hit, if expected	–	
$\lvert d_0^{\mathrm{vtx}} \rvert$	–	< 1.5 mm	< 1.0 mm
$\lvert \Delta z_0^{\mathrm{vtx}} \sin\theta \rvert$	–	< 1.5 mm	< 1.0 mm
Fit χ^2	–		< 6

Table 3.3: Criteria for meeting a few different track working points.

ensure the selection of tracks at analysis level is adequately pure and efficient. The specific criteria is known as the quality *working point*. Several of these are defined in ATLAS, such as `Loose`, `TightPrimary`, `MinBias`, `HILoose`, and `HITight`. For example, the `TightPrimary` definition requires

- $|\eta| < 2.5$,
- ≥ 9 hits across the pixel and SCT if $|\eta| < 1.65$, or ≥ 11 if $|\eta| > 1.65$,
- ≤ 2 SCT holes and no pixel holes,
- ≤ 1 shared pixel hit or ≤ 2 shared SCT hits (but not both), and
- ≥ 1 insertable B-layer or B-layer hit (if one is expected).

Definitions for `HILoose` and `HITight` are similarly cut-based; details for each selection are

provided in Table 3.3. The measurement presented in Chapter 4 selects tracks that meet the `HILoose` cut, and the one in Chapter 6 selects on the `TightPrimary` cut.

Fitting proceeds very similarly with the MS to produce muon trajectories near the detector periphery [242]. The MS track finding is initially performed independently of the ID. This is because the momentum of a muon in the MS may not be the same as in the ID due to potential energy loss in the calorimeters. Possible sets of hits matching a common trajectory are first identified with a Hough transform [243]. The hits are then fit to a common curve, including the possibility of incorrectly assigned hits, energy loss in the muon chambers, and detector misalignments. Reconstructed muons candidates can then be extrapolated back to the ID to create a match between an ID track and a candidate muon and recover the initial four-momentum. In rare cases, even calorimeter information can be utilized to aid with the ID-MS matching. There are several different possible types of muon trajectories output by the reconstruction:

- combined muons, which have both an ID and MS track,
- inside-out muons, which find a compatible MS track only when seeded by an ID track,
- extrapolated muons, which lack an ID track matched to the MS, and the MS trajectory must be extrapolated back to the IP,
- segment-tagged muons, which have an ID seed track matched to a segment in the MS (but not a full MS trajectory), and
- calorimeter-tagged muons, which have an ID track without an MS match, but leave a compatible minimally-ionizing signal in the calorimeter.

Muons with both an MS and an ID track are subject to a combined fit incorporating lost energy in the calorimeters to obtain as precise a measurement as possible. In offline analyses, muons must meet a quality standard for consideration, similar to normal ID tracks. This helps reduce background from cosmic rays, hadronic punch-through, and non-prompt muons resulting from pion or kaon decays in the detector. Typically, the `Medium` working point is used, which only includes

combined and inside-out muons. Of these two, the vast majority ($\sim 98\%$) of muons are combined, indicating the high identification efficiency of the MS relative to the ID.

Calorimeter Performance

Next, the reconstruction identifies photons, electrons, and jets from calorimeter signals. The calorimeter system provides 3-dimensional imaging of particle showers. This enables not only measuring energy deposits, but also the shapes of showers in angle and depth. This is heavily exploited in the EMCal in particular, where the shapes of EM showers are used to discriminate electrons, photons, and hadrons. For example, hadrons will traverse a longer path length before interacting since $\lambda > X_0$. Thus the EM component to a hadronic shower will develop deeper in the calorimeter and deposit more energy in layer 3 than layer 1. Comparing the energies deposited in these layers thus offers a discriminant of hadron backgrounds. Electrons and photons are further distinguished by comparing against the ID: electrons should be reconstructed as a track, while neutral photons do not interact with the ID (see Fig. 3.3).

A good hadronic calorimeter will respond in a balanced manner to EM and hadronic showers. Thus the ratio of the electron (e) and non-EM (h) average responses e/h serves as a performance indicator. The total non-EM response component (the bottom half of Fig. 3.10) can be decomposed into contributions from ionization losses, spallation protons, neutron evaporation, and invisible losses. e/h can be related to the ratio e/π where π represents the average response to a pion of the same energy:

$$\frac{e}{\pi} = \frac{e/h}{1 + \langle f_{\mathrm{EM}} \rangle \, (e/h - 1)}. \tag{3.6}$$

In practice, e/π is directly measured by comparing the response to a beam of electrons versus a beam of pions and is used to extract e/h. If e/h differs too far from unity, then fluctuations in the EM component f_{EM} – which are large and non-Poissonian – will make the response non-uniform and lead to a worse detector resolution. Typically $\langle f_{\mathrm{EM}} \rangle$ is described by a power law as ultra-relativistic particles will have a large EM fraction (and thus are "easier" to measure) [228, 244]:

$$\langle f_{\mathrm{EM}} \rangle = 1 - \left(\frac{E}{E_0} \right)^{k-1} . \tag{3.7}$$

Calorimeters with $e/h \simeq 1$ are said to be *compensating*; values above or below unity make it *non-compensating*. In addition to suffering from worse resolution, non-compensating calorimeters will exhibit a non-linear hadronic response – meaning the response varies with the incident energy – which is undesireable during a numerical inversion calibration. This can be directly observed by measuring the energy-dependent response $\pi(E)$. In practice, the hadronic response is inherently non-linear to some extent, and thus isolating the average EM component of a hadronic shower is essential to a correct energy scale calibration.

The basic inputs to calorimeter-based reconstruction of electrons, photons, and jets are the calibrated four-momenta associated with each readout channel. To determine the calibration factors that convert current to ADC counts and then finally an energy, each calorimeter section was bombarded with electron and hadron beams in the CERN SPS facility with energies ranging from a few to hundreds of GeV [208, 245–247]. This determines the energy-dependent responses in a highly controlled, empirical manner. Fluctuations in response contribute to a (dimensionless) finite resolution $\sigma(E)/E$, which for a single cell can be parameterized as the quadrature sum of a stochastic component a and a constant b, the latter of which reflects how non-compensating the calorimeter is[4]

$$\frac{\sigma(E)}{E}[\%] = \frac{a}{\sqrt{E/1\,\mathrm{GeV}}} \oplus b. \tag{3.8}$$

For the EMB, the energy response was found to be linear with $(a, b) = (10\%, 0.17\%)$ when exposed to an electron beam. In the HEC, $(a, b) = ((21.4 \pm 0.1)\%, 0\%)$ for electrons, but when bombarded with pions $(a, b) = ((70.6 \pm 1.5)\%, (5.8 \pm 0.2)\%)$, indicating the drastically worse resolution for hadronic versus EM showers. Performance of the FCal and tile calorimeter were also studied with qualitatively similar results [249, 250].

[4] The correct form for a non-compensating calorimeter is actually $\frac{\sigma(E)}{E} = \frac{a}{\sqrt{E/1\,\mathrm{GeV}}} \oplus a' \left(\frac{E}{E_0} \right)^{l-1}$, though typically $l \lesssim 1$ and so this term can be approximated by a constant except at the highest energies [248].

Jet Reconstruction

Jets are well-defined theoretical objects, but in experiment, they can become murkier due to resolution and background effects. The ATLAS heavy-ion jet reconstruction – described here – is a fully calorimetric measurement of energy flow [251]. As input, the reconstruction takes the total energy deposited in groups of calorimeter cells and then feeds that as a four-momentum vector to the jet-clustering algorithm, with an assumed mass of zero. This strategy can be problematic when there are substantial amounts of background energy in the calorimeter with a different physical origin than the core of a jet. Such background energy can lead to substantial fake jet rates, incorrect jet energies, reconstruction inefficiencies, and misplaced jets. Therefore it is critical to subtract off this component.

At the LHC, background can arise from two sources. The first is from pileup events, the rate of which can be tuned by varying the beam configuation. It is rare to produce a high p_{T} jet in any given event, but with decreasing p_{T}, jets become more ubiquitous. If pileup is high, it can be difficult to allocate calorimeter energy to each jet. Mitigating the effect of pileup typically involves subtracting off the expected energy, which when the pileup rate is high, fluctuates only mildly event-to-event. (A typical fluctuation for $R = 0.4$ jets in pp collisions with $\mu \sim 20$ is only on the scale of $2 - 3\,\mathrm{GeV}$, or thereabouts [230].)

In heavy-ion collisions there is also the *underlying event* (UE) background, which refers to the myriad particles produced in unrelated processes during the same nucleus-nucleus (or proton-nucleus) collision [252]. The UE background completely dominates over pileup in heavy-ion collisions, where $\mu \ll 1$. Unlike pileup, UE particles come from the same ion-ion collision and tend to be azimuthally correlated due to final-state dynamics. Additionally, there can be significant event-to-event fluctuations in both the strength of the correlations as well overall magnitude, both of which are driven by collision centrality: one event can be glancing and the next might be head-on. This necessitates the global correlations to be accounted for somehow, as well as event-by-event estimates of the underlying event.

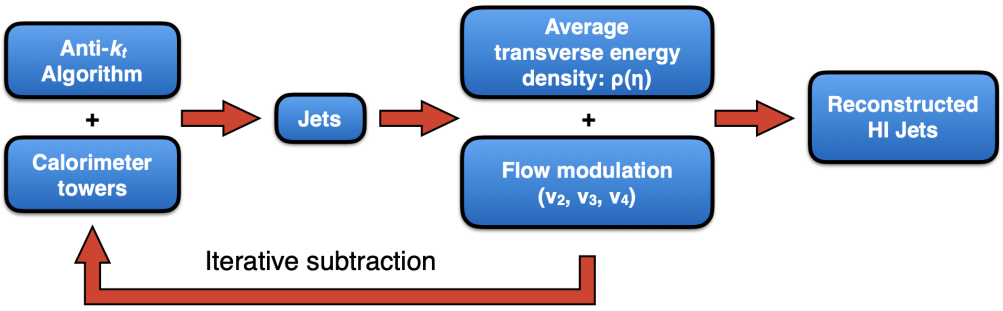


Figure 3.20: Flowchart of the heavy-ion jet reconstruction procedure described in the text.

In ATLAS, jets are defined by the anti-k_t algorithm, typically with radius parameter $R = 0.4$. The FastJet implementation of the algorithm is used [253]. The calorimeter cells input to the algorithm are grouped in clusters of fixed angular size $\Delta\eta \times \Delta\phi = 0.1 \times 0.1$ (called *towers*), which cover the calorimeter uniformly between $-4.9 \leq \eta \leq 4.9$ and $-\pi \leq \phi < \pi$. The tower energy is determined by summing the energy deposited in cells within the tower. Jets are reconstructed at the EM scale which correctly measures the energy left by EM showers in each tower. Reconstructed ("reco.") jets are later calibrated to the hadronic scale by studying the EM response function.

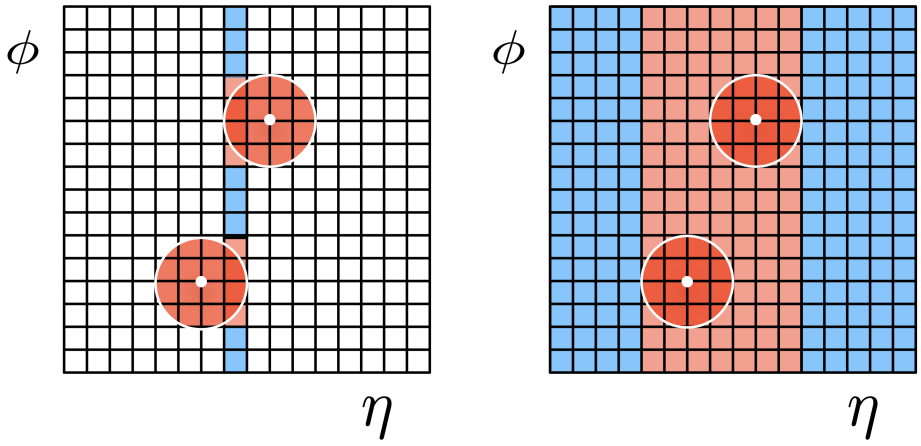
The heavy-ion underlying event is subtracted with an iterative procedure that provides estimates for the UE energy density in each tower. In each cell, the energy can be decomposed into contributions from a jet and the UE,

$$\frac{d^2E_{\mathrm{T}}^{\mathrm{total}}}{d\eta d\phi} = \frac{d^2E_{\mathrm{T}}^{\mathrm{jet}}}{d\eta d\phi} + \frac{d^2E_{\mathrm{T}}^{\mathrm{UE}}}{d\eta d\phi}. \tag{3.9}$$

The iterative procedure generates a model of the UE component where

$$\frac{d^2E_{\mathrm{T}}^{\mathrm{UE}}}{d\eta d\phi}(\eta,\phi) = \rho(\eta)\left\{1 + 2\sum_{n=2}^{N} v_n \cos\left[n\left(\phi - \Psi_n\right)\right]\right\}. \tag{3.10}$$

This quantity is intended to be evaluated tower-by-tower and thus depends on η and ϕ, where $\rho(\eta) = \left\langle \frac{d^2E_{\mathrm{T}}}{d\eta d\phi}(\eta) \right\rangle_{\phi}$ is the ϕ-averaged energy density describing the overall UE amplitude, and v_n, Ψ_n η-are independent parameters describing the anisotropic flow. The "n" subscripted components account for the orientation and strength of the global momentum correlations exhibited by the UE. For Pb+Pb and Xe+Xe data in Run 2, $N = 4$, however for the pp and p+Pb data used in this



(a) Inputs to $\rho(\eta)$ fits **(b)** Inputs to v_n fits

Figure 3.21: Illustrations detailing which towers are **included (blue)** and **excluded (red)** from the fits to **(a)** $\rho(\eta)$ and **(b)** v_n due to their association with seed jets. Each square has area $\Delta\eta \times \Delta\phi = 0.4 \times 0.4$. Figure reproduced from Ref. [254].

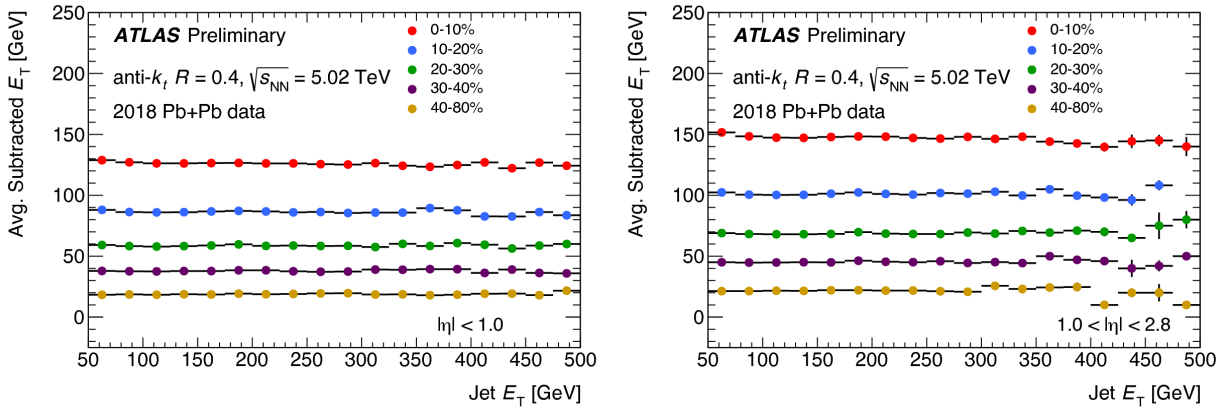
dissertation no anisotropic component is allowed (i.e. $N = 0$) in the fit due to the relatively low multiplicity of pp and p+Pb collisions in comparison to Pb+Pb.

In performing the fit, it is important to only include towers in which there is no jet present. Towers identified as jet constituents – meaning they are within $\Delta R < 0.4$ of an identified jet meeting a discrimination requirement [251] – are excluded from the fitting procedure. An initial set of "seed" jets tell the algorithm which towers to exclude during the initial UE fit. Each tower is then assigned a new UE-subtracted energy

$$E_{\mathrm{T}}^{\mathrm{tower}}\Big|_{\mathrm{sub.}} = E_{\mathrm{T}}^{\mathrm{tower}}\Big|_{\mathrm{unsub.}} - \frac{d^2 E_{\mathrm{T}}^{\mathrm{UE}}}{d\eta d\phi}(\eta_{\mathrm{tower}}, \phi_{\mathrm{tower}}) \times \Delta\eta_{\mathrm{tower}} \times \Delta\phi_{\mathrm{tower}}. \tag{3.11}$$

Subsequent jet collections are clustered from the tower subtracted energies, and the UE estimate can be improved by excluding towers matched to these new jets. By iteratively refeeding the newer jets to the UE estimation procedure, the jet collection can be refined. The algorithm performs the iteration twice, once with the initial UE estimate with seed jets excluded, the second with the first set of calorimeter jets excluded, and then finally returning the reclustered calorimeter jets.

The UE subtraction procedure is also performed separately at each layer of the calorimeter to allow for differences in calorimeter response to the UE compared to jets. Fig. 3.22 shows the



(a) $|\eta| < 1.0$ **(b)** $1.0 < |\eta| < 2.8$

Figure 3.22: The average subtracted transverse energy $E_{\mathrm{T}}^{\mathrm{sub.}}$ for jets in Pb+Pb collisions is plotted as a function of jet transverse energy for jets at **(a)** mid-rapidity and **(b)** forward rapidity, for a range of different centralities. Figure reproduced from Ref. [255].

average subtracted energy for jets in Pb+Pb collisions; little is subtracted in peripheral events, but for central events, up to $\sim 10^2$ GeV can be subtracted off for $R = 0.4$ jets. Additional details regarding the heavy-ion jet reconstruction can be found in [251, 254].

To evaluate the performance of the jet reconstruction, the HI jets are often compared against the so-called "truth jets" in Monte Carlo studies. These are the jets defined by the anti-k_t algorithm of the same radius where the inputs are the four momenta of truth particles with lifetime $> 10\,\mathrm{ps}$ (excluding muons and neutrinos, because they are not expected to deposit their energy in any of the calorimeter systems). Because truth particles are only defined in simulated events, these jets are only available in simulation (MC) samples.

Energy scale calibration

While individual calorimeter cells are themselves calibrated, they are only calibrated to the EM fraction of the hadronic shower. A variety of effects allow for only partial recovery of a jet's energy (e.g. dead material, gaps between cells, signal losses, etc. [229]). For this reason the energy scale of reco. jets needs to be calibrated to the full energy scale of the incident jet. The full calibration sequence is presented in Ref. [256] and exemplified later in Chapter 6; here we summarize

the main points. Jets after the UE subtraction are subject to two sequential calibrations:

(1) the EM+JES MC-based calibration to recover the truth energy scale in MC, including the origin correction,

(2) the cross-calibration & in-situ / η-intercalibration to account for MC-data differences.

The MC-based EM+JES calibration applies the large correction of the two and is derived from `Pythia8` dijet events simulated through the `GEANT` model of the detector. It is the component of the calibration sequence that corrects for the energy scale component common to data and MC. The per-jet energy scale correction is derived through a *numerical inversion* (NI) procedure [256–258]. The formalism is reviewed in [259]; the main idea is to invert the response function f to obtain the "correction function" f^{-1} which returns a best-estimate of the *truth*-level energy as a function of *reco.*-level energy:

$$f\left(E_{\text{truth}}\right) = \hat{E}_{\text{reco.}} \iff f^{-1}\left(E_{\text{reco.}}\right) = \hat{E}_{\text{truth}} \tag{3.12}$$

where $\hat{x}$ represents the modal value of x given the argument of the response function. To obtain an estimate of the truth-level energy $\hat{E}_{\text{truth}}$, *we assume* the random variable $E_{\text{reco.}}$ is at the expected reco. energy $\hat{E}_{\text{reco.}}$ for $\hat{E}_{\text{truth}}$, i.e. $E_{\text{reco.}} = \hat{E}_{\text{reco.}} = f\left(\hat{E}_{\text{truth}}\right)$. This is why the numerical inversion is powerful: the jet-by-jet calibration is performed by simply evaluating f^{-1}, i.e.

$$E_{\text{reco.}} \mapsto \hat{E}_{\text{truth}} = f^{-1}\left(E_{\text{reco.}}\right). \tag{3.13}$$

Though in general, the NI procedure to obtain f^{-1} is ill-defined mathematically and thus the final accuracy or *closure* of the energy scale correction must be carefully studied *post hoc*. Particularly, non-linear response functions are not guaranteed to close under NI.[5] Details of the numerical inversion procedure will be examined via a case study using the 2016 p+Pb data set in Chapter 6.

Typical jet energy scale corrections range from $f^{-1}\left(E_{\text{reco.}}\right) \sim 1.2 - 2$. This part of the calibration sequence also applies a minor correction to the jet pseudorapidity to counteract the implicit assumption of $v_z = 0$ during the reconstruction procedure (the "origin correction"). In

[5] An example of a response function where scaling by the inverse does not lead to closure is $f(x) \propto \sqrt[3]{x}$ [259].

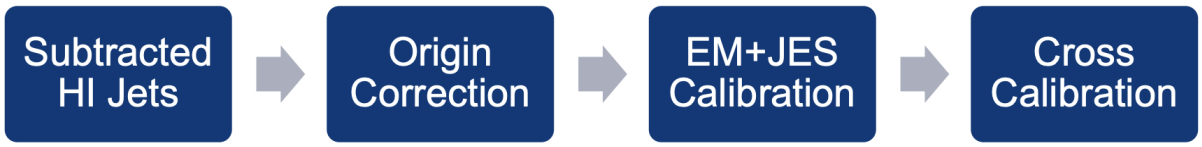


Figure 3.23: The heavy-ion jet calibration sequence.

reality, the collision vertex coordinate v_z is distributed along the beam line approximately normally; the consequence is that jets in the exact same position in the detector will have their pseudorapidity fluctuate slightly event-to-event, with a net bias that scales with the width of the v_z distribution. This correction is generally small and at the level of $\Delta\eta \sim 0.01 - 0.02$. The beamspot can also in principle fluctuate in the xy-plane and thus affect the ϕ coordinate of the jet, but generally $|v_x|, |v_y| \ll |v_z|$ because each beam is tightly focused in the longitudinal directions. Therefore any effect is generally ignored.

The second calibration component is only applied to jets in data and accounts for the fact that MC does not perfectly describe data. These are the *in situ* and η-intercalibration which provide residual corrections to the jet energy scale. The *in situ* correction is based on the p_{T} balance in $\gamma+$jet and $Z+$jet events, where data-MC differences in the momentum balance are used to calibrate mid-rapidity jets. The η-intercalibration is based on dijet events, where the well-understood mid-rapidity jets are used to calibrate partner jets at forward rapidity. In this way, jets at mid-rapidity can be accurately calibrated, and then used to bootstrap calibration factors for forward-rapidity jets in a data-driven manner. Both factors have been well-studied and documented for jets based on the EM topo-clusters (EMTopo) within ATLAS, though they cannot be directly applied to HI jets due to the difference in inputs. The purpose of the cross-calibration is to then account for additional differences in response between HI and fully calibrated EMTopo jets. This allows the performance of HI jets to be fully characterized within the EMTopo jet framework. However, this also leads to an additional cross-calibration uncertainty on the jet energy scale.

In data, only the cross-calibrated jets are used as this is the best jet energy scale estimate in data. In simulation, jets are generally only subject to the EM+JES calibration as this correction

is optimized for simulated events. However, jets in simulation with data overlay that are not truth-matched are assumed to come from the original data event, and therefore they must be cross-calibrated as well.

e/γ reconstruction

Electrons and photons are reconstructed primarily from ID and EMCal detector signals. In the second half of Run 2, the older sliding window reconstruction procedure [260] was superceded by the newer supercluster (SC) reconstruction [261, 262]. The purpose of this update was twofold. First, it improves performance at low-p_{T} by adding the ability to recover softer components of the EM shower, primarily low-energy bremmstrahlung photons. Second, the SC takes dynamical topological clusters (*topo-clusters*) as input, allowing the cluster size to grow with the shower Molière radius, which itself grows with the incident energy. The topo-clusters are formed locally around cells with a statistically significant energy deposit $\varsigma_{\mathrm{em}} = |E_{\mathrm{em}}/\sigma_{\mathrm{em}}|$ (where E_{em} and σ_{em} represent the cell signal and noise). In heavy ions, the cell energy is taken after an azimuthally-modulated UE subtraction similar to the one performed for jets. Though, the angular area of a topo-cluster is substantially smaller than that of a jet, so much less total energy is subtracted for an electron than a jet with similar momentum. Proto-clusters are formed by cells with $\varsigma_{\mathrm{em}} > 4$, and adjacent cells with $\varsigma_{\mathrm{em}} > 2$ are added to the cluster recursively. Finally, neighbor cells with $\varsigma_{\mathrm{em}} \geq 0$ are added. Clusters with multiple local maxima can be split into separate topo-clusters using a weighting scheme to assign cell energies. EM topo-clusters, which are passed to the SC algorithm, are defined to deposit at least 50% of their total energy in the main EMCal, excluding the presamplers. This cut was motivated from studies of simulated electrons and maintains the maximal identification efficiency.

The showers of electrons and photons are very similar; tracking information is therefore crucial in distinguishing the two. First, EM topo-clusters that pass a loose set of hadronic rejection criteria are seeded to a track refitting based on a Gaussian Sum Filter. Tracks are geometrically matched to the EM topo-clusters based on the solid angle distance ΔR. For a topo-cluster to be

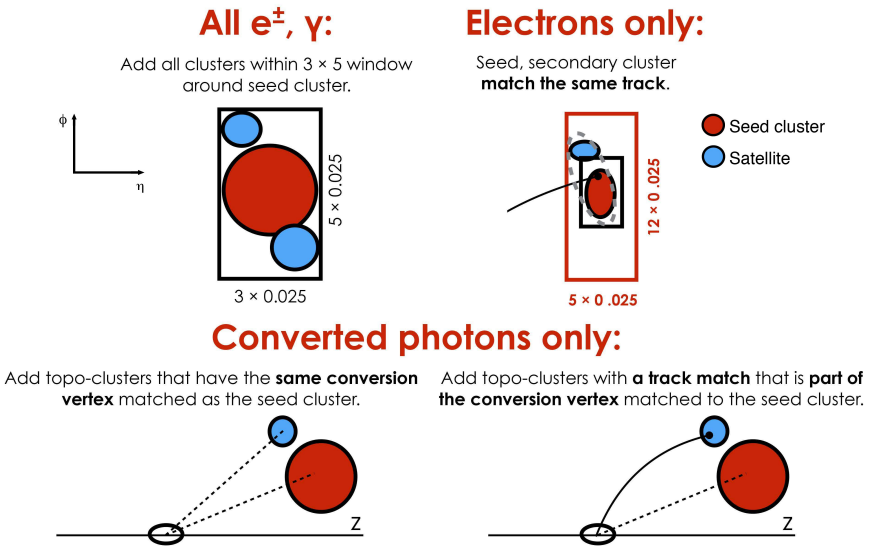


Figure 3.24: Illustration of how an electron supercluster is formed from a **seed cluster (red)** and nearby **satellite clusters (blue)**. Figure reproduced from Refs. [261, 262].

seeded to the electron SC reconstruction, it must possess at least 1 GeV and be track-matched. This can be compared with photons, which cannot be track-matched. Photon-candidate topo-clusters must also have at least 1.5 GeV to improve purity. The SC stage then searches for and adds satellite clusters to all seed clusters in order of descending p_{T}. Only clusters within a given area of solid angle $\Delta\eta \times \Delta\phi = 0.075 \times 0.125$ are considered to avoid excessively large SCs, though satellites within a 0.125×0.3 area can be added if they are matched to the same track as the seed. Topo-clusters that build the final electron candidates are restricted to a range

$$\Delta\eta = 0.025 \times \begin{cases} 3 & \text{in the barrel} \\ 5 & \text{in the end-caps.} \end{cases} \tag{3.14}$$

This restriction helps ensure the lateral shower leakage outside the included clusters is linearly related to the deposited energy, which reduces systematic uncertainties associated with the final energy scale.

Once the SC has been found, clusters associated with the candidate electron are then summed and the final energy is calibrated using a multivariate analysis algorithm [262]. Typically the SC reconstruction is $\gtrsim 97\%$ efficient at detecting electrons across a wide range of truth energies in pp

collisions. Finally, offline analyses use a likelihood-based identification procedure to reject remnant non-electron backgrounds [263]. The likelihood discriminant is calculated using 19 shower shape and tracking variables as well as the energy and angular position of the candidate. To accommodate the HI underlying event, the likelihood discriminant was optimized separately for heavy-ion and pp collisions as well [264]. Validation of the final electron energy scale, as well as effects of a finite energy scale resolution and residual background contributions to Z boson studies, will be further examined in Chapter 4.

Chapter 4

Z^0–Hadron Correlations in Pb+Pb Collisions

In Chapter 2, we explored how electroweak bosons are impervious to the strongly-coupled plasma and therefore serve as a probe of the initial state. This includes processes such as the tree-level Feynman diagrams shown in Fig. 4.1. When the boson is produced in conjunction with a high momentum parton, the boson-parton duo offers a clean probe of medium dynamics. In this spirit, this Chapter presents a new measurement of Z^0 boson-hadron correlations (referred to hereafter as a Z boson) performed with ATLAS Run 2 data.

At the LHC, studies of electroweak processes in heavy-ion collisions have already commenced with the abundant collision data from Run 2. Data from 2015 was used in a coordinated $W^{\pm}/Z$ measurement effort to map out isospin effects in Pb+Pb and validate the Glauber model scaling of hard processes [63, 265, 266]. The $W^{\pm}$ and Z lifetimes are extremely short – on the order of 0.1 fm/c – so they immediately decay to other particles. When the decay is leptonic, the products can be

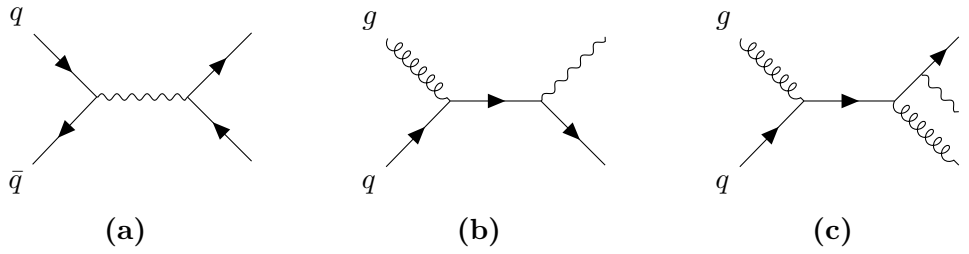


Figure 4.1: Examples of tree-level Feynman diagrams for electroweak boson production at the LHC are shown: **(a)** Drell-Yan production of a γ^*/Z^0, **(b)** hard radiation of a boson from a quark, and **(c)** final-state radiation. Each diagram is associated with the formation of at least 0, 1, or 2 jets, respectively. Note that on-shell photons are only created in the **(b)** ("direct") and **(c)** ("fragmentation") diagrams.

directly observed in the detector and analyzed to reconstructed the parent particle.[1] On the other hand, stable photons are directly observed in the calorimeter. Their production was thoroughly studied previously in Run 1 [267]. These investments in the lepton and photon reconstruction have led to advanced frameworks for dealing with electroweak bosons in the heavy-ion environment. In turn, these can be further used as a precise event-by-event tag to probe parton dynamics in the QGP. Photons in particular are the most abundant probe due to their zero mass. For the first time by ATLAS, photons were used to probe jet structure modification in Run 2 [112, 113, 158, 268–270]. However, the rarer leptonic Z decays have a very high signal purity due to the dilepton coincidence requirement. This translates into a high confidence that each observed event truly contains a Z. With the availability of sufficiently large data sets, such Z-tagged jet-quenching measurements are now statistically feasible and being carried out by multiple experiments [271–273].

The primary objective for the measurement presented in this Chapter is to count the number of charged hadrons recoiling against a Z as a function of their relative azimuthal angle to the Z ($\Delta\phi_{hZ}$) and momentum ($p_{\mathrm{T}}^{\mathrm{ch}}$).[2] The core idea is that the distribution of these particles is indicative of the final state energy of the parton scattering off the Z. First, Z boson candidates are reconstructed from their dilepton $Z \to ee$ or $Z \to \mu\mu$ decays. Such events are extremely rare within the context of the entire heavy-ion data set; the $Z \to ee$ and $Z \to \mu\mu$ cross sections only account for about 20 billionths of the total nucleon-nucleon cross section at 5.02 TeV. This selection alone thus greatly reduces the set of events that are considered. Then, the distribution of charged hadrons in those events is estimated. In each event, the observed *per-Z yield* of charged particles is corrected to the best estimate of the true yield by applying track-by-track correction factors. Events are averaged together using event-level acceptance corrections related to the probability that each real Z produced in a collision successfully enters the event selection. At sufficiently high-p_{T}, hadron and jet production coincide (by definition all high-p_{T} hadrons *must* lie within a jet); thus the production

[1] For the Z, both (charged) decay leptons are observed, but for the $W^{\pm}$, only a single lepton is observed. Missing transverse momentum in the detector can be used to infer the presence of a neutrino. If the Z decays into neutrinos then it is completely lost.

[2] To distinguish kinematics of the Z from charged hadrons we use the subscripts / superscripts "ch" for charged hadrons and "Z" for the Z boson.

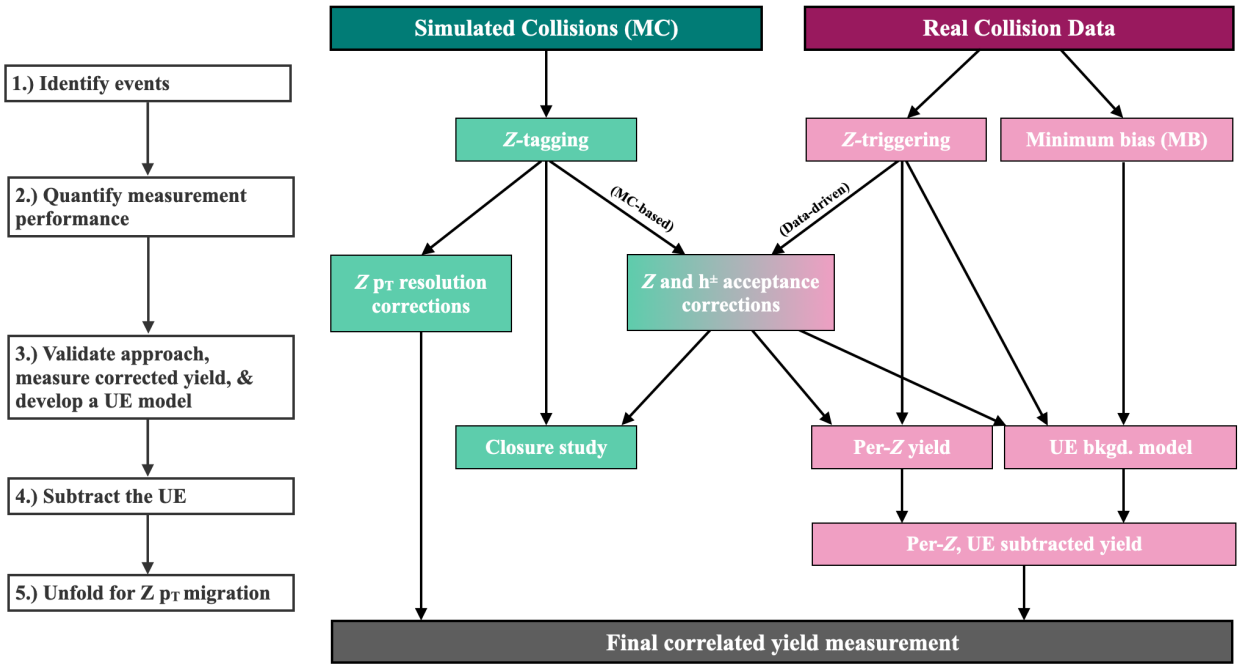


Figure 4.2: A roadmap illustrating a high-level, schematic overview of this measurement.

of high-p_{T} charged hadrons serves as a high-p_{T} resolution estimate for jet production. At lower p_{T}, the jet resolution deteriorates substantially, and the rate of fake jets grows considerably. Though hadronic backgrounds grow too (as we will see), the momentum resolution remains reliably precise down to very low values. This allows the hadron yield to serve as a competitive metric of the showering tree-level parent parton for low to moderate momentum transfers (Q^2). In fact, we will find that the hadron yield is actually sensitive to new physics that is inaccessible with jets alone.

This Chapter will be structured in the following way. First, the per-trigger yield is defined and motivated by relating it to more ubiquitous quenching metrics – nominally, the nuclear modification factor R_{AA} (Sec. 4.1). We will comment on the nontriviality of the underlying event (UE) and motivate a particular UE definition that maximizes sensitivity to the final state parton shower and medium response effects. The vast majority of the Chapter will discuss the technicalities of the measurement, including basic event selection and simulation configurations (Sec. 4.2), lepton reconstruction and performance (Secs. 4.3 and 4.4), analysis of the reconstructed Z kinematics (Sec. 4.5), charged-hadron reconstruction performance studies (Sec. 4.6), underlying event model

construction (Sec. 4.7), and a discussion of statistical and systematic uncertainties (Sec. 4.8). A roadmap illustrating how these all help build the final per-trigger yield is shown in Fig. 4.2. The main results will be presented subsequently in Chapter 5. A discussion on analysis validation can be found in the appendices (Appendices A.2 and A.3).

4.1 Per-Trigger Yields

The fundamental metric we use is the per-trigger or per-Z normalized charged-hadron yield Y, which is defined in terms of the *number of triggers* N_Z (i.e., the number of Z bosons) and the *total number of charged particles* $N_{\rm ch}$ in those triggered events,

$$\frac{d^2Y}{dp_{\rm T}^{\rm ch}d\Delta\phi_{hZ}} = \frac{1}{N_Z}\frac{d^2N_{\rm ch}}{dp_{\rm T}^{\rm ch}d\Delta\phi_{hZ}}. \tag{4.1}$$

The derivatives in $p_{\rm T}^{\rm ch}$ and $\Delta\phi_{hZ}$ are meant to indicate that Y is evaluated as a function of charged-particle $p_{\rm T}$ ($p_{\rm T}^{\rm ch}$) and relative transverse angle to the Z boson $\Delta\phi_{hZ}$. Compared to a inclusive cross section $\sigma(p_{\rm T}^{\rm ch})$, which is evaluated over all events as an ensemble,

$$\frac{d\sigma}{dp_{\rm T}^{\rm ch}} = \frac{1}{\mathcal{L}}\frac{dN_{\rm ch}}{dp_{\rm T}^{\rm ch}}, \tag{4.2}$$

the yield can be extracted event-by-event and averaged in the final measurement. Using the experimental definition of a cross section as $N_Z = \sigma^{Z+X} \times \mathcal{L}$, the per-$Z$ normalized yield in A + A collisions can be contextualized in terms of the differential hadron cross section in Z-tagged events:

$$dY_{\rm AA} = \frac{1}{\sigma_{\rm AA}^{Z+X}\mathcal{L}_{\rm AA}}dN_{\rm ch} = \frac{1}{\sigma_{\rm AA}^{Z+X}}d\sigma_{\rm AA}^{Z+h+X}. \tag{4.3}$$

We have adopted the notation $dN \equiv d^2N/dp_{\rm T}^{\rm ch}d\Delta\phi_{hZ}$ for brevity. Thus we see that the total yield Y can be schematically written as a convolution of the Z-tagged charged-hadron differential cross section with the pure Z cross section.

With per-trigger yield measurements, it is particularly interesting to isolate the component correlated with the Z boson, as this is the component most sensitive to final state parton shower. The operational assumption for per-trigger measurements is that hadrons in an A+A $\rightarrow Z+h+X$ –

where h represents hadrons (and not, for example, Higgs' bosons, H^0) – event originate from either a correlated, *hard-scatter* (HS) component or an uncorrelated, *underlying event* (UE) component which occurs in the remaining A+A collision, "independently" from the Z:

$$dN_{\rm ch}^{\rm AA,total} = \underbrace{dN_{\rm ch}^{{\rm AA}\to Z}}_{\text{HS term}} + \underbrace{dN_{\rm ch}^{\rm AA}}_{\text{UE term}}. \tag{4.4}$$

We label the HS and UE components $dN_{\rm ch}^{\rm HS}$ and $dN_{\rm ch}^{\rm UE}$. Note that in this measurement, the HS yield is defined to be the *correlated* component only. This nominally includes particles representative of same hard scattering event that produced the Z, but also particles that would otherwise exist as a part of the underlying A+A collision but are somehow affected by the hard scattering. The background is therefore strictly the uncorrelated yield, and any potential "correlated background" shown in Fig. 4.3 – from, for example, medium response – is considered a part of the the signal. To remove the background, a subtraction must be applied:

$$Y_{\rm AA}^{\rm sub} = \frac{1}{N_{\rm AA}^{Z}} dN_{\rm ch}^{\rm HS} = \frac{1}{N_{\rm AA}^{Z}} \left[dN_{\rm ch}^{\rm AA,total} - dN_{\rm ch}^{\rm UE} \right]. \tag{4.5}$$

The ratio of the correlated per-Z yields – which we denote by $I_{\rm AA}$ – can then be compared against the more traditional nuclear modification factor $R_{\rm AA}$. We define $I_{\rm AA}$ to be the ratio between the subtracted yield $Y^{\rm sub}$ in A+A collisions and the QCD vacuum reference system ("ref"),

$$I_{\rm AA} \equiv \frac{Y_{\rm AA}}{Y_{\rm ref}} = \frac{N_Z^{\rm ref}}{N_Z^{\rm AA}} \frac{dN_{\rm ch}^{\rm AA}}{dN_{\rm ch}^{\rm ref}} = \frac{\sigma_{\rm ref}^{Z+X}}{\sigma_{\rm AA}^{Z+X}} \frac{d\sigma_{\rm AA}^{Z+h+X}}{d\sigma_{\rm ref}^{Z+h+X}}. \tag{4.6}$$

The reference is usually (and for the remainder of this dissertation will be) taken from pp collisions, though in principle other systems could be used. On the right hand side we notice that we can reframe the ratio in terms of cross sections for particular processes – the luminosity factors cancel in the double ratio. Crucially, the per-trigger yield ratio $I_{\rm AA}$ differs from the nuclear modification factor $R_{\rm AA}$ due to the explicit consideration of a background source of hadrons. Recall that the nuclear modification factor of process A + A $\to X$ is determined purely from the cross sections $d\sigma_{\rm AA}^{X}$ and $d\sigma_{pp}^{X}$,

$$R_{\rm AA}^{X} \equiv \frac{1}{\langle N_{\rm coll} \rangle} \frac{d\sigma_{\rm AA}^{X}}{d\sigma_{pp}^{X}}. \tag{4.7}$$

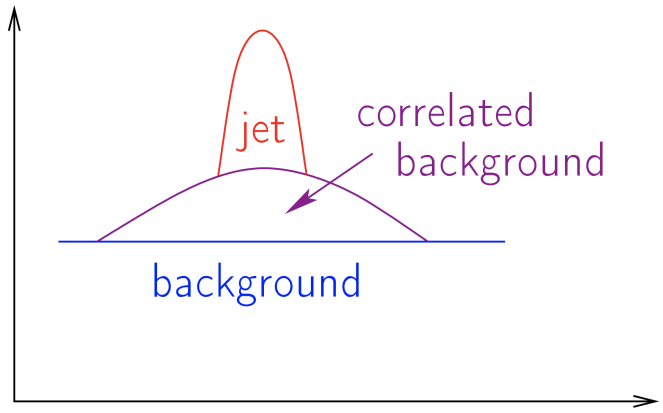


Figure 4.3: Cartoon illustration of the *correlated* and *uncorrelated* (background) event flow in the presence of a jet. The axes are generic: the x-axis might represent ΔR, ϕ, or η and the y-axis dE_{T}/dx or dN_{ch}/dx. Figure produced by Korinna Zapp.

Then the ratio $N^{Z}_{pp}/N^{Z}_{\mathrm{AA}}$ reduces to a factor of $\langle N_{\mathrm{coll}}\rangle$ and R^{Z+X}_{AA}. We finally obtain

$$I_{\mathrm{AA}} = \frac{N^{pp}_{Z}}{N^{\mathrm{AA}}_{Z}}\frac{dN^{\mathrm{HS,AA}}_{\mathrm{ch}}}{dN^{\mathrm{HS},pp}_{\mathrm{ch}}} = \frac{1}{\langle N_{\mathrm{coll}}\rangle \times R^{Z+X}_{\mathrm{AA}}}\frac{\mathcal{L}_{pp}}{\mathcal{L}_{\mathrm{AA}}}\frac{dN^{\mathrm{HS,AA}}_{\mathrm{ch}}}{dN^{\mathrm{HS},pp}_{\mathrm{ch}}} = \frac{1}{R^{Z+X}_{\mathrm{AA}}} \times \frac{1}{\langle N_{\mathrm{coll}}\rangle}\frac{d\sigma^{Z+h+X}_{\mathrm{HS,AA}}}{d\sigma^{Z+h+X}_{\mathrm{HS},pp}}, \tag{4.8}$$

or more simply,

$$I_{\mathrm{AA}} = \underbrace{\left(\frac{1}{R^{Z+X}_{\mathrm{AA}}}\right)}_{Z\text{ nucl. mod. factor}} \times \underbrace{\left(\frac{1}{\langle N_{\mathrm{coll}}\rangle}\frac{d\sigma^{Z+h+X}_{\mathrm{HS},AA}}{d\sigma^{Z+h+X}_{\mathrm{HS},pp}}\right)}_{Z-\text{correlated } h^{\pm}\text{ nucl. mod. factor}} . \tag{4.9}$$

The first term here is unsurprising – we already demonstrated that the per-trigger yield can be expressed as a convolution between the pure Z cross section and some kind of charged-hadron cross section, so the appearance of the Z nuclear modification factor is trivial. However we can identify the right hand component of this expression as a variant on the charged-hadron nuclear modification factor. In particular, only the cross sections for the *Z-correlated* yield of hadrons are used. At high-p_{T}, where $dN^{\mathrm{HS}}_{\mathrm{ch}} \gg dN^{\mathrm{UE}}_{\mathrm{ch}}$, we expect $d\sigma^{Z+h+X}_{\mathrm{HS,AA}} \to d\sigma^{Z+h+X}_{\mathrm{AA}}$ and $d\sigma^{Z+h+X}_{\mathrm{HS},pp} \to d\sigma^{Z+h+X}_{pp}$, so in this limit $I_{\mathrm{AA}} \to R^{Z+h+X}_{\mathrm{AA}}/R^{Z+X}_{\mathrm{AA}}$. Thus we expect the measurement of I_{AA} to match onto previous measurements of jet quenching in this regime. However at low-p_{T}, this limit does not hold, and thus we can see that the two might diverge. In fact, we will see that the low-p_{T} I_{AA} is sensitive to medium response physics that cannot be easily accessed from the nuclear modification factor.

One noteworthy aspect of the per-trigger yield is that it is inherently intrinsic with respect to

the number of events recorded in both the pp and Pb+Pb, the keyword here being *intrinsic*. Unlike a cross-section measurement, which is essentially "number of observations per unit luminosity", the per-trigger yield can be evaluated with an arbitrary subset of recorded events. If, for example, a small subset of events exhibit pathological behavior and cannot be reliably used, then the luminosity must be re-evaluated appropriately. One must look back at the data taking and evaluate how much luminosity was delivered in the affected portions of data, recalculate the delivered luminosity, and possibly re-evaluate the luminosity uncertainty. Clearly, this process can lead to additional uncertainties or potential mistakes. For the per-trigger yield, a situation like this is trivial to resolve: the "bad" events are rejected, so they no longer enter neither the numerator (the total number of charged particles over all triggering events) nor the denominator (the total number of triggering events).

In fact, the per-trigger yield ratio I_{AA} has been previously studied copiously at RHIC in photon-tagged events by PHENIX and STAR [274–276]. These measurements were performed in the lower temperature QGP formed in Au+Au collisions at $\sqrt{s_{\mathrm{NN}}} = 200$ GeV, and a modest away-side hadron suppression was observed, which is understood as a classic signature for jet quenching. This directly motivates similar measurements at the LHC in either the same channel or the qualitatively novel one offered by the Z.

Background engineering

It is easy to see why the background estimation forms a core part of the analysis. Understanding the expected properties and nuances of the background is essential for the analyzer to build an appropriate UE model. To illustrate this point, consider the following scenarios.

(1) A Z is radiated from a jet-forming parton via the right diagram in Fig. 4.1. There are then multiple partonic jets in the event (a "multi-jet"), each of which can experience quenching, and the Z kinematics do not uniquely determine the total exchanged transverse momentum. When, if ever, should the jets be considered a part of the background?

(2) In pp collisions, an isolated 1 GeV π^+ is emitted at a relative angle $\Delta\phi_{hZ} = \pi/2$. Is the π^+ correlated with the triggering Z?

(3) Suppose that a Z scatters back-to-back off a quark via the central diagram in Fig. 4.1. If the evolution of the background is dependent on the parton evolution (it must be – the parton will lose energy in the QGP, which must be redistributed *somewhere*), then does the jet become part of the background? (Does the background become part of the jet?)

The resolution of each situation is purposely ambiguous, and demonstrates an important point: the per-trigger yield Y is foundationally a *defined* measurement. It is subject to a particular definition of the UE, and different UE definitions can lead to different results. Experimentalists frequently motivate particular definitions based on their heightened sensitivity to underlying event particles. Possibilities include

- the random-cone method, where the charged-particle yield in randomly drawn cones at least $\Delta R \geq \Delta R_{\text{min}}$ away from a jet serves as an estimate of the UE yield within the jet core [111, 277, 278],
- the hemispheres-method, where the charged-particle yield in the Z-going hemisphere (i.e. all charged particles $\Delta\phi_{hZ} < \pi/2$) serves as the UE estimate,
- the zero-yield-at-minimum (ZYAM) method, where the background component of Y is defined as its global minimum versus $\Delta\phi_{hZ}$ (this method has been used frequently in the aforementioned RHIC measurements), or
- the mixed-event method, where the charged-particle yield in separate, independent events with similar global characteristics defines the UE.

To see how these might differ, consider for example the hemispheres method. In the multijet event (scenario 1), any jets that incidentally are in the same hemisphere of the Z would be included in the UE definition. This would naturally lead to a significantly more active UE at high-p_{T} due to

System	Year	$\mathcal{L}_{\text{int}}$	Good runs list (GRL)
pp	2017	$256.8\,\text{pb}^{-1}$	data17_5TeV.periodAllYear_DetStatus-v98-pro21-16_Unknown_PHYS _StandardGRL_All_Good_25ns_ignore_GLOBAL_LOWMU.xml
Pb+Pb	2018	$1.717\,87\,\text{nb}^{-1}$ (toroid on & off)	data18_hi.periodAllYear_DetStatus-v106-pro22-14_Unknown_PHYS _HeavyIonP_All_Good_ignore_TOROIDSTATUS.xml
		$1.438\,45\,\text{nb}^{-1}$ (toroid on)	data18_hi.periodAllYear_DetStatus-v106-pro22-14_Unknown_PHYS _HeavyIonP_All_Good.xml

Table 4.1: List of good runs lists used in the data sets for this analysis, with the appropriate integrated luminosities. Note that two GRLs are used for the 2018 Pb+Pb data to indicate the toroid status.

the coincidental multi-jet production. If the intended signal is only back-to-back Z-single parton scatterings, then including multi-jets in the background could be advantageous. On the other hand, if the background is meant to subtract everything originating elsewhere from the hard scattering, then multi-jets should be a part of the signal. We emphasize here that there is no *a priori* "best" method to define the UE. They simply lead to different results as they are sensitive to different physics.

The presented Z-charged-hadron correlation measurement applies the mixed-event definition with a particular set of matched global characteristics. The motivation for this is that mixed-event is uncorrelated with the Z – thus subtracting the mixed-event yield should leave only the correlated hadron yield, including any "correlated background" effect. We will revisit what this contribution could look like in the results. In Pb+Pb, we require the trigger event (the Z-tagged event) and associated event (the matched event) to have similar centrality, flow, and run number; the latter accounts for any variation in beam or detector conditions. The associated event is taken from minimum bias data. In pp, we take the associated event from low-p_{T} Z events, though no matching aside from run number is performed.

4.2 The Basics: Data Sets & Event Selection

The Pb+Pb collision data set used in this analysis was recorded by the ATLAS detector during the heavy-ion run in November and December 2018. pp collision data is used as a QCD vacuum reference, and was recorded during the November 2017 low-μ run. In each run, the nucleon-nucleon center of mass energy was $\sqrt{s_{\mathrm{NN}}} = 5.02$ TeV. For the pp run, a total of 13 runs pass the good runs list (GRL) selection. Similarly, only runs passing the GRL are used in the Pb+Pb analysis. For the $Z \to ee$ channel, 45 runs pass the GRL from the 2018 data-taking. For the $Z \to \mu\mu$ channel, a separate GRL is used to select a subset of these runs in which the toroid system was fully operational. The GRLs used in this analysis are shown in Table 4.1, in addition to their respective integrated luminosities.

In the offline analysis, events are required to meet several conditions, in addition to the good run list previously mentioned. Throughout the analysis, all events are required to have a reconstructed primary vertex, defined to be the vertex with at least two associated tracks and the highest sum of track p_{T}. Events are also required to not have a flag raised by the liquid argon, tile calorimeter, or SCT inner detector systems as being non-operational during that event [279].

Additionally, in some portions of the 2018 Pb+Pb data taking, the B-layer became desynchronized [280], modifying the tracking efficiency relative to nominal conditions [281]. Affected events are rejected in this analysis.

Pile-up Removal

Events which are flagged as pile-up can bias the observables presented here and must be rejected. Two types of pile-up can enter this analysis. First, out-of-time pile-up occurs when signal from a collision that occurred in a previous bunch crossing is still present in the detector during a subsequent collision. This can be problematic as the subsequent event may be measured to have a negative energy in the forward calorimeter, which affects the centrality measurement.[3] Events

[3] "Negative energy" frequently occurs when the integration time of the calorimeter signal is much longer than the average time between collisions, i.e. the bunch crossing rate divided by μ. The pulses from multiple collisions

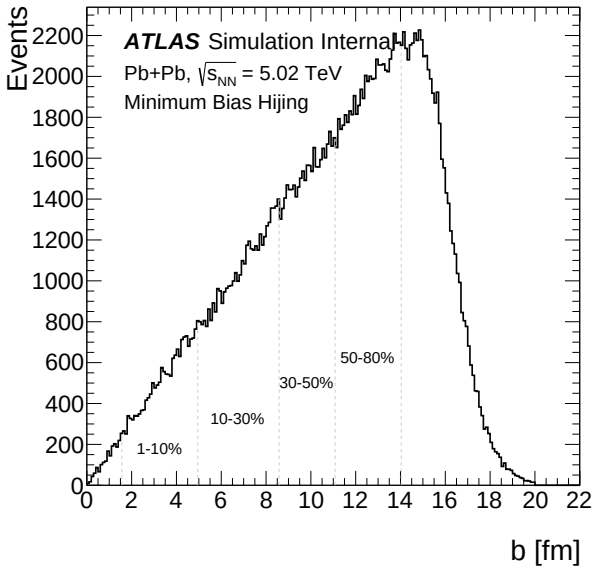


Figure 4.4: Truth Pb+Pb impact parameter distribution in minimum bias HIJING samples. Vertical dashed lines indicate centrality percentile cutoffs as designated: 1–10%, 10–30%, 30–50%, and 50–80%.

are flagged as out-of-time pile-up if they contain less than the mean ΣE_{T} minus four standard deviations in the calorimeter barrel as a function of the number of reconstructed charged particles, $N_{\mathrm{ch}}^{\mathrm{rec}}$ [282]. This corresponds to less than 0.5% of the data, over all $N_{\mathrm{ch}}^{\mathrm{rec}}$.

The other type is called in-time pile-up and occurs when multiple collisions occur during the same bunch crossing. In both pp and Pb+Pb, tracks must be associated with the primary vertex and therefore in-time pile-up does not directly affect the hadron yield measurements. However, having multiple collisions presents a problem with calorimetric measurements, particularly in the Pb+Pb. When multiple collisions contribute to the same total calorimeter energy, it is indeterminable how to assign energy to each collision. The idea of a calorimetric centrality metric breaks down because the forward calorimeter energy no longer describes the centrality of a single collision. If you ignore this and attempt to measure a centrality anyways, the result will certainly be biased towards the more central events. Therefore the most substantial impact from in-time pile-up is in the most central collisions. To reject these kinds of events, the ZDCs are used in conjunction with the FCal.

interfere, and the negative part of the pulse from one collision destructively interferes with the subsequent collision, making the estimated energy in the second collision negative.

At a given $\Sigma E_{\mathrm{T}}^{\mathrm{FCal}}$, there is a distribution of how many spectator neutrons will be emitted by the disintegrating nuclei, which translates into some distribution of total ZDC energies (since each neutron carries, on average, 2.51 TeV at this collision energy). In general, increasingly central events produce fewer spectator neutrons as more and more of the nuclei overlap in the collision. Therefore in-time pileup events will produce far too many spectators as each collision, which both have an overestimated centrality, will produce more spectators than expected. To quantitatively understand where these events begin to appear, the ZDC pulses were fitted and calibrated to the appropriate energy scale using the latest 2018 calibration [283]. After this calibration, the maximum allowed number of neutrons in the ZDC was evaluated as a function of $\Sigma E_{\mathrm{T}}^{\mathrm{FCal}}$. Events with a ZDC energy above this limit are very likely in-time pileup and are rejected. In pp collisions, there is no explicit removal of in-time pile-up events in this manner, although at the analysis level, all particles must come from the same primary vertex in both pp and Pb+Pb, and events with multiple collision vertices (i.e., pile-up vertices) are discarded.

Centrality Determination

Centrality is, of course, of pivotal interest in studying Pb+Pb collisions. In this measurement, a variety of metrics are used to determine event-by-event centrality values. Certain heavy-ion event generators, such as HIJING, directly provide initial state information like impact parameter (b). Thus for the HIJING Monte Carlo samples used in the analysis, centrality is determined from the minimum bias distribution of b. The derivation of the percentile cuts in this variable can be seen in Fig. 4.4. A few divisions are shown visually and further specified numerically in Table 4.2.

However, we cannot directly measure impact parameter in data, so we are forced to resort to proxy variables. A frequent choice is the total transverse energy deposited in the forward calorimeters ($\Sigma E_{\mathrm{T}}^{\mathrm{FCal}}$). Although peripheral collisions produce more forward-traveling beam remnants, these products have pseudorapidities of essentially 0, and they travel parallel to the magnetic field (at least within the main detector body). Thus the energy deposited in the forward calorimeter can be safely assumed to reflect to overall event activity and therefore strongly anti-correlates with

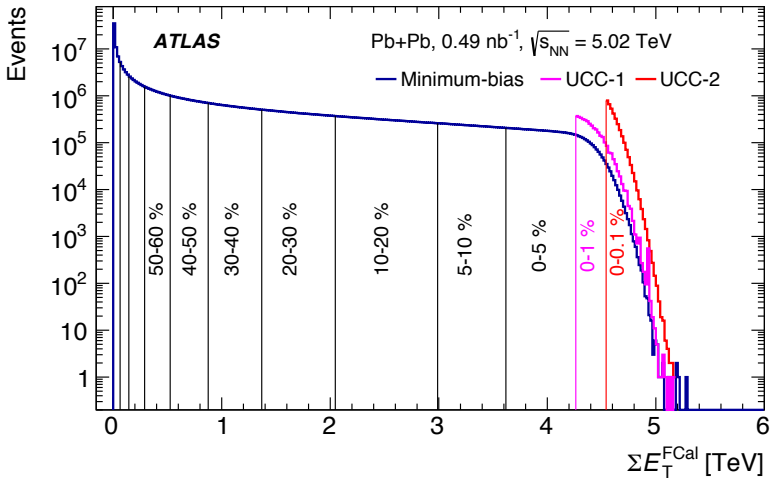


Figure 4.5: The distribution of $\Sigma E_{\mathrm{T}}^{\mathrm{FCal}}$ values in minimum bias Pb+Pb collisions at 5.02 TeVis shown, as well as two samples of ultra-central collisions (UCCs) in the range 0–1%. Vertical divisions indicate percentiles of the minimum bias distribution. Figure reproduced from Ref. [284].

the impact parameter of the collision [59, 90, 284]. The distribution of $\Sigma E_{\mathrm{T}}^{\mathrm{FCal}}$ values in minimum bias Pb+Pb collisions from 2015, along with percentile divisions, is shown in Fig. 4.5. The distributions in two samples of ultra-central or UCC Pb+Pb collisions are also overlaid. Other quantities commonly used in centrality determination include the total particle multiplicity $N_{\mathrm{ch}}^{\mathrm{rec}}$. We point out that this measurement counts charged particles in the rapidity interval $|\eta| < 2.5$, so using a multiplicity-based centrality metric would directly bias the charged-particle yield as they are autocorrelated.

The centrality categories used here were defined as percentiles of the $\Sigma E_{\mathrm{T}}^{\mathrm{FCal}}$ distribution from minimum bias Pb+Pb collisions recorded in 2015 [285]. Percentiles derived from the newer 2018 data set were found to match their 2015 counterparts. These divisions are listed in Table 4.2, as well as corresponding impact parameter values taken directly from Glauber model simulations of Pb+Pb collisions. Only three sets of cuts are shown here, as this measurement is performed in three centrality classes: 30–80% (“peripheral”), 10–30% (“mid-central”), and 0–10% (“central”). These will be frequently referred to throughout this chapter.

Percentile	$\Sigma E_{\mathrm{T}}^{\mathrm{FCal}}$ values [TeV]	Impact parameters [fm]
0–10%	$2.99594 - 5.$	$0 - 4.952$
10–30%	$1.37892 - 2.99594$	$4.952 - 8.582$
30–80%	$0.066402 - 1.37892$	$8.582 - 14.031$

Table 4.2: Shown are the percentile cuts on the ΣE_{T} in the forward calorimeters for Pb+Pb MB events with corresponding impact parameter cuts derived from Glauber modeling. These cuts define the centrality bins used in this analysis. The final results are reported in only three bins, from 30–80%, 10–30%, and 0–10%.

Triggering

First, events with a Z must be selected. Therefore events with candidate Z bosons are selected from the respective single muon trigger (`HLT_mu14`) or the appropriate single electron trigger (`HLT_e15_lhloose_ion_L1EM12` in the Pb+Pb or `HLT_e15_lhloose_L1EM12` in the low-μ pp reference). These triggers are found in the "HardProbes" data stream for Pb+Pb and the "Main" stream for pp. For events with electrons, there are two primary differences between the "ion" and "non-ion" triggers, stemming from the large underlying event activity in Pb+Pb collisions. First, for the "ion" trigger, only an E_{T} cut is used, i.e., no shower shapes are checked. Second, in heavy-ion systems the UE varies dramatically event-to-event, so an event-by-event underlying event subtraction is performed by the HLT algorithm [286]. These triggers were unprescaled throughout all of the runs used, so the event sample size should be maximized. However, to correct for potential trigger biases, a per-event efficiency correction is derived from single-lepton tag-and-probe studies in data.

Minimum Bias Events

In addition to single-lepton events, minimum bias (MB) events in the 2018 Pb+Pb data are also used to build the UE model. These events are required to be included in the GRL which ignores the toroid status as information from the MS is not needed. Unlike previous data sets, there are two

MB data streams in the 2018 Pb+Pb data. These are the "central collisions" (CC) and "peripheral collisions" (PC) streams. Events in the CC stream must fire the `HLT_noalg_cc_L1TE600.0ETA49` trigger, which requires $\Sigma E_{\mathrm{T}} > 600$ GeV (total E_{T} of calorimeter towers in the barrel, but only including those above an online E_{T} threshold). This online cut corresponds to approximately 0–55% central Pb+Pb collisions ($\Sigma E_{\mathrm{T}}^{\mathrm{FCal}} > 0.4$ TeV). The PC stream takes events tha fire one of two triggers. The first is `HLT_mb_sptrk_L1ZDC_A_C_VTE50`, which fires on events that leave a signal (above some threshold) in both the A- and C- side ZDC modules, and have $\Sigma E_{\mathrm{T}}^{\mathrm{FCal}} < 50$ GeV ($\gtrsim 75\%$ centrality Pb+Pb events). The second is `HLT_noalg_pc_L1TE50_VTE600.0ETA49`, which fires on events with between $50 < \Sigma E_{\mathrm{T}} < 600$ GeV in the calorimeters (approximately 55–75% central Pb+Pb events) [287].

MB data is not trigger prescale-corrected as it is only used to build the UE model and is therefore not sensitive to prescaling. However, there will be some modest shuffling if the prescale correction is not applied in centrality region 50–60% where the PC and CC streams overlap, as shown in Fig. 4.6. Here, because of online vs. offline differences in calculating ΣE_{T}, as well as fluctuations in ΣE_{T} in the barrel vs. the forward calorimetry, there is not a sharp cutoff between streams but instead a short turn-on and turn-off. Given this occurs in a region of low relative Z production and in a region where the physics of quenching is least observed, the impact should be minimal. Furthermore, given the prescale correction would just be reweighting contributions from identical distributions, the observed impact would be statistical and is therefore neglected. However, to mitigate any effect on the charged-hadron yields, events from the CC and PC stream in the 30–80% centrality range are randomly sampled at the analysis level. In the CC stream, only a subset of peripheral (30–80%) events are selected, since fewer Zs are produced in the peripheral bin, while all events in 0–30% are used. As a minor side effect, this also helps to reduce offline file sizes to improve analysis runtime. The PC stream is then sampled such that the flat tops of the 30–80% centrality distributions match, as can be seen in Fig. 4.6. To check that the flat tops match, the ratio of the PC flat top height is calculated with respect to that in CC. This quantity is a relative prescale between the two streams, and should be close to 1 to mitigate potential bias in

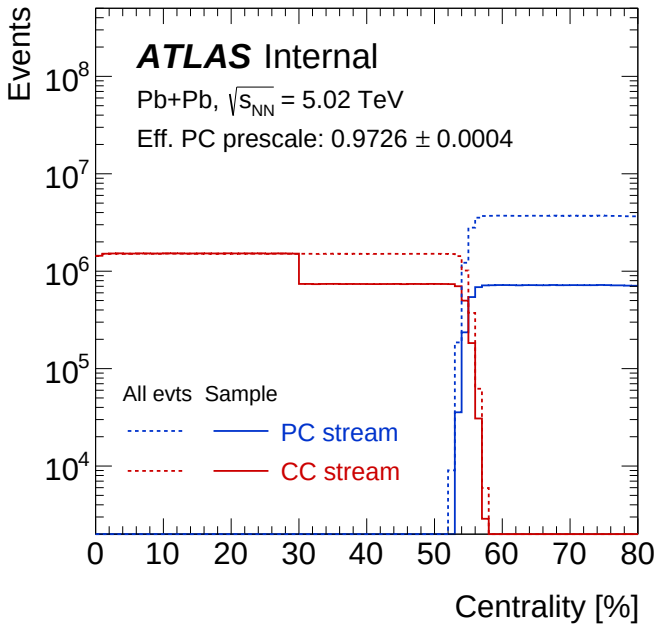


Figure 4.6: Contributions to the minimum bias centrality distribution from the PC and CC streams are shown. In the dashed lines, all recorded events are shown, whereas the resampled events are shown in solid lines. For 30–80% events in the CC stream, the probability of using an event at the analysis level is artificially reduced from 1 such that events in the 50–60% region are correctly sampled from the two data sets. The relative prescale of the PC stream compared to the CC stream is also reported.

the crossover region (roughly 50–60%). After resampling the PC stream, the final relative prescale is found to be within 3% of 1, so any possible bias arising from trigger combination should be minimized.

Monte Carlo Simulations

The Monte Carlo samples of Z bosons used in this analysis were generated with the POWHEG Monte Carlo event generator [288] interfaced with the PYTHIA v8.1 parton showering program [289]. Event generation is divided amongst the two such that POWHEG produces the hard-scattering signal (i.e. the process producing the Z), while PYTHIA handles the parton showering, hadron recombination, and pp underlying event. The CT10 parton distribution function (PDF) set [290] was used in the matrix element, while the CTEQ6L1 PDF set [291] and AZNLO tune [292] were used

to describe the initial-state parton shower. Hard-scattering processes in Pb+Pb collisions occur from a combination of individual pp, pn, np, and nn collisions. This can in principle affect the events in which a Z is produced, so the samples are divided into these four categories of nucleon-nucleon collisions. Ignoring neutron skin effects (i.e., a different radial distribution of neutrons compared to protons in the Pb nucleus), the number of events in each category is impact parameter independent and is calculated from the probability of drawing the nucleon pair from each nucleus. For example, the fraction of simulated nucleon-nucleon collisions that are pp collisions is given by

$$f_{pp} = \left(\frac{Z}{A}\right) \times \left(\frac{Z}{A}\right) \times 100\% \approx 15.5\%. \tag{4.10}$$

Samples of events that are backgrounds to the Z bosons (not the charged-particle background), namely $Z \to \tau\tau$ decays and $t\bar{t}$, have also been produced in this configuration. A full table detailing the samples used in this analysis can be seen in Table 4.3.

Data Overlay

To model the substantial underlying event present in central Pb+Pb collisions, simulated Z events are embedded into MB events from the 2018 Pb+Pb data during the digitization process. This helps model reconstruction effects that depend on the level of event activity and are expected to impact the reconstruction process in a data-driven manner. These effects potentially include quantities such as the lepton energy scales and resolutions, identification efficiencies, or fake track rate, which depend on the event-to-event detector occupation. Triggering is not necessary in these simulations so there is no trigger information saved during the reconstruction phase. Lastly, in order to guarantee that the distribution of event centralities in simulation match that in data, simulated events are weighted such that the $\Sigma E_{\mathrm{T}}^{\mathrm{FCal}}$ distributions have the same shape.

Hijing Samples

For greater control over the study of MC closure later in the analysis, additional events were sampled with the Hijing generator (version 1.383) [81]. This generator provides a full Monte

Overview of MC Samples

Description	Filters	# Events	σ[pb] ($pp/pn/nn$)	$\varepsilon_{\text{filter}}$ ($pp/pn/nn$)
$Z \to ee$	–	1M	642.8	1
$Z \to \mu\mu$	–	3.36M	642.8	1
$Z \to ee$ with Data Overlay	–	2.758M	642.8/656.5/665.3	1
	$p_{\text{T}}^{Z} > 25\,\text{GeV}$	2.76M		0.179/0.179/0.180
	$\lvert y_Z \rvert > 1.75$	2.76M		0.368/0.373/0.379
$Z \to \mu\mu$ with Data Overlay	–	2.399M	642.8/656.5/665.3	1
	$p_{\text{T}}^{Z} > 25\,\text{GeV}$	2.4M		0.179/0.179/0.180
	$\lvert y_Z \rvert > 1.75$	2.4M		0.368/0.373/0.379
$Z \to \tau\tau$ with Data Overlay	–	200k	642.9	1
$t\bar{t}$ with Data Overlay	–	70k	56.70	0.544
Hijing	–	300k	–	–
	$b < 7\,\text{fm}$	500k		
$Z \to ee$ with Hijing Overlay	–	100k	642.8	1
	$b < 7\,\text{fm}$	250k		
$Z \to \mu\mu$ with Hijing Overlay	–	100k	642.8	1
	$b < 7\,\text{fm}$	250k		

Table 4.3: Table of Monte Carlo samples generated for this measurement, including the event filter (if applicable), sample size, and cross-section σ, and filter efficiency $\varepsilon_{\text{filter}}$. For the Pb+Pb, samples are further subdivided into pp, pn, np, and nn nucleon-nucleon collisions, each of which has a slightly different σ and $\varepsilon_{\text{filter}}$, so the value for each isospin configuration is reported where appropriate (note that pn and np are identical in the eyes of the generator).

Carlo-based simulation of the high occupancy Pb+Pb collision environment, as opposed to the data overlay method which uses a hybrid MC-data approach. These events were divided amongst five samples placed at z-vertex positions of 0 mm, ±24 mm and ±64 mm. Additional "semicentral" (SC) event samples were generated with an impact parameter $b < 7\,\text{fm}$ filter to enhance the sampling of central events. This value very roughly corresponds to the 30% centile. Finally, $pp \to Z$ events generated with the Powheg interfaced to Pythia were embedded in the Hijing Pb+Pb events during detector simulation similar to the data overlay. As before, both $Z \to ee$ and $Z \to \mu\mu$ events were simulated, though multiple isospin configurations were not generated. Thus, 30 samples were

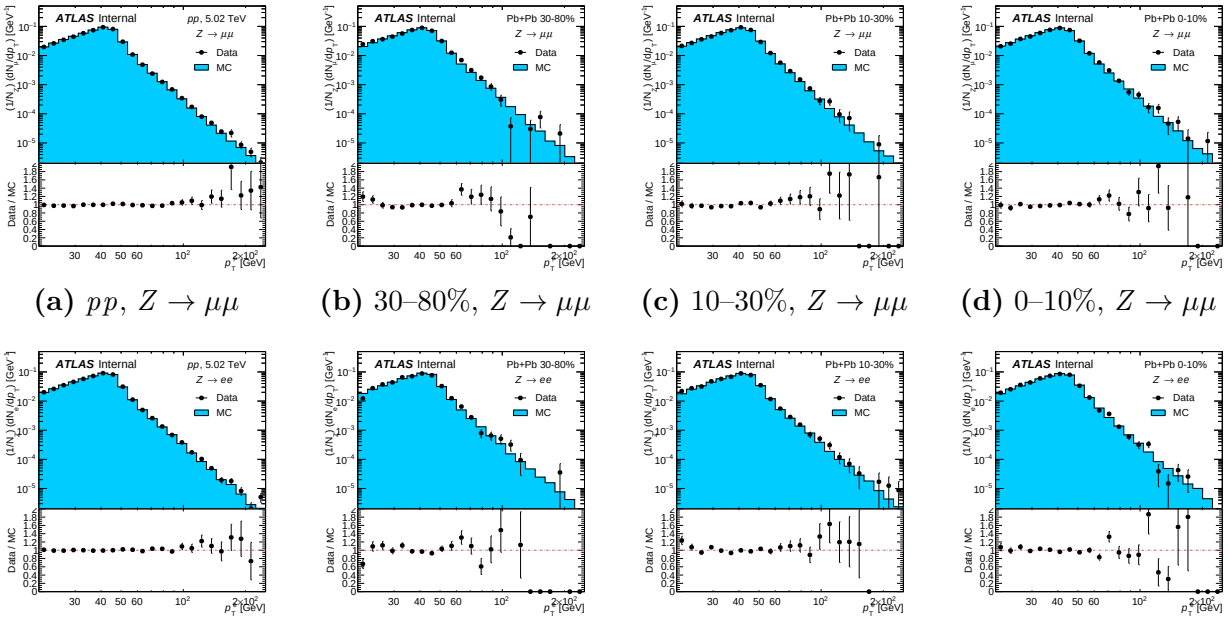
generated in total (5 per z-vertex position $\times$ 2 per centrality filter $\times$ 2 per channel + 1 without Z embedding = 30). These are listed in Table 4.3. For technical reasons, these samples were also used to estimate the tracking purity in Pb+Pb collisions (the fake rate cannot be measured in the data overlay samples).

4.3 Muon Channel

In this analysis, Z bosons are identified through their decays to either opposite-sign electron or muon pairs. To ensure the Z boson selection is well-controlled, first the performance of lepton reconstruction must be studied in detail. This is performed for each channel separately; we begin with the muon channel in this section. First, we will consider the probability that a real Z in data makes it to the event selection in our offline analysis. This probability can be thought of as an efficiency factor as it reflects our ability as experimentalists to maximize the sample size. If the efficiency depends on the properties of the event in substantial ways, then this can indicate bias on the final measurement which must be accounted for. Second, we consider the energy scale of the leptons and their impact on the boson kinematics. After calibrating the single-lepton energies, the resulting p_{T} spectra of Z decay leptons in data and MC can be seen in Fig. 4.7. A clear peak is observed at approximately 40–45 GeV or about half of the nominal Z mass. Events around this peak can be understood as fluctuations in the relevant degrees of freedom: the p_{T} and rapidity y of the parent, and the decay orientation in the center of mass frame.

Before diving into these details, let us consider the basic lepton requirements. To be considered in the Z reconstruction, candidate muons must meet a set of basic criteria in the offline selection. This helps maintain high sample purity and good kinematic resolution. These candidates must nominally

- have transverse momentum $p_{\mathrm{T}}^{\mu} > 20$ GeV,
- be reconstructed within the allowed pseudorapidity range $|\eta| < 2.5$,
- meet the `Medium` quality criterion [293],



(a) pp, $Z \to \mu\mu$ **(b)** 30–80%, $Z \to \mu\mu$ **(c)** 10–30%, $Z \to \mu\mu$ **(d)** 0–10%, $Z \to \mu\mu$

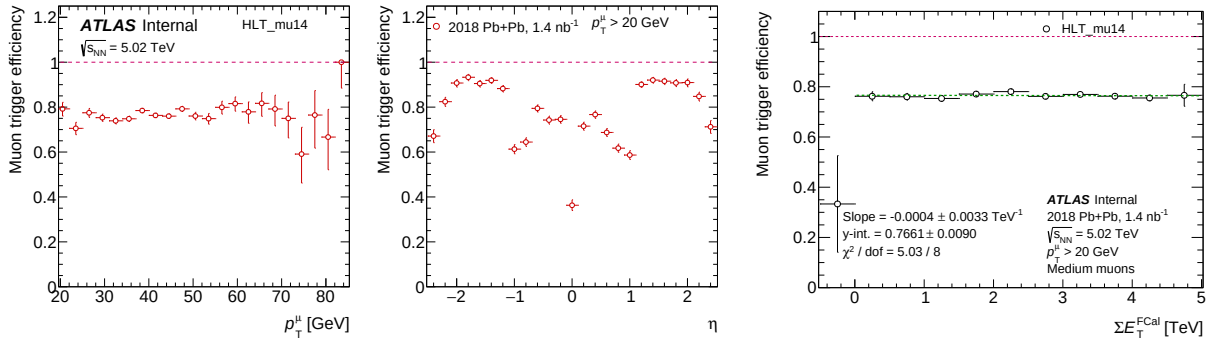
(e) pp, $Z \to ee$ **(f)** 30–80%, $Z \to ee$ **(g)** 10–30%, $Z \to ee$ **(h)** 0–10%, $Z \to ee$

Figure 4.7: Shown are the p_{T} distributions of single muons **(a–d)** and electrons **(e–h)** from tagged $Z \to \ell\ell$ decays, ranging from **(a,e)** pp to **(d,h)** 0–10% central Pb+Pb.

- meet a cut on the absolute value of the d_0 significance (defined as the d_0 uncertainty divided by its central value) $\left|\sigma_{d_0}/d_0\right| < 3$, and
- meet a cut on the z_0 parameter $\left|\Delta z_0^{\mathrm{vtx}} \sin\theta\right| < 0.5\,\mathrm{mm}$, where $\Delta z_0^{\mathrm{vtx}}$ is the distance in z to the primary vertex and θ is the polar angle of the track.

We note that the tracking parameters are taken from the inner detector track associated to the muon. Geometrically, this last condition is non-trivial. It essentially allows forward tracks to have a larger $\Delta z_0^{\mathrm{vtx}}$ than mid-rapidity tracks, which are presumably well-reconstructed and pass very close to the primary vertex.

Although the lepton minimum p_{T} is rather high, as the spectrum appears to have contributions below 20 GeV from Fig. 4.7, it matches the one used in previous Z measurements and is intended to keep the combinatoric di-muon background low in Pb+Pb events [63]. After applying these cuts and selecting events with reconstructed Z bosons (as described in Sec. 4.5), the p_{T} distribution of candidate Z decay muons can be seen top row of Fig. 4.7. From this figure the



(a) **(b)** **(c)**

Figure 4.8: The single muon trigger efficiency in the 2018 Pb+Pb data is investigated. Projections of the efficiency versus **(a)** p_{T}^{μ} and **(b)** η_{μ} are shown. **(c)** Dependence on centrality via $\Sigma E_{\mathrm{T}}^{\mathrm{FCal}}$ is also shown (right) and fitted to a linear function.

spectra in pp and Pb+Pb generally match, within statistics, though further study of inefficiencies and possible backgrounds is necessary to confirm there is no bias which appears in one data set but not the other.

$Z \to \mu\mu$ Acceptance Considerations

In this analysis, real Z bosons may be missed due to inefficiencies from two main sources: the first is the single-lepton trigger, and the second is the reconstruction and identification. We investigate both in this section for $Z \to \mu\mu$ events. First, we consider the trigger efficiency, which is driven by differences in the offline reconstruction of muons to the trigger algorithm. Essentially, these differences cause the trigger to miss some events erroneously. To determine how frequently this occurs, we implement a data-driven tag-and-probe method [294]. First, candidate $Z \to \mu\mu$ events are selected by searching for events that fire the single muon trigger and have an opposite-sign reconstructed muon pair with an invariant mass in the core of the $Z \to \mu\mu$ resonance, $76 < m_{\mu\mu} < 106$ GeV. One of these muons, called the "tag", must meet stringent criteria: it must have a $p_{\mathrm{T}}^{\mu} > 30$ GeV, meet the `Tight` identification criteria, and be matched to an HLT object which fired the trigger. By selecting on only one of the muons, we can check whether the other muon, called the "probe", is also matched to an HLT object which would fire the trigger; but, due to the

coincidence requirement we can be highly confident that it represents a real muon. This is helped by requiring additionally that the probe meet the `Medium` muon identification criteria.

What we have described is, in essence, a binomial experiment. The success rate of this experiment reflects the trigger efficiency:

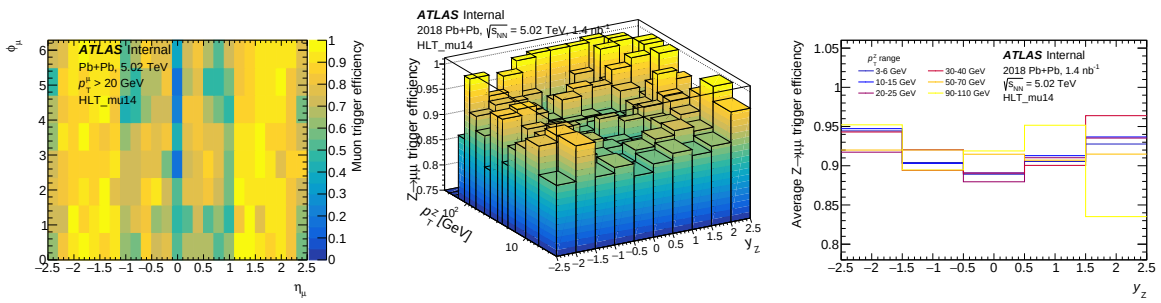
$$\varepsilon_{\mu}^{\text{trig}} = \frac{\#\text{ of successes}}{\#\text{ of attempts}} = \frac{N_{\mu}^{\text{HLT-matched}}}{N_{\mu}^{\text{probe}}}\left(\eta_{\mu}, \phi_{\mu}\right), \tag{4.11}$$

where $\varepsilon_{\mu}^{\text{trig}}$ is the trigger efficiency, $N_{\mu}^{\text{HLT-matched}}$ is the number of the HLT-matched probe muons, and N_{μ}^{probe} is the total number of probe muons. Because $\varepsilon_{\mu}^{\text{trig}}$ is taken to be binomial distributed, it has an estimated variance

$$\sigma^2_{\varepsilon_{\mu}^{\text{trig}}} = \frac{\varepsilon_{\mu}^{\text{trig}}\left(1-\varepsilon_{\mu}^{\text{trig}}\right)}{N_{\mu}^{\text{probe}}}. \tag{4.12}$$

These criteria select approximately 97,000 and 114,000 probe leptons in the electron and muon channels in pp collisions, with a wide distribution to be used for the tag and probe study, and $11,400$ and $12,700$ probe leptons for each channel in Pb+Pb collisions (integrated over all centralities).

Fig. 4.8 summarizes the primary results of the trigger efficiency measurement. Due to finite statistics, the dependence of the trigger efficiency can only be determined as a function of a few variables at most. The p_{T}^{μ} dependence is considered first, since the trigger is designed to only fire on muons with $p_{\text{T}}^{\mu} > 14$ GeV. Versus p_{T}^{μ}, the trigger efficiency is approximately constant, so this potential dependence is not further considered. It is then re-evaluated as a function of η_{μ} and ϕ_{μ}, to which more substantial dependence is observed. This is generally attributed to the structure of the detector affecting the trigger performance. Muons must pass through the entire detector and reach the muon chambers, so if they might have a heightened interaction probability in some directions, it is possible for the trigger efficiency to deteriote in those directions. For example, around $\eta_{\mu} \approx 0, \pm 1$, we can clearly see the efficiency dips somewhat; these dips are understood to be artifacts of the detector support structures affecting performance. Dependence on centrality via $\Sigma E_{\text{T}}^{\text{FCal}}$ is also studied and fitted to a linear function to quantify any occupancy dependence, although this is not observed as the fit is consistent with a flat line. This qualitatively fits in with our prior understanding, as most particles in Pb+Pb collisions are various low-p_{T} hadrons, which



(a) **(b)** **(c)**

Figure 4.9: **(a)** Final muon trigger efficiencies are shown for the 2018 Pb+Pb data as a function of η_μ and ϕ_μ. **(b)**,**(c)** The average trigger efficiency for the $Z \to \mu\mu$ decay is shown versus the reconstructed Z rapidity and p_{T}.

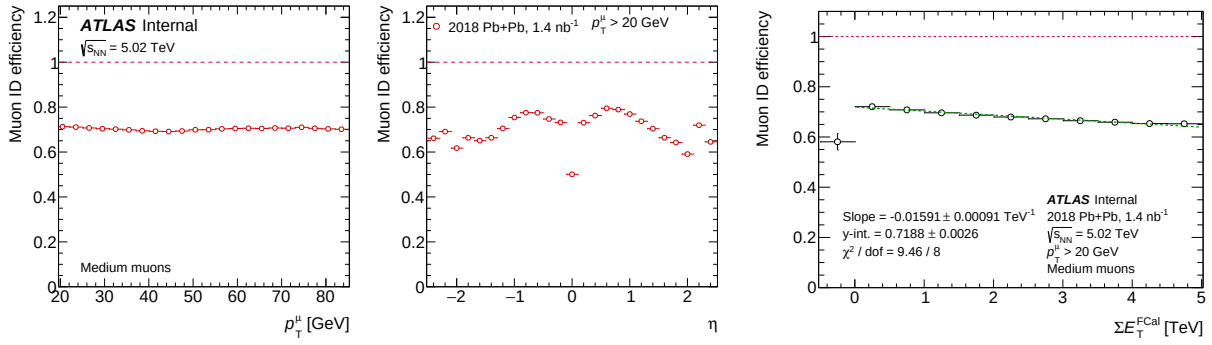
have a very low probability of reaching the MS.

The final efficiency map used to calculate the corresponding acceptance correction is shown in Fig. 4.9. To correct for trigger inefficiency, candidate events are weighted by the inverse of the efficiency, which accounts for similar events that were missed by the trigger. For single-lepton events, this efficiency is as described above. However for Z bosons, the probability of not triggering on an event is given by the probability of not triggering on either lepton. Therefore the appropriate trigger correction factor for Z boson events $1/\varepsilon$ is calculated on an event-by-event basis as

$$\varepsilon^{\mathrm{trig}}_{\mathrm{Z}\to\mu\mu} = 1 - \left[1 - \varepsilon^{\mathrm{trig}}_{\mu}\left(\eta_{\mu_1}, \phi_{\mu_1}\right)\right] \times \left[1 - \varepsilon^{\mathrm{trig}}_{\mu}\left(\eta_{\mu_2}, \phi_{\mu_2}\right)\right]. \tag{4.13}$$

To see how this efficiency varies with the Z kinematics (and therefore what kind of effect it will have in this analysis), profiles of the reconstruction efficiency are replotted versus the Z kinematics in Fig. 4.9. Since only one lepton must fire the trigger, there are effectively two attempts to fire the trigger with every event, and so the Z boson trigger efficiency is generally higher than that of single leptons. There is a minor dependence on rapidity which is corrected for by weighting these events.

Once an event has been recorded, it is then further possible for real muons to be missed by the reconstruction and identification procedure. In practice, the identification efficiency is not completely independent of the trigger efficiency. If a muon successfully manages to fire the trigger,



(a) **(b)** **(c)**

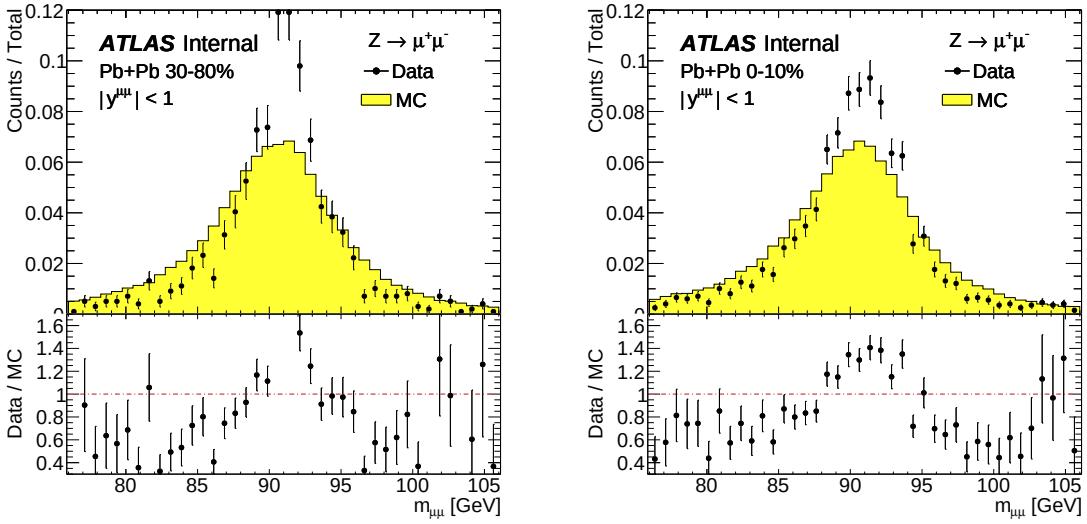
Figure 4.10: The single muon identification efficiency in the 2018 Pb+Pb data is investigated. Projections of the efficiency versus **(a)** p_{T}^{μ} and **(b)** η_{μ} are shown. **(c)** Dependence on centrality via $\Sigma E_{\mathrm{T}}^{\mathrm{FCal}}$ is also shown (right) after correcting for the η_{μ} and ϕ_{μ} dependencies, and is fitted to a linear function.

there is probably some characteristic of its interaction with the detector that will make it more likely to be successfully reconstructed. For simplicity, we assume here that the two are *not* correlated in this way, since the overall impact of the corrections on the final results is generally $\lesssim 2\%$ anyways (see Sec. A.5).

Unlike the trigger efficiency, we evaluate this reconstruction efficiency in simulation and apply it to data. Tag truth muons are first selected in simulated Z boson events (note that all of the simulated events contain a Z boson). These muons must have a pseudorapidity $|\eta| < 2.5$ and have a truth barcode < 10000, indicating that it was produced in the Powheg + Pythia hard-scattering event. Then each truth muon is matched to a reconstructed muon meeting the `Medium` identification criteria [242]. Muons are considered matched if they are separated geometrically by $\Delta R < 0.3$. Some probe truth muons will lack a reconstructed partner – this represents the combined inefficiency between the reconstruction and identification procedure. Therefore the efficiency is the binomial success rate:

$$\varepsilon_{\mu}^{\mathrm{reco}} = \frac{N_{\mu}^{\mathrm{reco.-matched}}}{N_{\mu}^{\mathrm{truth}}}\left(\eta_{\mu}, \phi_{\mu}, \Sigma E_{\mathrm{T}}^{\mathrm{FCal}}\right). \tag{4.14}$$

For muons, the efficiency is usually evaluated differentially in η_{μ} and ϕ_{μ}. The dependence in p_{T}^{μ} was also checked and is observed to be constant, as seen in Fig. 4.10.



(a) 30–80% Pb+Pb **(b)** 0–10% Pb+Pb

Figure 4.11: Normalized distributions of mid-rapidity opposite-signed dimuon invariant masses ($m_{\mu\mu}$) in data (black markers) and MC (yellow shaded region) are shown for **(a)** 30–80% peripheral and **(b)** 0–10% central Pb+Pb collisions. Muon kinematics are measured using the combined ID+MS track; the MS kinematics are used instead in Fig. 4.13.

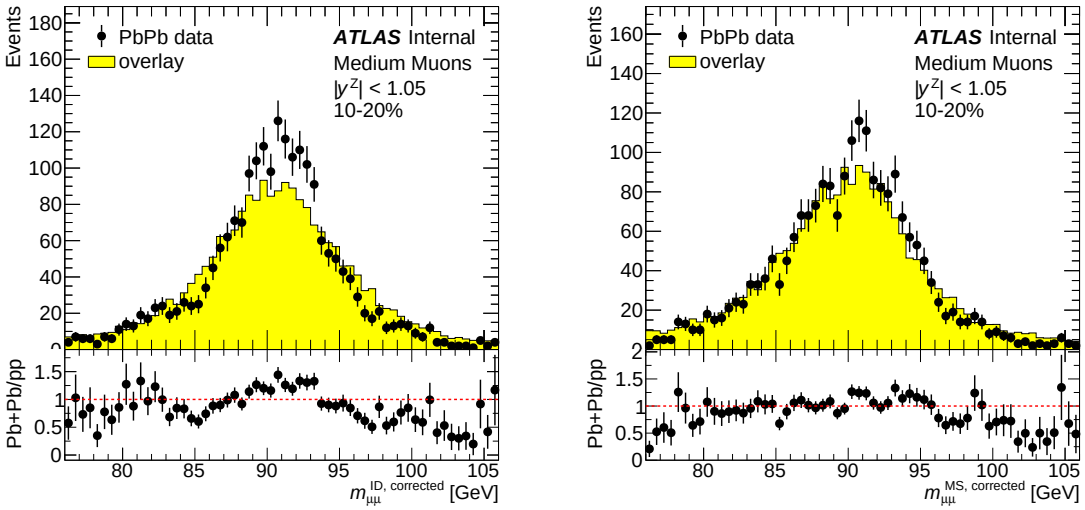
Note that at the trigger level, only one muon must be detected. However in the reconstruction it is required that both muons be reconstructed and identified to obtain a Z candidate. So to correct for these inefficiencies in the final result, $Z \to \mu\mu$ events are weighted by a factor calculated from both decay muons:

$$\varepsilon^{\text{reco}}_{Z\to\mu\mu} = \varepsilon^{\text{reco}}_{\mu}\left(\eta_{\mu_1}, \phi_{\mu_1}, \Sigma E_{\text{T}}^{\text{FCal}}\right) \times \varepsilon^{\text{reco}}_{\mu}\left(\eta_{\mu_2}, \phi_{\mu_2}, \Sigma E_{\text{T}}^{\text{FCal}}\right). \tag{4.15}$$

Energy Calibration and Smearing

In brief, reconstructed muons are characterized using the latest calibration and sagitta tags (`Recs2018_05_20` and `sagittaBiasDataAll_03_02_19_DataYY`, where $YY = 17, 18$ denotes the years the pp and Pb+Pb data were taken, respectively) [293].

To arrive at these calibrations, the dimuon invariant mass ($m_{\mu\mu}$) distribution is typically used as a data-driven indicator of the single muon energy scale and resolution. In other words, the invariant mass is used to adjust the accuracy and indicate the precision of the muon energy



(a) ID tracks **(b)** MS tracks

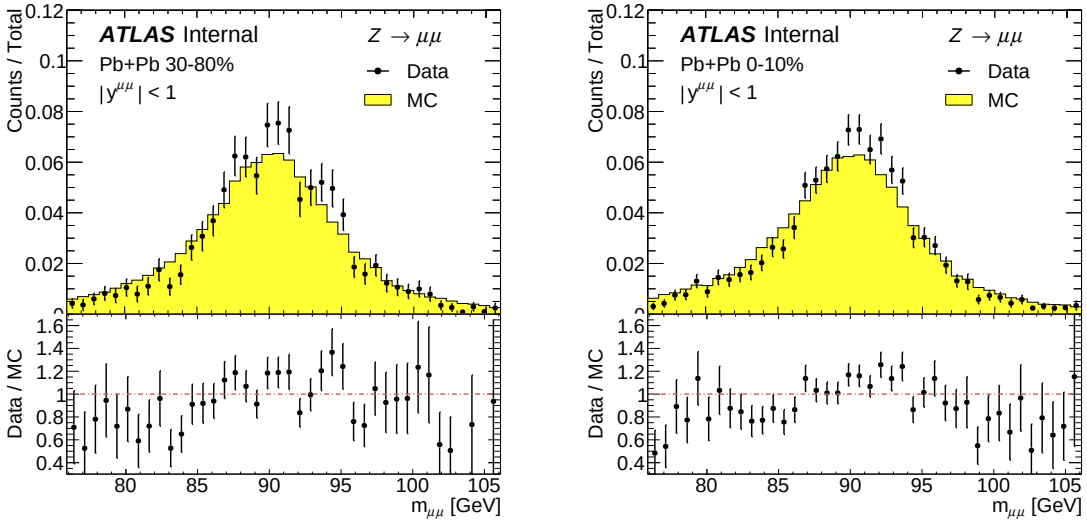
Figure 4.12: Normalized distributions of mid-rapidity opposite-signed dimuon invariant masses ($m_{\mu\mu}$) in data (black markers) and MC (yellow shaded region) are shown for 10–20% central Pb+Pb collisions. The muon kinematics are taken from the muon **(a)** ID track or **(b)** MS track.

measurement. This is because $m_{\mu\mu}$ can be expressed as

$$m_{\mu\mu}^2 = 2E_{\mu_1}E_{\mu_2}\left(1 - \cos\alpha\right) \tag{4.16}$$

if the muons are relativistic. In practice, α – the opening angle between the muons – is very well measured event-to-event from the precision tracking. To calibrate the energy scale, the distribution is carefully adjusted in the vicinity of known $\mu\mu$ scattering poles, such as the J/Ψ, Υ, or Z. These poles serve as standard candles for lepton calibration studies because they are very easily detectable in experiment: they are sharp and occur at very well-known invariant masses. By multiplicatively shifting the $m_{\mu\mu}$ distributions, the dimuon events can be calibrated as an ensemble, with the requisite shifting factors being imparted to the individual muon energies E_{μ_1} and E_{μ_2} as a calibration factor. While the smearing around the poles represents some real physics (namely, the decay width of the resonance), there is also a detector resolution component that can be studied this way.

To this end, the structure of the $m_{\mu\mu}$ distribution near the $Z \to \mu\mu$ resonance has been studied for each collision system in both data and MC. In Fig. 4.11, $m_{\mu\mu}$ histograms are plotted



(a) 30–80% Pb+Pb **(b)** 0–10% Pb+Pb

Figure 4.13: Normalized distributions of mid-rapidity opposite-signed dimuon invariant masses ($m_{\mu\mu}$) in data (black markers) and MC (yellow shaded region) are shown for **(a)** 30–80% peripheral and **(b)** 0–10% central Pb+Pb collisions. Muon kinematics are measured using the MS track only; the combined ID+MS kinematics are used instead in Fig. 4.11.

for 30–80% and 0–10% Pb+Pb collisions across both data and MC. In these comparisons, it is immediately apparent in these figures that the muon peak is wider in the MC than the Pb+Pb data, both in the peripheral and central event selections. Simultaneously, no significant difference between pp and Pb+Pb data was observed, indicating that the muon energy scale and resolution are similar in both collision data sets. This is expected as the Pb+Pb occupancy effect is primarily hadronic, so the resolution of the muon spectrometer should remain competitive even in central Pb+Pb. Therefore the Pb+Pb data-MC resolution difference must be exclusive to muons in the MC with data overlay.

To further investigate this discrepancy, we broke up the muon tracks into their purely ID versus MS fits and reperformed the invariant mass study. In Fig. 4.12, histograms of $m_{\mu\mu}$ for each track type are compared between data and MC in a narrow selection of 10–20% central Pb+Pb events. The dense tracking environment here should generally deteriorate the muon p_{T} resolution as measured by the ID, as hadrons from the Pb+Pb UE will increase the ID occupancy. Meanwhile, the MS should be relatively unaffected by a Pb+Pb occupancy effect. The observations do not

quite match the expectations, however. In the ID, the mass peak is found to be wider in the simulation than in data, which indicates that the MC does not fully describe the data here. This is contrasted with the MS version, shown on the right, which demonstrates decent agreement between data and simulation. We note that the specific, root cause of the wider ID peak in MC is currently unresolved. To mitigate any effect in this analysis, muon kinematics in Pb+Pb are estimated solely from the MS track. This means that muons are still selected from the combined track information; for example, the d_0 cut on muons is applied to the ID track, which has a better d_0 resolution. In the Z boson reconstruction, however, the combined track kinematics are substituted with the MS kinematics. In pp, no resolution effect is observed between data and simulation, so muon kinematics are measured from the combined track. Updated invariant mass peaks using MS kinematics can then be seen in Fig. 4.13. The data-to-MC resolution discrepancy is now much less with the MS kinematics.

Because of the switch to the MS kinematics, an effect on the systematic uncertainties should be expected. This is indeed found to be the case when performing lepton energy scale variations. However the muon energy scale is not the dominant source of uncertainty, so further investigation into this effect is not strictly necessary.

4.4 Electron Channel

In addition to the $Z \to \mu\mu$ channel, we select events in the $Z \to ee$ channel with similar methods. Candidate decay electrons are first selected from offline reconstructed electrons that

- have a $p_{\mathrm{T}} > 20$ GeV,
- are reconstructed within the allowed pseudorapidity range $|\eta| < 2.47$ and be outside the EMCal crack regions, $1.37 < |\eta| < 1.56$,
- meet the `LHLoose` (likelihood loose) or `LHLoose_HI` quality criterion [263],
- meet a significance cut on the d_0 parameter $\left|\sigma_{d_0}/d_0\right| < 5$, and

- meet a cut on the z_0 parameter $\left|\Delta z_0^{\text{vtx}} \sin\theta\right| < 0.5\,\text{mm}$.

The `LHLoose` (pp) or `LHLoose_HI` (Pb+Pb) identification criteria are used in this analysis to reject background electrons. The `LHLoose` or "likelihood loose" ID tag has been optimized to be 93% efficient in pp collisions. Similarly the HI variant has been optimized to have a 90% ID efficiency independent of collision centrality, but using the older sliding window reconstruction [264]. Prior to the 2018 data-taking, the performance of the supercluster reconstruction was also validated within this identification framework [295]. A minor decrease in efficiency was found, though the likelihood identification was not re-optimized for the new reconstruction. The energy resolution was also found to deteriorate mildly with the new reconstruction, which we will address below.

$Z \to ee$ Acceptance Considerations

First, we consider the probability that real $Z \to ee$ events are missed by the analysis procedure as a means to investigate potential biases entering the event selection. This follows the same general procedure as the muons, so here we will just highlight the details. Two unprescaled electron triggers were enabled during the 2018 Pb+Pb data-taking, `HLT_e15_lhloose_ion_L1EM12` and `HLT_e20_loose_ion`. Only the first trigger is used in this analysis, as it offers a better background rejection at the cost of a slightly lower efficiency – this was observed in a previous study using the tag-and-probe method [286]. Here, we again apply the tag-and-probe procedure. Events are first selected that contain two opposite-sign reconstructed electrons with an invariant mass near the Z boson, $76 < m_{ee} < 106$ GeV. To reduce background, the "tag" electron is required to satisfy the `LHMedium` criteria (`LHMedium_HI` in Pb+Pb), have $p_{\text{T}}^{e} > 30$ GeV, and be matched to an HLT electron object which fired the trigger. The probe is then the other reconstructed electron which satisfies the `LHLoose(_HI)` criteria. Both electrons must be reconstructed in the pseudorapidity range $0 < |\eta_e| < 1.37$ or $1.56 < |\eta_e| < 2.47$. The resulting efficiency curves are shown in Fig. 4.14 as a function of electron p_{T}, electron η, and collision centrality. Due to there being globally more total energy deposited in the calorimeters in central events, the trigger efficiency is expected to depend

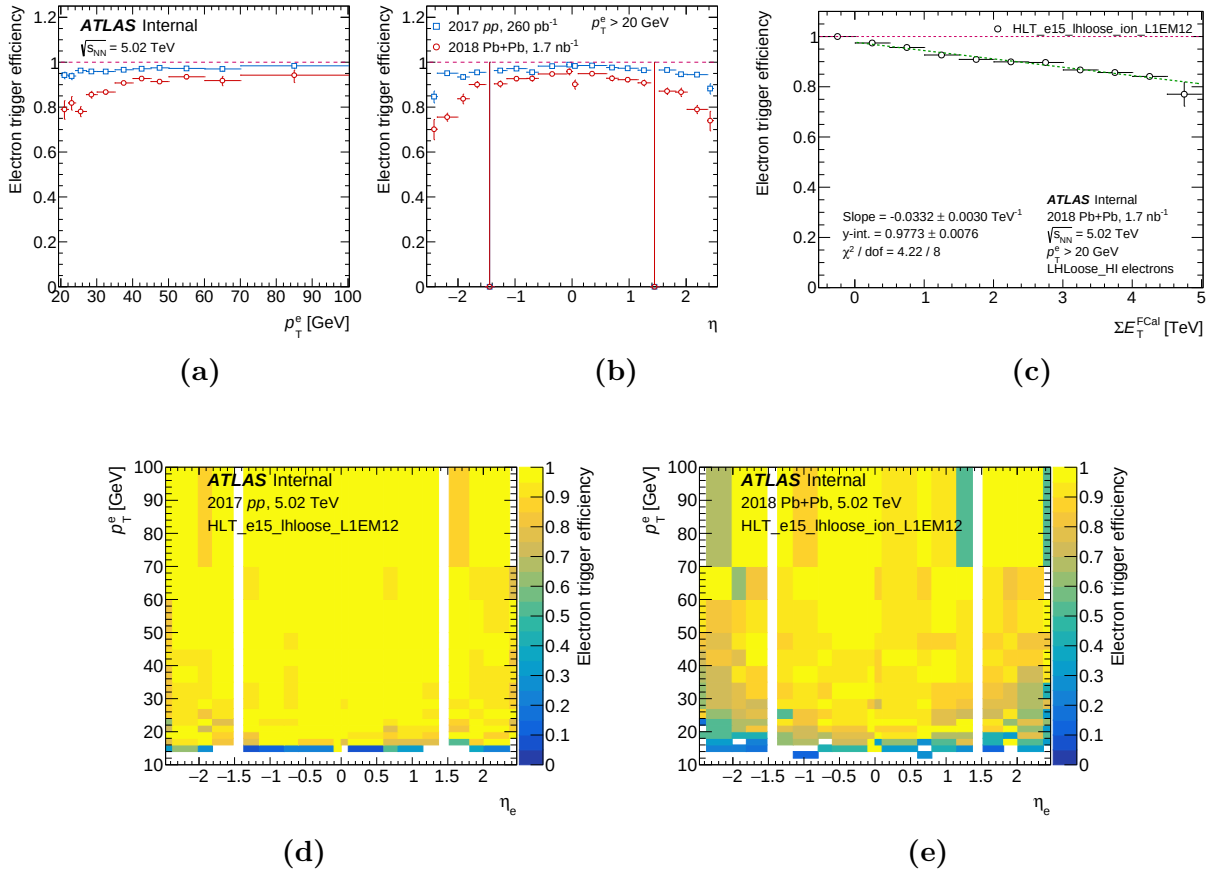


Figure 4.14: The single electron trigger efficiency in 2017 low-μ pp and 2018 Pb+Pb data is investigated. Projections of the efficiency versus **(a)** p_{T}^{e} and **(b)** η_e are shown. **(c)** Dependence on centrality via $\Sigma E_{\mathrm{T}}^{\mathrm{FCal}}$ is also shown after correcting for the p_{T}^{e} & η_e dependencies, and is fitted to a linear function. The full 2-dimensional efficiency versus $(\eta_e, p_{\mathrm{T}}^{e})$ is shown in **(d)** pp and **(e)** Pb+Pb.

on $\Sigma E_{\mathrm{T}}^{\mathrm{FCal}}$. The centrality dependence is quantified by fitting the efficiency to a linear function, which is then used to interpolate the efficiency event-by-event. This can be seen on the top right in Fig. 4.14.

To correct for the trigger efficiency, events are weighted by an efficiency factor calculated as a function of the electron pair used to identify Z candidates. Like the muons, this factor can be derived by relating it to the probability of not triggering on either electron:

$$\varepsilon_{\mathrm{Z}\to\mathrm{ee}}^{\mathrm{trig}} = 1 - \left[1 - \varepsilon_{e}^{\mathrm{trig}}\left(p_{\mathrm{T}}^{e_1}, \eta_{e_1}, \Sigma E_{\mathrm{T}}^{\mathrm{FCal}}\right)\right] \times \left[1 - \varepsilon_{e}^{\mathrm{trig}}\left(p_{\mathrm{T}}^{e_2}, \eta_{e_2}, \Sigma E_{\mathrm{T}}^{\mathrm{FCal}}\right)\right]. \tag{4.17}$$

Unlike the muons, we note that the efficiency is now differential in three variables: p_{T}^{e}, η_e, and

$\Sigma E_{\mathrm{T}}^{\mathrm{FCal}}$.

In addition to the trigger performance, the probability of correctly reconstructing and identifying electrons in candidate events must also be taken into account. This can be measured in $Z \to ee$ simulated events, as done with the muons. Truth electrons are selected in candidate events within the fiducial detector cuts ($0 < |\eta_e| < 1.37$ or $1.56 < |\eta_e| < 2.47$). The truth particle barcode is required to be < 10000. These truth electrons are then matched to reconstructed electrons that satisfy the identification criteria (`LHLoose` in pp or `LHLoose_HI` in Pb+Pb). Electrons are considered matched if they are separated by $\Delta R < 0.3$. The fraction of truth electrons with a reconstructed and identified match is then the corresponding efficiency:

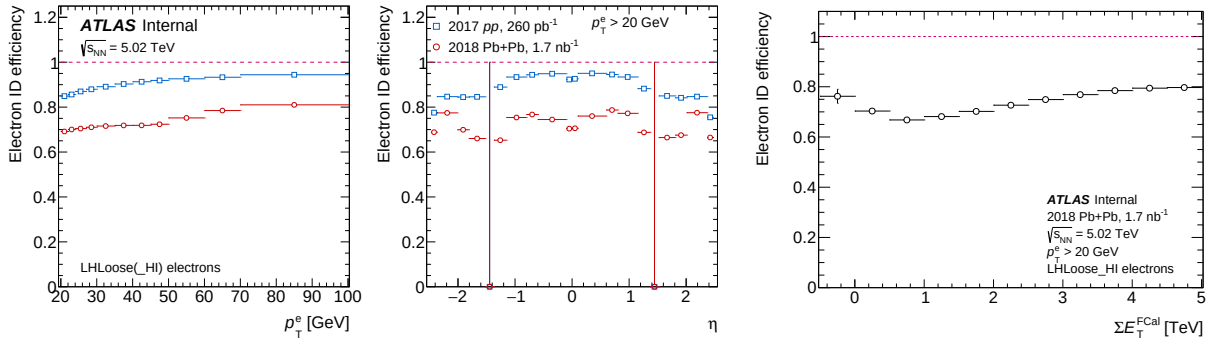
$$\varepsilon_e^{\mathrm{reco}} \equiv \frac{N_e^{\mathrm{reco.-matched}}}{N_e^{\mathrm{truth}}} \left(p_{\mathrm{T}}^{e}, \eta^{e}, \Sigma E_{\mathrm{T}}^{\mathrm{FCal}} \right). \tag{4.18}$$

This quantity is calculated as a function of $p_{\mathrm{T}}^{\mathrm{e}}$, η_e and is shown in Fig. 4.15. Additionally, the efficiency of the `LHLoose_HI` criterion is calculated as a function of centrality to study its performance using the supercluster reconstruction. This can be seen of the right side of the figure, where the identification efficiency actually slightly increases as a function of centrality, increasing from $\sim 65\%$ in the most peripheral collisions to $\sim 80\%$. Essentially the same behavior was previously observed prior to data-taking in the aforementioned HI supercluster reconstruction studies [295].

To correct for the reconstruction and identification inefficiency, each Z boson event is weighted by a factor

$$\varepsilon_{Z\to ee}^{\mathrm{reco}} = \varepsilon_e^{\mathrm{reco}} \left(p_{\mathrm{T}}^{e_1}, \eta_{e_1}, \Sigma E_{\mathrm{T}}^{\mathrm{FCal}} \right) \times \varepsilon_e^{\mathrm{reco}} \left(p_{\mathrm{T}}^{e_2}, \eta_{e_2}, \Sigma E_{\mathrm{T}}^{\mathrm{FCal}} \right). \tag{4.19}$$

We note that, despite this series of acceptance corrections to reduce bias on the Z kinematic selections, the overall impact on the correlated charged-hadron yields is generally small. A quantitative demonstration of this assertion is documented in Appendix A.5. Consequently these procedures are not treated as a source of systematic uncertainty.



(a) **(b)** **(c)**

Figure 4.15: Efficiency of reconstructing and correctly identifying electrons as measured in simulated $Z \to ee$ events with Pb+Pb data overlay. The efficiency is plotted as a function of **(a)** p_{T}^{e} and **(b)** η_e. In **(c)**, the efficiency is plotted as a function of $\Sigma E_{\mathrm{T}}^{\mathrm{FCal}}$ after correcting for the electron kinematic dependence.

Energy Scale Calibration

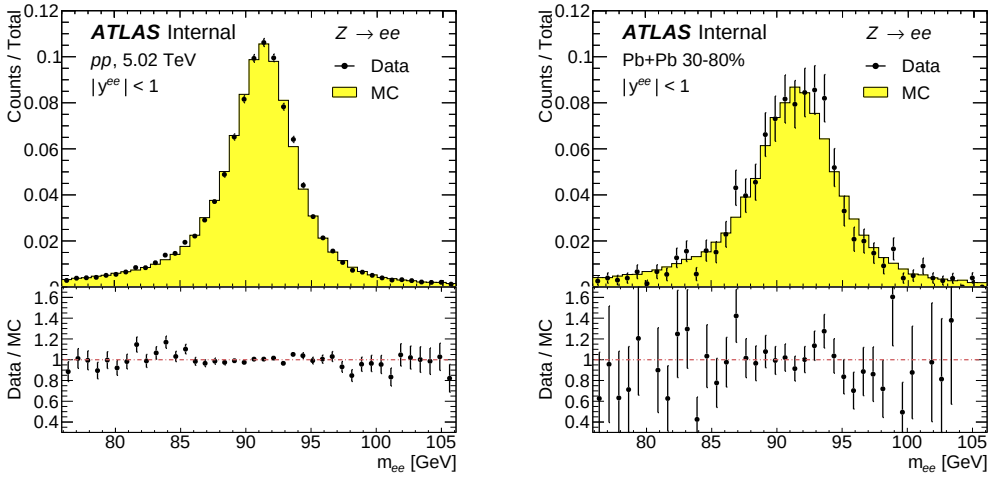
In both the pp reference and the Pb+Pb data, electrons are calibrated with the proper configuration (calibration tags `es2017_R21_v1` for the 2017 low-μ pp data and `es2017_R21_ofc0_v1` for the Run 2 $\mu \sim 0$ data) [261]. In Fig. 4.7 we have already seen p_{T} spectrum of $Z \to ee$ decay electrons; however, the energy scale of single electrons still needs to be validated. Like the muons, the $Z \to ee$ invariant mass peak should be centered at the nominal Z mass of 91.2 GeV [12]; deviations from this value can be used to calibrate and re-validate the single electron energy scale. This is done as a function of both centrality, to identify potential occupancy dependence, and rapidity, in case the electromagnetic end-caps behave slightly differently from the barrel on average.

In general, the $Z \to ee$ resonance is observed to be wider in central Pb+Pb events than, for example, its counterpart in pp. This is a known consequence of the supercluster reconstruction in the HI environment. Recall that superclusters can grow in size radially outward from the incident electron, possibly to a greater size than the sliding window. In pp, this allows more of the shower to be recovered, but in a high occupancy Pb+Pb collision this additional area introduces more fluctuating degrees of freedom dominated by UE contributions [295]. The net effect is an occupancy-dependent degradation of the resolution.

Additionally, a minor residual shift between data and MC is observed via their ratio in the Pb+Pb case. This reflects a possible electron energy scale shift which is either not accounted for in data or not modeled correctly in the MC. A shift towards lower values of m_{ee} common to both data and MC was also observed and found to be centrality dependent. Both of these differences present potential issues in selecting $Z \to ee$ events, so the electron energy scale must corrected in compensation. First, the center of each mass peak is extracted numerically by fitting the core to Gaussians and taking the mean (μ) parameter. Next, scaling factors – defined as ratios of μ between different data sets – are calculated. To avoid introducing an external value of the Z mass (such as the accepted PDG value [12]), each scaling factor (SF) is first derived to match the Pb+Pb simulation to pp ($\mathrm{SF_{MC}} \equiv \frac{\mu_{pp,\mathrm{MC}}}{\mu_{\mathrm{Pb+Pb,MC}}}$), and then second to match the Pb+Pb data to simulation ($\mathrm{SF_{data}} \equiv \mathrm{SF_{MC}} \times \frac{\mu_{\mathrm{Pb+Pb,MC}}}{\mu_{\mathrm{Pb+Pb,data}}}$). These are numerically listed in Table 4.4. The correction is calculated separately for electrons at mid-rapidity versus forward rapidity by categorizing in Z rapidity ranges to $|y_Z| \lesseqgtr 1$, as the energy scale precision is generally worse at higher $|\eta|$ values. To then correct each electron momentum vector, the appropriate scale factors are applied multiplicatively electron-by-electron. These corrections are generally very small and range from ~ 0.1–3% in absolute value. The final m_{ee} peaks can be seen in Fig. 4.16 after these corrections are applied. Good agreement between pp and Pb+Pb in the peak position as well as data-MC is now observed, indicating the $Z \to ee$ reconstruction should now be acceptably accurate.

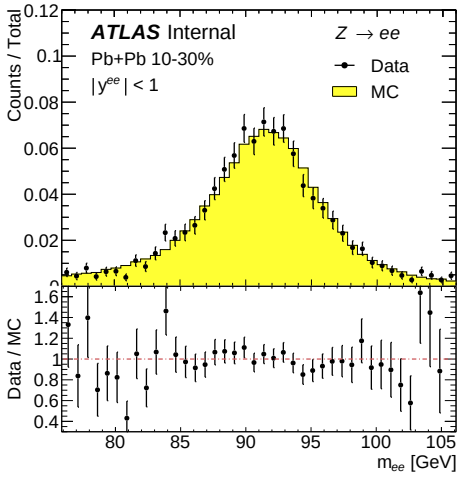
	MC scale factors, $\mathrm{SF_{MC}}$		Data scale factors, $\mathrm{SF_{data}}$	
Pb+Pb Centrality	$\lvert\eta_{\mathrm{e}}\rvert < 1$	$\lvert\eta_{\mathrm{e}}\rvert > 1$	$\lvert\eta_{\mathrm{e}}\rvert < 1$	$\lvert\eta_{\mathrm{e}}\rvert > 1$
30–80%	1.00327	1.0162	0.999731	1.007863
10–30%	1.01058	1.02528	1.01154	1.016304
0–10%	1.01624	1.03133	1.011729	1.024273

Table 4.4: Residual electron energy scale factors derived from the m_{ee} mass peak at the Z in both data and simulation, as a function of Pb+Pb event centrality and electron pseudorapidity. Scale factors for MC and data are shown in the left and right columns, respectively.

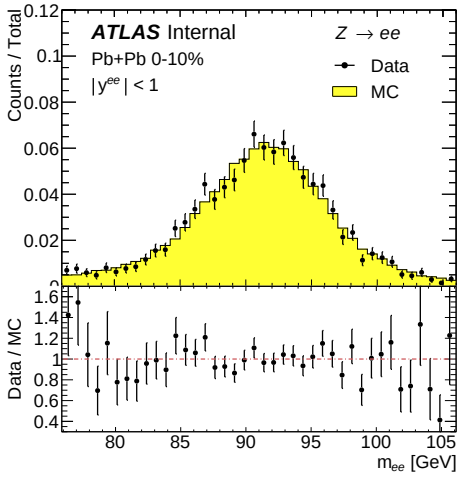


(a) pp

(b) 30–80% Pb+Pb



(c) 10–30% Pb+Pb



(d) 0–10% Pb+Pb

Figure 4.16: Normalized distributions of mid-rapidity opposite-signed dielectron invariant masses (m_{ee}) in data (black markers) and MC (yellow shaded region) are shown for **(a)** pp, **(b)** 30–80%, **(c)** 10–30%, and **(d)** 0–10% Pb+Pb collisions. The electron energy scales are corrected using the factors listed in Table 4.4.

4.5 Characterizing the Event Sample

On top of the single-lepton requirements, in order to enter the sample of Z bosons, each lepton pair must also

- have opposite charge signs and

- have an invariant mass $76 < m_{\ell\ell} < 106$ GeV.

Previous ATLAS measurements sensitive to the total Z yield use a relatively wide mass selection of $|m_{\ell\ell} - 91 \text{ GeV}| < 25$ GeV to minimize the statistical uncertainties, as a Z boson is produced rather rarely in hadronic collisions [63, 265]. This comes at the cost of larger background components, which are relatively maximal in the tails of the mass peak. The improvement in statistics from the tails is marginal however, so we choose to further restrict the allowed masses to $|m_{\ell\ell} - 91 \text{ GeV}| < 15$ GeV. This effectively guarantees a higher Z purity without much impact on the final measurement.

Table 4.5 details the total yield within these selections. Roughly 59,000 events have been tagged with a Z boson in the low-μ pp reference in the dielectron channel, and 80,000 in the dimuon channel. In the Pb+Pb, about 7,800 and 10,000 dielectron and dimuon candidates have been tagged as Z bosons, respectively. In both cases, about 20% of reconstructed Z bosons have $p_{\mathrm{T}} > 25$ GeV. Additionally, in the 10–30% and 0–10% centrality bins, there are roughly the same number of Zs, with 30–80% having about half of that amount. So as a rule-of-thumb, the yield of Z bosons across the three centralities approximately follows a $1 : 2 : 2$ ratio. To further check for any residual run dependence on the yield of Z boson events, the number of reconstructed events per microbarn of luminosity was plotted as a function of run number in Fig. 4.17. The luminosity used corresponds to the correct luminosity after rejecting events in lumiblocks excluded by the GRL and affected by B-layer desynchronization as described in Sec 4.2. The number of Z bosons per microbarn is generally different between the muon and electron channels due to differences in lepton reconstruction efficiency, but the normalized yield is consistent run-to-run which indicates the event sample does not suffer from systematic run-to-run effects.

The main objective of this measurement is the charged-hadron yield azimuthally opposite to a high-p_{T} Z boson. Minimally, this implies the Z kinematics should be controlled for and well understood. A more complete investigation of the Z kinematics is shown in Appendix A.1, though we summarize some the main points here. First, in Fig. 4.18, the Z p_{T} spectrum is shown for

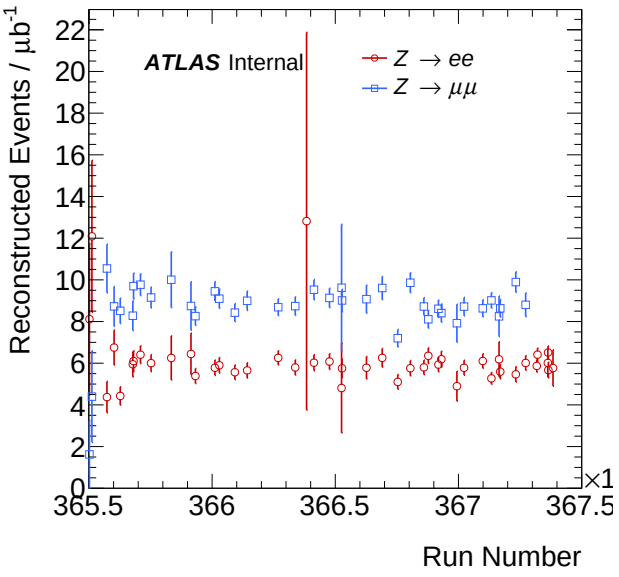


Figure 4.17: The yield of $Z \to ee$ (red) and $Z \to \mu\mu$ (blue) events per unit of recorded luminosity is plotted for each 2018 Pb+Pb run. The luminosity used corresponds to the correct luminosity after rejecting lumiblocks rejected by the GRL and affected by the B-layer desynchronization.

both the $Z \to ee$ and $Z \to \mu\mu$ channels, for events in pp versus 0–10% central Pb+Pb. The spectrum is observed to cover a broad p_{T}^{Z} range, with a distinctive peak around 4–6 GeV. This is due to the Jacobian transverse area factor of $1/p_{\mathrm{T}}$ that is not included in the y-axis definition. We can see that Z boson observations persist to very high-p_{T} thanks to the large data sets used; counts above 200 GeV are observed even in the Pb+Pb case. No pathological behavior is seen from these figures: data matches values from simulation, pp matches Pb+Pb, and $Z \to ee$ decays match $Z \to \mu\mu$ decays. If we look at instead the Z rapidity distributions (Fig. 4.19), we actually do see some deviations between the $Z \to \mu\mu$ and $Z \to ee$ channels. In particular, the $Z \to \mu\mu$ rapidity is found to be relatively flatter than its $Z \to ee$ counterpart. However, this is understood to be a consequence of the different electron pseudorapidity acceptance from the muons. While muons reconstructed anywhere in $|\eta_\mu| < 2.5$ will meet the selection criteria, electrons must avoid the EMCal crack region between $|\eta_e| = 1.37$ and 1.56. This can easily affect which Z bosons are accepted as a function of their rapidity. Overall, we see from these distributions that the Z boson selection is well understood via the MC comparison, and the most important quantities (invariant

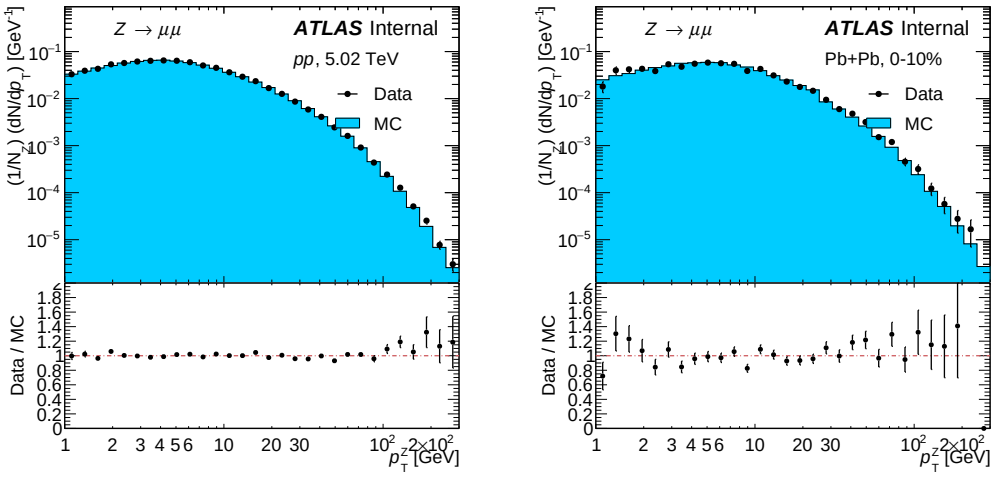
p_{T}^{Z} Range	Decay channel	pp	30–80%	10–30%	0–10%	Pb+Pb total
15–30 GeV	$Z \to ee$	12,422	293	772	868	1,933
	$Z \to \mu\mu$	16,301	455	944	944	2,343
30–60 GeV	$Z \to ee$	6,536	170	397	497	1,064
	$Z \to \mu\mu$	8,387	241	554	477	1,272
$>$ 60 GeV	$Z \to ee$	2,410	59	170	170	399
	$Z \to \mu\mu$	3,002	101	186	193	480
Total $>$ 15 GeV	$Z \to ee$	21,368	522	1,339	1,535	3,396
	$Z \to \mu\mu$	27,690	797	1,684	1,614	4,095

Table 4.5: Detailed yield of Z-tagged events in each centrality selection, broken down in 3 p_{T}^{Z} bins. The p_{T}^{Z} distribution of Z bosons peaks around 9 GeV.

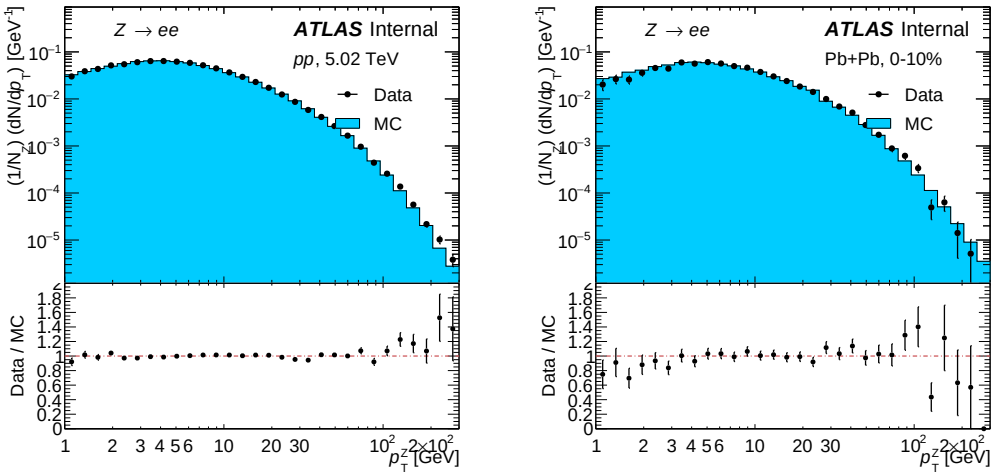
mass and p_{T}) match well between Pb+Pb and pp, as well as $Z \to ee$ and $Z \to \mu\mu$.

One of the advantages of the Z boson probe is that it can be reconstructed to arbitrarily low-p_{T} with negligible background. These low-p_{T} events can even be seen to occur rather frequently. This is unlike the photon, which becomes increasingly contaminated by QCD-induced backgrounds below $p_{\mathrm{T}} \sim 50$ GeV, and physically cannot be at rest, $\left|\vec{p_{\gamma}}\right| = 0$. We note that at the lowest momenta, Drell-Yan production of Z bosons ($q\overline{q} \to \gamma^{*}/Z \to \ell\ell$) becomes more ubiquitous. To lowest order, these kinds of events leave no correlated parton in the final state (though higher order initial state radiations can still leave these kinds of signals). If these events are accompanied by an incidental hard scattering elsewhere in the nucleus-nucleus collision, the two can mimic a $Z+$jets signal. But, these kinds of incidental $Z+$jets events are statistically subtracted by the UE subtraction, so this is not an issue, strictly speaking.

In the yield measurement, we integrate over relatively wide bins in p_{T}^{Z}. The detailed bins used and the yield of Z bosons in each bin are shown in Table 4.5.



(a) $Z \to \mu\mu$ in pp **(b)** $Z \to \mu\mu$ in 0–10% Pb+Pb



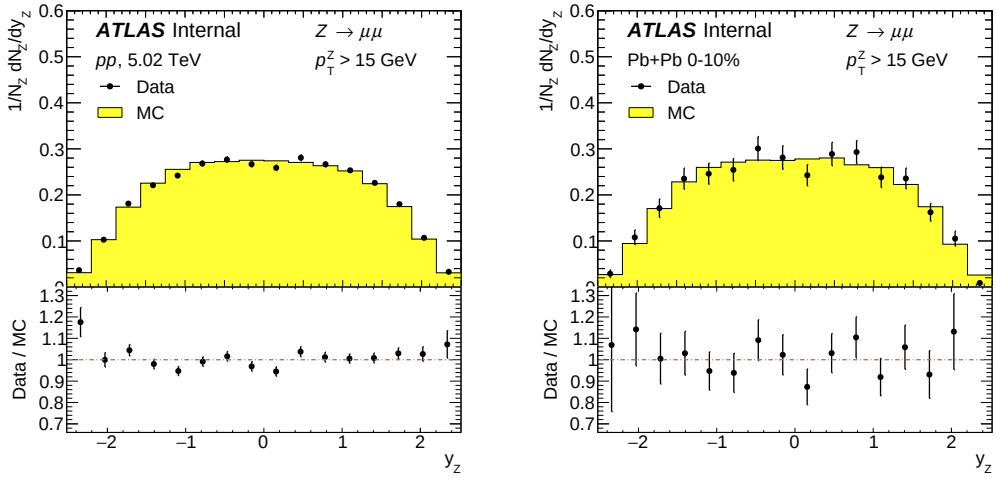
(c) $Z \to ee$ in pp **(d)** $Z \to ee$ in 0–10% Pb+Pb

Figure 4.18: A few p_{T} distributions of Z bosons in **(a,b)** dimuon and **(c,d)** dielectron channel are shown in both **(a,c)** pp and **(b,d)** 0–10% Pb+Pb collisions in data and MC.

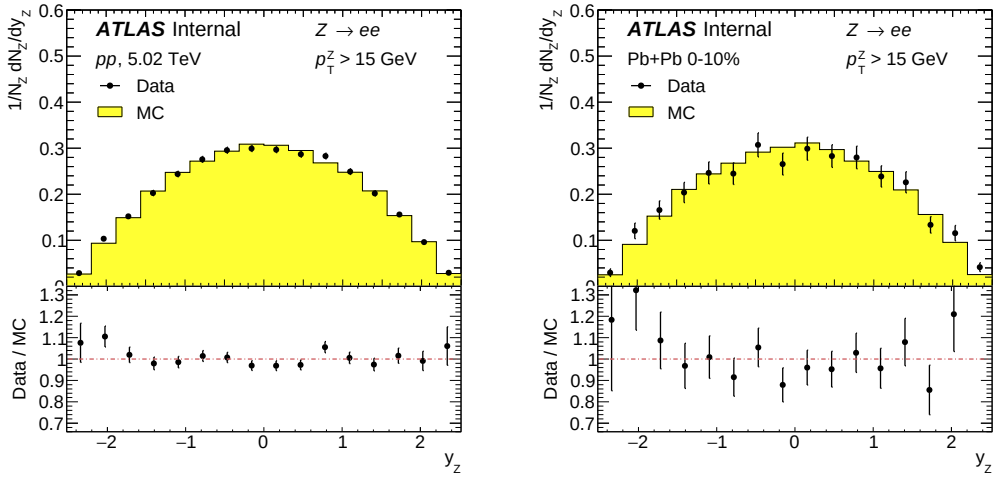
Background Events

In this section, we consider contamination due to Z background. If the rate is small, then it should have a minor (and therefore negligible) impact on the hadron yield measurement. Here, we consider the three most significant background sources to evaluate this hypothesis. These are

- the multi-jet QCD background,



(a) $Z \to \mu\mu$ in pp **(b)** $Z \to \mu\mu$ in 0–10% Pb+Pb



(c) $Z \to ee$ in pp **(d)** $Z \to ee$ in 0–10% Pb+Pb

Figure 4.19: A few rapidity distributions of Z bosons in **(a),(b)** dimuon and **(c,d)** dielectron channel are shown in both **(a,c)** pp and **(b,d)** 0–10% Pb+Pb collisions in data and MC. The invariant p_{T} is at least 15 GeV.

- $t\bar{t}$ decays into leptons, and
- $Z \to \tau\tau$ decays into leptons.

These contributions are motivated from an earlier study of the Pb+Pb Z cross section using the 2015 Pb+Pb collision data [296].[4] Changes to the reconstruction and a modified event selection in

[4] There is also a potential $W \to \ell\nu_\ell$ background, though other measurements find this is completely negligible in comparison to the other three.

Background process	Fraction of $Z \to ee$ yield [%]	Fraction of $Z \to \mu\mu$ yield [%]
$Z \to \tau\tau$	0.02	0.01
$t\bar{t}$	0.04	0.05
QCD multijet	1.5	0.09

Table 4.6: Summary of Z boson background contributions as determined for this analysis, for both the $Z \to \mu\mu$ and $Z \to ee$ channels.

this measurement require these rates to be revisited. The earlier analysis found the largest source of background was the multi-jet QCD background due to the lack of a isolation requirement on the leptons, which accounted for 2% of reconstructed Z events in the electron channel (in the muon channel this dropped to 0.5%).[5] The event selection in this analysis only requires a subsample of Z bosons, rather than all Z bosons, so the selection is optimized to remove more of the background. In particular, the background fraction is higher farther away from the nominal Z mass, so imposing a narrower mass window will reject more background events. The mass selection used here is $76 < m_{\ell\ell} < 106$ GeV, which roughly corresponds to the nominal Z mass 91.2 ± 15 GeV (as opposed to ± 25 GeV).

Electroweak Backgrounds

We analyze the $t\bar{t}$ MC sample documented in Table 4.3 to estimate their contribution in data. Of the 67,734 MC events generated, 218 candidate events were found to meet the selection criteria used in this analysis. 86 of these are in the dielectron channel, and 132 are in the dimuon channel. Of course, selection inefficiencies can deflate these numbers artificially. For comparison, events in the signal samples lead to 371,202 $Z \to ee$ events (out of 2,669,466, $\sim 13.9\%$) and 402,263 $Z \to \mu\mu$ (out of 2,300,998, $\sim 17.5\%$) meeting our selection criteria. Accounting for the cross sections and

[5] For reference, in the 2015 data analysis, the $Z \to \tau\tau$ background amounted to 0.05% in the dimuon channel and 0.06% in the dielectron channel. The $t\bar{t}$ background was of comparable magnitude, amounting to 0.08% for muons and 0.05% for electrons.

filtering efficiencies the background fraction due to process X in the $\ell\ell$ channel is

$$\text{Rate}[\%] = 100\% \times \underbrace{\frac{N_X^{\text{bkg }(\ell\ell)}\sigma_X f_X}{N_X^{\text{gen}}}}_{\text{Background cross section}} \times \underbrace{\frac{N_{Z\to\ell\ell}^{\text{gen}}}{N_{Z\to\ell\ell}^{\text{reco}}\sigma_{Z\to\ell\ell}f_{Z\to\ell\ell}}}_{\text{Signal cross section}}. \tag{4.20}$$

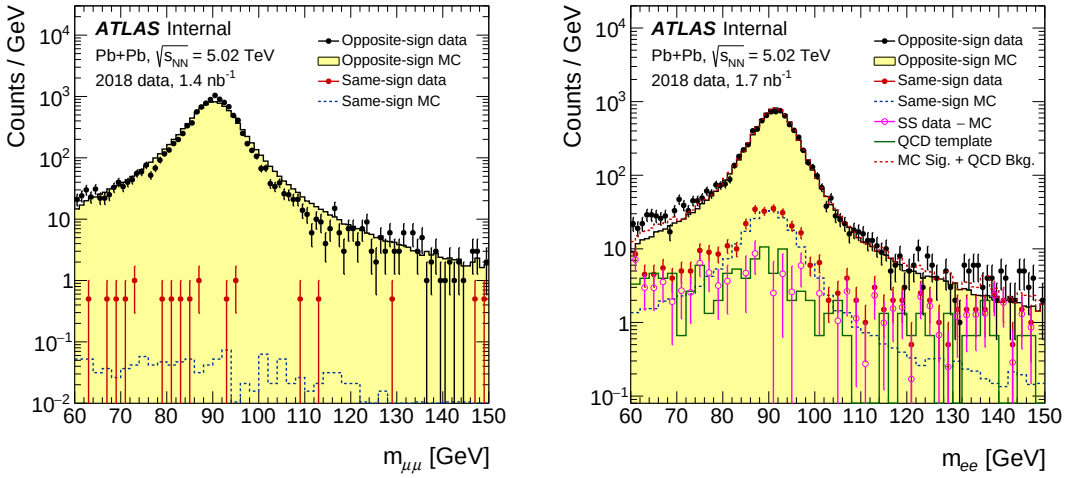
In this expression,

- σ_X is the generator-level cross section for process X; e.g. $\sigma_{t\bar{t}} = 56.695\,\text{pb}$ and $\sigma_{Z\to\tau\tau} = 642.820\,\text{pb}$,
- f_X is the simulation filter efficiency, representing the probability that the generated event is selected by the generator filter ($f_{Z\to\ell\ell} = 1$ since we can "force" the presence of a Z and that particular decay, but not for e.g. $t\bar{t}$ processes), and
- $N_X^{\text{bkg }(\ell\ell)}$ is the number of events from process X reconstructed as a candidate $Z \to \ell\ell$ event (note that *all* of the selection criteria must be met).

With this machinery, we find the fraction of events attributed to $t\bar{t}$ is 0.04% for electrons and 0.05% for muons. In the $Z \to \tau\tau$ channel, the backgrounds are comparable overall: 10 events in the sample (out of 193,395) are found to meet the event selection criteria, with 6 background $Z \to ee$ and 4 $Z \to \mu\mu$ events. The resulting fraction of events attributed to $Z \to \tau\tau$ decays is 0.02% for electrons and 0.01% for muons. As expected, both processes contribute negligibly small backgrounds to the event selection, exemplifying the versatility of the Z.

QCD Multijet Backgrounds

In contrast to the electroweak $t\bar{t}$ and $Z \to \tau\tau$ backgrounds, the QCD background – consisting of jets masquerading as or containing leptons – has a different origin. In heavy-ion collisions, jet production is more ubiquitous, and thus the QCD background should be more closely examined. We use a data-driven method for this purpose, and the method differs slightly between the electron and muon channels. The principle observation is that the lepton charges should be uncorrelated with each other if they are misidentified QCD jets. In short, lepton pairs with the same charge sign



(a) $Z \to \mu\mu$ **(b)** $Z \to ee$

Figure 4.20: Invariant mass distributions are shown for both candidate signal and QCD background events in Pb+Pb data and MC, in both the **(a)** $Z \to \mu\mu$ channel and **(b)** $Z \to ee$ channel.

originate nearly exclusively from QCD backgrounds, and serve as a means to identify the prevailing background in the opposite-sign Z sample. On the left in Fig. 4.20, the invariant mass distribution of opposite-sign muon pairs $m_{\mu\mu}$ is compared with same-sign pairs. We observe that same-sign pairs have a nonzero yield, but crucially lack the characteristic Z mass peak at ~ 90 GeV. In MC, a similar trend is observed, albeit with slightly enhanced statistics (note that the MC events are weighted, so the y-axis does not represent a pure count in this case). Overall, only about 0.09% of the reconstructed $Z \to \mu\mu$ events are attributed to this background.

For electrons, shown on the right in Fig. 4.20, we notice there is a peak in the same-sign m_{ee} distribution in data. This is also observed in the MC. The explanation for this is that the electron charge resolution is slightly worse in general than the muons; some electrons are reconstructed with the wrong sign, come from photon conversions, or are outright fake electrons. In many of these cases, the electrons can still originate from a Z boson decay. Therefore the same-sign distribution does not represent the true background rate. In particular, the same-sign MC distribution contains *only* $Z \to ee$ events at truth level, but maintains the characteristic mass peak.

Instead, a template distribution for background electrons is built in data by requiring one

electron to meet the `LHLoose_HI` quality but then fail both the `LHMedium_HI` quality and an isolation criteria. Again, the idea is to restrict to electrons meeting the nominal selection criteria, but then amplify the probability that the electron is actually a misidentified jet. As an isolation cut, we use

$$\sum_{\Delta R<0.2} E_{\mathrm{T}} > \left(\frac{\Sigma E_{\mathrm{T}}^{\mathrm{FCal}}}{10\ \mathrm{TeV}} + 0.05 \right) p_{\mathrm{T}}, \tag{4.21}$$

where $\sum_{\Delta R<0.2} E_{\mathrm{T}}$ – colloquially called the `Etcone20` variable – is the E_{T} sum over all cells within $\Delta R < 0.2$ of the electron (η, ϕ) coordinates. Cells contributing to the electron measurement itself are excluded. The operating principle behind the isolation criterion is that electrons with higher isolation energies are more likely to be a part of a hadronic shower and thus represent jets in the detector. The $\Sigma E_{\mathrm{T}}^{\mathrm{FCal}}$ dependence provides more leeway for a large underlying event in central Pb+Pb collisions.

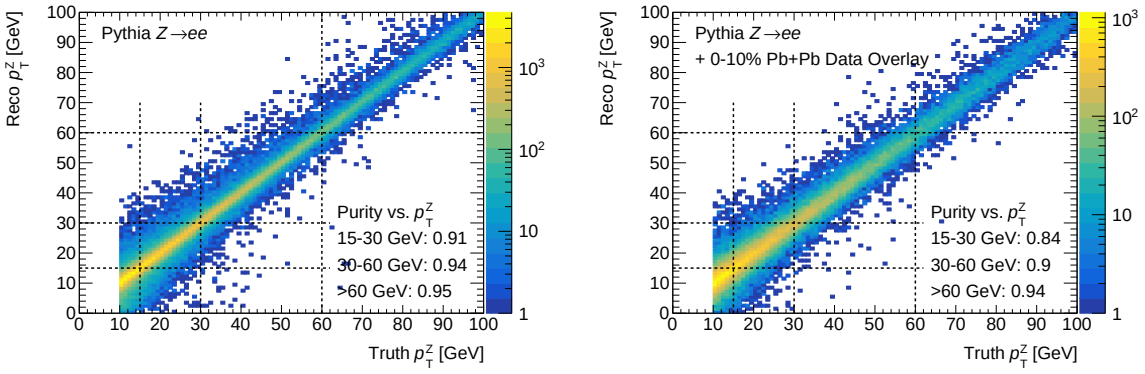
After making these selections, the template must be appropriately renormalized. For this we use the same-sign distribution in data after subtracting off the same-sign distribution in MC (shown as magenta open circles in Fig. 4.20). This leaves behind only the events attributed to the QCD background. The template is then scaled up so that the data-MC difference and the template have the same integral in the low-mass tail: m_{ee} = 60–70 GeV. The expected number of background events in the signal region is then the integral of the template in the fiducial mass acceptance 76–106 GeV. Applying the full procedure yields a background rate of about 1.5%, which is in agreement with previous findings ($\sim$ 2%); though, we note that the earlier estimate used the now-deprecated sliding window reconstruction and had a wider mass acceptance, so some differences are expected. However, with the newer reconstruction and narrower acceptance we still find the rate to be negligibly small. For this reason, as well as the minor expected impact on the away-side fragmentation pattern, the impact of background events is neglected.

Correcting for Z boson p_{T} resolution

With the Z boson selection broadly understood, we next turn to the kinematic resolution. The analysis reports charged-hadron yields in bins of Z boson p_{T}. However, due to the finite resolution in the lepton kinematics measurement and thus the measurement of Z boson kinematics, the reconstructed-level selection may pick out a set of Z bosons with a different p_{T} distribution than the corresponding truth-level selection. As the hadron yields are expected to depend on Z boson p_{T}, this could influence the measurement. In this section, the effects of the Z boson p_{T} migration on the charged-hadron yields are quantified.

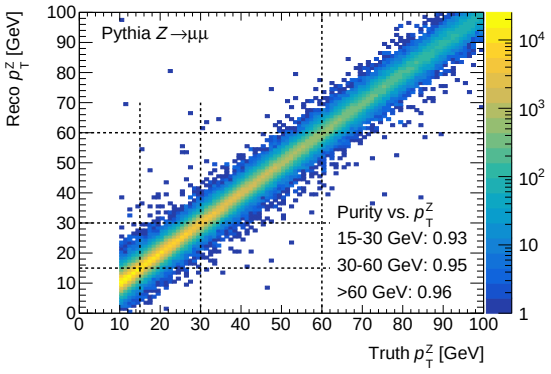
First, we investigate the 2-dimensional correlation between the true and measured Z boson p_{T} for both the electron and muon channels, and for each of the four different event types (pp and the three Pb+Pb centralities), using the Monte Carlo event samples. To determine this, Z candidates at the generator level were first selected; these must meet the same basic kinematic selections as the reconstructed leptons: minimum p_{T}, pseudorapidity, invariant mass, and opposite charge signs. Then, the reconstructed Z kinematics were determined by matching each truth decay lepton to a reconstructed lepton which passes all of the analysis cuts (pseudorapidity, ID, pointing cuts, etc.), and ensuring that the reconstructed Z passes boson-level cuts (the invariant mass). Fig. 4.21 shows 2-D scatterplots between the true and measured p_{T}^{Z} in the electron and muon channels, respectively, for pp and central Pb+Pb collisions. Different panels show different event classes: Pythia without (pp, left column) vs. with data overlay (0–10% Pb+Pb, right column) or decay channel $Z \to ee$ (top row) versus $Z \to \mu\mu$ (bottom row). The dashed lines correspond to the kinematic ranges used in the measurement.

As expected, the $Z \to ee$ truth-reco p_{T} correlation tightens onto the diagonal with increasing p_{T}, since the calorimetric electron p_{T} measurement becomes better with higher p_{T}, while the $Z \to \mu\mu$ correlation is only weakly dependent on p_{T} (recall that muons are not measured with the calorimeter at all). Additionally, the truth-reco p_{T} correlation is visibly broader in the more central Pb+Pb events, given the worse lepton energy resolution from underlying event fluctuations.

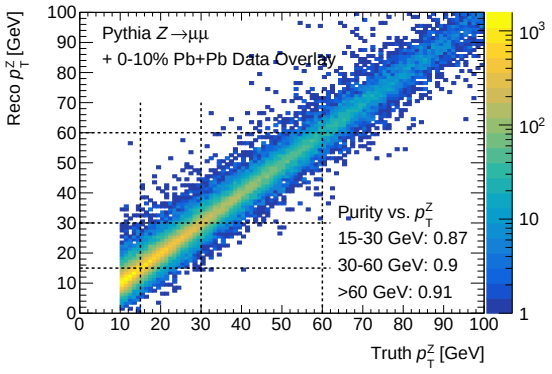


(a) $Z \to ee$ in pp

(b) $Z \to ee$ in 0–10% Pb+Pb



(c) $Z \to \mu\mu$ in pp



(d) $Z \to \mu\mu$ in 0–10% Pb+Pb

Figure 4.21: 2-dimensional correlation between true and reconstructed Z boson p_{T}, in the $Z \to ee$ channel (top row) and the $Z \to \mu\mu$ channel (bottom row). The dashed lines represent the p_{T} boundaries of the measurements, and the bin-by-bin purity within each reconstructed Z boson p_{T} range is shown in each panels.

We further define a selection purity based on the fraction of Z bosons in a given reconstructed p_{T} selection which originated from that same selection at the truth-level. The purity is given numerically in each panel. In every case, the purity is generally larger than 85%; in pp, it is always larger than 90%. It rises systematically with boson p_{T}, and it rises as the UE environment becomes smaller (i.e., decreases from 0–10% Pb+Pb to pp). On this basis, one expects the p_{T} migration effects to be smallest at high-p_{T}^Z and in pp events, and largest at low-p_{T}^Z in central Pb+Pb events.

Next, the impact of the impurity of the Z selection on the charged-hadron yield should be determined.[6] This impact of this effect can be determined in simulation by comparing the per-Z

[6] "Impurity" here refers to the presence of true Z bosons originating at a generator-level p_{T} which is outside the

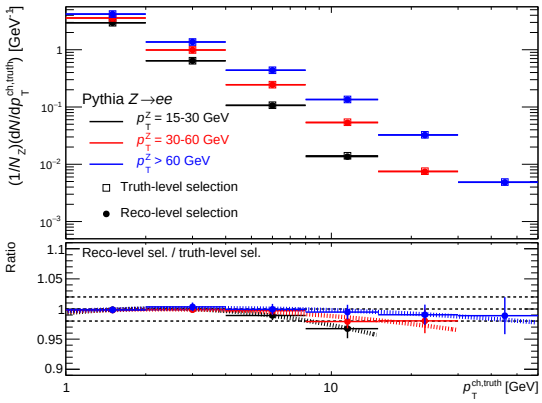
normalized truth-level charged-hadron yields (those with $|\Delta\phi| > 3\pi/4$ from the Z boson as in the analysis) for the cases when the Z boson selection is performed at the truth versus at the reconstructed level. This comparison thus includes the effects of the inflow of Z bosons from a different truth p_{T} bin, and the outflow of Z bosons born in this truth p_{T} selection out to a different reconstructed p_{T} selection.

Fig. 4.22 catalogs the impact on the charged-hadron yields when reported as a function of $p_{\mathrm{T}}^{\mathrm{ch}}$, for both the $Z \to ee$ and $Z \to \mu\mu$ channels in pp and central 0–10% Pb+Pb collisions. The bottom panels show the ratio of the per-Z yields between when the Z bosons are selected at the reco level to when this is done at the truth level. The horizontal dashed lines denote $\pm 2\%$ deviations. In pp collisions, the bin migration effect is negligibly small, with the ratios compatible with unity within the statistical uncertainties in the MC. Although, we still correct for it. In more central Pb+Pb events, or at lower Z p_{T} (where the purity is lower), the ratios may differ from unity by up to a few percent.

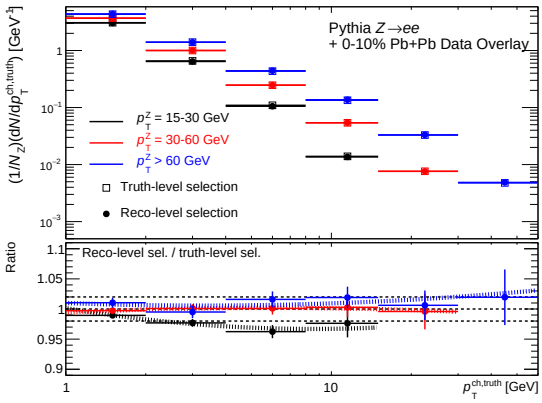
In a similar fashion, Fig. 4.23 catalogs the impact on the charged-hadron yields when reported as a function of $x_{hZ} = p_{\mathrm{T}}^{\mathrm{ch}}/p_{\mathrm{T}}^{Z}$. When reported versus x_{hZ}, the resolution of the p_{T}^{Z} measurement can also in principle cause a bin migration of the hadron yield between different bins of x_{hZ}, although we note that the bins are very large compared to the degree of migration. As in Fig. 4.22, the reconstructed-to-truth hadron yield ratios in pp collisions are typically within $\sim 1\%$ of unity. But, there are larger differences on the order of a few percent in the more central Pb+Pb events at low-p_{T}^{Z}, particularly at large values of $x_{hZ} > 0.5$, with deviations reaching $\sim$ 5–6%.

In summary, these effects reflect the impact of a finite p_{T}^{Z} resolution on the per-Z yields. Therefore the measurement must be corrected to counteract this bias. This is done through the use of multiplicative bin-by-bin correction factors determined from the reco./truth ratios in the figures presented here. These ratios are fit to a quadratic function $f(\log p_{\mathrm{T}}^{\mathrm{ch}})$ or $f(\log x_{hZ})$ so as to not introduce statistical fluctuations from the simulation into the correction. These are indicated as dashed lines in the bottom panels of the previous figures. Separate corrections are derived

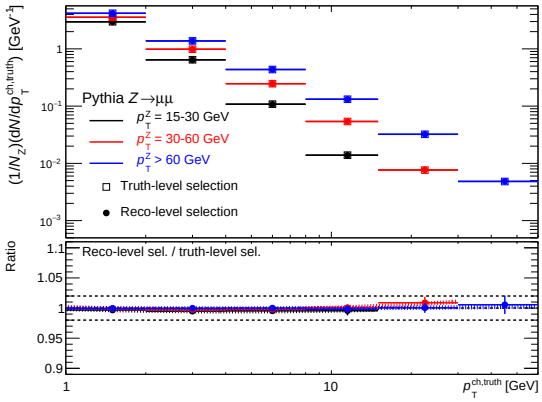
reconstructed p_{T} selection, and not from non-Z boson backgrounds.



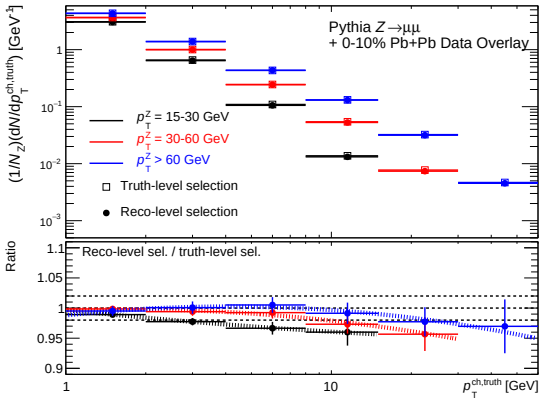
(a) $Z \to ee$ in pp



(b) $Z \to ee$ in 0–10% Pb+Pb



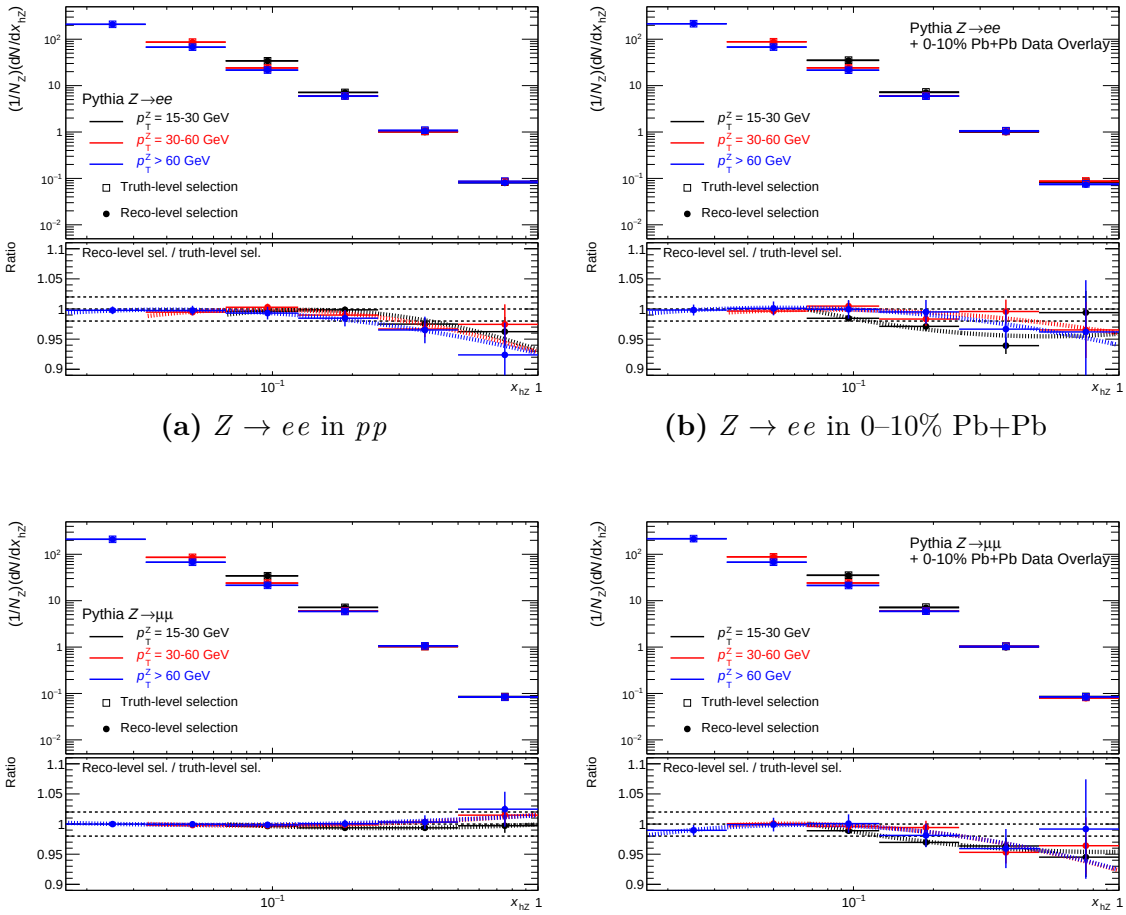
(c) $Z \to \mu\mu$ in pp



(d) $Z \to \mu\mu$ in 0–10% Pb+Pb

Figure 4.22: Comparison of per-Z truth-hadron yields versus $p_{\mathrm{T}}^{\mathrm{ch}}$ when the Z is selected at the truth-level (open squares) and reconstructed-level (filled circles). **(a)** $Z \to ee$ in pp, **(b)** $Z \to ee$ in 0–10% Pb+Pb, **(c)** $Z \to \mu\mu$ in pp, **(d)** $Z \to \mu\mu$ in 0–10% Pb+Pb. Fits to a quadratic function of $\log p_{\mathrm{T}}^{\mathrm{ch}}$ are overlaid.

independently for each event type. The measured yields in data are then corrected by the $p_{\mathrm{T}}^{\mathrm{ch}}$ or x_{hZ}-dependent multiplicative factor $1/f$: $Y_{\mathrm{meas}} \mapsto Y_{\mathrm{meas}}/f$. As the ratios are within $\approx 2\%$ percent of unity in most cases, and within 5% in the remaining cases, the impact on the results is well within the final uncertainties and their physics interpretation is minor. Importantly, a 2D unfolding procedure is not necessary.



(a) $Z \to ee$ in pp **(b)** $Z \to ee$ in 0–10% Pb+Pb

(c) $Z \to \mu\mu$ in pp **(d)** $Z \to \mu\mu$ in 0–10% Pb+Pb

Figure 4.23: Comparison of per-Z truth-hadron yields versus x_{hZ} when the Z is selected at the truth-level (open squares) and reconstructed-level (filled circles). **(a)** $Z \to ee$ in pp, **(b)** $Z \to ee$ in 0–10% Pb+Pb, **(c)** $Z \to \mu\mu$ in pp, **(d)** $Z \to \mu\mu$ in 0–10% Pb+Pb. Fits to a quadratic function of $\log x_{hZ}$ are overlaid.

Lepton & Z-tagging Uncertainties

Although the charged-hadron yield is normalized by the number of events, it is still possible for uncertainties on the Z-tagging to propagate to the final yield measurements. Uncertainties on the single-lepton energy scale in particular can shift the reconstructed Z kinematics; this might affect the $\Delta\phi$-integrated charged-hadron yield by shifting ϕ_Z, or vary the phase space explored by the showering partons by altering the estimated p_{T}^Z value. Because the p_{T}^Z migration is found to have a very minor effect overall, no large effect is expected from the Z-tagging. The predominant

source should pertain to the lepton reconstructions, with particular attention drawn to the energy scale. For both muons and electrons, the energy scale and its uncertainties are well-understood, and are determined on a lepton-by-lepton basis. For electrons, 69 uncertainties on the energy scale are assigned; for muons, there are 5. Since no large effect is expected, we use a simplified approach, rather than propagate the effect from each of the many sources. Essentially, we consider only the source which dominates the lepton p_{T} uncertainty. Because the energy scale of the leptons is correlated (e.g., if the energy scale is off by 1% for one lepton, it must also be off by 1% for the other), both leptons are raised or lowered by this amount together. This provides a complementary sample of Z bosons with slightly altered kinematics with which the measurement is reperformed; the difference to the nominal measurement represents the propagated systematic uncertainty. For electrons, this is at the level of 1% at most. For muons, we use the MS kinematics, though the uncertainty is assigned based on the combined track kinematics, and so the effect is a bit larger, rising up to 4% in central Pb+Pb.

4.6 Tracking Considerations

In addition to leptons, tracks are used extensively in this analysis, so the performance of the ID reconstruction should also be studied. For tracks to be considered at the analysis level, they must nominally

- meet the `HILoose` quality criterion,
- meet a d_0 significance cut $|d_0/\sigma_{d_0}| < 3$ (only in Pb+Pb),
- meet a $|z_0|$ significance cut $|z_0/\sigma_{z_0}| < 3$ (only in Pb+Pb),
- not be matched to the inner detector track associated with either decay lepton, and
- have $p_{\mathrm{T}}^{\mathrm{ch}} > 1$ GeV, unless otherwise specified.

Recall that the `HILoose` criterion refers to a set of cuts on the track-to-vertex association, number of hits, etc., which were defined in Table 3.3. In this section we detail the performance studies

pertaining to the final charged-particle yield measurement. These studies quantify the resilience of the tracking algorithms and selection criteria to accurate kinematic resolution, reconstruction efficiency, and background rejection. Throughout, some common tracking definitions are used with regard to reconstructed charged particles in simulated events:

- The truth-matching probability is the is probability that a reconstructed track corresponds to any truth track. It is defined by the expected number vs. observed number of hits between a given truth track (see [297]):

$$\mathcal{P}\left[\text{truth-matched}\right] = \frac{10 \times N_{\text{pixel}}^{\text{common}} + 5 \times N_{\text{SCT}}^{\text{common}} + 1 \times N_{\text{TRT}}^{\text{common}}}{10 \times N_{\text{pixel}}^{\text{track}} + 5 \times N_{\text{SCT}}^{\text{track}} + 1 \times N_{\text{TRT}}^{\text{track}}}. \tag{4.22}$$

  Distributions of truth-matching probabilities for `HILoose` tracks above $p_{\text{T}} > 1$ GeV are shown in Fig. 4.24.

- A track is considered truth-matched if $\mathcal{P}\left[\text{truth-matched}\right] > 0.5$.

- A track is fake if it is not truth-matched.

- A track is secondary if it is truth-matched but originates in the G4 simulation (e.g. electrons produced in an electromagnetic shower). Particles with truth barcode $\notin (0, 200000)$ are secondary.[7]

- A track is primary if it is neither fake nor secondary.

Four issues are explicitly addressed in the tracking performance studies. The first is the tracking purity, which accounts for fake and secondary tracks. These contaminate the sample of primary charged hadrons, and should not be included in the measurement. The track reconstruction efficiency then accounts for real tracks which are not reconstructed: essentially, these are tracks "missed" by the track finding algorithm. A lepton rejection study then verifies whether tracks associated with the Z decay leptons are properly accounted for, as these cannot be identified as charged hadrons. Lastly, to check whether a momentum-space unfolding procedure is needed, the

[7] Particles with barcode 0-10000 originate from PYTHIA while barcodes 10000-200000 originate in HIJING simulations.

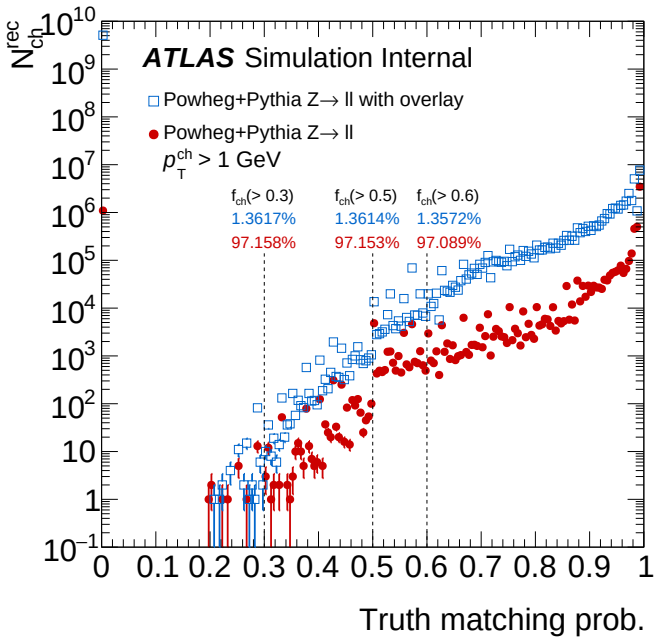


Figure 4.24: The distribution of truth matching probabilities is shown for both pp (red circles) and Pb+Pb (blue squares) MC. Vertical lines denote different proposed cuts on the truth matching probability. For each proposed cut, the fraction of tracks (f_{ch}) above that cut is shown.

effect of a finite momentum resolution on the truth yield was studied. Various aspects of these studies are used as the basis for several systematic uncertainties, which will be discussed in a later section.

Fakes & Secondaries

First, we account for backgrounds entering the charged-particle selection. Primary tracks are of main interest as these tracks can be associated with the collision at the primary vertex. Therefore the backgrounds to this are the fake and secondary tracks that did not originate in this physics process of interest. They can then contaminate the sample of charged hadrons that this analysis aims to study. A simulation-based approach is used to estimate their combined rate across a broad range of charged-particle kinematics. We use the Powheg + Pythia Z samples with (Pb+Pb) and without (pp) Hijing overlay from Table 4.3 for this purpose. The Hijing overlay simulates the effect of the Pb+Pb environment, as a detector occupancy dependence is expected.

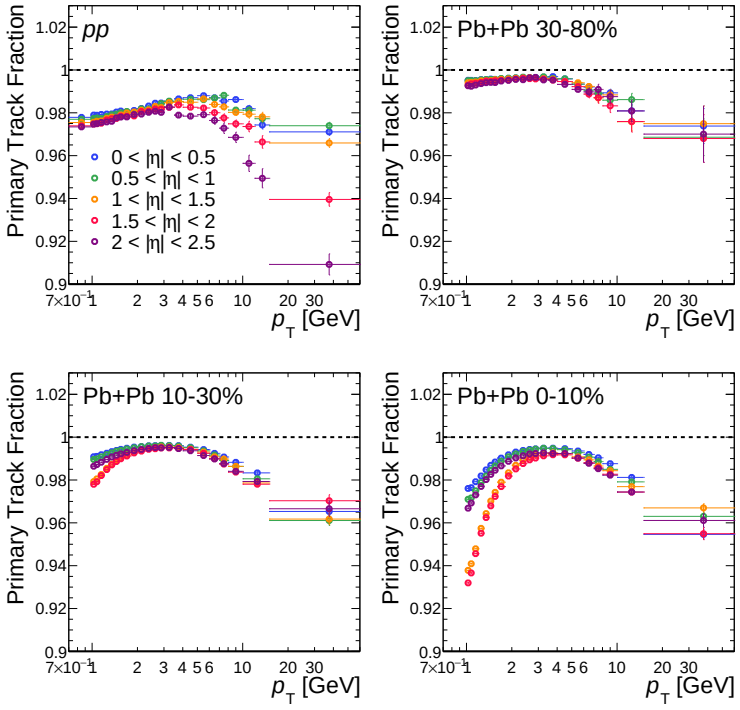


Figure 4.25: Projections of the primary track fraction at various pseudorapidity intervals are plotted for pp (left-most) through 0–10% central Pb+Pb (right-most), as a function of p_{T}.

As a metric for the fake and secondary rates, we use the combined primary rate, because all tracks must fall into one these three categories. The sum of the fake and secondary rates is equal to $1 - f_{\mathrm{primary}}$, where f_{primary} is the fraction of primary tracks (colloquially, the tracking "purity") and is defined as

$$f_{\mathrm{primary}}(p_{\mathrm{T}}, \eta) = \frac{N_{\mathrm{ch}}^{\mathrm{primary}}(p_{\mathrm{T}}, \eta)}{N_{\mathrm{ch}}^{\mathrm{reco.}}(p_{\mathrm{T}}, \eta)}. \tag{4.23}$$

Akin to the lepton efficiency studies, $N_{\mathrm{ch}}^{\mathrm{primary}}$ and $N_{\mathrm{ch}}^{\mathrm{reco.}}$ essentially represent the total passes and trials of a binomial experiment. Fig. 4.25 shows projections of f_{primary} for pp and the three Pb+Pb centrality selections (different panels) at various $|\eta|$ selections (different colors). In general, there is a clear $p_{\mathrm{T}}^{\mathrm{ch}}$ and η dependence, as well as a centrality dependence in Pb+Pb. The purity rises slowly up to $\sim$ 4–5 GeV where it begins to decrease again.

In general, there is a $p_{\mathrm{T}}^{\mathrm{ch}}$ and η dependence, as well as a centrality dependence in Pb+Pb. The purity is at the level of 98–99% for hadron $p_{\mathrm{T}} \sim 3$ GeV, but drops to $\gtrsim 97\%$ at low-$p_{\mathrm{T}}^{\mathrm{ch}}$ in

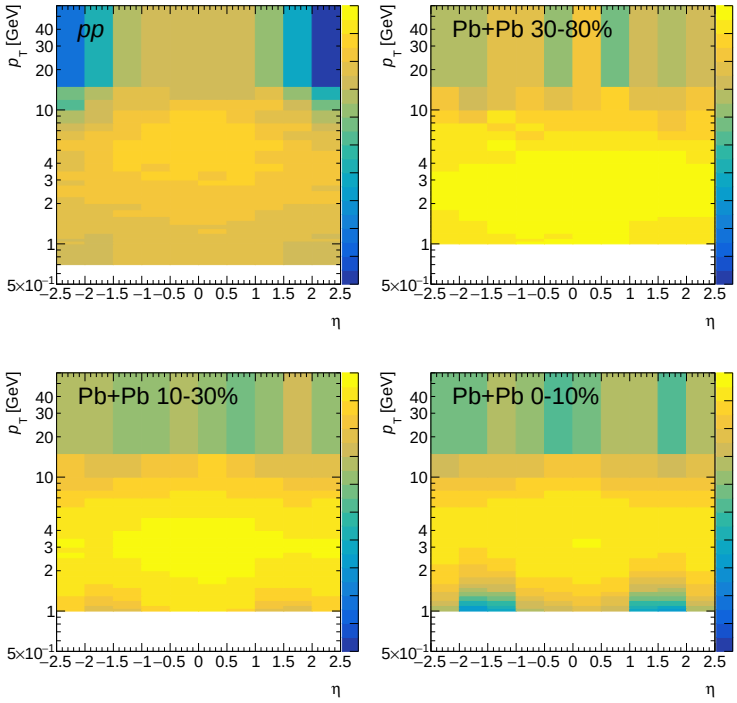


Figure 4.26: The full p_{T} and η dependencies of the primary track fraction for pp (left-most) through 0–10% central Pb+Pb (right-most) are shown. In Pb+Pb, the numerator and denominator are weighted such that the centrality selection in simulated events matches that in Z-tagged data.

pp and peripheral Pb+Pb. In central Pb+Pb, the purity can be as low as $\sim$ 93–94% at high $|\eta|$ and low-$p_{\mathrm{T}}^{\mathrm{ch}}$. In all cases, the purity also drops at high-$p_{\mathrm{T}}^{\mathrm{ch}}$ to $\sim$ 96%, although the drop is a bit larger for high $|\eta|$. The absolute normalization on the purity is also considered when evaluating systematic uncertainties in Sec. 4.8, although it is a subdominant source of uncertainty.

The full purity correction however is derived more differentially in η. In Fig. 4.26, this full $p_{\mathrm{T}}^{\mathrm{ch}}, \eta$ dependence of the purity is shown as a 2D heatmap. To account for the finite purity on the nominal track yields, a multiplicative per-track weighting factor is applied. Without any prior knowledge of a given track, the probability that a given track is a primary track is given by the purity. Therefore, the expected yield of primary tracks Y_{expected} in a given bin x is the sum of all tracks, weighted by the primary probability:

$$Y_{\mathrm{primary}}(x) = \sum_{\{\text{tracks at } x\}} f_{\mathrm{primary}}(x). \tag{4.24}$$

Reconstruction Efficiency

In reconstructing detector hits, real tracks can be missed by the reconstruction procedure. This is accounted for by calculating and correcting for imperfect track reconstruction efficiency ε_{trk}. The purpose of estimating ε_{trk} is to understand how many tracks were missed (not reconstructed) for each track that was reconstructed. Like previous studies, the efficiency is also assessed with a binomial experiment in simulation. Data-driven studies have been used to validate tracking performance studies, for example energy loss in the B-layer (dE/dx) to extract fake rate estimates, or comparisons between track working points to match the working point dependence of the efficiency [225]. Though, they have not been repeated for this measurement. In pp, the sample of Z boson events generated by Powheg + Pythia is used. For Pb+Pb, the sample of MC events are also from Powheg + Pythia Z bosons, but embedded in the MB with data overlay. (The Hijing overlay samples are *not* used, as the data overlay is a more accurate model of Pb+Pb occupancy effects.) The tracking efficiency is then defined as the fraction of truth-matched, primary charged hadrons $N_{\text{ch}}^{\text{truth}}$ that have a matching reconstructed track partner ($N_{\text{ch}}^{\text{reco.}-\text{matched}}$) that passes all track selection cuts:

$$\varepsilon_{\text{trk}}(p_{\text{T}}, \eta) = \frac{N_{\text{ch}}^{\text{reco.}-\text{matched}}(p_{\text{T}}^{\text{truth}}, \eta_{\text{truth}})}{N_{\text{ch}}^{\text{truth}}(p_{\text{T}}^{\text{truth}}, \eta_{\text{truth}})}. \tag{4.25}$$

Note that the charged hadrons are binned in the original truth-level kinematics. If the momentum response is perfect, can be well approximated this way, or the efficiency varies slowly with p_{T}, then the truth-level kinematics can be reasonably substituted with the reco.-level kinematics to obtain a per-track efficiency factor.

The efficiency is evaluated as a function of both truth p_{T} and η. Projections for five $|\eta|$ selections can be seen for each event type in the lower row of Fig. 4.27. The full 2-dimensional efficiency as a function of p_{T} and η is shown in the upper row. There is a clear, slowly varying p_{T}^{ch} dependence to the efficiency as a well as a centrality dependence. This is expected, as the detector becomes increasingly saturated at high levels of event activity. The peripheral Pb+Pb and pp do not generally match because events in the "peripheral" Pb+Pb bin are biased towards the central

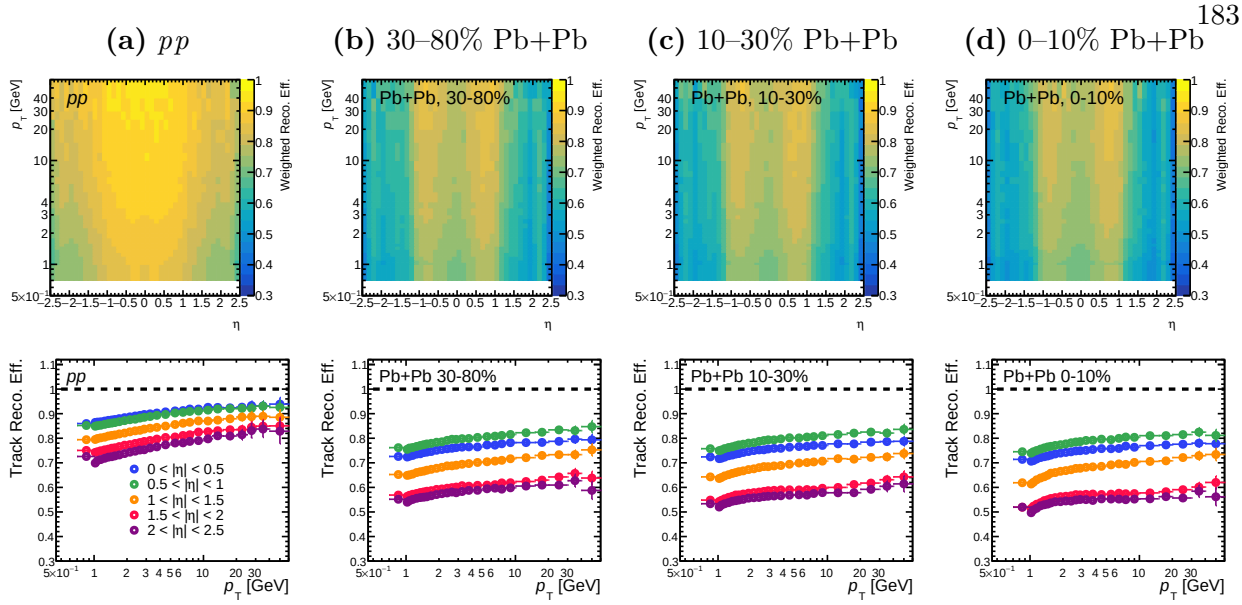


Figure 4.27: Shown are track reconstruction efficiencies as calculated in simulated events as a function of track p_{T} and η, for events ranging from **(a)** pp to **(d)** 0–10% Pb+Pb. Top row: The full 2D heatmap of efficiencies in (η, p_{T}) space is shown. Bottom row: Projections at various selections of $|\eta|$ are shown.

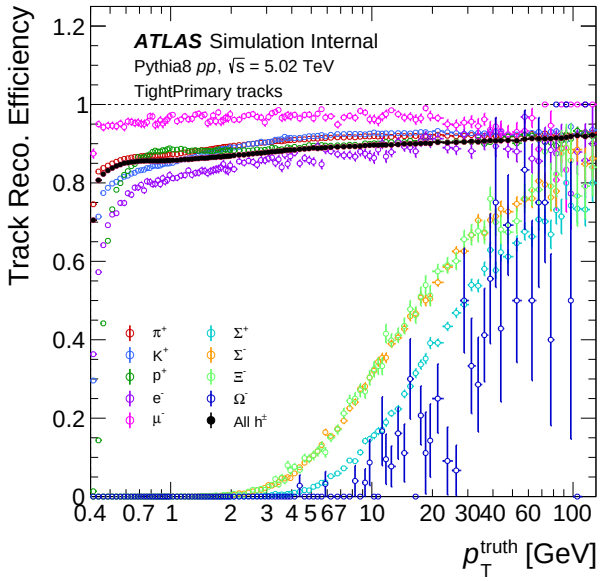


Figure 4.28: The track reconstruction efficiency for particles of different species as determined in simulated pp dijet events. Note that these factors apply to the measurement presented in Chapter 6.

end of the range due to N_{coll}-scaling of Z production.

When computing the reconstruction efficiency, we must also consider which kinds of particles

enter the sample. Different particle types at the same 3-momentum vector have various energies and can interact with the detector in different ways. To illustrate how the efficiency can vary with particle type, Fig. 4.28 shows an evaluation of the reconstruction efficiency for a wide variety of different species, as determined by dijet samples used in a measurement of jet-hadron correlations (see Chapter 6). Strange baryons in particular suffer from a poor reconstruction efficiency at low-p_{T}; this is because they have a tendency to decay within the detector. At high-p_{T}, they become sufficiently boosted to improve their reconstruction efficiency. Pions, kaons, and protons are all more consistent in general, with variations on the order of $\sim$ 5–10%. For starters, we are only interested in the number of charged hadrons per reconstructed track; i.e., electrons and muons are not of interest. So, non-hadronic charged particles are explicitly excluded. However the distribution of hadron species in MC is not expected to completely agree with data. If the two disagree substantially, then the reconstruction efficiency will be mismodeled. The particle species composition in the MC thus presents a source of systematic uncertainty, which is evaluated by reevaluating the efficiency exclusively for charged pions. The vast majority of charged hadrons are pions, so this represents a conservative evaluation of any potential effect.

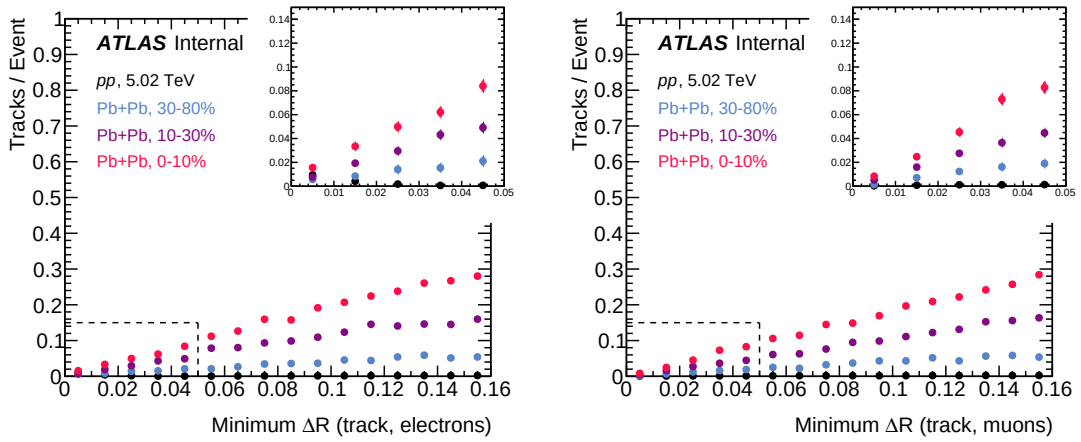
To correct for the reconstruction efficiency, tracks must be weighted by the expected number of truth tracks for each reconstructed track. In a given bin, this is the inverse of the reconstruction efficiency multiplied by the number of tracks in that bin. This is, of course, mathematically equivalent to weighting each track by the inverse of the efficiency to obtain a final yield Y_{final},

$$Y_{\mathrm{final}}(x) = \frac{Y_{\mathrm{primary}}(x)}{\varepsilon_{\mathrm{trk}}(x)} = \frac{1}{\varepsilon_{\mathrm{trk}}(x)} \sum_{\{\text{tracks at } x\}} f_{\mathrm{primary}}(x) = \sum_{\{\text{tracks at } x\}} \frac{f_{\mathrm{primary}}(x)}{\varepsilon_{\mathrm{trk}}(x)}. \tag{4.26}$$

The corresponding statistical uncertainty that accompanies the yield measurement will be assessed in Sec. 4.8.

Lepton Rejection

We next consider how tracks corresponding to the decay leptons are rejected. Because this measurement narrows in on the yield of charged hadrons azimuthally opposite the Z boson, extra



(a) $Z \to ee$ **(b)** $Z \to \mu\mu$

Figure 4.29: The distributions of ΔR between tracks and the closer Z decay lepton are shown for **(a)** $Z \to ee$ events and **(b)** $Z \to \mu\mu$ events, after rejecting tracks which kinematically match the Z decay leptons. The region enclosed by the dashed lines is shown in the plot insets.

particles nearby leptons are unlikely to enter the main results ($Y(p_{\mathrm{T}}^{\mathrm{ch}})$), though they can still enter the $Y(\Delta\phi)$ measurements. In this study we look at tracks in collision data that approximately match to the lepton geometrically. For each track entering the acceptance of this measurement, the minimum ΔR (defined below) to the decay leptons is calculated (each track is closer to only one of the decay leptons – only the closer match is considered):

$$\Delta R = \sqrt{\left(\eta_{\mathrm{lepton}} - \eta_{\mathrm{track}}\right)^2 + \left(\phi_{\mathrm{lepton}} - \phi_{\mathrm{track}}\right)^2}. \tag{4.27}$$

The distributions of minimum ΔR values are shown in Fig. 4.29 for electron events (left) and muon events (right).

In the reconstruction software, tracks nearby the lepton can be either matched or not matched to the lepton. Tracks matched to the lepton are obviously excluded because they are not hadronic. If they are not matched, they can further represent either coincidental hadron production, lepton shower-induced particle production, or a bad lepton-ID track match. Ideally, all tracks in a narrow ΔR range from the lepton will be from coincidental hadron production. Versus ΔR, these three cases exhibit different behavior, and can thus be identified. Coincidental hadrons tend to be produced more at larger relative angles due to the Jacobian area factor. Therefore the hadron

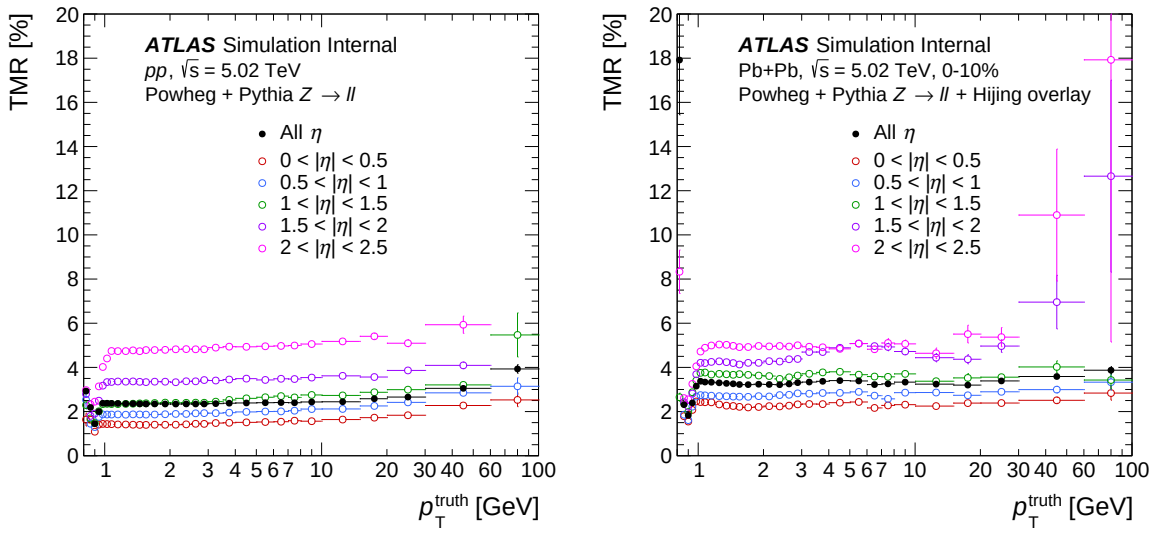
production component will scale approximately linearly with ΔR. The exact ΔR dependence is not trivial for the other two, however they will be largest near $\Delta R \approx 0$.

In Fig. 4.29, this is exactly what is observed. For each event type, there is an approximately linear component to the distribution in the regime $\Delta R \sim 0$–0.15. The slope is clearly steeper for central Pb+Pb, indicative of the large UE. There is also a noticeable uptick in the distribution in its first two bins, particularly for the pp events. This represents the persistent lepton correlations from either particle showers or incorrect ID track associations. It is larger for electrons, which could indicate the higher relative probability of an electron interaction with the ID compared to muons. However, from these figures it is clear that the coincidental hadron production strongly dominates these tracks. The conclusion is that there should be no substantial impact on the charged-hadron yield. Nevertheless, we treat poor lepton-associated-track rejection as a source of systematic uncertainty by adding an additional $\Delta R(\text{lepton}, \text{track}) > 0.02$ cut on tracks to both leptons. This associated uncertainty is almost always less than 1.5% and subdominant to other uncertainties.

Momentum Resolution

One of the advantages of a charged-particle measurement sensitive to jet quenching is the improved momentum resolution as compared to, for example, calorimetric jets, which inherit the resolution of the hadronic calorimeter. This greatly reduces the need for *unfolding* schemes to counteract resolution smearing effects, which introduce a degree of freedom to the measurement and create a source of potential systematic uncertainty. As long as the momentum-variable ($p_{\mathrm{T}}^{\mathrm{ch}}$ or x_{hZ}) bins are sufficiently wide compared to the momentum resolution, then the vast majority of tracks will fall in the same bin at the truth and reconstructed levels. Because the Z is rare to begin with, this measurement uses a relatively wide binning with logarithmic bin widths $\Delta \log\left(p_{\mathrm{T}}^{\mathrm{ch}}/1\ \mathrm{GeV}\right) \approx \log 2$. Thus as long as the track momentum resolution (TMR) is sufficiently better than $\approx 100\%$, any unfolding will have a very minor impact.

First, the TMR is calculated in simulated events as a function of truth $p_{\mathrm{T}}^{\mathrm{ch}}$ and η using a



(a) pp **(b)** Pb+Pb

Figure 4.30: The track momentum resolution (TMR) is shown versus truth charged-hadron p_{T} for **(a)** pp and **(b)** Pb+Pb, for different $|\eta|$ selections (open circles) and for an $|\eta|$-integrated selection (solid circles).

Gaussian fit procedure to the adimensional quantity $p_{\mathrm{T}}^{\mathrm{reco}}/p_{\mathrm{T}}^{\mathrm{truth}}$. For this simplified study, the TMR is defined as the width parameter of the fitted Gaussian. (Other more involved studies might use a slightly different functional form or the interquartile range to reduce sensitivity to outliers.) Only primary tracks were considered in this calculation to ensure good truth matches. The TMR is then shown in Fig. 4.30 for both pp and 0–10% Pb+Pb (which is taken from the HIJING with embedded Z boson MC samples).

In general, the TMR is quite good, averaging about 2.5% in pp in the region of interest, and only rising slightly to about 3.5% in 0–10% central Pb+Pb, despite the much greater detector occupancy. This alone assures that no unfolding is necessary. However to further solidify this approach, we investigated the impact of smearing the results in simulation by the TMR. For simplicity, we only perform this to the truth-level hadron yields in pp simulation. For each truth-level charged hadron, a smeared momentum $p_{\mathrm{T}}^{\mathrm{smeared}} = p_{\mathrm{T}}^{\mathrm{truth}} \times R$ was assigned by sampling a random smearing factor R

$$R \sim \mathcal{N}\left(1, \left(\frac{\mathrm{TMR}}{100\%}\right)^2\right). \tag{4.28}$$

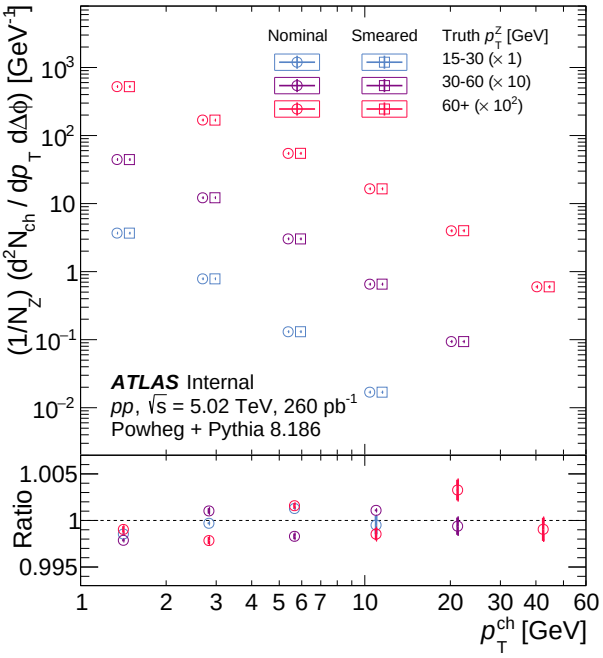


Figure 4.31: Truth-level Z-tagged hadron yields are compared with (open squares) and without (open circles) a track momentum resolution smearing applied. The ratio of Smeared / Nominal is shown below.

This was then compared to the result without any smearing applied; both can be seen in Fig. 4.31. In the bottom panel, which shows the ratio, the impact of smearing is found to be $\lesssim 0.3\%$ everywhere. Moreover, as the TMR is similar between pp and Pb+Pb, the effect of the smearing is going to be similar in Pb+Pb and therefore cancel in the ratio I_{AA}. We conclude that unfolding the yield measurement would have a very marginal benefit (and possibly introduce additional systematic uncertainties). Consequently, no unfolding for the charged-hadron momentum resolution is performed.

Tracking uncertainties

There are four sources of uncertainty attributed to the charged-particle tracking. The largest is the track identification uncertainty. Nominally, tracks must meet the `HILoose` working point. This set of criteria is optimized for a high reconstruction efficiency in Pb+Pb at the cost of a slightly lower tracking purity. A common alternative in the heavy-ion environment is `HITight`,

which sacrifices some reconstruction efficiency for an improved tracking purity. Because the yield is efficiency and purity corrected, it should not matter which working point is used; therefore, switching the working point accounts for potential uncertainties that may enter at this stage. After re-evaluating the efficiency and purity for the alternative track quality criteria, the uncertainty is found to be at the level of a few percent in Pb+Pb. In pp, it is about 1%. We note that the low relative uncertainty exemplifies the resilience of the ID reconstruction to potential backgrounds and inefficiencies.

Other sources include a particle composition uncertainty, where differences in the frequency of each particle type between data and simulation is considered. This is evaluated somewhat conservatively by restricting the tracking efficiency to charged pions, and is not allowed to cancel in the UE subtraction; though it is not a substantial source of uncertainty. We also apply a variation on the fake rate normalization, since the fake rate in dense environments (notably, the cores of high-p_{T} jets) is not very well constrained. This uncertainty is about 25% on the fake rate, though after propagation the effect is $\lesssim$ 1% because the fake rate is small to begin with. Lastly, an uncertainty from lepton-track associations is assigned where tracks in a small window $\Delta R < 0.02$ around the decay leptons are rejected. This uncertainty is only above 1.5% in the lowest p_{T}^{Z} bin in 0–10% Pb+Pb where more tracks come from the UE. This could be reduced by reevaluating the UE model in this variation, but it is not required since the measurement is acceptably precise to begin with.

4.7 Underlying Event

As already alluded to, developing the UE background model is a cornerstone of this measurement. Recall that we define the signal component to be Z-correlated yield, which is sensitive to both the parton shower and possible medium response. This leaves the Z-uncorrelated hadron yield, which is assigned as the background and subtracted. This latter component is estimated via a data-driven mixed event model, whereby the charged particles in each Z-triggered event are substituted with those in a minimum bias (MB) event with similar global characteristics. The premise

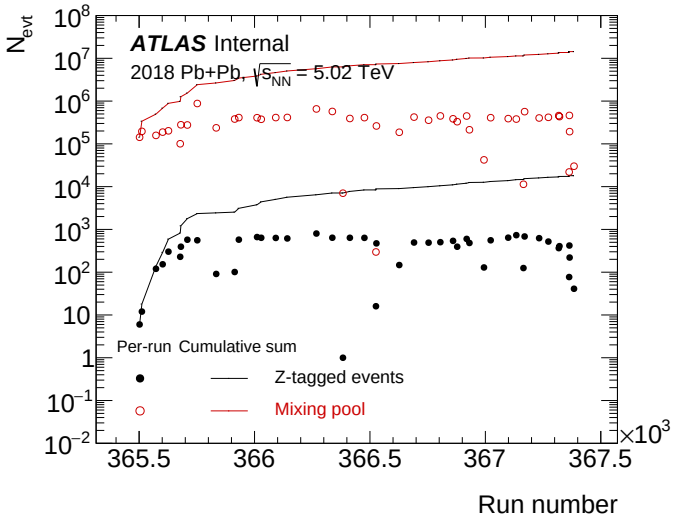


Figure 4.32: The number of Z boson events (black circles) and minimum bias (red circles) are shown for each run in the Pb+Pb data set. The lines correspond to the cumulative totals.

is that the two events are completely independent of each other, so measuring the distribution of charged hadrons in the mixed event serves as an estimate of the uncorrelated yield in the Z-tagged event. Furthermore, by subsampling the MB and matching the global characteristics of the Z sample, any differing samples properties are forced into agreement, improving the model accuracy. Such MB events are selected from a pool of events meeting the basic event selection: they must fire a MB trigger, meet the GRL and detector status cuts, possess a single collision vertex, and not be identified as pileup. The amount of Z events that must be mixed and potential MB events can be seen in Fig. 4.32 in red as a function of run number.

UE Model in Pb+Pb

In Pb+Pb, the mixed events must have similar characteristics in a few key categories, to ensure that the MB event accurately estimates the Z event. First and foremost is the event centrality, which correlates strongly with the overall magnitude of the UE. However, other categories such as run number or the flow vector (defined below) are also considered to account for run-to-run variation and multi-particle correlations in the UE. The flow vectors q_n describe the anisotropic

Pb+Pb Run Group	Run No. Range
Group A	365502 - 365709
Group B	365752 - 365834
Group C	365914 - 365932
Group D	366011 - 366092
Group E	366142 - 366337
Group F	366383 - 366476
Group G	366526 - 366805
Group H	366860 - 367023
Group I	367099 - 367165
Group J	367170 - 367273
Group K	367318 - 367384

Table 4.7: Run categorization used for mixing Z bosons with MB events in Pb+Pb collisions.

flow of the event and are usually measured in the forward calorimeter,

$$q_n = \frac{1}{\Sigma E_{\mathrm{T}}} \begin{pmatrix} \Sigma E_{\mathrm{T}} \cos(n\phi) \\ \Sigma E_{\mathrm{T}} \sin(n\phi) \end{pmatrix}, \tag{4.29}$$

where the sums are performed over all towers in the forward calorimeters. Though $q_n \neq 0$ for many $n = 2, 3, 4, \ldots$, q_2 is the most significant as it directly correlates with the initial nucleon geometry immediately prior to the collision.

In this analysis, each Z boson is mixed with at least 40 unique, but random MB events with a similar run number, centrality and event plane angle Ψ_2. For peripheral (30–80%) events, 160 MB events are mixed instead of 40 to reduce the associated background modeling uncertainty. Similarly, in semi-central (10–30%) events, 80 MB events are mixed. Increasing the mixing rate in the peripheral bins helps reduce the statistical uncertainty, and is feasible because N_{coll} scaling ensures that in more peripheral events, fewer and fewer events will possess a Z, so more MB events can be matched to each Z event.

First, events are matched in 11 run groups denoted Groups A through K, as shown in Table 4.7. These groups are arranged chronologically so that runs with similar detector conditions fall into the same groups. Some divisions are naturally provided by changing conditions during data-

$\Sigma E_{\mathrm{T}}^{\mathrm{FCal}}$ bin edges (TeV)							
0.066402	0.072411	0.078834	0.085729	0.093071	0.100928	0.109333	0.118249
0.127745	0.137874	**0.148625**	0.160033	0.172097	0.184922	0.198428	0.212684
0.227751	0.243588	0.260219	0.277742	**0.29617**	0.315523	0.335738	0.356885
0.378968	0.402144	0.426354	0.451509	0.477734	0.505085	**0.533608**	0.548435
0.563263	0.578667	0.59407	0.610058	0.626047	0.642658	0.659269	0.676438
0.693606	0.711429	0.729251	0.747778	0.766305	0.785456	0.804607	0.824399
0.844192	0.864682	**0.885172**	0.906377	0.927582	0.949534	0.971487	0.994174
1.01686	1.04029	1.06371	1.08795	1.1122	1.13727	1.16233	1.18812
1.21391	1.24049	1.26707	1.29459	1.32212	1.35052	**1.37892**	1.4081
1.43729	1.46742	1.49754	1.5288	1.56005	1.59219	1.62434	1.65741
1.69047	1.72477	1.75906	1.7944	1.82974	1.86623	1.90273	1.94037
1.97802	2.0169	**2.05577**	2.09597	2.13617	2.17752	2.21888	2.26168
2.30447	2.34879	2.39311	2.43893	2.48475	2.53216	2.57956	2.62858
2.6776	2.72864	2.77968	2.8327	2.88571	2.94082	**2.99594**	3.02452
3.0531	3.08169	3.11027	3.14012	3.16997	3.19982	3.22967	3.26092
3.29217	3.32341	3.35466	3.38739	3.42011	3.45284	3.48557	3.51983
3.55408	3.58834	3.6226	3.6587	3.6948	3.7309	3.767	3.80535
3.84371	3.88206	3.92041	3.96115	4.0019	4.04264	4.08338	4.12846
4.17355	4.21863	4.26372	4.33735	4.41098	4.4846	4.55823	4.63186
4.70549	4.77912	4.85274	4.92637	**5**			

Table 4.8: $\Sigma E_{\mathrm{T}}^{\mathrm{FCal}}$ bin edges used in the centrality matching for the Pb+Pb mixed event. 10% increments are indicated by the bolded values.

taking; for example, runs up to 366476 had a bunch spacing of 100 ns, later runs used a tighter spacing of 75 ns for higher collision rates. This might affect pileup rates, which could still propagate to the measurement as not all pileup events will necessarily be rejected. Thus matching in run conditions helps ensure these effects cancel in the background subtraction to avoid compounding any issues. While we could do this by matching the run numbers, creating run groups helps smooth out run-to-run fluctuations in the number of MB events recorded per Z-trigger event, since MB trigger prescales in particular can fluctuate quite a bit.

To then further match in centrality, events must fall into the same $\Sigma E_{\mathrm{T}}^{\mathrm{FCal}}$ bins, with bin edges defined as in Table 4.8. In general, the bin widths are a function of centrality, due to the distance between $\Sigma E_{\mathrm{T}}^{\mathrm{FCal}}$ centrality cuts growing wider for more central events:

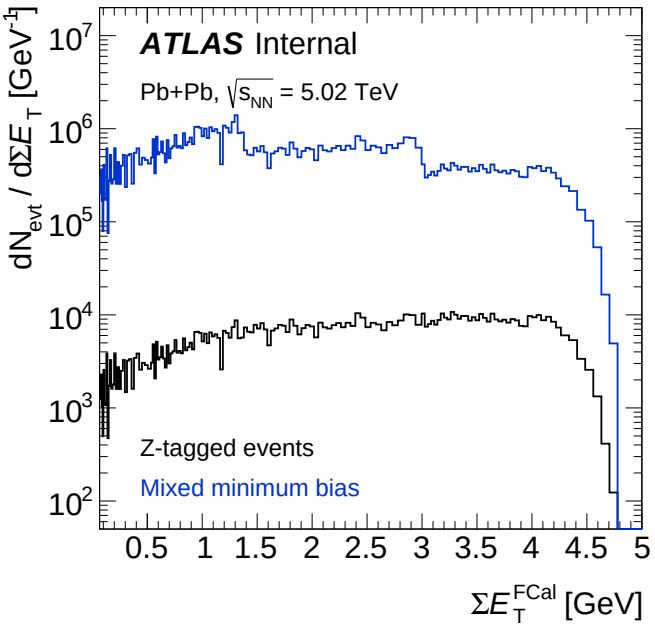


Figure 4.33: The distributions of $\Sigma E_{\mathrm{T}}^{\mathrm{FCal}}$ in Z-tagged events (black) and mixed events (blue) are shown.

- for 50–80%, bins are 1% wide
- for 10–50%, bins are about 0.5% wide
- for 1–10%, bins are about 0.25% wide, and
- for 0–1%, bins are about 0.1% wide.

The $\Sigma E_{\mathrm{T}}^{\mathrm{FCal}}$ distribution both for the Z-tagged and mixed events can be seen in Fig. 4.33. Even though the events represent MB data, their centrality distribution matches that of the Z-tagged events by construction. The two distributions have the exact same shape, including the same statistical fluctuations, up to step-function behavior from decreases in the number of MB events used from 160 to 80 at 30%, and then 80 to 40 at 10%.

In addition to centrality, the flow of the event must be considered when matching events. In particular, the event plane angle $\Psi_2 \equiv \frac{1}{2}\arg(q_2) \in [0, \pi)$ describes the orientation of the dominating anisotropy vector q_2 in the transverse plane. We note there is physical motivation to *not* match

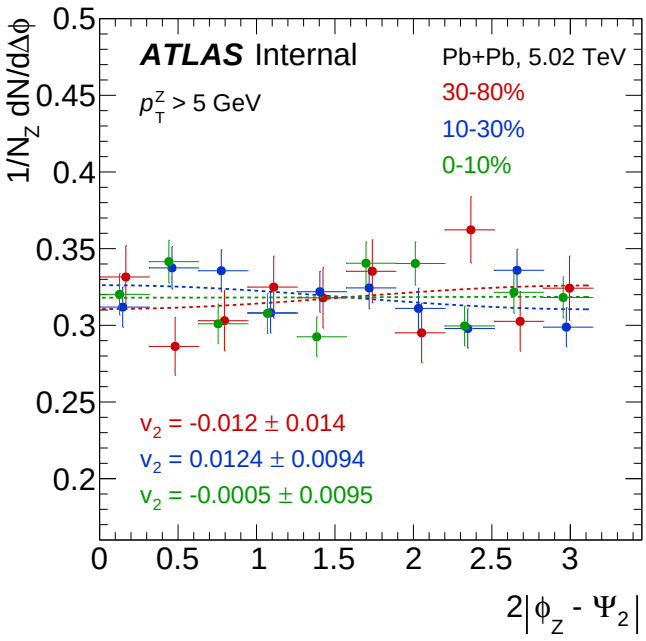


Figure 4.34: The azimuthal distribution of Z bosons is shown, relative to the event plane axis Ψ_2. Fits to the Fourier series as defined in Eq. 4.30 are overlaid. The coefficient v_2 represents the azimuthal anisotropy of Z boson production.

events according to their Ψ_2 values. The Z boson is color neutral and understood to not interact with the QGP. Because the q_2 vector arises due to final state interactions, there should be no physical correlation between the Z momentum angle ϕ_Z and the event plane Ψ_2. To check this, the distribution of ϕ_Z angles with respect to the event plane is shown in Fig. 4.34. Any potential azimuthal anisotropy of reconstructed Zs is quantified by expressing the yield as the first two terms in a Fourier series

$$\frac{1}{N_Z}\frac{dN_Z}{d\phi} = C\left(1 + 2v_2\cos\left(2(\phi - \Psi_2)\right)\right) \tag{4.30}$$

where the overall factor C is sensitive to the height of the distribution and v_2 is the standard metric of azimuthal ellipticity. The coefficients v_2 are calculated for each Pb+Pb centrality and listed in Fig. 4.34. As expected, they are compatible with 0, indicating the Z boson direction is independent of the event plane angle.

But, despite no *physical* correlation between the Z and Ψ_2, a dependence on the event plane angle can still manifest in this measurement. This can be due to either

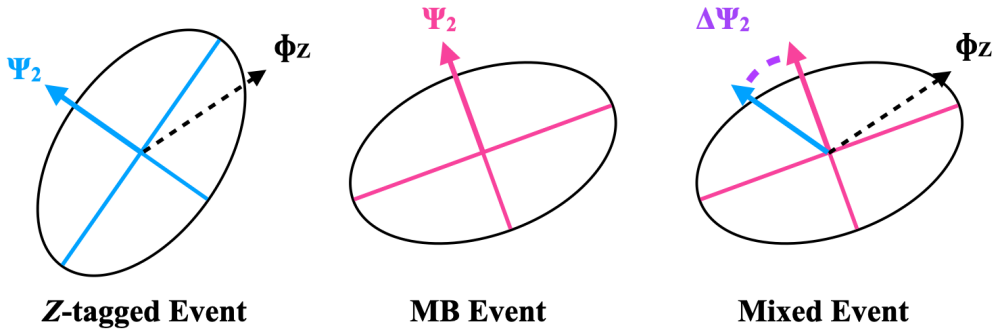
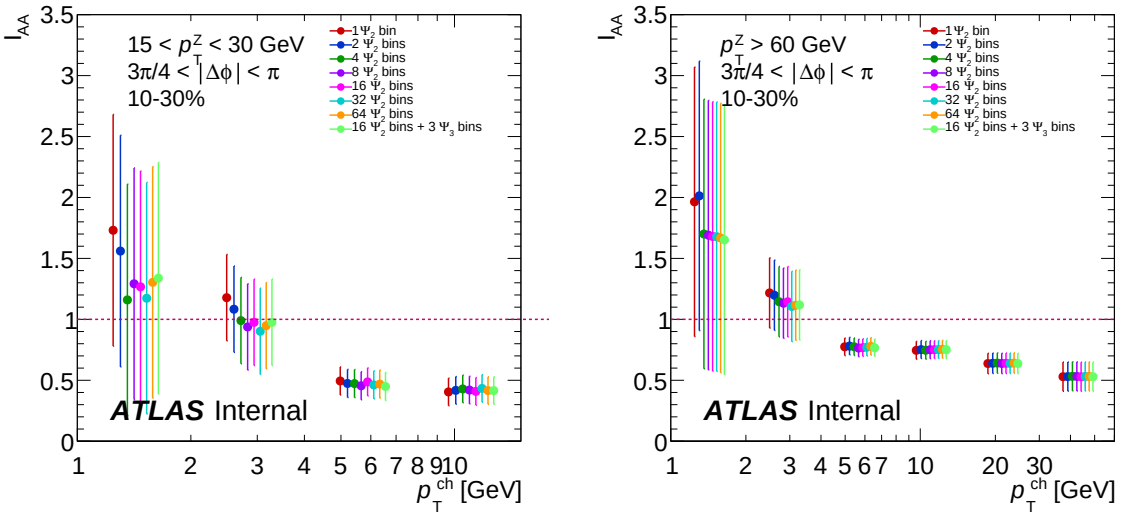


Figure 4.35: Diagram showing how the event plane angle (Ψ_2) matching is performed. The transverse plane profiles of a Z event, a minimum bias event, and a mixed event are illustrated. The difference in Ψ_2 between the events, $\Delta\Psi_2$, is required to be smaller than a value parameterized by N_{bins} for a good mixed event matching.

- finite statistics, e.g. a sample of one Z event would require the background to be estimated from minimum bias events similarly oriented in the detector to ensure the mixed event average converges to the correct background yield, and/or
- systematic detector and reconstruction effects; for example, the electron reconstruction performs a subtraction of the estimated energy deposited in the EMCal by the UE.

In the limit of infinite statistics and a perfect detector, any increase or decrease in the mixed-event hadron yield due to imperfect event plane mixing will average out, as the distribution of $\phi_Z - \Psi_2$ is flat. However, we are not entirely in this limit, so it is possible for mismatched event plane angles to bias the mixed-event yield somehow. Previous studies indicate that a mismatch of Ψ_2 provides a relatively small effect of about 0.5% on the UE yield [278], however this can substantially affect the UE subtracted yield due to the relative abundance of UE particles in a central Pb+Pb event. Consequently it is necessary to further study and correct for these effects.

The sensitivity to Ψ_2 matching was studied by gradually varying the matching criteria. These additional mixing criteria were imposed based on the relative difference in Ψ_2 between the Z-producing event and the candidate MB event, as illustrated in Fig. 4.35. Essentially, the matching criterion $\Delta\Psi_2 \equiv \Psi_2^Z - \Psi_2^{\text{MB}}$ was required to lie in increasingly small intervals, to more accurately capture the dependence of the UE on the orientation of the Z with respect to the reaction



(a) $p_{\mathrm{T}}^{Z} = 15$–30 GeV **(b)** $p_{\mathrm{T}}^{Z} > 60$ GeV

Figure 4.36: The impact of event plane angle (Ψ_2) matching on the I_{AA} is investigated in 10–30% mid-central Pb+Pb, as described in the text, for **(a)** low-p_{T}^{Z} events and **(b)** high-p_{T}^{Z} events. Various colors indicate different mixing schemes. Uncertainties shown are statistical and are correlated between each scheme.

plane. The maximum tolerated difference $\Delta\Psi_2$ was parameterized in terms of a number of bins via $\Delta\Psi_2 = \pi/N_{\mathrm{bins}}$ in this study. For the central values in this analysis, $N_{\mathrm{bins}} = 16$ is used to fix the Ψ_2 matching criteria. This value approximately corresponds to a best-case scenario for the Ψ_2 resolution in the forward calorimeters (see for example [298] for more details on the event plane resolution). Finer matching cuts are expected to not lead to discernible differences due to the resolution limit.

Fig. 4.36 shows the main results scanning through N_{bins}. The most significant effect on the results is at low-$p_{\mathrm{T}}^{\mathrm{ch}}$, where many more of the observed hadrons are associated with the UE rather than the hard scatter. At high-$p_{\mathrm{T}}^{\mathrm{ch}}$, the probability that a hadron is in the away-side jet grows substantially, so essentially no effect is observed. Additionally, as N_{bins} grows, the results converge around the central value for $N_{\mathrm{bins}} = 16$ (shown in magenta), as expected. Even by $N_{\mathrm{bins}} = 4$, essentially all of the difference between 1 bin (i.e. no Ψ_2 mixing) and the nominal $N_{\mathrm{bins}} = 16$ is accounted for. This is related to the choice of a wide charged-particle acceptance

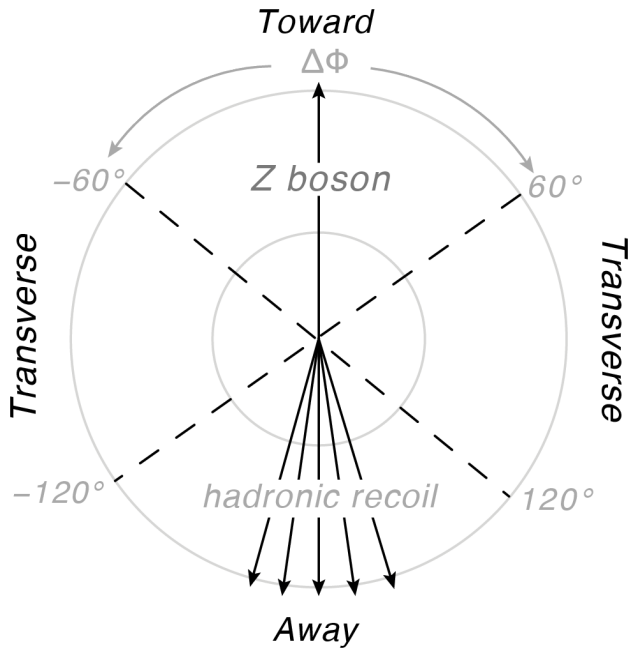


Figure 4.37: Illustration of the Z transverse plane. In particular, the transverse "trans-min" and "trans-max" regions are defined perpendicular to ϕ_Z. Figure reproduced from [299].

window $\Delta\phi_{\mathrm{ch},Z} > 3\pi/4$. Note that for $N_{\mathrm{bins}} = 4$, the maximum allowed event plane angle difference is $|\Delta\Psi_2| < \pi/4 = \pi - 3\pi/4$. Therefore using this wide window should reduce sensitivity to the event plane matching beyond $N_{\mathrm{bins}} = 4$.[8] The statistical UE modeling uncertainty is of the order 10–20% in the lowest $p_{\mathrm{T}}^{\mathrm{ch}}$ bin (see Sec. 4.8, which is generally consistent with (if not larger than) the variation between the highest N_{bins} selections, so the minor fluctuations seen in Fig. 4.36 can be attributed to statistical fluctuations resulting from the event mixing analysis selecting different event pairs. Furthermore, matching the third order event plane angle $\Psi_3 \equiv \frac{1}{3}\arg(q_3) \in [0, 2\pi/3)$ shows no additional systematic effect within the uncertainties. As a result, no additional systematic uncertainty associated with event categories in Pb+Pb is assigned.

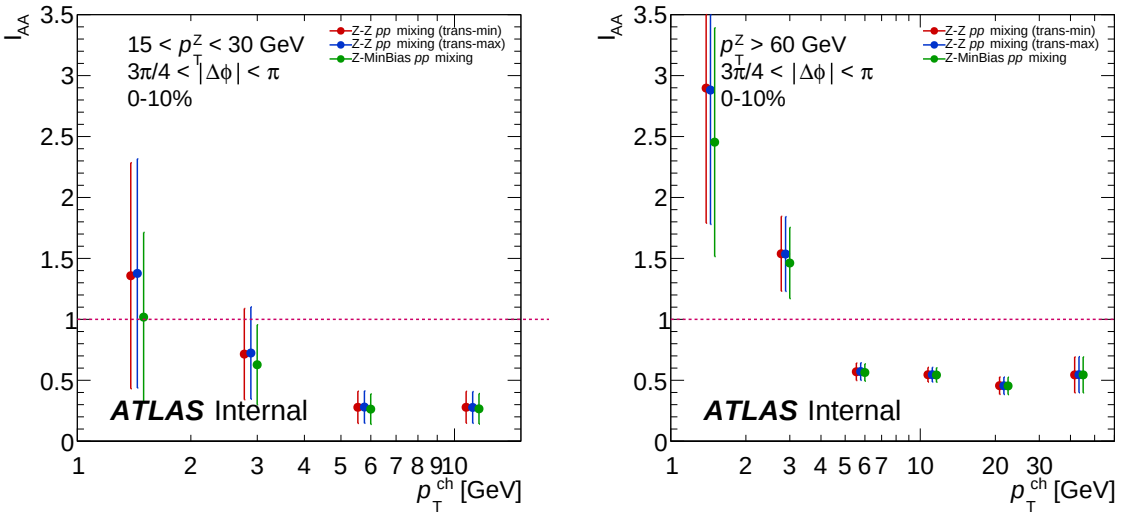
UE Model in *pp*

We must also develop a UE model in pp to keep the correlated yield definitions consistent. In Pb+Pb, by design the UE due to all nucleon-nucleon binary collisions is subtracted, including the UE produced by the nucleon-nucleon collision which produced the Z. This is because the $\Sigma E_{\mathrm{T}}^{\mathrm{FCal}}$ value in each collision has components from the background and the Z hard scattering, but the two cannot be accurately separated event-by-event. Each matched MB event will be slightly too central, and so our UE model should very slightly over-estimate the actual UE. Thus, the UE from the nucleon-nucleon (proton-proton) collision producing the Z must also be subtracted in the pp measurement, to ensure the modification ratio I_{AA} is comparing analogous quantities in pp and Pb+Pb. The underlying event in a typical pp event is substantially less than Pb+Pb, so this procedure doesn't have as significant of an impact on the final results as the Pb+Pb mixed event.

In pp, we also model the UE background with a data-driven mixed event approach. However, it is not immediately clear how to construct a mixed event. For example, it is known that the UE in an event with a Z is more "active" than a typical pp collision, which provides motivation that MB mixing might not be optimal. Additionally, diffractive collisions contribute to pp MB collisions at a much greater rate than to any of the Pb+Pb centralities. Such events are topologically distinct from events where a hard scattering occurs, and therefore should not be used in the UE model in pp events with Z bosons.

This necessitates a modification to the procedure. We employ a qualitatively novel method – the "same-event mixing" procedure – for modeling the UE in pp collisions. Inspired by studies of UE characteristics in Z-triggered pp events [299, 300], we draw a pool of mixed events from a complementary set of Z-tagged events in the same data set with a very low Z p_{T} of 1–12 GeV. The lower bound reduces cases where the Z azimuthal direction is poorly defined, while the upper bound provides adequate kinematic separation between the mixed event pool and the lowest reported p_{T}^{Z} selection of 15–30 GeV.

[8] In the limit of an inclusive acceptance, the results should be *completely* insensitive to event plane matching, because the UE orientation should not affect the total yield.



(a) $p_{\mathrm{T}}^{Z} = 15$–30 GeV **(b)** $p_{\mathrm{T}}^{Z} > 60$ GeV

Figure 4.38: Variations on the pp event matching are considered by investigating their effect on the I_{AA} in 0–10% central Pb+Pb, for **(a)** low-p_{T}^{Z} events and **(b)** high-p_{T}^{Z} events. Various colors indicate different mixing schemes. Uncertainties shown are statistical and are correlated between each scheme.

To accurately capture the underlying event in a pp collision producing a Z boson, real Z bosons (the "trigger" event) are mixed with other Z boson events (the "associated" or "mixed" event). However, Zs must be mixed in a way that the associated jet is not accidentally subtracted. Previous analyses which aim to study the UE in Z events typically look at the transverse plane in regions roughly perpendicular to the Z [299, 300]. In such analyses, the transverse plane is divided into four regions relative to ϕ_Z, as illustrated in Fig. 4.37:

- a "towards" region $< \pi/3$ from the ϕ_Z,
- an "away" region $> 2\pi/3$ from ϕ_Z, and
- two transverse regions ("trans-min" and "trans-max") between $\pi/3$ and $2\pi/3$ from ϕ_Z.

We use the two transverse regions to develop our UE model. These can be distinguished by the level of event activity on either side. The transverse region with a lower $\sum p_{\mathrm{T}}$ is designated as the trans-min while the higher of the two is the trans-max. The UE in Z boson events can then be estimated using charged hadrons in these regions.

The mixing procedure then proceeds between the triggering and associated events using hadrons in the transverse regions. Similar to the Pb+Pb event mixing, the trigger and associated pp events must meet certain criteria:

- First, to reduce the chance of an away-side jet peak biasing the UE estimate, the associated Z must have a relatively low-p_{T}^{Z} in the range $1 < p_{\mathrm{T}}^{Z} < 12$ GeV.
- Second, the trigger Z must be nearly opposite to the trans-min region of the associated Z in the transverse plane, with an allowed margin of $\pm\pi/8$.

The second criteria specifies the trans-min region to be used so that in the case of a multi-jet event, the yield from perpendicular jets is reduced. The margin of $\pm\pi/8$ ensures no overlap with a possible away-side jet peak at $\Delta\phi > 3\pi/4$. The main downside to this method is that the size of the mixing pool is limited by the Z statistics. If each associated event can only be matched once, then very few mixings can be performed. Due to the relatively low effect of the UE on the total yield in pp collisions, only a single mixing is performed for each trigger event.

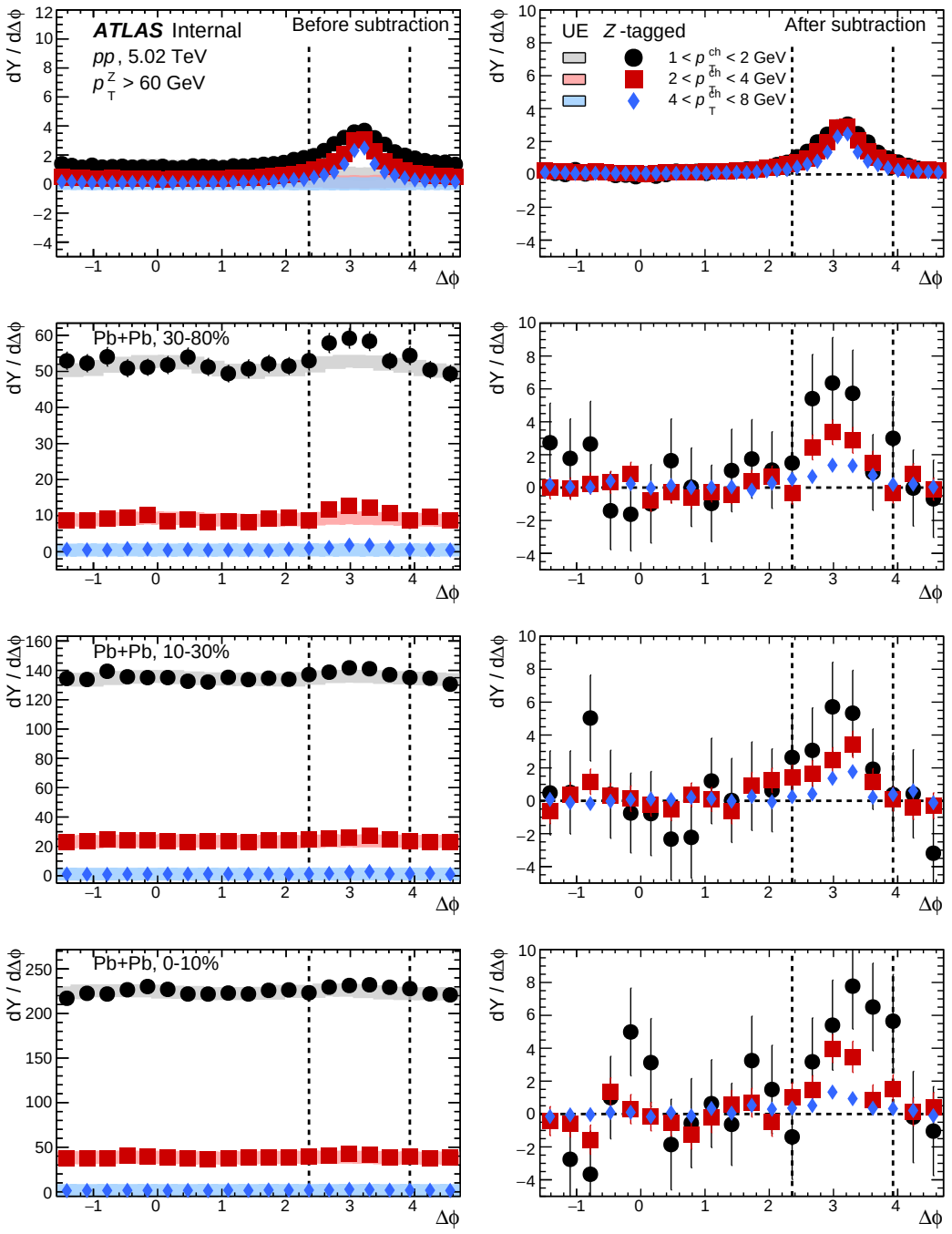
Some details of the UE model are similar to the Pb+Pb case. Like the Pb+Pb, the matching is performed randomly and uniquely. Run dependence is performed more simply, however, as the trigger and associated events must simply come from the same run number, instead of run groups. This is because both events are sampled from the same trigger, and so the number of associated events per trigger event should be consistent run-to-run (unlike in the Pb+Pb). A more subtle difference is that only hadrons opposite the trigger Z by $|\Delta\phi| < \pi/8$ are considered, with the smaller integration window properly scaled out in the subtraction procedure. This last difference helps ensure that the away-side jet peak in the associated event does not accidentally enter the UE model.

A summary of the impact on the final I_{AA} measurement from this novel approach to the UE is illustrated in Fig. 4.38. Two variations are performed for comparison. In green, we consider a different approach where the UE model is assessed nearly identically to in Pb+Pb: mixed events are drawn from MB pp collisions (firing the `HLT_mb_sptrk` trigger), and each Z-trigger event in

pp is mixed 40 times. In red, the nominal result where each trigger Z is mixed with charged hadrons in the trans-min region of the associated event. In blue, charged hadrons in the trans-max are shown instead. The only discernible difference between each variation is in the lowest two $p_{\mathrm{T}}^{\mathrm{ch}}$ bins. There is an approximately 40% effect going from the MB method to the Z method; this is mostly attributed to improved rejection of diffractive events, which have a lower charged-particle yield. Going from the green points to the red points increases the pp UE estimate, decreasing the signal component, and therefore increasing the I_{AA} ratio. However, varying the matching from the trans-min to the trans-max region does not have any notable impact on the measurement. This provides further evidence that the measurement is generally insensitive to the pp UE model – as such, no systematic uncertainty is assigned.

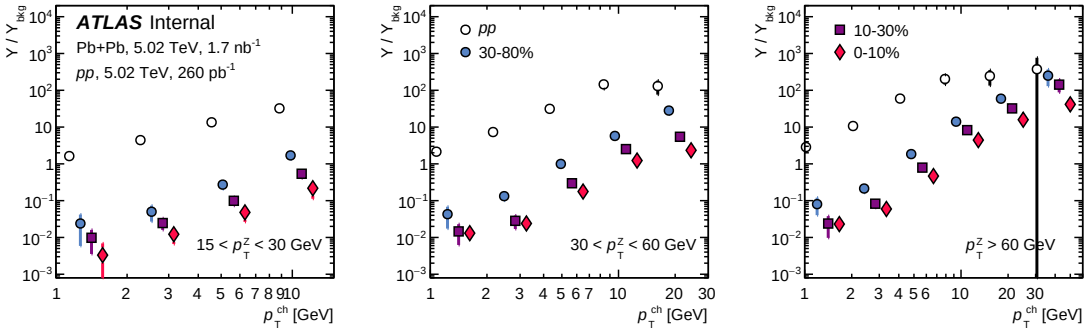
This new method solves the two aforementioned issues with MB mixing by directly evaluating the UE in the Z events themselves. We mentioned that the downside is that there are a similar number of associated and trigger events. This means each Z cannot be mixed many times. In fact, for the p_{T}^{Z} ranges defined here, only a single mixing per Z can be performed. But, if enough Z events are sampled and the measurement is not statistically limited (as is the case in the pp), this method is expected to be preferable because it automatically accounts for the Z-induced UE in a consistent manner without substantially increasing the uncertainties. In short, it automatically accounts for any systematic effects. Though, when the measurement is statistically limited rather than systematically (as is the case in the Pb+Pb), it is more important to subtract off a more basic model of the UE with high statistical precision to avoid increasing the statistical uncertainties due to the limited number of potential mixings.

In Fig. 4.39, the full subtraction procedure for Pb+Pb and pp is illustrated. In the left column, the $\Delta\phi$-differential yield is shown for the Z-tagged data and the background estimate. The Z-tagged yield consists of the correlated (signal) yield, plus the uncorrelated background. The UE yield is generally flat due to it being completely independent of the mixed Z boson. The subtracted (or "Z-correlated") yield is then shown on the right. A strong peak near $\Delta\phi \approx \pi$ (often called the away-side or "jet" peak) is observed both in pp and Pb+Pb, after the subtraction is



(a) Before subtraction **(b)** After subtraction

Figure 4.39: **(a)** Raw per-event track yields in pp (top) and each Pb+Pb centrality category (bottom 3 rows) are shown as a function of $\Delta\phi$. The mixed event yield is shown as shaded bands. **(b)** The UE subtracted yield is shown. Different colors correspond to different $p_{\mathrm{T}}^{\mathrm{ch}}$ selections. In these plots, the Z boson must have $p_{\mathrm{T}}^{Z} > 60$ GeV. Vertical dashed lines indicate the region $|\Delta\phi| > 3\pi/4$.



(a) $p_{\mathrm{T}}^{Z} = 15$–30 GeV **(b)** $p_{\mathrm{T}}^{Z} = 30$–60 GeV **(c)** $p_{\mathrm{T}}^{Z} > 60$ GeV

Figure 4.40: The ratio of the UE subtracted yield to the background (i.e., the signal-to-background ratio) is shown as a function of $p_{\mathrm{T}}^{\mathrm{ch}}$ for each Pb+Pb centrality category (various colors) or pp (open circles). The ratio is separated for Zs in the ranges **(a)** $15 < p_{\mathrm{T}}^{Z} < 30$ GeV, **(b)** $30 < p_{\mathrm{T}}^{Z} < 60$ GeV, and **(c)** $p_{\mathrm{T}}^{Z} > 60$ GeV.

performed. We see from these distributions that by subtracting the UE, which is essentially flat versus $\Delta\phi$ but very large in the Pb+Pb, the jet peak can be isolated for further study. Finally, in Fig. 4.40, the relative size of the UE background is displayed via the signal-to-background (S/B) ratio. As expected, the S/B is lowest at low-$p_{\mathrm{T}}^{\mathrm{ch}}$; it is of order 10^{-3}–10^{-2} for central Pb+Pb at low-p_{T}^{Z}.

4.8 Discussion of Uncertainties

We have already alluded to how many sources of uncertainty are accounted for. In this section, we summarize the effects of these and comment on how different sources compare. Because (1) Z bosons are rare in hadronic collisions and (2) most tracks in Pb+Pb come from the UE, this measurement is statistically limited in general. Therefore we first turn to how statistical uncertainties are addressed.

Statistical Uncertainties

For rare, independent events such as counts of Z bosons, it is standard to assign uncertainties assuming the count observed in experiment, N_Z, is Poisson distributed, so the statistical uncer-

tainty on the count is $\sigma = \sqrt{N_Z}$. However, charged particles within the same collision are neither independent nor rare. Even in single, high-energy pp collisions, up to $\sim 10^2$ particles can be expected (let alone the 10^4–10^5 particles in central Pb+Pb collisions). Furthermore, these particles are certainly not independent due to their common point of origin. Therefore the total number of charged particles in a given histogram bin cannot be assumed to be Poisson distributed.

To evaluate the statistical uncertainties, the standard deviation of the per-Z yield is first determined over all events. In a single event i, there is only one Z[9] , and so the per-Z yield in a given bin x, $Y_i(x)$, is simply given by

$$Y_i(x) = \frac{1}{N_Z^i}\frac{dN_{\text{ch}}^i}{dx} \xrightarrow[N_Z^i=1]{} \frac{dN_{\text{ch}}^i}{dx} \to \frac{1}{\Delta x}\sum_{\{\text{tracks at } x\}} \frac{f_{\text{primary}}(x)}{\varepsilon_{\text{trk}}(x)} \tag{4.31}$$

The last expression here represents a sum over all tracks in bin x, and comes from Eq. 4.26, where the primary fraction and reconstruction efficiency are properly accounted for. On its own, each $Y_i(x)$ is a random variable that must follow some distribution. One characteristic of this distribution is its "true" mean $Y(x)$, which can be extracted from the event-average yield of charged particles at x. This is itself evaluated from the ensemble of events,

$$\langle Y(x)\rangle_{\text{evt}} = \frac{1}{N_{\text{evt}}}\sum_{i\in\{\text{events}\}} Y_i(x). \tag{4.32}$$

The event average is accompanied by the (unbiased) standard deviation of per-Z charged-particle yields, which describes the spread of $Y(x)$ over all Z bosons in the sample,

$$\begin{aligned}\text{STD}\left[Y(x)\right]^2 &= \frac{1}{N_{\text{evt}}-1}\sum_{i\in\{\text{events}\}}\left(Y_i(x) - \langle Y(x)\rangle_{\text{evt}}\right)^2 \\ &= \frac{1}{N_{\text{evt}}-1}\left[\left(\sum_{i\in\{\text{events}\}} Y_i(x)^2\right) - N_{\text{evt}}\langle Y(x)\rangle_{\text{evt}}^2\right].\end{aligned} \tag{4.33}$$

Of course, the estimator for the true mean $Y(x)$ is simply the sample average $\langle Y(x)\rangle_{\text{evt}}$. This is simply a consequence of the central limit theorem, which (in this case) asserts that $\langle Y(x)\rangle_{\text{evt}} \sim$

[9] Realistically, only one Z can be observed in a single Pb+Pb collision, or at absolute most ~ 2, though the argument here can be easily generalized to these cases.

$\mathcal{N}(Y(x), \sigma_Y(x)^2)$. The uncertainty associated with this estimate of the true mean (i.e., the uncertainty on the mean) is related to the standard deviation,

$$\sigma_Y(x)^2 = \frac{\mathrm{STD}\left[Y(x)\right]^2}{N_{\mathrm{evt}}}. \tag{4.34}$$

In this manner, the per-Z yield of charged hadrons is measured independently in every event, with the uncertainty assigned from the statistical spread of the sample. Alternatively, the uncertainty on the mean can be extracted from the diagonal entries of the more general (unbiased) covariance matrix, which quantifies bin-to-bin correlations in hadron yields:

$$\begin{aligned}\mathrm{cov}\left[Y(x_1), Y(x_2)\right] &= \frac{1}{N_{\mathrm{evt}} - 1} \sum_{i \in \{\mathrm{events}\}} \left(Y_i(x_1) - \langle Y(x_1) \rangle_{\mathrm{evt}}\right) \left(Y_i(x_2) - \langle Y(x_2) \rangle_{\mathrm{evt}}\right) \\ &= \frac{1}{N_{\mathrm{evt}} - 1} \left[\left(\sum_{i \in \{\mathrm{events}\}} Y_i(x_1) Y_i(x_2) \right) - \left(N_{\mathrm{evt}} \langle Y(x_1) \rangle_{\mathrm{evt}} \langle Y(x_2) \rangle_{\mathrm{evt}} \right) \right]. \end{aligned} \tag{4.35}$$

Note that the second line of Eq. 4.35 allows a two-dimensional histogram storing the covariance matrix to be filled simultaneously with the averages being evaluated and therefore no additional algorithmic complexity is introduced.

One advantage of evaluating statistical uncertainties this way is that track-by-track and event-by-event weights can be accounted for in a straightforward manner. Track-by-track weights – namely the primary fraction and reconstruction efficiency – affect the measured yield in single events, as documented in Eq. 4.31. Event-by-event weights on the other hand affect the averaging procedure, effectively replacing each sum with a weighted variant

$$\sum_{i \in \{\mathrm{events}\}} \xrightarrow[\text{Replace with}]{} \sum_{i \in \{\mathrm{events}\}} \tilde{w}^i_{\mathrm{evt}}, \tag{4.36}$$

where $\tilde{w}^i_{\mathrm{evt}}$ is the normalized per-event weight factor for event i. For this analysis, recall that we weight by the Z acceptance factor, possibly accompanied by a MC sample combining factor w_{MC},

$$w^i_{\mathrm{evt}} = \left(\varepsilon^{\mathrm{trig}}_{Z \to \ell\ell} \times \varepsilon^{\mathrm{reco}}_{Z \to \ell\ell}\right)^{-1} \times \begin{cases} 1 & \text{if data} \\ w_{\mathrm{MC}} & \text{if MC} \end{cases}. \tag{4.37}$$

Essentially, w_{MC} allows samples with different filters to be combined. Each sample possesses a process cross section σ, a filter efficiency $\varepsilon_{\mathrm{filter}}$, and a number of generated events N_{evt} – these are

listed in Table 4.3. Standard practice for combining samples assigns a per-sample weight of

$$w_{\mathrm{MC}} = \frac{\sigma \times \varepsilon_{\mathrm{filter}} \times \mathcal{L}}{N_{\mathrm{evt}}}. \tag{4.38}$$

Each is a property of the MC sample as listed in Table 4.3. Notably, the filter efficiency $\varepsilon_{\mathrm{filter}}$ nontrivially appears in the numerator of Eq. (6.4). Naïvely, if there exists an efficiency associated with events in the MC sample, events should be weighted by $1/\varepsilon_{\mathrm{filter}}$. What $\varepsilon_{\mathrm{filter}}$ really represents is the probability that a given generated event is accepted by the MC sample filter; e.g. the probability that a $p_{\mathrm{T}} > 25$ GeV Z boson is produced in a high-p_{T} filtered sample. Because the MC event generation continues until N_{evt} events are generated, in the eyes of the generator (such as Pythia, which provides the sample cross section) the *actual* number of generated events is $N_{\mathrm{evt}}/\varepsilon_{\mathrm{filter}}$. In this context, we see that the purpose of the filter efficiency is actually in correcting N_{evt} to make it compatible with the provided cross section, and thus it migrates to the numerator.

Formally, a factor of the sampled data luminosity $\mathcal{L}$ is also present to cancel the units dependence, though this is effectively a constant for all of the samples, and it cancels between the numerator and the denominator.

Systematic Uncertainties

In addition to statistical sources of uncertainty, a variety of systematic uncertainties stemming from multiple aspects of the procedure are considered. These generally fall into one of three categories: Z-tagging, tracking, or the UE model. A summary of systematic uncertainty sources and their relative sizes is shown in Table 4.9.

We see from these tabulated values that the largest uncertainties pertain to the UE model. There are two main components to this. The first is a statistical uncertainty which can be reduced by raising the number of event mixings – for central Pb+Pb, 40 mixings are performed. This uncertainty maximizes in the neighborhood of 7–23%, with the exact value depending on the p_{T}^{Z} bin. In pp, because the S/B ratio is so big to begin with, this uncertainty is $\lesssim 1\%$. The second component is the non-closure uncertainty, which enters via the UE modeling and accounts for

Source	Max. Size in pp [%]		Max. Size in 0–10% Pb+Pb [%]	
	$p_{\mathrm{T}}^{Z} = 15 - 30$ GeV	$p_{\mathrm{T}}^{Z} > 60$ GeV	$p_{\mathrm{T}}^{Z} = 15 - 30$ GeV	$p_{\mathrm{T}}^{Z} > 60$ GeV
Track ID Cuts	1%	1%	3%	2%
Particle Composition	0.8%	0.8%	1%	1%
Purity Correction	0.5%	0.9%	0.7%	1%
Lepton Rejection	$< 0.5\%$	$< 0.5\%$	3%	$< 0.5\%$
Electron Energy Scale	$< 0.5\%$	$< 0.5\%$	$< 0.5\%$	0.8%
Muon Energy Scale	1%	1%	1%	4%
Channel dependence	1%	$< 0.5\%$	9%	$< 0.5\%$
Bkg. Stat. Unc.	0.8%	1%	23%	7%
MC Non-Closure	1%	1%	47%	13%

Table 4.9: Summary of systematic uncertainty sources considered in this analysis. All uncertainties quoted refer to their value in the UE subtracted yield as a function of $p_{\mathrm{T}}^{\mathrm{ch}}$. The first four source pertain to the tracking, the next three to the Z-tagging, and finally the last two to the UE modeling.

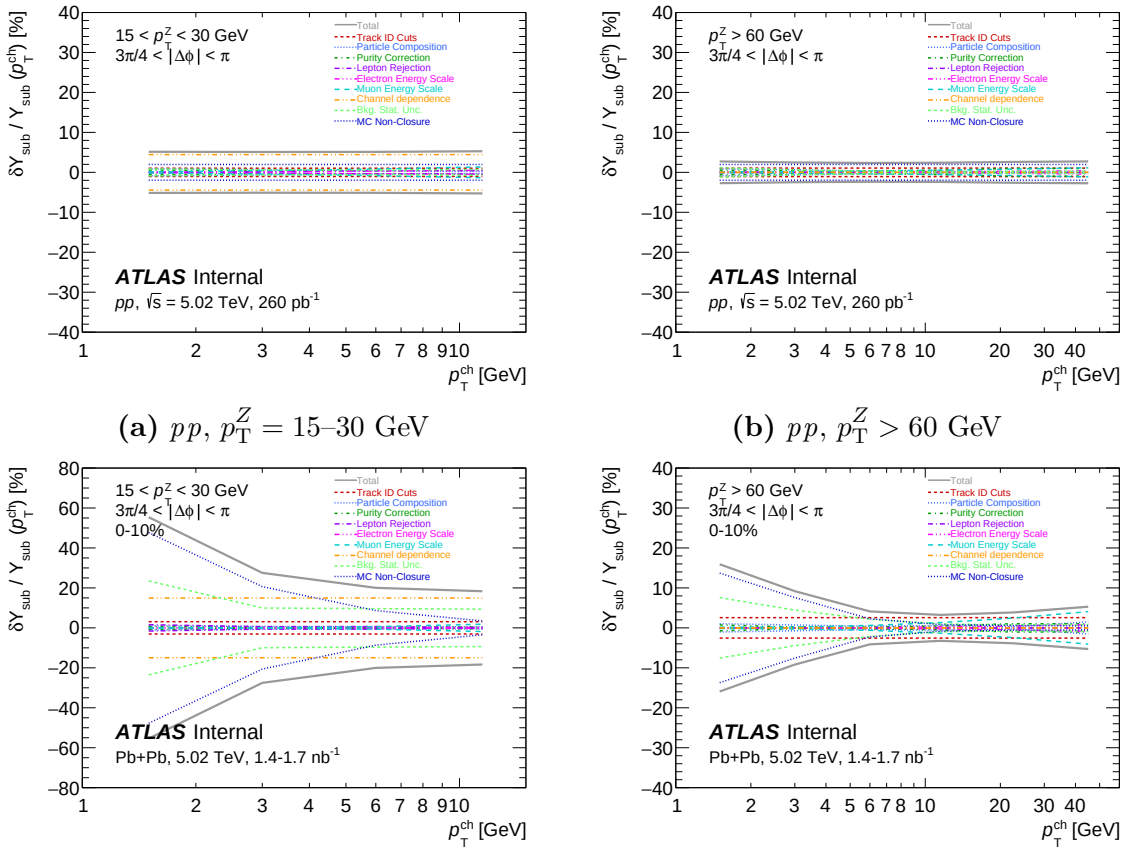
systematic effects entering the mixed event procedure. Though it has an visibly strong effect on the yield measurement, this uncertainty corresponds to approximately a 0.3% uncertainty on the yield of UE tracks, which is very competitive with similar measurements of, for example, jet fragmentation in Pb+Pb collisions [111].

In most cases, systematic uncertainties are propagated by raising or lower the relevant quantities and re-evaluating the yield measurements. To further propagate to the ratio I_{AA}, several sources are treated as correlated between the numerator and denominator because they are common to both. For example, the formulae for obtaining lepton energy scale uncertainties are essentially the same between Pb+Pb and pp, and therefore they are allowed to cancel when propagating them to I_{AA}. The standard way to do this is by, under variation X, taking the uncertainty on I_{AA} to be

$$\delta I_{\mathrm{AA}}|_{X} = \left.\frac{Y_{\mathrm{Pb+Pb}}}{Y_{pp}}\right|_{X} - \frac{Y_{\mathrm{Pb+Pb}}}{Y_{pp}}. \tag{4.39}$$

If the numerator and denominator are uncorrelated they are instead summed in quadrature,

$$\left.\frac{\delta I_{\mathrm{AA}}}{I_{\mathrm{AA}}}\right|_{X} = \left.\frac{\delta Y_{\mathrm{Pb+Pb}}}{Y_{\mathrm{Pb+Pb}}}\right|_{X} \oplus \left.\frac{\delta Y_{pp}}{Y_{pp}}\right|_{X}. \tag{4.40}$$

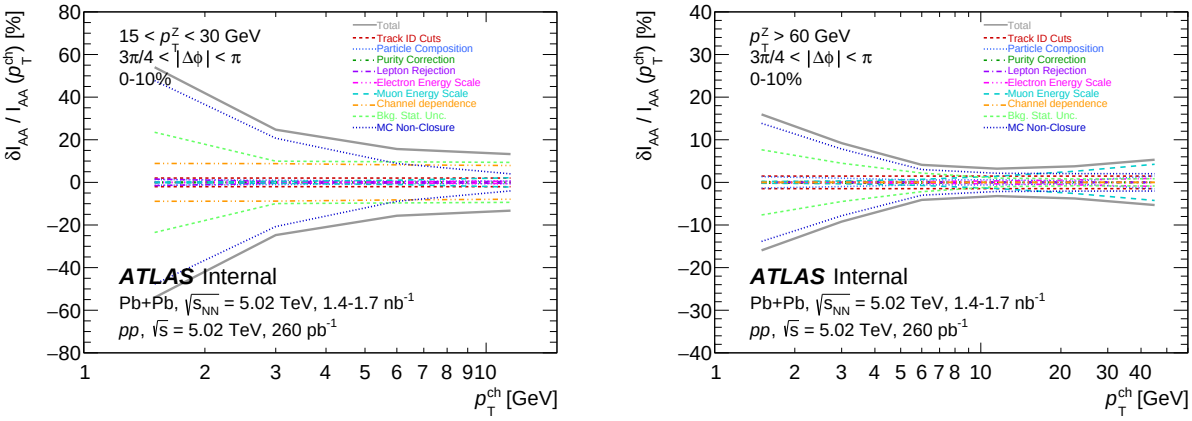


(a) pp, $p_{\mathrm{T}}^{Z} = 15$–30 GeV **(b)** pp, $p_{\mathrm{T}}^{Z} > 60$ GeV

(c) 0–10%, $p_{\mathrm{T}}^{Z} = 15$–30 GeV **(d)** 0–10%, $p_{\mathrm{T}}^{Z} > 60$ GeV

Figure 4.41: Relative uncertainties on the UE subtracted track yield as a function of $p_{\mathrm{T}}^{\mathrm{ch}}$ are shown for different p_{T}^{Z} bins: **(a,c)** $p_{\mathrm{T}}^{Z} = 15$–30 GeV, **(b,d)** $p_{\mathrm{T}}^{Z} > 60$ GeV) in **(a,c)** pp and **(b,d)** 0–10% Pb+Pb collisions. Each source is shown as a dashed line and the quadrature sum as grey lines.

Most of the uncertainty sources are treated as correlated between the numerator and denominator. This includes the track identification, particle species composition, fake rate normalization, lepton-track associations, and lepton energy scale. Statistical uncertainties are, of course, uncorrelated, though the channel dependence (which was observed to be worse in the Pb+Pb) and particularly the non-closure uncertainties are characteristically distinct between the Pb+Pb and pp, and so are treated as uncorrelated. Consequently the final I_{AA} ratio uncertainties are dominated by the non-closure at low-$p_{\mathrm{T}}^{\mathrm{ch}}$, but other sources, such as the muon energy scale, dominate the systematic uncertainties at high-$p_{\mathrm{T}}^{\mathrm{ch}}$. However, we reiterate that in the final measurement,



(a) 0–10%, $p_{\mathrm{T}}^{Z} = 15$–30 GeV **(b)** 0–10%, $p_{\mathrm{T}}^{Z} > 60$ GeV

Figure 4.42: Relative systematic uncertainties on I_{AA} as a function of $p_{\mathrm{T}}^{\mathrm{ch}}$ are shown for different p_{T}^{Z} bins: **(a)** $p_{\mathrm{T}}^{Z} = 15$–30 GeV and **(b)** $p_{\mathrm{T}}^{Z} > 60$ GeV) in 0–10% Pb+Pb collisions.

the uncertainties are dominated by the statistical component rather than any of these systematic sources.

Chapter 5

Results of the Z^0-Hadron Correlations Measurement

With all of the analysis validation and proper corrections in hand, we can proceed to look at the final results of the per-Z charged-hadron yield measurement. First, we show the correlation function in azimuth, $Y(\Delta\phi_{hZ})$. Recall it is defined as

$$\frac{d^2Y(p_{\mathrm{T}}^{\mathrm{ch}},\Delta\phi_{hZ})}{dp_{\mathrm{T}}^{\mathrm{ch}}d\Delta\phi_{hZ}} = \left(\frac{1}{N_Z}\right)\left(\frac{d^2N_{\mathrm{ch}}}{dp_{\mathrm{T}}^{\mathrm{ch}}d\Delta\phi_{hZ}}\right). \tag{5.1}$$

The away-side jet peak is expected to be prominently visible in this distribution, so it is important to validate this expectation. In Fig. 5.1, the azimuthally-dependent yields are summarized for charged hadrons in pp and 0–30% central Pb+Pb at low-$p_{\mathrm{T}}^{\mathrm{ch}}$ values 2–4 GeV (left column) and high values > 4 GeV (right column). Each row indicates a different p_{T}^{Z} bin, with $p_{\mathrm{T}}^{Z} > 60$ GeV on top and $p_{\mathrm{T}}^{Z} = 15$–30 GeV on the bottom. In every case, a distinct peak at $\Delta\phi_{hZ} \sim \pi$ is observed; this is the away-side jet peak, and represents the correlated jet yield. In the low-$p_{\mathrm{T}}^{\mathrm{ch}}$ selection, the pp and Pb+Pb distribution shapes appear compatible within the uncertainties. In the high-$p_{\mathrm{T}}^{\mathrm{ch}}$ selection, the Pb+Pb peak is consistently smaller – this is the jet-quenching effect. High-momentum partons shower as they pass through the plasma, dispersing their energy elsewhere in the event. Because the hadron p_{T} spectrum falls steeply as a power law, fewer hadrons in the parton shower are reconstructed within a given $p_{\mathrm{T}}^{\mathrm{ch}}$ bin in Pb+Pb than in pp. Thus, when quenching occurs, high-p_{T} particles migrate to lower p_{T} values, and consequently the quenched yield is less than an unquenched one.

The p_{T}^{Z} dependence of the measurement is novel and pushes jet-quenching measurements to a qualitatively new regime. Even for events with $p_{\mathrm{T}}^{Z} = 15$–30 GeV, the signatures of jet quenching are

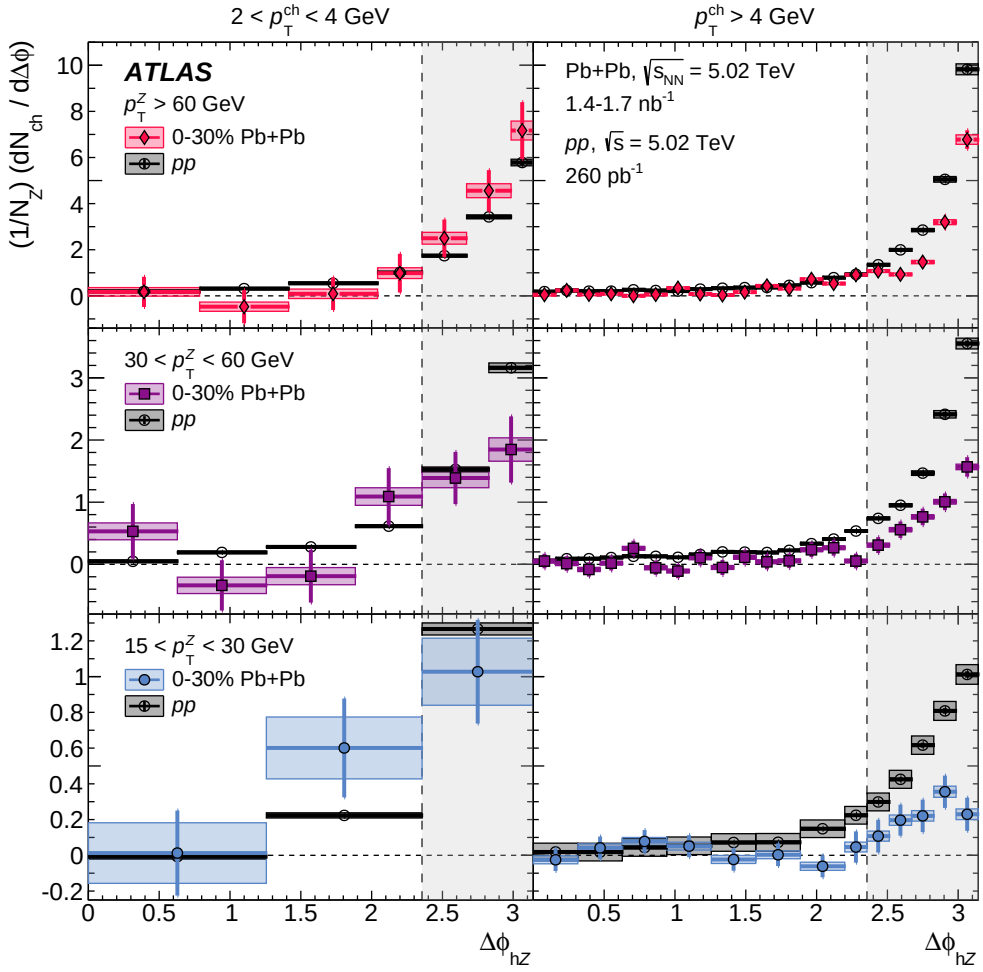


Figure 5.1: The azimuthal distribution of charged hadrons relative to a Z is shown in pp and 0–30% central Pb+Pb. From top to bottom, events are separated by p_{T}^{Z}: >60 GeV, 30–60 GeV, and 15–30 GeV. Charged hadrons with $p_{\mathrm{T}}^{\mathrm{ch}} = 2$–4 GeV are in the left column; those with $p_{\mathrm{T}}^{\mathrm{ch}} > 4$ GeV are on the right. The shaded region indicates $\Delta\phi_{hZ} > 3\pi/4$.

unmistakable. This demonstrates that the dynamics of jet quenching persist into a regime where models of soft particle dynamics (such as hydrodynamics) become relevant.

The jet peak is found to be strongest opposite the Z in the approximate range $\Delta\phi_{hZ} > 2.5$. As a choice, we therefore integrate the yield over the window $\Delta\phi_{hZ} > 3\pi/4$, denoted by the shaded area.[1] This allows us to look at the yield differentially in $p_{\mathrm{T}}^{\mathrm{ch}}$. Simultaneously, the yield was also measured differentially in the dimensionless variable $x_{hZ} \equiv p_{\mathrm{T}}^{\mathrm{ch}}/p_{\mathrm{T}}^{Z}$, which is more sensitive to the

[1] A tighter choice like $\Delta\phi_{hZ} > 7\pi/8 \approx \pi - 0.4$ would be more comparable with jet fragmentation measurements because the window width in ϕ would be similar to the very frequently used jet radius of $R = 0.4$. However the jet can also swing in ϕ due to jet drift [301], so the wider window accounts for this effect.

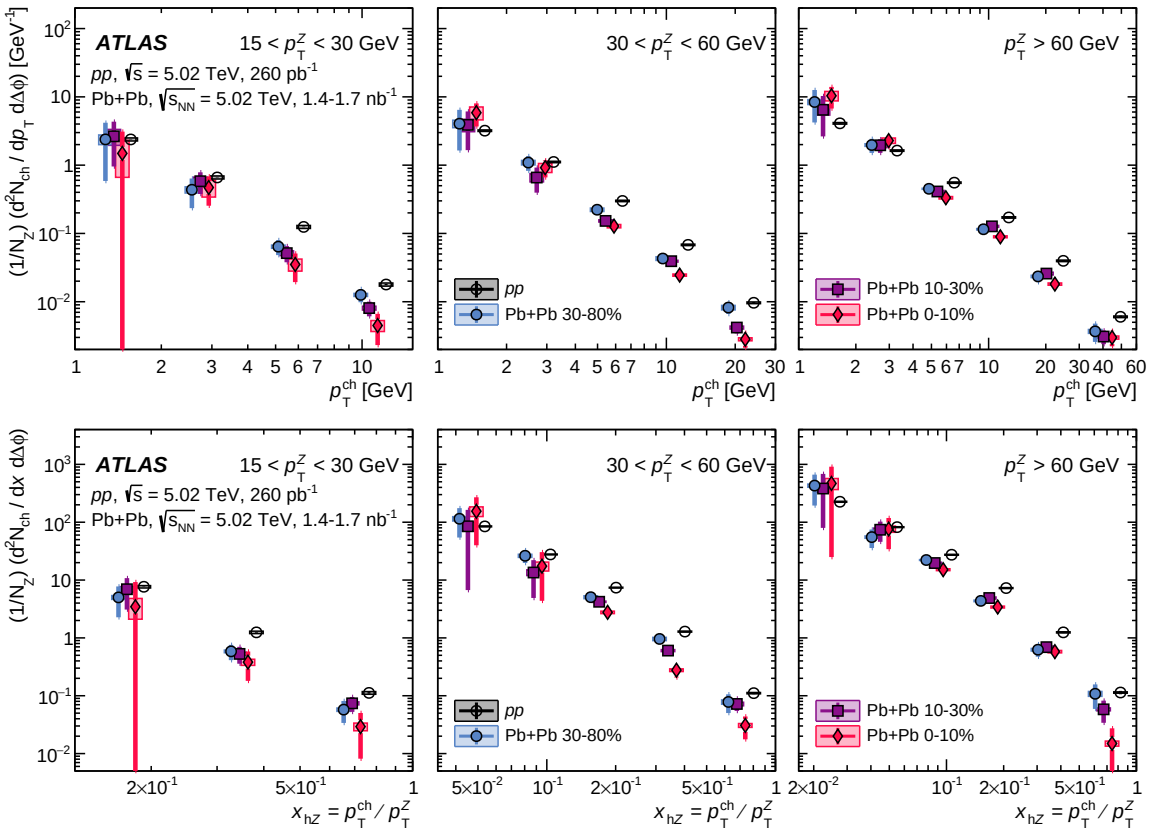


Figure 5.2: The mean yield of charged hadrons opposite a Z boson with $\Delta\phi_{hZ} > 3\pi/4$ is shown versus $p_{\mathrm{T}}^{\mathrm{ch}}$ (top) or $x_{hZ} \equiv p_{\mathrm{T}}^{\mathrm{ch}}/p_{\mathrm{T}}^{Z}$ (bottom). Events are separated based on the p_{T} of the Z, with p_{T}^{Z} = 15–30 GeV on the left and $p_{\mathrm{T}}^{Z} > 60$ GeV on the right. For visibility, each collision system is slightly horizontally offset by a fixed multiplicative factor.

momentum fraction carried by a particular hadron in the parton shower. The resulting spectra are shown in Fig. 5.2. The top row shows the yield versus hadron $p_{\mathrm{T}}^{\mathrm{ch}}$, while the bottom row shows the yield versus the dimensionless x_{hZ} variable. Plots from left to right show p_{T}^{Z} bins in increasing order: p_{T}^{Z} = 15–30 GeV is shown on the far left, and $p_{\mathrm{T}}^{Z} > 60$ GeV is shown on the far right.

The spectra are found to be steeply falling; the distribution is approximately linear on the log-log scale, indicating the aforementioned power law shape. At the highest $p_{\mathrm{T}}^{\mathrm{ch}}$ values, there is a clear separation between the pp (black) and Pb+Pb (assorted colors): the pp points are higher. The reduced phase space allotted to the showering parton due to the energy loss effect pushes high-$p_{\mathrm{T}}^{\mathrm{ch}}$ particles to lower values, increasing the yield of the low-$p_{\mathrm{T}}^{\mathrm{ch}}$ hadrons. These two effects – fewer

high-$p_{\mathrm{T}}^{\mathrm{ch}}$ hadrons and more low-$p_{\mathrm{T}}^{\mathrm{ch}}$ hadrons – combine together to make the spectrum steeper in central Pb+Pb than pp, which is readily apparent just from the spectral shapes shown in Fig. 5.2. Events with the highest momentum Zs $p_{\mathrm{T}}^{Z} > 60$ GeV – the right-most panels – exemplify this effect.

In the bottom row, the dependence of the yield versus x_{hZ} is shown. Immediately, we see that the statistical uncertainties on this measurement are larger than its $p_{\mathrm{T}}^{\mathrm{ch}}$ counterpart, even though the event samples are the same. This is understood as a consequence of the wide p_{T}^{Z} bins coupled with large UE fluctuations event-to-event. Essentially, the UE is strongly dependent on $p_{\mathrm{T}}^{\mathrm{ch}}$ but not so strongly on x_{hZ}. This translates to the statistical uncertainty on $Y(p_{\mathrm{T}}^{\mathrm{ch}})$ being heavily concentrated in the lowest $p_{\mathrm{T}}^{\mathrm{ch}}$ bin because this is where the UE is largest. But, in the second row, the x_{hZ} variable scales the x-axis down by the p_{T}^{Z} value (which itself can vary event-to-event by up to a factor of 2), thereby redistributing the UE-induced uncertainty to a broader set of bins. Future studies could reduce these uncertainties by performing more thorough systematic analyses or simply by taking more data.

5.1 Nuclear Modification

Of course, the end goal is to compare the quenched system (Pb+Pb) with the unquenched vacuum baseline (pp). Because of the power law nature of the spectra, it is difficult to make a quantitative comparison from the yields alone. Therefore we turn to the I_{AA} modification ratios. Recall I_{AA} is defined as

$$I_{\mathrm{AA}}(p_{\mathrm{T}}^{\mathrm{ch}}) = \frac{Y_{\mathrm{PbPb}}(p_{\mathrm{T}}^{\mathrm{ch}})}{Y_{pp}(p_{\mathrm{T}}^{\mathrm{ch}})}. \tag{5.2}$$

I_{AA} is plotted as a function of both $p_{\mathrm{T}}^{\mathrm{ch}}$ and x_{hZ} in Fig. 5.3. As before, the top row shows $I_{\mathrm{AA}}(p_{\mathrm{T}}^{\mathrm{ch}})$ and the bottom row shows $I_{\mathrm{AA}}(x_{hZ})$. Events are broken into centrality and p_{T}^{Z} categories, with panels from left to right showing events with increasing p_{T}^{Z}, and each Pb+Pb centrality shown with a different color and marker style.

Here the consequence of energy loss is on full display. In the regimes $p_{\mathrm{T}}^{\mathrm{ch}} \gtrsim 3$–$4$ GeV and $x_{hZ} \gtrsim 0.03$, a suppression of charged hadrons is consistently and systematically observed across all

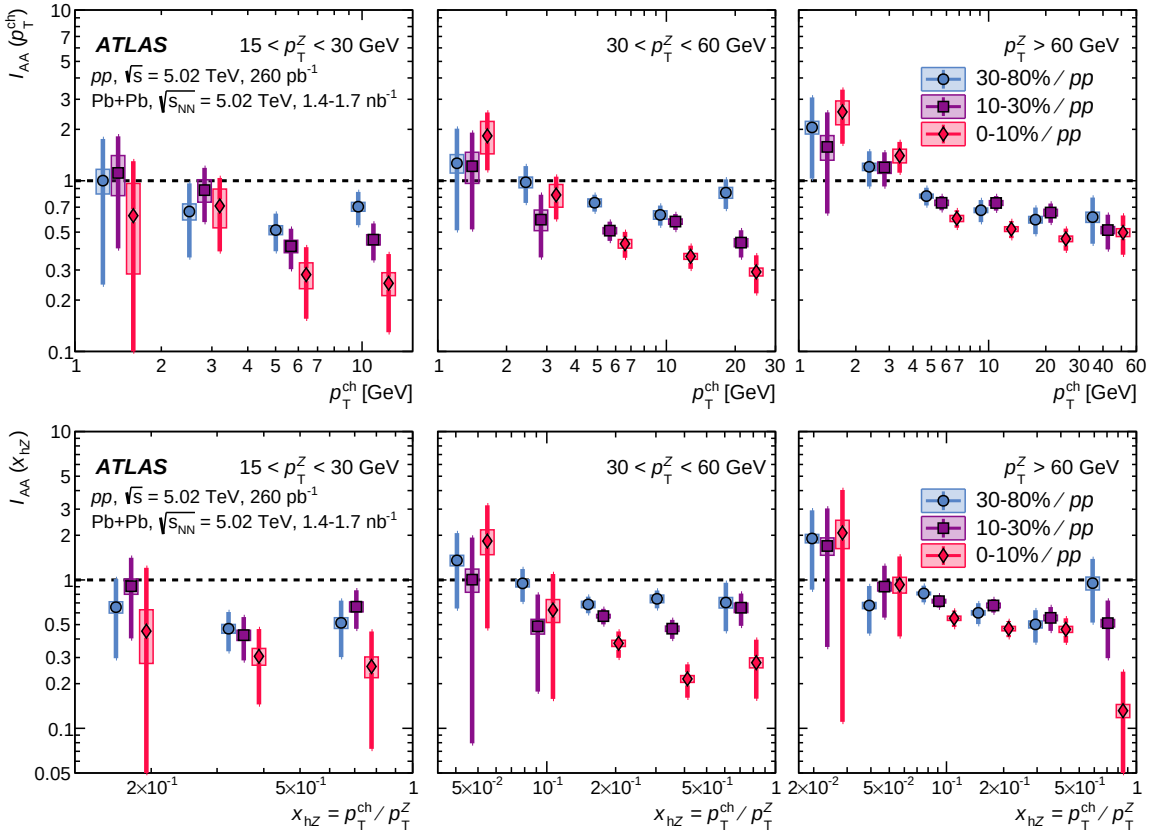
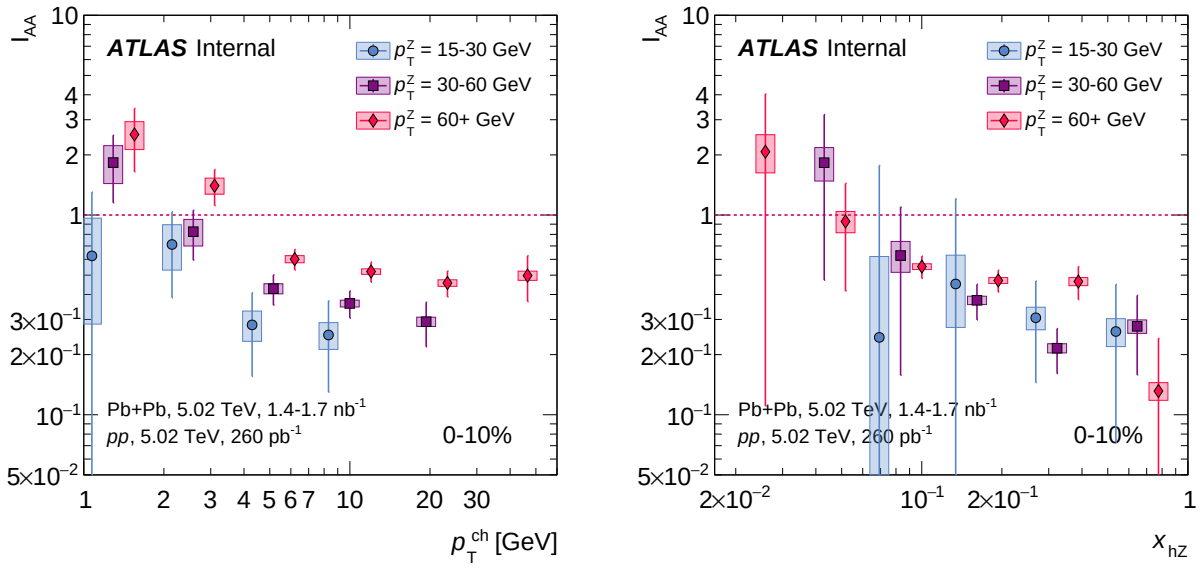


Figure 5.3: Nuclear modification ratio of Z-tagged charged-hadron yields I_{AA} for charged hadrons opposite a Z boson by $\Delta\phi_{hZ} > 3\pi/4$ versus $p_{\mathrm{T}}^{\mathrm{ch}}$ (top) or $x_{hZ} \equiv p_{\mathrm{T}}^{\mathrm{ch}}/p_{\mathrm{T}}^{Z}$ (bottom). Events are separated based on the p_{T} of the Z, with $p_{\mathrm{T}}^{Z} = 15$–30 GeV on the left and $p_{\mathrm{T}}^{Z} > 60$ GeV on the right. For visibility, each centrality selection is slightly horizontally offset by a fixed multiplicative factor.

of the Pb+Pb selections. Partons that would normally give rise to these final-state hadrons instead are forced to fragment into lower momentum hadrons, which may be observed more frequently relative to the vacuum baseline. At low-$p_{\mathrm{T}}^{\mathrm{ch}}$ and x_{hZ}, hints of this enhancement are observed, notably in central Pb+Pb where energy loss is greatest. This observation has important implications which will be further discussed later in the context of jet-quenching theory.

The p_{T}^{Z} dependence – examined in Fig. 5.4 – is also striking. In the left panel, charged hadrons opposite a low-p_{T} Z are consistently more suppressed than those in a high-p_{T}^{Z} event. This observation is consistent with the picture that the parton virtuality – which scales with p_{T}^{Z} in the leading order picture – is affecting the energy loss process. Thus in the right panel, if we rescale



(a) $I_{\mathrm{AA}}(p_{\mathrm{T}}^{\mathrm{ch}})$ **(b)** $I_{\mathrm{AA}}(x_{hZ})$

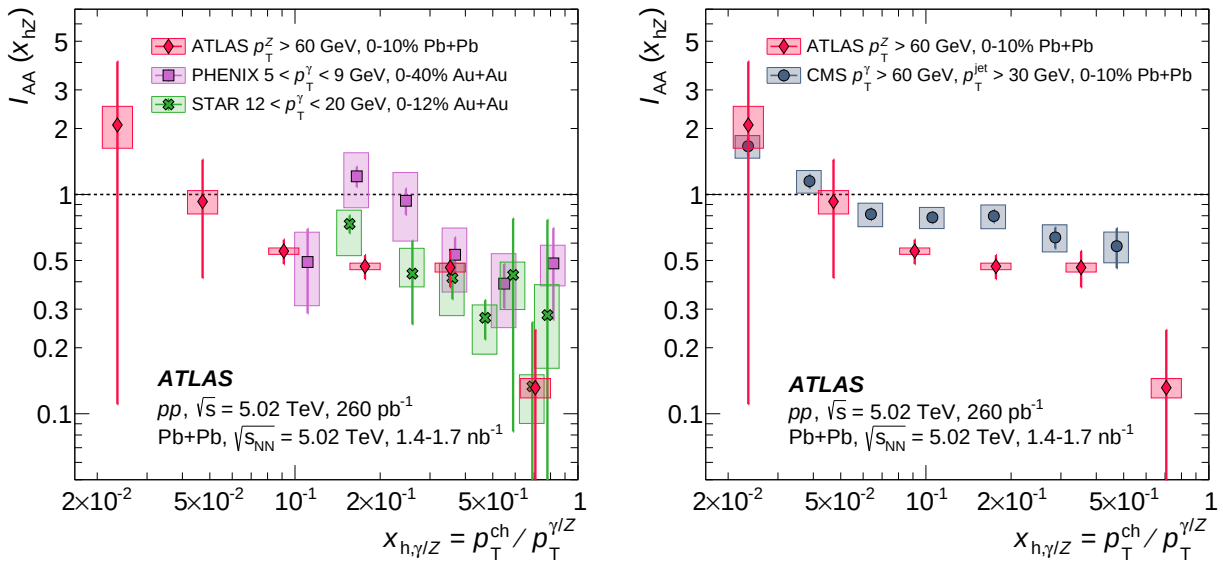
Figure 5.4: Z-tagged charged-hadron I_{AA} in 0–10% Pb+Pb collisions across p_{T}^{Z} bins (different colors and marker styles) as a function of **(a)** $p_{\mathrm{T}}^{\mathrm{ch}}$ and **(b)** x_{hZ}. For visibility, each centrality selection is slightly horizontally offset by a fixed multiplicative factor.

the hadron p_{T} by the Z momentum, then the data appears to align on a common curve. This strongly suggests z-scaling of the energy loss, where z represents the p_{T} fraction relative to the initial parton, $z = p_{\mathrm{T}}^{\mathrm{ch}}/p_{\mathrm{T}}^{\mathrm{parton}}$. Recalling the discussion from Chapter 2 on splitting functions, then if the quenching is the manifestation of modified in-medium splitting functions, the energy loss would be primarily a function of the momentum fraction z. In the calibrated Z-hadron picture, the best estimate for z is in fact x_{hZ}, so this observation is consistent with the modified splitting function scenario. This approach breaks down, however, as we approach the medium temperature scale $\sim \Lambda_{\mathrm{QCD}}$ where nonperturbative effects become important. Consequently, we expect I_{AA} to deviate from x_{hZ}-scaling in the low-x regime. With the large uncertainties, however, it is not currently possible to test for this deviation.

5.2 Comparisons to γ-tagged Data

While the Z-hadron correlation function is only accessible in LHC programs due to the high required Q^2, the overarching vector boson + jet ($V+$jet) physics program has a rich history dating to the early 2010s at RHIC in the $\gamma+$jet channel. The only differences between the two channels are the possible inclusion of Drell-Yan in Z production (which, as previously stated, can be suppressed via minimum transverse momentum cuts) and the relatively harder scatterings required to produce Z bosons. It is possible that this latter difference can lead to a slightly modified selection of incoming states in the final measurement compared to the $\gamma+$jet case, and therefore the population of final-state partons might be slightly modified correspondingly. In short, the fraction of gluon-initiated versus quark-initiated jets in Z-tagged versus γ-tagged events could be slightly different due to the modified Q^2. Though, both partons should be quenched, and even high-p_{T} γ events require a large virtuality so that the production mechanism is well-established to be perturbative. Regardless, if there is a strong virtuality dependence, the Z boson channel offers an insight to this. With these points in mind, it is therefore interesting to compare our findings with similar $\gamma+$jet channel measurements.

A suite of comparisons to both RHIC and LHC data are shown in Fig. 5.5. First, the left panel shows the comparison to PHENIX [274] and STAR [276] γ-tagged hadron data. These data sets are shown with the purple and green markers, respectively. Because of the different calibrated probe, the x-axis represents $x_{h\gamma} = p_{\mathrm{T}}^{\mathrm{ch}}/p_{\mathrm{T}}^{\gamma}$ for the RHIC data, while the ATLAS data uses x_{hZ}. The physics interpretation of this variable is similar, however. Because of the lower RHIC collision energy, the PHENIX and STAR results only cover the range $x_{h\gamma} \gtrsim 0.1$, below which hydrodynamics begins to dominate. In the high-x tail, the ATLAS measurement is consistent with STAR $\gamma+$jet data, including the strong depletion in the range $x_{h,\gamma/Z} > 0.5$. Some tension can be seen against the PHENIX data (notice that the PHENIX points are slightly higher than the ATLAS points), however the PHENIX centrality interval 0–40% includes more peripheral events, where presumably there is less quenching.



(a) Comparison to RHIC data **(b)** Comparison to CMS data

Figure 5.5: (a) Comparison of Z-tagged I_{AA} to PHENIX (purple) [274] and STAR (green) [276] γ-tagged data. **(b)** Comparison to CMS data (dark blue) [112]. Note that the CMS data requires the presence of a 30 GeV jet, and the PHENIX event selection is somewhat different from the ATLAS and STAR measurements.

In the right panel, a comparison to CMS γ-tagged jet fragmentation function data [112] is shown in dark blue. Recall from Chapter 1 that the definition of the fragmentation function $D_{\mathrm{jet}\to h}$ is very similar to Y:

$$D_{\mathrm{jet}\to h}(x_{h\gamma}) = \frac{1}{N_{\mathrm{jet}}} \frac{dN_{\mathrm{ch}}}{dx_{h\gamma}}, \tag{5.3}$$

and is measured as a function of $x_{h\gamma}$, akin to the RHIC data (at least for the CMS data shown here). More precisely, Fig. 5.5 compares the I_{AA} from this study to the ratio of fragmentation functions $R_{D(x_{h\gamma})}$ in Pb+Pb versus pp,

$$R_{D(x_{h\gamma})} = \frac{D_{\mathrm{PbPb}}(x_{h\gamma})}{D_{pp}(x_{h\gamma})}. \tag{5.4}$$

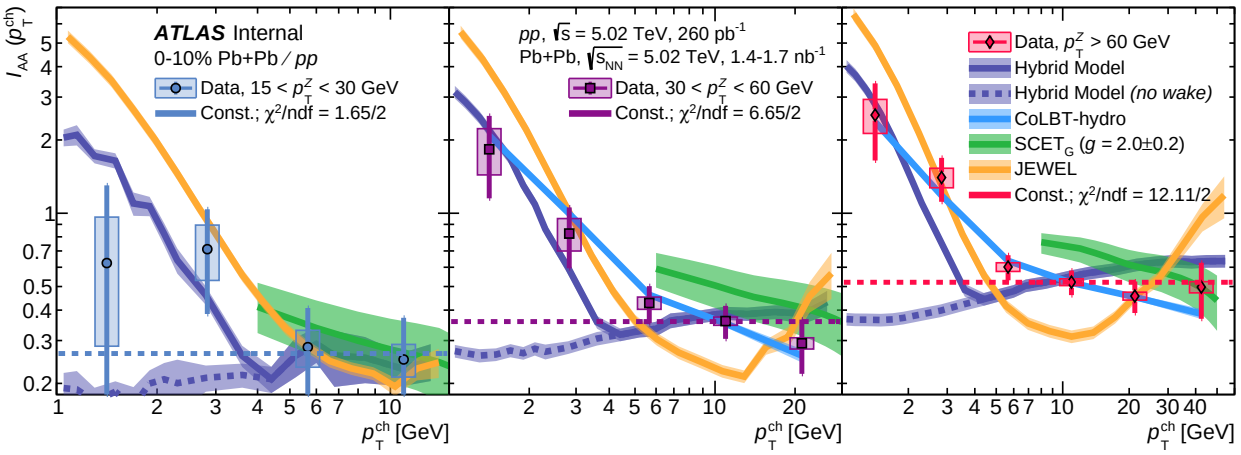
At the LHC, the entire hard scattering is more boosted than at RHIC, and therefore both ATLAS and CMS can push to the regime $x_{h,\gamma/Z} \gtrsim 0.015$. However, it is the high-x regime which is of interest here, where the impact of the jet selection bias is highlighted. Note that the analysis details nearly match: the vector boson has $p_{\mathrm{T}} > 60$ GeV and the events are 0–10% Pb+Pb at

5.02 TeV. The key difference is that while the CMS measurement requires the particles to lie within the cone of an $R = 0.4$ jet meeting $p_{\mathrm{T}}^{\mathrm{jet}} > 30$ GeV, the ATLAS study presented here does not impose this requirement, and instead all particles $\Delta\phi_{hZ} > 3\pi/4$ are considered. With this in mind, we find that for $x_{h,\gamma/Z} \gtrsim 0.05$, the CMS points are above the ATLAS points. In other words, jet fragmentation functions are less suppressed than inclusive hadron yields. Thus, if you require a jet, you anti-select on heavily quenched scenarios. While this may seem trivial, it exemplifies the important point that when our probe is related to our event topology, we reduce our sensitivity to the physics we want to study. Of course, the pitfall to the inclusive hadron approach is the much larger irreducible UE background fluctuations which increase the uncertainties at low-x_{hZ} values.

5.3 Implications for Jet-Quenching Models

Finally, we compare the results against jet-quenching models in Fig. 5.6. These panels show both the data and various model comparisons for each p_{T}^{Z} bin (from left to right, 15–30 GeV, 30–60 GeV, and > 60 GeV) in 0–10% Pb+Pb collisions. Even on the logarithmic scale, the suppression of high-p_{T} hadrons above 3–4 GeV is stark in all of the models shown. Moreover, the transition to a low-p_{T} enhancement is matched in all models with medium backreaction effects, stressing the importance of including this effect for the description of the jet-quenching phenomenon. In particular, the Hybrid Model increases by a factor ~ 10 at the low end of the range when the jet wake is included, and is within one standard deviation of the lowest $p_{\mathrm{T}}^{\mathrm{ch}}$ datum in each panel. High-$p_{\mathrm{T}}^{\mathrm{ch}}$ behavior in this model doesn't quite match the data; however as p_{T}^{Z} is lowered, the model comes more in agreement with the data.

The Jewel model also reproduces the qualitative trends in the data, and also predicts a high-$p_{\mathrm{T}}^{\mathrm{ch}}$ enhancement that is not observed. In the literature [157], this is understood as a hardening of the jet core. Conceptually, the argument is that two-body parton-parton cross section decreases as the incident high-p_{T} parton rises in energy, and therefore the only surviving high-p_{T} hadrons are the ones that don't scatter. As such, the yield of high-p_{T} hadrons is biased towards the less quenched jets. In traditional jet fragmentation functions, where the hadron p_{T} is compared against



(a) $p_{\mathrm{T}}^{Z} = 15$–30 GeV **(b)** $p_{\mathrm{T}}^{Z} = 30$–60 GeV **(c)** $p_{\mathrm{T}}^{Z} > 60$ GeV

Figure 5.6: Comparison of the Z-tagged charged-hadron I_{AA} with jet-quenching models, including the Hybrid Strong/Weak Coupling model (with and without the jet wake) [163, 165, 181], a coupled Linear Boltzmann Transport and hydrodynamics model (CoLBT-hydro) [176, 302], calculations for the Z-tagged hadron invariant yields in soft collinear effective theory with Glauber gluons [152, 160, 303, 304], and the pQCD-based JEWEL model [148, 156, 157] with medium-recoils included. Model uncertainties are all statistical, except for the $\mathrm{SCET_G}$ prediction, which varies the jet-medium coupling by $\Delta g = \pm 0.2$. Each panel shows a different p_{T}^{Z} bin in 0–10% Pb+Pb events (compared to the pp baseline): **(a)** $p_{\mathrm{T}}^{Z} = 15$–30 GeV, **(b)** $p_{\mathrm{T}}^{Z} = 30$–60 GeV, and **(c)** $p_{\mathrm{T}}^{Z} > 60$ GeV. Horizontal dashed lines indicate a constant fit to the data, with test statistic χ^2 per degree of freedom reported on each panel.

the quenched jet p_{T}, this can lead to an enhancement because the denominator becomes smaller, but the numerator remains effectively unchanged. In short, the high-p_{T} tracks are more collimated within the jet core. However, when the tag is a calibrated Z boson, it is unclear how this generates an enhancement ($I_{\mathrm{AA}} > 1$) rather than a return to unity ($I_{\mathrm{AA}} = 1$), as the Z is color-neutral and unquenched. Two-dimensional jet fragmentation functions [278] may offer further insight to this issue.

$\mathrm{SCET_G}$ is also effective at matching the high-$p_{\mathrm{T}}^{\mathrm{ch}}$ suppression, though the nominal parton-medium coupling $g = 2.0$ is systematically biased towards an insufficient energy loss. Although the prediction can only be compared with 2–3 points per panel, with all panels combined, the shape of the theory curve matches astonishingly well to the trend in data. Increasing the coupling to $g \approx 2.2$ (the lower bound on the uncertainty shown in the figure) should result in a remarkably

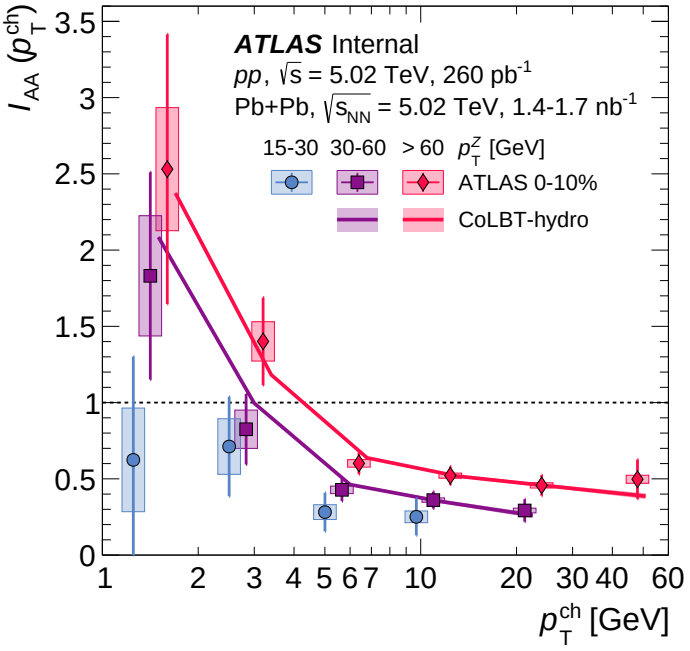


Figure 5.7: Comparison of the Z-tagged charged-hadron I_{AA} with a coupled Linear Boltzmann Transport and hydrodynamics model (CoLBT-hydro) [176, 302]. Model uncertainties are statistical. Each color and marker style shows a different p_{T}^{Z} bin in 0–10% Pb+Pb events (compared to the pp baseline). For visibility, points are slightly horizontally offset by a fixed multiplicative factor.

close agreement. This indicates that SCET$_{\mathrm{G}}$ is a powerful effective theory tool for describing radiative processes.

Finally, CoLBT-hydro reproduces the data fully in the center and right panels (it is not provided in the 15–30 GeV bin). Because of the good agreement, this comparison is highlighted further in Fig. 5.7. Recall that this approach treats the jet and medium as a single coevolving system, albeit a semiclassical one. This is perhaps the most conceptually appealing approach as the system should realistically be treated in a unified way. Despite its success, we point out that this model is actually a *post*-diction (not a *pre*-diction), and should be treated with care.[2] The statistical uncertainties appear too small and constant with $p_{\mathrm{T}}^{\mathrm{ch}}$, against expectation, as a model with a coevolving jet and medium should, in principle, have a similar $p_{\mathrm{T}}^{\mathrm{ch}}$-dependence to the uncertainties in data.[3] Moreover, a model this successful should provide a full set of systematic

[2] If free parameters in the model are tuned to match the data, then the agreement is artificially constructed.

[3] Even if the background can be perfectly subtracted, the uncertainties should grow with $\sqrt{Y(p_{\mathrm{T}}^{\mathrm{ch}})}$ as $p_{\mathrm{T}}^{\mathrm{ch}}$ is

uncertainties to allow a closer level of scrutiny. A subsequent publication by the authors [178] in fact shows modestly higher uncertainties on the prediction than the ones provided to ATLAS (as are shown here). Ultimately, it is our objective as scientists to prove our theories wrong, and without a complete understanding of their accuracy, we hinder ourselves.

Although the quenching effect is significant above $p_{\mathrm{T}}^{\mathrm{ch}} \sim 4$ GeV, the uncertainties below this cut are larger and therefore it is also of interest to quantify the significance of their apparent enhancement. In addition to jet-quenching model fits, a simple constant suppression model is also shown as a dashed line. The constant is evaluated as the average of all points with $p_{\mathrm{T}}^{\mathrm{ch}} > 4$ GeV. A test statistic χ^2 per degree of freedom is then calculated from the two points with $p_{\mathrm{T}}^{\mathrm{ch}} < 4$ GeV. Thus, this test checks for how compatible the low-$p_{\mathrm{T}}^{\mathrm{ch}}$ points are with being suppressed. Because the χ^2/ndf values are large in the center and right panels (both have at least χ^2/ndf > 3), it is unlikely that the low-$p_{\mathrm{T}}^{\mathrm{ch}}$ yields are suppressed by the same magnitude as the high-$p_{\mathrm{T}}^{\mathrm{ch}}$ points.

5.4 Key Messages

In summary, there are a few key takeaway messages from this measurement:

(1) There is a strong suppression of high-p_{T} hadrons opposite a Z boson, and a corresponding enhancement at low-$p_{\mathrm{T}}^{\mathrm{ch}}$. The suppression is indicative of partonic energy loss, while the enhancement is sensitive to energy redistribution and medium backreaction effects.

(2) x_{hZ}-scaling of I_{AA} is observed, and no low-x deviations are observed within current uncertainties. This is consistent with picture that medium-modified parton splittings play a significant role in energy loss phenomena.

(3) Jet fragmentation function measurements are inherently biased towards situations with less energy loss. The CMS-to-ATLAS comparison in the right panel of Fig. 5.5 means that the jet fragmentation function $D_{\mathrm{jet}\to h}(z)$ cannot serve as a proxy for $D_{p\to h}(z)$ because of the difference in event topologies. Even in vacuum, there is a distinction between $D_{\mathrm{jet}\to h}(z)$

lowered. Thus, uncertainties at low-$p_{\mathrm{T}}^{\mathrm{ch}}$ should be much larger than at high-$p_{\mathrm{T}}^{\mathrm{ch}}$.

as an "average" $D_{p\to h}(z)$ because this association requires a model for the population of partons p to average over. The point here is that in medium, there is also the jet-quenching bias.

(4) A form of medium backreaction is necessary in jet-quenching models. The rise in $I_{\rm AA}$ with decreasing $p_{\rm T}^{\rm ch}$ is an artifact of high momentum partons imparting their energy to the medium. The characteristic scale of 3–4 GeV separates the wake from the in-medium equivalent of vacuum jet fragments. In the future, jet-quenching studies are expected to narrow in on these effects. Recent theoretical developments have demonstrated that the low-$p_{\rm T}^{\rm ch}$, near-side yield should offer a surprising degree of sensitivity to the wake [178].

Chapter 6

Constraining Final-State Energy Loss in p+Pb

The per-trigger yield of charged hadrons introduced in the previous chapter can be more broadly used as a probe of jet quenching in a variety of situations. In this chapter, we turn to the case of small systems, which exhibit qualitatively unique phenomena. Collisions of large nuclei such as Pb+Pb, Au+Au, or Xe+Xe create nuclei-sized droplets of Quark-Gluon Plasma (QGP) in which quarks and gluons exist in a deconfined state. Small system collisions such as p+Pb at the LHC or d+Au at RHIC were not traditionally expected to form a long-lived QGP droplet, though they are now understood to exhibit some characteristics of QGP formation. For example, elliptic flow is a phenomenon which translates initial-state geometric anisotropies into global momentum-space correlations via pressure gradients in large systems, and has been observed across a variety of small systems [185, 305, 306], begging the question of whether a QGP is indeed formed in these collisions.

While hydrodynamic behavior is consistently observed, small collision systems show little to no indications of any quenching effect. Nuclear modification to hadronic [186, 187, 307, 308] and jet cross sections [189, 190] or jet structure [277, 309] is close to unity in p+Pb collisions for hadronic probes, indicating minimal energy loss is occurring, at least within current uncertainties. However, particles at high-p_{T}, i.e., those associated with high-Q^2 scatterings in the initial collision, have been found to exhibit elliptic flow-like momentum correlations [185]. In Pb+Pb collisions, differential energy loss is one common explanation for high-p_{T} momentum anisotropy (see Chapter 2 for a review) [310]. If a QGP droplet is indeed formed in p+Pb, and differential energy loss is the mechanism giving rise to a high-p_{T} v_2, one might expect measurable changes to jet production and

structure, depending on the phase lifetime. Such explanations however fail as they predict a large suppression of high-p_{T} particles, i.e. $R_{p\mathrm{Pb}} < 1$, as in Ref. [311], for example, where $R_{p\mathrm{Pb}}$ is defined as

$$R_{p\mathrm{Pb}} = \frac{1}{\langle N_{\mathrm{coll}} \rangle} \frac{d^2\sigma_{p\mathrm{Pb}}/dp_{\mathrm{T}}dy}{d^2\sigma_{pp}/dp_{\mathrm{T}}dy}. \tag{6.1}$$

If no modifications are observed such that jets appear to be fragmenting in vacuum, then the properties of these droplets can be constrained, including their spatial and temporal extent or possible temperature profile, since, at least empirically, the droplet can be described hydrodynamically [75].

One particular experimental challenge is that to measure $R_{p\mathrm{Pb}}$, not just in minimum bias collisions but in high-multiplicity events, one has to have a precision estimate of the average number of binary collisions $\langle N_{\mathrm{coll}} \rangle$ or equivalently the nuclear thickness seen by the projectile $\langle T_{p\mathrm{Pb}} \rangle$. Such estimates within the Monte Carlo Glauber framework have more sizable uncertainties in p+Pb compared with Pb+Pb, and the multiplicity selection (depending on the pseudorapidity and p_{T} range of the selection) can bias these values – see Refs. [186, 312, 313] for detailed discussions.

Since previous measurements already constrain jet-quenching effects in p+Pb collisions to be small, the measurement detailed in this chapter is carried out with the goals of (1) introducing minimal dependence on the specific event categorization and on Monte Carlo Glauber matching, and (2) focusing on providing a precision constraint on jet quenching in the regime where momentum anisotropies are known to exist. To that end, we focus on the per-jet normalized charged-hadron yield Y as a function of p_{T} measured in pp and p+Pb (which is functionally similar to the per-Z normalized charged-hadron yield)

$$\frac{d^2Y}{dp_{\mathrm{T}}^{\mathrm{ch}} d\Delta\phi_{h,\mathrm{jet}}} = \left(\frac{1}{N_{\mathrm{jet}}}\right)\left(\frac{dN_{\mathrm{ch}}}{dp_{\mathrm{T}}^{\mathrm{ch}} d\Delta\phi_{h,\mathrm{jet}}}\right). \tag{6.2}$$

To identify modification to the spectra associated with the presence of the Pb ion, the p+Pb-to-pp ratio $I_{p\mathrm{Pb}}$ is then measured

$$I_{p\mathrm{Pb}} = \frac{\langle Y_{p\mathrm{Pb}} \rangle}{\langle Y_{pp} \rangle}. \tag{6.3}$$

As compared with the nuclear modification factor $R_{p\mathrm{Pb}}$, the quantity $I_{p\mathrm{Pb}}$ does not explicitly depend on $\langle N_{\mathrm{coll}} \rangle$ or equivalently the nuclear thickness seen by the projectile $\langle T_{p\mathrm{Pb}} \rangle = \langle N_{\mathrm{coll}} \rangle / \sigma_{pp}^{\mathrm{inel.}}$.

Moreover, the yield of charged hadrons can be precisely determined at moderate p_{T} values $\sim$ 5–50 GeV due to the excellent track momentum resolution and relative abundance of these particles compared to very high-energy jets. Akin to the previous chapter, we define an underlying event via the uncorrelated yield of charged hadrons, which is extracted from a similar mixed event modeling procedure.

In addition, we utilize the energy deposited in the zero degree calorimeter (ZDC) in the Pb-going direction to sort events into categories with varying N_{coll} central tendencies. (Note that all N_{coll} binary collisions occur between the same proton projectile and assorted nucleons within the Pb nucleus.) Using the ZDC is different to other p+Pb measurements which have utilized the total energy in the Pb-going forward calorimeter $\Sigma E_{\mathrm{T}}^{\mathrm{FCal,Pb}}$ or the track multiplicity around mid-rapidity ($|\eta| < 2.5$) [185, 189, 314]; both of these quantities are known to have correlations that can bias the Monte Carlo Glauber estimators [186, 312]. This effectively eliminates the autocorrelation bias between the centrality and our jet-quenching metrics, enhancing the accuracy of the final jet-quenching constraint.

Because many of the technical details for this measurement are similar to their counterparts in Chapter 4, this chapter will focus on aspects that are unique to this jet-centric measurement. In that spirit, the chapter is organized in the following way. After a summary of the basic data selection (Sec. 6.1), we discuss how the ZDC can be uniquely used to measure centrality in p+Pb (Sec. 6.2). We then proceed to document the jet calibration sequence and necessary cross-validation studies (Sec. 6.3). The next two sections – the main results of the track reconstruction studies (Sec. 6.4) and the underlying event subtraction (Sec. 6.5) – are similar to studies in the previous chapter, so we summarize the main points and differences relevant to the p+Pb. Next, we perform an unfolding procedure to deconvolve detector resolution smearing (Sec. 6.6). Finally, we summarize the main uncertainties (Sec. 6.7). The main results will be presented subsequently in Chapter 7.

Overview of Data Sets			
System (Year)		p+Pb (2016)	pp (2017)
Good runs list (GRL)		`data16_hip5TeV.periodAllYear_DetStatus-v105-pro22-13_Unknown_PHYS_HeavyIonP_All_Good.xml`	See Table 4.1
Minimum Bias (MB) trigger		`HLT_mb_sptrk_L1MBTS_1`	`HLT_mb_sptrk`
Jet (J50) trigger		`HLT_j50_ion_L1J10`	`HLT_j50_L1J15`
$\mathcal{L}_{\text{int}}$	Total (after vetoes)	$355.981\,\mu\text{b}^{-1}$	$256.824\,\text{pb}^{-1}$
	Sampled by MB Trig.	$25.1334\,\mu\text{b}^{-1}$	$2.655\,13\,\text{nb}^{-1}$
	Sampled by J50 Trig.	$355.544\,\mu\text{b}^{-1}$	$3.574\,87\,\text{pb}^{-1}$

Table 6.1: Overview of the data sets used for this measurement, with good runs lists, triggers, and integrated luminosities after event vetoes. Data for pp is repeated from Chapter 4.

6.1 The Basics: Data Sets & Event Selection

The 2016 5.02 TeV p+Pb data set recorded by ATLAS is optimal for this type of measurement for a few reasons. The first is that the 5.02 TeV low-μ pp data set from 2017 serves as an excellent QCD vacuum reference. No reference data set exists to accompany the larger 8.16 TeV p+Pb data set, immediately limiting any precision study of jet quenching with this data. Though the 5.02 TeV data set has a significantly smaller integrated luminosity than the 8.16 TeV data by a factor of ~ 500, jets with moderate p_{T} ($p_{\text{T}}^{\text{jet}}$) are abundant, so we will see that the final measurement is systematically-limited at most charged-hadron p_{T} (p_{T}^{ch}), and only becomes statistically limited in the high-$z = p_{\text{T}}^{\text{ch}}/p_{\text{T}}^{\text{jet}}$ tails. Data on very high-p_{T} momentum-space correlations is limited anyways, so jets with the highest transverse momenta are not the focus – it is really the intermediate values that we hope to access. Lastly, the ZDCs are well-calibrated for this ultra-low-pileup p+Pb data set, thus enabling a centrality classification unique to this data [315].

Thus, this analysis uses six out the of seven runs from the 2016 p+Pb run at 5.02 TeV.[1] The beams during these runs were oriented such that the proton (beam 1) was traveling from the A side to the C side of the detector (i.e., positive η to negative η) and the lead ion (beam 2) was traveling in the reverse direction. This configuration features a nucleon-nucleon center-of-mass

[1] Run 312649 is excluded because it contributes negligible luminosity and lacks a level 1 ZDC trigger in the C-side (thus preventing calibration of the A-side ZDC).

Run no.	312649	312796	312837	312937	312945	312968	314199
Peak $\langle\mu\rangle$ ($\times 10^{-3}$)	5.246	0.3147	0.2342	0.2309	0.1480	0.2504	0.2825
Run no.	340644	340683	340697	340718	340814	340849	340850
Peak $\langle\mu\rangle$	4.031	3.975	4.086	4.021	4.318	4.014	3.993
Run no.	340910	340925	340973	341027	341123	341184	
Peak $\langle\mu\rangle$	3.969	1.999	2.998	3.217	3.364	2.048	

Table 6.2: Peak pile-up rates $\langle\mu\rangle$ are shown for each of the 2016 p+Pb runs (top row) and 2017 pp runs (bottom two rows) at 5.02 TeV meeting the GRL.

boost of $\Delta y = -0.465$ due to a mismatch in beam energies: beam 1 had an energy of 4 TeV while beam 2 had an energy per-nucleon of $\frac{Z}{A} \times 4$ TeV $\simeq 1.58$ TeV. Table 6.2 shows the highest instantaneous pile-up rate $\langle\mu\rangle$ for each run used in this analysis.[2] Also used are the 13 low-μ pp runs passing GRL cuts at 5.02 TeV taken in 2017. Details for the sampled luminosity of each data set, as well as good runs lists, can be found in Table 6.1.

Event selection

As usual, events must pass the GRL. These are listed in Table 6.1. Although not included in the GRL by default, reconstructed events that trigger an error in the LAr, Tile, or SCT are not used in this analysis and are rejected at this stage. After the GRL, events are selected if they fire one of the triggers of interest – this will be discussed momentarily.

To reduce the impact of pile-up, vertexing is also considered for event selection. In each event, the primary vertex is defined to be the vertex with the largest $\sum p_{\mathrm{T}}^2$ over all associated tracks. Others are denoted as pile-up or possibly secondary vertices, in the event of a particle decay. Pile-up vertices – defined as all other vertices with at least 2 tracks – indicate separate but simultaneous collisions, and may be found elsewhere in the detector. Jets and tracks should both be associated with the same collision. Jets in particular are tough to associate with a particular vertex without looking at tracking information, so the easiest solution is to outright reject events with pile-up vertices. Furthermore, to ensure the tracking reconstruction is well-behaved, events

[2] Technically, the highest $\langle\mu\rangle$ value is reported over the run. Because of beam losses, events near the beginning of the run usually exhibit more pile-up of average than events later in the run.

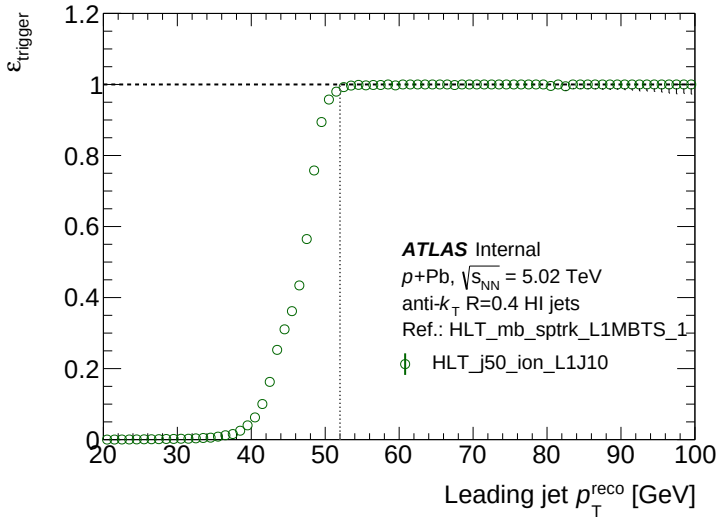


Figure 6.1: The trigger efficiency of the `HLT_j50_ion_L1J10` trigger used in 5.02 TeV p+Pb collisions is plotted as a function of the offline, post-calibration leading jet p_{T}. The vertical dashed line indicates the first bin where the efficiency reaches 99%.

must also have their primary vertex z coordinate within 150 mm of the origin. Unlike the Z-hadron correlations measurement, no out-of-time pile-up cut is applied, since the collision rate is extremely small in this p+Pb data set. No calorimeter-based pile-up cut is performed in pp, though the single primary vertex cut is also applied.

One unique feature of this analysis is the use of the ZDC energy percentiles as a proxy for collision centrality. However, events with a total ZDC energy of exactly 0 often indicate issues with the pulse-fitting in the ZDC calibration code. These events can originate from any centrality, so they must be rejected. Specifically, we reject any event in data with A-side ZDC energy $\Sigma E^{\mathrm{ZDC,A}} == 0$.

Triggers

Two main types of triggers are used in this analysis. First, events with a hard scattering (i.e., jet production) are selected using single jet triggers in the "Main" data streams. The p+Pb beam configuration had very low collision rates, so the `HLT_j50_ion_L1J10` is the first unprescaled single jet trigger in this data set, and is therefore the primary jet trigger used in p+Pb. In the

pp data, the collision rate is much higher (typical μ values range from 1 to 4) so the relevant jet trigger was prescaled, meaning it only records a small fraction of events. The trigger we use is the `HLT_j50_L1J15`, as this matches the kinematic selection as in the p+Pb case. With the prescale, this trigger records roughly 1.4% of triggered events. Both the `HLT_j50_ion_L1J10` and `HLT_j50_L1J15` (referred to as "`j50`" triggers) are designed to fire when an anti-k_t $R = 0.4$ jet with $p_{\mathrm{T}} > 50$ GeV is detected. The primary difference between the two is that the "ion" trigger is allowed to perform an underlying event subtraction at the HLT level. These triggers are used to sample events in which there is a jet above 60 GeV. To validate this choice of offline p_{T} threshold, Fig. 6.1 shows the efficiency of the p+Pb `j50` trigger, as well as the point at which it is 99% efficient, which is found to be ~ 52 GeV. (The efficiency of the pp trigger has been studied extensively as well [310, 316].) In both cases, the trigger is fully efficient in the selected kinematic range.

Events with lower momentum transfer Q^2 (i.e., lower momentum jets) are also of interest in this analysis. To select on events with a jet above $p_{\mathrm{T}} > 30$ GeV, no suitable single jet trigger (i.e., no jet trigger with ample phase space to avoid turn-on biases) is available, so events are selected from minimum bias (MB) data. In p+Pb, the `HLT_mb_sptrk_L1MBTS_1`, which requires a hit in the MBTS at level-1 and the `sptrk` algorithm to fire at the HLT level is used. In pp collisions, MB events are selected with the very similar `HLT_mb_sptrk` trigger which only lacks the level-1 MBTS seed (it is instead seeded by the random L1 trigger `L1_RD0_FILLED`). A more complete discussion of the MB trigger algorithms can be found in Chapter 3.

In pp, there is a known mistiming of the `L1_RD0_FILLED` trigger which seeds the `HLT_mb_sptrk` trigger at the HLT stage. This has been linked to a minor inefficiency of the `HLT_mb_sptrk` trigger at high jet p_{T}. To avoid this effect, a timing cut is recommended and applied in this analysis. Events firing this trigger must have a timing within 10 ns of the start of the bunch crossing to enter the analysis.

Overview of MC Samples

Description	System	Filter	N_{events}	σ[nb]	$\varepsilon_{\text{filter}}$
Pythia dijets	pp	JZ0	8M	6.7890×10^{7}	9.9713×10^{-1}
		JZ1	8M	6.789×10^{7}	2.8748×10^{-3}
		JZ2	8M	6.3996×10^{5}	4.2952×10^{-3}
		JZ3	8M	4.7195×10^{3}	5.2994×10^{-3}
		JZ4	8M	2.6602×10^{1}	4.5901×10^{-3}
		JZ5	8M	2.2476×10^{-1}	2.1846×10^{-3}
Pythia dijets + boost	p+Pb	JZ1	2M	6.789×10^{7}	2.8689×10^{-3}
		JZ2	2M	6.3996×10^{5}	4.295×10^{-3}
		JZ3	2M	4.7197×10^{3}	5.3006×10^{-3}
Pythia dijets + boost & Data Overlay	p+Pb	JZ0	4M	6.789×10^{7}	9.9726×10^{-1}
		JZ1	2M	6.789×10^{7}	2.8689×10^{-3}
		JZ2	2M	6.3996×10^{5}	4.295×10^{-3}
		JZ3	2M	4.7197×10^{3}	5.3006×10^{-3}
Hijing	p+Pb	–	5M	–	–

Table 6.3: Detailed information about the Monte Carlo samples used in this analysis. JZ slices sample different regions of the total pp cross-section and must be reweighted by $\sigma \times \varepsilon$ when combined. The Hijing sample is not combined with any other sample and so this quantity is not reported.

Monte Carlo samples

Simulated collisions are important for characterizing and correcting for detector effects in this analysis. Proton-proton collisions with the presence of a high-p_{T} jet are generated with the Pythia generator. These are generated with the A14 ATLAS tune and NNPDF23LO pdf set [317]. Dijet events are filtered using the JZ*R04 ("JZ") filters which select events containing an anti-k_t $R = 0.4$ jet in specific p_{T} ranges.

Proton-lead collisions are simulated in two ways. The first is the data overlay, in which Pythia events are simulated at the truth-level as described above, but are embedded in real, minimum bias p+Pb collisions. Only the Pythia pp configuration is used (rather than a combination of pp and pn) because this analysis is not expected to be sensitive to isospin effects. Then the full, combined events are reconstructed and analyzed. In this way the higher p+Pb detector occupancy

is accounted for in a straightforward manner which does not introduce any generator bias. However, the rate of fake tracks cannot be estimated from the data overlay because real, data tracks will be incorrectly identified as fake tracks. This motivates the second sample of events without the use of data overlay, which are generated with the HIJING heavy-ion event generator [81], which is solely used to categorize the tracking performance (more details can be found in Sec. 6.4).

For the data overlay samples, 2 million events of `JZ1` through `JZ3` are generated due to the minimum jet p_{T} selection and very small integrated luminosity in data. A somewhat larger 4 million event sample of `JZ0` was used to counter the relatively imprecise sampling in the 20−−25 GeV regime, a consequence of upward fluctuations in jet energy response at very low p_{T} below 20 GeV. For this analysis, 48 million previously generated pp dijet events are used, with 8 million events in each `JZ0` through `JZ5`. Though, the `JZ4` and `JZ5` samples cover a very high-p_{T} range that is not studied in this analysis, and thus they are only used for characterizing the jet performance. Lastly, 5 million minimum bias p+Pb HIJING events are used as well. Each sample is documented in Table 6.3.

MC weighting

The `JZ*04` sampling scheme is useful for increasing high-Q^2 statistics and thus introduces event-selection biases that must be corrected for. The standard method to do this is to reweight events according to their relative probability of occurring. Events in a given `JZ` slice are assigned an event weight w_{evt}

$$w_{\mathrm{evt}} = \frac{\sigma \times \varepsilon_{\mathrm{filter}} \times \mathcal{L}}{N_{\mathrm{evt}}} \tag{6.4}$$

where σ is the generator cross section, $\varepsilon_{\mathrm{filter}}$ is the filter efficiency, and N_{evt} is the number of events. Recall that $\mathcal{L}$ is the luminosity of the data sample and cancels out the units dependence, though it is constant for a given collision system. This analysis uses $\mathcal{L}_{pp} = 3.574\,87\,\mathrm{pb}^{-1}$ and $\mathcal{L}_{p+\mathrm{Pb}} = 0.355\,545\,\mathrm{nb}^{-1}$, which represent the prescale-corrected luminosities of the respective $p_{\mathrm{T}}^{\mathrm{jet}} > 50$ GeV triggers as returned by `lumicalc`.

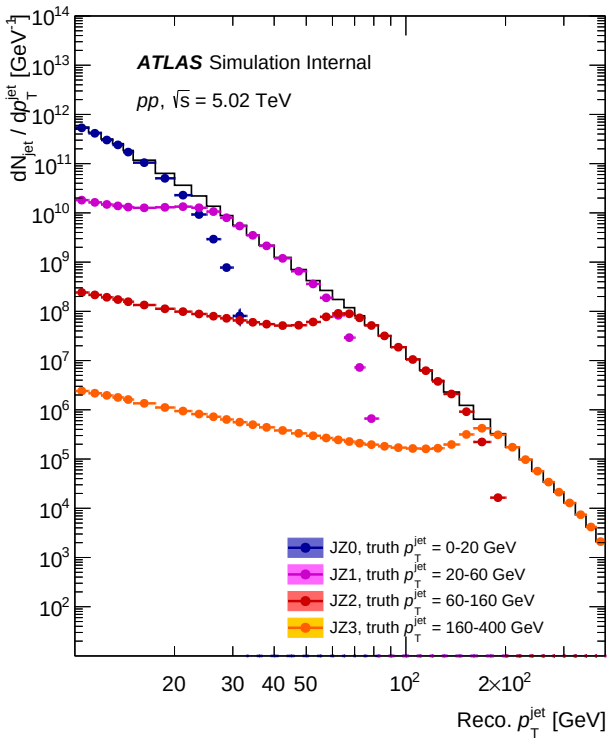


Figure 6.2: The p_{T} spectrum of reconstructed jets in simulated pp data is plotted, broken into different `JZ` samples in various colors. The sample-integrated spectrum is shown in black.

To avoid sampling the same truth jet p_{T} range with multiple samples (this can lead to issues with de-weighted statistical uncertainties) events should only be used in each `JZ` slice if the leading truth jet is within the given p_{T} range. The appropriate anti-k_t $R = 0.4$ truth jet p_{T} ranges can be found in Table 6.4. However due to resolution effects, the `JZ` slices overlap slightly as a function of reconstructed p_{T}; this can be seen for example in the MC samples with pp conditions in Fig. 6.2.

It is well-known that, because the `JZ0` and `JZ1` are produced with Pythia `SoftQCD` while `JZ2` and above are produced with Pythia `HardQCD`, there is a slight discontinuity in the inclusive, truth-level jet spectrum at 60 GeV, even with the nominal `JZ` weights applied. To smooth this discontinuity, the truth spectrum is fitted to 2 power law functional forms covering the region 25–50 GeVand 70–120 GeV. The `JZ2` and above samples are then weighted by an additional factor 0.859275, which is taken from the ratio of these functional fits at 60 GeV.

	JZ0	JZ1	JZ2	JZ3	JZ4	JZ5
Min. p_{T} [GeV]	0	20	60	160	400	800
Max. p_{T} [GeV]	20	60	160	400	800	1300

Table 6.4: Sampled anti-k_t $R = 0.4$ truth jet p_{T} ranges for each JZ slice. Events in a given slice should only be used if their leading truth jet is within the specified p_{T} range to avoid drawing the same region of the truth spectrum from multiple samples.

6.2 Centrality

In large system collisions, such as Pb+Pb, recall that the volume of the QGP droplet created is related to the impact parameter or "centrality" of the collision. Many observables sensitive to QGP interactions depend on the centrality of the collision, so controlling for this parameter is of primary interest. Typically the energy at forward rapidities (in ATLAS the total energy in the forward calorimeter $\Sigma E_{\mathrm{T}}^{\mathrm{FCal}}$) is demonstrated to strongly correlate with collision centrality via fitting to a particle production model. This allows event-by-event estimates of the collision centrality based on the $\Sigma E_{\mathrm{T}}^{\mathrm{FCal}}$ value.

In small systems such as p+Pb, centrality is still known to play a important role. We emphasize here that though the term "centrality" is still used colloquially, the more important factor is the number of binary nucleon-nucleon collisions, or alternatively the total charged-particle multiplicity, rather than impact parameter *per se*. For example, the cross sections for high-Q^2 processes scale with the number of binary nucleon-nucleon collisions (N_{coll}) due to purely geometrical effects [95, 190, 318]. In these systems the $\Sigma E_{\mathrm{T}}^{\mathrm{FCal}}$ value in the ion-going direction still correlates with collision centrality and can be used as a proxy in a similar fashion [319, 320]. However such projectile-on-target collision systems leave much of the ion relatively intact and therefore not nearly as much energy is deposited in the forward calorimetry as large systems. This allows centrality biases to be more prominent in p+Pb than Pb+Pb collisions. In particular, jet production at mid-rapidity has been shown to auto-correlate with forward particle production in certain event generators and therefore the presence of a jet has the potential to shift the $\Sigma E_{\mathrm{T}}^{\mathrm{FCal}}$ distribution independently of the true collision centrality [312]. Consequently, centrality estimates in events with a jet can

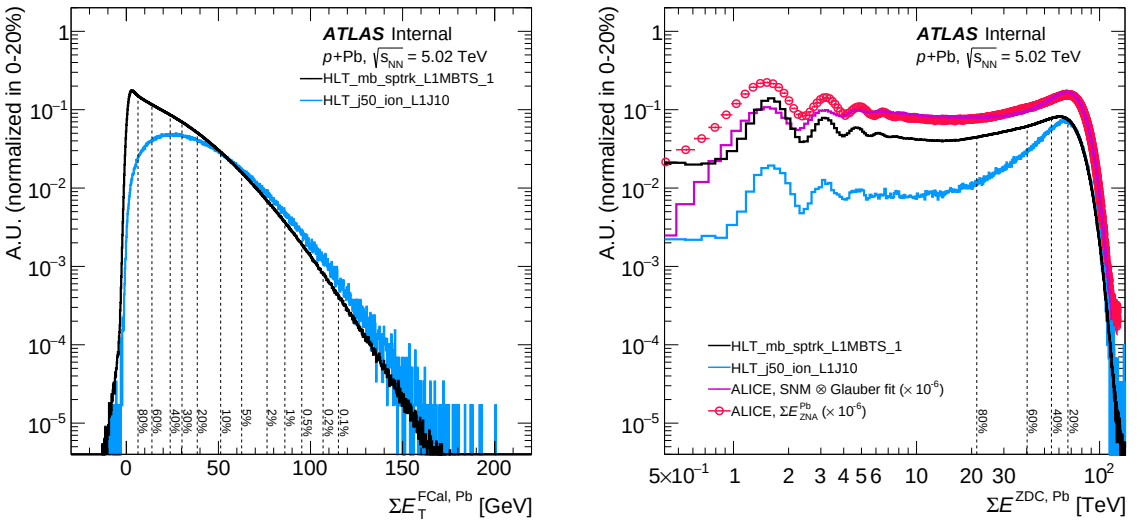
potentially be overestimated via this method. As explained earlier, one goal of this measurement is to minimize such biases.

In the Run 2 p+Pb data at 5.02 TeV, the pile-up rate was low ($\mu \lesssim 0.01$) so the zero-degree calorimeter (ZDC) energy scale has been successfully calibrated for 6 out of the 7 runs (the runs used in this analysis) [315]. The remaining run, 312649, cannot be calibrated due to its lack of a C-side L1 ZDC trigger, though it contributes negligible luminosity. This detector, in particular the A-side ZDC due to the beam configuration, is sensitive to energy deposited by spectator neutrons emitted during the breakup of the ion that are nearly co-linear with the ion beam. Therefore the total energy deposited in the ZDC ($\Sigma E^{\mathrm{ZDC,Pb}}$) is typically expressed in TeV.

Figure 6.3 shows the two centrality variables in both minimum bias and jet-triggered p+Pb events. The left plot shows the distributions of $\Sigma E_{\mathrm{T}}^{\mathrm{FCal,Pb}}$ and the right shows distributions of $\Sigma E^{\mathrm{ZDC,Pb}}$. Each plot is normalized to the 20% highest value events and the bottom panels show the ratio of jet-triggered events to minimum bias. The single peaks seen are the $\Sigma E^{\mathrm{ZDC,Pb}}$ distribution at low values represent the signal left by integer numbers of neutrons in the ZDC (convolved with the calorimeter response). Because each neutron carries an average of 1.58 TeV, the position of the single neutron peak is used to calibrate the energy scale of the ZDC modules [315, 321]. The corresponding energy resolution of the ZDC in the 5.02 TeV, low-μ p+Pb data was determined to be about $\sigma_E/E \approx 22\%$ [315].

The ZDC energy can be challenging to relate to N_{coll} as it depends on the number of spectator nucleons from the Pb-nucleus, and also on the nuclear fragmentation pattern since some spectator neutrons will be bound into larger, electrically charged nuclei (e.g., He, C, O, etc.) and thus be swept away from the ZDC by the LHC magnets. We highlight that we do not require the quantitative value of $\langle N_{\mathrm{coll}} \rangle$ to calculate $I_{p\mathrm{Pb}}$; however, it is important to have an estimate of this value to enable theoretical calculation comparisons with the experimental measurements.

The ALICE Collaboration has shown by fitting the energy in a similar detector (the "ZNA" or A-side neutron ZDC) from minimum bias p+Pb collisions to a neutron emission model, that the centiles of the ZNA distribution roughly but monotonically map onto N_{coll} values [186]. In this



(a) $\Sigma E_{\mathrm{T}}^{\mathrm{FCal,Pb}}$ **(b)** $\Sigma E^{\mathrm{ZDC,Pb}}$

Figure 6.3: Distribution of **(a)** $\Sigma E_{\mathrm{T}}^{\mathrm{FCal,Pb}}$ and **(b)** $\Sigma E^{\mathrm{ZDC,Pb}}$ values in events triggering on a **high-p_{T} jet (light blue)** or **minimum bias (black)**. The ATLAS distributions are normalized in the 20% high-side tail. In each plot, vertical lines denote percentiles of the distribution derived from the minimum bias events. The $\Sigma E^{\mathrm{ZDC,Pb}}$ distributions are overlaid with $\Sigma E^{\mathrm{ZNA,Pb}}$ distributions published by ALICE [186], shown in **red**, and their SNM $\otimes$ Glauber model fit in **purple**.

way, the centiles of the ZDC distribution can be used as a complementary definition of centrality unique to p+Pb. Moreover, the physical mechanism explaining the origin of spectator neutrons is unrelated to jet production, and so this centrality metric crucially lacks the aforementioned auto-correlation centrality bias. In this analysis the A-side ZDC centiles are similarly used as the primary indicator of event centrality. The results of the ALICE Glauber-SNM model fit to the ZDC energy distribution, as reported in [186], are listed in Table 6.5. The main idea for the measurement presented here is not to repeat this detailed ALICE analysis; rather, we utilize their published values combined into our planned coarser centrality intervals (i.e., 0–20%, 20–40%, …80–100%). Though values of N_{coll} do not explicitly enter the measurement of $I_{p\mathrm{Pb}}$, and therefore these values do not affect the measurement in any way, they are still useful for theory comparisons where N_{coll} is often viewed as a tuneable parameter.

Now we detail how the ZDC centiles are defined in this analysis. As with FCal centrality studies, events are selected with the p+Pb minimum bias trigger (see Sec. 6.1) and must have ≤ 6

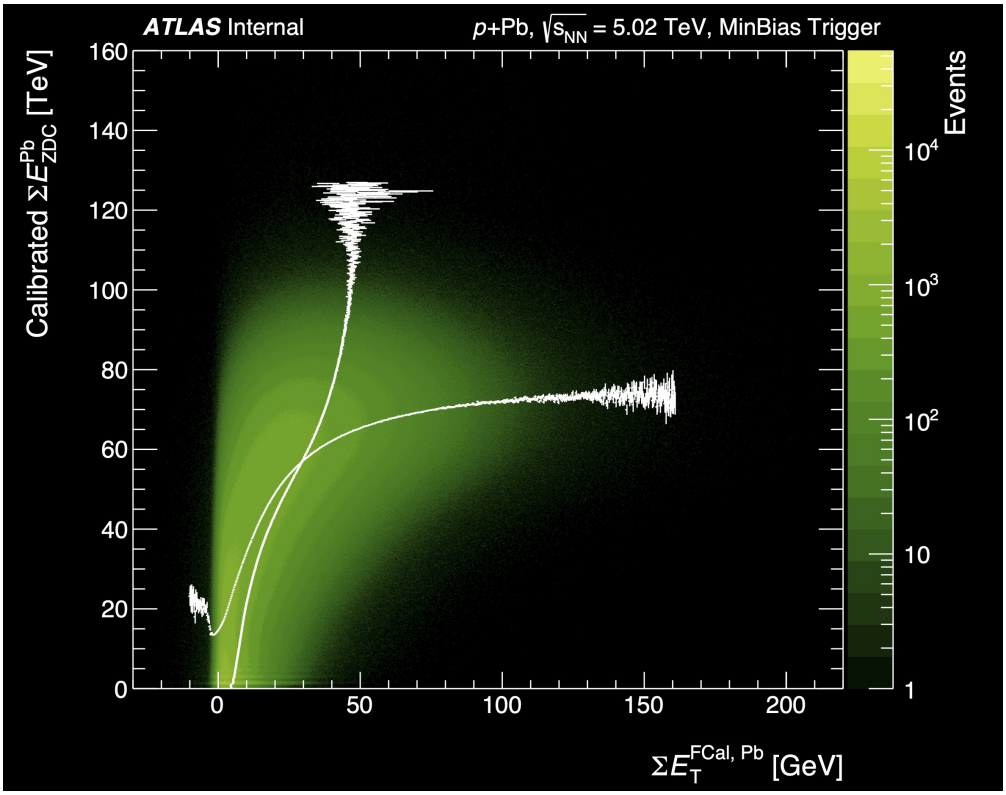


Figure 6.4: 2D correlation plot between A-side $\Sigma E_{\mathrm{T}}^{\mathrm{FCal}}$ and ΣE^{ZDC} in the 5.02 TeV p+Pb data. Profiles along each axis are shown as white curves.

Centile	0–5%	5–10%	10–20%	20–40%	40–60%	60–80%	80–100%	0–100%	0–20%
Max. $\Sigma E_{\mathrm{ATLAS}}^{\mathrm{ZDC}}$ [TeV]	159.875	80.7312	74.8377	67.1273	54.5756	40.1944	21.3314	159.875	159.875
Min. $\Sigma E_{\mathrm{ATLAS}}^{\mathrm{ZDC}}$ [TeV]	80.7312	74.8377	67.1273	54.5756	40.1944	21.3314	0	0	67.1273
$\langle N_{\mathrm{coll}} \rangle_{\mathrm{ALICE}}$	15.7	13.9	12.4	9.99	6.53	3.04	1.24	6.88	13.6
$\sigma_{\mathrm{Glauber}}$	10%	10%	10%	8.8%	6.6%	4.3%	2.0%	8%	10%
σ_{SNM}	7%	5%	2%	2%	4%	4%	8%	–	4%
$\sigma_{\mathrm{Glauber}} \oplus \sigma_{\mathrm{SNM}}$	12.2%	11.2%	10.2%	9%	7.7%	5.9%	8.2%	8%	10.8%

Table 6.5: Centile cuts of the ion-side $\Sigma E^{\mathrm{ZDC,Pb}}$ distribution derived from minimum bias 5.02 TeV p+Pb collisions as measured by ATLAS. Average values of the number of binary collisions (N_{coll}) in each zero-degree neutron calorimeter ("ZNA") centrality as reported by the ALICE Collaboration [186]. Values are extracting by fitting the ZNA distribution to a slow-neutron emission (SNM) model as described in the text. Reported uncertainties on $\langle N_{\mathrm{coll}} \rangle$ due to the Glauber and SNM modeling are repeated, and in the bottom row we compute the quadrature sum assuming the two uncertainties are independent.

tracks associated with any non-primary vertices, as done in [320].

Particular types of diffractive events leave the nucleus completely unaffected, instead exciting the proton, and therefore no signal is measured in the nucleus-side ZDC or FCal across *all* N_{coll} values [319]. Additionally ultra-peripheral (UPC) collisions are not included in the Monte Carlo Glauber model. Such events therefore cannot be mapped onto any value of N_{coll}. Both types of events constitute a background when classifying centrality and should not be included in the distributions shown in Fig. 6.3. The `HLT_mb_sptrk_L1MBTS_1` trigger requirement, which is sensitive to mid-rapidity charged-particle production, generally reduces the rate of these events, though some fraction persists to the analysis level. This can be seen for example in the right plot in Fig. 6.3, wherein a large number of real events are observed to have $\Sigma E^{\text{ZDC,Pb}} = 0$.

In other analyses a level-1 ZDC trigger requirement is typically used to indicate breakup of the nucleus and assist in removing this background. However, this requirement would introduce an auto-correlation effect in the $\Sigma E^{\text{ZDC,Pb}}$ distribution and thus cannot be performed here. Gap cuts are useful for rejecting some of these backgrounds. Diffractive events in particular can leave the proton in an excited state, and are associated with large rapidity gaps in the nucleus-going direction. Consequently, their effect can be reduced by selecting events with no large rapidity gap [319]. In this centrality study, events must have rapidity gap on the nucleus-going side $\Delta\eta_{\text{Pb}} < 1.8$, as defined and motivated in [320].

However no additional cut is performed to reject background events, and so their effect must be considered. Because such processes usually do not fire the ZDC trigger, they will be concentrated around the first bin, near $\Sigma E^{\text{ZDC,Pb}} \sim 0$. We reject events with energy of *exactly* 0 to eliminate events with pulse-fitting errors; this eliminates about 4% of events. Though, this does not necessarily reject all background events; a discussion of persisting UPC backgrounds is provided in Appendix B.1. In short, we find that while some rate of UPC-like events make it to this level of the analysis, they are suppressed by more than a factor of 10 to a negligible fraction when a high-$p_{\text{T}}^{\text{jet}}$ selection is superimposed.

Table 6.5 details the cutoffs for the ZDC-derived centrality percentiles. The main results of this analysis select events in the 0–20% centile for which there is no provided value for $\langle N_{\text{coll}} \rangle$.

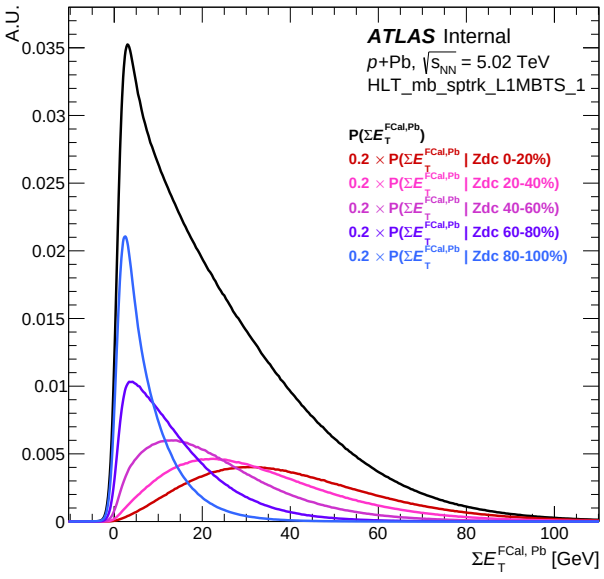


Figure 6.5: Normalized projections of Fig. 6.4 onto $\Sigma E_{\mathrm{T}}^{\mathrm{FCal,Pb}}$ (the x-axis) at 5 different ZDC centile ranges are shown, plus the inclusive selection in black.

Given the estimates for $\langle N_{\mathrm{coll}} \rangle$ by ALICE (detailed in [186] and repeated in Table 6.5), we calculate that in the 0–20% events selected in this analysis

$$\langle N_{\mathrm{coll}} \rangle = 0.25 \times 15.7 + 0.25 \times 13.9 + 0.5 \times 12.4 = 13.6,$$

and the uncertainties, assuming total correlation in $\langle N_{\mathrm{coll}} \rangle$ between centralities, are 10% from the Glauber modeling component, and 4.2% from the SNM component. Though these values do not affect the per-jet yield measurement in any way, they are important for predictions in theory models where N_{coll} is the tune-able parameter for controlling collision centrality.

For performance considerations – particularly with MC studies and in the underlying event estimation procedure – the forward calorimeter transverse energy is still used as a centrality indicator. We highlight that there is no accurate MC simulation of forward neutron production.

Cross-checks

The ZDC centrality definition can be compared to the usual FCal one. Fig. 6.4 shows the 2D correlation plot between the measured ZDC and FCal energies in the ion-going direction. There

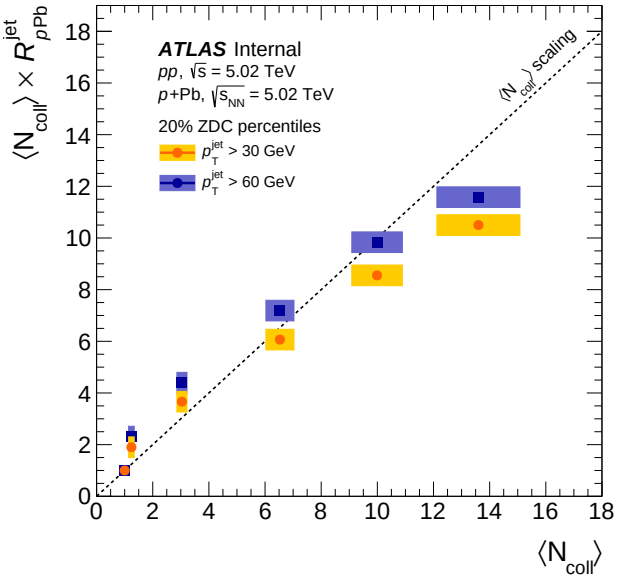


Figure 6.6: The $R_{p\mathrm{Pb}}$ of jets above **30 GeV (orange)** and **60 GeV (blue)** are plotted as a function of $\langle N_{\mathrm{coll}} \rangle$ in each p+Pb ZDC-determined centrality, plus pp at $\langle N_{\mathrm{coll}} \rangle = 1$. Error bars represent the statistical uncertainty (lines) combined with the uncertainty on $\langle N_{\mathrm{coll}} \rangle$ (boxes).

is a rather direct correlation between the two observables and then for $\Sigma E_{\mathrm{T}}^{\mathrm{FCal,Pb}}$ greater than 50–60 GeV the $\Sigma E^{\mathrm{ZDC,Pb}}$ saturates to around 70 TeV. Projections of the ZDC-FCal correlation from Fig. 6.4 are shown Fig. 6.5, where the five different colored distributions show the conditional probability distribution for a particular $\Sigma E_{\mathrm{T}}^{\mathrm{FCal,Pb}}$ value given the percentile range for $\Sigma E^{\mathrm{ZDC,Pb}}$. Events that are identified as central with the ZDC have probability distributions shifted towards higher $\Sigma E_{\mathrm{T}}^{\mathrm{FCal,Pb}}$, and vice versa. This is consistent with the picture that both $\Sigma E^{\mathrm{ZDC,Pb}}$ and $\Sigma E_{\mathrm{T}}^{\mathrm{FCal,Pb}}$ are sensitive to N_{coll}, and that selecting events with higher $\Sigma E^{\mathrm{ZDC,Pb}}$ will select higher N_{coll} events.

To further demonstrate the correlation between N_{coll} and $\Sigma E^{\mathrm{ZDC,Pb}}$, a check was performed of how jet production scales with $\langle N_{\mathrm{coll}} \rangle$. Jets selected for each bin in this analysis were counted in the centrality bins reported in Table 6.5. We then compared the p+Pb result to pp via the nuclear modification factor $R_{p\mathrm{Pb}}$. The results are shown in Fig. 6.6, where the p_{T}-integrated $R_{p\mathrm{Pb}}$ for jets selected in this analysis is shown as a function of the $\langle N_{\mathrm{coll}} \rangle$ values provided by ALICE [186]. We

calculate the $p_{\mathrm{T}}^{\mathrm{jet}}$-integrated nuclear modification factor here via [94, 189]

$$R_{p\mathrm{Pb}} = \frac{N_{p\mathrm{Pb}}^{\mathrm{jet}} \sigma_{pp}^{\mathrm{tot.}}}{\langle N_{\mathrm{coll}} \rangle \, N_{p\mathrm{Pb}}^{\mathrm{MB}} \sigma_{pp}^{\mathrm{jet}}}. \tag{6.5}$$

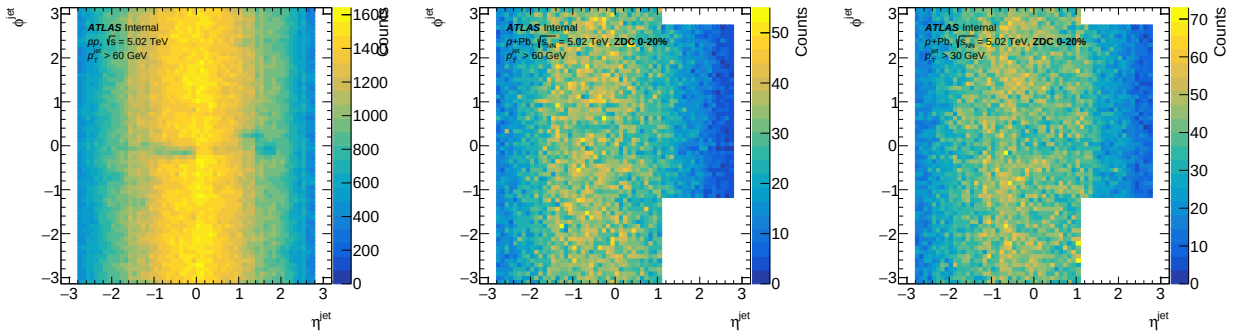
The pp inelastic cross section at 5.02 TeV is taken to be $\sigma_{pp}^{\mathrm{inel.}} = 67.6\,\mathrm{mb}$ [61] and the number of minimum bias events $N_{p\mathrm{Pb}}^{\mathrm{MB}}$ is taken from the number of events firing the minimum bias trigger in that centrality category, scaled to the appropriate luminosity. Thus, we take $N_{p\mathrm{Pb}}^{\mathrm{MB}} = 1129.17065$ per mb^{-1} of luminosity, per 10% of events.

The number of jets in more central p+Pb events is found to roughly scale with $\langle N_{\mathrm{coll}} \rangle$, as seen in Fig. 6.6. A constant trend ("N_{coll} scaling") is drawn for both $p_{\mathrm{T}}^{\mathrm{jet}}$ selections as the dashed 45° line. The right plot shows simply the $R_{p\mathrm{Pb}}$ (i.e. by taking the left plot scaled down by $\langle N_{\mathrm{coll}} \rangle$, i.e. the y-coordinates are divided by the x-coordinates) to check for deviations from linearity. The peripheral p+Pb events show an enhancement, though there are a variety of possible explanations for this. Potential EM processes which occur at rate independent of N_{coll} could be affecting the peripheral bins in particular due to the lower overall jet yield and their tendency to lower $\Sigma E^{\mathrm{ZDC,Pb}}$ values – we investigate these contributions in the next section. It is also likely that the ALICE $\langle N_{\mathrm{coll}} \rangle$ values are too high in central p+Pb and too low in peripheral (this is cited as a possibility in Ref. [186]). In short, observation of this scaling effect indicates that selecting events with higher ZDC energies really does separate events that produce jets more frequently, and therefore tend to higher N_{coll} values.

6.3 The p+Pb Jet Calibration Sequence

Charged hadrons are of primary interest in this measurement, and they are tagged by the presence of a jet measured in the calorimeter. Tagging jets must meet a basic set of requirements for consideration: they must have $p_{\mathrm{T}} > 30$ GeV and lie within the main calorimeter barrel at $|\eta| < 2.8$ (i.e. not lie within the forward calorimeters).

Some jets can originate from uninteresting background processes and affect certain features of the event. To avoid correlating hadrons with such jets, jets are additionally required to satisfy the



(a) pp, $p_{\mathrm{T}}^{\mathrm{jet}} > 60$ GeV **(b)** p+Pb, $p_{\mathrm{T}}^{\mathrm{jet}} > 60$ GeV **(c)** p+Pb, $p_{\mathrm{T}}^{\mathrm{jet}} > 30$ GeV

Figure 6.7: Example (η, ϕ) distributions of accepted jets are shown in **(a)** pp and **(b,c)** p+Pb.

`LooseBad` jet cleaning requirement (with `DoUgly` set to `false`). This is a high efficiency working point designed to reject only 0.5–1% of EMTopo jets in 13 TeV collisions [322]. In our set of simulated pp events at 5.02 TeV, we find that up to 2% of HI jets are rejected by this cut, which is negligibly small.

There is also the issue of the disabled channels in the hadronic end-cap (colloquially referred to as the "disabled HEC" or HEC). During the 2016 p+Pb data-taking a set of channels in the 4^{th} quadrant of the A-side HEC were disabled due to a faulty LV power supply [323]. The affected region in phase space is roughly $(\eta, \phi) \in (1.5, 3.2) \times (-\pi, -\pi/2)$. Because only the electromagnetic calorimeter is fully operational in this region, jets are susceptible to having their response mischaracterized. Moreover jets have angular extent and so jets that are nearby the disabled HEC can also be negatively affected. Therefore jets reconstructed with $(\eta, \phi) \in (1.5 - R, 3.2 + R) \times (\pi - R, \pi] \cup (-\pi, -\pi/2 + R)$ are rejected in this analysis, where $R = 0.4$ is the jet radius. This cuts out jets falling in a rectangular shaped region of (η, ϕ) space.

The net effect is a bias acceptance where, assuming jets in pp and p+Pb have the same pseudorapidity distribution, jets selected in this analysis in p+Pb will be less likely to have pseudorapidity $\eta > (1.5 - R)$ than in pp. Therefore, an area-based acceptance correction should be applied. In p+Pb, jets (and likewise the charged particles correlated with such jets) which lie outside the disabled quadrant but have a compatible pseudorapidity $\eta > (1.5 - R)$ are reweighted by

		Number of selected jets						
Trigger	$p_{\mathrm{T}}^{\mathrm{jet}}$ range	pp	80–100%	60–80%	40–60%	20–40%	0–20%	p+Pb total
MinBias	30–60 GeV	33,590	17,352	33,025	54,173	75,503	91,278	271,331
J50	60–300 GeV	3,230,973	14,418	27,148	43,750	59,134	67,948	212,398

Table 6.6: The numbers of jets in pp and each p+Pb centrality bin for the low-p_{T} and high-p_{T} selections are reported.

w_{jet},

$$w_{\mathrm{jet}} = \frac{2\pi}{2\pi - \left(\frac{\pi}{2} + 2R\right)} \approx 1.6 \text{ for } R = 0.4. \tag{6.6}$$

Because jets are distributed uniformly in detector ϕ – which has been verified in the pp to the 1% level – this quantity represents the inverse of the probability that an accepted jet with $\eta > (1.5 - R)$ will also meet the disabled HEC selection criteria, and thus weighting these jets by this factor accounts for the additional acceptance effect.

Fig. 6.7 shows examples of the jet (η, ϕ) acceptance in pp and p+Pb. In addition to the reduced p+Pb acceptance, we also notice that in p+Pb the average jet pseudorapidity is visibly shifted by $\Delta\eta \approx -0.5$, which is expected by the higher beam energy of the proton compared to the ion.

MC-based Calibration

Recall that there are two principal components to the HI jet calibration sequence: the first is the MC-based EM+JES calibration, and the second is the data-driven cross-calibration. Here, we provide an example of the jet calibration sequence for use in 2016 p+Pb data. For the 5.02 TeV pp data used in this measurement, the EM+JES calibration and cross-calibration have been previously derived and studied in extensive detail [256]. However, this calibration cannot be directly applied to the p+Pb without further study. In particular, the EM+JES calibration used for the 5.02 TeV pp cannot be used in the p+Pb due to the possibility of a different average jet response at fixed detector η in the p+Pb compared to the pp. This is a nontrivial effect that arises due to a combination of

- different average detector responses to quark- vs. gluon-initiated jets,

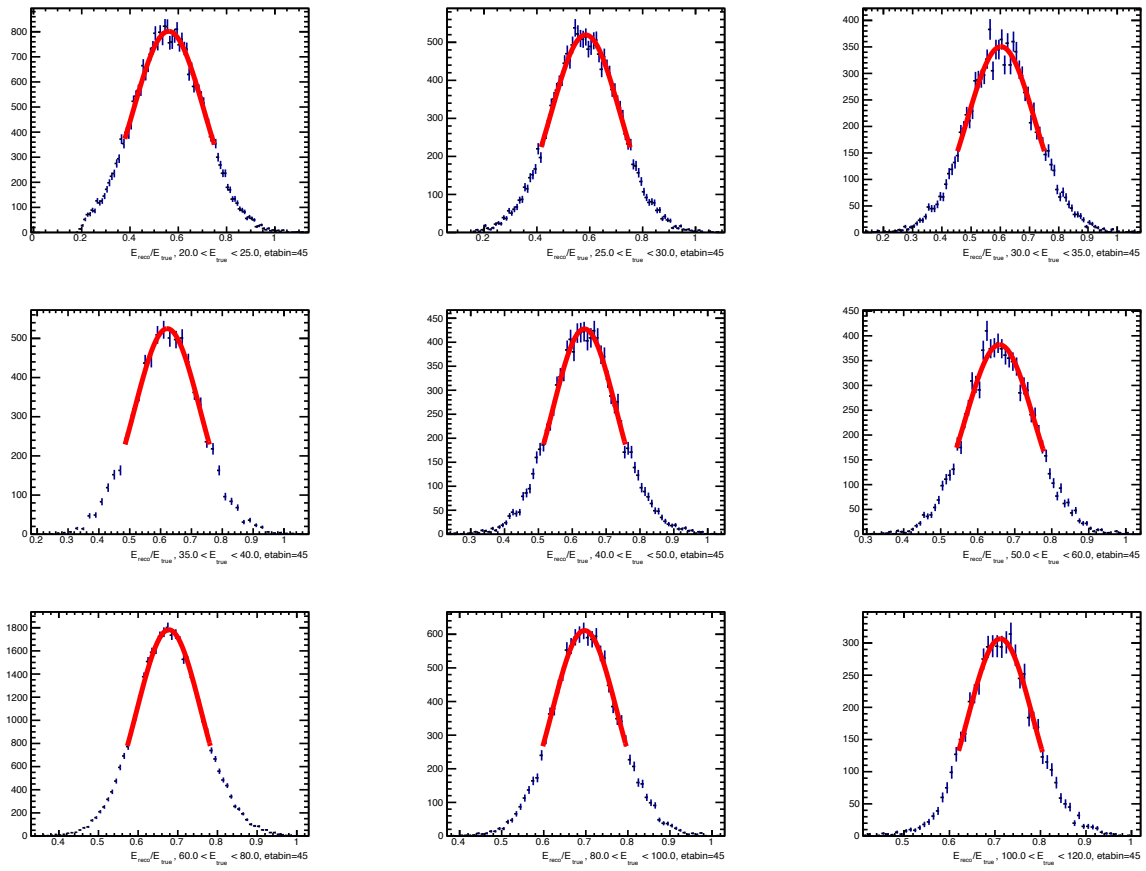


Figure 6.8: Examples of energy response distributions for anti-k_t $R = 0.4$ HI jets in 5.02 TeV collisions with 2016 p+Pb detector conditions are shown. Each panel shows a different truth energy range. Gaussian fits are overlaid as the red curves.

- η dependence of the fraction of jets initiated by a quark (f_q) vs. a gluon (f_g), and
- the center-of-mass boost in the p+Pb.

Therefore a dedicated EM+JES calibration was derived for the p+Pb data. In this section, we show how the numerical inversion (NI) procedure works by considering the p+Pb as a case study. We will use a common set of variables referring to jet energies at various levels of calibration as follows:

- E_{truth} represents the energy of a jet in a simulated collision, as returned by the anti-k_t algorithm run over truth particles.

- $E_{\text{reco.}} = E_{\text{EM}}$ represents the raw, uncalibrated jet energy recovered by the detector. This is the energy deposited via electromagnetic (EM) interactions.
- r denotes the fraction of a jet's energy recovered during the reconstruction, $r = E_{\text{reco.}}/E_{\text{truth}}$.
- $\hat{E}_{\text{truth}}$ represents our best-estimate of the truth-level jet energy.
- $E_{\text{EM+JES}}$ represents the output of MC-based EM+JES calibration sequence. Exclusively in MC, $\hat{E}_{\text{truth}} = E_{\text{EM+JES}}$.

For jets reconstructed by ATLAS, a common software framework is used to perform the NI of simulated jets. Central to the NI process is the conditional probability distribution of reco. jet energies $P\left[E_{\text{truth}}\right]$,

$$P\left[E_{\text{truth}}, \eta\right] = \mathcal{P}\left(E_{\text{reco.}} | E_{\text{truth}}, \eta\right). \tag{6.7}$$

Note that the distribution is differential in both E_{truth} and η, since the EM fraction changes with jet energy, and the detector properties vary significantly in η. We also define a related but more commonly used probability distribution of normalized reco. jet energies $p\left[E_{\text{truth}}, \eta\right]$,

$$p\left[E_{\text{truth}}, \eta\right] = \mathcal{P}\left(r | E_{\text{truth}}, \eta\right). \tag{6.8}$$

For simplicity, we will not further write the η dependence explicitly; it should be assumed.

First we evaluate these probability distributions by studying how truth jets are reconstructed. Truth jets are paired with reco. jets to form "truth-reco. matches" by geometrically matching all possible pairings. Candidate matches are formed by all pairs with sufficiently low $\Delta R < 0.75R$. To ensure a high matching accuracy, matches with other nearby jets above a small p_{T} value, at either the truth ($\Delta R < 2.5R$ and $p_{\text{T}}^{\text{jet}} > 7$ GeV) or reco. ($\Delta R < 1.5R$ and $p_{\text{T}}^{\text{jet}} > 7$ GeV) levels, are rejected. Then, the reco. and truth level energies are compared; examples of the $p\left[E_{\text{truth}}\right]$ distributions are shown in Fig. 6.8 for jets in the pseudorapidity interval $\eta \in (0, 0.1)$. Each panel shows a different narrow bin in E_{truth}. These distributions are Gaussian in shape, which indicates the response is nearly ideal; however this is neither exactly nor necessarily the case. For example, low-energy jets can have non-Gaussian tails in their responses.

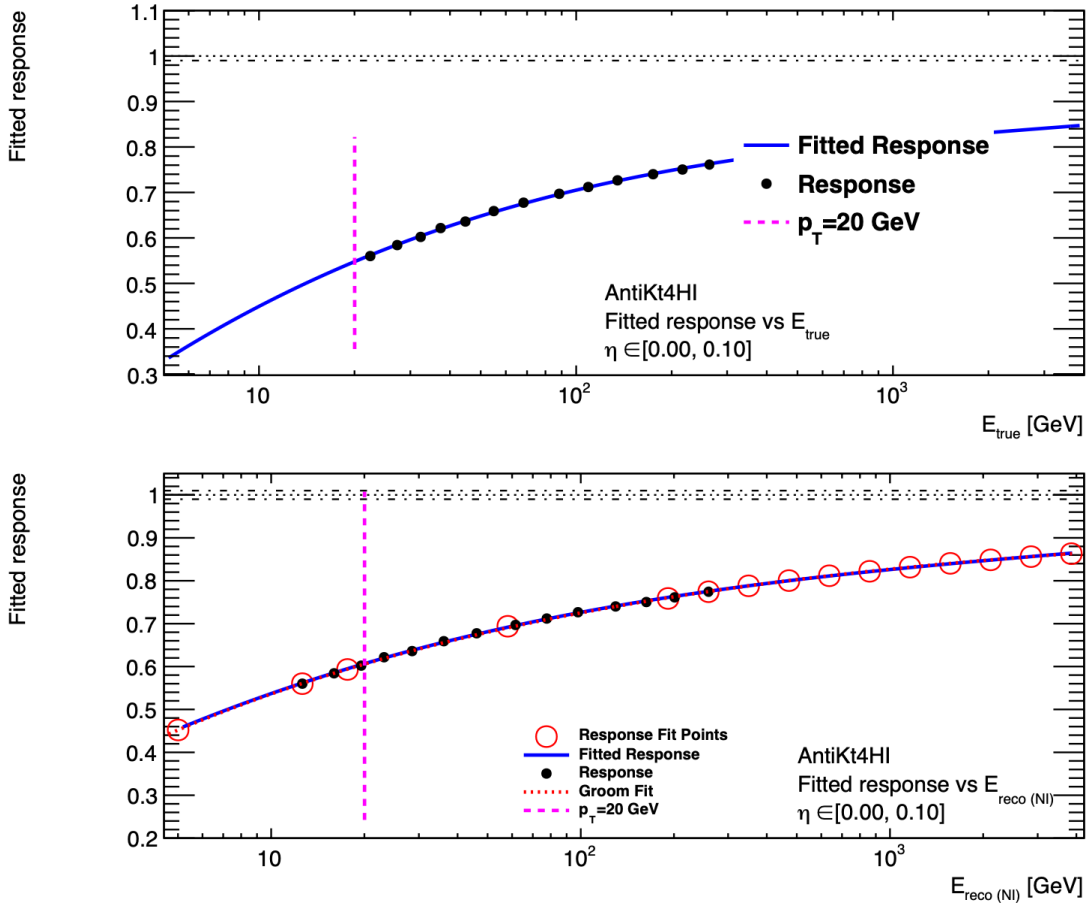
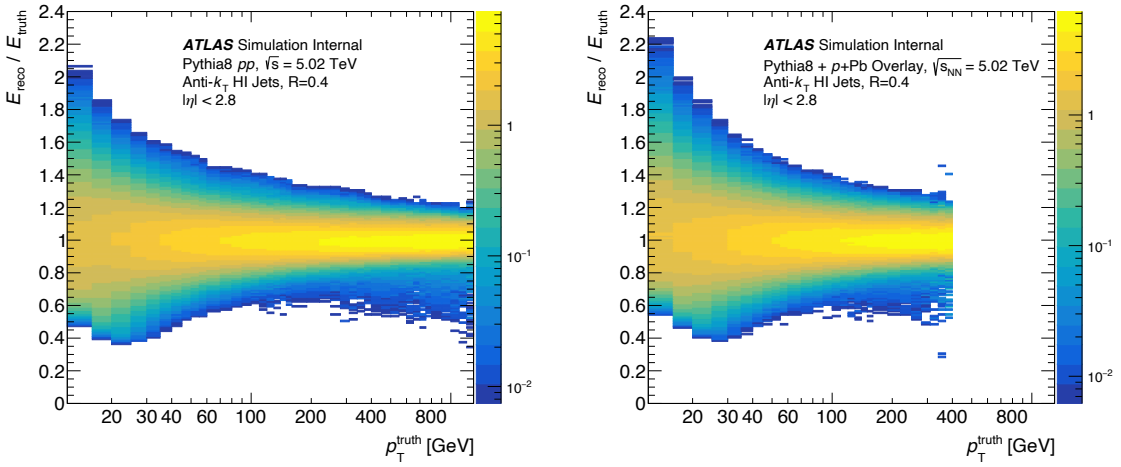


Figure 6.9: Examples of normalized fits to the mode energy response $f\left(E_{\text{truth}}\right)/E_{\text{truth}}$ for anti-k_t $R = 0.4$ HI jets in 5.02 TeV collisions with 2016 p+Pb detector conditions are plotted versus truth energy (top) and mode reco. energy (bottom).

Next, we define the *response function* f via the distribution $P\left[E_{\text{truth}}\right]$. Specifically, we set $f\left(E_{\text{truth}}\right)$ to return the most probable (modal) reco. energy $\hat{E}_{\text{reco}}$ of P:

$$f\left(E_{\text{truth}}\right) = \text{mode}\left[P\left[E_{\text{truth}}\right]\right] = E_{\text{truth}} \times \text{mode}\left[p\left[E_{\text{truth}}\right]\right]. \tag{6.9}$$

To extract the mode, we fit the distribution p to a Gaussian with arbitrary normalization; the mean parameter μ then indicates the peak of the distribution. In the literature, this is often referred to as the mean response, however we point out that because it is picking out the peak, it is actually identifying the *mode*. Example fits are overlaid with their distributions in Fig. 6.8. We then define the mode reco. energy $\hat{E}_{\text{reco.}}$ via $\mu = \hat{E}_{\text{reco.}}/E_{\text{truth}}$.



(a) pp **(b)** p+Pb

Figure 6.10: Best-estimates of the truth jet energy $\hat{E}_{\text{truth}}$ (denoted $E_{\text{reco.}}$) are plotted versus the truth momentum $p_{\text{T}}^{\text{truth}}$ for simulated MC events with **(a)** pp and **(b)** p+Pb conditions. The distributions of $E_{\text{reco.}}/E_{\text{truth}}$ are normalized at each $p_{\text{T}}^{\text{truth}}$ bin so that they can be interpreted as a probability distribution. Note that for the p+Pb case, the MC event generation terminates at JZ3, which samples a maximum $p_{\text{T}}^{\text{truth}}$ of 400 GeV.

The next steps can be seen visually in Fig. 6.9. First, the sampled values of f are fitted to a smooth function versus E_{truth}. This provides a full characterization of the response via an interpolation across the entire range of E_{truth} values. Conceptually, this forms a large set of associations $E_{\text{truth}} \leftrightarrow \hat{E}_{\text{reco.}}$. With these associations, we can then plot instead the initial energy E_{truth} versus $\hat{E}_{\text{reco.}}$ (this is essentially the step where $x \leftrightarrow y$ are swapped), so the inverse function $f^{-1}\left(\hat{E}_{\text{reco.}}\right)$ can be directly evaluated and refitted. This crucial step is seen in the bottom panel, where the response function is plotted instead versus the most likely value. In the ATLAS implementation, both f and f^{-1} are defined as n^{th}-order empirical polynomials in $\log E$ (where $n \leq 6$) [324].

Finally, the calibration can be applied by assuming the reco. energy is the most probable value $E_{\text{reco.}} \overset{\text{assume}}{=} \hat{E}_{\text{reco.}}$ for some truth energy, and evaluating f^{-1}:

$$E_{\text{reco.}} \xrightarrow[\text{EM+JES calibration}]{} E_{\text{EM+JES}} = f^{-1}\left(E_{\text{reco.}}\right). \tag{6.10}$$

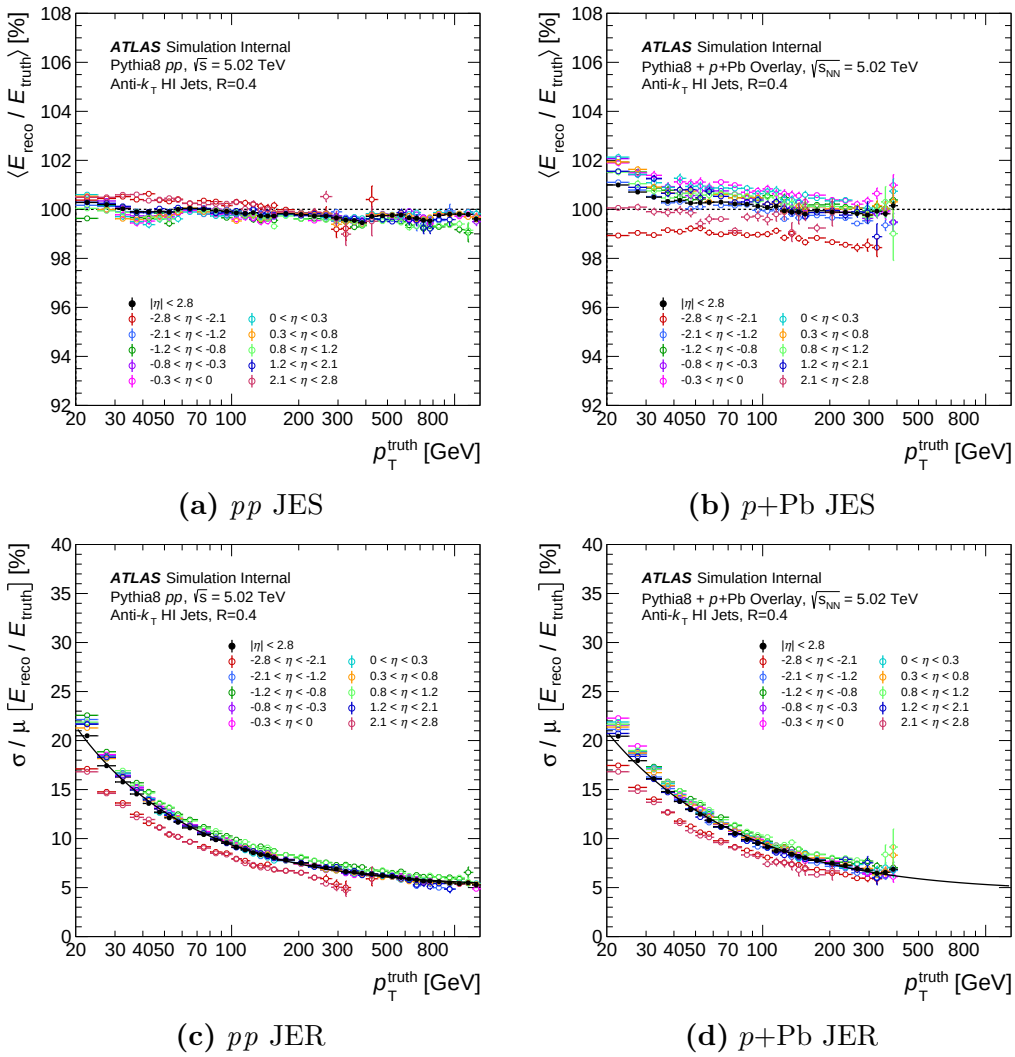
JES and JER

After this procedure, the post-calibration jet energy response must be validated. While the provided software framework performs the NI, this separate check builds confidence in the final calibration by demonstrating closure independently. In this study, jets must be isolated with respect to all other jets with $p_{\mathrm{T}} > 7$ GeV by at least $\Delta R = 2.5R$ at the truth level, where $R = 0.4$ is the jet radius. A reconstructed jet-truth jet pair is only considered matched if $\Delta R < 0.75R$.[3] The results are presented in Fig. 6.10. The y-axis of each panel shows the post-calibration energy response ratio $E_{\mathrm{reco.}}/E_{\mathrm{truth}}$ across a broad range of $p_{\mathrm{T}}^{\mathrm{truth}}$ values. Closure is obtained if the most likely response is unity, i.e., the reco. jet energy matches the truth energy. By eye, this is achieved for $E_{\mathrm{truth}} \gtrsim 20$ GeV. Though, a more quantitative assessment is performed by estimating the modal response via the Gaussian fit method. Frequently, the μ parameter is defined as the *jet energy scale* (JES). Concurrently the *jet energy resolution* (JER) is defined as σ/μ; this latter component encapsulates the precision to which single jet energies can be measured. Thus, the closure condition can be reframed as the observation $\mu \approx 1$.

The JES and JER are presented in Fig. 6.11 for both the pp and p+Pb MC samples. In both collision systems, closure is observed for jets above $p_{\mathrm{T}} \sim 30$ GeV to within 2% across the entire acceptance. This indicates that jet energies are well-characterized on average. Residual minor non-closures are expected due to differences in how the calibration factors are derived versus how the JES is computed in this study. In particular, the p+Pb NI is only derived from pp MC samples with appropriate detector conditions – i.e., no data overlay is present to simulate the higher UE in p+Pb. While this is primarily expected to affect the JER via fluctuations, biases in the UE subtraction procedure as well as sample independence can lead to some non-closure. This difference explains why the pp demonstrates better closure than the p+Pb.

The JER can also be compared to expectations based on our knowledge of hadronic showers.

[3] Note that ΔR and R denote separate quantities here – ΔR represents the distance between jets in (η, ϕ) space, while R represents the jet radius.



(a) pp JES **(b)** p+Pb JES

(c) pp JER **(d)** p+Pb JER

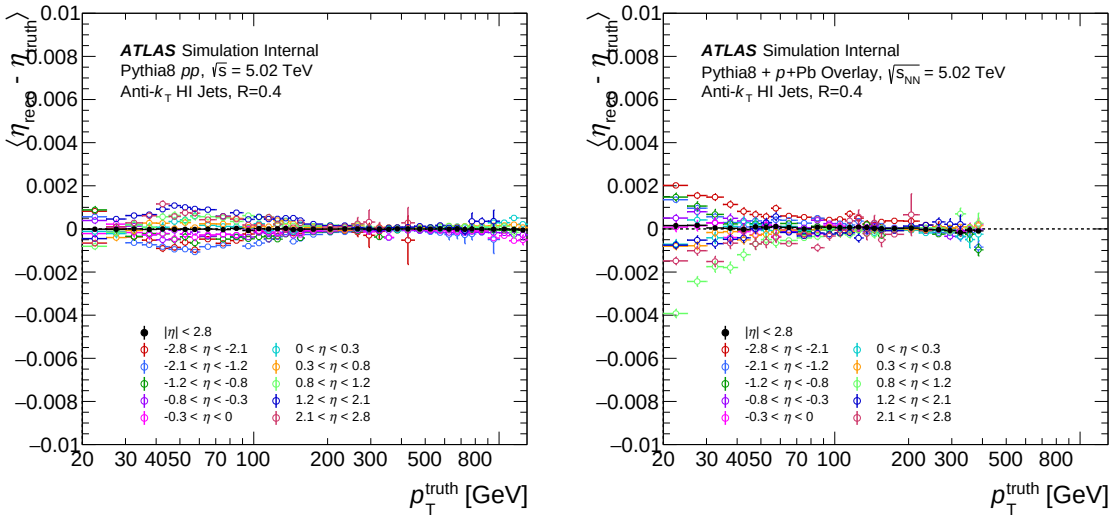
Figure 6.11: The jet energy **(a,b)** scale and **(c,d)** resolution are plotted for anti-k_t $R = 0.4$ jets after the EM+JES calibration in **(a,c)** pp MC and **(b,d)** MC with p+Pb data overlay.

The JER is understood to obey the functional form

$$\text{JER}\,(E)\,[\%] = 100\% \times \frac{\sigma}{\mu}\,[E] = 100\% \times \left[C \oplus \frac{S}{\sqrt{E}} \oplus \frac{N}{E}\right]. \tag{6.11}$$

where C represents the constant term, S the stochastic component, and N the noise component that varies with the size of the underlying event (or pileup). Fits to this form are overlaid in Fig. 6.11. Conceptually, we see that the JER asymptotes to a constant (C) as $E \to \infty$; this is expected as the EM fraction of the shower increases with energy due to phase space considerations.

Fig. 6.12 then presents the closure of the jet pseudorapidity after the origin correction is



(a) pp **(b)** p+Pb

Figure 6.12: The most probable difference between jet origin-corrected and truth-level pseudorapidities is plotted for anti-k_t $R = 0.4$ jets after the origin calibration in **(a)** pp MC and **(b)** MC with p+Pb data overlay.

applied. This plot considers the average difference in jet pseudorapidity at the fully-corrected reconstruction level and truth level. Because the basic quantity is a difference and not a quotient, the closure condition is instead that the most likely value is 0 (not 1). While the η correction is fairly modest most of the time, a previous measurement with this data showed that the breakup of the lead ion can very slightly pull jets towards the A-side of the detector [325]. In the current study, some minor non-closure in the pseudorapidity can be seen, though the effect introduces an uncertainty on η of at most $\delta\eta \sim 0.005$ and therefore is completely negligible in magnitude.

Beyond confirming our basic expectations, quantifying the JER in particular is also important in this measurement for defining additional jet selection criterion in MC. Recall that the data overlay method is used to simulate the p+Pb collision environment by embedding MC-generated events within real minimum bias data. By construction, there is some small but nonzero rate that real high-p_{T} jets will be embedded in the MC event, and eventually be reconstructed alongside their MC jet partners. While this is a relatively rare occurrence, the consequence is that there are real jets that lack a truth-matched partner. In particular, this will bias the per-jet hadron yield as measured

in MC because these data jets will contribute real reconstructed tracks, but lack the truth level particles. In brief, the reco.-level yield will be artificially inflated relative to the truth-level yield.

To reject such jets, geometric matching between truth and reconstructed jets can first reduce their impact. This enhances the probability that any given reco. jet actually has a truth-level partner. However, because the reco. jets are fully calorimeter based, it is completely impossible to identify scenarios where one reco. jet corresponds to the superposition of two or more real jets. Because each simulated event contains at least one truth jet by construction, there will be some rate where jets in data become superimposed on the truth jets, thus impacting the JES. Geometric matching alone is not sufficient to discern these situations, so additional criteria are required. For this, we turn to the JER.

If two jets are geometrically matched with a ΔR-based cut, we can then consider the conditional probability p from before,

$$p\left[E_{\text{truth}}\right] = \mathcal{P}\left(r|E_{\text{truth}}\right) \sim \mathcal{N}\left(\text{JES}, \text{JER}\right). \tag{6.12}$$

On the right hand side, we now explicitly state the Gaussian form of the distribution from before, showing us the full power of the JES and JER characterizations. What these *really* do is parameterize this probability in terms of a normal distribution, allowing us to talk about z-scores, which lets us talk about p-values for the response. Assuming a perfect JES for simplicity, we take the z-score of the match to be[4]

$$z\left[\text{match}\right] \equiv \frac{1}{\frac{\sigma}{\mu}\left[E_{\text{truth}}\right]}\left(\frac{E_{\text{reco.}} - E_{\text{truth}}}{E_{\text{truth}}}\right) \approx \frac{1}{\frac{\sigma}{\mu}\left[E_{\text{truth}}\right]}\left(\frac{p_{\text{T}}^{\text{reco.}} - p_{\text{T}}^{\text{truth}}}{p_{\text{T}}^{\text{truth}}}\right). \tag{6.13}$$

This reframes the match quality question into a hypothesis testing problem. Given a truth-reco. jet match, our null hypothesis is that the match is "good", meaning the there is no jet in data dramatically biasing the reco.-level energy. The alternative hypothesis is that the match is "bad", or that a real jet in the data event is being overlaid with the truth jet, leading to a significant bias on the final energy. If the null hypothesis is true, we are exceedingly likely to have low $|z|$ values.

[4] The right side approximation stems from the assumptions that (1) $m \ll p_{\text{T}}$ and (2) $\eta_{\text{reco.}} \approx \eta_{\text{truth}}$.

If the alternative hypothesis is true, we are much more likely to find a high $|z|$ values because the shape of p will be vastly different. Jets from data are well-known to follow a power law in energy, so at a fixed E_{truth} value the response probability distribution will be strongly peaked at very low values of $E_{\text{reco}} \ll E_{\text{truth}}$. In this situation, the jet should be rejected.

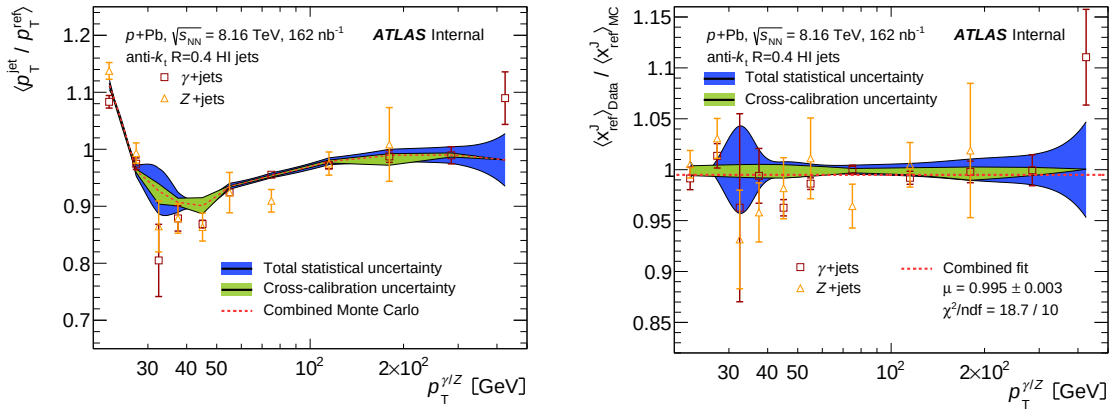
Thus, in addition to our geometric matching criterion, we perform this experiment on a jet-by-jet basis in MC events to evaluate the validity of the jet. As a choice, we reject the null hypothesis – thereby rejecting the jet – if $|z| > 3$. This corresponds to $p < 0.0027$, so we expect a very low false positive rate (meaning we reject jets erroneously very rarely).

Cross-calibration

The cross-calibration is, essentially, a bootstrapped, data-driven jet calibration exclusive to HI jets. It builds on the EM+JES sequence by accounting for differences in the jet response between data & MC. This makes it applicable only to data (since the EM+JES completely calibrates the MC). The main idea is to quantify the performance of the post-EM+JES-calibration HI jets relative to fully calibrated EM topo-cluster (EMTopo) jets. Differences in the two jet inputs are assumed to be largely $\sqrt{s}$-independent and can be evaluated in a data set with abundant statistics – namely, 13 TeV pp collisions with similar detector conditions (i.e., pile-up rates) to the 5.02 TeV heavy-ion data sets. Vector boson probes – which are required to perform an *ab initio* derivation of the *in situ* calibration factors – are very rare, so sufficiently large data sets are needed, hence the use of the large 13 TeV Run 2 data set. Central to the cross-calibration is the jet-by-jet response ratio $\mathcal{R}$ of the EM+JES scale energy $\hat{E}_{\text{EM+JES}}$ for HI jets and the fully calibrated energy scale $\hat{E}_{\text{truth}}$ for EMTopo jets,

$$\mathcal{R} \equiv \frac{\hat{E}^{\text{HI}}_{\text{EM+JES}}}{\hat{E}^{\text{EMTopo}}_{\text{truth}}}. \tag{6.14}$$

Jets must be appropriately matched between collections to form a good set of HI $\leftrightarrow$ EMTopo associations. $\mathcal{R}$ is usually evaluated in bins of $\hat{E}^{\text{HI}}_{\text{truth}}$. The modal response $\hat{\mathcal{R}}$ is extracted using a Gaussian function, smoothed to an empirical curve versus $\hat{E}^{\text{HI}}_{\text{EM+JES}}$, and finally used to calibrate



(a) Modal x^j_{ref} **(b)** Data-to-MC ratio

Figure 6.13: **(a)** Modal x^j_{ref} values in p+Pb data and MC simulations and **(b)** their ratios between data and MC. $\gamma+$jet and $Z+$jet points are shown separately. Shaded bands show the statistical uncertainty **(blue)** on the combined result as well as the total cross-calibration uncertainty **(green)**.

the HI jets up to the best-estimate of the truth jet energy scale:

$$E^{\text{HI}}_{\text{reco.}} \xrightarrow[\text{EM+JES calibration}]{} \hat{E}^{\text{HI}}_{\text{EM+JES}} = f^{-1}\left(E^{\text{HI}}_{\text{reco.}}\right) \xrightarrow[\text{Cross-calibration}]{} \hat{E}^{\text{HI}}_{\text{truth}} = \frac{\hat{E}^{\text{HI}}_{\text{EM+JES}}}{\hat{\mathcal{R}}\left(\hat{E}^{\text{HI}}_{\text{EM+JES}}\right)}. \quad (6.15)$$

We note that $\hat{R}$ is only used as a multiplicative correction, rather than a full numerical inversion; this is valid as long as $\hat{R} \approx 1$. This correction factor introduces an additional jet energy scale uncertainty which can be characterized *post hoc*. However, the single jet energy response is strongly correlated between the HI and EMTopo algorithms, since the JER is mainly driven by event-to-event variation in the hadronic showers. Thus, $\hat{\mathcal{R}}$ is known rather precisely in comparison to the overall jet energy resolution.

For the p+Pb data, the cross-calibration was not directly derived; rather factors derived from the 2015 pp were validated for use in the 2016 data. Akin to the calculation of the *in situ* calibration factors, this was performed with a momentum balance study in $\gamma+$jet and $Z+$jet events (referred to together as $V+$jet events). A momentum balance variable x^j_{ref} for the nearly back-to-back $V+$jet pairs was defined event-by-event via

$$x^j_{\text{ref}} = \frac{p^{\text{jet}}_{\text{T}}}{p^{\gamma \text{ or } Z}_{\text{T}} \cos\Delta\phi}, \quad (6.16)$$

and studied in both the data and MC. Again, this allows the jet energy calibration to bootstrap off the more precise γ/Z calibrations. If the jet energy scale in data is accurate, then the momentum balance at a fixed value of γ/Z p_{T} should be comparable in both data and MC because high-p_{T} $V+\mathrm{jet}$ production is well-understood to be dominated by tree-level diagrams with a $q+\gamma/Z$ final state. This assumes, of course, that the p+Pb jets are not being quenched; however we do not expect to be sufficiently statistically sensitive to any such effect in the vector boson channels, if one is present.

Similar to the EM+JES calibration, the modal x^{j}_{ref} values are picked out by fitting their distributions to a Gaussian, though the distributions are not shown here. In Fig. 6.13, these values are shown versus the p_{T} of the boson. Values for $\gamma+\mathrm{jet}$ and $Z+\mathrm{jet}$ processes are shown separately but are expected to be compatible. A combined MC prediction with both $\gamma+\mathrm{jet}$ and $Z+\mathrm{jet}$ processes is also shown. Two uncertainty bands are provided here. The first is the cross-calibration uncertainty, shown in green, which is generally at the 0.5–1% in this study. The second is the total statistical uncertainty on the combined $\gamma+\mathrm{jet}$ and $Z+\mathrm{jet}$ results. We see that the data is compatible with the MC – this is particularly noticeable in the data/MC ratio on the right, where the combined channel fit in red visibly lies within 1σ of unity at all p_{T} values. This indicates that the cross-calibration is working to an acceptable level, and no additional uncertainty pertaining to differences in detector conditions from 2015 to 2016 is necessary.

Jet Energy Scale Uncertainties

We consider the jet energy measurement as a source of systematic uncertainty. First, a standard set of uncertainties on the EM+JES energy scale are provided within the ATLAS software by the JetEtMiss subgroup. These uncertainties are evaluated with the `JetUncertaintiesTool` at the AOD level in simulated data with the `GlobalReduction` configuration [326]. Only the first 16 jet energy scale nuisance parameters are studied (the 17^{th} is an uncertainty that only applies to data taken in 2018). The relative effect on Y is evaluated in MC and then propagated to data to assign the final uncertainty. Because the calibrations were derived in the same manner in pp

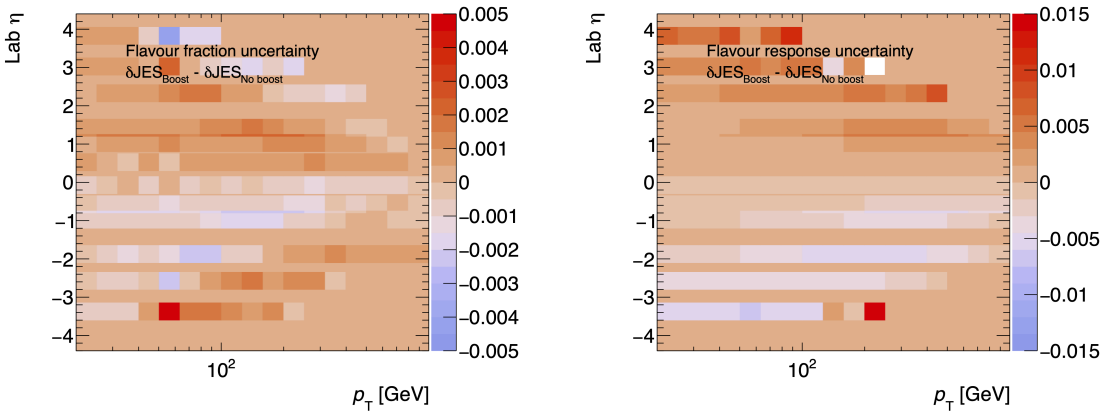
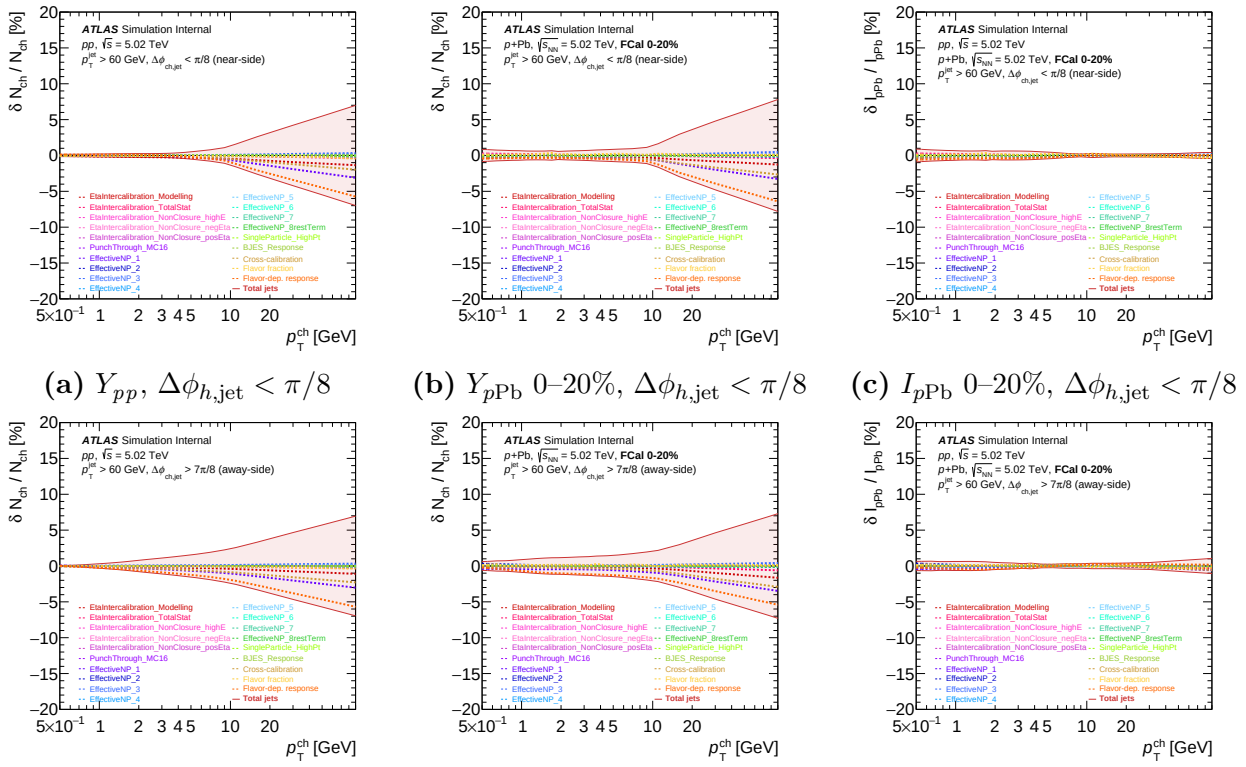


Figure 6.14: The difference in flavor-fraction (left) and flavor-response (right) uncertainties on the JES (in units of % uncertainty on the JES) between p+Pb ("boost") and pp ("no boost") is shown as a function of jet p_{T} and η in the lab reference frame.

and p+Pb, each source is treated as completely correlated between pp and p+Pb, and thus each is allowed to cancel when computing the ratio $I_{p\mathrm{Pb}}$. HI jets in data also must undergo the cross-calibration which introduces an additional cross-calibration uncertainty. But again, this is applied identically between pp and p+Pb and thus also allowed to cancel in the ratio $I_{p\mathrm{Pb}}$.

The flavor of jets in MC also affects the jet calibration and must be considered as a source of uncertainty. Quark-initiated and gluon-initiated jets are known to fragment differently, which will affect, for example the EM fraction of the total hadronic response. This is known as the flavor-dependent response and leads to two sources of uncertainty. The first is associated with our description of flavor-dependence itself. If you have incorrectly estimated the average gluon-jet response at a given flavor-fraction then this will shift the jet energy scale. The second is associated with uncertainty on the fraction of jets that are gluon-initiated, f_g. If you have incorrectly estimated the fraction of gluon-initiated jets (or equivalently the fraction of quark-initiated jets f_q) with a given flavor-dependence, then this will shift the jet energy scale as well.

Both systematic uncertainties are provided as a function of jet p_{T} and η. However the uncertainties are only provided for pp, and cannot be applied directly to the p+Pb. This is because at fixed detector η, f_g will differ between pp and p+Pb due to the rapidity boost of the latter.



(a) Y_{pp}, $\Delta\phi_{h,\text{jet}} < \pi/8$ **(b)** $Y_{p\text{Pb}}$ 0–20%, $\Delta\phi_{h,\text{jet}} < \pi/8$ **(c)** $I_{p\text{Pb}}$ 0–20%, $\Delta\phi_{h,\text{jet}} < \pi/8$

(d) Y_{pp}, $\Delta\phi_{h,\text{jet}} > 7\pi/8$ **(e)** $Y_{p\text{Pb}}$ 0–20%, $\Delta\phi_{h,\text{jet}} > 7\pi/8$ **(f)** $I_{p\text{Pb}}$ 0–20%, $\Delta\phi_{h,\text{jet}} > 7\pi/8$

Figure 6.15: Systematic uncertainties on the yield measurement related to the jet energy scale are plotted as a function of charged-particle p_{T} in **(a–c)** the near-side ($\Delta\phi < \pi/8$) and **(d–f)** the away-side ($\Delta\phi > 7\pi/8$) for events with a jet above 60 GeV.

However R_g and R_q will be approximately the same as these reflect a property of the detector. For this reason, the flavor dependence uncertainties have been reevaluated using the boosted kinematics for f_g but non-boosted kinematics for R_g. The difference between the pp and p+Pb uncertainties are shown in Fig. 6.14, though in general the JES uncertainty is found to change only by a fraction of a percent in most cases.

Of the two, the flavor-dependent response is typically the larger uncertainty. We treat the flavor-dependent response as correlated between the pp and p+Pb because it reflects a property of the detector, however, the flavor fraction uncertainty is not assumed to be correlated to account for any possible bias due to the rapidity boost in p+Pb. Though, the total uncertainty is a very small overall, amounting to a fraction of a percent. For the 30 GeV jets, the effect is slightly larger

but bounded around $\lesssim 1\%$. A breakdown of all the jet energy scale uncertainties, including the non-cancelling flavor fraction uncertainty, is shown in Fig. 6.15.

6.4 Tracking Considerations

With the set of events selected by our jet requirements defined and in hand, we next turn to building our sample of charged hadrons from charged-particle tracks in the inner detector. Many of the technical details of the tracking studies are common with Chapter 4, so we suggest the reader first read Sec. 4.6.

The main tool we have to study charged-hadron yields is the yield of charged particles. Charged-particle trajectories or "tracks" are reconstructed using hits left by charged particles traversing the inner detector. Each reconstructed track can originate either from the true collision or from extraneous background sources. To mitigate the contributions of background sources, tracks are required to pass a set of selection criteria, reflecting the "quality" of the track. Different pre-optimized sets of criteria exist and the particular choice of criteria is referred to the working point. The resilience of the working point to reconstruction efficiency and background rejection must be considered, and is discussed here.

In this measurement, we require tracks meet a basic set of criteria, including

- $|\eta| < 2.5$,
- $p_{\mathrm{T}}^{\mathrm{ch}} > 0.4$ GeV,
- meet the `TightPrimary` working point (see Table 3.3),
- meet a cut on the center of mass rapidity, $\left|\eta^*\right| = \left|\eta_{\mathrm{lab}} - y^*\right| > 2.035$.

Recall from Chapter 4 that tracks in MC are considered truth-matched if the truth-matching probability is greater than 0.5; truth-matching probability distributions for MC samples used in this analysis can be found in Fig. 6.16. A track is then either fake if it is not truth-matched,

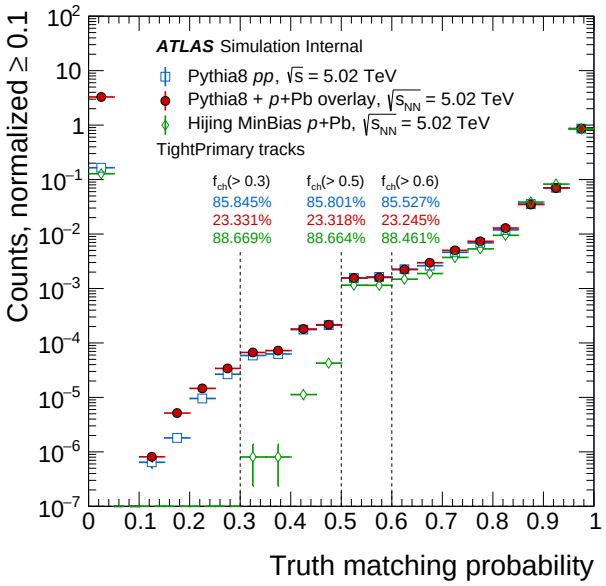


Figure 6.16: Truth-matching probability distributions for tracks reconstructed in PYTHIA pp dijets **(light blue)**, PYTHIA pp dijets with p+Pb data overlay **(red)**, and HIJING minimum bias p+Pb **(green)** simulated events. Labels indicate the fraction of tracks $f_{\text{ch}}(x)$ reconstructed above truth-matching probability x.

secondary if it is truth-matched but originates from a particle shower, or primary if it is neither fake nor secondary.

Notably, the last criterion reduces the charged-particle rapidity acceptance compared to the usual one. Under the assumption that the p+Pb jet-tagged yield is identically distributed in rapidity y to pp in the center-of-mass (CM) frame, some particles will be boosted outside of the tracker acceptance in p+Pb, thus affecting the pp-to-p+Pb comparison. For charged particles in the limit $p_{\text{T}} \gg m$, if $|\eta^*| = |\eta_{\text{lab}} - y^*_{\text{CM}}| > 2.5 - |y^*_{\text{CM}}|$ then the particle will not be reconstructed, where $y^*_{\text{CM}} = 0$ in the pp data and -0.465 in p+Pb. To avoid comparing charged-particle yields at different rapidities, as an analysis choice all charged particles must have pseudorapidity

$$|\eta_{\text{CM}}| = |\eta_{\text{lab}} - y_{\text{CM}}| < 2.5 - 0.465 = 2.035. \tag{6.17}$$

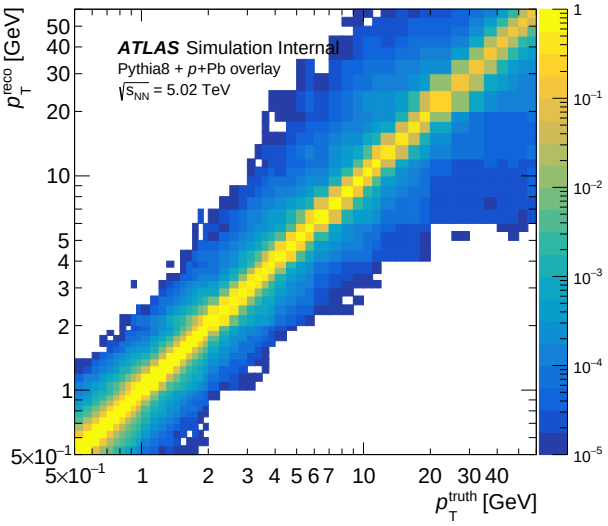


Figure 6.17: 2D scatterplots of reconstructed versus truth p_{T} for charged particles in p+Pb simulated events. The distributions along the y-axis are normalized at each p_{T} bin (so that the reconstructed p_{T} probability distribution is normalized at each truth p_{T} bin).

Momentum Response

First, we examine the charged-particle momentum response, which closely parallels the study of the jet energy response. In simulation, truth-matched particles frequently have an imperfect match between truth and reconstructed (reco.) level momenta.[5] This can be seen for example in Fig. 6.17, where the 2D scatterplot of truth versus reco. charged-particle p_{T} is shown to have a strong correlation – note the logarithmic z-axis.

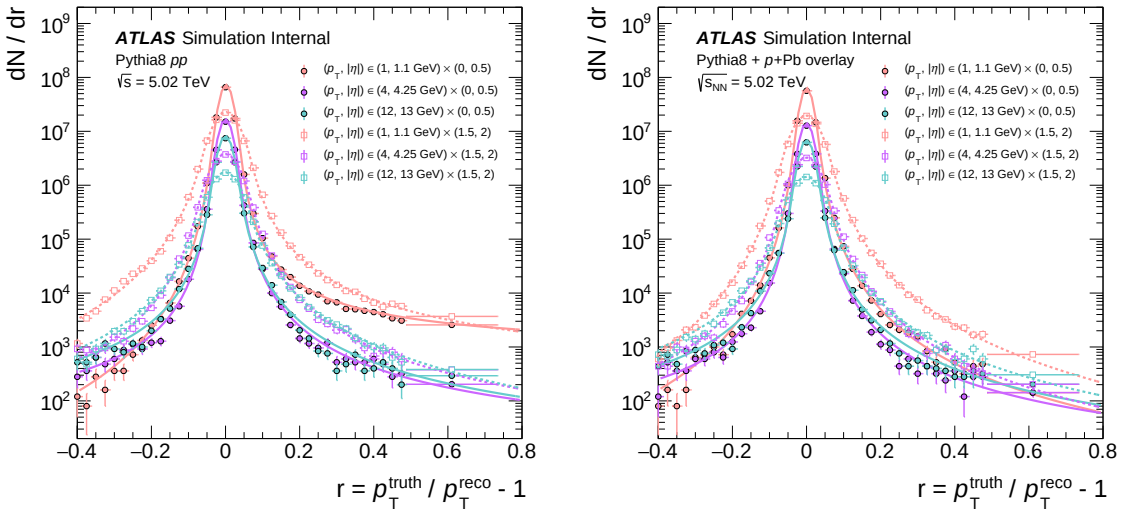
For truth-matched charged particles, we define the p_{T} response r track-by-track in simulated events via [327]:

$$r = \frac{p_{\mathrm{T}}^{\mathrm{truth}} - p_{\mathrm{T}}^{\mathrm{reco}}}{p_{\mathrm{T}}^{\mathrm{reco}}}. \tag{6.18}$$

The distribution of r is measured as a function of $p_{\mathrm{T}}^{\mathrm{truth}}$ and η_{truth} from primary tracks in simulation, as demonstrated in Fig. 6.18. To smooth out fluctuations, r is fitted to a modified double-sided Crystal ball function[6] motivated by [327],

[5] We note that the treatment of the TMR in Chapter 4 was simplified and used to argue against the need for an unfolding. Here, the p_{T} bins are much narrower and the desired precision is much higher, so a more thorough treatment is needed.

[6] Note that Ref. [327] uses the sum of two Gaussians with floating parameters for the core of the fit. We found



(a) pp **(b)** p+Pb

Figure 6.18: Examples of fits of the track momentum response (r) distributions (dN/dr) to the double-Crystal ball functional form $f(r)$ in **(a)** pp and **(b)** p+Pb, for a few different truth p_{T} ranges at midrapidity (filled circles and solid lines) and forward rapidity (open squares and dashed lines).

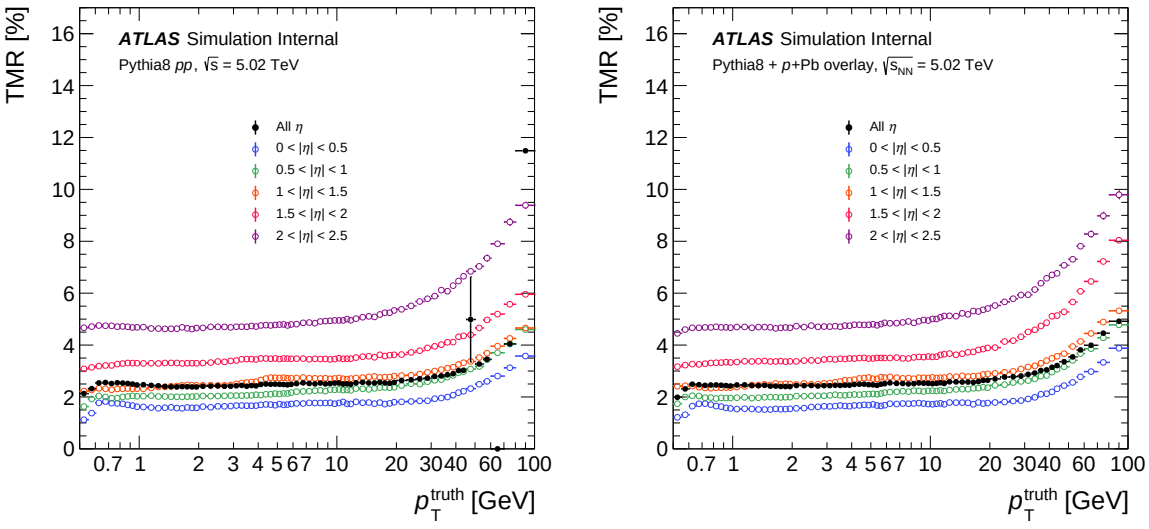
$$f(r) = \begin{cases} \exp\left\{A_n + B_n |r|^{c_n}\right\} & \text{if } r < t_n \\ A_0 \exp\left\{\frac{1}{2}\frac{(r-r_0)^2}{\sigma_0^2}\right\} & \text{if } t_n < r < t_p \\ \exp\left\{A_p + B_p |r|^{c_p}\right\} & \text{if } t_p < r. \end{cases} \tag{6.19}$$

Though $f(r)$ contains 11 parameters, only seven of them are independent due to the constraints that f be smooth and continuous at t_p, t_n (i.e. f and f' are continuous at t_p, t_n). In this analysis, we define that track momentum resolution as the width of the Gaussian core component of $f(r)$,

$$\mathrm{TMR}[\%] = 100\% \times \sigma_0. \tag{6.20}$$

Analytically we find that the dependent parameters are A_n, A_p, B_n, B_p, though the fit to $f(r)$ is still complicated due to the seven remaining free parameters. For a fit to be performed, histograms are required to have at least 1000 entries. Stable fits were attained by fitting to the logarithm of

that this particular form is difficult to constrain due to the strong correlation between the parameters of the two Gaussians, and thus use a single Gaussian to estimate the momentum resolution in this analysis. Other methods frequently used include the interquartile range (IQR) of the r distribution.



(a) pp **(b)** p+Pb

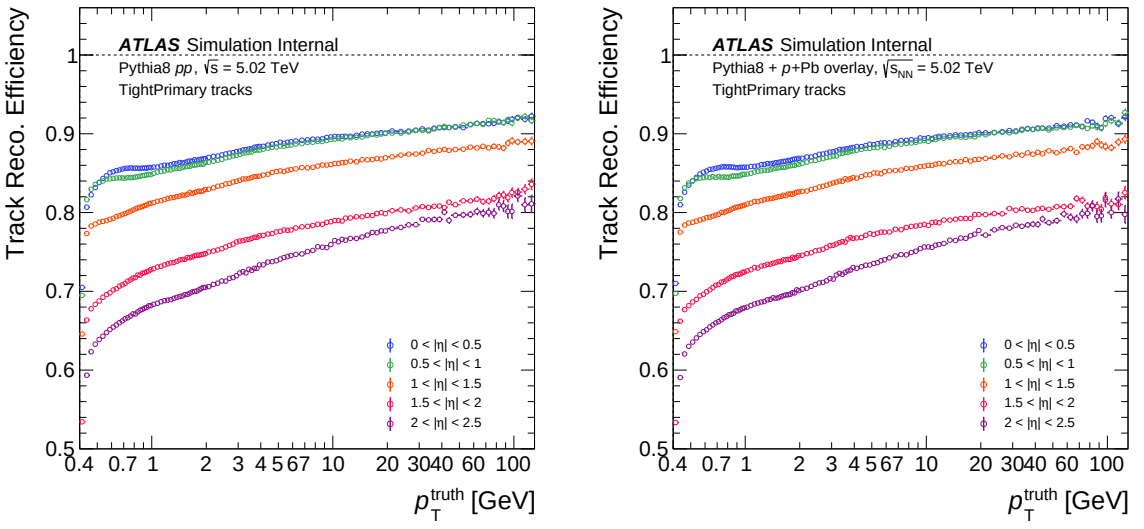
Figure 6.19: The extracted track momentum resolution (TMR) is plotted as a function of truth particle p_{T} and η for **(a)** pp and **(b)** p+Pb.

the r distribution, with bins with 0 counts discarded. Consequently the fit was performed with the χ^2 minimization / least-squares method, similar to how they were performed in [327].

Examples of the track resolution fits are overlaid in Fig. 6.18. From each fit, the TMR value was extracted and plotted as a function of truth p_{T} and η in Fig. 6.19. At fixed p_{T}, the resolution is best for midrapidity particles and worst for particles at forward rapidity. At fixed $|\eta|$, the resolution is roughly fixed until 10–20 GeV, at which point the the particle trajectory becomes less curved and the TMR increases (i.e. the resolution gets worse). For instance, a $p_{\mathrm{T}} \simeq 100$ GeV charged particle in a magnetic field $B \simeq 2\,\mathrm{T}$ will have a radius of curvature $R \simeq 170\,\mathrm{m}$ and thus a deflection angle of only $\sim 3^\circ$ over a 2 m distance.

Reconstruction efficiency

Next we consider the reconstruction efficiency, which encapsulates the probability that any given charged particle will be observed in the analysis. It is estimated in simulation by comparing the distributions of truth-matched reconstructed tracks and truth particles and described with a



(a) pp **(b)** p+Pb

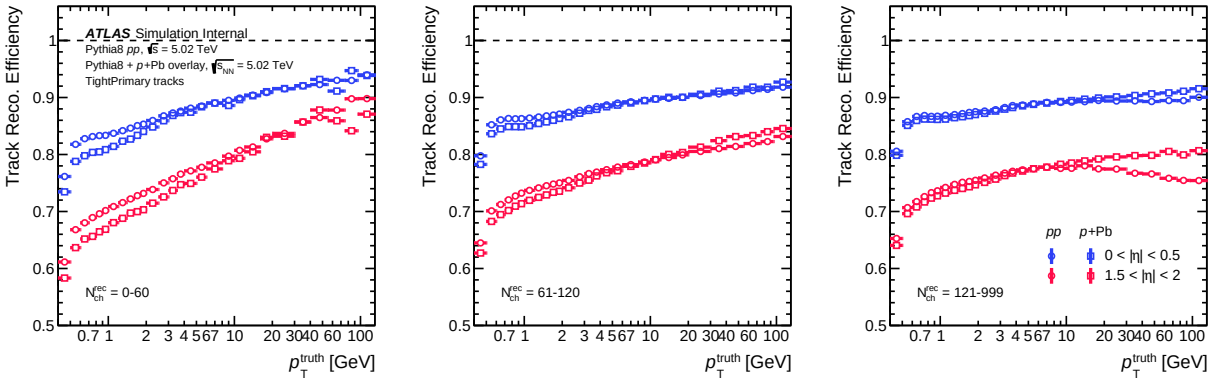
Figure 6.20: Projections of track reconstruction efficiency are plotted versus truth p_{T} at 5 different pseudorapidity selections, ranging from midrapidity (blue, green) to forward rapidity (red, purple) in **(a)** pp and **(b)** p+Pb.

binomial probability

$$f_{\mathrm{eff}}\left(p_{\mathrm{T}}^{\mathrm{truth}}, \eta_{\mathrm{truth}}\right) = \frac{N_{\mathrm{ch}}^{\mathrm{reco.}}\left(p_{\mathrm{T}}^{\mathrm{truth}}, \eta_{\mathrm{truth}}\right)}{N_{\mathrm{ch}}^{\mathrm{truth}}\left(p_{\mathrm{T}}^{\mathrm{truth}}, \eta_{\mathrm{truth}}\right)}. \tag{6.21}$$

Profiles of the tracking efficiency at different rapidities are shown in Fig. 6.20 to give a qualitative sense of how the efficiency varies with p_{T} and η separately. These plots integrate over all multiplicities and therefore lack any occupancy dependence. Projections separated into the multiplicity bins used for the nominal results are shown in Fig. 6.21. Around $p_{\mathrm{T}} \sim 0.5$ GeV the tracking efficiency ranges from $\sim$ 65–85% and reaches $\sim$ 82–92% by 100 GeV. Without filtering on detector occupancy, the efficiency is nearly identical in pp and p+Pb.

In Pb+Pb collisions, there is a known occupancy dependence of the efficiency. This is because generally the probability of reconstructing a track decreases when separate tracks become too close together. In this analysis, we also investigated the reconstruction efficiency in coarse bins in the track multiplicity $N_{\mathrm{ch}}^{\mathrm{rec}}$ – this is shown in Fig. 6.21. We mention however that the p+Pb tracking environment is relatively 'dilute' in comparison to Pb+Pb, and so no large difference to the multiplicity dependence from pp is expected. At low multiplicity, we see the two can differ by



(a) $N_{\mathrm{ch}}^{\mathrm{rec}} = 0$–$60$ **(b)** $N_{\mathrm{ch}}^{\mathrm{rec}} = 61$–$120$ **(c)** $N_{\mathrm{ch}}^{\mathrm{rec}} = 121$–$999$

Figure 6.21: Projections of track reconstruction efficiency are plotted versus truth p_{T} for particles at midrapidity **($0 < |\eta| < 0.5$; blue)** and forward rapidity **($1.5 < |\eta| < 2$; red)**. From left to right, events are divided by low to high multiplicity.

up to $\lesssim 3\%$. Since the overall multiplicity in p+Pb is usually higher than pp, this could indicate that the contribution from p+Pb events with downward fluctuations in the reconstruction efficiency are making a larger contribution than in pp, though this would require further study. The reverse of this behavior is that at high multiplicity and high-$p_{\mathrm{T}}^{\mathrm{ch}}$, the efficiency drops in the pp relative to the p+Pb. This can be explained by the fact high multiplicity pp events actually correspond to jets with a large number of high-$p_{\mathrm{T}}^{\mathrm{ch}}$ fragments, while in p+Pb either the jet can contain many high-$p_{\mathrm{T}}^{\mathrm{ch}}$ fragments or the underlying event can be more active. In the pp, all of these high-$p_{\mathrm{T}}^{\mathrm{ch}}$ particles *must* correspond to jets at the truth-level, but the density is so high, the efficiency suffers. In the p+Pb, the particles are more spread out in (η, ϕ) space, so the tracking efficiency at high-$p_{\mathrm{T}}^{\mathrm{ch}}$ does not deteriorate as much.

Fakes and Secondaries

Recall that only primary tracks are associated with the collision, so fake and secondary tracks must be rejected. There is no *a priori* method to discern primaries from fakes and secondaries, so tracks must be weighted by the probability that it is primary (colloquially called the "primary fraction" or "purity"). The primary fraction is evaluated in simulated events via a binomial probability

$$f_{\text{primary}}(p_{\text{T}},\eta) = \frac{N_{\text{ch}}^{\text{primary}}(p_{\text{T}},\eta)}{N_{\text{ch}}^{\text{reco.}}(p_{\text{T}},\eta)}. \tag{6.22}$$

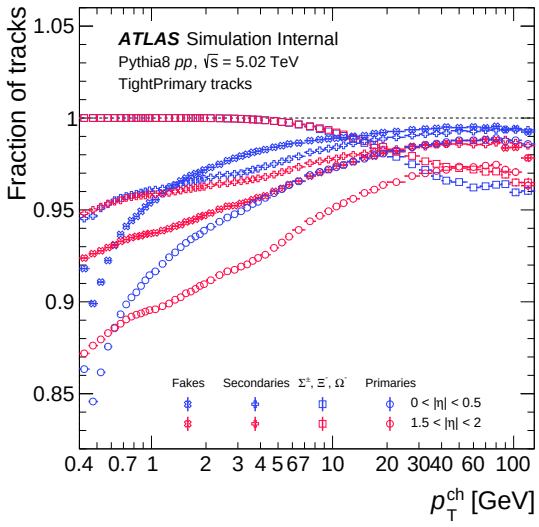
To estimate the purity, the usual MC samples in Table 6.3 are used. However, the heavy-ion data overlay samples cannot be used as real tracks from the data overlay will be falsely identified as fake tracks. This will bias the fake rate if left unaccounted for. To avoid this effect, the pure HIJING sample is used instead to estimate the purity in p+Pb. In pp, there is no overlay and therefore the non-boosted PYTHIA `JZ` samples are considered as usual.

In Fig. 6.22, we illustrate how the primary rate can be decomposed into the underlying fake and secondary rates. Because strange baryons ($\Sigma^+, \Sigma^-, \Xi^-$, and Ω^-) tend to decay in the detector and consequently suffer from poor reconstruction efficiency (see Fig. 4.28), the rate at which these particles appear is also shown for comparison. The lower panels show projections of the primary fraction at various pseudorapidity intervals. We see that for `TightPrimary` tracks, the primary fraction typically ranges from about 86–97% in pp across a broad p_{T} range. In p+Pb, the fraction is higher, ranging from 90–99%. Though the rate of secondaries is similar from pp to p+Pb, the fake rate is lower in the p+Pb, driving differences in the primary fraction that can be seen in the lower panels. For example, around $p_{\text{T}} \simeq 1$ GeV, about 94% of tracks are primaries in the p+Pb, contrasting with a rate of only about 91% in the pp.

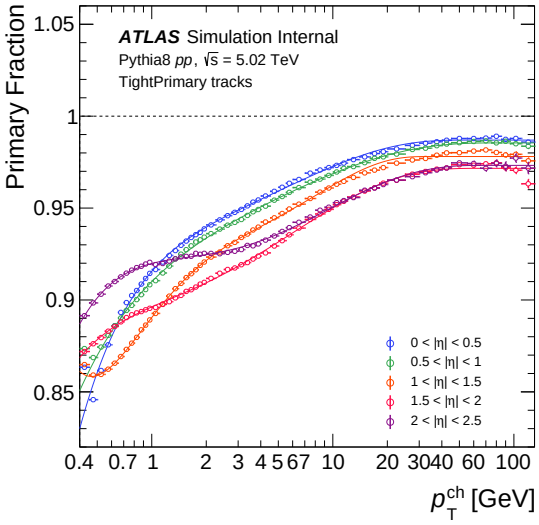
Because the p+Pb MC has no jet filter, statistical coverage at high-p_{T} is poor. To mitigate bin-to-bin variation, the fraction at each $|\eta|$ is fitted to an empirical piecewise function which is an $N = 4^{\text{th}}, 5^{\text{th}}, 6^{\text{th}}, \text{or } 7^{\text{th}}$ degree polynomial in $\log(p_{\text{T}})$ below some value $p_{\text{T}}^{\text{const.}}$, and a constant above that value:

$$f_{\text{primary}}^{\text{fit}}(p_{\text{T}}) = \begin{cases} \sum_{n=0}^{N} a_n (\log p_{\text{T}})^n & \text{if } p_{\text{T}} \leq p_{\text{T}}^{\text{const.}} \\ f_{\text{primary}}^{\text{fit}}\left(p_{\text{T}}^{\text{const.}}\right) & \text{otherwise.} \end{cases} \tag{6.23}$$

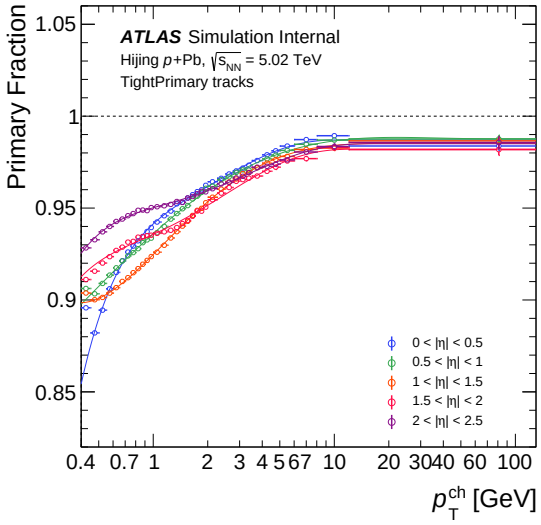
a_n and $p_{\text{T}}^{\text{const.}}$ are fitted parameters, though a_1 and a_2 are fixed relative to the other a_n such that the first two derivatives of $f_{\text{primary}}^{\text{fit}}$ are continuous at $p_{\text{T}}^{\text{const.}}$. The degree is set such that the goodness-of-fit test statistic (χ^2 per degree of freedom) is at most 4, with lower degree fits given priority. To account for points with unrealistically low uncertainties skewing the fit, each point is given a



(a) Fake and secondary components



(b) Primary fraction in pp



(c) Primary fraction in p+Pb

Figure 6.22: **(a)** The fraction of tracks in pp identified as fakes, secondaries, strange baryons, and primaries is plotted as a function of p_{T} for tracks at midrapidity (blue) and forward rapidity (red). Note that the complement to 1 is shown instead for the fake, secondary, and strange baryon rates so to fit on the scale. The primary fraction is also plotted as a function of p_{T} for 5 different η projections in **(b)** pp and **(c)** p+Pb. Fits to $f_{\mathrm{primary}}^{\mathrm{fit}}$ (defined in the text) are shown as curves of the same colors.

relative uncertainty of at least 0.5%. Fits to $f_{\mathrm{primary}}^{\mathrm{fit}}$ are then used to infer the appropriate track-by-track correction factor in this analysis. Examples of fitted functions are overlaid in Fig. 6.22.

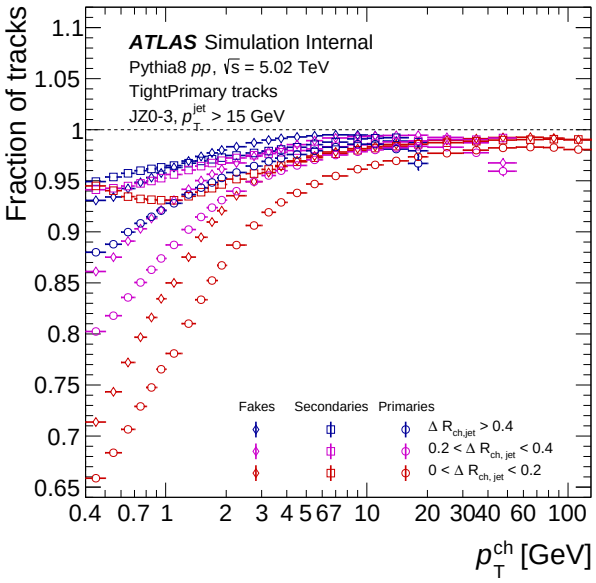


Figure 6.23: The fraction of fake, secondary, and primary tracks is studied as a function of the geometric distance ΔR to the nearest jet above 15 GeV in pp Pythia dijet MC samples. Note that the complement to 1 is shown instead for the fake and secondary rates so to fit on the scale. Tracks far away from the closest jet ($\Delta R > 0.4$) are shown in **blue**; tracks within the jet core ($\Delta R < 0.2$) are shown in **red**.

In general the fits describe the measured primary fractions very well across the entire acceptance. Though, the use of a fit to define the primary track fraction correction factor is taken as a source of systematic uncertainty by evaluating the corrections directly from the data points themselves.

However there is a side-effect of using the minimum bias Hijing MC samples to determine the fake rate in p+Pb. Notably, the fake rate is known to deteriorate in the cores of jets due to the highly collimated spray of particles saturating the ID layers [297]. In Fig. 6.23, we investigate how the fake and secondary rates evolve when looking inside the core of a jet. We use the pp dijet samples for this study, since we already determine the primary fraction in pp using these samples. At 1 GeV, we find that the fake rate increases by about $\sim 12\%$ when looking at particles outside a jet ($\Delta R > 0.4$) to particles in the very core of a jet ($\Delta R < 0.2$). At the lowest p_{T} values, the fake rate increases to nearly 25%. From this study, it is easy to see why the fake rate is lower in the pp samples: every pp dijet MC event contains a jet with many particles, negatively impacting the fake rate, while very few jets are in the p+Pb MC events. This leads to a minor issue where if

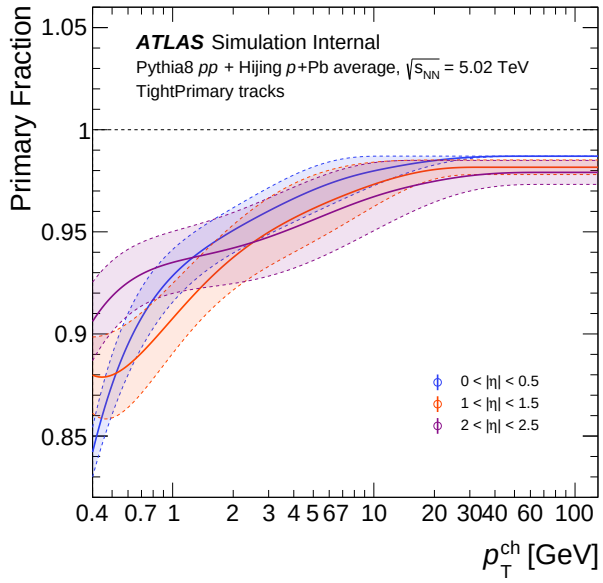


Figure 6.24: The average fraction of primary tracks between the PYTHIA dijet and HIJING p+Pb samples is plotted as a function of track momentum ($p_{\mathrm{T}}^{\mathrm{ch}}$) for three different $|\eta|$ selections. Shaded bands indicate the region between the PYTHIA and HIJING values where the true primary fraction in jet-tagged p+Pb events should lie.

the fake rate differs by Δf between the p+Pb signal and background events, the UE model will be biased by an amount $\Delta f/(S/B)$, where S/B is the signal-to-background ratio. If $S/B < 1$, which is generally the case below $p_{\mathrm{T}} \lesssim 2$ GeV in the p+Pb, then the bias is *amplified*. For example, recall that the difference in primary fractions between the pp and p+Pb was about $\Delta f \approx 3\%$ at 1 GeV; this translates to a bias of about $3\%/0.5 \approx 6\%$ on the final yield measurement. This is clearly unacceptable if we aim to make a precision constraint on jet quenching.

Fortunately, a straightforward solution exists. Note that the p+Pb jet-tagged data consists of particles which are either associated with the jet or the UE. In that case, the true primary fraction must lie *somewhere* between the jet-derived primary fraction used in pp and the HIJING MB-derived primary fraction intended for MB p+Pb. In other words, it cannot be lower than the pure pp (dijet) value and it cannot be higher than the MB value. To account for this effect, we use the average between the samples to obtain a "hybrid" primary fraction and apply it only in p+Pb jet-tagged events. (In pp events and in p+Pb matched events, the primary fraction is assumed to

already be well-modeled by the PYTHIA and HIJING samples, respectively.) Fig. 6.24 shows the result of taking the average between the dijet and MB rates, as well as an shaded band to indicate these lower and upper bounds. At midrapidity, the primary fraction uncertainty is only at the level of $\sim 1\%$, which would translate to an uncertainty of $\sim 2\%$ for a S/B ratio of 0.5. The difference increases at forward rapidity, with an associated uncertainty of $\sim 2\%$.

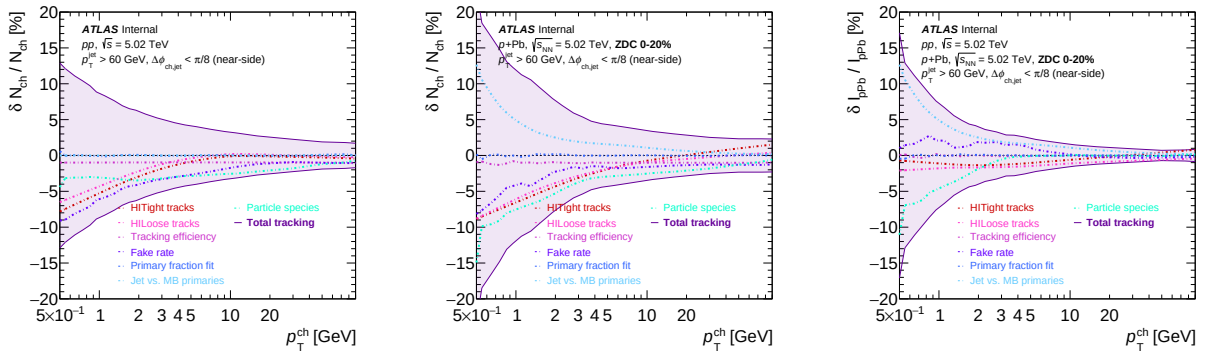
Tracking Uncertainties

We consider a variety of systematic uncertainties related to the charged-hadron selection. These pertain to the choice of track-quality working point, the reconstruction efficiency, the primary fraction & fake rate, and particle-species modeling. How each source compares and contributes to the total tracking uncertainty is illustrated by Fig. 6.25.

First, we evaluate a working point uncertainty by switching to `HILoose` and `HITight` quality criteria. In principle, use of an alternative working point can lead to slightly different results, which should be treated as a source of uncertainty. We apply two variations, though only the variation leading to a larger uncertainty is used. The efficiency and primary rates are reevaluated in each case and used to repeat the measurement. Typically, we find the yield is a few percent small with the alternative working points at the lowest $p_{\mathrm{T}}^{\mathrm{ch}}$ values. At higher values, all results converge to the roughly the same values. However, these variations pick out a slightly different sample of tracks, so this uncertainty is smoothed with a `LOWESS` smoother to reduce sensitivity to statistical uncertainties.

Next is an uncertainty on the reconstruction efficiency. One of the main factors in correctly modeling the track reconstruction is the detector simulation; an imperfect description of the detector will correspond to uncertainty on the model. An overall normalization uncertainty on the tracking efficiency, derived from the modeling of the ID material, must be applied. Essentially, it is a 0.4% uncertainty on the efficiency which grows at larger pseudorapidities,

$$\frac{\delta f_{\mathrm{eff}}(p_{\mathrm{T}},\eta)}{f_{\mathrm{eff}}} \times 100\% = \frac{1.8\% - 0.5\%}{2.4 - 0.05}\left(|\eta| - 0.05\right) + 0.5\%. \tag{6.24}$$



(a) Y_{pp}, $\Delta\phi_{h,\mathrm{jet}} < \pi/8$ **(b)** $Y_{p\mathrm{Pb}}$ 0–20%, $\Delta\phi_{h,\mathrm{jet}} < \pi/8$ **(c)** $I_{p\mathrm{Pb}}$ 0–20%, $\Delta\phi_{h,\mathrm{jet}} < \pi/8$

Figure 6.25: Systematic uncertainties related to tracking are plotted versus $p_{\mathrm{T}}^{\mathrm{ch}}$ in the near-side ($\Delta\phi < \pi/8$) for events with a jet above 60 GeV.

We treat this particular uncertainty as correlated between pp and p+Pb, so it cancels in their ratio.

Another source related to the tracking efficiency pertains to the model details. Similar to the measurement of Z-hadron correlations, we assign an uncertainty on the distribution of particle species in the MC by switching to the efficiency calculation for π^+ mesons. Unlike others, this uncertainty cancels in the pp/p+Pb ratio but *not* in the UE subtraction. Therefore, it is typically 3–4% in pp but can reach 9–10% in p+Pb.

There is also the possibility for uncertainty on the primary fraction f_{primary} to affect the charged-particle yield. One source comes from minor differences in the fake rate that have been observed between data and MC. A universal 100% variation on the `TightPrimary` fake rate is recommended and applied. This uncertainty also accounts for the increased fake rate at high occupancy (i.e., within the core of jets).

Independently, another source of uncertainty is considered in dealing with the fits to the primary fraction, $f_{\mathrm{primary}}^{\mathrm{fit}}$. This uncertainty deals with how well the fit models the true primary fraction, and can be related to, for example, mismodeling of the primary fractions plotted in Fig. 6.22 or uncertainty on the fit parameters. As a conservative estimate, the uncertainty is evaluated by taking the *ab initio* values for the primary fraction, i.e., it is instead evaluated from the points shown in Fig. 6.22. Because the fits capture the points qualitatively well, this uncertainty

is small.

Lastly, we consider an uncertainty associated with differences in the fake rate between the trigger event and matched event. While the 100% fake rate variation accounts for the fake rate in jets, it applies identically to both the trigger event and the matched event and therefore deals with the overall normalization. This additional uncertainty is meant to cover relative differences, and therefore enters in a manner that scales inversely with signal-to-background. We assign this uncertainty by varying the fake rate in p+Pb to the minimum bias HIJING value, rather than the "hybrid" value used for the central values. We find that at low-$p_{\mathrm{T}}^{\mathrm{ch}}$, this uncertainty codominates with the particles species and working point uncertainties (see below), and it drops to 0 at high-$p_{\mathrm{T}}^{\mathrm{ch}}$.

6.5 Underlying Event

Recall that particles can come from either the hard process producing the jet (i.e. are correlated with the presence of the jet tag) or from other processes that occur during the same collision (i.e. are not correlated with the jet). Contributions from the latter are referred to as underlying event (UE) particles. To access the contribution of jet-correlated particles to the total yield (also referred to as the signal yield), the UE background component must be subtracted.

Similar to Chapter 4, a mixed event procedure is used to construct a model for the UE contribution. Recall that in the Pb+Pb study, mixed events are taken from minimum bias data to reduce any final-state bias, and are matched to "trigger events" with similar event activity levels, flow orientation, detector conditions, etc. Schematically, the procedure works the following way:

(1) Select events with jets that meet the jet selection criteria ("trigger events").

(2) For each trigger event, find N_{mix} independent events with similar global properties ("associated events").

(3) For each trigger-associated event pair, take the jets from the trigger event and correlate them with charged particles from the associated event ("mixed event").

In this method, the UE in the trigger events should be similar to the UE in the associated events, but the associated events lack the signal component and therefore the mixed event yield serves as an estimate for the UE.

Underlying Event in p+Pb

Akin to the Pb+Pb measurement in the previous Chapter, our mixed event here is constructed to only match events with similar global properties. First and foremost are the detector conditions. In the Pb+Pb, we used "run groups" to smooth over run-to-run variations; however, we only use 6 of p+Pb data-taking runs, so we simply match events with the same run numbers. Next is the centrality component. Again, in the Pb+Pb case, this was accounted for by matching $\Sigma E_{\mathrm{T}}^{\mathrm{FCal}}$ values to the same percentile bins. In the p+Pb, we use the ZDC energy as a centrality measure, so events should lie in the same $\Sigma E^{\mathrm{ZDC,Pb}}$ percentile bins. Unfortunately however, the dynamic resolution of the ZDC is not sufficient for percent-level event matching. Instead, we match events with similar $\Sigma E_{\mathrm{T}}^{\mathrm{FCal,Pb}}$ values, analogous to the centrality matching in Pb+Pb. The exact matching criteria are defined via the 5% centiles as listed in Table 6.7. This ensures the broad centrality dependence of the mixed event matches the trigger event, though leaves open the possibility of a jet-induced auto-correlation effect. Though, we emphasize that any effect will be suppressed by the signal-to-background ratio S/B, so at high-p_{T} in particular, no bias is expected.

Lastly, in the Pb+Pb, an event-plane matching was performed to ensure the elliptic flow pattern was well-described by the mixed event. In this analysis, this is not completely feasible, as the resolution of the Ψ_2 event plane angle in p+Pb collisions is dramatically worse. This is because the amount of total energy deposited in the forward calorimeter is smaller in p+Pb than Pb+Pb by an order of magnitude. Furthermore, the event plane angle resolution cannot be explicitly studied because only the forward calorimeter on one side of the detector is sensitive to the post-collision nuclear dynamics. In other words, the proton-*nucleus* collision will be boosted towards the Pb-going direction for $N_{\mathrm{coll}} \gtrsim 3$ (since 4 TeV $\sim 3 \times 1.58$ TeV). As a source of systematic uncertainty, we consider the impact of matching event plane angles to within $|\Delta\Psi_2| < \pi/4$. In addition to

Percentile	p+Pb, ΣE_{T} [GeV]	pp, ΣE_{T} [GeV]		p+Pb, ΣE_{T} [GeV]	pp, ΣE_{T} [GeV]
100%	**-22.2**	**-30**			
99%	0.0677596	-24.6222	49%	18.9812	5.49487
98%	0.684615	-21.3904	48%	19.4842	5.79451
97%	1.12491	-19.0602	47%	19.9947	6.09663
96%	1.49227	-17.2364	46%	20.5142	6.4002
95%	**1.82253**	-15.7235	45%	**21.0414**	6.70706
94%	2.13	-14.4311	44%	21.5782	7.0163
93%	2.42523	-13.3116	43%	22.1218	7.32828
92%	2.71275	-12.3107	42%	22.6752	7.64442
91%	2.99725	-11.4091	41%	23.2379	7.96356
90%	**3.28119**	**-10.5869**	40%	**23.812**	**8.28745**
89%	3.56653	-9.82972	39%	24.3971	8.61429
88%	3.85525	-9.12723	38%	24.9922	8.94816
87%	4.14778	-8.47258	37%	25.5978	9.28612
86%	4.44518	-7.85873	36%	26.2153	9.6297
85%	**4.74739**	-7.27867	35%	**26.8471**	9.97898
84%	5.05454	-6.72811	34%	27.4941	10.3351
83%	5.36731	-6.20516	33%	28.1541	10.6972
82%	5.68585	-5.70685	32%	28.8268	11.067
81%	6.00807	-5.22992	31%	29.5164	11.4446
80%	**6.33632**	**-4.77168**	30%	**30.2226**	**11.8312**
79%	6.67007	-4.33132	29%	30.9459	12.2261
78%	7.00782	-3.90732	28%	31.6883	12.631
77%	7.35057	-3.49578	27%	32.4491	13.0468
76%	7.69867	-3.09669	26%	33.2327	13.4728
75%	**8.05047**	-2.70954	25%	**34.0429**	13.9107
74%	8.40802	-2.33286	24%	34.8777	14.3613
73%	8.76912	-1.96523	23%	35.7376	14.8253
72%	9.13477	-1.60704	22%	36.6289	15.3076
71%	9.50518	-1.25716	21%	37.5513	15.8053
70%	**9.87994**	**-0.914987**	20%	**38.5099**	**16.3202**
69%	10.2592	-0.579508	19%	39.5071	16.8539
68%	10.6438	-0.248996	18%	40.5473	17.4086
67%	11.0327	0.0760603	17%	41.6335	17.9901
66%	11.427	0.396522	16%	42.7742	18.5999
65%	**11.8256**	0.711449	15%	**43.9751**	19.2391
64%	12.2295	1.02234	14%	45.2438	19.9141
63%	12.6386	1.33038	13%	46.5895	20.6295
62%	13.0526	1.63634	12%	48.0207	21.3883
61%	13.4727	1.93899	11%	49.5591	22.2028
60%	**13.8972**	**2.23852**	10%	**51.2185**	**23.0819**
59%	14.3277	2.53702	9%	53.0235	24.0361
58%	14.7645	2.83444	8%	55.0084	25.0853
57%	15.2069	3.13034	7%	57.22	26.2534
56%	15.6559	3.42595	6%	59.7225	27.5764
55%	**16.111**	3.7205	5%	**62.6251**	29.109
54%	16.5727	4.01458	4%	66.0934	30.936
53%	17.0407	4.30907	3%	70.4484	33.2358
52%	17.5157	4.60449	2%	76.3949	36.3724
51%	17.9969	4.90021	1%	86.0756	41.5072
50%	**18.4852**	**5.19628**	0%	**219.8**	**219.8**

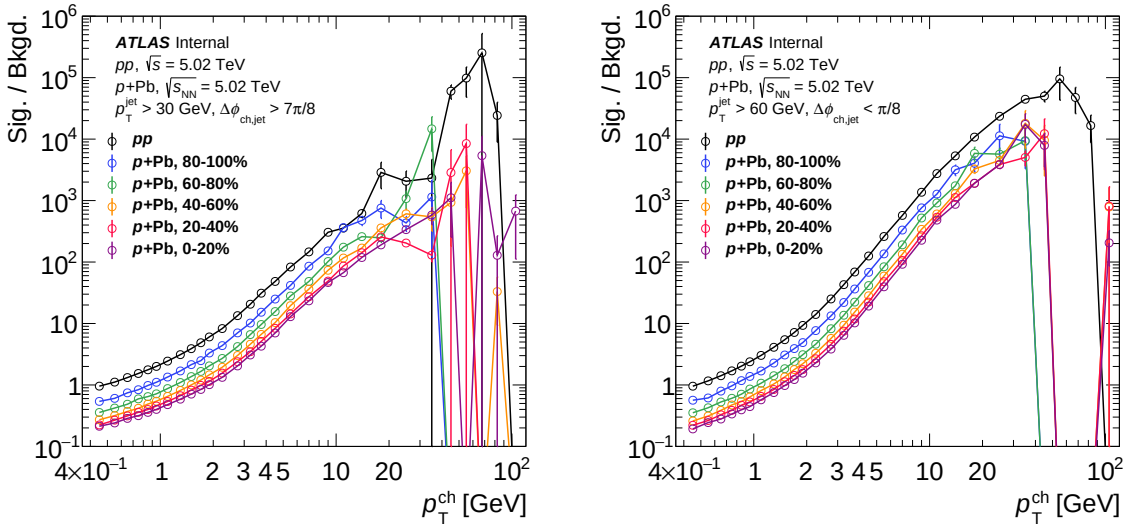
Table 6.7: $\Sigma E_{\mathrm{T}}^{\mathrm{FCal}}$ centiles used for the p+Pb (A-side only) and pp (A+C-side sum) event matching. Bolded values correspond to the bin edges used in the nominal analysis results; other values are used in variations on the matching.

incorporating sensitivity to differences event plane orientation, this is useful for discerning the impact of a potential jet bias. If, in fact, jets are biasing the measured $\Sigma E_{\mathrm{T}}^{\mathrm{FCal,Pb}}$ value, then because of their collimated nature they would naturally affect the Ψ_2 angle measurement because it is calorimetric (see Eq. (4.29)). If jets in both the trigger and associated event are affecting the Ψ_2 measurement, then this should impact the UE measurement and the final yield in some manner. However, this is not observed to within a fraction of a percent, so we conclude there is no discernible effect. Another systematic uncertainty is evaluated by varying the particular $\Sigma E_{\mathrm{T}}^{\mathrm{FCal,Pb}}$ matching criteria, though we find the results are completely insensitive to this variation.

Underlying Event in *pp*

Although smaller, there is also an underlying event in pp collisions. In the Z-hadron correlations measurement, the pp underlying event was evaluated within the same subset of Z-tagged events to match event characteristics as closely as possible. For jet events, this is not possible simply for the reason that we cannot define a complementary set of "at-rest" jets akin to our "at-rest" Z bosons. Thus we use minimum bias data to define the UE, thereby foregoing some amount of model accuracy in favor of definability.

We start by matching jet-trigger events with minimum bias events firing the `HLT_mb_sptrk` trigger. For matching criteria, again events must lie within the same run number. We also match in a notion of centrality to compensate for the fact that the minimum bias events can be topologically distinct from jet events. One way to understand this is that although $N_{\mathrm{coll}} \in \{0, 1\}$ in pp collisions, the proton has a nonzero volume and thus each pp collision still possesses some notion of centrality. As impact parameter decreases, more parton-parton scatterings might occur, which might lead to, for example, increased probability for multiparton interactions (MPIs). Thus, without accounting for this effect, associated events might be biased towards a lower probability of a multi-parton interaction than the trigger event would be. To account for this "pp centrality" notion, we match events with similar $\Sigma E_{\mathrm{T}}^{\mathrm{FCal,A+C}}$ values (note that the A and C sides are summed, unlike the p+Pb, as the collision system is rapidity-symmetric). We require events be in the same 10%-centiles, as



(a) $p_{\mathrm{T}}^{\mathrm{jet}} > 30$ GeV, away-side **(b)** $p_{\mathrm{T}}^{\mathrm{jet}} > 60$ GeV, near-side

Figure 6.26: Signal-to-background ratios are shown for pp and 5 different p+Pb centrality selections (determined with ZDC centiles) as a function of charged-particle p_{T}. **(a)** shows this quantity for the 30 GeV jet selection in the away-side, where the ratio tends to be smallest. **(b)** shows this quantity for the 60 GeV jet selection in the near-side, where the ratio tends to be largest.

designated by the bolded values in Table 6.7. Variations on the matching are applied to account for potential systematic uncertainty with this method, though, similar to the p+Pb variations, the results are completely insensitive to their effects.

The results of the mixed event procedure are shown with the main results later in Chapter 7. Though, in determining uncertainties related to the mixed event, it is useful to characterize the relative size of the background to the signal component, i.e., the signal-to-background ratio. These are shown in Fig. 6.26 for a variety of event selections. As expected, the signal-to-background ratio is smallest at low-$p_{\mathrm{T}}^{\mathrm{ch}}$ and in the most central p+Pb selection. It is also smaller in the away-side than the near-side, and for events with lower p_{T} jets. Roughly around a $p_{\mathrm{T}}^{\mathrm{ch}}$ value of 2 GeV, the signal-to-background is at least unity across all the selections. Above this value, it is more likely that any given charged particle is truly correlated with a jet rather than part of the underlying event background.

Event-Mixing Uncertainties

One source of uncertainty comes from imperfect modeling of the mixed event due to mismatches in global event characteristics. As an extreme example, if we imagine an event with $\Sigma {E_{\mathrm{T}}}^{\mathrm{FCal}} = 100$ GeV that was only matched with events with $\Sigma {E_{\mathrm{T}}}^{\mathrm{FCal}} = 90$ GeV, we might expect the average UE will be underestimated and therefore the signal component to be overestimated. To understand the impact of the matching criteria on the UE estimate, a few different variations are applied, labeled "Mixing Variation n" for $n \in \{1, 2, 3, 4, 5\}$. They are as follows:

(1) The $\Sigma E_{\mathrm{T}}^{\mathrm{FCal}}$ matching is more granular in pp collisions, where the trigger and matched event must have $\Sigma E_{\mathrm{T}}^{\mathrm{FCal}}$ in the same 2% bin, 100%, 98%, 96%, ..., 4%, 2%, 0%.

(2) The $\Sigma E_{\mathrm{T}}^{\mathrm{FCal}}$ matching is very granular in p+Pb collisions at the 1% level, i.e. 100%, 99%, 98%, ..., 2%, 1%, 0%.

(3) The $\Sigma E_{\mathrm{T}}^{\mathrm{FCal}}$ matching is offset in pp collisions. Instead of matching in 100%, 90%, 80%, ..., 20%, 10%, 0%, events are matched in a complementary range of $\Sigma E_{\mathrm{T}}^{\mathrm{FCal}}$ percentiles of the same width: 100%, 95%, 85%, 75%, ..., 25%, 15%, 5%, 0%.

(4) In addition the nominal matching, the event plane angle Ψ_2 determined with the A-side forward calorimeter, defined via sums performed over towers in the forward calorimeter

$$\tan\left(n\Psi_n\right) = \frac{\sum E_{\mathrm{T}} \sin\left(n\phi\right)}{\sum E_{\mathrm{T}} \cos\left(n\phi\right)}, \tag{6.25}$$

is required to match between the tagged and matched events to within $|\Delta\Psi_2| < \frac{\pi}{4}$ in the p+Pb data.

(5) The event plane angle Ψ_2, determined with from the combined A- and C-side sum, is matched to within $\frac{\pi}{4}$ in the pp, similar to (4).

In brief, the first three variations affect the centrality matching of the UE modeling. Variations 1 and 3 apply similarly to the pp measurement, and the maximum variation of the two is

taken at each bin in the analysis to avoid double-counting this uncertainty. Variation 2 applies to the p+Pb measurement and is treated independently from 1 and 3. The total pp and the p+Pb uncertainties are then added together in quadrature.

The other two variations – 4 and 5 – perform an event plane matching and affect the result independently from the centrality matching. Therefore, the relative uncertainties from the pp and p+Pb event plane matching are also added in quadrature when computing the ratio $I_{p\mathrm{Pb}}$. These are not expected to lead to a large effect in either system due to poor expected resolution of the Ψ_2 variable; however, if there is a jet bias in the FCal, this could bias the Ψ_2 measurement in the jet events and generate a bias across a wide $p_{\mathrm{T}}^{\mathrm{ch}}$ range. This is not observed however, suggesting the UE model is not sensitive to this.

This reflects the small UE in these collision systems, which generally leads to small uncertainties overall, at least compared to other sources. They are largest where the signal-to-background ratio is smallest, amounting to $\sim 2\%$ around 0.5 GeV in central p+Pb events.

6.6 Deconvolving the Detector Response

In Sec. 6.3 we talked about how the JER quantifies the p_{T} response fluctuations of the jet reconstruction. We also looked at the TMR to quantify the p_{T} response fluctuations of the track trajectory measurement. In general, the TMR is better than the JER by a factor of $\sim \times 3 - 4$ and the effect of p_{T} bin migration is expected to be small relative to our bin widths. However, it is well-known that the jet p_{T} response is dependent on the fragmentation pattern [328]. Constituents of harder fragmenting jets, for example, tend to have a larger EM fraction of their showers and so more of the jet energy is directly recovered. In short, this means that the track yield is somewhat autocorrelated with the particular jet p_{T} response.

To deconvolve these detector resolution effects, an *unfolding* procedure is necessary. The main goal of any unfolding is to build an estimator for the truth-level parameters or *causes* C_i $(1 \leq i \leq N_C)$ given a set of *effects* E_j $(1 \leq j \leq N_E)$, sometimes also referred to as the measurements or observations. In general, the response matrix, which translates causes into effects, either cannot

be inverted or the inverse exhibits pathological qualities. Thus extracting the truth-level parameters given a data set is a computationally challenging problem.

The most frequently used method in heavy-ion physics is the iterative, Bayesian-inspired procedure introduced by D'Agostini [329].[7] Central to this procedure is Bayes' theorem, which helps us tackle the probability of each cause C_i given a particular observation E_j,

$$\mathcal{P}\left(C_i|E_j\right) = \frac{\mathcal{P}\left(E_j|C_i\right)\mathcal{P}\left(C_i\right)}{\mathcal{P}\left(E_j\right)} = \frac{\mathcal{P}\left(E_j|C_i\right)\mathcal{P}\left(C_i\right)}{\sum_{i'=1}^{N_\mathrm{C}}\mathcal{P}\left(E_j|C_{i'}\right)\mathcal{P}\left(C_{i'}\right)}. \tag{6.26}$$

The power in this equation, which D'Agostini recognized, is that the posterior probability of C_i can be recursively updated from known values given a data set, even if our previous knowledge $\mathcal{P}\left(C_i\right)$ (the prior) is limited. Essentially, Bayes' theorem above allows us to update our belief of any particular cause given some set of data $\left\{E_j\right\}$. Typically, the likelihood $\mathcal{P}\left(E_j|C_i\right)$, which transfers causes into effects, is evaluated in Monte Carlo studies with detector simulation. Thus the likelihood encapsulates the response, and is related to the 2D correlation between causes and effects; examples for the response matrix for jets can be seen in Fig. 6.28. (The complete set of response matrices is shown in Appendix B.2.) At each cause ("truth-level $p_\mathrm{T}^\mathrm{jet}$"), there is a distribution of

[7] The iterative unfolding uses Bayes' theorem to recursively update the probability of each cause given a set of observations, but returns a fixed estimate for the number of causes $\hat{n}\left(C_i\right)$ instead of its distribution, and therefore is not entirely Bayesian. Note that the iterative step Eq. (6.28) is a fundamentally frequentist statement.

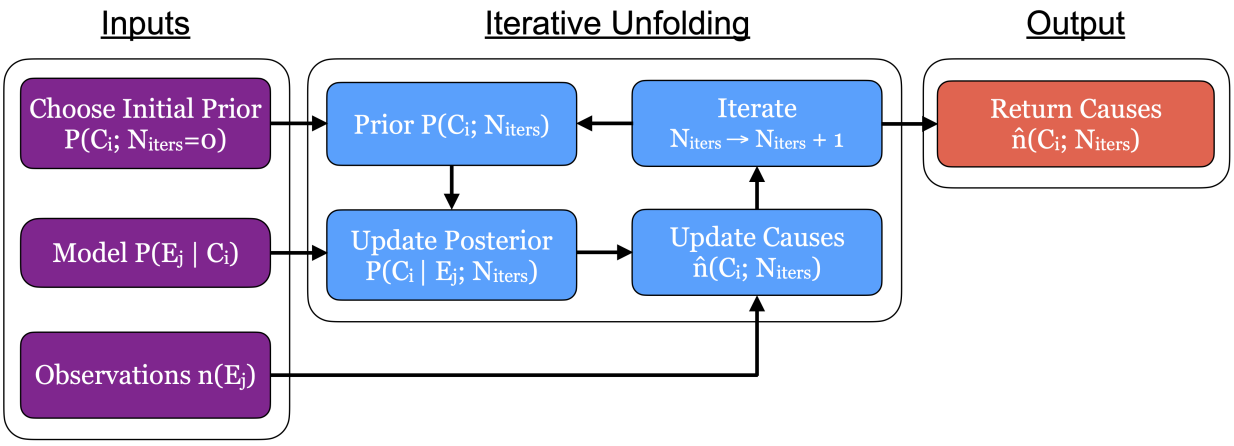
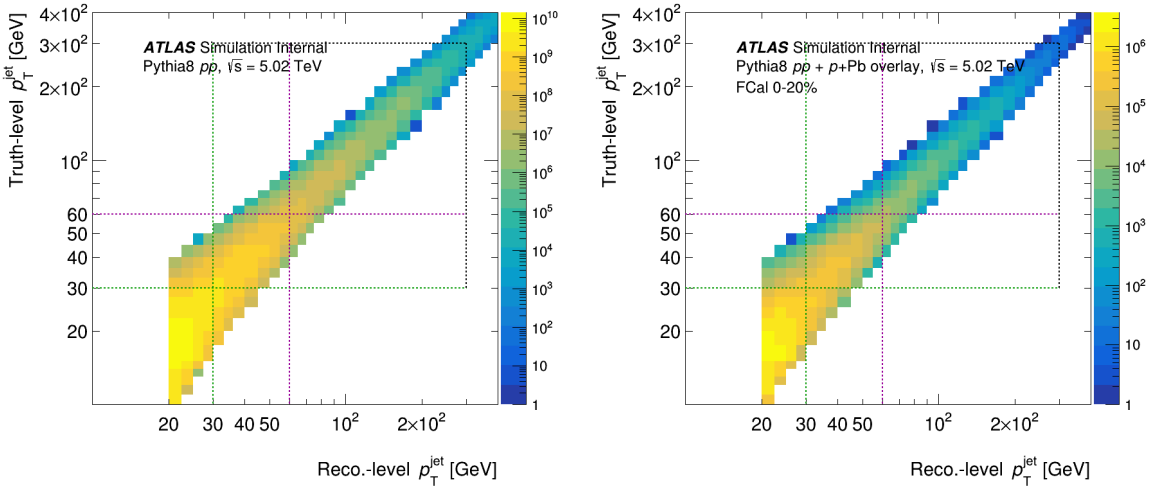


Figure 6.27: Flow chart of the iterative Bayesian-inspired unfolding procedure introduced by D'Agostini [329]. Inputs are shown on the left and outputs on the right. The iterative loop is shown in the center.



(a) pp **(b)** FCal 0–20% p+Pb

Figure 6.28: Examples of 1D response matrices for jets in **(a)** pp and **(b)** FCal 0–20% p+Pb collisions, which are input to the iterative unfolding. The fiducial ranges of the measurement is highlighted by the dashed lines. The full set of response matrices are in Appendix B.2.

effects ("reco.-level $p_{\mathrm{T}}^{\mathrm{jet}}$") that can occur. Normalizing this distribution gives us $\mathcal{P}\left(E_j|C_i\right)$. Putting everything together, we evaluate the posterior and update the expected number of causes $\hat{n}$, which can be written as a function of the number of observations n:

$$\hat{n}\left(C_i\right)|_{N_{\mathrm{iter}}} = \sum_{j=1}^{N_{\mathrm{E}}} \mathcal{P}\left(C_i|E_j\right)|_{N_{\mathrm{iter}}-1}\, n\left(E_j\right). \tag{6.27}$$

The subscripts N_{iter} indicate how these quantities evolve as we iterate the procedure. With $\hat{n}\left(C_i\right)$ in-hand, we define a new prior after N_{iter} iterations $\mathcal{P}\left(C_i\right)|_{N_{\mathrm{iter}}}$ via

$$\mathcal{P}\left(C_i\right)|_{N_{\mathrm{iter}}} = \frac{\hat{n}\left(C_i\right)|_{N_{\mathrm{iter}}}}{\sum_{i=1}^{N_C} \hat{n}\left(C_i\right)|_{N_{\mathrm{iter}}}}. \tag{6.28}$$

The operating principle is that this new prior incorporates our new knowledge from the data, and therefore represents an improvement in our model. We can then feed it back into Eq. (6.26) and repeat. In summary, the iterative unfolding algorithm is succinctly illustrated via a flow diagram as in Fig. 6.27.

Defining the Unfolding Problem

This analysis uses the implementation of the iterative unfolding algorithm in the `RooUnfold` software package [330]. Notably, there are two ingredients to our measurement that need to be unfolded:

- the total number of jet-correlated charged-particles N_i in bin i, and
- the total number of jets n_i in bin i.

Although we are primarily interested in N_i, it is important to also unfold the jet spectrum. For distinguishing the two, we refer to the numerator unfold ($N_i \to \hat{N}_i$) as the "2D unfold", since each bin i represents both a $p_{\mathrm{T}}^{\mathrm{ch}}$ and a $p_{\mathrm{T}}^{\mathrm{jet}}$ values, and the denominator ($n_i \to \hat{n}_i$) as the 1D unfold, since each bin i only represents a $p_{\mathrm{T}}^{\mathrm{jet}}$ value. To illustrate why both must be unfolded, consider a situation where many 29 GeV jets migrate to perhaps 31 GeV, but due to the power law nature of the jet spectrum, not as many 31 GeV jets migrate to 29 GeV. The 2D unfolding will identify this as an excess of total charged particles in the fiducial region and essentially scale up the yield appropriately. If the denominator is unchanged, then the final per-jet yield will be smaller than it should be, even though the contamination of lower p_{T} jets will be uncorrected for. To compensate, the number of selected events (the number of jets) must be similarly corrected to obtain the correct per-jet normalized yield. In fact, the N_{jet} unfold is much simpler: it is one-dimensional, and only uses a handful of $p_{\mathrm{T}}^{\mathrm{jet}}$ bins (for convenience, the same $p_{\mathrm{T}}^{\mathrm{jet}}$ bins are used as in the 2D unfolding).

But first, we need to relate these quantities to the average yield – which is the quantity we actually measure – via scaling up by the number of sampled jets. For instance,

$$N_i = n_i \times \left(\left. \frac{dY}{dp_{\mathrm{T}}^{\mathrm{ch}}} \right|_{\mathrm{subtracted}} \times \Delta p_{\mathrm{T}}^{\mathrm{ch}} \right), \tag{6.29}$$

where $dY/dp_{\mathrm{T}}^{\mathrm{ch}}$ is the UE-subtracted, per-jet charged-particle yield in bin i, and $\Delta p_{\mathrm{T}}^{\mathrm{ch}}$ is the bin width.

Next, we define the likelihood function via the response matrices in the MC samples. Response matrices are produced from truth-matched charged particles correlated with reconstructed

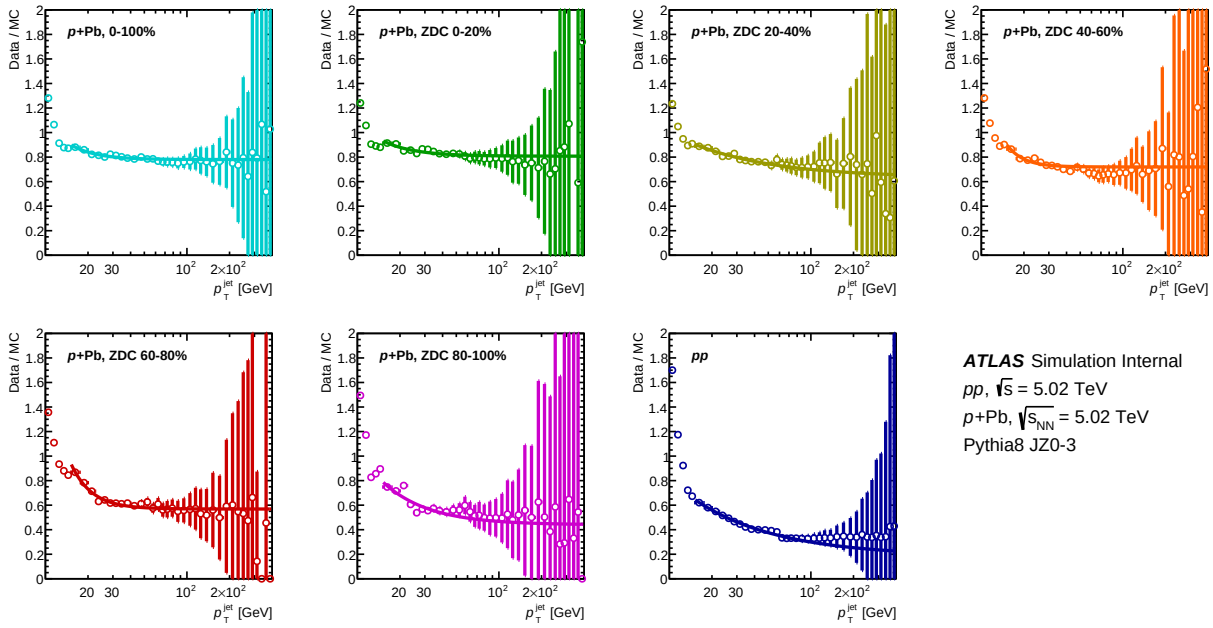


Figure 6.29: Jet-by-jet weights applied to MC in evaluating the response matrix, derived via the data / MC ratio of jet spectra. Each panel indicates a different p+Pb centrality or pp collisions.

jets in the MC samples (in the case of p+Pb, the MC with data overlay samples are used, though we note that tracks and jets in the overlay are suppressed by the truth-matching requirement). Thus separate response matrices are generated for charged particles nearby ($\Delta\phi < \pi/8$), away from ($\Delta\phi > 7\pi/8$) and perpendicular to ($\pi/3 < \Delta\phi < 2\pi/3$) a jet. To account for response inefficiencies in the nominal measurement (jets and/or charged particles that fall outside the nominal p_{T} acceptances), additional underflow/overflow bins are used. Several underflow bins span from $p_{\mathrm{T}}^{\mathrm{jet}} = 10$–$30$ GeV and 4 overflow bins span from $p_{\mathrm{T}}^{\mathrm{jet}} = 300$–$400$ GeV, respectively. For the charged hadron response, only one underflow/overflow bin on either end of the range is needed due to the excellent response $\lesssim 3\%$. One bin is used to cover underflow between $p_{\mathrm{T}}^{\mathrm{ch}} = 0.4$–$0.5$ GeV, and another covers the $p_{\mathrm{T}}^{\mathrm{ch}} = 90$–$120$ GeV range.

To enter the response matrix, jets are required to have truth $p_{\mathrm{T}}^{\mathrm{jet}} > 10$ GeV. Successfully reconstructed jets meet the event selection criteria outlined in Sec. 6.3 and have $p_{\mathrm{T}}^{\mathrm{jet}} > 20$ GeV. Both truth and reconstructed jets can have a maximum $p_{\mathrm{T}}^{\mathrm{jet}}$ of 400 GeV. Truth charged particles and reconstructed charged particles must have p_{T} in the range 0.4–120 GeV. Because the raw (pre-

unfolded) yield measurement is tracking-efficiency corrected, truth charged particles must have a reconstructed partner meeting the selection criteria outlined in Sec. 6.4 to enter the response matrix at all. However, truth jets can enter the response matrix if they do not have a reconstructed partner by calling the `RooUnfoldResponse::Miss` function, which enables a jet-efficiency correction. After unfolding, the final yield distributions can be computed by working backwards from Eq. 6.29:

$$\left.\frac{dY}{dp_{\mathrm{T}}^{\mathrm{ch}}}\right|_{\mathrm{unfolded}} = \frac{1}{\hat{n}_i}\frac{\hat{N}_i}{\Delta p_{\mathrm{T}}^{\mathrm{ch}}}. \tag{6.30}$$

In addition to all of this, it is important to ensure that the events filling the response matrix are have similar sample properties to data. In particular, the jet p_{T} spectrum should match between the two; otherwise, the unfold will be artificially biased towards the spectrum in MC. For this reason we reweight entries so that the spectrum matches between data and simulation. The weights are applied per-jet and derived by taking the ratio of the jet spectra in data and MC, which is smoothed by fitting to a functional form

$$f(p_{\mathrm{T}}) = \left(\frac{p_{\mathrm{T}}}{p_{\mathrm{T0}}}\right)^{\gamma} + C. \tag{6.31}$$

The final weights are shown in Fig. 6.29. Visually, the fits describe the ratio very well. At low-p_{T}, the data/MC ratio diverges due to fewer jets appearing in MC, though we note that soft jet production is not as well modeled in simulation as hard jets, so this behavior is not unreasonable. Additionally, the ratio is nearly constant in the fiducial acceptance 30–300 GeV, so we argue that the results should be somewhat insensitive to the weights in this range. Though, we do consider these to be a source of systematic uncertainty, which is evaluated by not applying the jet weights at all. This is labeled as an "Unfolding Prior" uncertainty.

Regularization

We have specifically avoided mention of when to exit the recursion. There is no *a priori* "best" number of iterations to use; instead, N_{iter} is treated as a regularization parameter. Ideally, increasing N_{iter} leads to a more accurate result, and changes to the distribution diminish with higher N_{iter}. However statistical uncertainties tend to increase without bound as more iterations

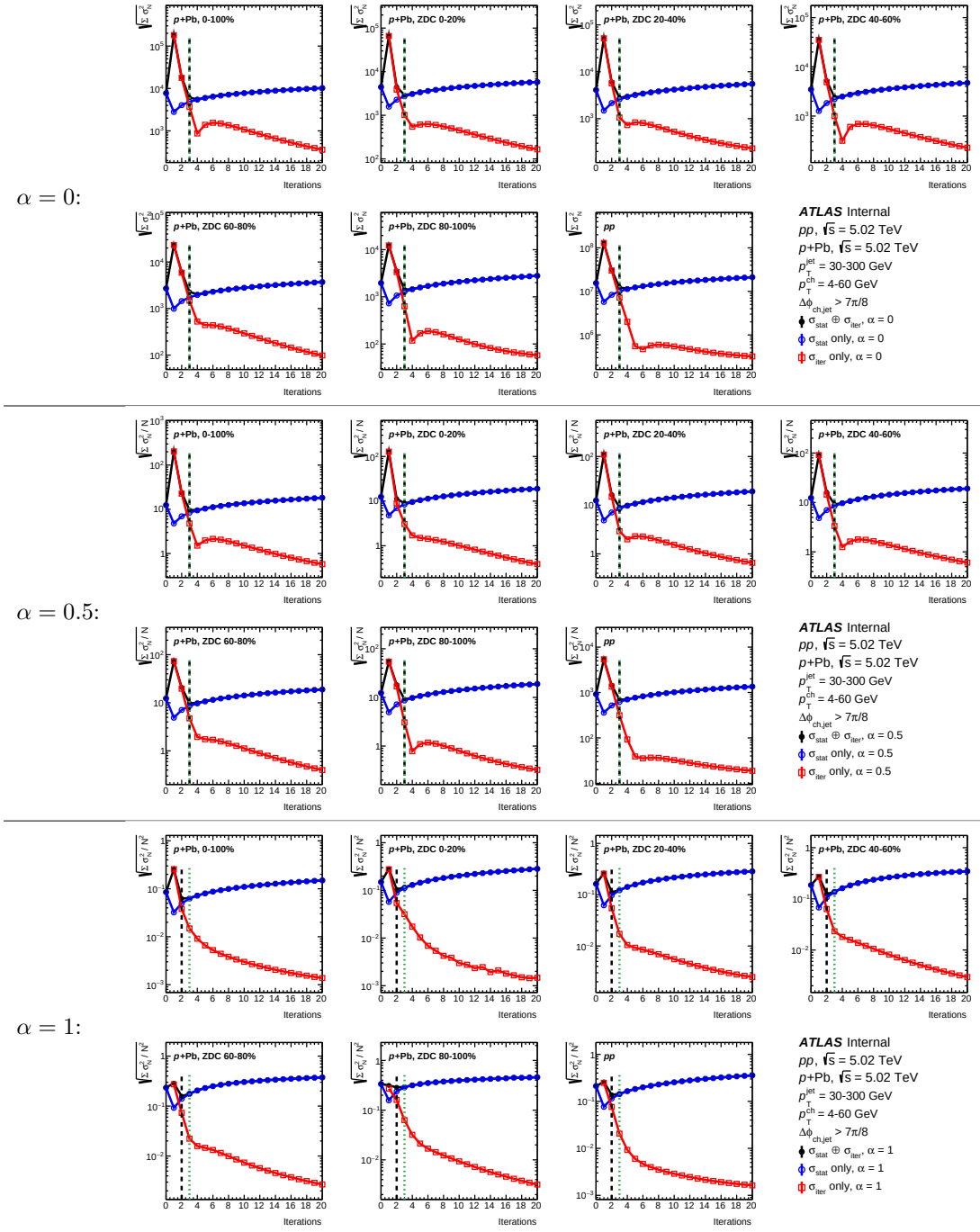


Figure 6.30: σ_{iter} (red squares) and σ_{stat} (blue circles) are plotted versus N_{iter} in data with $\alpha \in \{0, 0.5, 1\}$. **Black** vertical dashed lines indicate the lowest nonzero N_{iter} value ($N_{\text{iter}}^{\text{opt.}}$) where $\sigma_{\text{iter}} < \sigma_{\text{stat}}$ for all $N_{\text{iter}} > N_{\text{iter}}^{\text{opt.}}$ values. The **green** dotted lines indicate the value of $N_{\text{iter}}^{\text{opt.}}$ used in the analysis. Analogous plots for the near-side are shown in Fig. B.5 in Appendix B.3.

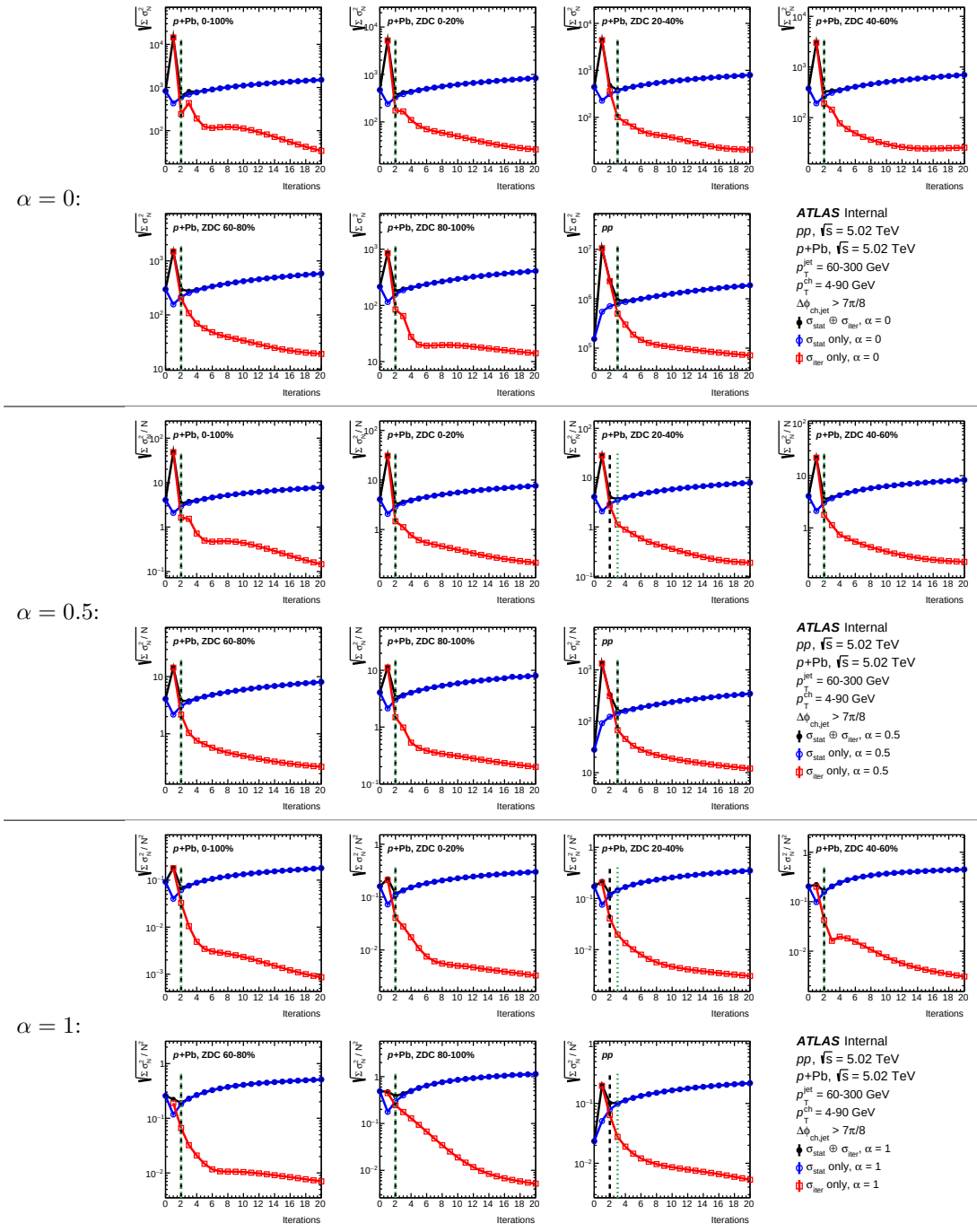


Figure 6.31: σ_{iter} (red squares) and σ_{stat} (blue circles) are plotted versus N_{iter} in data with $\alpha \in \{0, 0.5, 1\}$. **Black** vertical dashed lines indicate the lowest nonzero N_{iter} value ($N_{\text{iter}}^{\text{opt.}}$) where $\sigma_{\text{iter}} < \sigma_{\text{stat}}$ for all $N_{\text{iter}} > N_{\text{iter}}^{\text{opt.}}$ values. The **green** dotted lines indicate the value of $N_{\text{iter}}^{\text{opt.}}$ used in the analysis. Analogous plots for the near-side are shown in Fig. B.6 in Appendix B.3.

are performed, with increasingly marginal benefits in accuracy. Consequently N_{iter} is often tuned to balance these two competing effects. We use a data-driven approach to fix N_{iter} by examining the convergence of the unfold, setting it numerically by comparing the net effect of each iteration to the total uncertainty. Thus, we define a total statistical uncertainty σ_{stat} and an iterative difference σ_{iter} associated with going from N_{iter} to $N_{\text{iter}}+1$ iterations for this purpose. Note that this latter quantity indicates the relative effect of the unfold as $N_{\text{iter}} \to \infty$ and is not treated as a source of systematic uncertainty in the final result. Both are defined via sums on the unfolded distributions after N_{iter} iterations (denoted by $\hat{N}_{i,N_{\text{iter}}}$) over a range of bins $\{i\}$:

$$\sigma_{\text{stat}}\left(N_{\text{iter}};\alpha\right) = \bigoplus_i \frac{\sigma_{\hat{N}_{i,N_{\text{iter}}}}}{\left(\hat{N}_{i,N_{\text{iter}}}\right)^{\alpha}} \quad \text{and} \quad \sigma_{\text{iter}}\left(N_{\text{iter}};\alpha\right) = \sum_i \frac{\left|\hat{N}_{i,N_{\text{iter}}} - \hat{N}_{i,N_{\text{iter}}-1}\right|}{\left(\hat{N}_{i,N_{\text{iter}}}\right)^{\alpha}}. \tag{6.32}$$

A combined uncertainty is also taken from the quadrature sum $\sigma_{\text{total}} = \sigma_{\text{stat}} \oplus \sigma_{\text{iter}}$, though it does not affect our decision-making. As a choice, we optimize the unfold over bins i such that 30(60) GeV $< p_{\text{T}}^{\text{jet}} <$ 300 GeV and 4 GeV $\leq p_{\text{T}}^{\text{ch}} \leq$ 60(90) GeV.[8] The parameter $\alpha \in [0,1]$ in Eq. 6.32 specifies how the bins are combined according to their central values and uncertainties: $\alpha = 0$ means sum the *absolute* uncertainties, $\alpha = 1$ means sum the *relative* uncertainties. Thus, if $\alpha = 0$, then bins with high absolute uncertainties (bins with a large number of counts) will dominate the sum, whereas if $\alpha = 1$, then bins with high relative uncertainties (bins with a small number of counts) will dominate. Other values denote some hybrid of these extremes, and can be understood from an example where $\alpha = 0.5$. Equipped with a Poisson ansatz that $\sigma_{\hat{N}_i} \propto \sqrt{\hat{N}_i}$, then the $\hat{N}_i$ dependence mostly disappears in each term, so we expect each bin to contribute similarly to the sum. In this case, neither end of the range is favored. To determine when to terminate the iterations, we investigate how N_{iter} would be optimized differently for each situation.

Some selected results of this study are shown in Fig. 6.30 for the away-side of $p_{\text{T}}^{\text{jet}} > 30$ GeV jets. We see that a cross-over value for N_{iter} emerges such that $\sigma_{\text{iter.}} < \sigma_{\text{stat.}}$ above the cross-over. These are indicated by the vertical **black** dashed lines, and range from $\sim$ 2–3 iterations. They tend

[8] Recall that the 30–60 GeV jets are sampled from prescaled minimum bias data, whereas the 60 GeV jets are sampled with an unprescaled jet trigger, so there is a sampling discontinuity at $p_{\text{T}}^{\text{jet}} = 60$ GeV. Therefore we optimize N_{iter} separately for the $p_{\text{T}}^{\text{jet}} > 30$ GeV and $p_{\text{T}}^{\text{jet}} > 60$ GeV selections.

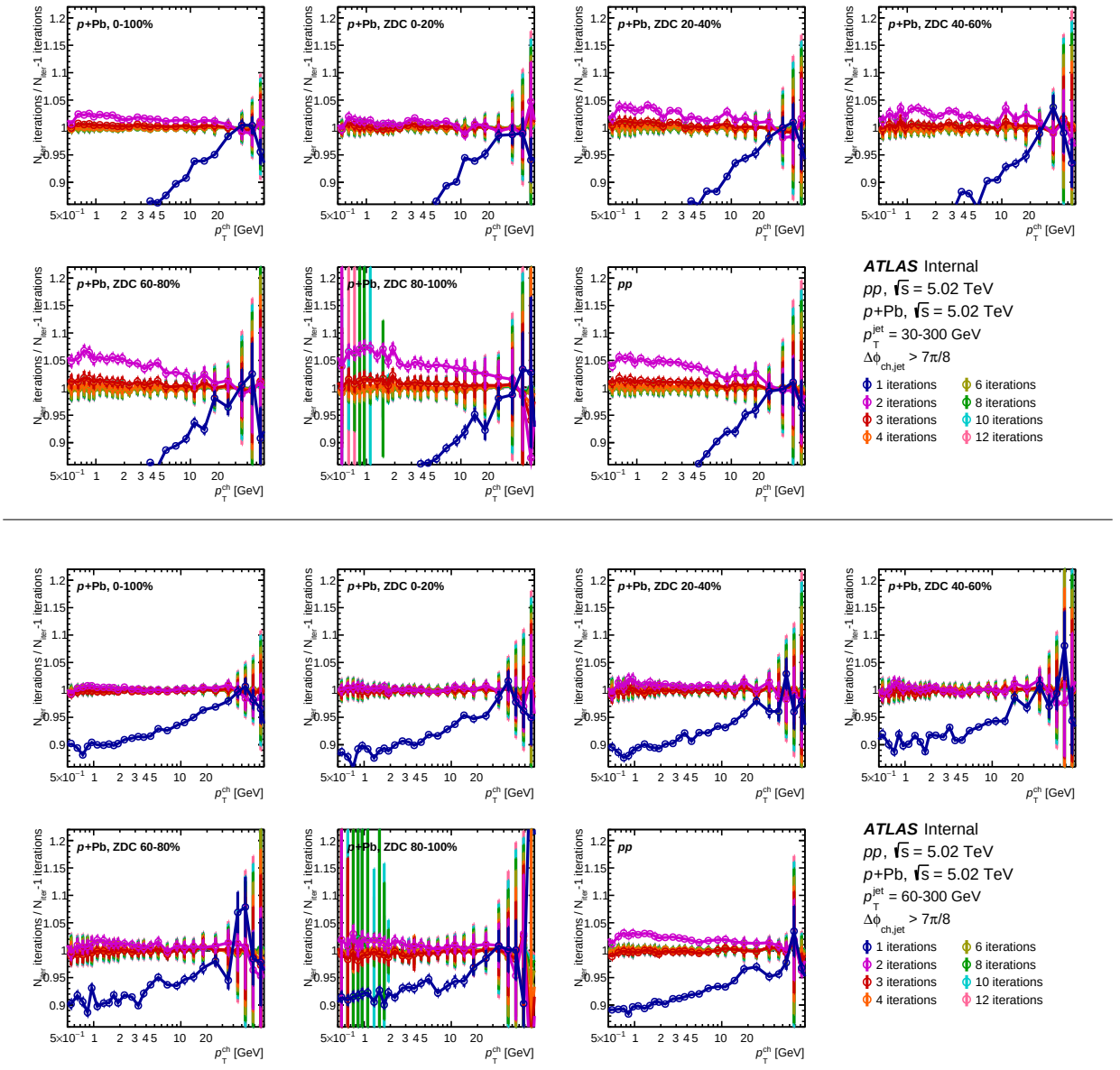


Figure 6.32: The convergence ratio is studied as a function of $p_{\mathrm{T}}^{\mathrm{ch}}$ and N_{iter}. Uncertainties represent solely the uncertainty on the numerator. Analogous plots for the near-side are shown in Fig. B.7 in Appendix B.3.

to be higher in bins with more jets, i.e., the centrality-integrated and central-most p+Pb events, due to their better statistical precision. We also notice that in each selection, the cross-over values are very stable across $\alpha \in \{0, 0.5, 1\}$, typically differing by at most 1 iteration across the entire range. This indicates that the regularization can be simultaneously optimized for both the high-$p_{\mathrm{T}}^{\mathrm{ch}}$

and low-$p_{\mathrm{T}}^{\mathrm{ch}}$ bins. As a choice, we define the optimal number of iterations $N_{\mathrm{iter}}^{\mathrm{opt.}}$ to the be the largest value across $\alpha \in \{0, 0.5, 1\}$. In each panel, $N_{\mathrm{iter}}^{\mathrm{opt.}}$ is indicated numerically by the **green** vertical dotted line, and by construction always lies on top of or to the right of the **black** dashed lines.

In Fig. 6.31 we repeat this study for the away-side of $p_{\mathrm{T}}^{\mathrm{jet}} > 60$ GeV jets. We see very similar behavior in these panels, with 2–3 iterations being favored for this selection as well. As a choice, we again set $N_{\mathrm{iter}}^{\mathrm{opt.}}$ based on the maximum $N_{\mathrm{iter}}^{\mathrm{opt.}}$ across each α value for the $p_{\mathrm{T}}^{\mathrm{jet}} > 60$ GeV selection. These optimized values are again indicated by the **green** vertical dotted lines.

To validate these choices, we also explicitly investigate the convergence of the unfold as N_{iter} increases. Ideally, the posterior will quickly converge to some value, and we hope that

$$\lim_{N_{\mathrm{iter}} \to \infty} \frac{\hat{n}_i \left(N_{\mathrm{iter}}\right)}{\hat{n}_i \left(N_{\mathrm{iter}} - 1\right)} = 1. \tag{6.33}$$

To this end, this ratio – plotted versus $p_{\mathrm{T}}^{\mathrm{ch}}$– is shown in Figs. 6.32 and B.7 for a range of N_{iter} values. Initially, the unfold has a dramatic effect – which is expected – and the ratio is observed to converge to unity as more iterations are added. This suggests the unfolding is convergent as $N_{\mathrm{iter}} \to \infty$, as desired. Visually, by approximately $N_{\mathrm{iter}} \sim 3$, additional iterations have a very marginal effect (within about 1% everywhere). We can also see that the $p_{\mathrm{T}}^{\mathrm{jet}} > 30$ GeV measurement converges less quickly than the $p_{\mathrm{T}}^{\mathrm{jet}} > 60$ GeV selection, reflecting the more precise JER at higher $p_{\mathrm{T}}^{\mathrm{jet}}$.

We also highlight the convergence ratio going from $N_{\mathrm{iter}}^{\mathrm{opt.}}$ iterations to $N_{\mathrm{iter}}^{\mathrm{opt.}}+1$ in Fig. 6.33. In each panel, the additional iteration is shown as a systematic band on the nominal value. We see that this variation leads to effects that are – at the very most (and typically much less than) – of order 1%, and diminish with $p_{\mathrm{T}}^{\mathrm{ch}}$. For comparison, this is much smaller than the systematic uncertainties (discussed later in Sec. 6.7), and thus we conclude that this choice of N_{iter} simultaneously provides an acceptably stable and accurate result.

Separate from the 2D unfold, the number of iterations in the 1D unfold for the denominator is also optimized. This follows very similarly, and here we summarize the findings. The iterations study is performed again with $\alpha \in \{0, 0.5, 1\}$ and the results are shown in Figs. 6.34 and 6.35. We note that, when integrating over jets above 60 GeV, a local maximum structure appears around

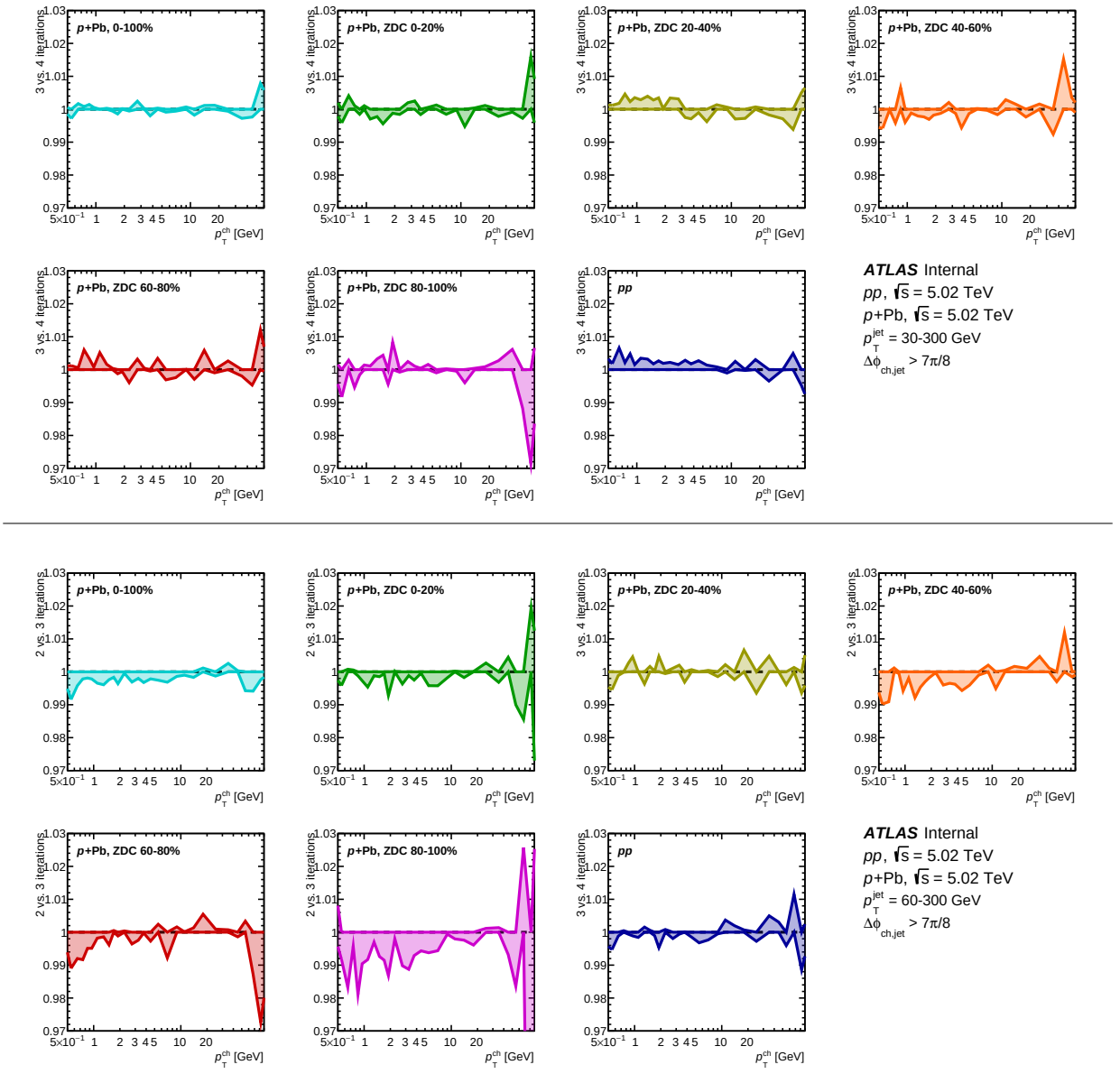


Figure 6.33: The convergence ratio at $N_{\mathrm{iter}}^{\mathrm{opt.}}$ is studied as a function of $p_{\mathrm{T}}^{\mathrm{ch}}$. The uncertainty band shows the effect of the additional iteration. Analogous plots for the near-side are shown in Fig. B.8 in Appendix B.3.

7–10 iterations, however this peak is well within the statistical uncertainties and can be ignored. In fixing N_{iter} for the jet spectrum, we note that it is better to optimize with respect to the absolute uncertainty ($\alpha = 0$) rather than the relative uncertainty ($\alpha = 1$) as the spectrum of jets is falling, and therefore the lower $p_{\mathrm{T}}^{\mathrm{jet}}$ bins are – in a sense – more important than the high-$p_{\mathrm{T}}^{\mathrm{jet}}$ bins, because

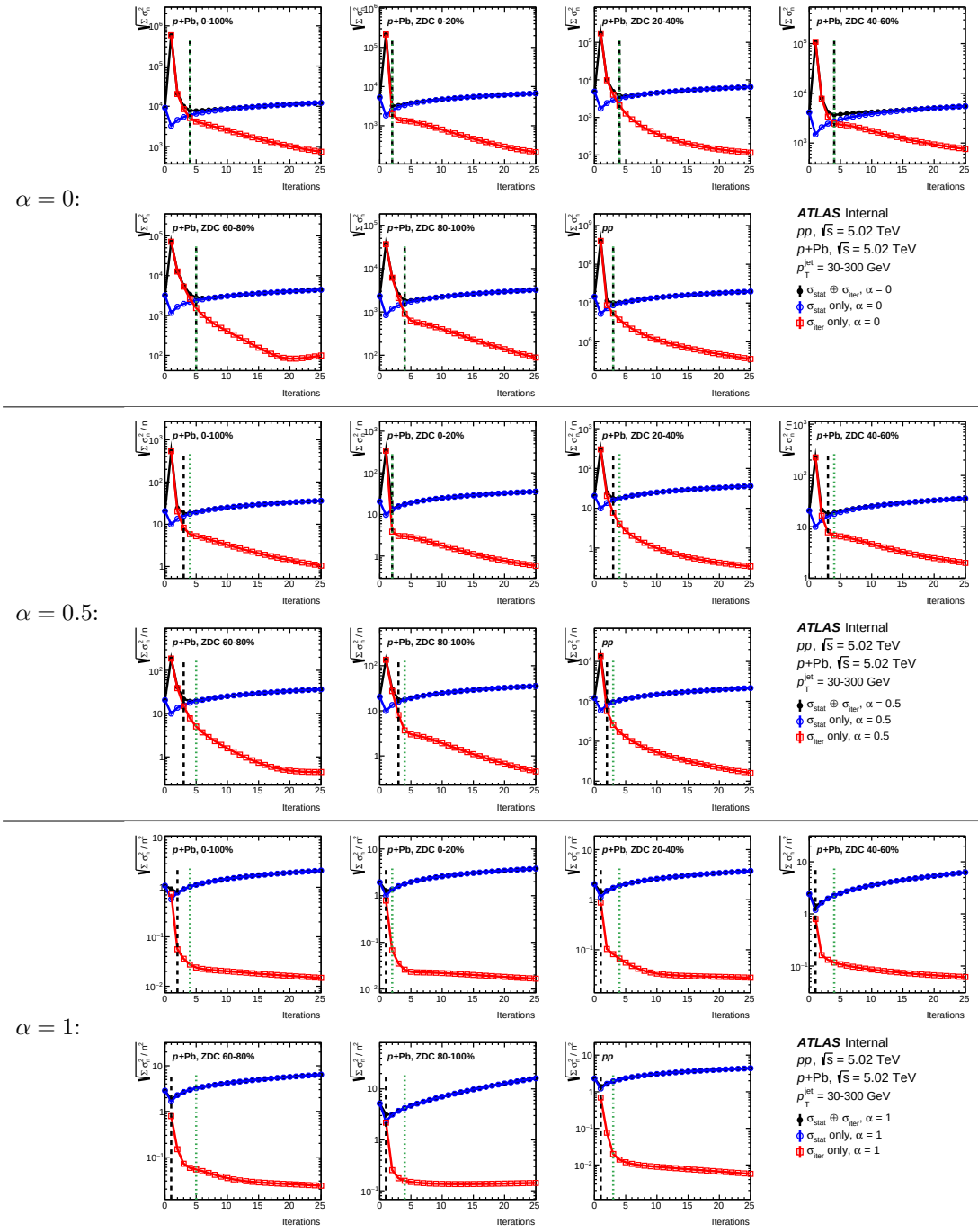


Figure 6.34: From top to bottom, the number of iterations study is performed on the jet spectra in data with parameters $\alpha \in \{0, 0.5, 1\}$. Each panel corresponds to a different p+Pb centrality selection, or pp in the lower right. Bins are considered in the sums if $p_{\mathrm{T}}^{\mathrm{jet}} = 30$–$300$ GeV. **Black** vertical dashed lines indicate the lowest nonzero N_{iter} value where $\boldsymbol{\sigma_{\mathrm{iter}}}$ **(red squares)** is less than $\boldsymbol{\sigma_{\mathrm{stat}}}$ **(blue circles)** for all higher N_{iter} values. The **green** dotted lines indicate the value of N_{iter} used in the analysis.

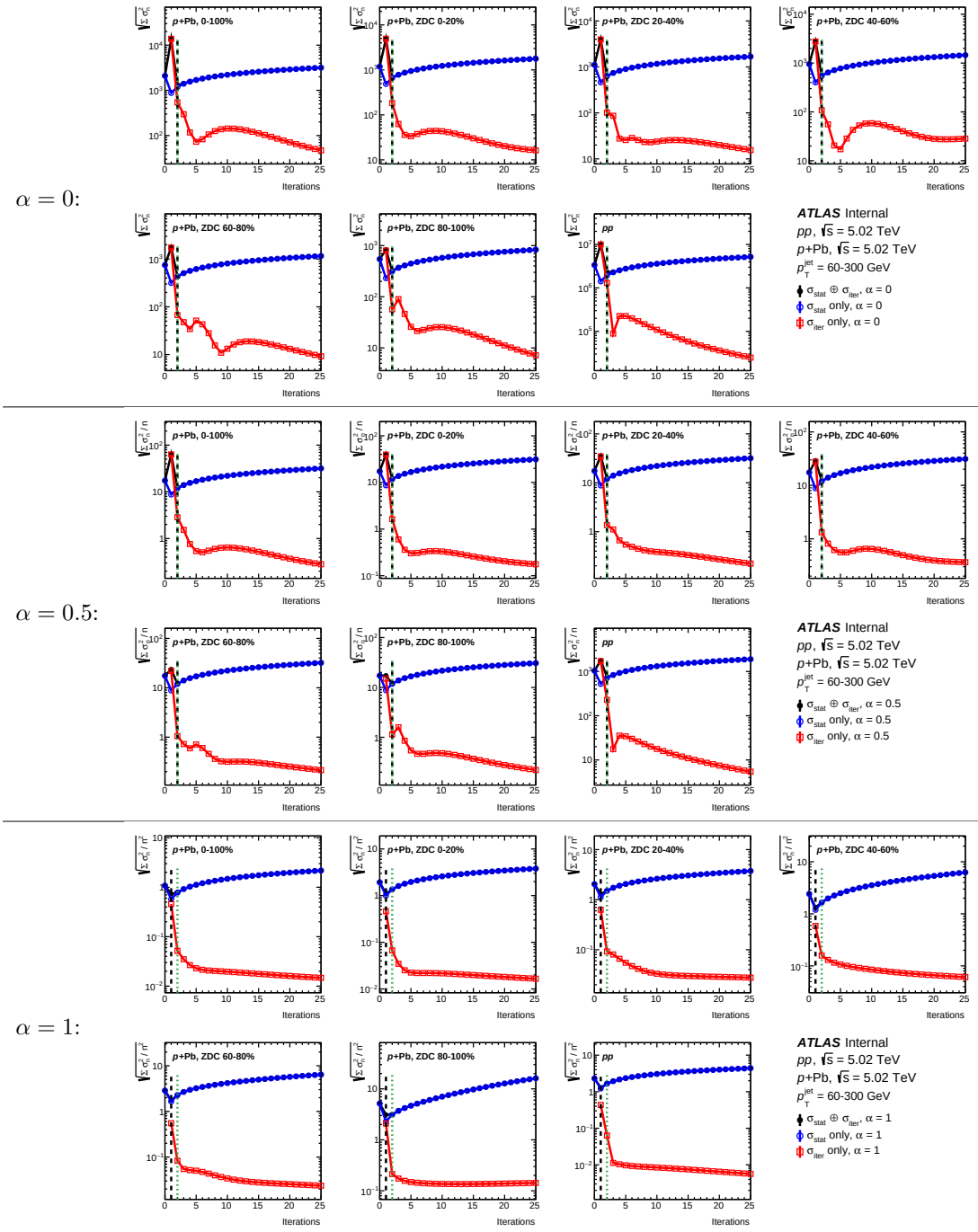


Figure 6.35: From top to bottom, the number of iterations study is performed on the jet spectra in data with parameters $\alpha \in \{0, 0.5, 1\}$. Each panel corresponds to a different p+Pb centrality selection, or pp in the lower right. Bins are considered in the sums if $p_{\mathrm{T}}^{\mathrm{jet}} = 60$–$300$ GeV. **Black** vertical dashed lines indicate the lowest nonzero N_{iter} value where $\boldsymbol{\sigma_{\mathrm{iter}}}$ **(red squares)** is less than $\boldsymbol{\sigma_{\mathrm{stat}}}$ **(blue circles)** for all higher N_{iter} values. The **green** dotted lines indicate the value of N_{iter} used in the analysis.

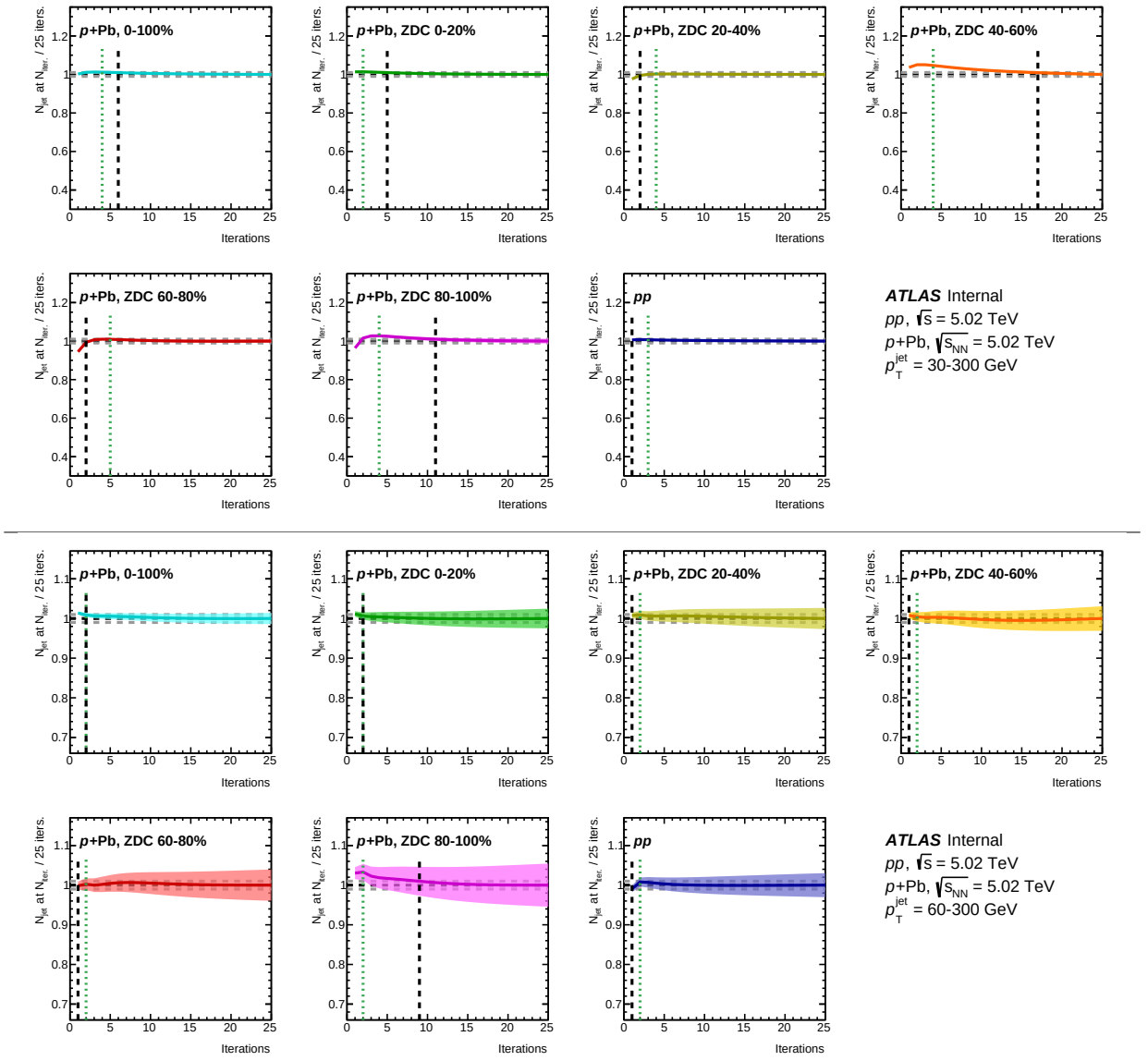


Figure 6.36: The convergence of the N_{jet} normalization is plotted a function of N_{iter}. Each panel corresponds to a different p+Pb centrality selection, or pp in the lower right. The uncertainties represent solely the uncertainty on the numerator.

they contribute more events to the average. Thus the optimal N_{iter} is chosen here from the $\alpha = 0$ plots.

The convergence of the unfold with N_{iter} is also examined to identify any substantial features in Fig. 6.36. Again, we see that the ratio of the distributions at N_{iter} to $N_{\text{iter}} - 1$ iterations rapidly converges onto unity for the nominal selection in the range 30–300 GeV, demonstrating

that the unfolded distribution is stable, at least within the fiducial range of the measurement from 30–300 GeV. Further validation of these regularization choices is performed by checking our ability to recover the truth-level spectra in Monte Carlo. This is discussed in detail in Appendix B.4.

Refolding Cross-Checks

A frequent data-driven cross-check on the accuracy of the unfolding procedure is to apply a *refolding* whereby the unfolded distribution is resmeared according to the response matrix. If the unfolded data and the response matrix are accurate, then this should return the measured distribution.

Fig. 6.37, for example, shows the ratios of the refolded charged particle distribution opposite to ($\Delta\phi > 7\pi/8$) jets above 30 GeV and 60 GeVat various numbers of iterations on the unfolding. In each analysis bin, the refolded distribution is found to match the raw data within a few percent by the second iteration, and subsequent iterations have only a modest impact. This provides additional evidence that the unfolding procedures have converged on accurate representations of the truth distributions in data.

In addition, Fig. 6.38 examines the effect of the refolding on the per-jet normalization factor as more iterations are used. These plots demonstrate that the unfolded jet spectrum is able to reproduce the raw normalization factor within 2–3 iterations, generally. This corroborates the findings from Fig. 6.37 and the previous section that only a few iterations are necessary to obtain a stable, unfolded result.

6.7 Discussion of Uncertainties

We provide both statistical and systematic uncertainties for this measurement. The statistical uncertainties are evaluated in an identical manner to the previous Z-hadron correlations measurement; we refer the reader to Sec. 4.8 for a discussion on these.

In general, this measurement is limited by systematic uncertainties, despite the very small amount of p+Pb data. At least for the $p_{\mathrm{T}}^{\mathrm{jet}} > 60$ GeV measurement, the statistical uncertainty

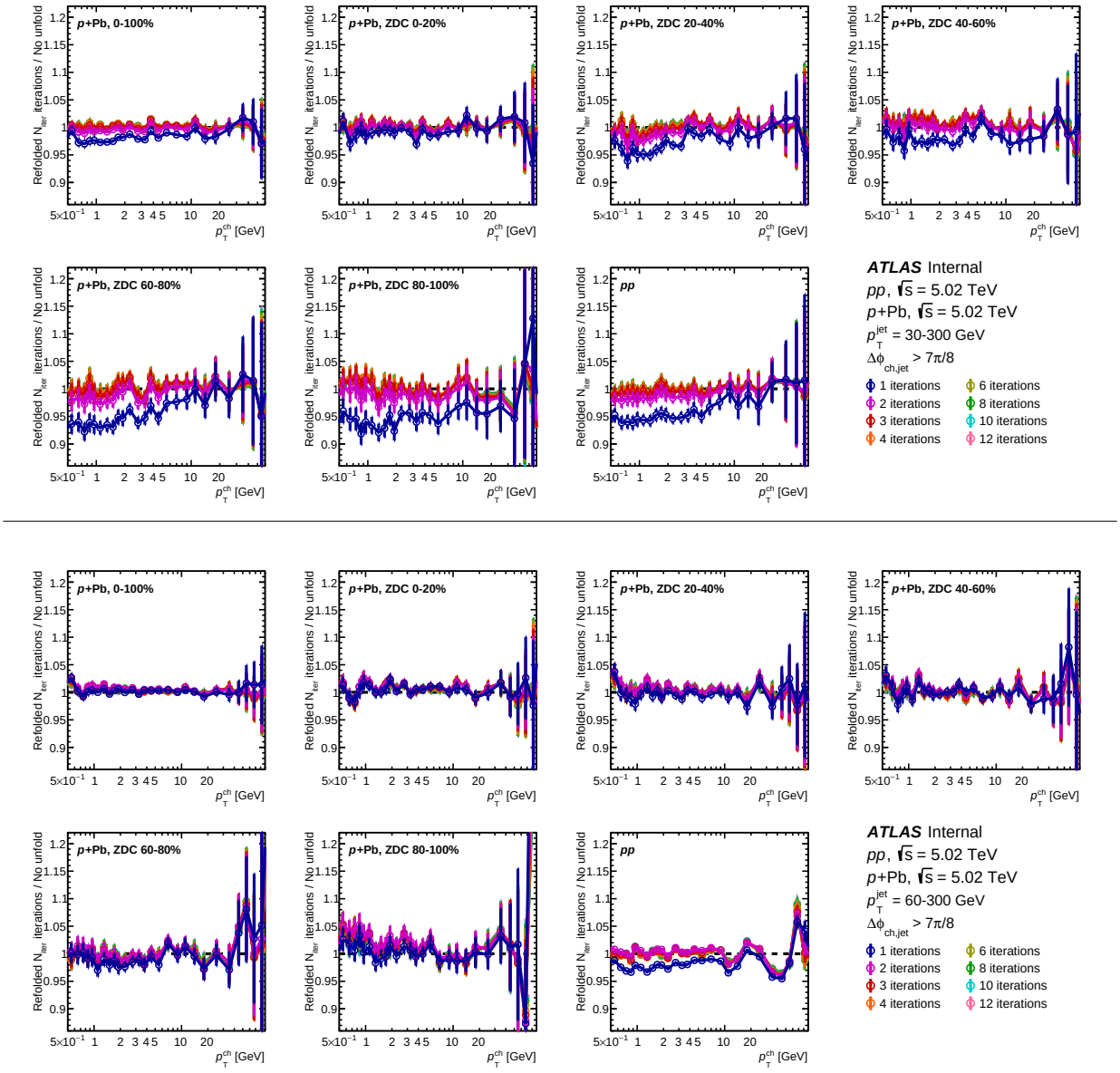


Figure 6.37: The refolded distribution of charged particles is studied as a function of $p_{\mathrm{T}}^{\mathrm{ch}}$ and the number of iterations. The y-axis shows the ratio of the refolded distribution away-side charged particle yield $\hat{N}$, integrated over $p_{\mathrm{T}}^{\mathrm{jet}} = 30$–$300$ GeV (top) and $p_{\mathrm{T}}^{\mathrm{jet}} = 60$–$300$ GeV (bottom), at N_{iter} iterations to that prior to the unfolding (i.e. the "raw" distribution). Each panel corresponds to a different p+Pb centrality selection or pp in the lower right. The uncertainties represent solely the uncertainty on the denominator. Analogous plots for the near-side are shown in Fig. B.9 in Appendix B.3.

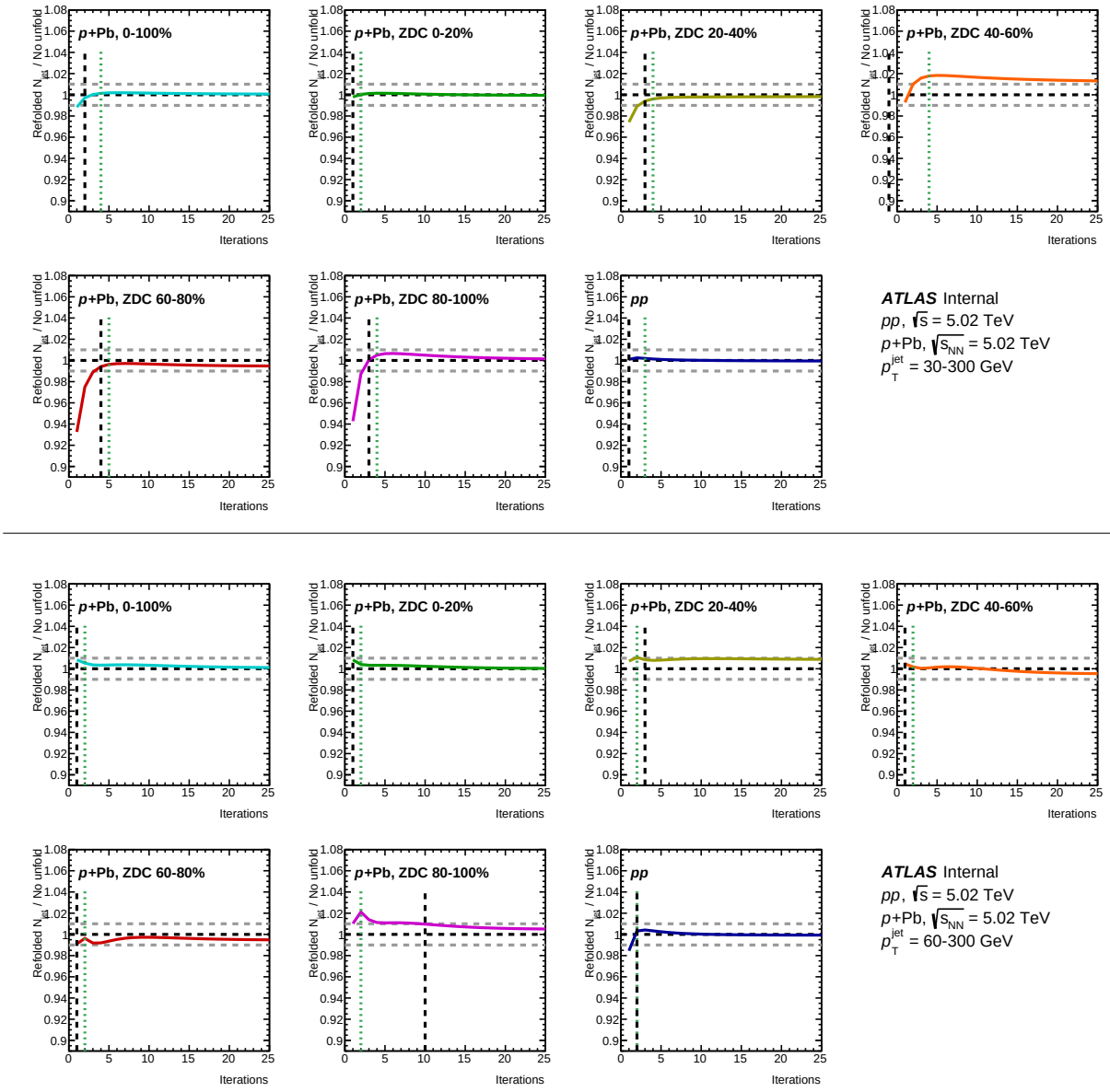


Figure 6.38: The number of jets N_{jet} in the window 30–300 GeV (top) and 60–300 GeV (bottom) is calculated from the refolded jet spectrum and compared to the raw, pre-unfolded value. The x-axis shows the number of iterations on the unfold while the y-axis shows the ratio of the refolded N_{jet} to the raw value. Each panel corresponds to a different p+Pb centrality selection or pp in the lower right. The uncertainties represent solely the uncertainty on the denominator.

only dominates in the high-z fragment tail ($p_{\mathrm{T}}^{\mathrm{ch}} \gtrsim 70$ GeV), or in bins with poor coverage, i.e., peripheral p+Pb. Analogous plots for the $p_{\mathrm{T}}^{\mathrm{jet}} > 30$ GeV show that measurement is completely systematically limited. Here, we examine where these uncertainties are coming from. First a breakdown of these into statistical plus three types of systematic sources is shown in Fig. 6.39. These three sources correspond to the jet-tagging procedure, the charged-hadron reconstruction, and the signal extraction. A more full decomposition of all sources of systematic uncertainty is provided in Appendix B.5.

First, the jet-tagging uncertainties lead to an effect on the charged-particle yield via the event selection, but also affect the per-jet normalization (i.e. the denominator). Additionally, there are significant correlations between pp and p+Pb, so there is typically no large net effect on the ratio. The jet uncertainties generally dominate the yield of high-z jet fragments, and therefore affect the measurement most at high $p_{\mathrm{T}}^{\mathrm{ch}} \gtrsim 10$ GeV. The jet energy scale uncertainties are also reduced in the away-side compared to the near-side. This is explained by the fact that the away-side measurement integrates over all possible jet configurations, while charged particles on the near-side are much more likely to represent the fragments of the tagging jet; in short, this represents the autocorrelation between the jet energy scale and the charged-hadron yield.

Second, the tracking uncertainties are typically largest where the acceptance corrections are substantial, i.e. at small $p_{\mathrm{T}}^{\mathrm{ch}} \lesssim 5$ GeV and large $|\eta|$. They are typically the largest uncertainties in this measurement. We see that the tracking uncertainties are more strongly dependent on $p_{\mathrm{T}}^{\mathrm{ch}}$ than the jet uncertainties, but again this is expected. As $p_{\mathrm{T}}^{\mathrm{ch}}$ rises, they decrease nearly monotonically, reaching about 2–3% at the highest reported $p_{\mathrm{T}}^{\mathrm{ch}}$ values. They are also similar in magnitude between the near and away-sides.

Finally, there a set of uncertainties related to the signal extraction. This catch-all term is meant to include uncertainties on the unfolding prior, analysis closure studies, and event-matching criteria; though, only the first two dominate. Recall that the unfolding prior uncertainty is evaluated by applying no per-jet weights to the MC to obtain a different prior. Because the unfolding converges so quickly, the alternate prior *also* converges within a few iterations, and the resulting

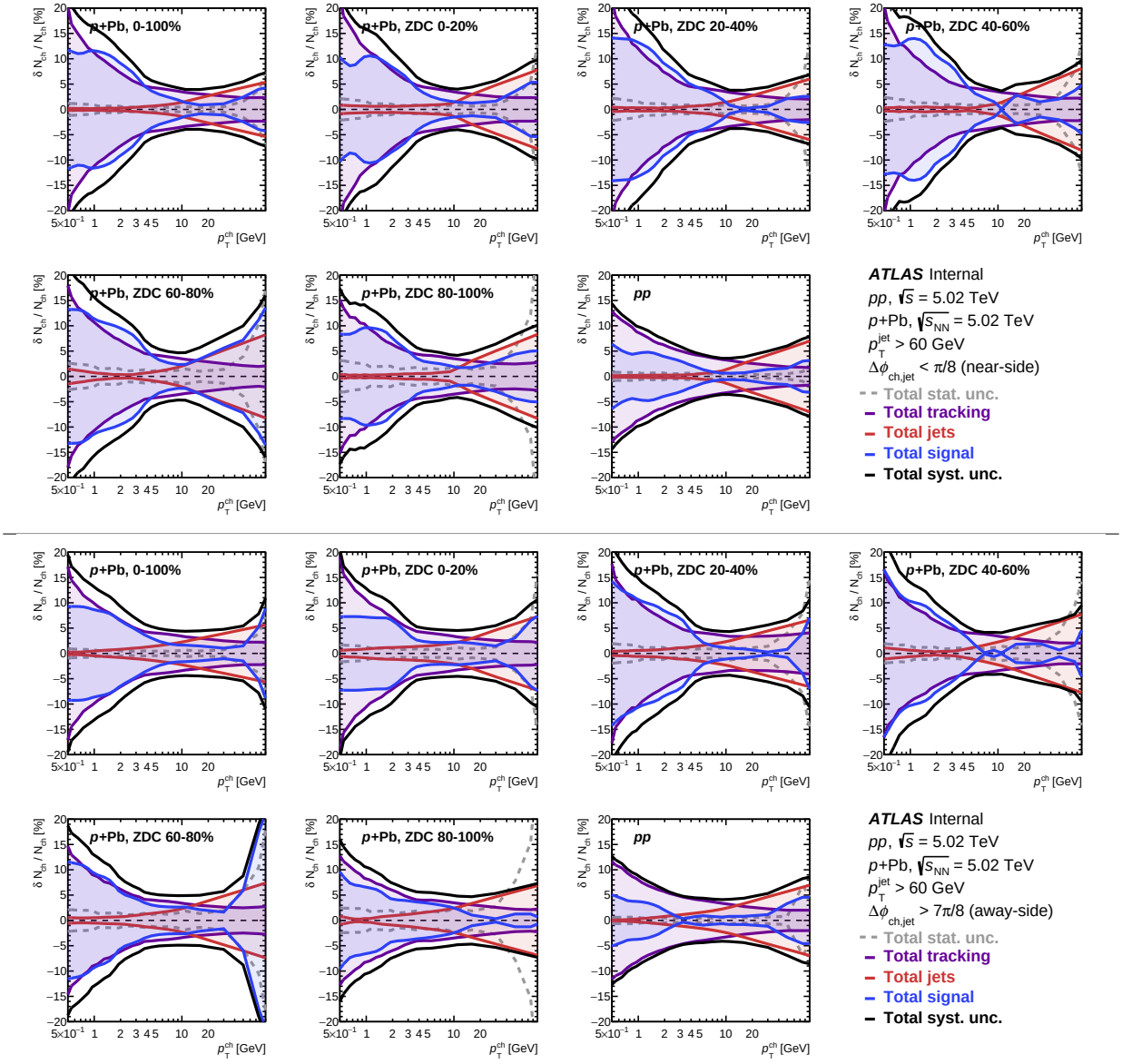


Figure 6.39: Total systematic uncertainties for each source (**UE modeling & signal extraction; blue**, **charged-particle tracking; violet**, and **jet-tagging; maroon**) and the **total (black)** are plotted versus $p_{\mathrm{T}}^{\mathrm{ch}}$ in the near-side ($\Delta\phi < \pi/8$; top rows) and the away-side ($\Delta\phi > 7\pi/8$; bottom rows) for events with a jet above 60 GeV. The total statistical (**gray**) and total systematic uncertainty **(black)** are also shown.

uncertainty is typically non-dominant, only reaching 2–3% in a specific extremities: in pp at high $p_{\mathrm{T}}^{\mathrm{ch}}$ (60–90 GeV) in correlation with a high p_{T} jet ($p_{\mathrm{T}}^{\mathrm{jet}} > 60$ GeV). Because the uncertainty has a very similar effect in pp and p+Pb – an expected consequence of the unfolding being performed with very similar response matrices, since pp and p+Pb share the same MC generator – it mostly cancels in the $I_{p\mathrm{Pb}}$ ratio.

These is also the issue of non-closure in MC, which provides us with a metric of the measurement accuracy, and must be treated as a source of systematic uncertainty. Because the closure does not change substantially with the number of iterations, as seen in Figs. B.13 and B.15 to B.17, we use the closure at 2 iterations to assign the uncertainty, and some smoothing is applied. At low-$p_{\mathrm{T}}^{\mathrm{ch}}$, it is typically 10–15% and drops to only a few percent at high-$p_{\mathrm{T}}^{\mathrm{ch}}$, where the unfolding uncertainty dominates instead. In pp, the low-$p_{\mathrm{T}}^{\mathrm{ch}}$ uncertainty is much lower than the p+Pb uncertainty; at high-$p_{\mathrm{T}}^{\mathrm{ch}}$ there is some minor non-closure but the pp and p+Pb match. This can be explained by the uncertainty being related to the unfolding procedure, which we note is performed identically in pp and p+Pb. We therefore allow the non-closure uncertainty to cancel in the $I_{p\mathrm{Pb}}$ ratio, and it is visibly smaller there, decreasing to $< 1\%$ at high-$p_{\mathrm{T}}^{\mathrm{ch}}$.

Chapter 7

Results of the Jet-Hadron Correlations Measurement

Now we proceed to detail the main findings from the study of jet-hadron correlations in p+Pb discussed in Chapter 6. First, the average jet-tagged charged-hadron yield Y is measured versus azimuthal separation $\Delta\phi_{h,\mathrm{jet}}$. Examples of these distributions in ZDC-determined 0–20% p+Pb and pp collisions are featured in Fig. 7.1. Horizontal dashed lines indicate the underlying event background estimate. In these figures it is clear that most of the correlated yield is concentrated at the extremities $\Delta\phi \sim 0$ (the *near-side*) and $\Delta\phi \sim \pi$ (the *away-side*); these regions are indicated by the shaded areas. Unlike the Z-tagged hadron yield measurement, the trigger jet is made up of charged hadrons, leading to the distinct near-side peak. To conserve momentum, the trigger particle in both cases is often produced with a recoiling partner which leads to charged-hadron production (the recoil jet). As $p_{\mathrm{T}}^{\mathrm{jet}}, p_{\mathrm{T}}^{Z} \ll \sqrt{s}/2$, there is some freedom to how momentum must be conserved, so other topologies such three-jet "Mercedes" events can smear the away-side peak. Therefore, the away-side in Fig. 7.1 looks broader and somewhat flatter than the near-side. Further, as $p_{\mathrm{T}}^{\mathrm{ch}}$ is raised, both the near and away-sides become much steeper, which is a result of high-p_{T} fragments being more likely to lie in the core of the jet, since the jet axis is a momentum-average. One notable feature we see visually is that 6–8 GeV charged particles opposite a $p_{\mathrm{T}} > 30$ GeV jet are already substantially rarer than either 2–4 GeV particles or those opposite a $p_{\mathrm{T}} > 60$ GeV jet. This is likely due to their high-z fraction $z \gtrsim 0.2$ in the dijet partner.[1]

To help us further understand the characteristics of the jet samples going into these figures,

[1] Recall the definition of the momentum fraction variable $z = \left|\vec{p}_h \cdot \vec{p}_{\mathrm{jet}}\right| / \left|\vec{p}_{\mathrm{jet}}\right|^2$.

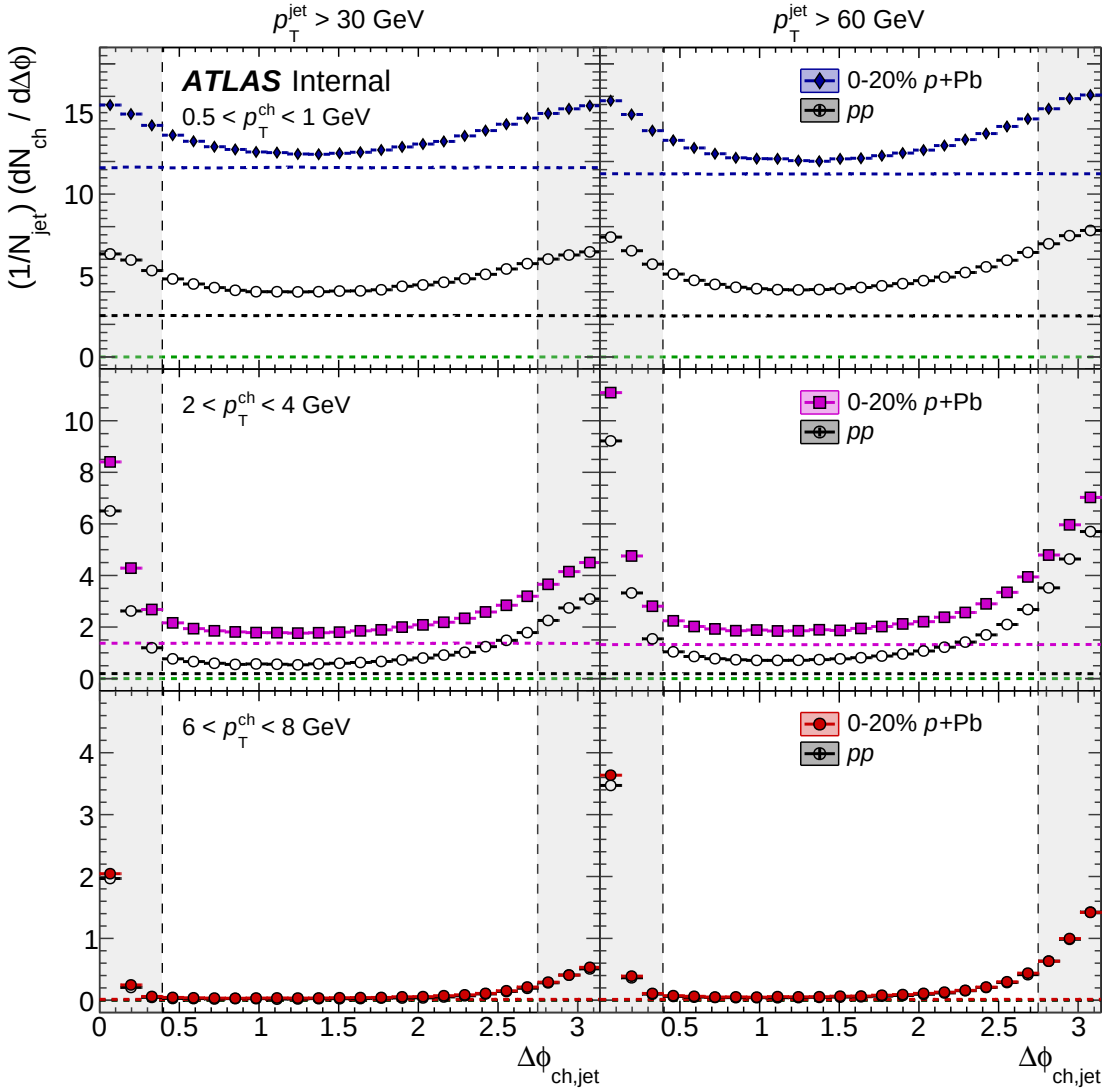


Figure 7.1: Examples of jet-hadron azimuthal correlation distributions for jets above 30 GeV (left) or 60 GeV (right). Each row indicates a different $p_{\mathrm{T}}^{\mathrm{ch}}$ selection. Horizontal dashed lines indicate the estimated background from the mixed event. Vertical dashed lines indicate the near-side $\Delta\phi < \pi/8$ and the away-side $\Delta\phi > 7\pi/8$.

we compute the mean of the unfolded jet spectra input to the N_{jet} normalization. These mean $p_{\mathrm{T}}^{\mathrm{jet}}$ values are reported in Table 7.1, along with their statistical uncertainties. From these, we see that the average jet p_{T} in the >60 GeV selection is roughly $77--78$ GeV and consistent between pp and p+Pb. Similarly, the average for jets above $p_{\mathrm{T}}^{\mathrm{jet}} = 30$ GeV is about $39--40$ GeV and generally consistent between pp and p+Pb. The primary focus of this measurement is to identify

	$\left\langle p_{\mathrm{T}}^{\mathrm{jet}} \right\rangle$ [GeV] (±stat.)						
Min. $p_{\mathrm{T}}^{\mathrm{jet}}$	pp	80–100%	60–80%	40–60%	20–40%	0–20%	0–100%
30 GeV	39.89 ± 0.04	40.07 ± 0.08	39.97 ± 0.06	39.95 ± 0.04	39.85 ± 0.04	39.72 ± 0.03	39.87 ± 0.02
60 GeV	77.55 ± 0.24	77.51 ± 0.42	77.26 ± 0.30	77.54 ± 0.24	77.18 ± 0.20	76.81 ± 0.18	77.17 ± 0.11

Table 7.1: The average jet p_{T} after unfolding for each of the event selections, with statistical uncertainties.

or limit modification to the p_{T} distribution of these charged hadrons, and therefore the near-side and away-side yields are integrated over regions as marked in gray boxes and quantified below.

We now integrate over the near-side window ($\Delta\phi < \pi/8$), as well as separately over the away-side window ($\Delta\phi > 7\pi/8$), and detail the $I_{p\mathrm{Pb}}$ as a function of charged-hadron p_{T} per jet trigger with $p_{\mathrm{T}} > 60$ GeV.[2] Recall that the ratio $I_{p\mathrm{Pb}}$ in p+Pb is defined similarly to I_{AA} in A+A collisions:

$$I_{p\mathrm{Pb}} = \frac{Y_{p\mathrm{Pb}}}{Y_{pp}}. \tag{7.1}$$

The away-side ratio is shown in Fig. 7.2 while the near-side ratio is shown in Fig. 7.3. In each figure, the top two rows show $I_{p\mathrm{Pb}}$ for charged particles correlated with a jet meeting $p_{\mathrm{T}}^{\mathrm{jet}} > 30$ GeV. The bottom rows correlate particles with a jet meeting $p_{\mathrm{T}}^{\mathrm{jet}} > 60$ GeV. Different panels and colors show each p+Pb centrality class, plus an inclusive 0–100% centrality category.

$I_{p\mathrm{Pb}}$ in the away-side is essentially flat and consistent with one over the entire p_{T} range (0.5–60 GeV) within statistical and systematic uncertainties. There is a hint of a few percent enhancement above one (or "bump") for $p_{\mathrm{T}} \approx$ 1–4 GeV and a deficit below this range, where $p_{\mathrm{T}} \approx$ 0.5–1 GeV. Though, we point out that these points have the lowest signal-to-background ratios. The near-side distribution is also flat for $p_{\mathrm{T}} \gtrsim 4$ GeV, but approximately 5–10% above unity. Below 4 GeV, there is again a bump approximately in the range 1–4 GeV. Further below 1 GeV, $I_{p\mathrm{Pb}}$ again decreases below unity. However, the data does not rule out whether the characteristics of the bump are in fact different between each of these selections.

One of the stated goals for this analysis is to push limits on jet quenching to events with lower

[2] In Appendix C, Figs. C.3 and C.4 show the full jet-correlated charged-hadron spectra in the away-side and near-side, respectively.

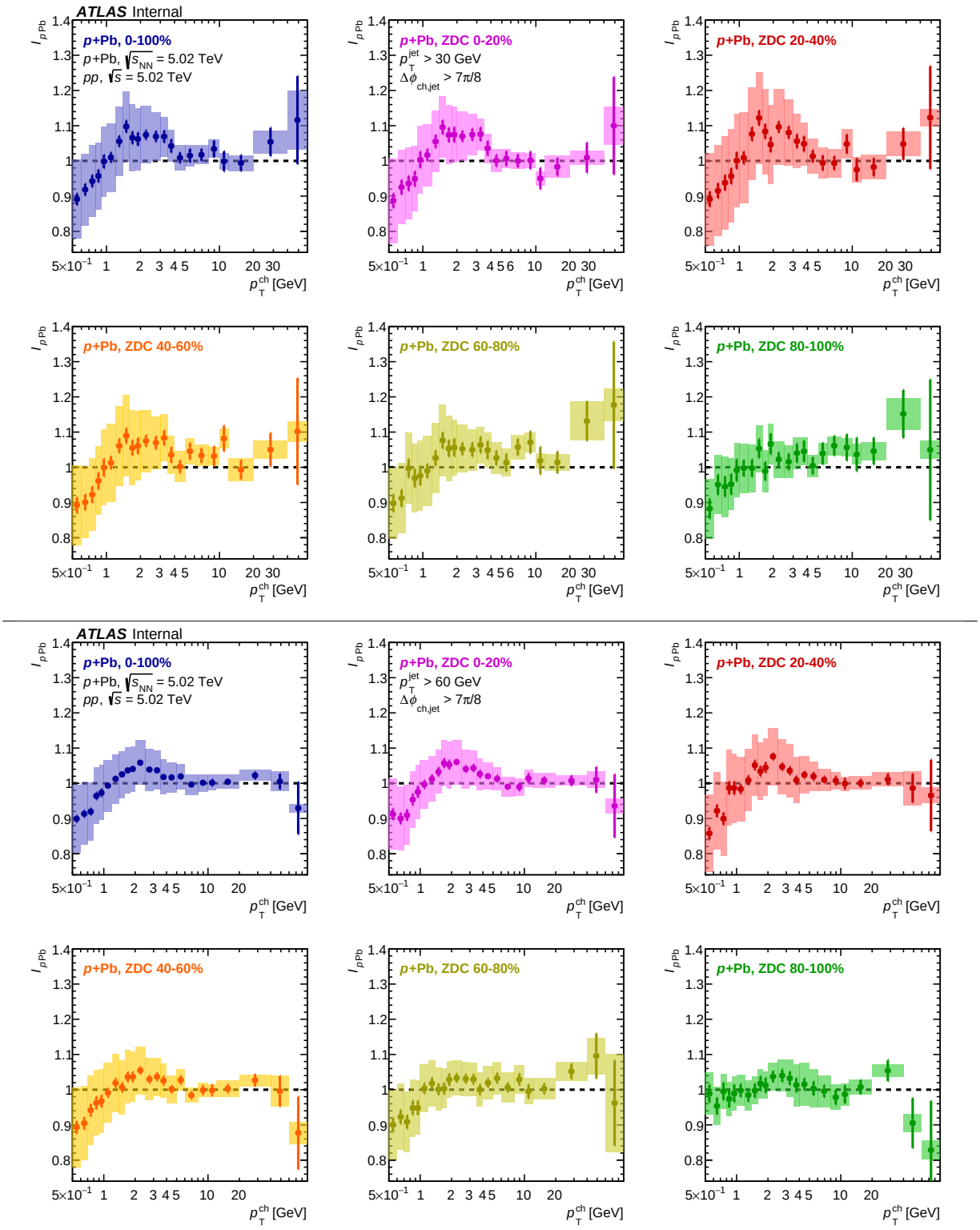


Figure 7.2: Away-side ($\Delta\phi > 7\pi/8$) nuclear modification ratio of jet-tagged hadrons $I_{p\mathrm{Pb}}$ in each p+Pb ZDC-selected centrality. Particles are correlated with a jet above 60 GeV (top rows) or 30 GeV (bottom rows).

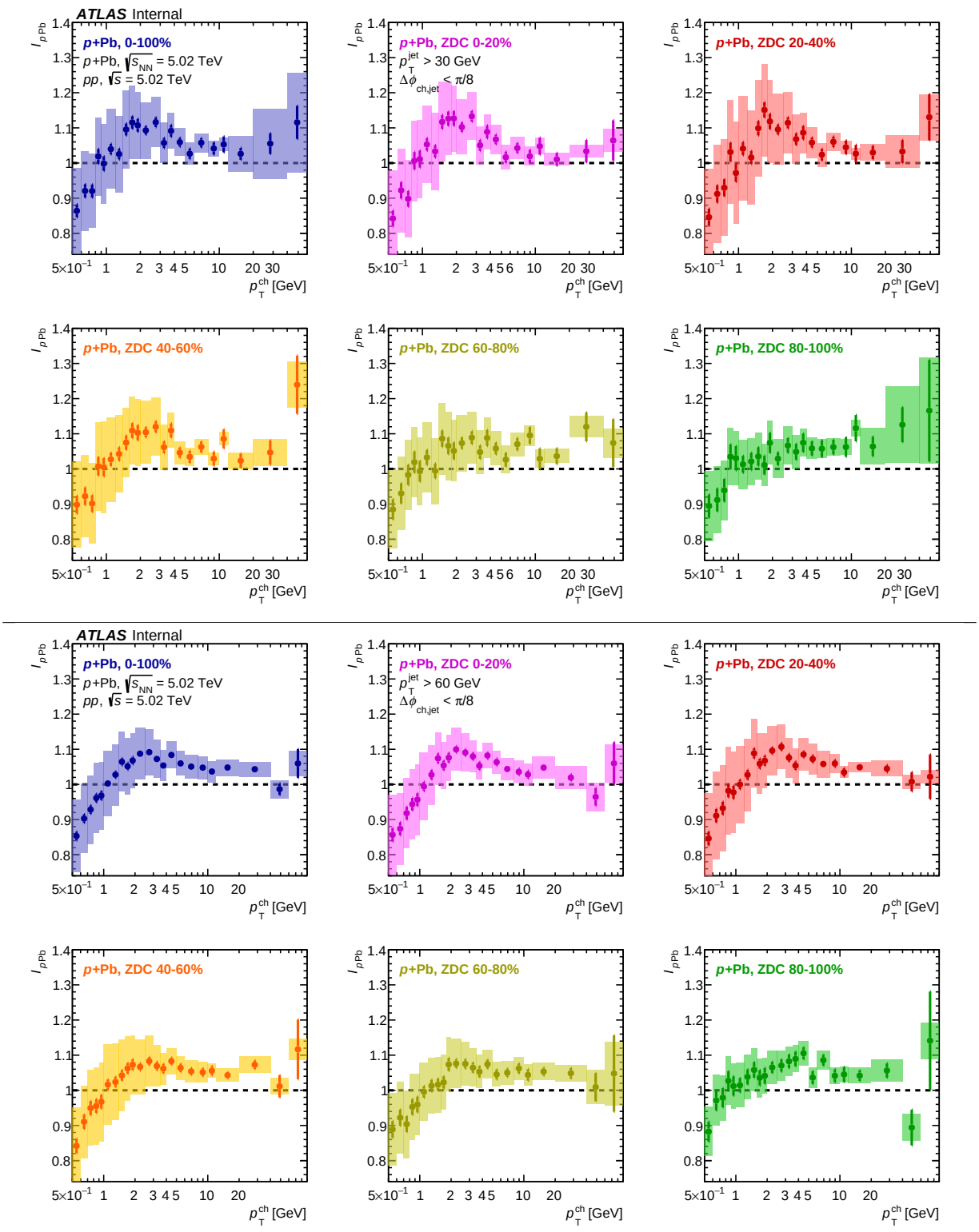


Figure 7.3: Near-side ($\Delta\phi < \pi/8$) nuclear modification ratio of jet-tagged hadrons $I_{p\mathrm{Pb}}$ in each p+Pb ZDC-selected centrality. Particles are correlated with a jet above 60 GeV (top rows) or 30 GeV (bottom rows).

momentum transfer in the hard scattering. This selects final-state partons with lower momentum that lie in a regime where collectivity is known to persist [185]. Recall that in A+A collisions, this is the regime where we observe both flow and jet modification. For the $p_{\mathrm{T}}^{\mathrm{jet}} > 30$ GeV selection, the overall spectra look similar, and the away-side $I_{p\mathrm{Pb}}$ is consistent with a constant ~ 1 at high-p_{T} with a similar local maximum ("bump") around 2 GeV. Unlike the $p_{\mathrm{T}}^{\mathrm{jet}} > 60$ GeV selections, this bump is larger, with central values reaching $I_{p\mathrm{Pb}} \sim 1.2$ in some cases. It also appears to be more significant – i.e., the points are not as compatible with $I_{p\mathrm{Pb}} \sim 1$ at the given uncertainties.

Lastly, we can also comment on the centrality dependence. In the $I_{p\mathrm{Pb}}$ figures, the 2 GeV bump visibly persists from the most central to nearly peripheral event selections (approx. 0–80%), though its magnitude is centrality-dependent. Simultaneously, each centrality bin is consistent with $I_{p\mathrm{Pb}} = 1$ within the uncertainties above 4 GeV, providing strong constraints on potential jet-quenching scenarios. The 3–4% enhancement of particles on the near-side to jets above 60 GeV also persists across all centralities. Given that the average jet p_{T} in the > 60 GeV selection is roughly 82 GeV and consistent between pp and p+Pb, there does not appear a jet energy scale bias inducing this, so we must treat this as a real physics effect.

In inclusive charged-hadron yield measurements (for example, the one detailed in Ref. [187]), a similar bump occurs and is colloquially referred to as the *Cronin* effect, named after James Cronin [193]. This effect is conventionally explained via k_t broadening, whereby partons exiting a hard scattering subsequently rescatter in the nuclear collision. This imparts an RMS k_t to each parton of order ~ 1 GeV, thus smearing the steeply-falling final state p_{T} spectra at low values. When nuclear systems are compared with pp, a suppression of charged particles at the lowest p_{T} values is observed, followed by a modest enhancement around ~ 1 GeV, which manifests as a bump. What the data here suggests is that, in central p+Pb collisions, partons inducing high-p_{T} jets also undergo k_t broadening, since the bump persists after the underlying event is subtracted. The bump fades in the peripheral selection, as well, further suggesting that the k_t broadening effect is centrality dependent, and strongest in central events.

In the scenario that jet quenching is occurring in these p+Pb collisions, high-p_{T} partons

should have their momenta redistributed in p_{T} slightly, which would be observed as a change in slope to the away-side per-jet charged-particle yields from Figs. C.3 and C.4. Because the $I_{p\mathrm{Pb}}$ ratios in Fig. 7.2 are very close to unity across a wide $p_{\mathrm{T}}^{\mathrm{ch}}$ range from approximately 3–4 GeV up to the statistical limit near $\sim$ 50–60 GeV, this indicates $Y_{p\mathrm{Pb}}$ and Y_{pp} match not only very closely in value but also in slope. Therefore these results pose very constraining limits on jet quenching in p+Pb collisions. Recall from Chapter 2 that differential energy loss is one possible explanation for high-p_{T} flow in p+Pb, based on its success in Pb+Pb at explaining the jet v_2. However, this measurement strongly favors scenarios with no energy loss. Therefore this phenomenon (high-p_{T} flow in p+Pb) is likely to have a different cause.

7.1 Comparison to Fragmentation Function Measurements

Although this is not a jet fragmentation function (FF) measurement, a comparison can be made to previous measurements of the jet FF in small systems. Recall from Chapter 1 that the definition of the FF ($D_{\mathrm{jet}\to h}(p_{\mathrm{T}}^{\mathrm{ch}})$) is very similar to $Y(p_{\mathrm{T}}^{\mathrm{ch}})$:

$$D_{\mathrm{jet}\to h}(p_{\mathrm{T}}^{\mathrm{ch}}) = \frac{1}{N_{\mathrm{jet}}}\frac{dN_{\mathrm{ch}}}{dp_{\mathrm{T}}^{\mathrm{ch}}}. \tag{7.2}$$

The difference between $D(p_{\mathrm{T}}^{\mathrm{ch}})$ and $Y(p_{\mathrm{T}}^{\mathrm{ch}})$ is in the fiducial charged-particle acceptance. The FF is restricted to charged particles that can be identified as jet fragments, so they must lie within the cone of the jet. In comparison, this measurement takes particles nearby/away from the jet in azimuth but potentially separated by up to several units in rapidity. From the more limited acceptance of the FF we then expect $Y(p_{\mathrm{T}}^{\mathrm{ch}}) \gtrsim D(p_{\mathrm{T}}^{\mathrm{ch}})$.[3] Thus it is more appropriate to compare $I_{p\mathrm{Pb}}$ with the *modification* of the FF, which is described by the ratio to pp:

$$R_{D(p_{\mathrm{T}})} = \frac{D_{p\mathrm{Pb}}(p_{\mathrm{T}}^{\mathrm{ch}})}{D_{pp}(p_{\mathrm{T}}^{\mathrm{ch}})}. \tag{7.3}$$

The slightly different acceptance in this measurement should thus cancel in the ratio, and we are left with the expectation that $R_{D(p_{\mathrm{T}})} \sim I_{p\mathrm{Pb}}$.

[3] Since $\pi/8 \approx 0.4$, the solid angle acceptance of $Y(p_{\mathrm{T}}^{\mathrm{ch}})$ is strictly larger than that of $D(p_{\mathrm{T}}^{\mathrm{ch}})$.

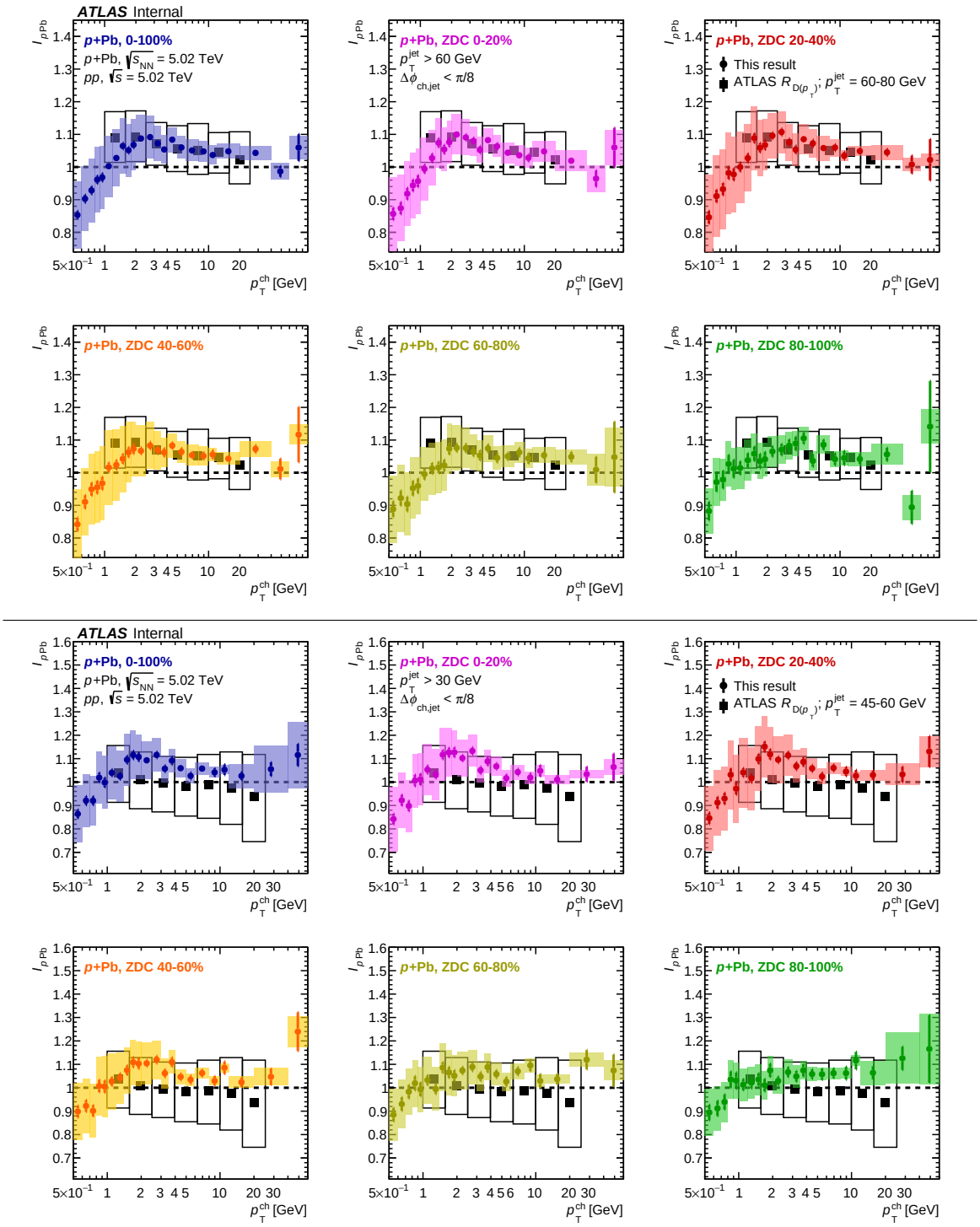


Figure 7.4: Near-side ($\Delta\phi < \pi/8$) $I_{p\mathrm{Pb}}$ in each p+Pb ZDC-selected centrality are compared to jet fragmentation functions measured by ATLAS [277]. Particles are correlated with a jet above 60 GeV (top rows) or 30 GeV (bottom rows). The fragmentation function measurement corresponds to jets in the range $p_{\mathrm{T}}^{\mathrm{jet}} = 60$–$80$ GeV (top rows) or $p_{\mathrm{T}}^{\mathrm{jet}} = 45$–$60$ GeV (bottom rows). The fragmentation function measurements are identical in each centrality selection.

The FF has been previously measured by both CMS [309] and ATLAS [277]. We note that neither experiment has measured the centrality dependence of the FF in p+Pb. The comparison with the ATLAS FF measurement [277] – explored in Fig. 7.4 – shows the results are systematically compatible. For the $p_{\mathrm{T}}^{\mathrm{jet}} > 60$ GeV measurement, the points are in remarkably close agreement, though we point out that the jet FF measurement was primarily limited by systematic uncertainties on the jet energy scale, and the heavy-ion jet reconstruction (for small systems) has remain largely unchanged since Run 1. However, the input data sets are completely independent: the p+Pb data in [277] was taken in Run 1, and the pp data was taken in 2015. (The jet energy scale uncertainties could not fully cancel between Run 1 and Run 2, explaining the larger systematic uncertainties on the FF measurement.) We point out that the UE modeling is completely different between the two analyses, which could partially drive some of the observed differences at low-$p_{\mathrm{T}}^{\mathrm{ch}}$.

In Fig. C.5 in Appendix C, we compare against CMS data [309]. In general, we see that the two are compatible within their systematic uncertainties. However, the $I_{p\mathrm{Pb}}$ uncertainties are noticeably smaller, and the addition of the centrality dependence should be invaluable for teasing out potential final-state energy loss effects. We also note that the CMS measurement is preliminary and interpolates the Run 1 pp reference between 2.76 TeV and 7 TeV.

7.2 Small System Model Predictions

The near-side enhancement discussed in the previous section is also an intriguing effect, and begs to be understood. One possibility is that a cold nuclear matter effect such as isospin is driving this observation. Under this hypothesis, if more high-p_{T} up-type quarks are scattered in p+Pb, then perhaps there is a bias towards more charged particles in the fragmentation pattern.

To test this hypothesis, we compare the near-side $I_{p\mathrm{Pb}}$ against the Angantyr model provided with Pythia (version 8.306) [82].[4] Recall from Chapter 1 that this model is designed to simulate heavy-ion collisions without making any assumption that a hot, dense plasma is formed.

[4] We note that these MC samples are generated privately and not run through the ATLAS G4 simulation – only generator-level information is used.

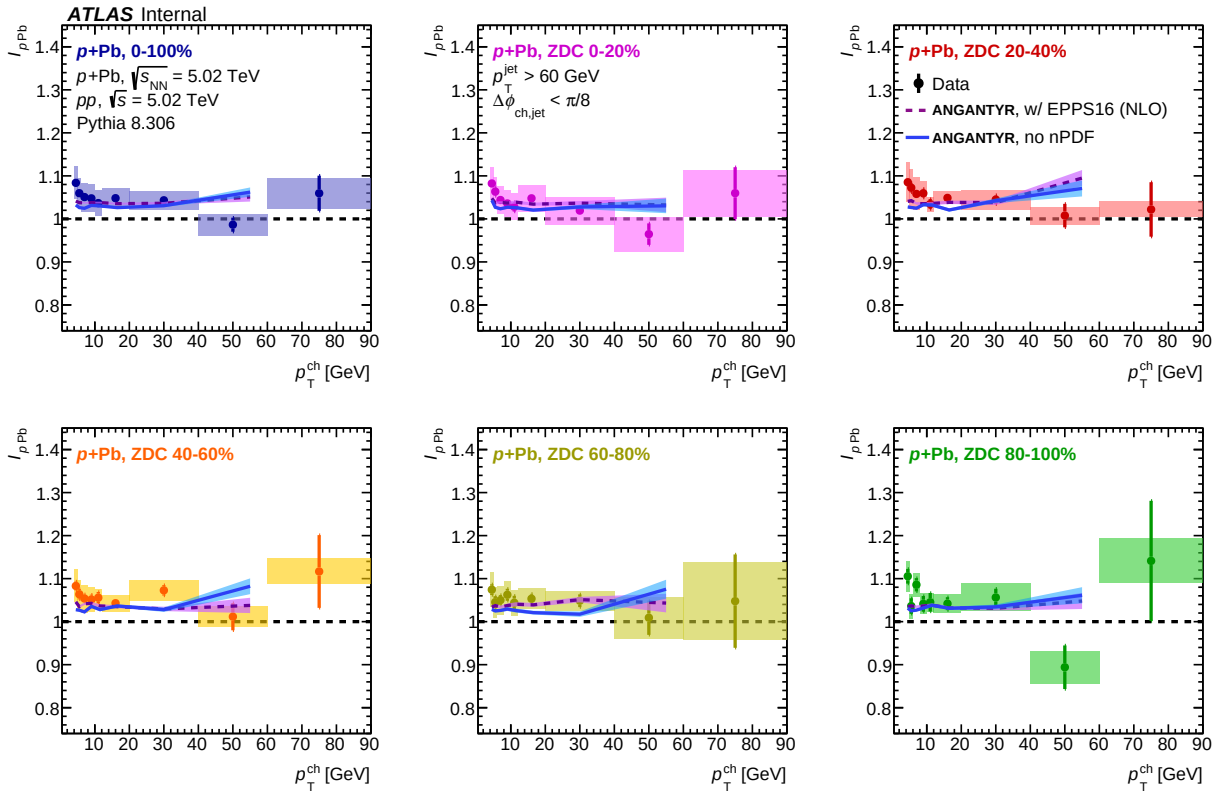
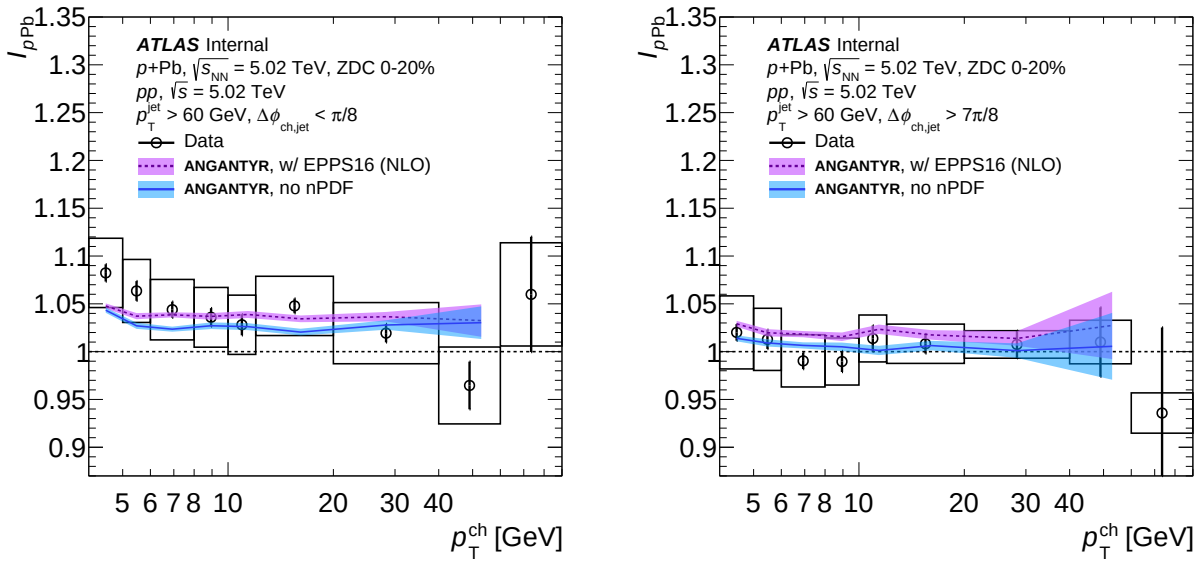


Figure 7.5: Near-side ($\Delta\phi < \pi/8$) $I_{p\mathrm{Pb}}$ in each p+Pb ZDC-selected centrality compared to ANGANTYR predictions. Particles are correlated with a jet above 60 GeV. Two curves are drawn on each panel: the **purple dashed** line represents the nominal ANGANTYR model, with isospin and nPDF effects enabled. In the **blue solid** line, the nPDF is disabled. Uncertainties on the model prediction are statistical only.

As basic ingredients, it uses a Glauber-Gribov color fluctuation model to generate initial positions of nucleons [67, 331–334], a PYTHIA-based model for nucleon-nucleon sub-collisions, and the string fragmentation model for final-state hadron production. We ran the ANGANTYR mode in PYTHIA using the settings

(1) `HardQCD:all = on` to generate jet events, with `PhaseSpace:pTHatMin = 20` or 50 to sample jets above 30 GeV or 60 GeV, respectively,

(2) `MPI:allowRescatter = on` to enable partonic rescattering, a common explanation for the Cronin enhancement at moderate p_{T} values $\sim$ 2–5 GeV (though the effect of rescattering is expected to be suppressed at higher p_{T} values),



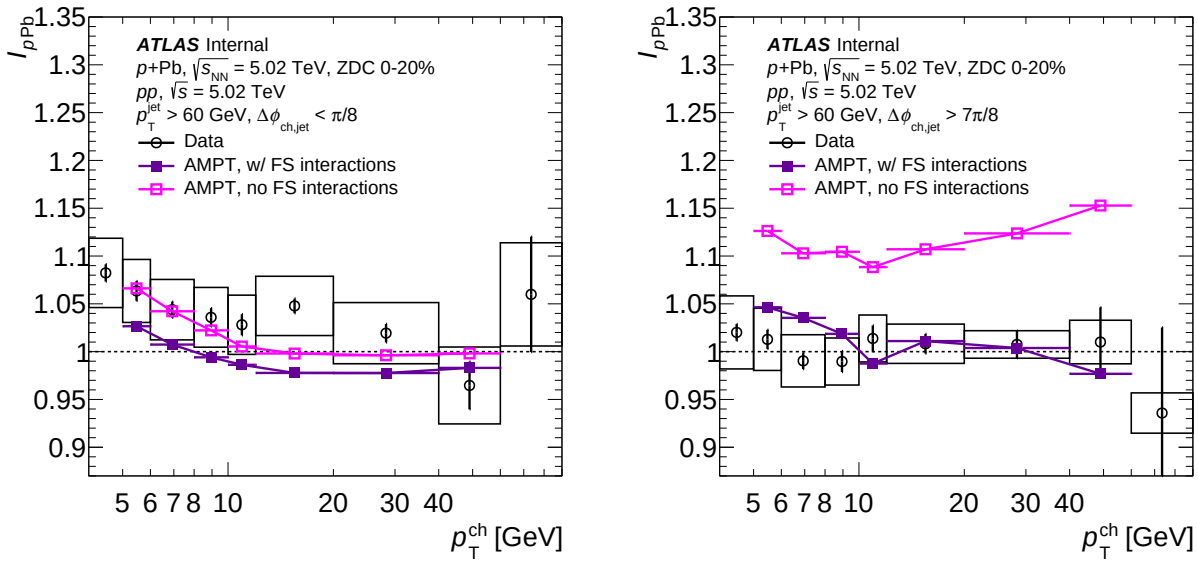
(a) $\Delta\phi < \pi/8$ **(b)** $\Delta\phi > 7\pi/8$

Figure 7.6: $I_{p\mathrm{Pb}}$ in 0–20% central p+Pb on the **(a)** near-side ($\Delta\phi < \pi/8$) and **(b)** away-side ($\Delta\phi > 7\pi/8$) compared to ANGANTYR predictions [82]. Particles are correlated to a jet above 60 GeV. Two curves are drawn on each panel: the **purple dashed** line represents the nominal ANGANTYR model, with isospin and nPDF effects enabled. In the **blue solid** line, the nPDF is disabled. Uncertainties on the model prediction are statistical only. In data, points below 4 GeV have been truncated.

(3) `PDF:useHardNPDFA = on` (or off) and `PDF:nPDFSetA = 3` to enable the use of nPDFs in sampling initial state partons, with nPDF set "3" corresponding to the EPPS16 (NLO) fits [51], with isospin effects explicitly enabled.

We note that the ANGANTYR model simulates the nucleon types & positions in the nucleus and therefore should include isospin effects by default. So, the last step where we turn on nPDF effects should not be explicitly necessary to investigate an isospin effect. In addition to the above options, we also include the effect of the boost by tuning the beam energies separately to 1.58 TeV (Pb beam) and 4 TeV (proton beam). To determine the collision centrality, we take percentiles of the N_{coll} distribution from minimum bias events.

Because the ANGANTYR model simulates the entire p+Pb collision, there will also be a UE contribution to the charged-particle yield. As discussed in Chapter 6, this can bias the p+Pb jet energy scale if left unaccounted for. Thus, we also apply a UE background subtraction to the



(a) $\Delta\phi < \pi/8$ **(b)** $\Delta\phi > 7\pi/8$

Figure 7.7: Jet-tagged $I_{p\mathrm{Pb}}$ in 0–20% central p+Pb on the **(a)** near-side ($\Delta\phi < \pi/8$) and **(b)** away-side ($\Delta\phi > 7\pi/8$) compared to AMPT predictions [78]. Particles are correlated to a jet above 60 GeV. Two predictions are drawn on each panel: the **violet solid square** markers denote the prediction by AMPT with final state (FS) interactions effects enabled, and the **magenta open square** markers indicates the prediction with FS interactions disabled. In data, points below 4 GeV have been truncated.

jets clustered from the PYTHIA events. We use the FASTJET 3.4.0 software package [253] to both cluster the jets and perform and area-based subtraction. For simplicity, we do not perform a UE subtraction on the charged-particle yield, analogous to what is performed in data. Thus, below $\sim$ 2–4 GeV the ratio begins to rise due to background. Therefore, we only show the predicted $I_{p\mathrm{Pb}}$ above 4 GeV.

The ANGANTYR model shows a striking similarity to the data in Fig. 7.5, where the near-side $I_{p\mathrm{Pb}}$ is compared to all of the p+Pb centrality selections. Similarly, in Fig. 7.6, the away-side and near-side comparisons are shown for 0–20% p+Pb collisions. The model produces a slight enhancement of charged particles in p+Pb collisions at the level of approximately 4%, strongly suggesting this is potentially a cold nuclear matter effect. The configuration with the nPDF option disabled is not visibly different from the curve with this option enabled, suggesting the enhancement is not strongly related to nPDF effects. We note that a significant nPDF-induced enhancement of

charged particles was not expected.

We also have investigated modification predicted in AMPT [78]. Recall from Chapter 1 that AMPT is a publicly available heavy-ion Monte Carlo which explicitly considers the formation of a bulk medium with partonic degrees of freedom. The collision is initialized by the hard scattering of partons from the underlying HIJING generator, and therefore can be used to make jet-quenching predictions with medium response. It has been shown in Ref. [191] that $R_{p\mathrm{Pb}}$ for charged hadrons in this model is approximately 0.5 almost independently of $p_{\mathrm{T}}^{\mathrm{ch}}$, in strong disagreement with data from ATLAS [187], CMS [307], and ALICE [186, 308].[5] This has been done in some recent studies, for example Ref. [335]. However, the default AMPT only includes hadronization by coalescence via spatial proximity and hence the authors caution against over-interpreting high p_{T} results. We show our results with the AMPT generator in Fig. 7.7; the predictions are truncated below 5 GeV to avoid the UE effects. Here, we find that the $I_{p\mathrm{Pb}}$ results in 0–20% p+Pb collisions on the near and away side are consistent with 1. However, other nuclear effects appear to enhance the away side yield by +10% (as seen when running AMPT without partonic or hadronic interactions), which is then counterbalanced by energy loss effects of approximately -10%.[6] This can be seen in the left panel of Fig. 7.7. Thus, while the current AMPT implementation of high-p_{T} parton interactions and hadronization is already ruled out by the $R_{p\mathrm{Pb}}$ for hadrons and jets, the more modest $I_{p\mathrm{Pb}}$ effect it predicts may be due to a selection or geometry bias when finding a jet with $p_{\mathrm{T}} > 60$ GeV.

7.3 Key Messages

Like the Z-hadron measurement, we can summarize the findings from the jet-hadron correlations measurement as the following:

(1) The yield of high-p_{T} hadrons $p_{\mathrm{T}}^{\mathrm{ch}} \gtrsim 4$ GeV opposite high-p_{T} jets in central p+Pb collisions matches that in pp to $\lesssim 4\%$ across the entire centrality range. The yield of these particles

[5] Our simulations have confirmed this result, and also find that anti-k_t $R = 0.4$ jet $R_{p\mathrm{Pb}}$ in 0–20% central events is approximately 0.75.

[6] Disabling the interactions is equivalent to skipping the parton and hadron cascades in AMPT. Therefore, the curve with no final-state interactions represents primarily a crude Monte Carlo model based on HIJING initial conditions with string melting and coalescence.

follows an approximate power law, ensuring $I_{p\mathrm{Pb}}$ is strongly sensitive to partonic energy loss effects. This places a precision constraint on potential small system energy loss scenarios. Differential energy loss is therefore disfavored as an explanation for high-p_{T} flow.

(2) The behavior of $I_{p\mathrm{Pb}}$ at low-p_{T} may suggest the Cronin effect is also present in jet fragmentation patterns. The 2–3 GeV bump observed in central p+Pb is characteristic of the bump in $R_{p\mathrm{Pb}}$ measurements, known as the Cronin effect. This is known to occur in minimum bias collisions and traditionally explained by rescattering effects in the cold nucleus, which causes a broadening of the p_{T} spectrum at the $\sim$ few GeV level. However, this enhancement does not vanish after the background is subtracted, suggesting that jet-inducing partons may also experience this effect.

(3) Cold nuclear matter Monte Carlo models are consistent with the data, but predict a small excess of particles in both the away-side and near-side. While this could represent a lingering jet energy subtraction issue, the near-side ANGANTYR prediction matches the data better than the away-side prediction, the latter of which is slightly above the data. This leaves open the possibility of a small energy loss effect corresponding to a $\sim 2\%$ suppression, which is not ruled out by the data.

(4) Kinetic theory might suggest a competing nuclear effect can negate small system energy loss signals. While coalescence is not an accurate model of vacuum jet fragmentation, a yet undiagnosed cold nuclear matter effect predicting similar behavior may also wash away the energy loss effect. This is very speculative, however, and would require further study.

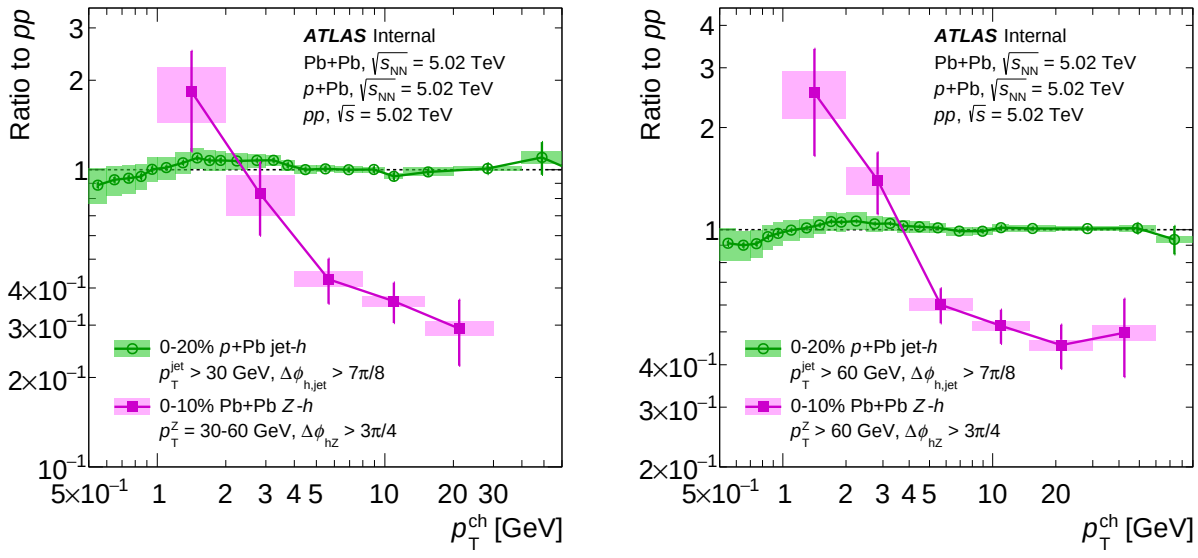
Chapter 8

Conclusions & Outlook

This thesis presents two new measurements of hadron yields exploiting calibrated probes of large and small nuclear systems. In large systems, the degrees of freedom are understood to be partonic rather than hadronic, implying a quark-gluon plasma has formed, which we can then study experimentally. In small systems, it is not currently understood whether a smaller volume of the A+A QGP forms, prompting us to rethink our expectations for QGP phases. Probes of jet quenching are therefore important for fully characterizing this phase of matter.

In large systems, Z bosons offer a calibrated probe of hard-scattering events due to their color neutrality. Their kinematics can be compared against the recoil component of the final state seen in the detector to obtain a before-and-after picture of medium-induced energy loss. Hadron yields are particularly sensitive to energy loss, and are found to be heavily suppressed at high-p_{T}, indicating the hadrons migrate to lower p_{T} as a consequence of this effect. At the lowest momenta $p_{\mathrm{T}} \gtrsim \Lambda_{\mathrm{QCD}}$, additional hadrons can be found due to a combination of this p_{T} feed-down effect and medium backreaction. The suppression observed at the LHC maps cleanly onto RHIC γ-tagged measurements, but direct comparisons with fragmentation functions reveal the implicit $\sum p_{\mathrm{T}}$ bias in the latter. As mentioned in Chapter 5, this is consistent with the energy loss mechanism being only weakly Q^2-dependent.

One of the main findings from this study is that jet-quenching theory must take the backreaction into account somehow in order to fully describe the jet evolution. Detection of the jet-induced wake is important theoretically because it offers a new perspective on the parton-medium interac-



(a) $p_{\mathrm{T}}^{\mathrm{tag}} > 30$ GeV **(b)** $p_{\mathrm{T}}^{\mathrm{tag}} > 60$ GeV

Figure 8.1: Comparison of nuclear modification ratios I_{AA} in 0–10% Pb+Pb or $I_{p\mathrm{Pb}}$ in 0–20% p+Pb between the Z-hadron and jet-hadron measurements from Chapters 5 and 7. Charged hadrons are correlated with the Z or jet calibrated tag with minimum transverse momentum **(a)** 30 GeV and **(b)** 60 GeV.

tion. The pQCD-based JEWEL treats the interaction as a sequence of perturbative $n \to m$ scattering processes that can be simulated as a cascade in Monte Carlo. The backreaction is then simulated by including the medium partons "kicked" by the high-p_{T} parton in the event record. Meanwhile, the Hybrid model treats the backreaction as a small perturbation on the energy-momentum tensor $T^{\mu\nu}$ which then perturbs the Cooper-Frye spectrum at freeze-out. These methods generally work, but are slightly *ad hoc*. On the other hand, CoLBT-hydro works with a ground-up description, but makes a semiclassical approximation and thus may fail close to the transition temperature or in smaller systems, where quantum effects may be more important. In the future, it would be interesting to see additional ground-up approaches to jet-medium coevolution that make more realistic sets of assumptions.

We have then used the same calibrated-probe analysis technology to obtain precision limits on jet-quenching scenarios in p+Pb collisions. In this case, jets are used as the calibrated tag instead of Z bosons due to the limited statistics of Z bosons in the p+Pb data. One possible explanation for

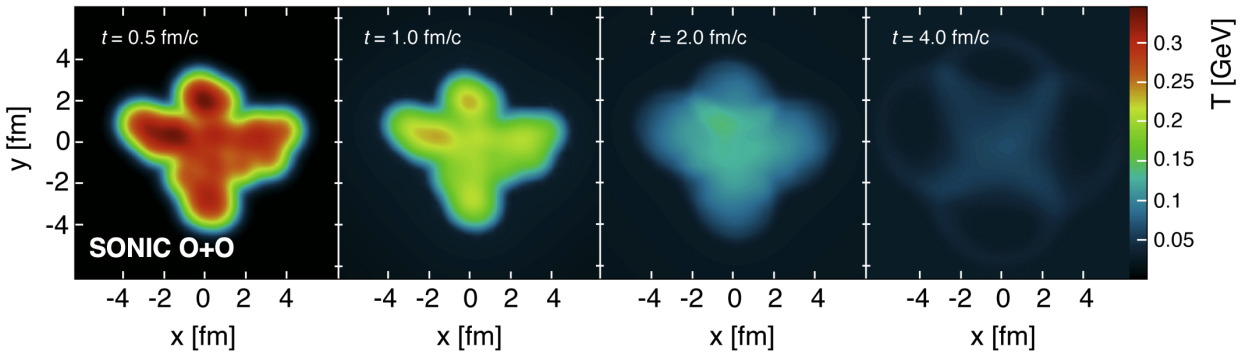


Figure 8.2: Time series of a hydrodynamically evolving O+O collision in SONIC. Figure reproduced from Ref. [336].

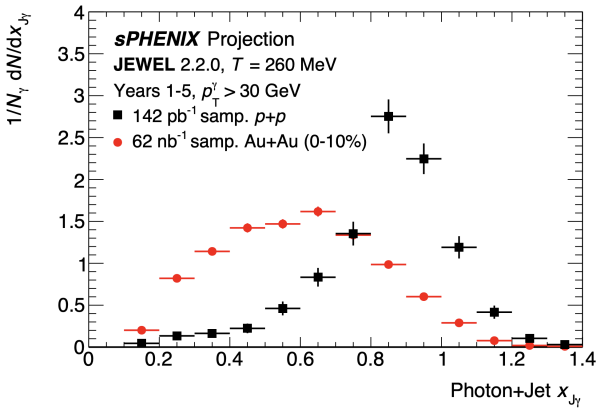
the high-p_{T} v_2 in this system is a differential energy loss mechanism correlated with the geometry of a hydrodynamic medium. We find that hadron yields opposite jets are unmodified in p+Pb relative to the pp baseline within 4% across all centrality bins. The accuracy of this measurement is further improved by using the ATLAS zero-degree calorimeter to minimize the jet-autocorrelation bias with the centrality metric. The most important take-away message from this measurement is that the flat, near-unity $I_{p\mathrm{Pb}}$ in central p+Pb strongly constrains hypothesized jet-quenching scenarios. To contextualize the lack of any jet-quenching signal, Fig. 8.1 directly compares central Pb+Pb I_{AA} from the Z-hadron study to the central p+Pb $I_{p\mathrm{Pb}}$ from this measurement. While hadrons above $p_{\mathrm{T}}^{\mathrm{ch}} \sim 3$–4 GeV are heavily suppressed in Pb+Pb, analogous hadrons in p+Pb are not redistributed in p_{T} whatsoever. Relating back to the small system $R_{\mathrm{AA}} + v_2$ puzzle, to explain the observed high-p_{T} flow via differential energy loss, the lack of *any* p_{T} redistribution must be reconciled.

Simultaneously, comparisons between data and theoretical models suggest that cold nuclear matter effects can disguise energy loss effects. Of course, this has been long understood in heavy ions, and disentangling cold versus hot nuclear effects remains a driving factor for studying small systems. However, this is readily seen from AMPT predictions for the jet-correlation hadron yield, and may also be present in simulations using the ANGANTYR model.

There are several ongoing efforts to further refine our understanding of jet-medium interactions. In 2022, the LHC will resume operations and take Pb+Pb data again at 5.02 TeV. This



(a) sPHENIX HCal Sectors



(b) Projections for the $\gamma+$jet balance

Figure 8.3: **(a)** Outer (left) and inner (right) sPHENIX hadronic calorimeter ("HCal") sectors being outfitted with electronics at Brookhaven National Laboratory. Chair for scale. **(b)** Statistical projections for the $\gamma+$jet momentum balance using the JEWEL event generator assuming 5 years of data-taking. Figure produced by Ahmed Alenezi and Dennis Perepelitsa.

will increase the current data set by a factor ~ 3. Rare probes, like Z bosons, will be numerous, enabling more precise measurements in this channel. Perhaps more interesting is an expected O+O run later in Run 3 [337]. This system pushes the limits of the traditional distinction between "small" and "large" nuclear collision systems. A hydrodynamic description of this system can be obtained [336], which is less surprising given the state of small systems research [75], and searching for jet quenching should yield additional insight to the limiting formation of QGP droplets. In fact, parton energy loss may be sensitive to the speculated 4-α cluster ^{16}O nuclear geometry (illustrated with the hydrodynamic simulations in Fig. 8.2) via path length dependence, and therefore jet-quenching observables (e.g., jet v_4) could even be used as a tool to study the structure of cold nuclear matter.

In 2023, the sPHENIX upgrade to the PHENIX experiment [338] will come online and once again study jet quenching at RHIC energies. The main purpose of the upgrade is to equip the detector with a dedicated hadronic calorimeter, enabling a fully-calorimeter-based jet reconstruction for the first time at RHIC energies. Fig. 8.3 shows off a few of the feature of the sPHENIX experiment. The calorimeter will have 3 layers; in order of increasing radius, they are the electromagnetic, and

inner and outer hadronic calorimeters. This will enable a new suite of precision measurements at RHIC energies in the coming years. For example, the $\gamma +$ jet balance – shown on the right – will be a key observable in the sPHENIX program. At RHIC energies, the QGP temperature is understood to be lower than the LHC. Loosely speaking, lower temperature plasmas are more strongly coupled, so understanding the impact on jet quenching is vital in obtaining a full characterization of the QGP created in nuclear collisions. JEWEL, for example, predicts a broad suppression of jets in the γ-tag channel, which will be interesting to compare against when the data is collected. While work presented in this thesis has enabled us to make more definitive statements on the strength and extent of jet quenching, it is certainly not the final word in the story.

Bibliography

[1] S. W. Hawking, **A Brief History of Time: From the Big Bang to Black Holes**, London, UK: Bantam Press, 1988, ISBN: 978-0-553-17698-8, 978-3-499-62600-5, 978-0-553-38016-3 (cit. on p. 2).

[2] S. Durr et al., *Ab-Initio Determination of Light Hadron Masses*, Science **322** (2008) 1224, arXiv: 0906.3599 [hep-lat] (cit. on p. 3).

[3] C. Ratti, *Lattice QCD and heavy ion collisions: a review of recent progress*, Rept. Prog. Phys. **81** (2018) 084301, arXiv: 1804.07810 [hep-lat] (cit. on pp. 3, 14).

[4] J. M. Maldacena, *The Large N limit of superconformal field theories and supergravity*, Adv. Theor. Math. Phys. **2** (1998) 231, arXiv: hep-th/9711200 (cit. on p. 3).

[5] US Department of Energy, *DOE Explains...the Standard Model of Particle Physics*, https://www.energy.gov/science/doe-explainsthe-standard-model-particle-physics (cit. on p. 7).

[6] J. C. Collins and M. J. Perry, *Superdense Matter: Neutrons Or Asymptotically Free Quarks?*, Phys. Rev. Lett. **34** (1975) 1353 (cit. on pp. 7, 13).

[7] R. P. Feynman, **QED: The Strange Theory of Light and Matter**, Princeton, NJ: Princeton University Press, 1986, ISBN: 978-0-691-02417-2 (cit. on pp. 7, 16).

[8] E. Eichten, K. Gottfried, T. Kinoshita, K. D. Lane, and T. .-. Yan,
Charmonium: The model, Phys. Rev. D **17** (11 1978) 3090,
URL: https://link.aps.org/doi/10.1103/PhysRevD.17.3090 (cit. on p. 9).

[9] D. J. Gross and F. Wilczek, *Ultraviolet Behavior of Nonabelian Gauge Theories*,
Phys. Rev. Lett. **30** (1973) 1343, ed. by J. C. Taylor (cit. on p. 9).

[10] H. D. Politzer, *Reliable Perturbative Results for Strong Interactions?*,
Phys. Rev. Lett. **30** (1973) 1346, ed. by J. C. Taylor (cit. on p. 9).

[11] F. Bissey, A. I. Signal, and D. B. Leinweber,
Comparison of gluon flux-tube distributions for quark-diquark and quark-antiquark hadrons,
Physical Review D **80** (2009), ISSN: 1550-2368,
URL: http://dx.doi.org/10.1103/PhysRevD.80.114506 (cit. on p. 10).

[12] M. Tanabashi et al., *Review of Particle Physics*, Phys. Rev. D **98** (3 2018) 030001,
URL: https://link.aps.org/doi/10.1103/PhysRevD.98.030001
(cit. on pp. 10, 18, 20, 21, 23, 89, 99, 160, 161).

[13] M. Gell-Mann,
THE EIGHTFOLD WAY: A THEORY OF STRONG INTERACTION SYMMETRY,
(1961), URL: https://www.osti.gov/biblio/4008239 (cit. on p. 11).

[14] Y. Ne'eman, *Derivation of strong interactions from a gauge invariance*,
Nucl. Phys. **26** (1961) 222, ed. by R. Ruffini and Y. Verbin (cit. on p. 11).

[15] S. Jain and S. R. Wadia, *The Science of Murray Gell-Mann*, Curr. Sci. **117** (2019) 10,
arXiv: 1909.07354 [physics.hist-ph] (cit. on p. 12).

[16] V. E. Barnes et al., *Observation of a Hyperon with Strangeness Minus Three*,
Phys. Rev. Lett. **12** (8 1964) 204,
URL: https://link.aps.org/doi/10.1103/PhysRevLett.12.204 (cit. on p. 12).

[17] R. Hagedorn, "Thermodynamics of strong interactions", CERN, Geneva, 1970 - 1971, CERN, Geneva: CERN, 1971 mult. p, URL: https://cds.cern.ch/record/318595 (cit. on p. 13).

[18] A. Bazavov et al., *The QCD Equation of State to $\mathcal{O}(\mu_B^6)$ from Lattice QCD*, Phys. Rev. D **95** (2017) 054504, arXiv: 1701.04325 [hep-lat] (cit. on p. 13).

[19] N. Cabibbo and G. Parisi, *Exponential Hadronic Spectrum and Quark Liberation*, Phys. Lett. B **59** (1975) 67 (cit. on p. 13).

[20] J. Rafelski, *Melting Hadrons, Boiling Quarks*, Eur. Phys. J. A **51** (2015) 114, arXiv: 1508.03260 [nucl-th] (cit. on p. 14).

[21] A. Bazavov et al., *Equation of state in (2+1)-flavor QCD*, Phys. Rev. D **90** (2014) 094503, arXiv: 1407.6387 [hep-lat] (cit. on p. 15).

[22] A. Aprahamian et al., *Reaching for the horizon: The 2015 long range plan for nuclear science*, (2015) (cit. on pp. 15, 30, 32).

[23] L. Kumar, *Identified Particle Production from the BES at RHIC*, (2011), arXiv: 1109.5313 [nucl-ex] (cit. on p. 15).

[24] D. Tlusty, "The RHIC Beam Energy Scan Phase II: Physics and Upgrades", **13th Conference on the Intersections of Particle and Nuclear Physics**, 2018, arXiv: 1810.04767 [nucl-ex] (cit. on p. 15).

[25] J. Schükraft, *Heavy-ion physics at the LHC*, (2006), URL: https://cds.cern.ch/record/935632 (cit. on p. 15).

[26] M. G. Alford, A. Schmitt, K. Rajagopal, and T. Schäfer, *Color superconductivity in dense quark matter*, Rev. Mod. Phys. **80** (2008) 1455, arXiv: 0709.4635 [hep-ph] (cit. on p. 16).

[27] M. G. Alford, K. Rajagopal, and F. Wilczek,
Color flavor locking and chiral symmetry breaking in high density QCD,
Nucl. Phys. B **537** (1999) 443, arXiv: hep-ph/9804403 (cit. on p. 16).

[28] B. P. Abbott et al.,
GW170817: Observation of Gravitational Waves from a Binary Neutron Star Inspiral,
Phys. Rev. Lett. **119** (2017) 161101, arXiv: 1710.05832 [gr-qc] (cit. on p. 16).

[29] K. Chatziioannou, K. Yagi, A. Klein, N. Cornish, and N. Yunes,
Probing the Internal Composition of Neutron Stars with Gravitational Waves,
Phys. Rev. D **92** (2015) 104008, arXiv: 1508.02062 [gr-qc] (cit. on p. 16).

[30] G. F. Chew and S. C. Frautschi, *Principle of Equivalence for All Strongly Interacting Particles Within the S Matrix Framework*, Phys. Rev. Lett. **7** (1961) 394 (cit. on p. 17).

[31] M. N. Rosenbluth, *High Energy Elastic Scattering of Electrons on Protons*,
Phys. Rev. **79** (4 1950) 615, URL: https://link.aps.org/doi/10.1103/PhysRev.79.615
(cit. on p. 17).

[32] J. C. Collins, D. E. Soper, and G. F. Sterman, *Factorization of Hard Processes in QCD*,
Adv. Ser. Direct. High Energy Phys. **5** (1989) 1, arXiv: hep-ph/0409313 (cit. on p. 18).

[33] J. D. Bjorken, *Asymptotic Sum Rules at Infinite Momentum*, Phys. Rev. **179** (1969) 1547
(cit. on p. 20).

[34] T.-J. Hou et al., *New CTEQ global analysis of quantum chromodynamics with high-precision data from the LHC*, Phys. Rev. D **103** (2021) 014013,
arXiv: 1912.10053 [hep-ph] (cit. on pp. 21, 22).

[35] S. Catani and M. Grazzini,
Collinear Factorization and Splitting Functions for Next-to-next-to-leading Order QCD Calculations. NEXT-TO-NEXT-TO-LEADING-ORDER,
Phys. Lett. B **446** (1998) 143, latex, 10 pages, minor corrections in the references

Report-no: CERN–TH/98-325, ETH–TH/98-27,
URL: https://cds.cern.ch/record/368357 (cit. on p. 23).

[36] V. N. Gribov and L. N. Lipatov, *Deep inelastic e p scattering in perturbation theory*, Sov. J. Nucl. Phys. **15** (1972) 438 (cit. on p. 23).

[37] G. Altarelli and G. Parisi, *Asymptotic Freedom in Parton Language*, Nucl. Phys. B **126** (1977) 298 (cit. on p. 23).

[38] Y. L. Dokshitzer, *Calculation of the Structure Functions for Deep Inelastic Scattering and e+ e- Annihilation by Perturbation Theory in Quantum Chromodynamics.*, Sov. Phys. JETP **46** (1977) 641 (cit. on p. 23).

[39] D. de Florian, R. Sassot, M. Epele, R. J. Hernández-Pinto, and M. Stratmann, *Parton-to-Pion Fragmentation Reloaded*, Phys. Rev. D **91** (2015) 014035, arXiv: 1410.6027 [hep-ph] (cit. on p. 24).

[40] ATLAS Collaboration, "Event Displays from 2009 Collision Data", Available online, 2009, URL: https://twiki.cern.ch/twiki/bin/view/AtlasPublic/EventDisplay2009PublicResults (cit. on p. 25).

[41] M. Cacciari, G. P. Salam, and G. Soyez, *The anti-k_t jet clustering algorithm*, JHEP **04** (2008) 063, arXiv: 0802.1189 [hep-ph] (cit. on pp. 25, 26).

[42] Y. Dokshitzer, G. Leder, S. Moretti, and B. Webber, *Better jet clustering algorithms*, Journal of High Energy Physics **1997** (1997) 001, ISSN: 1029-8479, URL: http://dx.doi.org/10.1088/1126-6708/1997/08/001 (cit. on p. 25).

[43] M. Wobisch and T. Wengler, "Hadronization corrections to jet cross-sections in deep inelastic scattering", **Workshop on Monte Carlo Generators for HERA Physics (Plenary Starting Meeting)**, 1998, arXiv: hep-ph/9907280 (cit. on p. 25).

[44] S. Catani, Y. Dokshitzer, M. Seymour, and B. Webber,
Longitudinally-invariant $k_\perp$-clustering algorithms for hadron-hadron collisions,
Nuclear Physics B **406** (1993) 187, ISSN: 0550-3213,
URL: https://www.sciencedirect.com/science/article/pii/055032139390166M
(cit. on p. 25).

[45] S. D. Ellis and D. E. Soper, *Successive combination jet algorithm for hadron collisions*,
Physical Review D **48** (1993) 3160, ISSN: 0556-2821,
URL: http://dx.doi.org/10.1103/PhysRevD.48.3160 (cit. on p. 25).

[46] G. P. Salam and G. Soyez, *A practical seedless infrared-safe cone jet algorithm*,
Journal of High Energy Physics **2007** (2007) 086, ISSN: 1029-8479,
URL: http://dx.doi.org/10.1088/1126-6708/2007/05/086 (cit. on p. 25).

[47] B. Andersson, G. Gustafson, G. Ingelman, and T. Sjöstrand,
Parton fragmentation and string dynamics, Phys. Rept. **97** (1983) 31 (cit. on p. 26).

[48] T. Sjöstrand, S. Mrenna, and P. Skands, *A brief introduction to PYTHIA 8.1*,
Comput. Phys. Commun. **178** (2008) 852, arXiv: 0710.3820 [hep-ph] (cit. on p. 27).

[49] G. Corcella et al., *HERWIG 6: an event generator for hadron emission reactions with interfering gluons (including supersymmetric processes)*, JHEP **01** (2001) 010,
arXiv: hep-ph/0011363 (cit. on p. 28).

[50] T. Gleisberg et al., *Event generation with SHERPA 1.1*, JHEP **02** (2009) 007,
arXiv: 0811.4622 [hep-ph] (cit. on p. 28).

[51] K. J. Eskola, P. Paakkinen, H. Paukkunen, and C. A. Salgado,
EPPS16: Nuclear parton distributions with LHC data, Eur. Phys. J. C **77** (2017) 163,
arXiv: 1612.05741 [hep-ph] (cit. on pp. 29, 306).

[52] N. Armesto, *Nuclear shadowing*, J. Phys. G **32** (2006) R367, arXiv: hep-ph/0604108
(cit. on p. 28).

[53] S. Acharya et al., *Inclusive J/ψ production at forward and backward rapidity in p-Pb collisions at $\sqrt{s_{\mathrm{NN}}}$ = 8.16 TeV*, JHEP **07** (2018) 160, arXiv: 1805.04381 [nucl-ex] (cit. on p. 29).

[54] K. Kovarik et al., *nCTEQ15 - Global analysis of nuclear parton distributions with uncertainties in the CTEQ framework*, Phys. Rev. D **93** (2016) 085037, arXiv: 1509.00792 [hep-ph] (cit. on p. 29).

[55] F. Cooper and G. Frye, *Single-particle distribution in the hydrodynamic and statistical thermodynamic models of multiparticle production*, Phys. Rev. D **10** (1 1974) 186, URL: https://link.aps.org/doi/10.1103/PhysRevD.10.186 (cit. on p. 32).

[56] B. Schenke, S. Jeon, and C. Gale, *(3+1)D hydrodynamic simulation of relativistic heavy-ion collisions*, Phys. Rev. C **82** (2010) 014903, arXiv: 1004.1408 [hep-ph] (cit. on p. 32).

[57] S. Ryu et al., *Importance of the Bulk Viscosity of QCD in Ultrarelativistic Heavy-Ion Collisions*, Phys. Rev. Lett. **115** (2015) 132301, arXiv: 1502.01675 [nucl-th] (cit. on p. 32).

[58] M. Byres, S. H. Lim, C. McGinn, J. Ouellette, and J. L. Nagle, *Bulk viscosity and cavitation in heavy ion collisions*, Phys. Rev. C **101** (2020) 044902, arXiv: 1910.12930 [nucl-th] (cit. on pp. 32, 38).

[59] M. L. Miller, K. Reygers, S. J. Sanders, and P. Steinberg, *Glauber modeling in high energy nuclear collisions*, Ann. Rev. Nucl. Part. Sci. **57** (2007) 205, arXiv: nucl-ex/0701025 (cit. on pp. 33, 35, 141).

[60] C. Loizides, J. Nagle, and P. Steinberg, *Improved version of the PHOBOS Glauber Monte Carlo*, SoftwareX **1-2** (2015) 13, arXiv: 1408.2549 [nucl-ex] (cit. on p. 33).

[61] C. Loizides, J. Kamin, and D. d'Enterria,
Improved Monte Carlo Glauber predictions at present and future nuclear colliders,
Phys. Rev. C **97** (2018) 054910, [Erratum: Phys.Rev.C 99, 019901 (2019)],
arXiv: 1710.07098 [nucl-ex] (cit. on pp. 33, 34, 240).

[62] A. Adare et al., *Beam Energy and Centrality Dependence of Direct-Photon Emission from Ultrarelativistic Heavy-Ion Collisions*, Phys. Rev. Lett. **123** (2019) 022301,
arXiv: 1805.04084 [hep-ex] (cit. on p. 35).

[63] ATLAS Collaboration, *Z boson production in Pb+Pb collisions at* $\sqrt{s_{NN}}$= 5.02 *TeV measured by the ATLAS experiment*, Phys. Lett. B **802** (2020) 135262,
arXiv: 1910.13396 [hep-ex] (cit. on pp. 35, 129, 148, 163).

[64] CMS Collaboration,
The production of isolated photons in PbPb and pp collisions at $\sqrt{s_{NN}} = 5.02$ *TeV*,
JHEP **07** (2020) 116, arXiv: 2003.12797 [hep-ex] (cit. on p. 35).

[65] ATLAS Collaboration, *Measurement of the pseudorapidity and transverse momentum dependence of the elliptic flow of charged particles in lead–lead collisions at* $\sqrt{s_{NN}} = 2.76$ *TeV with the ATLAS detector*, Phys. Lett. B **707** (2012) 330,
arXiv: 1108.6018 [hep-ex] (cit. on p. 36).

[66] C. Loizides, *Glauber modeling of high-energy nuclear collisions at the subnucleon level*,
Phys. Rev. C **94** (2016) 024914, arXiv: 1603.07375 [nucl-ex] (cit. on p. 36).

[67] M. Alvioli and M. Strikman, *Color fluctuation effects in proton–nucleus collisions*,
Physics Letters B **722** (2013) 347, ISSN: 0370-2693,
URL: http://dx.doi.org/10.1016/j.physletb.2013.04.042 (cit. on pp. 36, 305).

[68] P. Romatschke and U. Romatschke,
Relativistic Fluid Dynamics In and Out of Equilibrium,
Cambridge Monographs on Mathematical Physics, Cambridge University Press, 2019,
ISBN: 978-1-108-48368-1, arXiv: 1712.05815 [nucl-th] (cit. on p. 37).

[69] P. Kovtun, D. T. Son, and A. O. Starinets,
Viscosity in strongly interacting quantum field theories from black hole physics,
Phys. Rev. Lett. **94** (2005) 111601, arXiv: hep-th/0405231 (cit. on p. 38).

[70] P. Arnold, G. D. Moore, and L. G. Yaffe,
Transport coefficients in high temperature gauge theories (I): leading-log results,
Journal of High Energy Physics **2000** (2000) 001, ISSN: 1029-8479,
URL: http://dx.doi.org/10.1088/1126-6708/2000/11/001 (cit. on pp. 38, 65).

[71] J. Adam et al., *Centrality dependence of the pseudorapidity density distribution for charged particles in Pb-Pb collisions at* $\sqrt{s_{\mathrm{NN}}} = 5.02$ *TeV*, Phys. Lett. B **772** (2017) 567,
arXiv: 1612.08966 [nucl-ex] (cit. on p. 39).

[72] U. Heinz and R. Snellings, *Collective flow and viscosity in relativistic heavy-ion collisions*,
Ann. Rev. Nucl. Part. Sci. **63** (2013) 123, arXiv: 1301.2826 [nucl-th] (cit. on p. 40).

[73] P. Romatschke, *Relativistic Hydrodynamic Attractors with Broken Symmetries: Non-Conformal and Non-Homogeneous*, JHEP **12** (2017) 079,
arXiv: 1710.03234 [hep-th] (cit. on p. 41).

[74] M. P. Heller, R. Jefferson, M. Spaliński, and V. Svensson,
Hydrodynamic Attractors in Phase Space, Phys. Rev. Lett. **125** (2020) 132301,
arXiv: 2003.07368 [hep-th] (cit. on p. 41).

[75] R. D. Weller and P. Romatschke, *One fluid to rule them all: Viscous hydrodynamic description of event-by-event central p+p, p+Pb and Pb+Pb collisions at s=5.02 TeV*,
Physics Letters B **774** (2017) 351, ISSN: 0370-2693,
URL: http://dx.doi.org/10.1016/j.physletb.2017.09.077
(cit. on pp. 41, 42, 77, 80, 224, 313).

[76] J. L. Nagle and W. A. Zajc,
Small System Collectivity in Relativistic Hadronic and Nuclear Collisions,

Ann. Rev. Nucl. Part. Sci. **68** (2018) 211, arXiv: 1801.03477 [nucl-ex]
(cit. on pp. 42, 80).

[77] P. Romatschke, *Do nuclear collisions create a locally equilibrated quark–gluon plasma?*,
Eur. Phys. J. C **77** (2017) 21, arXiv: 1609.02820 [nucl-th] (cit. on p. 43).

[78] Z.-W. Lin, C. M. Ko, B.-A. Li, B. Zhang, and S. Pal,
A Multi-phase transport model for relativistic heavy ion collisions,
Phys. Rev. C **72** (2005) 064901, arXiv: nucl-th/0411110 (cit. on pp. 43, 307, 308).

[79] B. Alver and G. Roland,
Collision geometry fluctuations and triangular flow in heavy-ion collisions,
Phys. Rev. C **81** (2010) 054905, [Erratum: Phys.Rev.C 82, 039903 (2010)],
arXiv: 1003.0194 [nucl-th] (cit. on p. 44).

[80] J. L. Nagle and J. Orjuela Koop, *A Quasiparticle Transport Explanation for Collectivity in the Smallest of Collision Systems ($p+p$ and e^+e)*,
Nucl. Phys. A **982** (2019) 455, ed. by F. Antinori et al., arXiv: 1807.04619 [nucl-th]
(cit. on pp. 44, 45).

[81] M. Gyulassy and X.-N. Wang, *HIJING 1.0: A Monte Carlo program for parton and particle production in high energy hadronic and nuclear collisions*,
Computer Physics Communications **83** (1994) 307, ISSN: 0010-4655,
URL: http://www.sciencedirect.com/science/article/pii/0010465594900574
(cit. on pp. 45, 145, 231).

[82] C. Bierlich, G. Gustafson, L. Lönnblad, and H. Shah,
The Angantyr model for heavy-ion collisions in Pythia8,
Journal of High Energy Physics **2018** (2018), ISSN: 1029-8479,
URL: http://dx.doi.org/10.1007/JHEP10(2018)134 (cit. on pp. 45, 304, 306).

[83] K. J. Eskola, H. Paukkunen, and C. A. Salgado,
EPS09: A New Generation of NLO and LO Nuclear Parton Distribution Functions,
JHEP **04** (2009) 065, arXiv: 0902.4154 [hep-ph] (cit. on p. 46).

[84] A. Bialas, M. Bleszynski, and W. Czyz,
Multiplicity Distributions in Nucleus-Nucleus Collisions at High-Energies,
Nucl. Phys. B **111** (1976) 461 (cit. on p. 46).

[85] J. D. Bjorken, "Energy loss of energetic partons in QGP: possible extinction of high pt jets in hadron-hadron collisions", FERMILAB-PUB-82-059-THY, 1982,
URL: http://lss.fnal.gov/archive/preprint/fermilab-pub-82-059-t.shtml
(cit. on pp. 47, 48).

[86] M. H. Thoma and M. Gyulassy,
Quark damping and energy loss in the high temperature QCD,
Nuclear Physics B **351** (1991) 491, ISSN: 0550-3213,
URL: https://www.sciencedirect.com/science/article/pii/S0550321305800318
(cit. on p. 48).

[87] M. H. Thoma, *Collisional energy loss of high energy jets in the quark-gluon plasma*,
Physics Letters B **273** (1991) 128, ISSN: 0370-2693,
URL: https://www.sciencedirect.com/science/article/pii/0370269391905658
(cit. on pp. 48, 69).

[88] C. Manuel, *The Stopping Power of Hot Nuclear Matter*, Physics **7** (2014) (cit. on p. 48).

[89] J. Noronha-Hostler, B. Betz, J. Noronha, and M. Gyulassy,
Event-by-Event Hydrodynamics + Jet *Energy Loss: A Solution to the* $R_{AA} \bigotimes v_2$ *Puzzle*,
Phys. Rev. Lett. **116** (25 2016) 252301,
URL: https://link.aps.org/doi/10.1103/PhysRevLett.116.252301
(cit. on pp. 49, 83, 84).

[90] ATLAS Collaboration, *Observation of a Centrality-Dependent Dijet Asymmetry in Lead–Lead Collisions at $\sqrt{s_{NN}} = 2.76$ TeV with the ATLAS Detector at the LHC*, Phys. Rev. Lett. **105** (2010) 252303, arXiv: 1011.6182 [hep-ex] (cit. on pp. 49, 50, 141).

[91] CMS Collaboration, *Observation and studies of jet quenching in PbPb collisions at $\sqrt{s_{NN}} = 2.76$ TeV*, Phys. Rev. C **84** (2011) 024906, arXiv: 1102.1957 [hep-ex] (cit. on p. 49).

[92] ATLAS Collaboration, *Measurement of jet p_T correlations in Pb+Pb and pp collisions at $\sqrt{s_{NN}} = 2.76$ TeV with the ATLAS detector*, Phys. Lett. B **774** (2017) 379, arXiv: 1706.09363 [hep-ex] (cit. on p. 49).

[93] ATLAS Collaboration, *Measurement of the production of neighbouring jets in lead-lead collisions at $\sqrt{s_{NN}} = 2.76$ TeV with the ATLAS detector*, Phys. Lett. B **751** (2015) 376, arXiv: 1506.08656 [hep-ex] (cit. on p. 50).

[94] ATLAS Collaboration, *Measurement of the nuclear modification factor for inclusive jets in Pb+Pb collisions at $\sqrt{s_{NN}} = 5.02$ TeV with the ATLAS detector*, Phys. Lett. B **790** (2019) 108, arXiv: 1805.05635 [hep-ex] (cit. on pp. 52, 240).

[95] ATLAS Collaboration, *Measurements of the Nuclear Modification Factor for Jets in Pb+Pb Collisions at $\sqrt{s_{NN}} = 2.76$ TeV with the ATLAS Detector*, Phys. Rev. Lett. **114** (2015) 072302, arXiv: 1411.2357 [hep-ex] (cit. on pp. 52, 233).

[96] CMS Collaboration, *Measurement of inclusive jet cross-sections in pp and PbPb collisions at $\sqrt{s_{NN}} = 2.76$ TeV*, Phys. Rev. C **96** (2017) 015202, arXiv: 1609.05383 [hep-ex] (cit. on p. 52).

[97] CMS Collaboration, *First measurement of large area jet transverse momentum spectra in heavy-ion collisions*, JHEP **05** (2021) 284, arXiv: 2102.13080 [hep-ex] (cit. on p. 52).

[98] A. Adare et al.,
Transverse momentum and centrality dependence of dihadron correlations in Au+Au collisions at s(NN) = 200-GeV: Jet-quenching and the response of partonic matter,
Phys. Rev. C **77** (2008) 011901, arXiv: 0705.3238 [nucl-ex] (cit. on p. 53).

[99] M. Connors, C. Nattrass, R. Reed, and S. Salur, *Jet measurements in heavy ion physics*,
Rev. Mod. Phys. **90** (2018) 025005, arXiv: 1705.01974 [nucl-ex] (cit. on p. 53).

[100] K. K. Hill, "Collective behavior of high-p_{T} particles in 8.16 TeV p+Pb collisions with the ATLAS detector", Talk presented at Quark Matter 2019, Wuhan, China, 2019
(cit. on p. 54).

[101] ATLAS Collaboration, *Measurement of the Azimuthal Angle Dependence of Inclusive Jet Yields in Pb+Pb Collisions at $\sqrt{s_{NN}} = 2.76$ TeV with the ATLAS detector*,
Phys. Rev. Lett. **111** (2013) 152301, arXiv: 1306.6469 [hep-ex] (cit. on p. 54).

[102] CMS Collaboration, *Azimuthal anisotropy of charged particles with transverse momentum up to 100 GeV/c in PbPb collisions at $\sqrt{s_{NN}} = 5.02$ TeV*, Phys. Lett. B **776** (2018) 195,
arXiv: 1702.00630 [hep-ex] (cit. on p. 54).

[103] ATLAS Collaboration,
Measurements of Jet Azimuthal Anisotropies in Pb+Pb collisions at $\sqrt{s_{NN}} = 5.02$ TeV,
ATLAS-CONF-2020-019, 2020, URL: https://cds.cern.ch/record/2720249
(cit. on p. 54).

[104] Y. L. Dokshitzer, V. A. Khoze, and S. I. Troyan,
On specific QCD properties of heavy quark fragmentation ('dead cone'),
Journal of Physics G: Nuclear and Particle Physics **17** (1991) 1602,
URL: https://doi.org/10.1088/0954-3899/17/10/023 (cit. on p. 56).

[105] A. Collaboration, *Direct observation of the dead-cone effect in QCD*, 2021,
arXiv: 2106.05713 [nucl-ex] (cit. on p. 56).

[106] G. Aad et al., *Measurement of the nuclear modification factor for muons from charm and bottom hadrons in Pb+Pb collisions at 5.02 TeV with the ATLAS detector*, (2021), arXiv: 2109.00411 [nucl-ex] (cit. on pp. 56, 57).

[107] M. Spousta and B. Cole,
Interpreting single jet measurements in Pb + Pb collisions at the LHC,
The European Physical Journal C **76** (2016), ISSN: 1434-6052,
URL: http://dx.doi.org/10.1140/epjc/s10052-016-3896-0 (cit. on p. 57).

[108] J. Brewer, "Separating quark and gluon jet distributions in heavy-ion collisions",
Poster presented at Quark Matter 2019, Wuhan, China (cit. on p. 57).

[109] O. Biebel, P. Nason, and B. R. Webber, *Jet fragmentation in e+e- annihilation*, (2001), arXiv: hep-ph/0109282 (cit. on p. 58).

[110] ATLAS Collaboration, *Measurement of inclusive jet charged-particle fragmentation functions in Pb+Pb collisions at* $\sqrt{s_{NN}} = 2.76$ *TeV with the ATLAS detector*,
Phys. Lett. B **739** (2014) 320, arXiv: 1406.2979 [hep-ex] (cit. on p. 59).

[111] ATLAS Collaboration, *Measurement of jet fragmentation in Pb+Pb and pp collisions at* $\sqrt{s_{NN}} = 5.02$ *TeV with the ATLAS detector*, Phys. Rev. C **98** (2018) 024908,
arXiv: 1805.05424 [hep-ex] (cit. on pp. 59, 61, 136, 207).

[112] CMS Collaboration, *Observation of Medium Induced Modifications of Jet Fragmentation in PbPb Collisions at* $\sqrt{s_{NN}} = 5.02$ *TeV Using Isolated Photon-Tagged Jets*,
Phys. Rev. Lett. **121** (2018) 242301, arXiv: 1801.04895 [hep-ex]
(cit. on pp. 60, 61, 130, 217).

[113] ATLAS Collaboration, *Comparison of Fragmentation Functions for Jets Dominated by Light Quarks and Gluons from pp and Pb+Pb Collisions in ATLAS*,
Phys. Rev. Lett. **123** (2019) 042001, arXiv: 1902.10007 [hep-ex] (cit. on pp. 60, 61, 130).

[114] H. Bethe and W. Heitler,
On the stopping of fast particles and on the creation of positive electrons,
Proc. R. Soc. **146** (1934) 83, ISSN: 0950-1207,
URL: https://royalsocietypublishing.org/doi/10.1098/rspa.1934.0140
(cit. on p. 62).

[115] R. Baier, Y. Dokshitzer, S. Peigné, and D. Schiff,
Induced gluon radiation in a QCD medium, Physics Letters B **345** (1995) 277,
ISSN: 0370-2693, URL: http://dx.doi.org/10.1016/0370-2693(94)01617-L
(cit. on p. 62).

[116] R. Baier, Y. Dokshitzer, A. Mueller, S. Peigné, and D. Schiff,
The Landau-Pomeranchuk-Migdal effect in QED, Nuclear Physics B **478** (1996) 577,
ISSN: 0550-3213, URL: http://dx.doi.org/10.1016/0550-3213(96)00426-9
(cit. on p. 62).

[117] B. G. Zakharov,
Fully quantum treatment of the Landau-Pomeranchik-Migdal effect in QED and QCD,
Journal of Experimental and Theoretical Physics Letters **63** (1996) 952, ISSN: 1090-6487,
URL: http://dx.doi.org/10.1134/1.567126 (cit. on p. 62).

[118] R. Baier, Y. Dokshitzer, A. Mueller, S. Peigné, and D. Schiff,
Radiative energy loss and $p_\perp$-broadening of high energy partons in nuclei,
Nuclear Physics B **484** (1997) 265, ISSN: 0550-3213,
URL: http://dx.doi.org/10.1016/S0550-3213(96)00581-0 (cit. on p. 62).

[119] R. Baier, Y. Dokshitzer, A. Mueller, S. Peigné, and D. Schiff, *Radiative energy loss of high energy quarks and gluons in a finite-volume quark-gluon plasma*,
Nuclear Physics B **483** (1997) 291, ISSN: 0550-3213,
URL: http://dx.doi.org/10.1016/S0550-3213(96)00553-6 (cit. on pp. 62, 63).

[120] B. G. Zakharov, *Radiative energy loss of high-energy quarks in finite-size nuclear matter and quark-gluon plasma*,
Journal of Experimental and Theoretical Physics Letters **65** (1997) 615, ISSN: 1090-6487,
URL: http://dx.doi.org/10.1134/1.567389 (cit. on p. 62).

[121] R. Baier, Y. Dokshitzer, A. Mueller, and D. Schiff, *Medium-induced radiative energy loss; equivalence between the BDMPS and Zakharov formalisms*,
Nuclear Physics B **531** (1998) 403, ISSN: 0550-3213,
URL: http://dx.doi.org/10.1016/S0550-3213(98)00546-X (cit. on p. 62).

[122] Y. MEHTAR-TANI, J. G. MILHANO, and K. TYWONIUK,
Jet physics in heavy-ion collisions,
International Journal of Modern Physics A **28** (2013) 1340013, ISSN: 1793-656X,
URL: http://dx.doi.org/10.1142/S0217751X13400137 (cit. on pp. 62, 63).

[123] R. Baier, *Jet quenching*, Nuclear Physics A **715** (2003) 209c, ISSN: 0375-9474,
URL: http://dx.doi.org/10.1016/S0375-9474(02)01429-X (cit. on p. 63).

[124] Y. Mehtar-Tani,
Gluon bremsstrahlung in finite media beyond multiple soft scattering approximation,
Journal of High Energy Physics **2019** (2019), ISSN: 1029-8479,
URL: http://dx.doi.org/10.1007/JHEP07(2019)057 (cit. on pp. 63, 64, 66).

[125] U. A. Wiedemann,
Gluon radiation off hard quarks in a nuclear environment: opacity expansion,
Nuclear Physics B **588** (2000) 303, ISSN: 0550-3213,
URL: http://dx.doi.org/10.1016/S0550-3213(00)00457-0 (cit. on pp. 64, 65).

[126] M. Gyulassy, P. Levai, and I. Vitev, *Reaction operator approach to non-abelian energy loss*,
Nuclear Physics B **594** (2001) 371, ISSN: 0550-3213,
URL: http://dx.doi.org/10.1016/S0550-3213(00)00652-0 (cit. on p. 64).

[127] M. Gyulassy, P. Lévai, and I. Vitev,
Jet quenching in thin quark–gluon plasmas I: formalism,
Nuclear Physics B **571** (2000) 197, ISSN: 0550-3213,
URL: http://dx.doi.org/10.1016/S0550-3213(99)00713-0 (cit. on p. 64).

[128] M. Djordjevic and M. Gyulassy, *Heavy quark radiative energy loss in QCD matter*,
Nucl. Phys. A **733** (2004) 265, arXiv: nucl-th/0310076 (cit. on p. 64).

[129] C. A. Salgado and U. A. Wiedemann, *Calculating quenching weights*,
Physical Review D **68** (2003), ISSN: 1089-4918,
URL: http://dx.doi.org/10.1103/PhysRevD.68.014008 (cit. on p. 65).

[130] N. Armesto, C. Salgado, and U. Wiedemann,
Medium-induced gluon radiation off massive quarks fills the dead cone,
Physical Review D **69** (2004), ISSN: 1550-2368,
URL: http://dx.doi.org/10.1103/PhysRevD.69.114003 (cit. on p. 65).

[131] P. Arnold, G. D. Moore, and L. G. Yaffe,
Photon emission from quark-gluon plasma: complete leading order results,
Journal of High Energy Physics **2001** (2001) 009, ISSN: 1029-8479,
URL: http://dx.doi.org/10.1088/1126-6708/2001/12/009 (cit. on p. 65).

[132] P. Arnold, G. D. Moore, and L. G. Yaffe,
Photon and gluon emission in relativistic plasmas,
Journal of High Energy Physics **2002** (2002) 030, ISSN: 1029-8479,
URL: http://dx.doi.org/10.1088/1126-6708/2002/06/030 (cit. on p. 65).

[133] S. Jeon and G. D. Moore, *Energy loss of leading partons in a thermal QCD medium*,
Physical Review C **71** (2005), ISSN: 1089-490X,
URL: http://dx.doi.org/10.1103/PhysRevC.71.034901 (cit. on p. 65).

[134] G.-Y. Qin et al., *Radiative and Collisional Jet Energy Loss in the Quark-Gluon Plasma at the BNL Relativistic Heavy Ion Collider*, Physical Review Letters **100** (2008),

ISSN: 1079-7114, URL: http://dx.doi.org/10.1103/PhysRevLett.100.072301 (cit. on p. 65).

[135] J. Casalderrey-Solana, H. Liu, D. Mateos, K. Rajagopal, and U. A. Wiedemann, **Gauge/String Duality, Hot QCD and Heavy Ion Collisions**, Cambridge University Press, 2014 (cit. on p. 66).

[136] X. Guo and X.-N. Wang, *Multiple Scattering, Parton Energy Loss, and Modified Fragmentation Functions in Deeply InelasticeAScattering*, Physical Review Letters **85** (2000) 3591, ISSN: 1079-7114, URL: http://dx.doi.org/10.1103/PhysRevLett.85.3591 (cit. on p. 66).

[137] X.-N. Wang and X. Guo, *Multiple parton scattering in nuclei: parton energy loss*, Nuclear Physics A **696** (2001) 788, ISSN: 0375-9474, URL: http://dx.doi.org/10.1016/S0375-9474(01)01130-7 (cit. on p. 66).

[138] A. Majumder, *Hard collinear gluon radiation and multiple scattering in a medium*, Physical Review D **85** (2012), ISSN: 1550-2368, URL: http://dx.doi.org/10.1103/PhysRevD.85.014023 (cit. on p. 66).

[139] U. A. Wiedemann, *Jet quenching versus jet enhancement: a quantitative study of the BDMPS-Z gluon radiation spectrum*, Nuclear Physics A **690** (2001) 731, ISSN: 0375-9474, URL: http://dx.doi.org/10.1016/S0375-9474(01)00362-1 (cit. on p. 68).

[140] G.-Y. Qin and X.-N. Wang, *Jet quenching in high-energy heavy-ion collisions*, International Journal of Modern Physics E **24** (2015) 1530014, ISSN: 1793-6608, URL: http://dx.doi.org/10.1142/S0218301315300143 (cit. on p. 68).

[141] H. Li, F. Liu, G.-l. Ma, X.-N. Wang, and Y. Zhu, *Mach Cone Induced by γ-Triggered Jets in High-Energy Heavy-Ion Collisions*, Physical Review Letters **106** (2011), ISSN: 1079-7114, URL: http://dx.doi.org/10.1103/PhysRevLett.106.012301 (cit. on pp. 68, 76).

[142] X.-N. Wang and Y. Zhu,
Medium Modification of γ Jets in High-Energy Heavy-Ion Collisions,
Physical Review Letters **111** (2013), ISSN: 1079-7114,
URL: http://dx.doi.org/10.1103/PhysRevLett.111.062301 (cit. on pp. 68, 76).

[143] Y. He, T. Luo, X.-N. Wang, and Y. Zhu, *Linear Boltzmann transport for jet propagation in the quark-gluon plasma: Elastic processes and medium recoil*, Physical Review C **91** (2015), ISSN: 1089-490X, URL: http://dx.doi.org/10.1103/PhysRevC.91.054908 (cit. on p. 68).

[144] I. P. Lokhtin and A. M. Snigirev, *A model of jet quenching in ultrarelativistic heavy ion collisionsand high-p_{T} hadron spectra at RHIC*,
The European Physical Journal C **45** (2006) 211, ISSN: 1434-6052,
URL: http://dx.doi.org/10.1140/epjc/s2005-02426-3 (cit. on p. 69).

[145] S. Mrowczynski, *Energy loss of a high-energy parton in the quark - gluon plasma*,
Phys. Lett. B **269** (1991) 383 (cit. on p. 69).

[146] A. Dainese, C. Loizides, and G. Paic,
Leading-particle suppression in high energy nucleus-nucleus collisions,
The European Physical Journal C **38** (2005) 461, ISSN: 1434-6052,
URL: http://dx.doi.org/10.1140/epjc/s2004-02077-x (cit. on p. 70).

[147] A. Buzzatti and M. Gyulassy,
Jet Flavor Tomography of Quark Gluon Plasmas at RHIC and LHC,
Physical Review Letters **108** (2012), ISSN: 1079-7114,
URL: http://dx.doi.org/10.1103/PhysRevLett.108.022301 (cit. on p. 70).

[148] K. C. Zapp, F. Krauss, and U. A. Wiedemann, *A perturbative framework for jet quenching*,
JHEP **03** (2013) 080, arXiv: 1212.1599 [hep-ph] (cit. on pp. 70, 71, 219, 423, 424).

[149] K. C. Zapp, *Monte Carlo simulations of jet quenching in heavy ion collisions*,
Nuclear Physics A **855** (2011) 60, ISSN: 0375-9474,
URL: http://dx.doi.org/10.1016/j.nuclphysa.2011.02.019 (cit. on p. 70).

[150] CMS Collaboration, *Study of high-p_T charged particle suppression in PbPb compared to pp collisions at $\sqrt{s_{NN}} = 2.76$ TeV*, Eur. Phys. J. C **72** (2012) 1945, arXiv: 1202.2554 [hep-ex] (cit. on pp. 71, 72).

[151] B. Abelev et al., *Centrality Dependence of Charged Particle Production at Large Transverse Momentum in Pb–Pb Collisions at $\sqrt{s_{\mathrm{NN}}} = 2.76$ TeV*, Phys. Lett. B **720** (2013) 52, arXiv: 1208.2711 [hep-ex] (cit. on pp. 71, 72).

[152] Z.-B. Kang, R. Lashof-Regas, G. Ovanesyan, P. Saad, and I. Vitev, *Jet quenching phenomenology from soft-collinear effective theory with Glauber gluons*, Phys. Rev. Lett. **114** (2015) 092002, arXiv: 1405.2612 [hep-ph] (cit. on pp. 71, 73, 219, 423, 424).

[153] J. D. Bjorken, *Highly Relativistic Nucleus-Nucleus Collisions: The Central Rapidity Region*, Phys. Rev. D **27** (1983) 140 (cit. on p. 71).

[154] T. Sjöstrand, S. Mrenna, and P. Z. Skands, *PYTHIA 6.4 Physics and Manual*, JHEP **05** (2006) 026, arXiv: hep-ph/0603175 (cit. on p. 72).

[155] K. Zapp, *JEWEL 2.0.0: directions for use*, The European Physical Journal C **74** (2014), ISSN: 1434-6052, URL: http://dx.doi.org/10.1140/epjc/s10052-014-2762-1 (cit. on p. 72).

[156] R. Kunnawalkam Elayavalli and K. C. Zapp, *Simulating V+jet processes in heavy ion collisions with JEWEL*, Eur. Phys. J. C **76** (2016) 695, arXiv: 1608.03099 [hep-ph] (cit. on pp. 72, 219, 423, 424).

[157] R. Kunnawalkam Elayavalli and K. C. Zapp, *Medium response in JEWEL and its impact on jet shape observables in heavy ion collisions*, Journal of High Energy Physics **2017** (2017), ISSN: 1029-8479, URL: http://dx.doi.org/10.1007/JHEP07(2017)141 (cit. on pp. 72, 218, 219, 423, 424).

[158] ATLAS Collaboration, *Measurement of photon-jet transverse momentum correlations in 5.02 TeV Pb+Pb and pp collisions with ATLAS*, Phys. Lett. B **789** (2019) 167, arXiv: 1809.07280 [hep-ex] (cit. on pp. 72, 130).

[159] Y.-T. Chien, "Jet Physics at High Energy Colliders", PhD thesis: Harvard University, 2013 (cit. on p. 73).

[160] G. Ovanesyan and I. Vitev, *Medium-induced parton splitting kernels from Soft Collinear Effective Theory with Glauber gluons*, Phys. Lett. B **706** (2012) 371, arXiv: 1109.5619 [hep-ph] (cit. on pp. 73, 219, 423, 424).

[161] P. M. Chesler, K. Jensen, A. Karch, and L. G. Yaffe, *Light quark energy loss in strongly coupled N=4 supersymmetric Yang-Mills plasma*, Physical Review D **79** (2009), ISSN: 1550-2368, URL: http://dx.doi.org/10.1103/PhysRevD.79.125015 (cit. on pp. 74, 75).

[162] L. McLerran, *Theory summary: Quark Matter 2006*, Journal of Physics G: Nuclear and Particle Physics **34** (2007) S583, ISSN: 1361-6471, URL: http://dx.doi.org/10.1088/0954-3899/34/8/S50 (cit. on p. 74).

[163] J. Casalderrey-Solana, D. C. Gulhan, J. G. Milhano, D. Pablos, and K. Rajagopal, *A Hybrid Strong/Weak Coupling Approach to Jet Quenching*, JHEP **10** (2014) 019, [Erratum: JHEP09,175(2015)], arXiv: 1405.3864 [hep-ph] (cit. on pp. 74, 75, 219, 423, 424).

[164] S. S. Gubser, D. R. Gulotta, S. S. Pufu, and F. D. Rocha, *Gluon energy loss in the gauge-string duality*, Journal of High Energy Physics **2008** (2008) 052, ISSN: 1029-8479, URL: http://dx.doi.org/10.1088/1126-6708/2008/10/052 (cit. on p. 75).

[165] J. Casalderrey-Solana, D. C. Gulhan, J. G. Milhano, D. Pablos, and K. Rajagopal, *Predictions for Boson-Jet Observables and Fragmentation Function Ratios from a Hybrid*

Strong/Weak Coupling Model for Jet Quenching, JHEP **03** (2016) 053, arXiv: 1508.00815 [hep-ph] (cit. on pp. 75, 219, 423, 424).

[166] S. Cao, T. Luo, G.-Y. Qin, and X.-N. Wang, *Linearized Boltzmann transport model for jet propagation in the quark-gluon plasma: Heavy quark evolution*, Physical Review C **94** (2016), ISSN: 2469-9993, URL: http://dx.doi.org/10.1103/PhysRevC.94.014909 (cit. on p. 76).

[167] S. Cao and X.-N. Wang, *Jet quenching and medium response in high-energy heavy-ion collisions: a review*, Reports on Progress in Physics **84** (2021) 024301, ISSN: 1361-6633, URL: http://dx.doi.org/10.1088/1361-6633/abc22b (cit. on p. 76).

[168] H. Song and U. Heinz, *Suppression of elliptic flow in a minimally viscous quark–gluon plasma*, Physics Letters B **658** (2008) 279, ISSN: 0370-2693, URL: https://www.sciencedirect.com/science/article/pii/S0370269307013913 (cit. on p. 77).

[169] H. Song and U. Heinz, *Causal viscous hydrodynamics in 2 + 1 dimensions for relativistic heavy-ion collisions*, Phys. Rev. C **77** (6 2008) 064901, URL: https://link.aps.org/doi/10.1103/PhysRevC.77.064901 (cit. on p. 77).

[170] Z. Qiu, C. Shen, and U. Heinz, *Hydrodynamic elliptic and triangular flow in Pb–Pb collisions at sNN=2.76A TeV*, Physics Letters B **707** (2012) 151, ISSN: 0370-2693, URL: https://www.sciencedirect.com/science/article/pii/S0370269311014985 (cit. on p. 77).

[171] L.-G. Pang, Y. Hatta, X.-N. Wang, and B.-W. Xiao, *Analytical and numerical Gubser solutions of the second-order hydrodynamics*,

Phys. Rev. D **91** (7 2015) 074027,

URL: https://link.aps.org/doi/10.1103/PhysRevD.91.074027 (cit. on p. 77).

[172] L. Pang, Q. Wang, and X.-N. Wang,

Effects of initial flow velocity fluctuation in event-by-event (3+1)D hydrodynamics,

Phys. Rev. C **86** (2 2012) 024911,

URL: https://link.aps.org/doi/10.1103/PhysRevC.86.024911 (cit. on p. 77).

[173] W. van der Schee, P. Romatschke, and S. Pratt,

Fully Dynamical Simulation of Central Nuclear Collisions,

Physical Review Letters **111** (2013), ISSN: 1079-7114,

URL: http://dx.doi.org/10.1103/PhysRevLett.111.222302 (cit. on p. 77).

[174] P. Romatschke,

Light-Heavy Ion Collisions: A window into pre-equilibrium QCD dynamics?,

Eur. Phys. J. C **75** (2015) 305, arXiv: 1502.04745 [nucl-th] (cit. on p. 77).

[175] M. Xie, X.-N. Wang, and H.-Z. Zhang,

γ-hadron spectra in p+Pb collisions at $\sqrt{s_{\mathrm{NN}}} = 5.02$ TeV, Physical Review C **103** (2021),

ISSN: 2469-9993, URL: http://dx.doi.org/10.1103/PhysRevC.103.034911

(cit. on p. 77).

[176] W. Chen, S. Cao, T. Luo, L.-G. Pang, and X.-N. Wang,

Effects of jet-induced medium excitation in γ-hadron correlation in A+A collisions,

Physics Letters B **777** (2018) 86, ISSN: 0370-2693,

URL: http://dx.doi.org/10.1016/j.physletb.2017.12.015

(cit. on pp. 77, 219, 220, 423).

[177] K. C. Han, R. J. Fries, and C. M. Ko,

Jet fragmentation via recombination of parton showers, Phys. Rev. C **93** (4 2016) 045207,

URL: https://link.aps.org/doi/10.1103/PhysRevC.93.045207 (cit. on p. 78).

[178] Z. Yang et al., *Search for the Elusive Jet-Induced Diffusion Wake in Z/γ-Jets with 2D Jet Tomography in High-Energy Heavy-Ion Collisions*, Phys. Rev. Lett. **127** (2021) 082301, arXiv: 2101.05422 [hep-ph] (cit. on pp. 78, 79, 221, 222).

[179] S. Cao, T. Luo, G.-Y. Qin, and X.-N. Wang, *Heavy and light flavor jet quenching at RHIC and LHC energies*, Physics Letters B **777** (2018) 255, ISSN: 0370-2693, URL: http://dx.doi.org/10.1016/j.physletb.2017.12.023 (cit. on p. 78).

[180] CMS Collaboration, *Modification of jet shapes in PbPb collisions at $\sqrt{s_{NN}} = 2.76$ TeV*, Phys. Lett. B **730** (2014) 243, arXiv: 1310.0878 [hep-ex] (cit. on p. 79).

[181] J. Casalderrey-Solana, D. C. Gulhan, J. G. Milhano, D. Pablos, and K. Rajagopal, *Angular structure of jet quenching within a hybrid strong/weak coupling model*, Journal of High Energy Physics **2017** (2017), ISSN: 1029-8479, URL: http://dx.doi.org/10.1007/JHEP03(2017)135 (cit. on pp. 79, 219, 423, 424).

[182] J. Adam et al., *Enhanced production of multi-strange hadrons in high-multiplicity proton-proton collisions*, Nature Phys. **13** (2017) 535, arXiv: 1606.07424 [nucl-ex] (cit. on p. 80).

[183] ALICE Collaboration, *Multi-strange baryon production in pPb collisions at $\sqrt{s_{\mathrm{NN}}} = 5.02$ TeV*, Physics Letters B **758** (2016) 389, ISSN: 0370-2693, URL: https://www.sciencedirect.com/science/article/pii/S0370269316301745 (cit. on p. 80).

[184] S. H. Lim et al., *Examination of flow and nonflow factorization methods in small collision systems*, Phys. Rev. C **100** (2019) 024908, arXiv: 1902.11290 [nucl-th] (cit. on p. 80).

[185] ATLAS Collaboration, *Transverse momentum and process dependent azimuthal anisotropies in $\sqrt{s_{NN}} = 8.16$ TeV p+Pb collisions with the ATLAS detector*, Eur. Phys. J. C **80** (2020) 73, arXiv: 1910.13978 [hep-ex] (cit. on pp. 81, 223, 225, 301).

[186] J. Adam et al., *Centrality dependence of particle production in p-Pb collisions at $\sqrt{s_{\mathrm{NN}}} = 5.02$ TeV*, Phys. Rev. C **91** (2015) 064905, arXiv: 1412.6828 [nucl-ex] (cit. on pp. 81, 82, 223–225, 234–236, 238–240, 308).

[187] ATLAS Collaboration, *Transverse momentum, rapidity, and centrality dependence of inclusive charged-particle production in $\sqrt{s_{NN}} = 5.02$ TeV p+Pb collisions measured by the ATLAS experiment*, Phys. Lett. B **763** (2016) 313, arXiv: 1605.06436 [hep-ex] (cit. on pp. 81, 223, 301, 308).

[188] CMS Collaboration, *Nuclear effects on the transverse momentum spectra of charged particles in pPb collisions at $\sqrt{s_{NN}} = 5.02$ TeV*, Eur. Phys. J. C **75** (2015) 237, arXiv: 1502.05387 [hep-ex] (cit. on p. 81).

[189] ATLAS Collaboration, *Centrality and rapidity dependence of inclusive jet production in $\sqrt{s_{NN}} = 5.02$ TeV proton-lead collisions with the ATLAS detector*, Phys. Lett. B **748** (2015) 392, arXiv: 1412.4092 [hep-ex] (cit. on pp. 81, 223, 225, 240).

[190] CMS Collaboration, *Measurement of inclusive jet production and nuclear modifications in pPb collisions at $\sqrt{s_{NN}} = 5.02$ TeV*, Eur. Phys. J. C **76** (2016) 372, arXiv: 1601.02001 [hep-ex] (cit. on pp. 81, 223, 233).

[191] J. L. Albacete et al., *Predictions for p+Pb Collisions at sqrt s_NN = 5 TeV*, Int. J. Mod. Phys. E **22** (2013) 1330007, arXiv: 1301.3395 [hep-ph] (cit. on pp. 82, 308).

[192] J. L. Albacete et al., *Predictions for Cold Nuclear Matter Effects in p+Pb Collisions at $\sqrt{s_{NN}} = 8.16$ TeV*, Nucl. Phys. A **972** (2018) 18, arXiv: 1707.09973 [hep-ph] (cit. on pp. 82–84).

[193] J. W. Cronin et al.,
Production of hadrons at large transverse momentum at 200, 300, and 400 GeV,
Phys. Rev. D **11** (11 1975) 3105,
URL: https://link.aps.org/doi/10.1103/PhysRevD.11.3105 (cit. on pp. 82, 301).

[194] B. Z. Kopeliovich, J. Nemchik, A. Schafer, and A. V. Tarasov,
Cronin effect in hadron production off nuclei, Phys. Rev. Lett. **88** (2002) 232303,
arXiv: hep-ph/0201010 (cit. on p. 82).

[195] R. Corke and T. Sjostrand, *Multiparton Interactions and Rescattering*,
JHEP **01** (2010) 035, arXiv: 0911.1909 [hep-ph] (cit. on p. 82).

[196] K. Hill,
"Investigations of p+Pb Collisions at Perturbative and Non-Perturbative QCD Scales",
PhD thesis: University of Colorado Boulder, 2020, arXiv: 2004.07920 [nucl-ex]
(cit. on p. 83).

[197] **LEP design report**, Copies shelved as reports in LEP, PS and SPS libraries,
Geneva: CERN, 1984, URL: https://cds.cern.ch/record/102083 (cit. on p. 85).

[198] E. Mobs,
The CERN accelerator complex - 2019. Complexe des accélérateurs du CERN - 2019,
(2019), General Photo, URL: https://cds.cern.ch/record/2684277 (cit. on p. 86).

[199] G. B. of World Records, *Largest Fridge*, Accessed: 2021-10-04,
URL: https://www.guinnessworldrecords.com/world-records/largest-fridge
(cit. on p. 86).

[200] R. Bailey and P. Collier, *Standard Filling Schemes for Various LHC Operation Modes*,
tech. rep., CERN, 2003, URL: http://cds.cern.ch/record/691782 (cit. on p. 87).

[201] J. Jowett et al., "The 2018 heavy-ion run of the LHC",
10th International Particle Accelerator Conference, 2019 WEYYPLM2 (cit. on pp. 87, 88).

[202] J. Wenninger, *Operation and Configuration of the LHC in Run 2*, (2019), URL: https://cds.cern.ch/record/2668326 (cit. on p. 88).

[203] J. Jowett et al., "The 2015 Heavy-Ion Run of the LHC",
7th International Particle Accelerator Conference, 2016 TUPMW027 (cit. on p. 88).

[204] J. Jowett et al., "The 2016 Proton-Nucleus Run of the LHC",
8th International Particle Accelerator Conference, 2017 (cit. on p. 88).

[205] M. Schaumann et al., "First Xenon-Xenon Collisions in the LHC",
9th International Particle Accelerator Conference, 2018 (cit. on p. 88).

[206] S. Baird, *Accelerators for pedestrians; rev. version*, tech. rep., CERN, 2007, URL: http://cds.cern.ch/record/1017689 (cit. on p. 89).

[207] A. Collaboration, *ATLAS Open Data 13 TeV Documentation*, Accessed: 2021-10-04, URL: http://opendata.atlas.cern/release/2020/documentation/atlas/experiment.html (cit. on p. 90).

[208] ATLAS Collaboration, *The ATLAS Experiment at the CERN Large Hadron Collider*, JINST **3** (2008) S08003 (cit. on pp. 90, 95, 98, 101, 103–106, 109, 111, 119).

[209] G. Aad et al.,
Expected Performance of the ATLAS Experiment - Detector, Trigger and Physics, (2009), arXiv: 0901.0512 [hep-ex] (cit. on p. 90).

[210] L. R. F. Castillo, "The ATLAS and CMS detectors",
The Search and Discovery of the Higgs Boson, 2053-2571,

Morgan & Claypool Publishers, 2015 4-1 to 4, ISBN: 978-1-6817-4078-2,
URL: http://dx.doi.org/10.1088/978-1-6817-4078-2ch4 (cit. on p. 91).

[211] A. Collaboration,
"Experiment Briefing: Keeping the ATLAS Inner Detector in perfect alignment",
General Photo, 2020, URL: https://cds.cern.ch/record/2723878 (cit. on p. 93).

[212] J. Pequenao,
"Computer generated images of the Pixel, part of the ATLAS inner detector.", 2008,
URL: https://cds.cern.ch/record/1095925 (cit. on p. 94).

[213] ATLAS Collaboration, *ATLAS Pixel Detector: Technical Design Report*,
ATLAS-TDR-11; CERN-LHCC-98-013, 1998, URL: https://cds.cern.ch/record/381263
(cit. on pp. 93–95).

[214] G. Aad et al., *ATLAS pixel detector electronics and sensors*, JINST **3** (2008) P07007,
URL: https://cds.cern.ch/record/1119279 (cit. on p. 93).

[215] ATLAS Collaboration, *ATLAS Insertable B-Layer: Technical Design Report*,
ATLAS-TDR-19; CERN-LHCC-2010-013, 2010,
URL: https://cds.cern.ch/record/1291633 (cit. on p. 95),
Addendum: ATLAS-TDR-19-ADD-1; CERN-LHCC-2012-009, 2012, URL:
https://cds.cern.ch/record/1451888.

[216] B. Abbott et al., *Production and integration of the ATLAS Insertable B-Layer*,
JINST **13** (2018) T05008, arXiv: 1803.00844 [physics.ins-det] (cit. on p. 95).

[217] A. Abdesselam et al., *The barrel modules of the ATLAS semiconductor tracker*,
Nuclear Instruments and Methods in Physics Research Section A: Accelerators,
Spectrometers, Detectors and Associated Equipment **568** (2006) 642, ISSN: 0168-9002,
URL: https://www.sciencedirect.com/science/article/pii/S016890020601388X
(cit. on p. 95).

[218] A. Ahmad et al., *The silicon microstrip sensors of the ATLAS semiconductor tracker*, Nuclear Instruments and Methods in Physics Research Section A: Accelerators, Spectrometers, Detectors and Associated Equipment **578** (2007) 98, ISSN: 0168-9002, URL: https://www.sciencedirect.com/science/article/pii/S0168900207007644 (cit. on p. 95).

[219] A. Abdesselam et al., *The ATLAS semiconductor tracker end-cap module*, Nuclear Instruments and Methods in Physics Research Section A: Accelerators, Spectrometers, Detectors and Associated Equipment **575** (2007) 353, ISSN: 0168-9002, URL: https://www.sciencedirect.com/science/article/pii/S0168900207003270 (cit. on p. 95).

[220] ATLAS Collaboration, *Operation and performance of the ATLAS semiconductor tracker*, JINST **9** (2014) P08009, arXiv: 1404.7473 [hep-ex] (cit. on p. 95).

[221] D. Besin et al., *Design and Evaluation of LAr Trigger Digitizer Board in the ATLAS Phase-I Upgrade*, (2018) 6 p, This manuscript for conference record of the 21st IEEE Real Time conference, arXiv: 1806.08046, URL: https://cds.cern.ch/record/2641641 (cit. on p. 96).

[222] A. S. Boldyrev et al., *The ATLAS transition radiation tracker*, Instruments and Experimental Techniques **55** (2012) 323, ISSN: 1608-3180, URL: https://doi.org/10.1134/S0020441212010125 (cit. on p. 96).

[223] A. S. Boldyrev and A. S. Maevskiy, *Simulation of the transition radiation detection conditions in the ATLAS TRT detector filled with argon and krypton gas mixtures*, Physics of Atomic Nuclei **78** (2015) 1552, ISSN: 1562-692X, URL: https://doi.org/10.1134/S1063778815130049 (cit. on p. 97).

[224] ATLAS Collaboration, *Performance of the ATLAS Transition Radiation Tracker in Run 1 of the LHC: tracker properties*, JINST **12** (2017) P05002, arXiv: 1702.06473 [hep-ex] (cit. on p. 97).

[225] ATLAS Collaboration, *Performance of the ATLAS track reconstruction algorithms in dense environments in LHC Run 2*, Eur. Phys. J. C **77** (2017) 673, arXiv: 1704.07983 [hep-ex] (cit. on pp. 97, 114, 115, 182).

[226] ATLAS Collaboration, *Performance of top-quark and W-boson tagging with ATLAS in Run 2 of the LHC*, Eur. Phys. J. C **79** (2019) 375, arXiv: 1808.07858 [hep-ex] (cit. on p. 97).

[227] G. Aad et al., *Drift Time Measurement in the ATLAS Liquid Argon Electromagnetic Calorimeter using Cosmic Muons*, The European Physical Journal C **70** (2010) 755, ISSN: 1434-6052, URL: http://dx.doi.org/10.1140/epjc/s10052-010-1403-6 (cit. on p. 101).

[228] R. Wigmans, **Calorimetry: Energy measurement in particle physics**, vol. 107, Oxford, UK: Oxford University Press, 2017 (cit. on pp. 102, 118).

[229] ATLAS Collaboration, *Jet energy measurement and its systematic uncertainty in proton–proton collisions at $\sqrt{s} = 7$ TeV with the ATLAS detector*, Eur. Phys. J. C **75** (2015) 17, arXiv: 1406.0076 [hep-ex] (cit. on pp. 102, 123).

[230] ATLAS Collaboration, *Determination of jet calibration and energy resolution in proton–proton collisions at $\sqrt{s} = 8$ TeV using the ATLAS detector*, Eur. Phys. J. C **80** (2020) 1104, arXiv: 1910.04482 [hep-ex] (cit. on pp. 102, 120).

[231] D. Drakoulakos, E. Gschwendtner, J. M. Maugain, F. Rohrbach, and Y. Sedykh, "The high precision X-ray tomograph for quality control of the ATLAS MDT muon spectrometer", **7th Asia Pacific Physics Conference**, 1997 (cit. on p. 107).

[232] P. Jenni, M. Nessi, and M. Nordberg, *Zero Degree Calorimeters for ATLAS*, tech. rep., CERN, 2007, URL: http://cds.cern.ch/record/1009649 (cit. on pp. 109, 110).

[233] M. A. L. Leite, "Performance of the ATLAS Zero Degree Calorimeter", **2013 IEEE Nuclear Science Symposium and Medical Imaging Conference (2013 NSS/MIC)**, 2013 1 (cit. on p. 109).

[234] ATLAS Collaboration, *Operation of the ATLAS trigger system in Run 2*, JINST **15** (2020) P10004, arXiv: 2007.12539 [hep-ex] (cit. on p. 111).

[235] ATLAS Collaboration, *Trigger Menu in 2016*, ATL-DAQ-PUB-2017-001, 2017, URL: https://cds.cern.ch/record/2242069 (cit. on p. 112).

[236] ATLAS Collaboration, *Trigger Menu in 2017*, ATL-DAQ-PUB-2018-002, 2018, URL: https://cds.cern.ch/record/2625986 (cit. on p. 112).

[237] ATLAS Collaboration, *Trigger Menu in 2018*, ATL-DAQ-PUB-2019-001, 2019, URL: https://cds.cern.ch/record/2693402 (cit. on p. 112).

[238] A. Sidoti, *Minimum Bias Trigger Scintillators in ATLAS Run II*, tech. rep., CERN, 2014, URL: https://cds.cern.ch/record/1708408 (cit. on pp. 112, 113).

[239] ATLAS Collaboration, *Readiness of the ATLAS Tile Calorimeter for LHC collisions*, The European Physical Journal C **70** (2010) 1193, ISSN: 1434-6052, URL: http://dx.doi.org/10.1140/epjc/s10052-010-1508-y (cit. on p. 113).

[240] ATLAS Collaboration, *Charged-particle distributions in $\sqrt{s} = 13$ TeV pp interactions measured with the ATLAS detector at the LHC*, Phys. Lett. B **758** (2016) 67, arXiv: 1602.01633 [hep-ex] (cit. on p. 113).

[241] R. Frühwirth, *Application of Kalman filtering to track and vertex fitting*, Nuclear Instruments and Methods in Physics Research Section A: Accelerators, Spectrometers, Detectors and Associated Equipment **262** (1987) 444, ISSN: 0168-9002, URL: https://www.sciencedirect.com/science/article/pii/0168900287908874 (cit. on p. 114).

[242] ATLAS Collaboration, *Muon reconstruction and identification efficiency in ATLAS using the full Run 2 pp collision data set at* $\sqrt{s} = 13$ *TeV*, Eur. Phys. J. C **81** (2020) 578, arXiv: 2012.00578 [hep-ex] (cit. on pp. 117, 152).

[243] J. Illingworth and J. Kittler, *A survey of the hough transform*, Computer Vision, Graphics, and Image Processing **44** (1988) 87, ISSN: 0734-189X, URL: https://www.sciencedirect.com/science/article/pii/S0734189X88800331 (cit. on p. 117).

[244] T. A. Gabriel, D. E. Groom, P. K. Job, N. V. Mokhov, and G. R. Stevenson, *Energy dependence of hadronic activity*, Nucl. Instrum. Meth. A **338** (1994) 336 (cit. on p. 118).

[245] C. Cojocaru et al., *Hadronic calibration of the ATLAS liquid argon end-cap calorimeter in the pseudorapidity region 1.6 < |η| < 1.8 in beam tests*, Nucl. Instrum. Meth. A **531** (2004) 481, ed. by V. Gostilo, arXiv: physics/0407009 (cit. on p. 119).

[246] J. P. Archambault et al., *Energy calibration of the ATLAS liquid argon forward calorimeter*, JINST **3** (2008) P02002 (cit. on p. 119).

[247] J. Pinfold et al., *Performance of the ATLAS liquid argon endcap calorimeter in the pseudorapidity region 2.5 < |eta| < 4.0 in beam tests*, Nucl. Instrum. Meth. A **593** (2008) 324 (cit. on p. 119).

[248] M. Livan and R. Wigmans, *Misconceptions about Calorimetry*, Instruments **1** (2017), ISSN: 2410-390X, URL: https://www.mdpi.com/2410-390X/1/1/3 (cit. on p. 119).

[249] J. P. Archambault et al., *Performance of the ATLAS liquid argon forward calorimeter in beam tests*, JINST **8** (2013) P05006 (cit. on p. 119).

[250] J. Abdallah et al., *Study of energy response and resolution of the ATLAS Tile Calorimeter to hadrons of energies from 16 to 30 GeV*, Eur. Phys. J. C **81** (2021) 549, arXiv: 2102.04088 [physics.ins-det] (cit. on p. 119).

[251] ATLAS Collaboration, *Jet energy scale and its uncertainty for jets reconstructed using the ATLAS heavy ion jet algorithm*, ATLAS-CONF-2015-016, 2015, URL: https://cds.cern.ch/record/2008677 (cit. on pp. 120, 122, 123).

[252] J. A. Hanks et al., *Method for separating jets and the underlying event in heavy ion collisions at the BNL Relativistic Heavy Ion Collider*, Phys. Rev. C **86** (2 2012) 024908, URL: https://link.aps.org/doi/10.1103/PhysRevC.86.024908 (cit. on p. 120).

[253] M. Cacciari, G. P. Salam, and G. Soyez, *FastJet user manual*, Eur. Phys. J. C **72** (2012) 1896, arXiv: 1111.6097 [hep-ph] (cit. on pp. 121, 307).

[254] A. Angerami et al., *Performance of Jet Reconstruction in Heavy Ion Collisions*, tech. rep., Supporting document for jet rcp paper which is in final pub com review.: CERN, 2011, URL: https://cds.cern.ch/record/1409453 (cit. on pp. 122, 123).

[255] S. Timoshenko et al., *Performance plots from 2018 Pb+Pb collisions at* $\sqrt{s_{NN}} = 5.02$ *TeV II.*, tech. rep., CERN, 2018, URL: https://cds.cern.ch/record/2650332 (cit. on p. 123).

[256] M. Krivos, M. Rybar, and M. Spousta, *Numerical inversion and cross-calibration for heavy-ion jet collections in 2017 pp and 2018 Pb+Pb*, tech. rep., CERN, 2020, URL: https://cds.cern.ch/record/2706256 (cit. on pp. 123, 124, 242).

[257] T. Kosek et al., *Numerical inversion for calibration of Heavy-ion jets*, tech. rep., CERN, 2014, URL: https://cds.cern.ch/record/1742072 (cit. on p. 124).

[258] J. Ouellette, *Calibration of Heavy Ion Jets in 2016 8.16 TeV p+Pb Collisions*, tech. rep., CERN, 2019, URL: https://cds.cern.ch/record/2655891 (cit. on p. 124).

[259] A. Cukierman and B. Nachman,
Mathematical properties of numerical inversion for jet calibrations,
Nuclear Instruments and Methods in Physics Research Section A: Accelerators, Spectrometers, Detectors and Associated Equipment **858** (2017) 1, ISSN: 0168-9002, URL: http://dx.doi.org/10.1016/j.nima.2017.03.038 (cit. on p. 124).

[260] ATLAS Collaboration,
Electron and photon energy calibration with the ATLAS detector using LHC Run 1 data,
Eur. Phys. J. C **74** (2014) 3071, arXiv: 1407.5063 [hep-ex] (cit. on p. 126).

[261] ATLAS Collaboration, *Electron and photon reconstruction and performance in ATLAS using a dynamical, topological cell clustering-based approach*, ATL-PHYS-PUB-2017-022, 2017, URL: https://cds.cern.ch/record/2298955 (cit. on pp. 126, 127, 160).

[262] ATLAS Collaboration, *Electron and photon performance measurements with the ATLAS detector using the 2015–2017 LHC proton–proton collision data*, JINST **14** (2019) P12006, arXiv: 1908.00005 [hep-ex] (cit. on pp. 126, 127).

[263] ATLAS Collaboration, *Electron reconstruction and identification in the ATLAS experiment using the 2015 and 2016 LHC proton–proton collision data at* $\sqrt{s} = 13$ *TeV*,
Eur. Phys. J. C **79** (2019) 639, arXiv: 1902.04655 [hep-ex] (cit. on pp. 128, 156).

[264] J. A. Kremer and I. Grabowska-Bold,
Optimization of electron likelihood identification in Pb+Pb collisions,
tech. rep. ATL-COM-PHYS-2016-1398, CERN, 2016,
URL: https://cds.cern.ch/record/2217208 (cit. on pp. 128, 157).

[265] ATLAS Collaboration, *Measurements of* W *and* Z *boson production in pp collisions at* $\sqrt{s} = 5.02$ *TeV with the ATLAS detector*, Eur. Phys. J. C **79** (2019) 128,
arXiv: 1810.08424 [hep-ex] (cit. on pp. 129, 163),
Erratum: Eur. Phys. J. C **79** (2019) 374.

[266] ATLAS Collaboration, *Measurement of $W^{\pm}$ boson production in Pb+Pb collisions at $\sqrt{s_{NN}} = 5.02$ TeV with the ATLAS detector*, Eur. Phys. J. C **79** (2019) 935, arXiv: 1907.10414 [hep-ex] (cit. on p. 129).

[267] ATLAS Collaboration, *Centrality, rapidity and transverse momentum dependence of isolated prompt photon production in lead–lead collisions at $\sqrt{s_{NN}} = 2.76$ TeV measured with the ATLAS detector*, Phys. Rev. C **93** (2016) 034914, arXiv: 1506.08552 [hep-ex] (cit. on p. 130).

[268] CMS Collaboration, *Studies of jet quenching using isolated-photon+jet correlations in PbPb and pp collisions at $\sqrt{s_{NN}} = 2.76$ TeV*, Phys. Lett. B **718** (2013) 773, arXiv: 1205.0206 [hep-ex] (cit. on p. 130).

[269] CMS Collaboration, *Study of jet quenching with isolated-photon+jet correlations in PbPb and pp collisions at $\sqrt{s_{NN}} = 5.02$ TeV*, Phys. Lett. B **785** (2018) 14, arXiv: 1711.09738 [hep-ex] (cit. on p. 130).

[270] CMS Collaboration, *Jet Shapes of Isolated Photon-Tagged Jets in PbPb and pp Collisions at $\sqrt{s_{NN}} = 5.02$ TeV*, Phys. Rev. Lett. **122** (2019) 152001, arXiv: 1809.08602 [hep-ex] (cit. on p. 130).

[271] CMS Collaboration, *Study of jet quenching with Z+jet correlations in PbPb and pp collisions at $\sqrt{s_{NN}} = 5.02$ TeV*, Phys. Rev. Lett. **119** (2017) 082301, arXiv: 1702.01060 [hep-ex] (cit. on p. 130).

[272] ATLAS Collaboration, *Medium-Induced Modification of Z-Tagged Charged Particle Yields in Pb+Pb Collisions at* 5.02 *TeV with the ATLAS Detector*, Phys. Rev. Lett. **126** (2021) 072301, arXiv: 2008.09811 [hep-ex] (cit. on p. 130).

[273] CMS Collaboration, *Using Z boson events to study parton–medium interactions in PbPb collisions*, (2021), arXiv: 2103.04377 [hep-ex] (cit. on p. 130).

[274] A. Adare et al.,
*Photon-Hadron Jet Correlations in p+p and Au+Au Collisions at s**(1/2) = 200-GeV*,
Phys. Rev. **C80** (2009) 024908, arXiv: 0903.3399 [nucl-ex] (cit. on pp. 135, 216, 217).

[275] PHENIX Collaboration, *Medium Modification of Jet Fragmentation in Au+Au Collisions at $\sqrt{s_{NN}} = 200$ GeV Measured in Direct Photon-Hadron Correlations*,
Phys. Rev. Lett. **111** (2013) 032301, arXiv: 1212.3323 [nucl-ex] (cit. on p. 135).

[276] STAR Collaboration,
Jet-like correlations with direct-photon and neutral-pion triggers at $\sqrt{s_{_{NN}}} = 200$ GeV,
Phys. Lett. B **760** (2016) 689, arXiv: 1604.01117 [nucl-ex] (cit. on pp. 135, 216, 217).

[277] ATLAS Collaboration, *Measurement of jet fragmentation in* 5.02 *TeV proton–lead and proton–proton collisions with the ATLAS detector*, Nucl. Phys. **A978** (2018) 65,
arXiv: 1706.02859 [hep-ex] (cit. on pp. 136, 223, 303, 304).

[278] ATLAS Collaboration,
Measurement of angular and momentum distributions of charged particles within and around jets in Pb+Pb and pp collisions at $\sqrt{s_{NN}} = 5.02$ TeV with the ATLAS detector,
Phys. Rev. C **100** (2019) 064901, arXiv: 1908.05264 [hep-ex] (cit. on pp. 136, 195, 219),
Erratum: Phys. Rev. C **101** (2019) 059903.

[279] Analysis Software Group, **General event information**,
URL: https://atlassoftwaredocs.web.cern.ch/ABtutorial/event_level/
(cit. on p. 138).

[280] **Pixel desynchronization in PbPb 2018 runs**,
URL: https://its.cern.ch/jira/browse/ATLHI-245 (cit. on p. 138).

[281] **HeavyIonAnalysis2018**, URL:
https://twiki.cern.ch/twiki/bin/view/AtlasProtected/HeavyIonAnalysis2018
(cit. on p. 138).

[282] Zou, Wenkai and Rybar, Martin and Derendarz, Dominik, **Out-of-time pileup removal**, URL: https://indico.cern.ch/event/825854/contributions/3455132/attachments/1862106/3060638/Weekly_OOT_0613_2019.pdf (cit. on p. 139).

[283] Steinberg, Peter, **ZdcAnalysisTool**, URL: https://twiki.cern.ch/twiki/bin/viewauth/Atlas/ZdcAnalysisTool (cit. on p. 140).

[284] ATLAS Collaboration, *Measurement of the azimuthal anisotropy of charged particles produced in $\sqrt{s_{NN}} = 5.02$ TeV Pb+Pb collisions with the ATLAS detector*, Eur. Phys. J. C **78** (2018) 997, arXiv: 1808.03951 [hep-ex] (cit. on p. 141).

[285] D. Perepelitsa, *Centrality determination in $\sqrt{s_{\mathrm{NN}}} = 5.02$ TeV Pb+Pb collision data in 2015, using the Glauber v3.2 model*, tech. rep. ATL-COM-PHYS-2019-340, CERN, 2019, URL: https://cds.cern.ch/record/2672348 (cit. on pp. 141, 376).

[286] ATLAS Collaboration, *Performance of electron and photon triggers in ATLAS during LHC Run 2*, Eur. Phys. J. C **80** (2020) 47, arXiv: 1909.00761 [hep-ex] (cit. on pp. 142, 157).

[287] ATLAS Collaboration, *Performance of the ATLAS Minimum Bias and Forward Detector Triggers in p+Pb collisions*, ATLAS-CONF-2013-104, 2013, URL: https://cds.cern.ch/record/1624013 (cit. on p. 143).

[288] P. Nason, *A new method for combining NLO QCD with shower Monte Carlo algorithms*, JHEP **11** (2004) 040, arXiv: hep-ph/0409146 (cit. on p. 144).

[289] P. Skands, S. Carrazza, and J. Rojo, *Tuning PYTHIA 8.1: the Monash 2013 Tune*, Eur. Phys. J. C **74** (2014) 3024, arXiv: 1404.5630 [hep-ph] (cit. on p. 144).

[290] J. Gao et al., *CT10 next-to-next-to-leading order global analysis of QCD*, Phys. Rev. D **89** (2014) 033009, arXiv: 1302.6246 [hep-ph] (cit. on p. 144).

[291] J. Pumplin et al.,
New Generation of Parton Distributions with Uncertainties from Global QCD Analysis,
JHEP **07** (2002) 012, arXiv: hep-ph/0201195 (cit. on p. 144).

[292] ATLAS Collaboration, *Measurement of the Z/γ^* boson transverse momentum distribution in pp collisions at $\sqrt{s} = 7$ TeV with the ATLAS detector*, JHEP **09** (2014) 145,
arXiv: 1406.3660 [hep-ex] (cit. on p. 144).

[293] ATLAS Collaboration, *Muon reconstruction performance of the ATLAS detector in proton–proton collision data at $\sqrt{s} = 13$ TeV*, Eur. Phys. J. C **76** (2016) 292,
arXiv: 1603.05598 [hep-ex] (cit. on pp. 147, 153).

[294] ATLAS Collaboration,
Performance of the ATLAS muon trigger in pp collisions at $\sqrt{s} = 8$ TeV,
Eur. Phys. J. C **75** (2015) 120, arXiv: 1408.3179 [hep-ex] (cit. on p. 149).

[295] S. Lim,
Validation of phton and electron reconstruction with superclusters in heavy-ion collisions,
tech. rep. ATL-COM-PHYS-2019-118, CERN, 2019,
URL: https://cds.cern.ch/record/2659626 (cit. on pp. 157, 159, 160).

[296] M. Dumancic, A. Milov, Z. H. Citron, P. A. Janus, and P. Steinberg,
Z boson production in Pb+Pb collisions at $\sqrt{s_{NN}}$=5.02 TeV,
tech. rep. ATL-COM-PHYS-2018-167, CERN, 2018,
URL: https://cds.cern.ch/record/2305729 (cit. on p. 167).

[297] ATLAS Collaboration, *Modelling of Track Reconstruction Inside Jets with the 2016 ATLAS $\sqrt{s} = 13$ TeV pp Dataset*, ATL-PHYS-PUB-2017-016, 2017,
URL: https://cds.cern.ch/record/2275639 (cit. on pp. 178, 265).

[298] S. Lim, Q. Hu, D. Perepelitsa, and J. L. Nagle,
Supporting note for heavy flavor muon flow in Run2 Pb+Pb collisions with ATLAS,

tech. rep. ATL-COM-PHYS-2019-999, CERN, 2019,
URL: https://cds.cern.ch/record/2685279 (cit. on p. 196).

[299] ATLAS Collaboration, *Measurement of distributions sensitive to the underlying event in inclusive Z boson production in pp collisions at $\sqrt{s} = 13$ TeV with the ATLAS detector*, Eur. Phys. J. C **79** (2019) 666, arXiv: 1905.09752 [hep-ex] (cit. on pp. 197–199).

[300] ATLAS Collaboration, *Measurement of distributions sensitive to the underlying event in inclusive Z-boson production in pp collisions at $\sqrt{s} = 7$ TeV with the ATLAS detector*, Eur. Phys. J. C **74** (2014) 3195, arXiv: 1409.3433 [hep-ex] (cit. on pp. 198, 199).

[301] L. Antiporda, J. Bahder, H. Rahman, and M. D. Sievert, *Jet Drift and Collective Flow in Heavy-Ion Collisions*, (2021), arXiv: 2110.03590 [hep-ph] (cit. on p. 211).

[302] T. Luo, S. Cao, Y. He, and X.-N. Wang, *Multiple jets and γ-jet correlation in high-energy heavy-ion collisions*, Physics Letters B **782** (2018) 707, ISSN: 0370-2693, URL: http://dx.doi.org/10.1016/j.physletb.2018.06.025 (cit. on pp. 219, 220, 423).

[303] R. B. Neufeld and I. Vitev, *Z^0-Tagged Jet Event Asymmetry in Heavy-Ion Collisions at the CERN Large Hadron Collider*, Phys. Rev. Lett. **108** (2012) 242001, arXiv: 1202.5556 [hep-ph] (cit. on pp. 219, 423, 424).

[304] Y.-T. Chien and I. Vitev, *Towards the understanding of jet shapes and cross sections in heavy ion collisions using soft-collinear effective theory*, JHEP **05** (2016) 023, arXiv: 1509.07257 [hep-ph] (cit. on pp. 219, 423, 424).

[305] ATLAS Collaboration, *Measurement of long-range pseudorapidity correlations and azimuthal harmonics in $\sqrt{s_{NN}} = 5.02$ TeV proton–lead collisions with the ATLAS detector*, Phys. Rev. C **90** (2014) 044906, arXiv: 1409.1792 [hep-ex] (cit. on p. 223).

[306] ATLAS Collaboration, *Observation of Long-Range Elliptic Azimuthal Anisotropies in $\sqrt{s} = 13$ and 2.76 TeV pp Collisions with the ATLAS Detector*, Phys. Rev. Lett. **116** (2016) 172301, arXiv: 1509.04776 [hep-ex] (cit. on p. 223).

[307] CMS Collaboration, *Charged-particle nuclear modification factors in PbPb and pPb collisions at $\sqrt{s_{NN}} = 5.02$ TeV*, JHEP **04** (2017) 039, arXiv: 1611.01664 [hep-ex] (cit. on pp. 223, 308).

[308] S. Acharya et al., *Nuclear modification factor of light neutral-meson spectra up to high transverse momentum in p-Pb collisions at $\sqrt{s_{NN}}$ = 8.16 TeV*, (2021), arXiv: 2104.03116 [nucl-ex] (cit. on pp. 223, 308).

[309] *Jet Fragmentation Function in pPb Collisions at sqrt(sNN) = 5.02 TeV and pp Collisions at sqrt(s) = 2.76 and 7 TeV*, tech. rep., CERN, 2015, URL: https://cds.cern.ch/record/2030077 (cit. on pp. 223, 304, 427).

[310] ATLAS Collaboration, *Measurements of azimuthal anisotropies of jet production in Pb+Pb collisions at $\sqrt{s_{NN}}$ = 5.02 TeV with the ATLAS detector*, (2021), arXiv: 2111.06606 [nucl-ex] (cit. on pp. 223, 229).

[311] X. Zhang and J. Liao, *Jet Quenching and Its Azimuthal Anisotropy in AA and possibly High Multiplicity pA and dA Collisions*, (2013), arXiv: 1311.5463 [nucl-th] (cit. on p. 224).

[312] A. Adare et al., *Centrality categorization forRp(d)+Ain high-energy collisions*, Physical Review C **90** (2014), ISSN: 1089-490X, URL: http://dx.doi.org/10.1103/PhysRevC.90.034902 (cit. on pp. 224, 225, 233).

[313] C. Loizides and A. Morsch, *Absence of jet quenching in peripheral nucleus–nucleus collisions*, Phys. Lett. B **773** (2017) 408, arXiv: 1705.08856 [nucl-ex] (cit. on p. 224).

[314] ATLAS Collaboration, *Measurements of long-range azimuthal anisotropies and associated Fourier coefficients for pp collisions at $\sqrt{s} = 5.02$ and 13 TeV and p+Pb collisions at $\sqrt{s_{NN}} = 5.02$ TeV with the ATLAS detector*, Phys. Rev. C **96** (2017) 024908, arXiv: 1609.06213 [hep-ex] (cit. on p. 225).

[315] J. L. Nagle, *ATLAS Zero Degree Calorimeter 2016 p+Pb Study*, tech. rep., CERN, 2019, URL: https://cds.cern.ch/record/2668872 (cit. on pp. 226, 234).

[316] ATLAS Collaboration, *Measurement of the dijet momentum balance in Pb+Pb and pp collisions at $\sqrt{s_{NN}} = 5.02$ TeV with the ATLAS detector*, ATLAS-CONF-2020-017, 2020, URL: https://cds.cern.ch/record/2720247 (cit. on p. 229).

[317] ATLAS Collaboration, *ATLAS Pythia 8 tunes to 7 TeV data*, ATL-PHYS-PUB-2014-021, 2014, URL: https://cds.cern.ch/record/1966419 (cit. on p. 230).

[318] ATLAS Collaboration, *Z boson production in $p + Pb$ collisions at $\sqrt{s_{NN}} = 5.02$ TeV measured with the ATLAS detector*, Phys. Rev. C **92** (2015) 044915, arXiv: 1507.06232 [hep-ex] (cit. on p. 233).

[319] D. Perepelitsa, B. Cole, and P. Steinberg, *Centrality Determination in the 2012 and 2013 p+Pb data in ATLAS*, tech. rep., CERN, 2013, URL: https://cds.cern.ch/record/1545591 (cit. on pp. 233, 237).

[320] K. K. Hill and D. Perepelitsa, *Centrality Calibration in 8.16 TeV p+Pb Collisions*, tech. rep., CERN, 2018, URL: https://cds.cern.ch/record/2301540 (cit. on pp. 233, 236, 237).

[321] *Energy calibration studies of the ATLAS Zero Degree Calorimeter with 5.02 TeV 2018 Pb+Pb data*, tech. rep., CERN, 2020, URL: https://cds.cern.ch/record/2729779 (cit. on p. 234).

[322] ATLAS Collaboration, *Selection of jets produced in 13 TeV proton–proton collisions with the ATLAS detector*,

ATLAS-CONF-2015-029, 2015, URL: https://cds.cern.ch/record/2037702 (cit. on p. 241).

[323] **LAr HEC Q3 impact on 2016 pPb data**, URL: https://its.cern.ch/jira/browse/ATLHI-100 (cit. on p. 241).

[324] ATLAS Collaboration, *Jet energy measurement with the ATLAS detector in proton–proton collisions at* $\sqrt{s} = 7$ *TeV*, Eur. Phys. J. C **73** (2013) 2304, arXiv: 1112.6426 [hep-ex] (cit. on p. 246).

[325] ATLAS Collaboration, *Dijet azimuthal correlations and conditional yields in pp and p + Pb collisions at* $\sqrt{s_{NN}} = 5.02$ *TeV with the ATLAS detector*, Phys. Rev. C **100** (2019) 034903, arXiv: 1901.10440 [hep-ex] (cit. on p. 249).

[326] ATLAS Collaboration, *Jet energy scale and resolution measured in proton–proton collisions at* $\sqrt{s} = 13$ *TeV with the ATLAS detector*, Eur. Phys. J. C **81** (2020) 689, arXiv: 2007.02645 [hep-ex] (cit. on p. 253).

[327] P. Balek and A. Milov, *Supporting note for the measurement of the charged hadron spectra in heavy-ion collisions at* $\sqrt{s_{NN}} = 5\,TeV$ *with the ATLAS detector at the LHC*, tech. rep., CERN, 2019, URL: https://cds.cern.ch/record/2702964 (cit. on pp. 258, 260).

[328] M. Rybar et al., *Jet Fragmentation in p+Pb Collisions*, tech. rep., CERN, 2015, URL: https://cds.cern.ch/record/2005223 (cit. on p. 275).

[329] G. D'Agostini, *A multidimensional unfolding method based on Bayes' theorem*, Nucl. Instrum. Meth. A **362** (1995) 487, ISSN: 0168-9002 (cit. on p. 276).

[330] T. Adye, *Unfolding algorithms and tests using RooUnfold*, 2011, arXiv: 1105.1160 [physics.data-an] (cit. on p. 278).

[331] H. Heiselberg, G. Baym, B. Blättel, L. L. Frankfurt, and M. Strikman, *Color transparency, color opacity, and fluctuations in nuclear collisions*,

Phys. Rev. Lett. **67** (21 1991) 2946,
URL: https://link.aps.org/doi/10.1103/PhysRevLett.67.2946 (cit. on p. 305).

[332] B. Blättel, G. Baym, L. L. Frankfurt, H. Heiselberg, and M. Strikman,
Hadronic cross-section fluctuations, Phys. Rev. D **47** (7 1993) 2761,
URL: https://link.aps.org/doi/10.1103/PhysRevD.47.2761 (cit. on p. 305).

[333] M. Alvioli, L. Frankfurt, V. Guzey, and M. Strikman,
Revealing "flickering" of the interaction strength in pA collisions at the CERN LHC,
Phys. Rev. C **90** (3 2014) 034914,
URL: https://link.aps.org/doi/10.1103/PhysRevC.90.034914 (cit. on p. 305).

[334] M. Alvioli, B. A. Cole, L. Frankfurt, D. V. Perepelitsa, and M. Strikman, *Evidence for x-dependent proton color fluctuations in pA collisions at the CERN Large Hadron Collider*,
Phys. Rev. C **93** (1 2016) 011902,
URL: https://link.aps.org/doi/10.1103/PhysRevC.93.011902 (cit. on p. 305).

[335] A. Luo, Y.-X. Mao, G.-Y. Qin, E.-K. Wang, and H.-Z. Zhang,
Jet shape and redistribution of the lost energy from jets in Pb+Pb collisions at the LHC in a multiphase transport model, (2021), arXiv: 2107.11751 [hep-ph] (cit. on p. 308).

[336] S. H. Lim et al., *Exploring New Small System Geometries in Heavy Ion Collisions*,
Phys. Rev. C **99** (2019) 044904, arXiv: 1812.08096 [nucl-th] (cit. on pp. 312, 313).

[337] J. Brewer, A. Mazeliauskas, and W. van der Schee,
"Opportunities of OO and pO collisions at the LHC",
Opportunities of OO and pO collisions at the LHC, 2021,
arXiv: 2103.01939 [hep-ph] (cit. on p. 313).

[338] A. Adare et al., *An Upgrade Proposal from the PHENIX Collaboration*, (2015),
arXiv: 1501.06197 [nucl-ex] (cit. on p. 313).

[339] J. Adam et al., *Centrality dependence of the pseudorapidity density distribution for charged particles in Pb-Pb collisions at* $\sqrt{s_{\mathrm{NN}}} = 5.02$ *TeV*, Phys. Lett. B **772** (2017) 567, arXiv: 1612.08966 [nucl-ex] (cit. on p. 373).

[340] ATLAS Collaboration, *Two-particle azimuthal correlations in photonuclear ultraperipheral Pb+Pb collisions at* 5.02 *TeV with ATLAS*, Phys. Rev. C **104** (2021) 014903, arXiv: 2101.10771 [hep-ex] (cit. on pp. 392, 393).

Appendix A

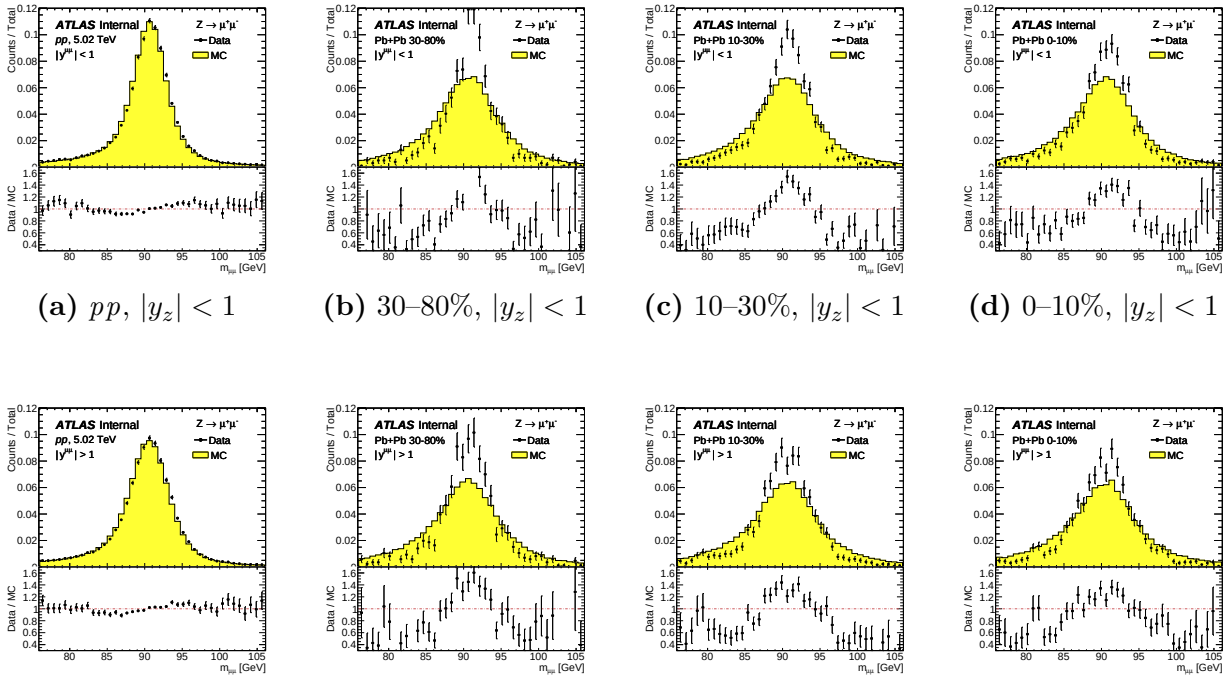
Auxiliary Material for the Z^0–Hadron Correlations Measurement

A.1 Characterizing the Z boson Sample

In the main text, we argued that, at least following the lepton energy scale studies, no pathological differences were observed in the Z kinematics between either Pb+Pb and pp or data and simulation. This is essential to allow the event sample in Pb+Pb to be compared with pp. The following sections exhaustively study the kinematic properties of reconstructed Z bosons across each of the bins in this analysis to fully demonstrate this claim. This include a complete set of Z resonance mass distributions (both before and after proper energy scale calibration), Z p_{T} spectra, rapidity & azimuth 2D heatmaps, and (pseudo-)rapidity distributions.

Some features of these figures are noteworthy. In Figs. A.1 to A.4, many of the energy scale issues discussed in Secs. 4.3 and 4.4 are on full display. For example, the muon peak mismatch between data and MC is readily visible in Fig. A.1, where the Z kinematics are drawn from the sum of the combined muon track momenta. In each of the Pb+Pb panels, the MC peak is wider than data. By restricting to the MS kinematics, as in Fig. A.2, the MC modeling is in better agreement with the data.

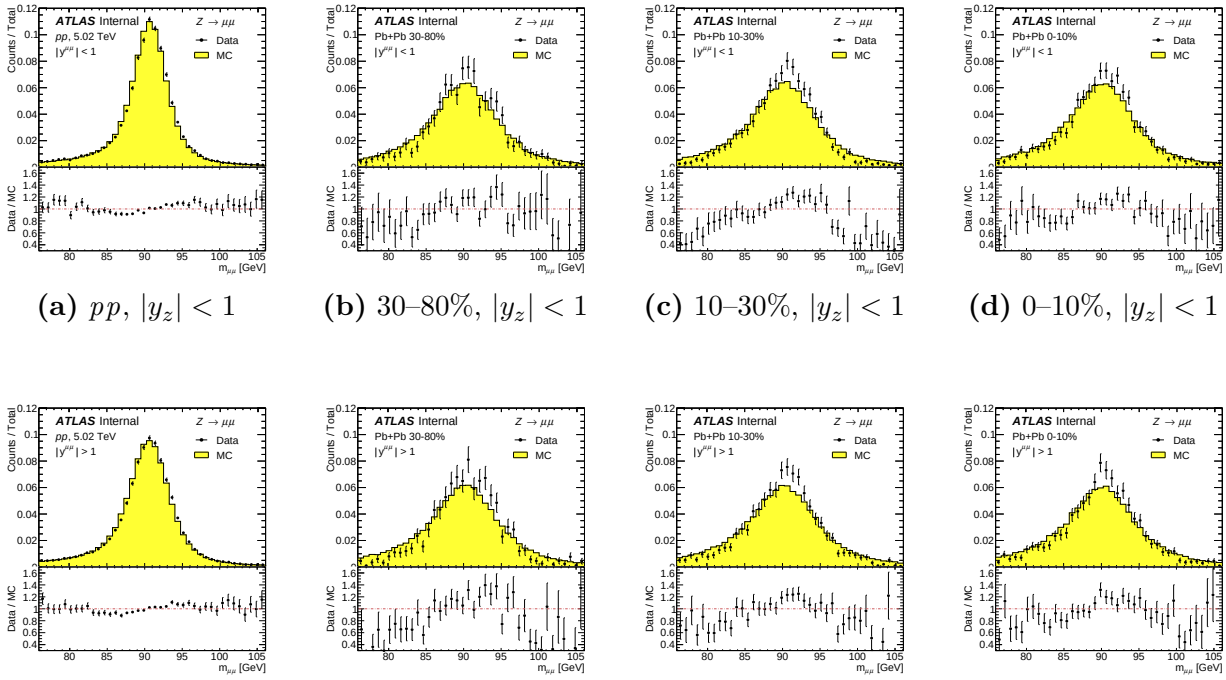
Later in Fig. A.8, we see the Z rapidity distribution is not consistent between the $Z \to ee$ and $Z \to \mu\mu$ channels; in particular, the $Z \to \mu\mu$ distribution is somewhat flatter near mid-rapidity. However, recall that the single electron pseudorapidity acceptance must account for the EMCal crack between $|\eta_e| = 1.37$ and 1.56, so we find we are less sensitive to Z bosons that can decay in this range. But, the effect is consistent between Pb+Pb and pp, so it can be ignored.



(a) pp, $|y_z| < 1$ **(b)** 30–80%, $|y_z| < 1$ **(c)** 10–30%, $|y_z| < 1$ **(d)** 0–10%, $|y_z| < 1$

(e) pp, $|y_z| > 1$ **(f)** 30–80%, $|y_z| > 1$ **(g)** 10–30%, $|y_z| > 1$ **(h)** 0–10%, $|y_z| > 1$

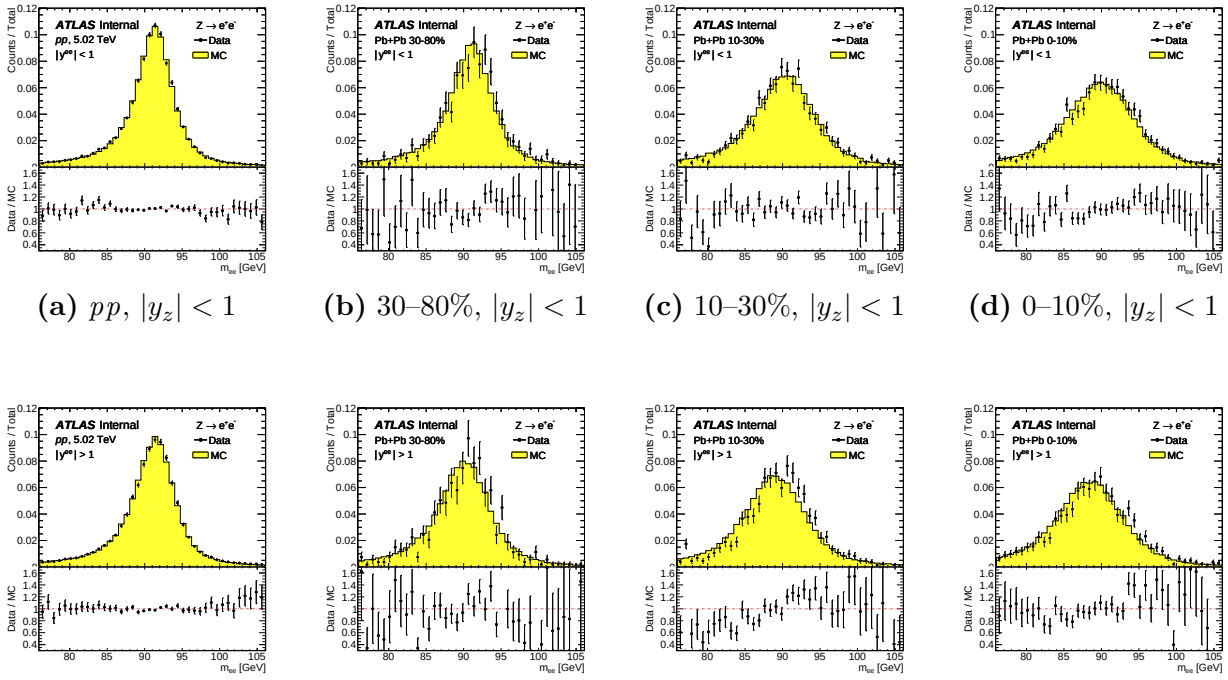
Figure A.1: Normalized distributions of mid-rapidity **(a–d)** and forward rapidity **(e–h)** opposite-signed dimuon invariant masses ($m_{\mu\mu}$) in data (black markers) and MC (yellow shaded region) are shown for **(a,e)** pp, **(b,f)** 30–80%, **(c,g)** 10–30%, and **(d,h)** 0–10% Pb+Pb collisions. Muon kinematics are measured using the combined track.



(a) pp, $|y_z| < 1$ **(b)** 30–80%, $|y_z| < 1$ **(c)** 10–30%, $|y_z| < 1$ **(d)** 0–10%, $|y_z| < 1$

(e) pp, $|y_z| > 1$ **(f)** 30–80%, $|y_z| > 1$ **(g)** 10–30%, $|y_z| > 1$ **(h)** 0–10%, $|y_z| > 1$

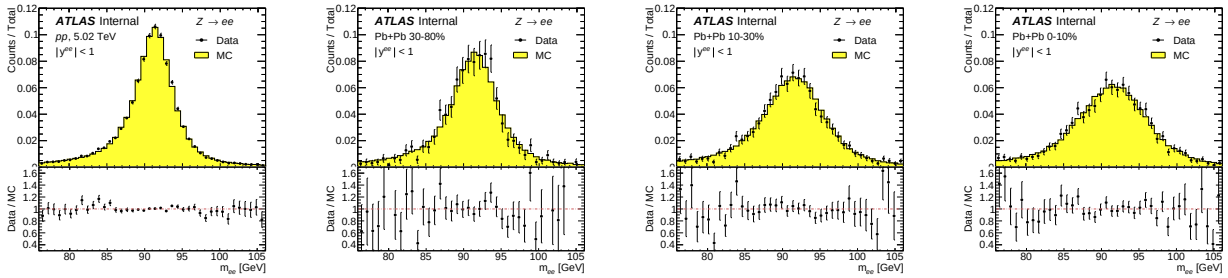
Figure A.2: Normalized distributions of mid-rapidity **(a–d)** and forward rapidity **(e–h)** opposite-signed dimuon invariant masses ($m_{\mu\mu}$) in data (black markers) and MC (yellow shaded region) are shown for **(a,e)** pp, **(b,f)** 30–80%, **(c,g)** 10–30%, and **(d,h)** 0–10% Pb+Pb collisions. Muon kinematics are measured using the MS track only.



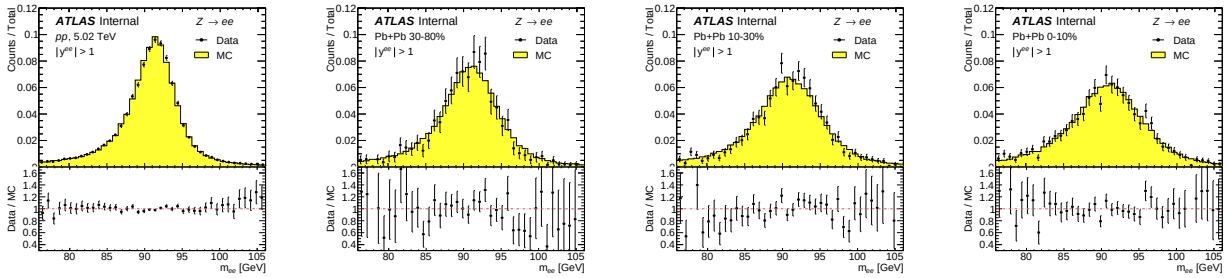
(a) pp, $|y_z| < 1$ **(b)** 30–80%, $|y_z| < 1$ **(c)** 10–30%, $|y_z| < 1$ **(d)** 0–10%, $|y_z| < 1$

(e) pp, $|y_z| > 1$ **(f)** 30–80%, $|y_z| > 1$ **(g)** 10–30%, $|y_z| > 1$ **(h)** 0–10%, $|y_z| > 1$

Figure A.3: Normalized distributions of mid-rapidity **(a–d)** and forward rapidity **(e–h)** opposite-signed dielectron invariant masses (m_{ee}) in data (black markers) and MC (yellow shaded region) are shown for **(a,e)** pp, **(b,f)** 30–80%, **(c,g)** 10–30%, and **(d,h)** 0–10% Pb+Pb collisions. Electron kinematics are *not* corrected by the scale factors in Table 4.4.

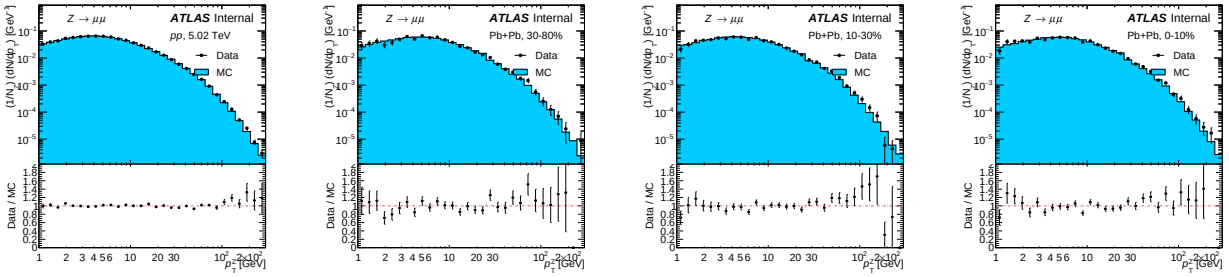


(a) pp, $|y_z| < 1$ **(b)** 30–80%, $|y_z| < 1$ **(c)** 10–30%, $|y_z| < 1$ **(d)** 0–10%, $|y_z| < 1$

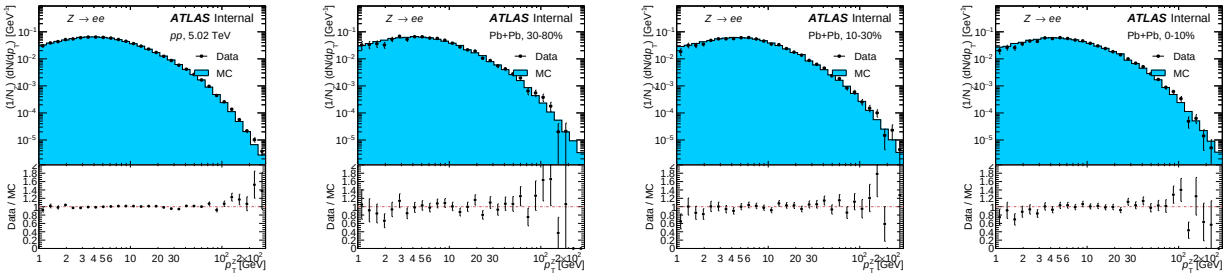


(e) pp, $|y_z| > 1$ **(f)** 30–80%, $|y_z| > 1$ **(g)** 10–30%, $|y_z| > 1$ **(h)** 0–10%, $|y_z| > 1$

Figure A.4: Normalized distributions of mid-rapidity **(a–d)** and forward rapidity **(e–h)** opposite-signed dielectron invariant masses (m_{ee}) in data (black markers) and MC (yellow shaded region) are shown for **(a,e)** pp, **(b,f)** 30–80%, **(c,g)** 10–30%, and **(d,h)** 0–10% Pb+Pb collisions. Electron kinematics have been corrected by the scale factors in Table 4.4.

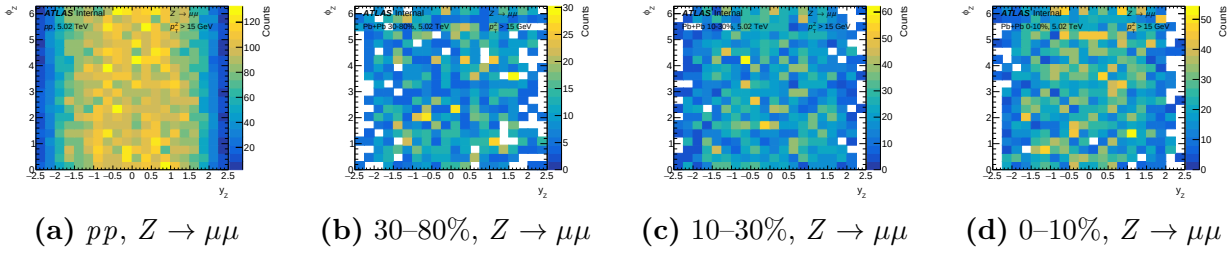


(a) pp, $Z \to \mu\mu$ **(b)** 30–80%, $Z \to \mu\mu$ **(c)** 10–30%, $Z \to \mu\mu$ **(d)** 0–10%, $Z \to \mu\mu$

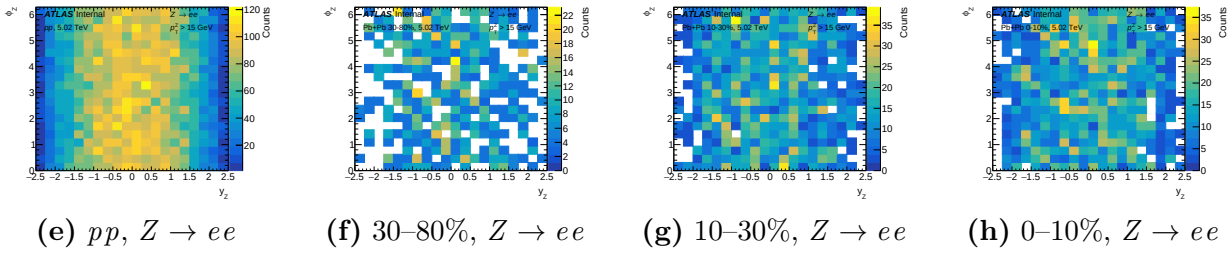


(e) pp, $Z \to ee$ **(f)** 30–80%, $Z \to ee$ **(g)** 10–30%, $Z \to ee$ **(h)** 0–10%, $Z \to ee$

Figure A.5: Normalized distributions of reconstructed Z p_{T} are shown for **(a,e)** pp, **(b,f)** 30–80%, **(c,g)** 10–30%, and **(d,h)** 0–10% Pb+Pb collisions in both the $Z \to \mu\mu$ **(a–d)** and $Z \to ee$ **(e–h)** decay channels.

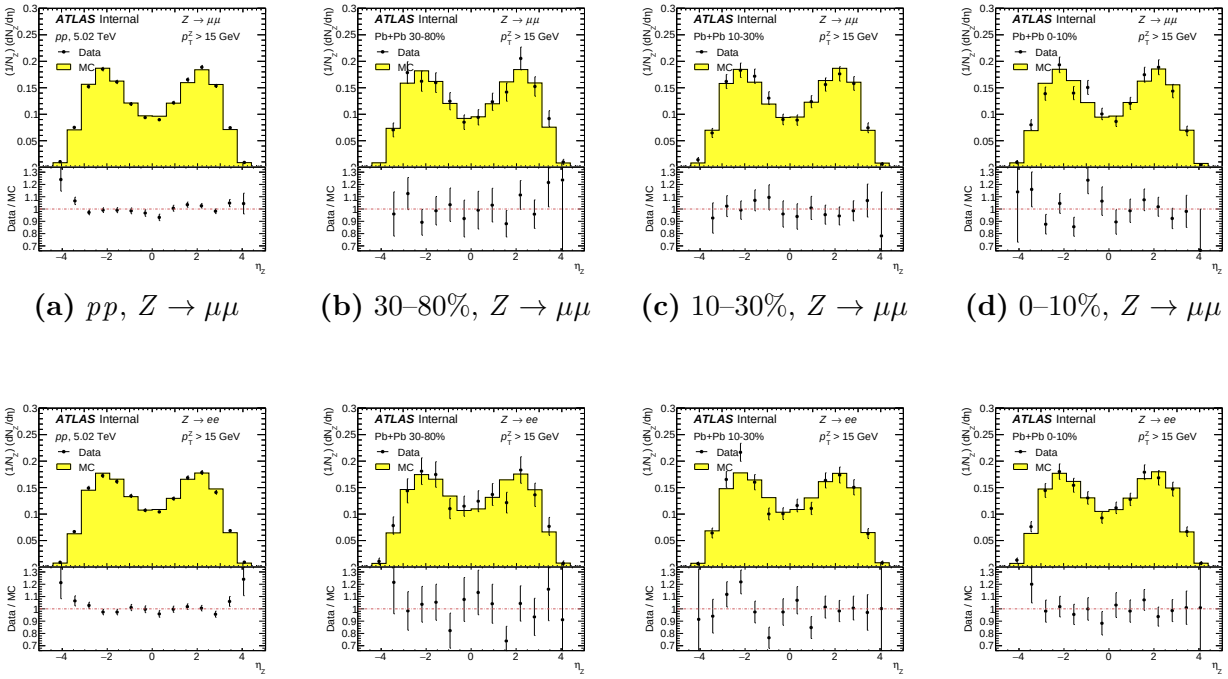


(a) pp, $Z \to \mu\mu$ **(b)** 30–80%, $Z \to \mu\mu$ **(c)** 10–30%, $Z \to \mu\mu$ **(d)** 0–10%, $Z \to \mu\mu$



(e) pp, $Z \to ee$ **(f)** 30–80%, $Z \to ee$ **(g)** 10–30%, $Z \to ee$ **(h)** 0–10%, $Z \to ee$

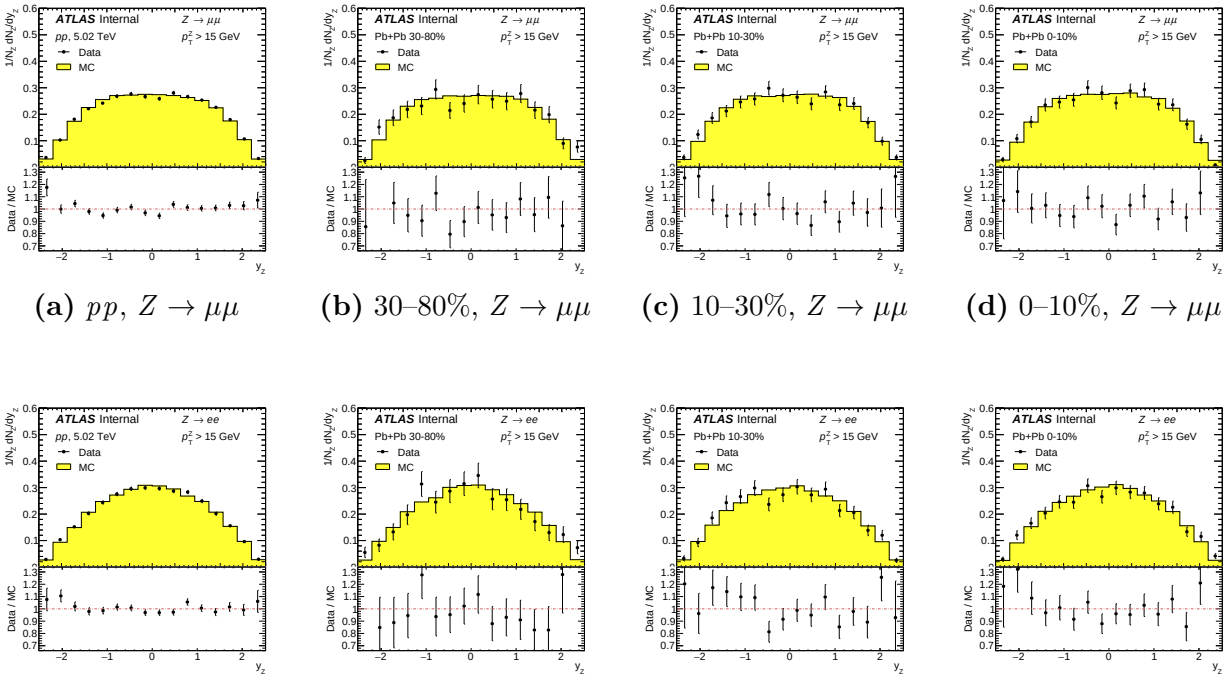
Figure A.6: 2D heatmaps of reconstructed Z boson azimuthal angles and rapidities (ϕ_Z and y_Z) are shown for **(a,e)** pp, **(b,f)** 30–80%, **(c,g)** 10–30%, and **(d,h)** 0–10% Pb+Pb collisions in both the $Z \to \mu\mu$ **(a–d)** and $Z \to ee$ **(e–h)** decay channels. The invariant p_{T} is at least 15 GeV.



(a) pp, $Z \to \mu\mu$ **(b)** 30–80%, $Z \to \mu\mu$ **(c)** 10–30%, $Z \to \mu\mu$ **(d)** 0–10%, $Z \to \mu\mu$

(e) pp, $Z \to ee$ **(f)** 30–80%, $Z \to ee$ **(g)** 10–30%, $Z \to ee$ **(h)** 0–10%, $Z \to ee$

Figure A.7: Normalized distributions of reconstructed Z boson pseudorapidities (η_Z) are shown for **(a,e)** pp, **(b,f)** 30–80%, **(c,g)** 10–30%, and **(d,h)** 0–10% Pb+Pb collisions in both the $Z \to \mu\mu$ **(a–d)** and $Z \to ee$ **(e–h)** decay channels. The invariant p_{T} is at least 15 GeV.



(a) pp, $Z \to \mu\mu$ **(b)** 30–80%, $Z \to \mu\mu$ **(c)** 10–30%, $Z \to \mu\mu$ **(d)** 0–10%, $Z \to \mu\mu$

(e) pp, $Z \to ee$ **(f)** 30–80%, $Z \to ee$ **(g)** 10–30%, $Z \to ee$ **(h)** 0–10%, $Z \to ee$

Figure A.8: Normalized distributions of reconstructed Z boson rapidities (y_Z) are shown for **(a,e)** pp, **(b,f)** 30–80%, **(c,g)** 10–30%, and **(d,h)** 0–10% Pb+Pb collisions in both the $Z \to \mu\mu$ **(a–d)** and $Z \to ee$ **(e–h)** decay channels. The invariant p_{T} is at least 15 GeV.

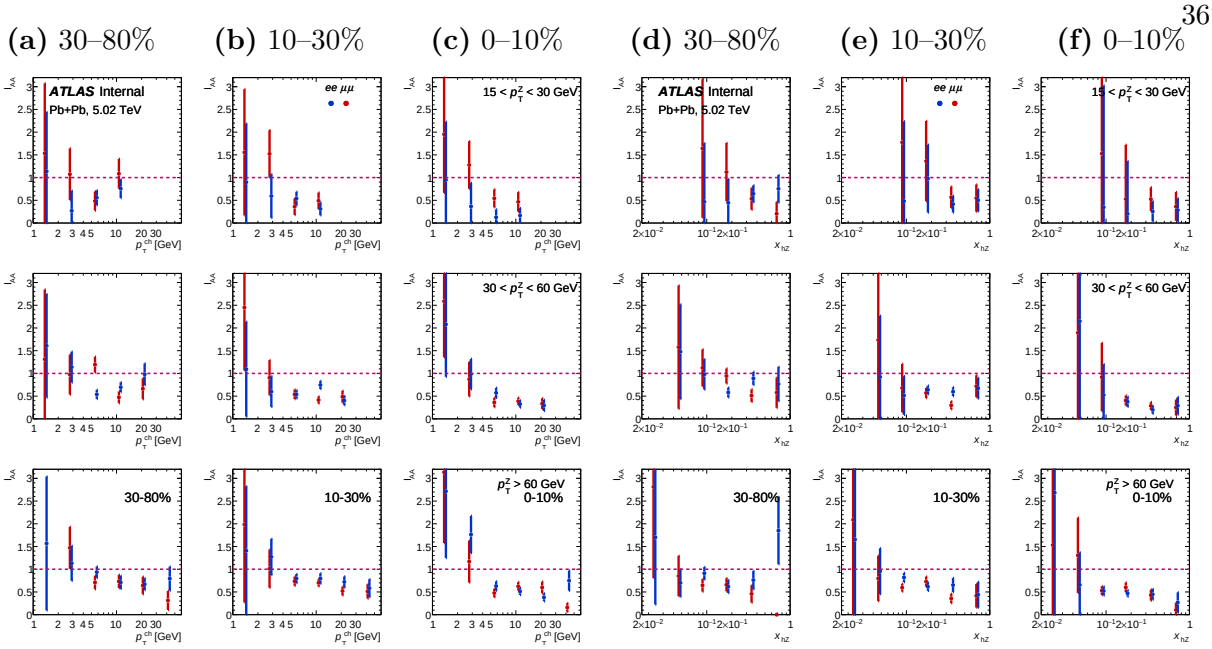


Figure A.9: I_{AA} is shown for events in each Z boson decay channel, as a function of $p_{\mathrm{T}}^{\mathrm{ch}}$ (**(a–c)**) and x_{hZ} (**(d-f)**), for each Z boson selection (top to bottom, $15 < p_{\mathrm{T}}^{Z} < 30$ GeV to $p_{\mathrm{T}}^{Z} > 60$ GeV) and centrality selection (left to right, **(a,d)** 30–80% to **(c,f)** 0–10%). The $Z \to \mu\mu$ channel is shown in red and the $Z \to ee$ channel is shown in blue.

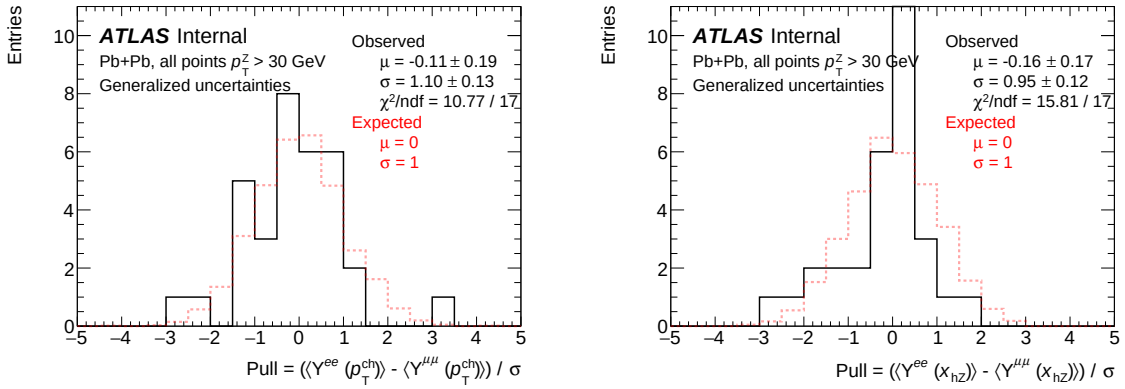
A.2 Channel Dependence Checks

As an internal cross-check on the results, potential Z decay channel dependence of the yield measurement was investigated. This was done by performing the analysis separately for each channel and comparing the I_{AA} ratios, as in Fig. A.9. To quantitatively assess potential differences, we define a statistical pull metric between the data sets,

$$\mathrm{Pull} = \frac{Y_{Z\to ee} - Y_{Z\to\mu\mu}}{\sqrt{\sigma^2_{Z\to ee} + \sigma^2_{Z\to\mu\mu}}}. \tag{A.1}$$

Because the event samples are independent, we expect the pull to be normally distributed, $\mathrm{Pull} \sim \mathcal{N}(0,1)$. This can be examined empirically by combining the yield measurement over all the reported bins. In the case of a systematic difference between the channels, we expect the *mean* parameter to differ from 0; in the case of invalid statistical uncertainties, we expect the *width* parameter to differ from 1.

First we look at the how the main results differ between the two channels. A direct comparison



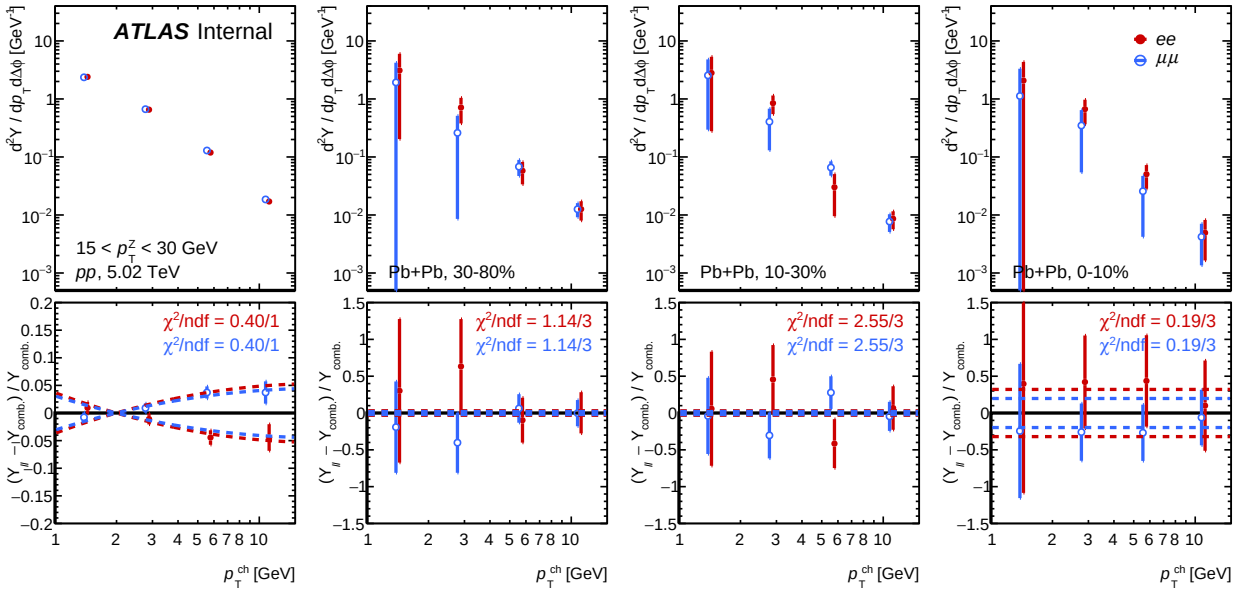
(a) Pull of $p_{\mathrm{T}}^{\mathrm{ch}}$ points **(b)** Pull of x_{hZ} points

Figure A.10: Distribution of pull values in Pb+Pb data. The yield measurement is performed in bin of **(a)** $p_{\mathrm{T}}^{\mathrm{ch}}$ and **(b)** x_{hZ}. The black histogram shows the observed pull distribution with the width quoted in the label, while the red histogram is the expectation from a normal distribution (width = 1). The quoted μ, σ values are determined from a log-likelihood fit to a Gaussian.

is shown in Fig. A.9: the $Z \to ee$ channel is shown in blue and the $Z \to \mu\mu$ channel in red. In the lower two rows, corresponding to events with $p_{\mathrm{T}}^{Z} > 30$ GeV, no substantial difference is observed between the channels. Though in the 15–30 GeV bins – shown in the top row – there is evidence for channel dependence to the main result which must be separately addressed. Therefore in quantifying the pull, all of the bins with $ptz > 30$ GeV are directly combined to make a distribution of pull values.

We see the distribution of pulls in Fig. A.10. The left panel shows the pulls where the measurement is binned in $p_{\mathrm{T}}^{\mathrm{ch}}$; the right panel shows the pulls binned in x_{hZ}. In each case the distribution visibly resembles a Gaussian, as expected. Compatibility with a Gaussian shape is directly evaluated by performing a log-likelihood fit to a normal distribution shape. The parameters μ and σ are reported on each panel, along with their uncertainties. In each case, the χ^2/ndf is modest, indicating the fit is appropriate. In each case, μ and σ are consistent with their expected values, further indicating that there is no systematic, channel-dependent bias in these bins that can be detected within the uncertainties, and that the statistical uncertainties are properly accounted for.

Now we turn to the difference observed in the 15–30 GeV bin. This could be caused by a few



(a) pp **(b)** 30–80% Pb+Pb **(c)** 10–30% Pb+Pb **(d)** 0–10% Pb+Pb

Figure A.11: Top row: the per-Z yield of hadrons is shown for $Z \to ee$ and $Z \to \mu\mu$ events separately, ranging from **(a)** pp to **(d)** 0–10% central Pb+Pb. Z bosons all have $p_{\mathrm{T}}^{Z} = 15$–30 GeV. Bottom row: the difference between the muon and electron channels is taken and scaled down by their sum. In pp, this quantity is fitted to a quadratic function. In Pb+Pb, a flat line is used instead. Each fit (dashed curves) is symmetrized around 0.

issues, such as sensitivity to the lepton energy scale or fluctuations in the UE background, as the lowest p_{T}^{Z} events have the smallest signal-to-background ratios. The root cause of this difference is not understood, however as a stop-gap measure, an additional systematic for this p_{T}^{Z} range must be assigned to account for this bias. We note that no substantial difference is observed as a function of x_{hZ} and therefore no systematic is assigned for those distributions.

In Fig. A.11, the procedure for evaluating this systematic is illustrated. The yields measured in the electron and muon channels are compared by calculating their difference to the combined channel in the bottom panels of each figure. However as the statistical uncertainty generally increases at low $p_{\mathrm{T}}^{\mathrm{ch}}$, fluctuations in the difference become large in this regime. So the difference must be scaled down by the average yield. In pp, fluctuations can be smoothed by performing a quadratic fit, however a conservative systematic uncertainty is assigned by taking half of the maximum difference between the electron and muon channels. In Pb+Pb, the uncertainty can

come from different or additional sources, and the uncertainties are larger, so a constant fit is used in Fig. A.11. Treating the points in the bottom panels as the maximum possible variation on the nominal measurement (a worst case uncertainty would be due to sampling all Z bosons in one decay channel) implies that the relative uncertainty can be treating the bottom panels as the extrema for a uniform distribution. The variance of this distribution is its width divided by $\sqrt{12}$, so the relative uncertainty assigned is taken from a fit to the relative electron-muon difference, divided by this numerical factor.

A.3 Monte Carlo Closure Studies

It is important to further demonstrate that, when the analysis procedure is performed on simulated events from Monte Carlo, the distributions with reconstructed charged particles capture the distributions at the generator or truth level. This test is an important check against the accuracy of the analysis procedure. If the truth-level distributions are recovered with reconstructed-level objects, then the analysis is said to achieve *closure*. Significant deviations away from the truth-level distribution signify *non-closure* and can represent unaccounted-for sources of systematic uncertainty or potential bias.

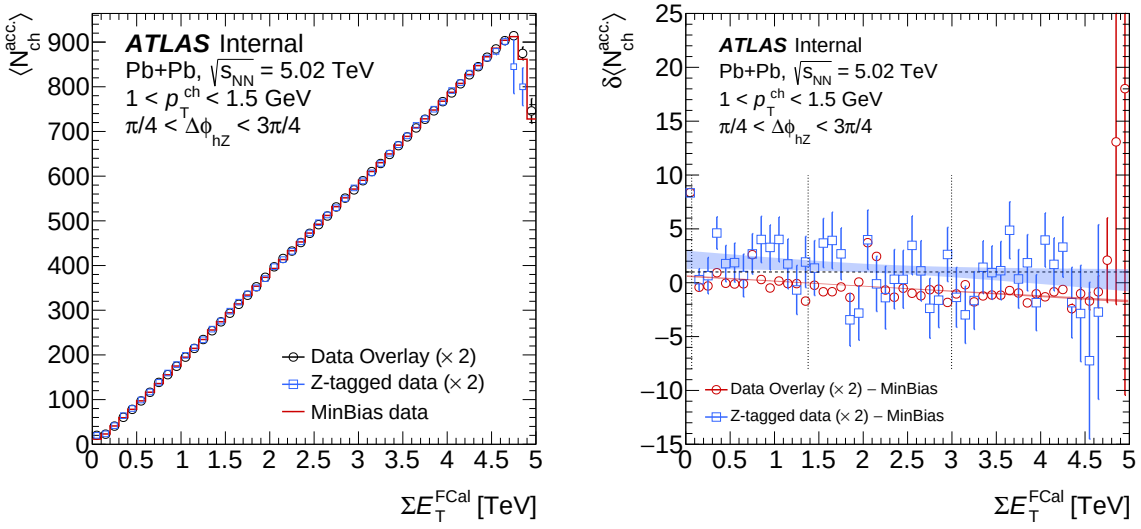
In this section we detail the MC closure studies. Like in the data, a particular definition of the signal component and the background must be adopted to demonstrate that the true signal is recovered. The specific definition does not need to *exactly* match that in data, but the signal-to-background ratios should at least be comparable. For the closure studies here, we define the signal component as the per-Z yield of charged hadrons in the main Powheg + Pythia event. This is the most convenient choice as the generator-level yield distributions can be readily accessed. Consequently, this means no background subtraction is necessary in the closure study for the pp measurement, because there is no background event overlaid. This is reasonable as the S/B in pp data is already very high anyways. For the Pb+Pb, the S/B deteriorates, so the Pb+Pb UE component must be accounted for. In fact due to the low S/B values of 10^{-3}–10^{-2}, the closure must be evaluated very carefully.

In Pb+Pb, nominally the closure study would be performed with the data overlay MC samples mixed with minimum bias (MB) data. Since the data overlay component to the MC events really is taken from MB data, this procedure really should work. However, an unfortunate sequence of technical issues with the overlay procedure required modifications to the mixing procedure. First, a slight tracking inefficiency was observed to be induced by the overlay. Essentially, we found that the UE is very slightly lower in the data overlay MC as compared to pure MB events. This is observed in the plots in Fig. A.12. The left panel shows the average total number of tracks

in a specific acceptance that is chosen to enhance the UE. These tracks must have a relatively low p_{T} in the range 1–1.5 GeV and, in simulated Z events, be azimuthal perpendicular to the Z $\pi/4 < |\Delta\phi_{hZ}| < 3\pi/4$ to minimize contributions from the away-side jet peak (the yield in these events is scaled up by 2 to account for the lost phase space). In all samples used, this multiplicity is strongly correlated with $\Sigma E_{\mathrm{T}}^{\mathrm{FCal}}$, which is expected and well-understood to represent an autocorrelation stemming from the larger UE in more central collisions. In the right panel of Fig. A.12, the differences between each set of points are shown. Particularly, the MC with data overlay is found to have fewer tracks on average per-event than MB data, even though the data overlay events are drawn from, essentially, the same MB event sample. This can be seen in the right panel, which shows the difference. This issue is technical in nature and is likely tied to the use of a dynamic detector alignment in the G4 simulation, although no fix is known. The interpretation is that the tracking efficiency is ever-so-slightly lower in data overlay MC samples than it is in real data. In the data, we correct by the tracking efficiency derived in the MC with data overlay, which we just argued does not completely describe the data. But, this does not pose a significant issue because the slight difference cancels in the background subtraction. It is only problematic in the MC closusre study, as when MC data overlay events are mixed with MB data, this effect does *not* cancel. Instead, it becomes amplified by the low S/B ratio.

We note that this is an effect unique to the data overlay samples. Therefore it can be avoided by simulating the Pb+Pb environment instead with a pure MC approach via Hijing event generation. Z bosons generated in Powheg + Pythia, as described in Sec. 4.2, were embedded in the Hijing backgrounds during the reconstruction procedure, similar to the data overlay. The set of Hijing events was also reconstructed in parallel with no Z embedding and used as a sample of MB events to test the event mixing. To enhance sampling of the most central events, additional, similarly configured samples of Hijing with a semicentral (SC) event filter were also used: these events require a central impact parameter $b < 7\,\mathrm{fm}$.

Despite this strategy, a separate issue pertaining to the $\Sigma E_{\mathrm{T}}^{\mathrm{FCal}}$ modeling was identified with these samples. In Pb+Pb collisions, the FCal energy strongly correlates with overall event



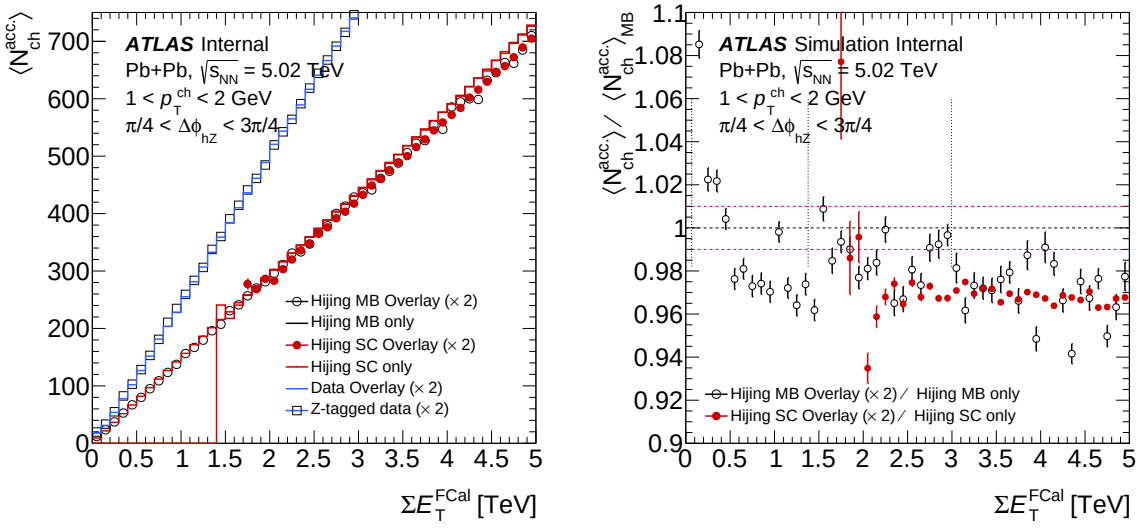
(a) $\langle N_{\mathrm{ch}}^{\mathrm{acc.}} \rangle$ **(b)** $\delta \langle N_{\mathrm{ch}}^{\mathrm{acc.}} \rangle$

Figure A.12: (a) The average number of charged particles in the acceptance – $1 < p_{\mathrm{T}}^{\mathrm{ch}} < 1.5$ GeV and $\pi/4 < |\Delta\phi| < 3\pi/4$ (only for MC and Z-tagged data) – is plotted as a function of $\Sigma E_{\mathrm{T}}^{\mathrm{FCal}}$ in MC with MB data overlay (black open circles), Z-tagged data events (blue open squares), and MB data events (red line). The y-axis is scaled up by a factor of 2 to account for this phase space factor. **(b)** The difference in MC events with data overlay (red circles) and Z-tagged data (blue squares) is taken with respect to MB data events as a function of $\Sigma E_{\mathrm{T}}^{\mathrm{FCal}}$. The differences are fitted to linear functions; 68% confidence intervals on these fits are shown in the shaded regions for Z-tagged data (blue) and MC overlay (red).

activity, such as the number of charged particles $N_{\mathrm{ch}}^{\mathrm{rec}}$. However it is observed that the signal and background samples exhibit different correlations between $\Sigma E_{\mathrm{T}}^{\mathrm{FCal}}$ and $N_{\mathrm{ch}}^{\mathrm{rec}}$. This was noticed in the plots shown in Fig. A.13. To focus on the UE behavior, the average charged-particle yield in a similarly specific acceptance $N_{\mathrm{ch}}^{\mathrm{acc.}}$ was studied instead of total multiplicity. Some known effects are readily apparent here. For example, version 1.383 of HIJING – the version interfaced with the ATLAS software – is already known to overpredict energy deposition at forward rapidities, so at a fixed $\langle N_{\mathrm{ch}}^{\mathrm{acc.}} \rangle$ value, the $\Sigma E_{\mathrm{T}}^{\mathrm{FCal}}$ tends to be overpredicted in HIJING as compared to data [339]. We see this directly in the left panel of Fig. A.13.[1]

When a Z event is embedded in the HIJING event, there can be a different number of accepted particles; however this difference should be, on average, centrality independent, because the two

[1] Although as shown in the right panel, this version of HIJING underpredicts the total particle production in each centrality class when compared with data. This could be due to the particular charged-particle acceptance used.

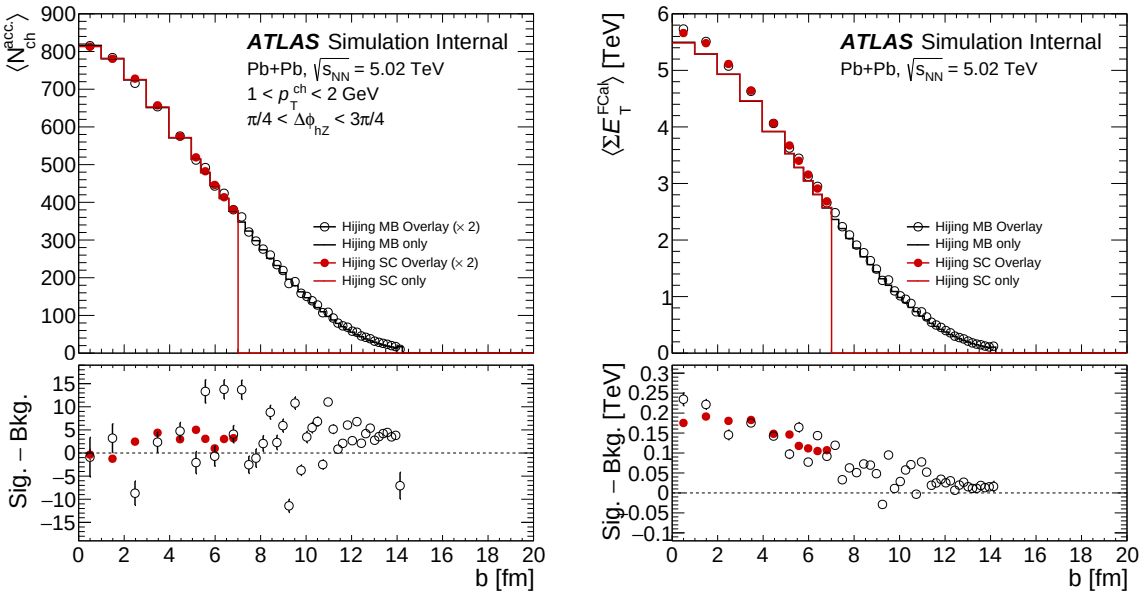


(a) $\langle N_{\mathrm{ch}}^{\mathrm{acc.}} \rangle$ **(b)** $\langle N_{\mathrm{ch}}^{\mathrm{acc.}} \rangle / \langle N_{\mathrm{ch}}^{\mathrm{acc.}} \rangle_{\mathrm{MB}}$

Figure A.13: (a) The average number of charged particles in the acceptance – $1 < p_{\mathrm{T}}^{\mathrm{ch}} < 2$ GeV and $\pi/4 < |\Delta\phi| < 3\pi/4$ (only for Z-tagged event) – is plotted as a function of $\Sigma E_{\mathrm{T}}^{\mathrm{FCal}}$ in MB Hijing MC (black line), SC Hijing (red line), MB Hijing with Z embedding (black open circles), SC Hijing with Z embedding (red solid circles), Z-tagged data events (black open squares), and data overlay samples (blue line). For events with a Z, the y-axis is scaled up by a factor of 2 to account for the reduced phase space. **(b)** The ratio in events with Z embedding is taken with respect to the corresponding background-only events as a function of $\Sigma E_{\mathrm{T}}^{\mathrm{FCal}}$. SC samples are shown in red solid circles, MB samples are in black open circles.

events do not know about each other. But, this is not what is observed. Instead we find that there are more particles in the non-overlay Hijing in a centrality-dependent manner, as shown by the approximately constant ratio ~ 0.97 plotted in the center panel. This effect is consistent between both the MB and SC Hijing events, so it is not specific to either sample.

To understand whether the issue can be linked to either the FCal simulation or another tracking inefficiency, both the average $N_{\mathrm{ch}}^{\mathrm{rec}}$ and $\Sigma E_{\mathrm{T}}^{\mathrm{FCal}}$ were further studied as a function of the truth Pb+Pb impact parameter, b. The advantage is that the impact parameter is certainly completely decoupled from the overlay procedure, so the separate overlay-induced effects on $\langle N_{\mathrm{ch}}^{\mathrm{acc.}} \rangle$ and $\left\langle \Sigma E_{\mathrm{T}}^{\mathrm{FCal}} \right\rangle$ should be illuminated by this check. How these variables evolve with b is examined in Fig. A.14. While the overlay samples possess a few more tracks on average than the background samples, and this difference is essentially independent of b. This is expected provided that the hard



(a) $\langle N_{\mathrm{ch}}^{\mathrm{rec}} \rangle$ **(b)** $\left\langle \Sigma E_{\mathrm{T}}^{\mathrm{FCal}} \right\rangle$

Figure A.14: **(a)** The average number of charged particles in the acceptance ($1 < p_{\mathrm{T}}^{\mathrm{ch}} < 2$ GeV and $\pi/4 < |\Delta\phi| < 3\pi/4$ for the overlay samples) and **(b)** average $\Sigma E_{\mathrm{T}}^{\mathrm{FCal}}$ are plotted as a function of impact parameter b in MB Hijing MC (black lines), SC Hijing (red lines), MB Hijing with Z embedding (black open circles), and SC Hijing with Z embedding (red solid circles). For events with a Z, the y-axis is scaled up by a factor of 2 to account for the reduced phase space. Bins along the x-axis are roughly 2% wide in impact parameter percentiles. The bottom panels show the difference of (points) − (lines) of the same color; e.g. Hijing MB Overlay − Hijing MB only.

scattering and underlying events evolve completely independently. However, the amount of extra energy in the FCal is clearly dependent on b, reaching ~ 200 GeV on average in the most central events. This indicates something is different about the FCal simulation between the overlay versus non-overlay samples, and therefore $\Sigma E_{\mathrm{T}}^{\mathrm{FCal}}$ cannot be used as a proxy for centrality in Hijing. Crucially, the mixed event procedure cannot use $\Sigma E_{\mathrm{T}}^{\mathrm{FCal}}$ to match event centralities, otherwise there would be a significant bias in the UE model.

Instead, impact parameter itself is used to define centrality for the closure study. As a reminder, these centrality categories were previously defined in Sec. 4.2. (An example impact parameter distribution from minimum bias Hijing events can be seen in Fig. 4.4, with a few centrality percentiles overlaid.) In general, centrality is defined similarly to in Sec. 4.2, but the procedure is quickly summarized here. Cuts for each centrality class are derived from Glauber

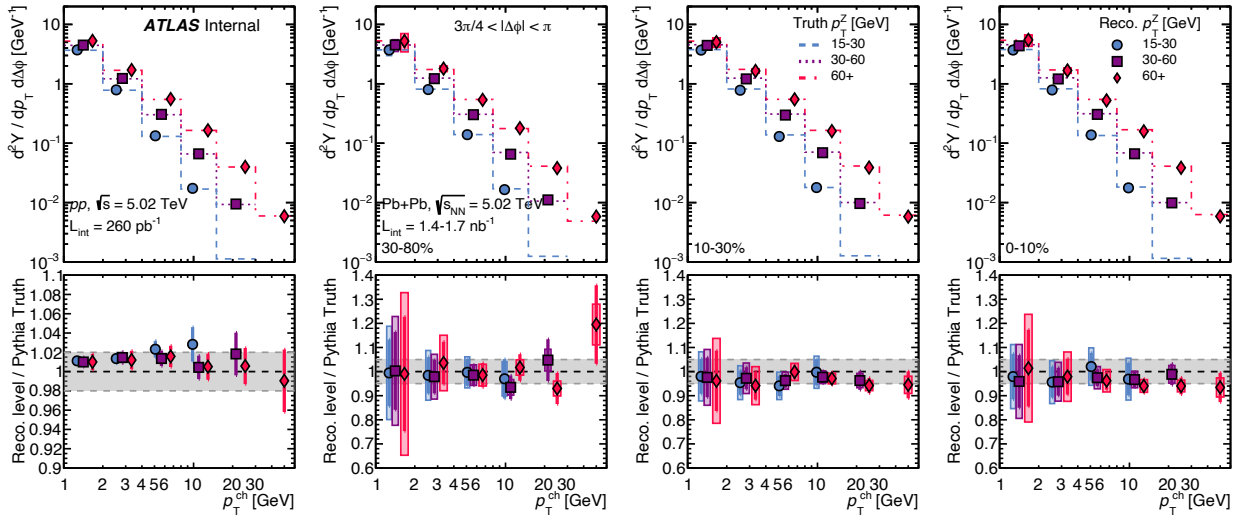
modeling, as is done with centrality determination in data [285]. Briefly, these cuts were found to be

- $b = 0 - 4.952\,\text{fm}$ for 0–10%
- $b = 4.952 - 8.582\,\text{fm}$ for 10–30%
- $b = 8.582 - 14.031\,\text{fm}$ for 30–80%.

Despite this change in centrality class definitions, the final uncertainty associated with the non-closure will be demonstrated to be insensitive to this centrality categorization.

Equipped with this new centrality definition, an initial closure check of the tracking corrections was performed using an "exact-event matching" method. This procedure exploits the fact that the underlying HIJING truth events are identical in both the Z overlay and background samples. I.e., each Z-containing event can be uniquely matched to a particular background event at the truth level. This directly avoids any potential complications with the event mixing procedure done in data. Thus, any non-closure tied to the tracking efficiency, purity, etc. can be identified. After performing this exact-event matching procedure, the per-Z normalized yields were compared to their truth-level quantities. The resultant distributions are shown in Figs. A.15 for each centrality, and pp as a comparison. The bottom panels of each figure show the reco.-level/truth-level ratio, which is colloquially referred to as the closure. In general, closure within 2% is observed in pp and 5% in Pb+Pb (up to statistical variations). For pp, a conservative systematic uncertainty of 2% (independent the x-axis variable) is assigned to account for this non-closure, although it is subdominant to other sources anyways.

We then proceed to understand how well the mixed event procedure models the UE by mixing the overlay and background events. In addition to the different centrality metric, a few minor modifications to the mixing procedure are made. First, to reduce the number of events generated, the uniqueness of the event matching was relaxed. This means background events could be reused in the mixing; though in general a different ϕ_Z would allow a different set of particles to enter the acceptance. This comes with the caveat that no two events could be matched more

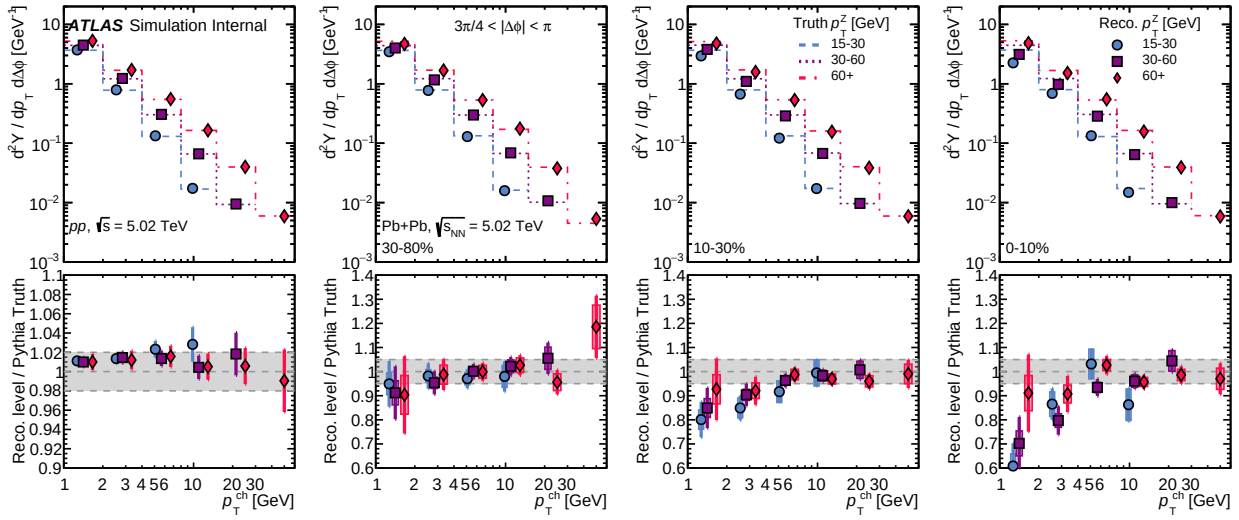


(a) pp **(b)** 30–80% Pb+Pb **(c)** 10–30% Pb+Pb **(d)** 0–10% Pb+Pb

Figure A.15: The reconstructed-level and truth-level yields of charged particles as a function of $p_{\mathrm{T}}^{\mathrm{ch}}$ is shown for **(a)** pp through **(d)** 0–10% central Pb+Pb. An exact-event matching is used to generate the UE model in Pb+Pb. No UE is subtracted in pp. Different colors refer to different p_{T}^{Z} selections. Systematic uncertainties, shown as boxes, represent solely the statistical uncertainty on the UE measurement. In the bottom panels, the reco./truth ratio (referred to as the closure) is shown. In pp (Pb+Pb), the shaded region corresponds to ±2% (±5%).

than once. Next, all Z events were mixed 10 times instead of the 160/80/40 used in data, for the same reason. This helped reduce potential biases related to the UE model while keeping the related statistical uncertainty low. Lastly, an event plane matching was similarly performed by cutting on the $\Delta\Psi_2$ value, but because the $\Sigma E_{\mathrm{T}}^{\mathrm{FCal}}$ quantity could not be trusted, the truth-level event plane was used instead. This variable is solely a property of the background event similar to the impact parameter, and is therefore completely independent of the overlay procedure.

With this mixed event prescription, the results of the mixed-event closure test can be seen in Fig. A.16. (Note that the leftmost column (pp) is the same as in the exact-event matching Fig. A.15 since no subtraction is applied here.) There is a considerable amount of non-closure (up to $\sim 30\%$) at low $p_{\mathrm{T}}^{\mathrm{ch}}$ and in central Pb+Pb, while high $p_{\mathrm{T}}^{\mathrm{ch}}$/ peripheral Pb+Pb points converge onto unity as previously seen. Because (1) the exact-event matching worked much better, and (2) the closure is worst in bins known to have a low signal-to-background ratio, this suggests that the non-closure must be related to the background normalization. In other words, there is an unaccounted for

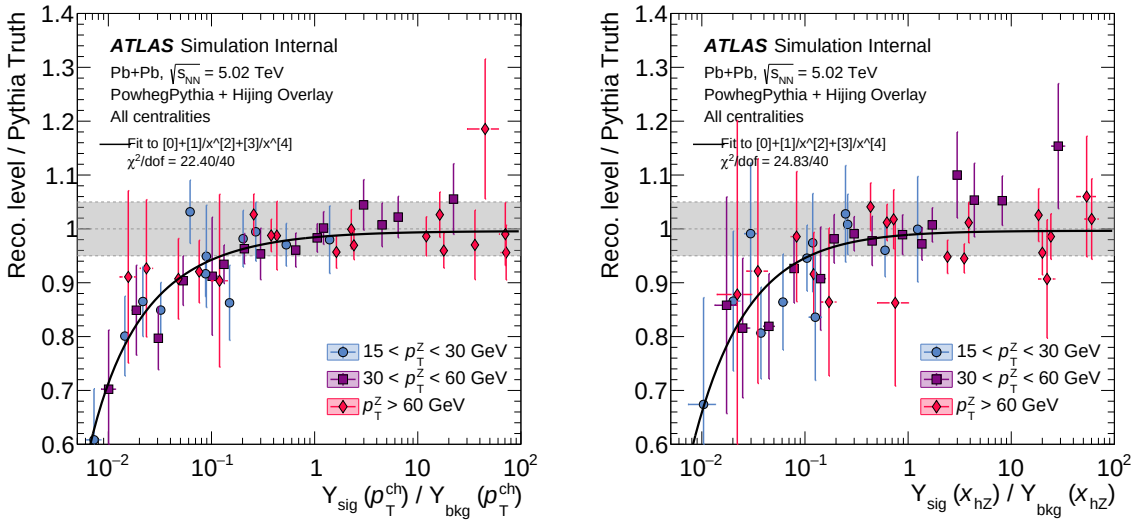


(a) pp **(b)** 30–80% Pb+Pb **(c)** 10–30% Pb+Pb **(d)** 0–10% Pb+Pb

Figure A.16: The reconstructed-level and truth-level yields of charged particles as a function of $p_{\mathrm{T}}^{\mathrm{ch}}$ is shown for **(a)** pp through **(d)** 0–10% central Pb+Pb. A mixed-event procedure is used to generate the UE model in Pb+Pb. No UE is subtracted in pp. Different colors refer to different p_{T}^{Z} selections. Systematic uncertainties, shown as boxes, represent solely the UE model statistical uncertainty. In the bottom panels, the reco./truth ratio (referred to as the closure) is shown. In pp (Pb+Pb), the shaded region corresponds to ±2% (±5%).

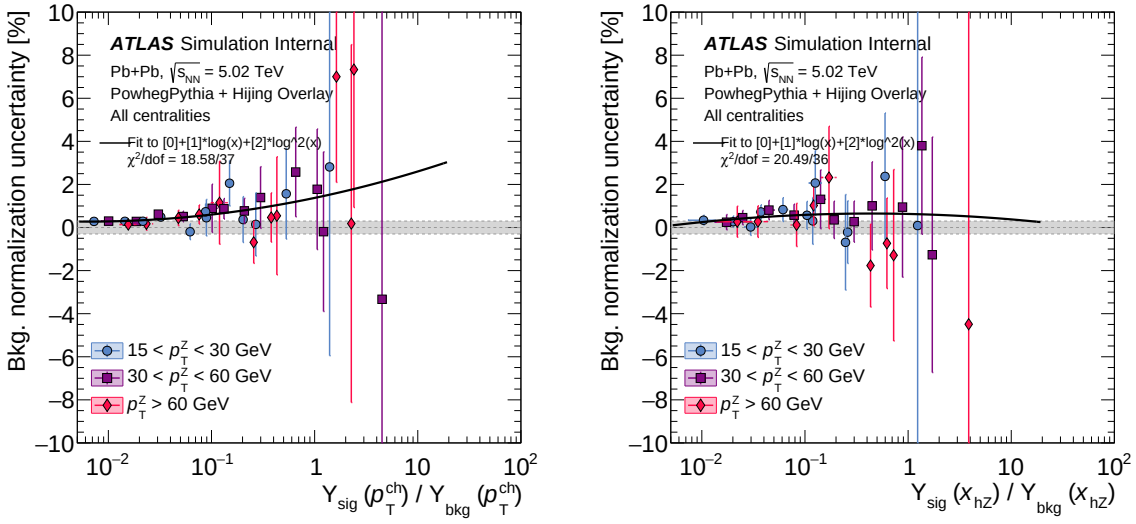
uncertainty on the UE model which is amplified by the S/B ratio in these ratios. This can be further tested by plotting the closure ratios as a function of S/B, as is done in Fig. A.17.

When the closure test is reframed this way, we find that each set of points (each centrality and p_{T}^{Z} selection) appears to align on a common curve as a function of S/B. At low S/B, the non-closure drops below 1, but asymptotes to 1 at higher S/B, with about $\sim 5\%$ of non-closure at a $S/B \sim 0.1$. Because we argue the non-closure can be interpreted as due to normalization uncertainty on the background, the percent-level uncertainty can be calculated by multiplying this 5% by $S/B \sim 0.1$. The result can be seen in Fig. A.18. To average over fluctuations, the uncertainty is fitted to a quadratic function in $\log(S/B)$. At the lowest S/B values, the uncertainty is roughly 0.3%. Previous ATLAS analyses found this uncertainty to be about 0.5%, showing a modest improvement to the UE model precision. At high S/B, the uncertainty is a bit larger, rising to $\sim 2\%$, although the actual uncertainty on the charged-hadron yield in this regime is quite small since much fewer of these particles are part of the background anyways.



(a) Versus $p_{\mathrm{T}}^{\mathrm{ch}}$ **(b)** Versus x_{hZ}

Figure A.17: The closure ratio for the HIJING mixed event procedure is shown for all Pb+Pb centralities and p_{T}^{Z} selections versus the S/B ratio for points binned in **(a)** $p_{\mathrm{T}}^{\mathrm{ch}}$ and **(b)** x_{hZ}. The shaded region represents ±5%. The points are fitted to a smooth empirical function of $\log(S/B)$ which asymptotes to 1.

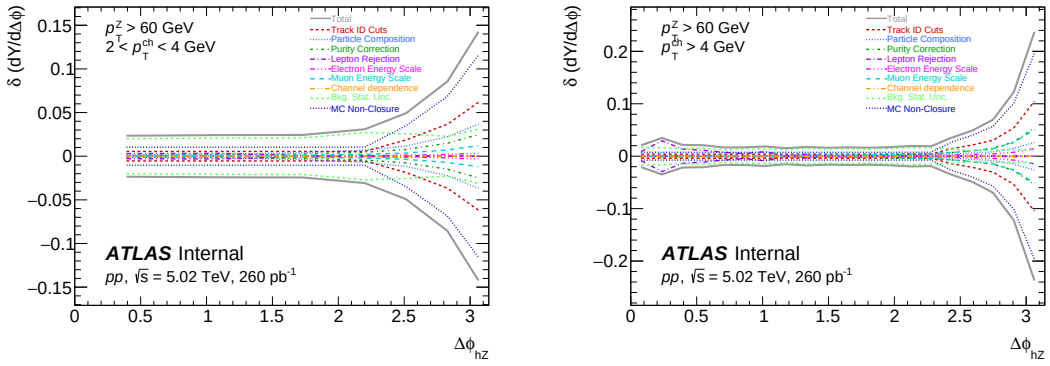


(a) Versus $p_{\mathrm{T}}^{\mathrm{ch}}$ **(b)** Versus x_{hZ}

Figure A.18: The closure ratio is interpreted as a background normalization uncertainty (in %) for the HIJING mixed event procedure by multiplying the points in Fig. A.17 by their S/B value (i.e., their x-coordinate). Points are shown for all Pb+Pb centralities and p_{T}^{Z} selections versus their S/B ratio for **(a)** $p_{\mathrm{T}}^{\mathrm{ch}}$ points and **(b)** x_{hZ}. The shaded region represents ±0.3%. The points are fitted to a smooth empirical function of $\log(S/B)$.

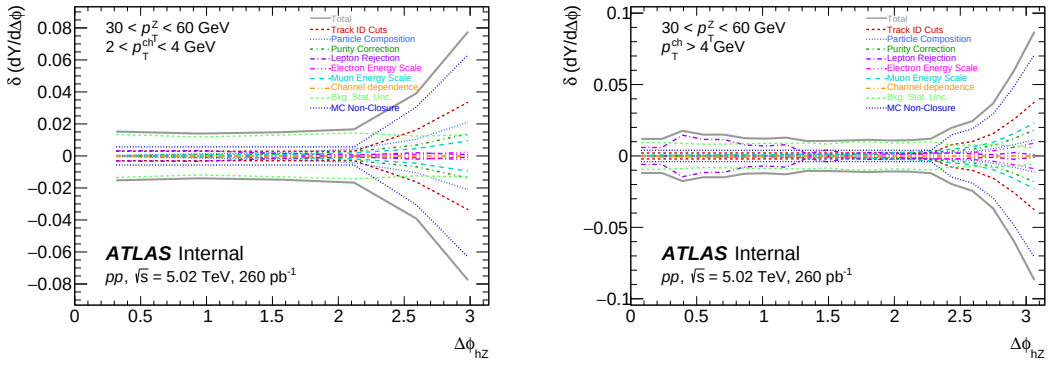
Summarizing, the pp measurement is observed to close within 2%. This remaining non-closure is assigned as systematic uncertainty in the data, though the uncertainty on the pp is subdominant on the final I_{AA} measurement. In the Pb+Pb, closure is obtained when the background can be exactly subtracted, or the S/B ratio is sufficiently high. Non-closure is observed when the background must be modeled via the mixed event, due to a previously unaccounted-for source of uncertainty on the UE background. This uncertainty is of the scale $\sim$ 0.3–2% but is amplified by the S/B ratio on the final yield measurement. Therefore in regions where the S/B is very low, the corresponding uncertainty can reach each $\sim$ 40–50%.

A.4 Decomposition of All Systematic Uncertainties



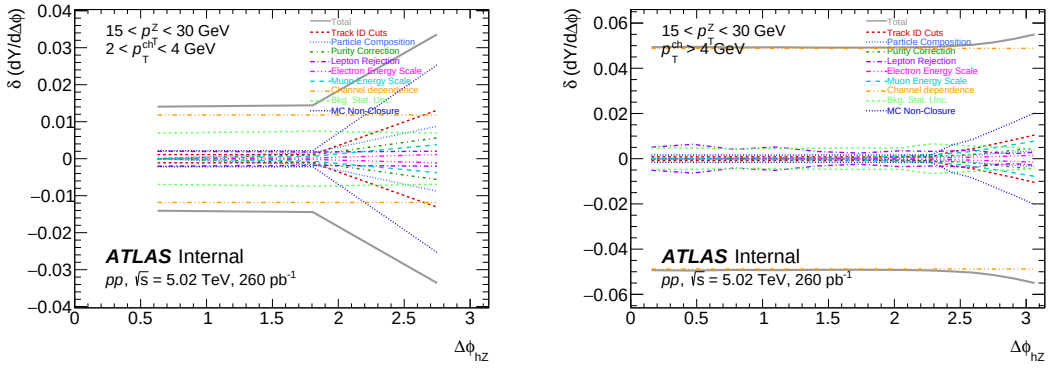
(a) $p_{\mathrm{T}}^{Z} > 60$ GeV, $p_{\mathrm{T}}^{\mathrm{ch}} = 2$–$4$ GeV

(b) $p_{\mathrm{T}}^{Z} > 60$ GeV, $p_{\mathrm{T}}^{\mathrm{ch}} > 4$ GeV



(c) $p_{\mathrm{T}}^{Z} = 30$–60 GeV, $p_{\mathrm{T}}^{\mathrm{ch}} = 2$–$4$ GeV

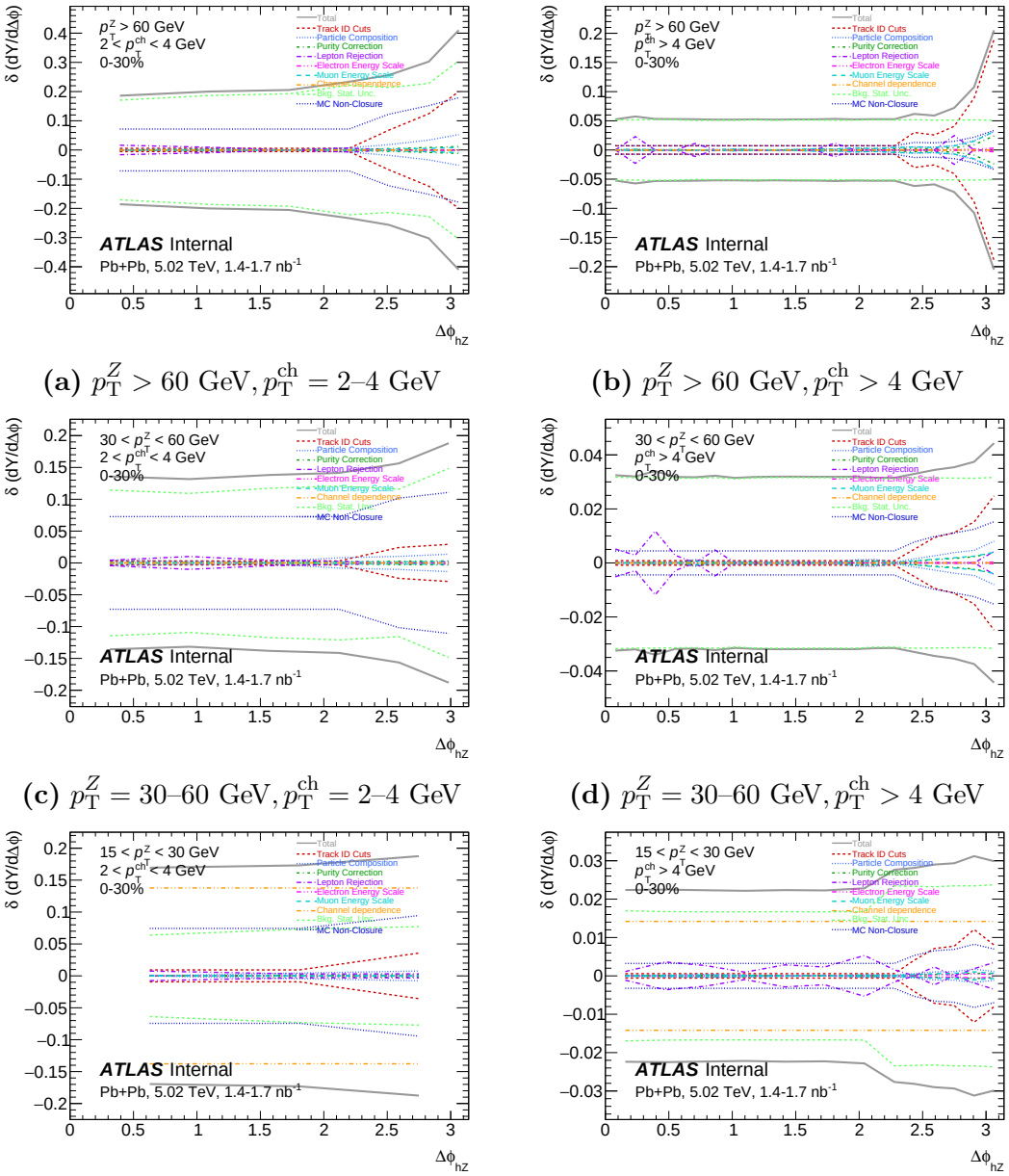
(d) $p_{\mathrm{T}}^{Z} = 30$–60 GeV, $p_{\mathrm{T}}^{\mathrm{ch}} > 4$ GeV



(e) $p_{\mathrm{T}}^{Z} = 15$–30 GeV, $p_{\mathrm{T}}^{\mathrm{ch}} = 2$–$4$ GeV

(f) $p_{\mathrm{T}}^{Z} = 15$–30 GeV, $p_{\mathrm{T}}^{\mathrm{ch}} > 4$ GeV

Figure A.19: Absolute systematic uncertainties on the UE subtracted track yield as a function of $\Delta\phi_{hZ}$ for different $p_{\mathrm{T}}^{\mathrm{ch}}$ selections: **(a,c,e)** $2 < p_{\mathrm{T}}^{\mathrm{ch}} < 4$ GeV, **(b,d,f)** $p_{\mathrm{T}}^{\mathrm{ch}} > 4$ GeV) and the 3 p_{T}^{Z} selections: **(a,b)** $p_{\mathrm{T}}^{Z} > 60$ GeV, **(c,d)** $30 < p_{\mathrm{T}}^{Z} < 60$ GeV, **(e,f)** $15 < p_{\mathrm{T}}^{Z} < 30$ GeV for pp events.



(a) $p_{\mathrm{T}}^{Z} > 60$ GeV, $p_{\mathrm{T}}^{\mathrm{ch}} = 2$–$4$ GeV

(b) $p_{\mathrm{T}}^{Z} > 60$ GeV, $p_{\mathrm{T}}^{\mathrm{ch}} > 4$ GeV

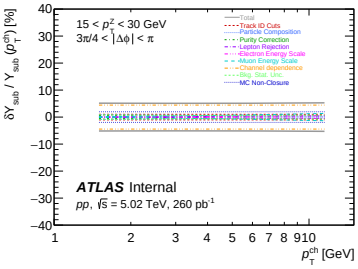
(c) $p_{\mathrm{T}}^{Z} = 30$–60 GeV, $p_{\mathrm{T}}^{\mathrm{ch}} = 2$–$4$ GeV

(d) $p_{\mathrm{T}}^{Z} = 30$–60 GeV, $p_{\mathrm{T}}^{\mathrm{ch}} > 4$ GeV

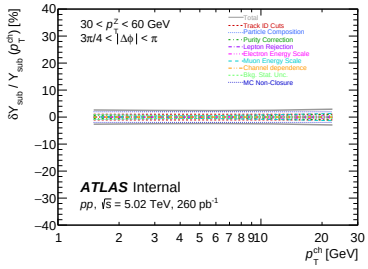
(e) $p_{\mathrm{T}}^{Z} = 15$–30 GeV, $p_{\mathrm{T}}^{\mathrm{ch}} = 2$–$4$ GeV

(f) $p_{\mathrm{T}}^{Z} = 15$–30 GeV, $p_{\mathrm{T}}^{\mathrm{ch}} > 4$ GeV

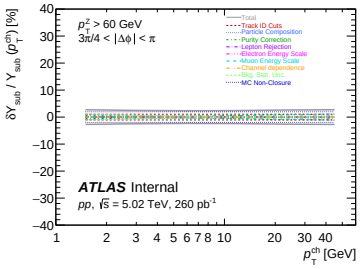
Figure A.20: Absolute systematic uncertainties on the UE subtracted track yield as a function of $\Delta\phi_{hZ}$ for different $p_{\mathrm{T}}^{\mathrm{ch}}$ selections: **(a,c,e)** $2 < p_{\mathrm{T}}^{\mathrm{ch}} < 4$ GeV, **(b,d,f)** $p_{\mathrm{T}}^{\mathrm{ch}} > 4$ GeV) and the 3 p_{T}^{Z} selections: **(a,b)** $p_{\mathrm{T}}^{Z} > 60$ GeV, **(c,d)** $30 < p_{\mathrm{T}}^{Z} < 60$ GeV, **(e,f)** $15 < p_{\mathrm{T}}^{Z} < 30$ GeV for 0–30% central Pb+Pb events.



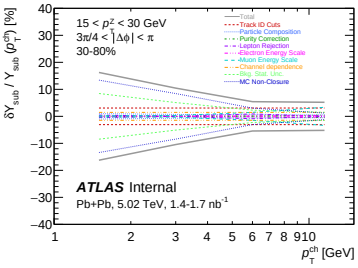
(a) pp, $p_{\mathrm{T}}^{Z} = 15$–30 GeV



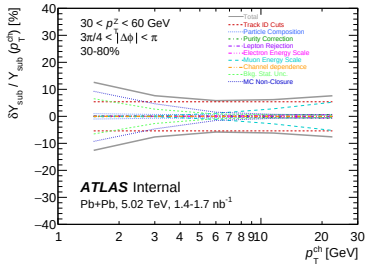
(b) pp, $p_{\mathrm{T}}^{Z} = 30$–60 GeV



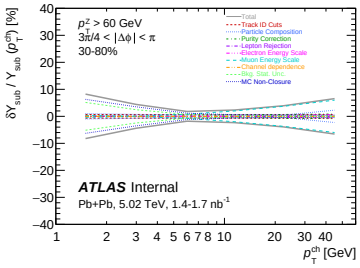
(c) pp, $p_{\mathrm{T}}^{Z} > 60$ GeV



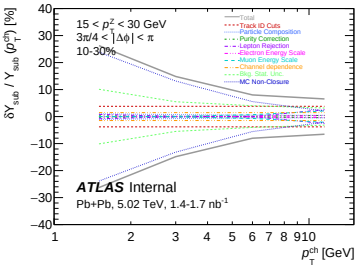
(d) 30–80%, $p_{\mathrm{T}}^{Z} = 15$–30 GeV



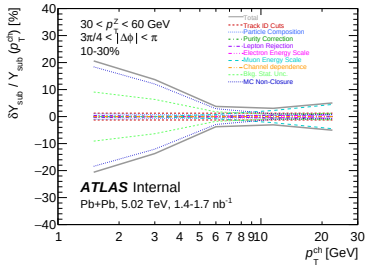
(e) 30–80%, $p_{\mathrm{T}}^{Z} = 30$–60 GeV



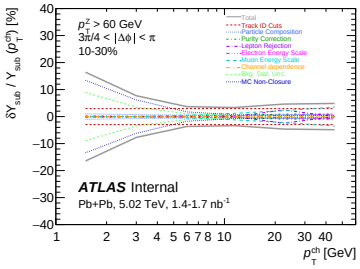
(f) 30–80%, $p_{\mathrm{T}}^{Z} > 60$ GeV



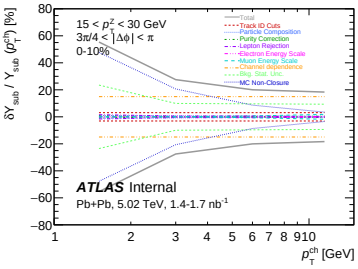
(g) 10–30%, $p_{\mathrm{T}}^{Z} = 15$–30 GeV



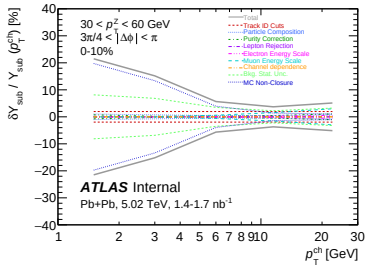
(h) 10–30%, $p_{\mathrm{T}}^{Z} = 30$–60 GeV



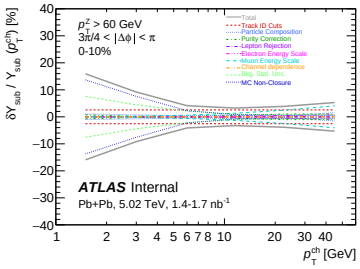
(i) 10–30%, $p_{\mathrm{T}}^{Z} > 60$ GeV



(j) 0–10%, $p_{\mathrm{T}}^{Z} = 15$–30 GeV

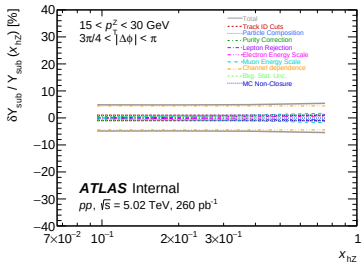


(k) 0–10%, $p_{\mathrm{T}}^{Z} = 30$–60 GeV

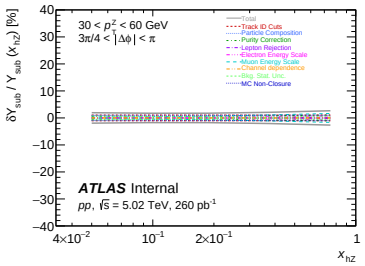


(l) 0–10%, $p_{\mathrm{T}}^{Z} > 60$ GeV

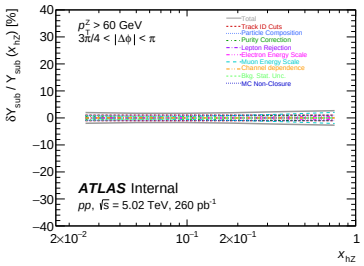
Figure A.21: Relative uncertainties on the UE subtracted track yield as a function of $p_{\mathrm{T}}^{\mathrm{ch}}$ are shown for different p_{T}^{Z} bins **(a,d,g,j)** $p_{\mathrm{T}}^{Z} = 15$–30 GeV, **(b,e,h,k)** $p_{\mathrm{T}}^{Z} = 30$–60 GeV, **(c,f,i,l)** $p_{\mathrm{T}}^{Z} > 60$ GeV) and **(a–c)** pp, **(d–f)** 30–80%, **(g–i)** 10–30%, and **(j–l)** 0–10% Pb+Pb collisions.



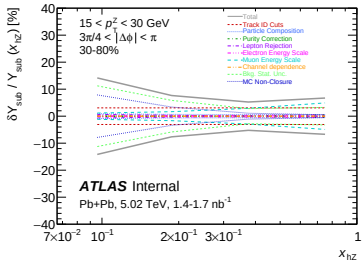
(a) pp, $p_{\mathrm{T}}^{Z} = 15$–30 GeV



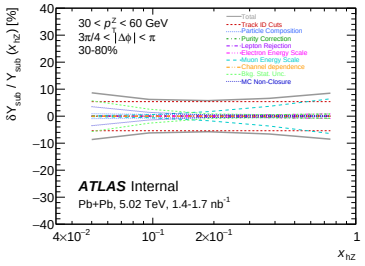
(b) pp, $p_{\mathrm{T}}^{Z} = 30$–60 GeV



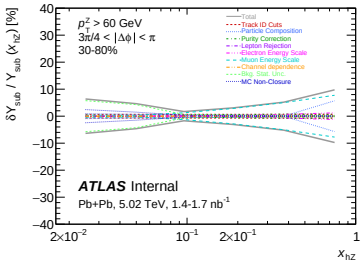
(c) pp, $p_{\mathrm{T}}^{Z} > 60$ GeV



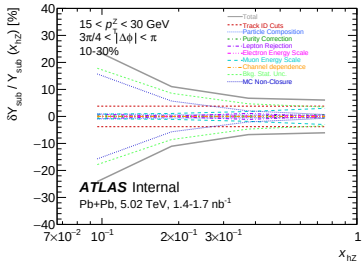
(d) 30–80%, $p_{\mathrm{T}}^{Z} = 15$–30 GeV



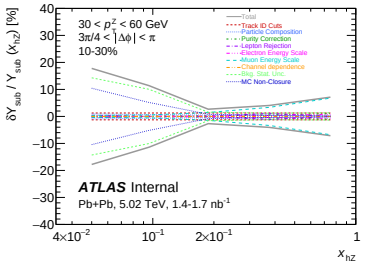
(e) 30–80%, $p_{\mathrm{T}}^{Z} = 30$–60 GeV



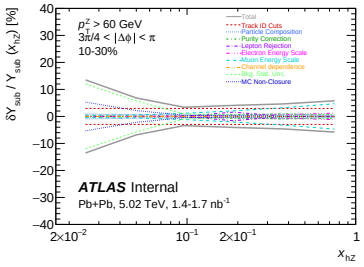
(f) 30–80%, $p_{\mathrm{T}}^{Z} > 60$ GeV



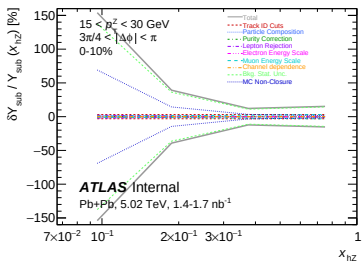
(g) 10–30%, $p_{\mathrm{T}}^{Z} = 15$–30 GeV



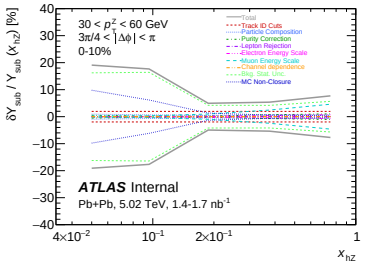
(h) 10–30%, $p_{\mathrm{T}}^{Z} = 30$–60 GeV



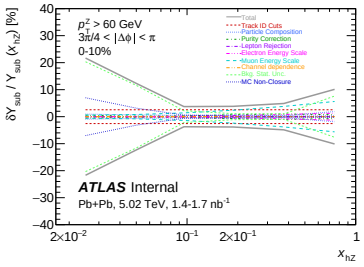
(i) 10–30%, $p_{\mathrm{T}}^{Z} > 60$ GeV



(j) 0–10%, $p_{\mathrm{T}}^{Z} = 15$–30 GeV

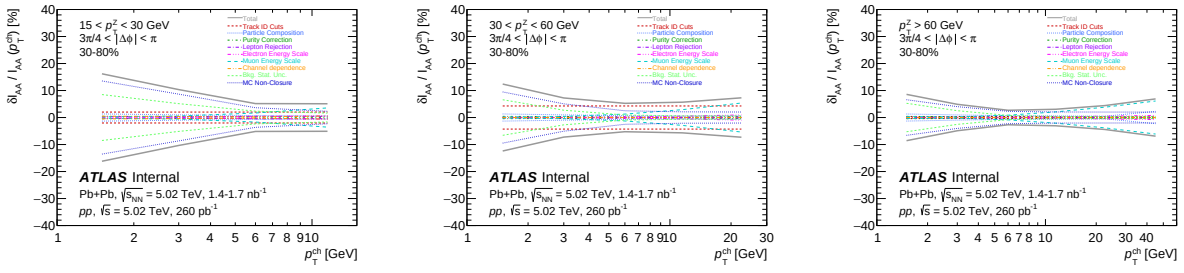


(k) 0–10%, $p_{\mathrm{T}}^{Z} = 30$–60 GeV



(l) 0–10%, $p_{\mathrm{T}}^{Z} > 60$ GeV

Figure A.22: Relative uncertainties on the UE subtracted track yield as a function of x_{hZ} are shown for different p_{T}^{Z} bins **(a,d,g,j)** p_{T}^{Z} = 15–30 GeV, **(b,e,h,k)** p_{T}^{Z} = 30–60 GeV, **(c,f,i,l)** $p_{\mathrm{T}}^{Z} > 60$ GeV) and **(a–c)** pp, **(d–f)** 30–80%, **(g–i)** 10–30%, and **(j–l)** 0–10% Pb+Pb collisions.

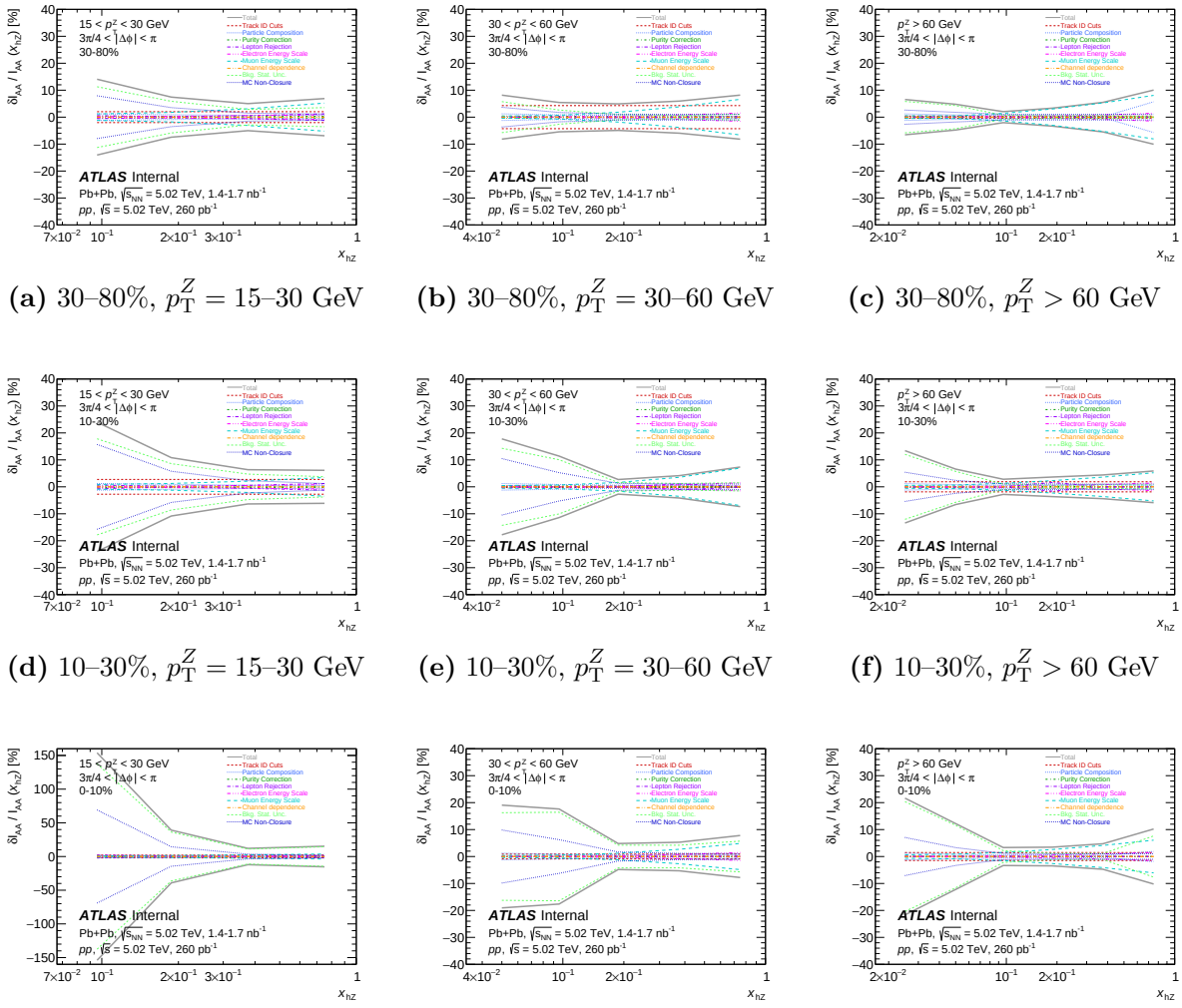


(a) 30–80%, $p_{\mathrm{T}}^{Z} = 15$–30 GeV **(b)** 30–80%, $p_{\mathrm{T}}^{Z} = 30$–60 GeV **(c)** 30–80%, $p_{\mathrm{T}}^{Z} > 60$ GeV

(d) 10–30%, $p_{\mathrm{T}}^{Z} = 15$–30 GeV **(e)** 10–30%, $p_{\mathrm{T}}^{Z} = 30$–60 GeV **(f)** 10–30%, $p_{\mathrm{T}}^{Z} > 60$ GeV

(g) 0–10%, $p_{\mathrm{T}}^{Z} = 15$–30 GeV **(h)** 0–10%, $p_{\mathrm{T}}^{Z} = 30$–60 GeV **(i)** 0–10%, $p_{\mathrm{T}}^{Z} > 60$ GeV

Figure A.23: Relative systematic uncertainties on I_{AA} as a function of $p_{\mathrm{T}}^{\mathrm{ch}}$ are shown for different p_{T}^{Z} bins **(a,d,g)** $p_{\mathrm{T}}^{Z} = 15$–30 GeV, **(b,e,h)** $p_{\mathrm{T}}^{Z} = 30$–60 GeV, **(c,f,i)** $p_{\mathrm{T}}^{Z} > 60$ GeV) and **(a–c)** 30–80%, **(d–f)** 10–30%, and **(g–i)** 0–10% Pb+Pb collisions.



(a) 30–80%, $p_{\mathrm{T}}^{Z} = 15$–30 GeV **(b)** 30–80%, $p_{\mathrm{T}}^{Z} = 30$–60 GeV **(c)** 30–80%, $p_{\mathrm{T}}^{Z} > 60$ GeV

(d) 10–30%, $p_{\mathrm{T}}^{Z} = 15$–30 GeV **(e)** 10–30%, $p_{\mathrm{T}}^{Z} = 30$–60 GeV **(f)** 10–30%, $p_{\mathrm{T}}^{Z} > 60$ GeV

(g) 0–10%, $p_{\mathrm{T}}^{Z} = 15$–30 GeV **(h)** 0–10%, $p_{\mathrm{T}}^{Z} = 30$–60 GeV **(i)** 0–10%, $p_{\mathrm{T}}^{Z} > 60$ GeV

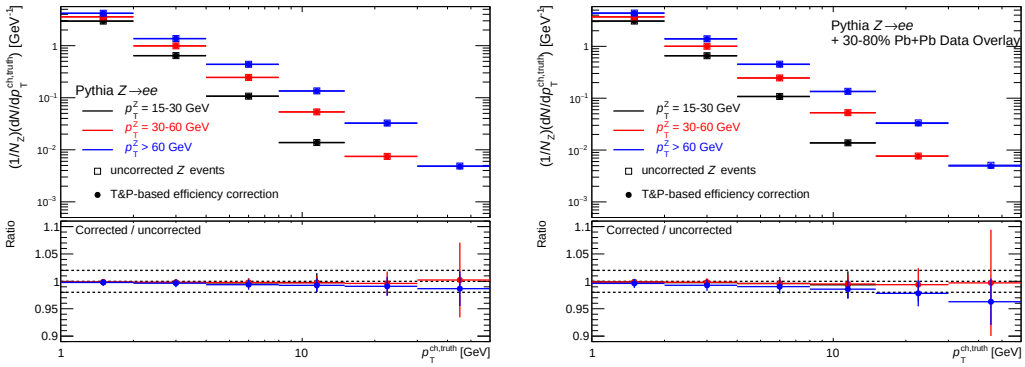
Figure A.24: Relative systematic uncertainties on I_{AA} as a function of x_{hZ} are shown for different p_{T}^{Z} bins **(a,d,g)** $p_{\mathrm{T}}^{Z} = 15$–30 GeV, **(b,e,h)** $p_{\mathrm{T}}^{Z} = 30$–60 GeV, **(c,f,i)** $p_{\mathrm{T}}^{Z} > 60$ GeV) and **(a–c)** 30–80%, **(d–f)** 10–30%, and **(g–i)** 0–10% Pb+Pb collisions.

A.5 Impact of Z-based Acceptance Corrections

The analysis reports charged-hadron yields in broad bins of Z boson p_{T}. However, due to the finite efficiency for the lepton trigger, reconstruction, and selection, the selected set of reconstructed Z events may pick out a biased set of Z bosons with a different p_{T} or η distribution than the full set of produced Z bosons within that kinematic range. As the hadron yields are expected to depend on Z boson p_{T}, this can influence the measurement. In this section, the effect of the Z boson inefficiency on the charged-hadron yields as a function of $p_{\mathrm{T}}^{\mathrm{ch}}$ and x_{hZ} is quantified. For clarity, the nominal results are corrected by inefficiencies. But, any systematic uncertainties related to these corrections will be related to the effect the corrections have on the measurement in the first place. Therefore understanding their impact is essential to evaluating a corresponding uncertainty.

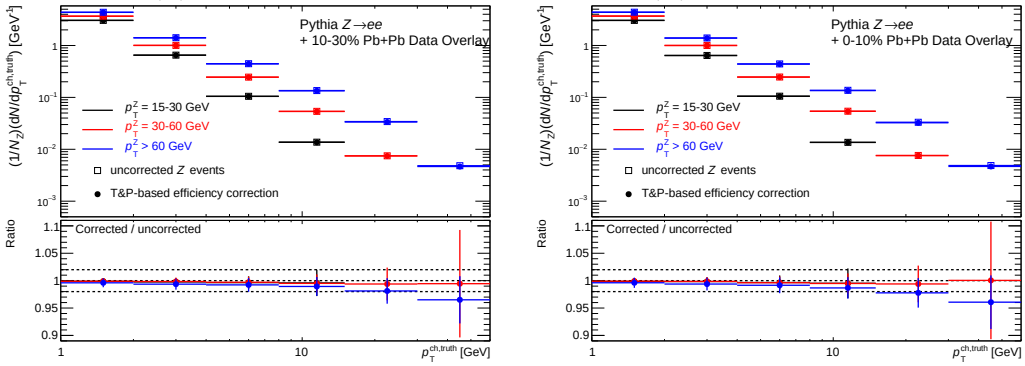
To understand the possible size of the Z boson acceptance corrections – i.e., the trigger and reconstruction efficiency factors – their effects are studied using the simulation samples, where there are many more events than the data. First, per-lepton reconstruction and selection efficiencies are determined using a tag-and-probe method. Candidate events are selected from opposite-sign lepton pairs which have invariant mass $76 < m_{\ell\ell} < 106$ GeV. For the dimuon channel, the tag muon is required to be `Medium` and pass pointing cuts, while the probe muon is required to only be a reconstructed muon with no additional requirement. The efficiency is then defined as the probability that the probe passes `Medium` + pointing cuts. For the dielectron channel, the tag electron is required to be `LHLoose` or `LHLoose_HI` (in pp and Pb+Pb, respectively) and pass pointing cuts, while the "probe" is only a reconstructed topocluster. The efficiency was then defined as the probability that the probe matches to a reconstructed electron and passes ID and pointing cuts. The efficiencies for both sets of leptons are determined as a function of lepton η, p_{T}, and separately for the four event types.

Then, the per-Z yields of truth-level charged hadrons is determined using the reconstructed set of Z bosons, and compared to the same set but with a per-boson weighting given by $1/(\varepsilon_{\ell_1}\varepsilon_{\ell_2})$, where ε_{ℓ_i} represents the p_{T}- and η-dependent efficiency for each decay lepton $i = 1, 2$ (which are



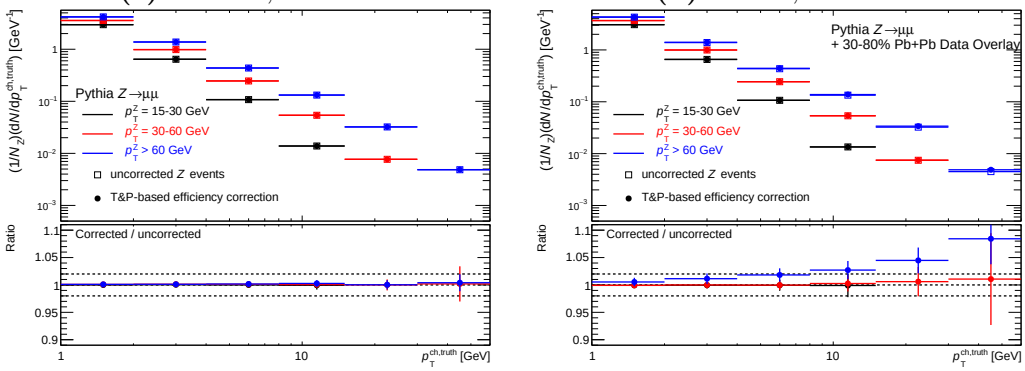
(a) pp, $Z \to ee$

(b) 30–80%, $Z \to ee$



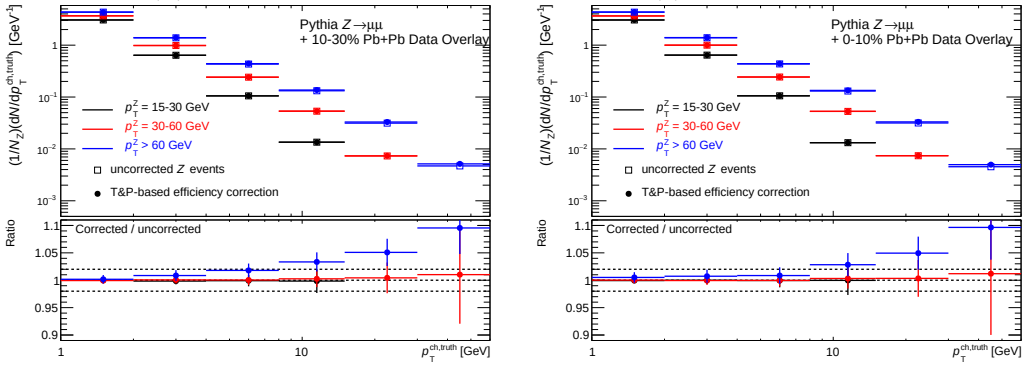
(c) 10–30%, $Z \to ee$

(d) 0–10%, $Z \to ee$



(e) pp, $Z \to \mu\mu$

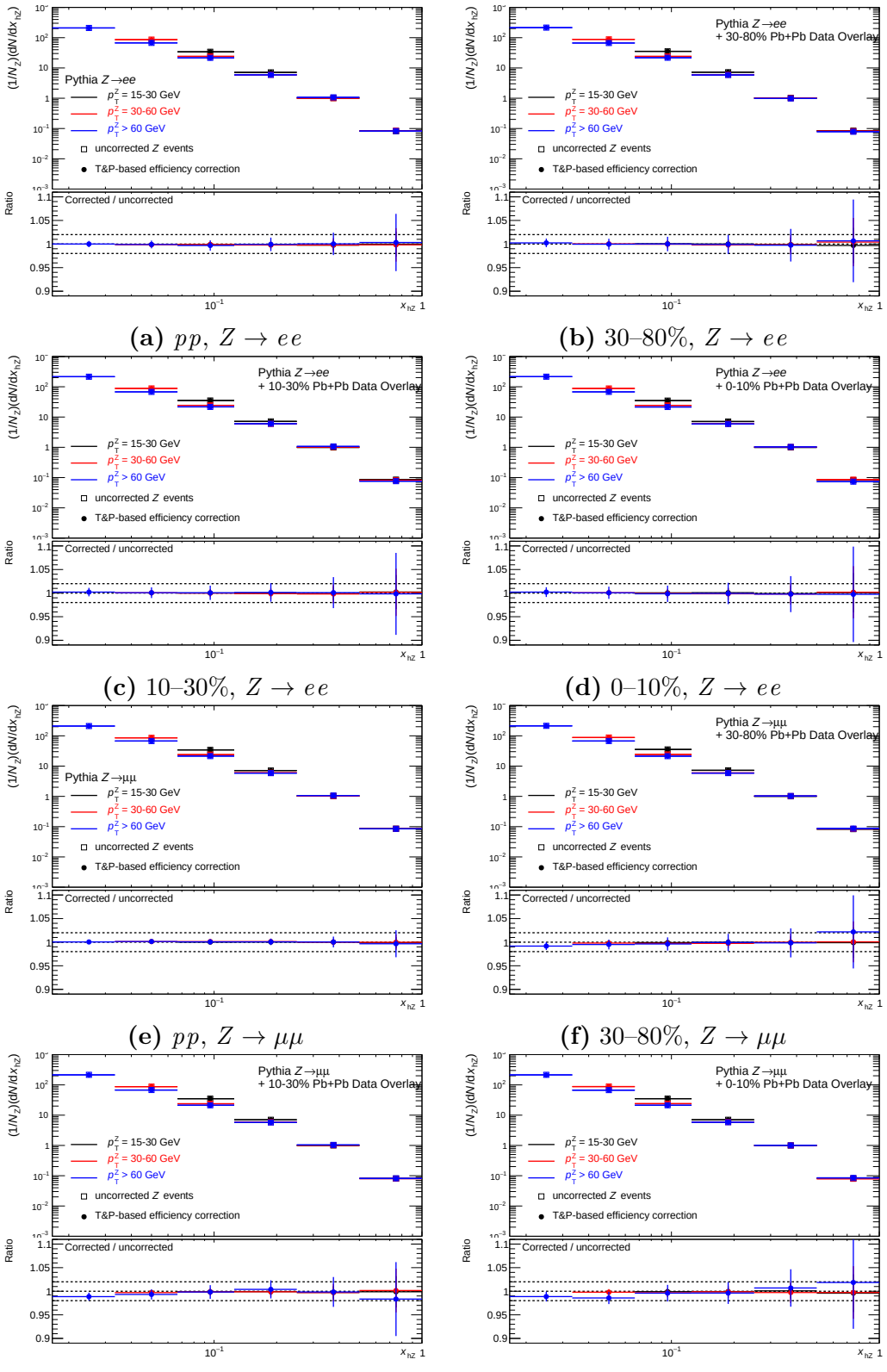
(f) 30–80%, $Z \to \mu\mu$



(g) 10–30%, $Z \to \mu\mu$

(h) 0–10%, $Z \to \mu\mu$

Figure A.25: Comparison of per-Z truth-hadron yields versus $p_{\mathrm{T}}^{\mathrm{ch}}$ for reconstructed Z events with (open squares) and without (filled circles) reconstruction inefficiency corrections, in **(a,e)** pp, **(b,f)** 30–80%, **(c,g)** 10–30%, and **(d,h)** 0–10% Pb+Pb collisions in both the $Z \to ee$ **(a–d)** and $Z \to \mu\mu$ **(e–h)** decay channels.



(a) pp, $Z \to ee$ **(b)** 30–80%, $Z \to ee$

(c) 10–30%, $Z \to ee$ **(d)** 0–10%, $Z \to ee$

(e) pp, $Z \to \mu\mu$ **(f)** 30–80%, $Z \to \mu\mu$

(g) 10–30%, $Z \to \mu\mu$ **(h)** 0–10%, $Z \to \mu\mu$

Figure A.26: Comparison of per-Z truth-hadron yields versus x_{hZ} for reconstructed Z events with (open squares) and without (filled circles) reconstruction inefficiency corrections, in **(a,e)** pp, **(b,f)** 30–80%, **(c,g)** 10–30%, and **(d,h)** 0–10% Pb+Pb collisions in both the $Z \to ee$ **(a–d)** and $Z \to \mu\mu$ **(e–h)** decay channels.

also centrality-dependent in Pb+Pb). Although the efficiencies vary with individual lepton η and p_{T}, the dependence of the efficiency on the Z kinematics is observed to be only modest, due to the broad correlation between the Z kinematics and the kinematics of any individual decay lepton.

Fig. A.25 catalogs the impact of the per-Z efficiency correction on the charged-hadron yields, for both the $Z \to ee$ and $Z \to \mu\mu$ channels in each of the four event selections. The bottom panels show the ratio of the per-Z yields between the Z boson with efficiency correction weighting, to that without the weighting (i.e. just using the reconstructed set of Z's). The horizontal dashed lines denote $\pm 2\%$ deviations. In almost all event types, channels, and p_{T}^{Z} selections, the ratios are compatible with unity (within the uncertainties in the MC) and the effect is negligible. The only exception is for the highest Z p_{T} selection in Pb+Pb events, at large $p_{\mathrm{T}}^{\mathrm{ch}}$, where the ratios can reach 5% below unity (5-10% above unity) in the electron (muon) channels.

Fig. A.26 catalogs the impact on the charged-hadron yields when reported as a function of $x_{hZ} = p_{\mathrm{T}}^{\mathrm{ch}}/p_{\mathrm{T}}^{Z}$, with a format analogous to that in Fig. A.25 above. When reported as a function of x_{hZ}, the impact of changing the sampled p_{T}^{Z} distribution is mostly cancelled out, such that this observable is less sensitive to the p_{T}^{Z} distribution within the broad p_{T} range. For all centrality and p_{T}^{Z} selections, the ratios are typically compatible with unity.

Recall that data events are corrected by the trigger and reconstruction efficiency. For the trigger efficiency, only one lepton must fire the trigger, so the trigger correction is expected to be less impactful. The reconstruction efficiency is then corrected for as described above in the nominal results, using the product of the single-lepton reconstruction efficiencies as measured in MC. The impact of these correction factors on the UE subtracted yields is then shown in Fig. A.27 for both decay channels. As seen in the MC, this correction affects the UE subtracted charged-hadron yield at the few percent level in data. This is well within the allotted uncertainties, so no systematic uncertainty is evaluated from the Z acceptance correction procedure.

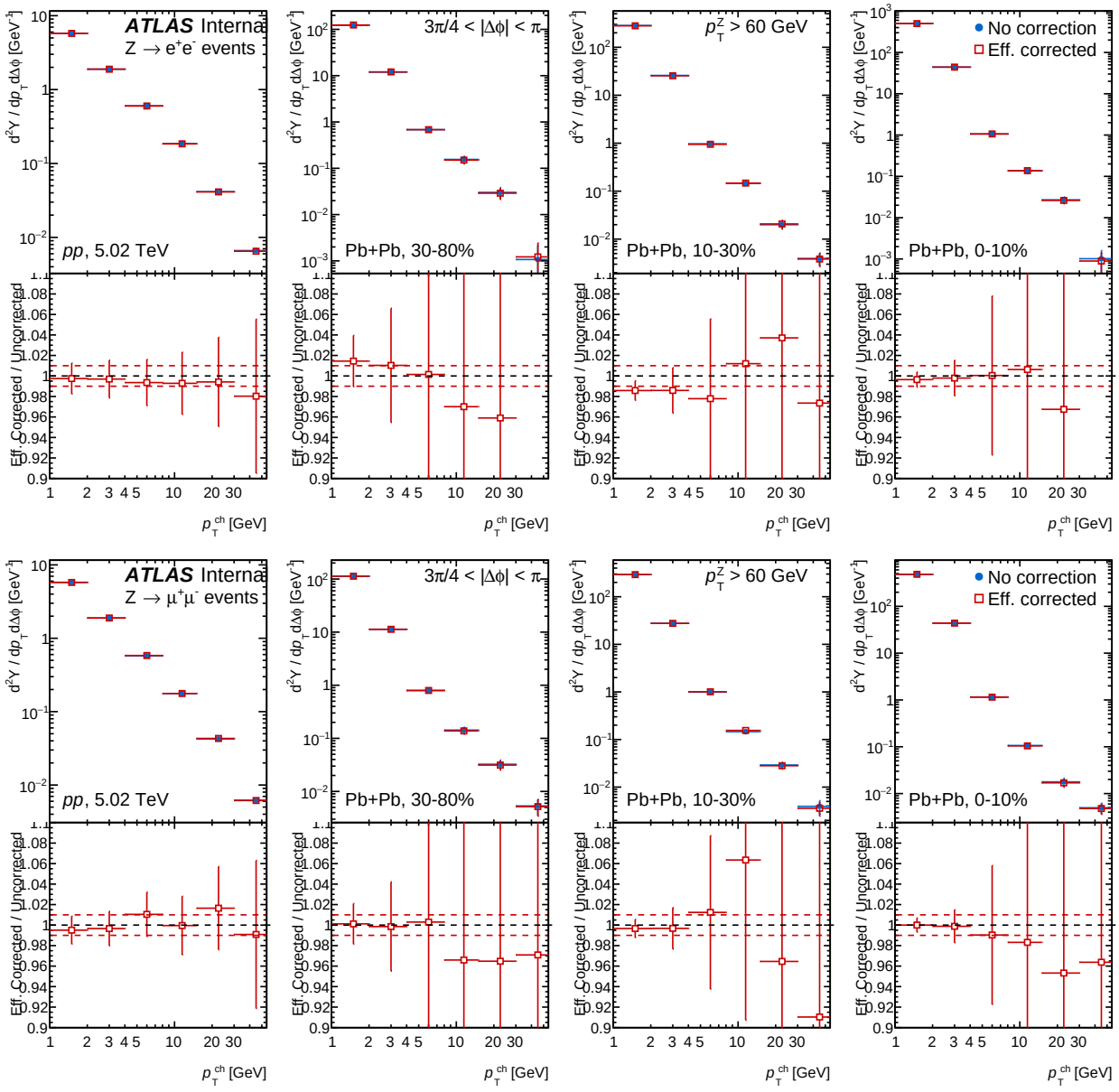


Figure A.27: The UE subtracted yield is compared between the results with and without per-Z efficiency weights in the $Z \to ee$ (top) and $Z \to \mu\mu$ (bottom) channel for events with $p_{\mathrm{T}}^{Z} > 60$ GeV.

Appendix B

Auxiliary Material for the Jet–Hadron Correlations Measurement

B.1 Electromagnetic Backgrounds

While this analysis is interested in hadronic types of p+Pb collisions, a separate category of EM processes comprise a substantial fraction of the total cross-section due to the high Z of the Pb nucleus. Such processes can occur via quasi-real photon exchange when the nuclei do not overlap and are known as ultra-peripheral collisions or UPCs. As previously mentioned, these types of collisions are not featured in the Glauber model and thus must be rejected when categorizing event centralities. To this end, we apply a topological cut on events to reduce contamination from these kinds of events, though it is of interest to retroactively evaluate how they persist in the final event selection, particularly given the apparent excess of jets in the peripheral bin.

UPC events are frequently identified topologically based on rapidity gaps between particles traveling in the direction of the emitted photon. A concise summary of how this works can be found in Ref. [340]. In short, we use the sum-of-gaps quantity, defined as the sum of rapidity gaps that are at least 0.5 between consecutive entries in a sorted list of track and cluster rapidities. Tracks must have $p_{\mathrm{T}} > 0.4$ GeV and meet the `HILoose` working point; clusters must have $p_{\mathrm{T}} > 0.2$ GeV. Unlike in [340], where UPCs were selected in a symmetric collision system by considering the sum of gaps on either side of the detector, here we focus on UPCs where the photon is emitted by the Pb nucleus and thus travels towards the A-side of the detector. In p+Pb, most UPCs will be of this type since the photon emission probability is substantially higher for nuclei with higher Z.

In Fig. B.1, we investigate the distribution of the sum-of-gaps quantity $\sum_{\mathrm{Pb}(\gamma)} \Delta\eta$ in the

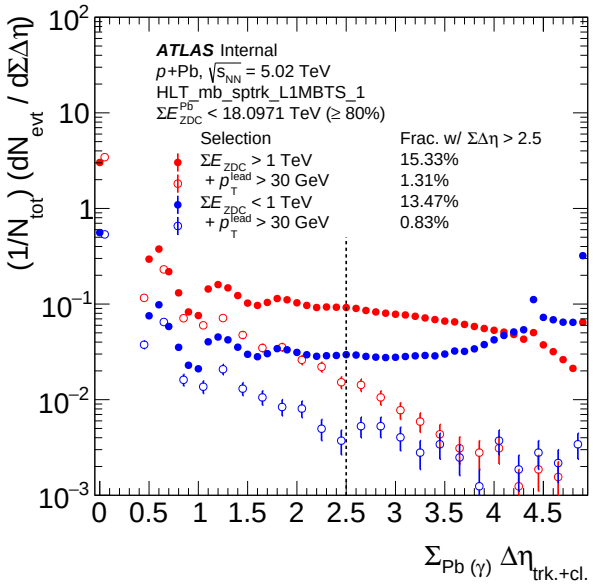


Figure B.1: The sum-of-gaps in the Pb (γ) going direction – the A-side of the detector – is shown for p+Pb events with ZDC energies in the peripheral-most selection 80–100%. Four selections are shown: events with $\Sigma E^{\mathrm{ZDC,Pb}} < 1$ TeV (**red**) or < 1 TeV (**blue**), and inclusive events (solid circles) versus events with a leading jet p_{T} above 30 GeV(open circles). Alongside each selection the fraction of events meeting that criteria with a sum-of-gaps above 2.5 is shown.

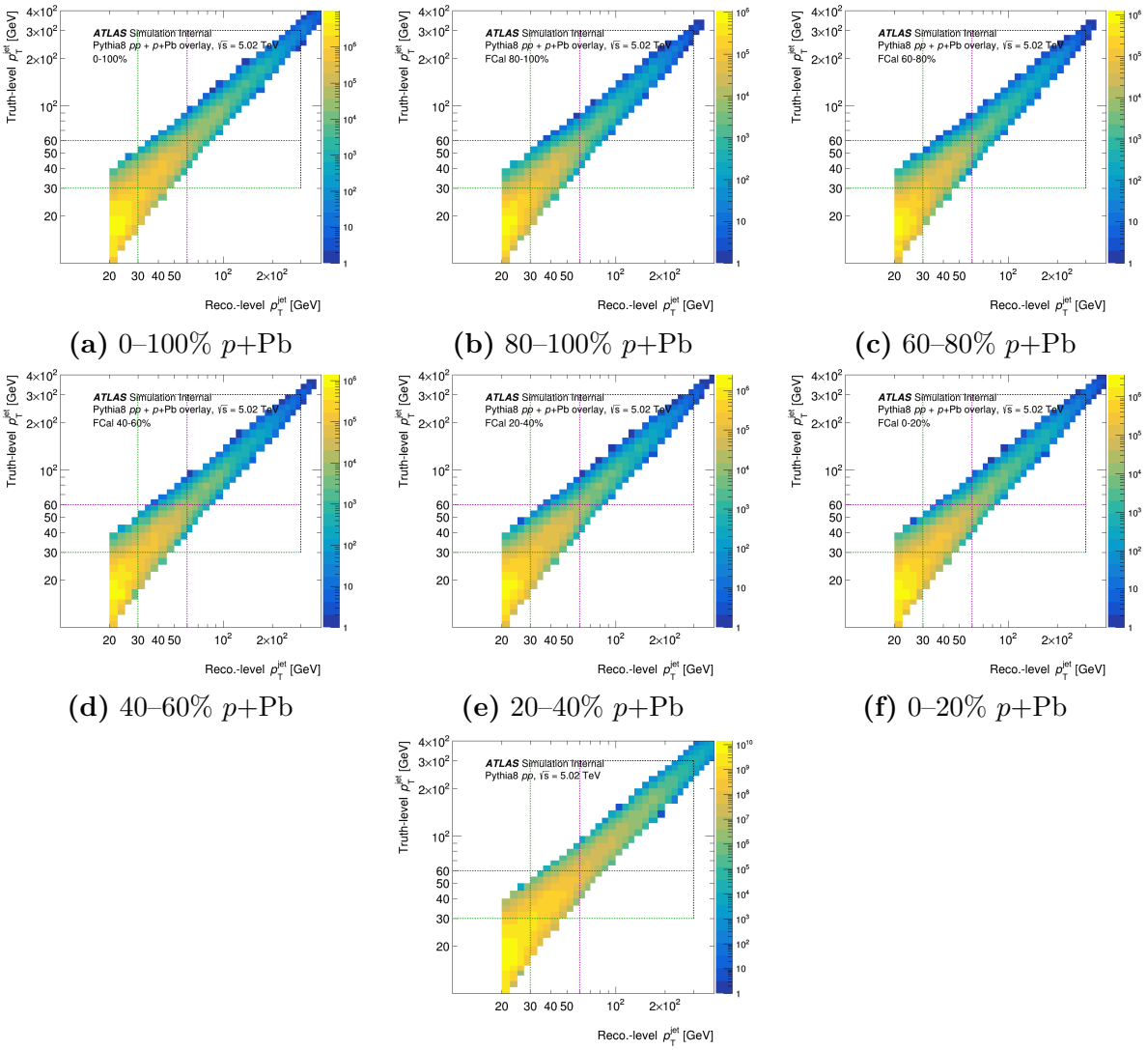
peripheral events to identify any substantial contribution from residual UPC topologies. In this figure, we divide the events based on their ZDC energies as UPCs tend to generate few if any spectator neutrons. This provides two samples: the sample with higher ZDC energies should have more hadronic events, while the sample with lower ZDC energies should have more UPC events, and enhance any of their features. We use the cut $\Sigma E^{\mathrm{ZDC,Pb}} = 1$ TeV to define these two categories. This energy cutoff is somewhat arbitrary, but is far enough below the single neutron peak at 2.51 TeV that these events can safely be categorized as having no neutrons.

We see in the solid markers in Fig. B.1 that events with lower ZDC energies have a bimodal sum of gaps distribution, with a peak at low $\sum_{\mathrm{Pb}(\gamma)} \Delta\eta$ corresponding to the hadronic interactions, but also a minor peak at high $\sum_{\mathrm{Pb}(\gamma)} \Delta\eta$ coming from the UPC events. Features at 0.5 and 1 are a consequence of the sum-of-gaps definition (only gaps $\Delta\eta > 0.5$ are summed). A division at 2.5, motivated by [340] and validated by the relative flatness of the distributions around that value, can be used to separate events with a UPC topology from a hadronic topology. We find that about

$\sim 29\%$ of all minimum bias events in the peripheral bin are observed to have $\sum_{\mathrm{Pb}(\gamma)} \Delta\eta > 2.5$ – this is indicated by the fractions on the figure.

We then further select events based on the presence of a jet. Jet production rates are not necessarily the same between UPCs and hadronic interactions because of the difference in physics; generally, selecting on hard processes such as jet production strongly favors collisions with real hadronic interactions. So, we expect the fraction of UPCs to diminish when requiring a high-p_{T} jet to be present in the event. Indeed, in the open markers, we see that further selecting on events with a jet above $p_{\mathrm{T}} = 30$ GeV reduces the total UPC-like fraction to only $\sim 2.1\%$. Moreover, the distributions for events with $\Sigma E^{\mathrm{ZDC,Pb}} \gtrless 1$ TeV have the same general shape above 2.5, corroborating that the UPC contribution is very small after applying the jet selection. Because the fraction appears to be so low, we conclude that this source of background is sufficiently small and therefore we neglect it.

B.2 Response Matrices

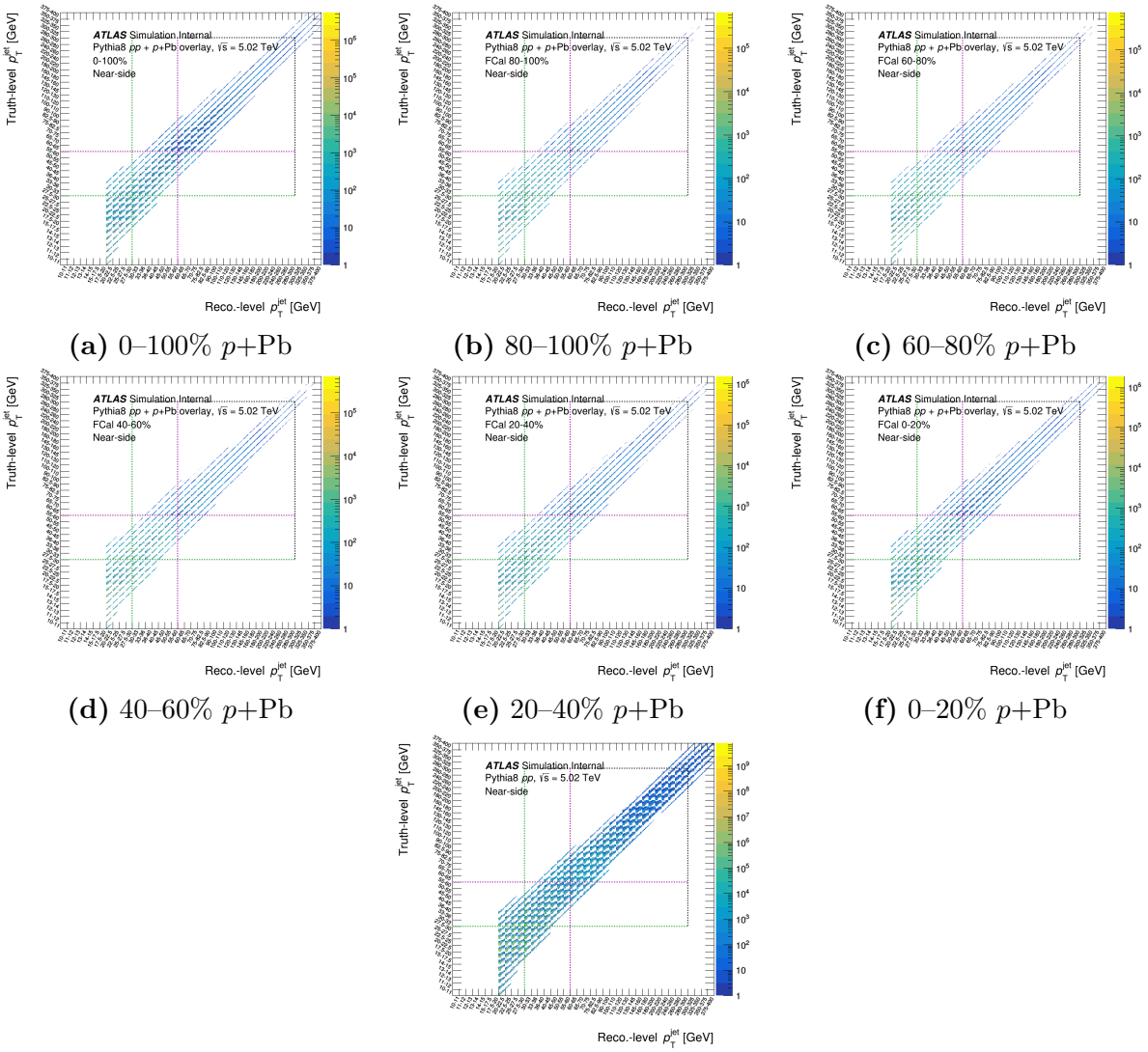


(a) 0–100% p+Pb **(b)** 80–100% p+Pb **(c)** 60–80% p+Pb

(d) 40–60% p+Pb **(e)** 20–40% p+Pb **(f)** 0–20% p+Pb

(g) pp

Figure B.2: 1D response matrices for jets in **(a–f)** p+Pb and **(g)** pp collisions are shown. The fiducial ranges of the measurement is highlighted by the dashed lines: the low $p_{\mathrm{T}}^{\mathrm{jet}}$ selection shown in **green** and high $p_{\mathrm{T}}^{\mathrm{jet}}$ selection in **purple**. Both selections are cut off at 300 GeV (**black**).

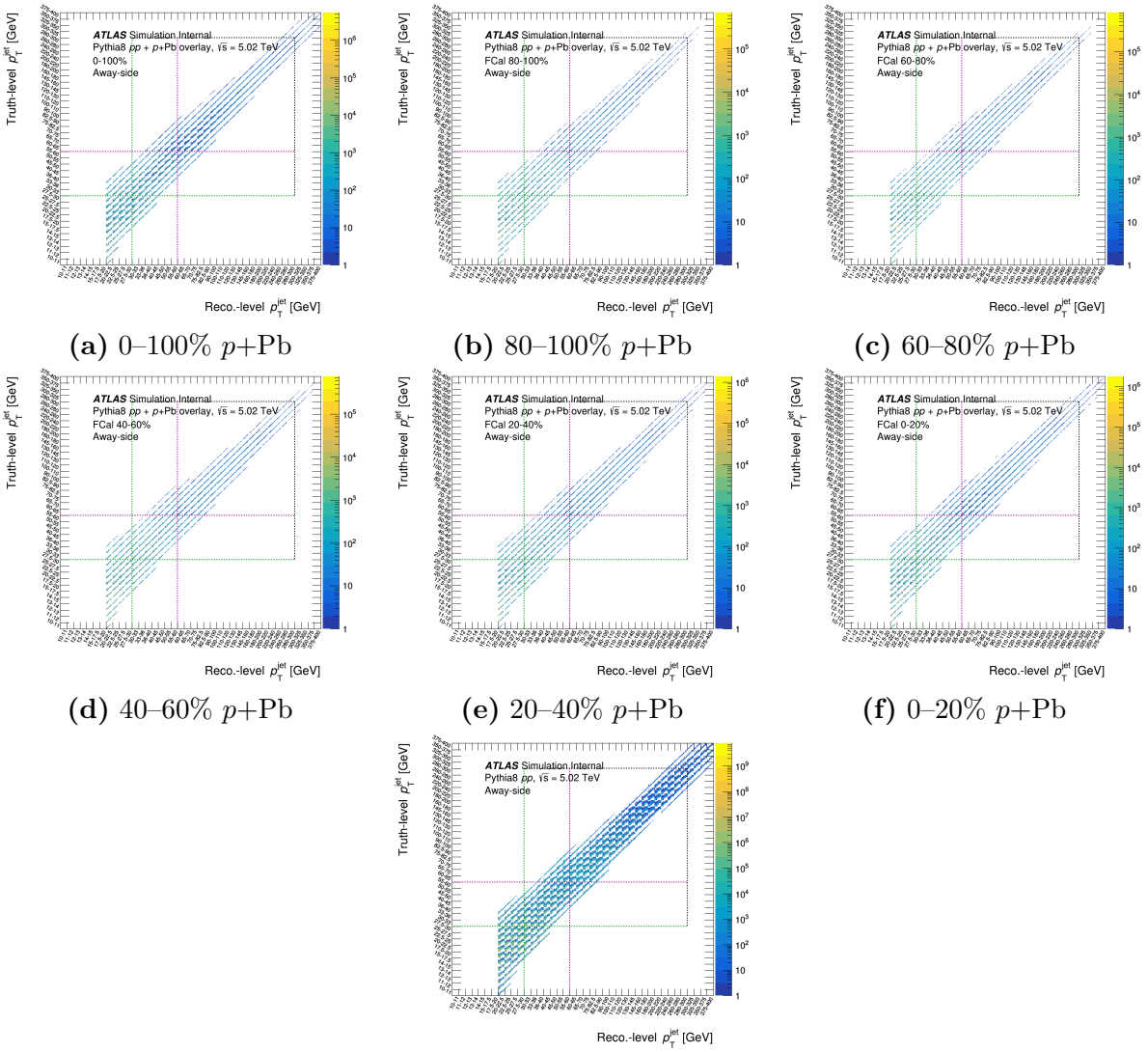


(a) 0–100% p+Pb **(b)** 80–100% p+Pb **(c)** 60–80% p+Pb

(d) 40–60% p+Pb **(e)** 20–40% p+Pb **(f)** 0–20% p+Pb

(g) pp

Figure B.3: 2D response matrices for charged particles nearby a jet ($\Delta\phi < \pi/8$) in **(a–f)** p+Pb and **(g)** pp collisions are shown. The fiducial ranges of the measurement is highlighted by the dashed lines: the low $p_{\mathrm{T}}^{\mathrm{jet}}$ selection shown in **green** and high $p_{\mathrm{T}}^{\mathrm{jet}}$ selection in **purple**. Both selections are cut off at 300 GeV (**black**).



(a) 0–100% p+Pb **(b)** 80–100% p+Pb **(c)** 60–80% p+Pb

(d) 40–60% p+Pb **(e)** 20–40% p+Pb **(f)** 0–20% p+Pb

(g) pp

Figure B.4: 2D response matrices for charged particles opposite a jet ($\Delta\phi > 7\pi/8$) in **(a–f)** p+Pb and **(g)** pp collisions are shown. The fiducial ranges of the measurement is highlighted by the dashed lines: the low $p_{\mathrm{T}}^{\mathrm{jet}}$ selection shown in **green** and high $p_{\mathrm{T}}^{\mathrm{jet}}$ selection in **purple**. Both selections are cut off at 300 GeV (**black**).

B.3 Unfolding Termination on the Near-side

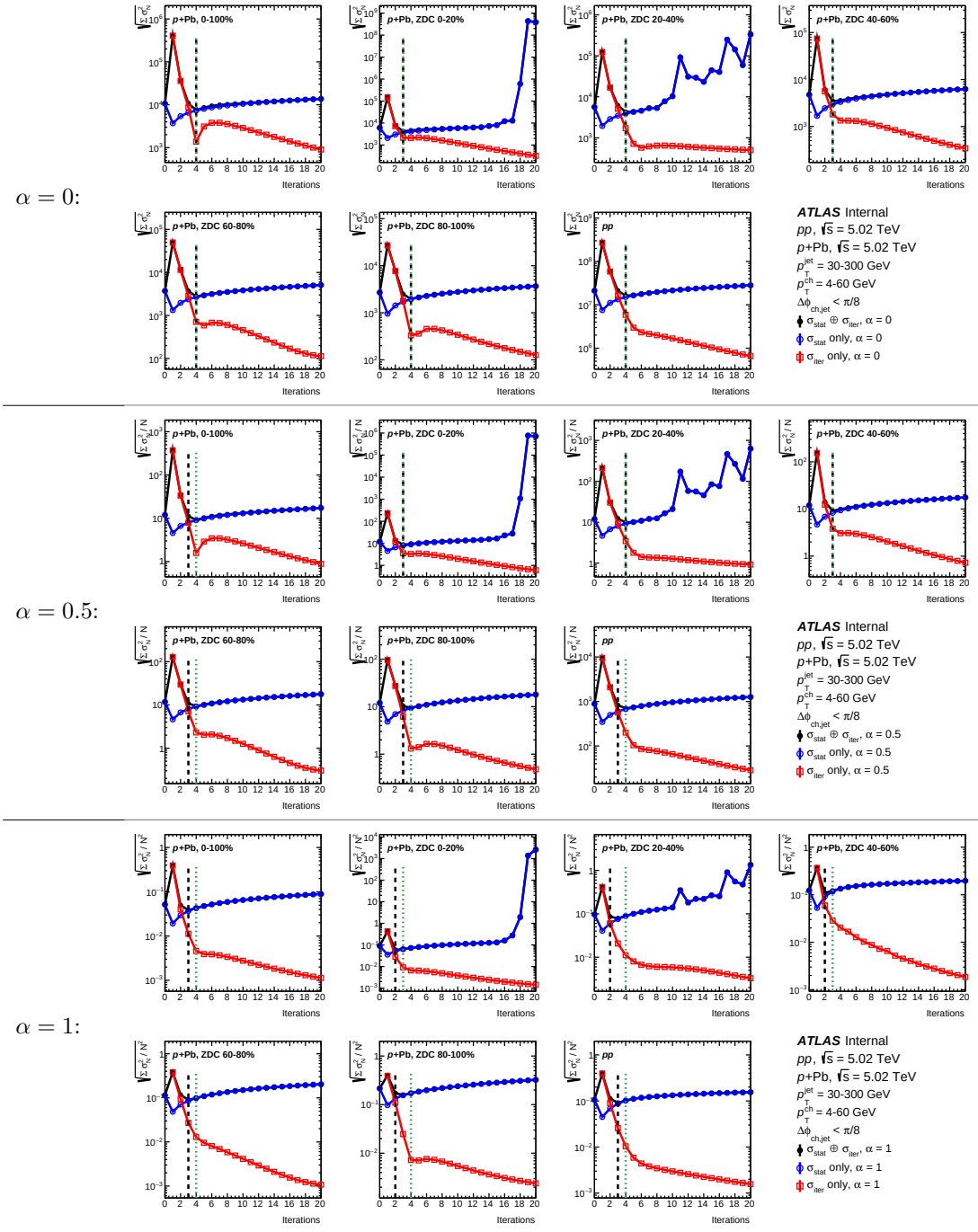


Figure B.5: σ_{iter} (red squares) and σ_{stat} (blue circles) are plotted versus N_{iter} in data with $\alpha \in \{0, 0.5, 1\}$. **Black** vertical dashed lines indicate the lowest nonzero N_{iter} value ($N_{\text{iter}}^{\text{opt.}}$) where $\sigma_{\text{iter}} < \sigma_{\text{stat}}$ for all $N_{\text{iter}} > N_{\text{iter}}^{\text{opt.}}$ values. The **green** dotted lines indicate the value of $N_{\text{iter}}^{\text{opt.}}$ used in the analysis. These plots are analogous to the ones for the away-side shown in Fig. 6.30 in Sec. 6.6.

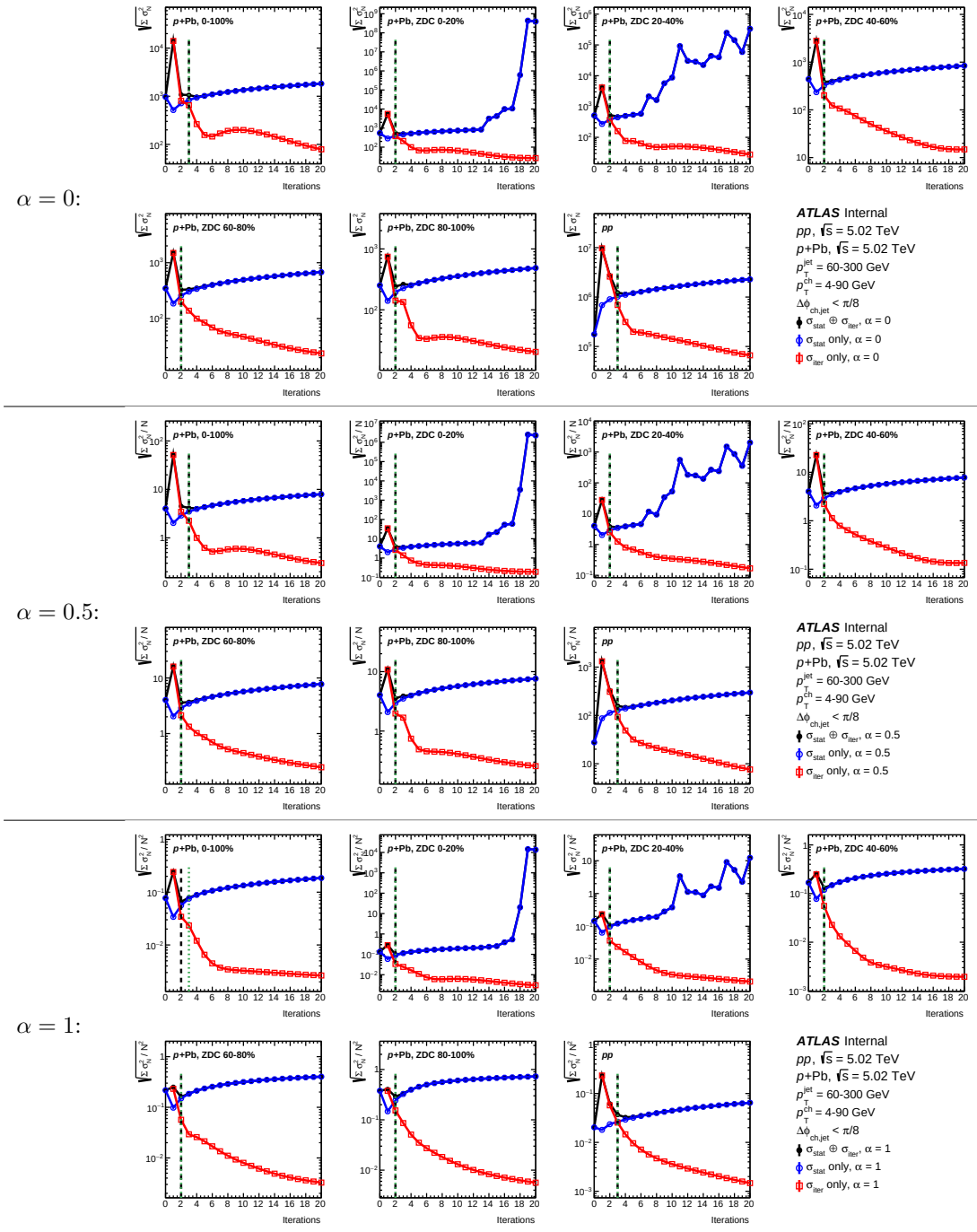


Figure B.6: $\boldsymbol{\sigma_{\text{iter}}}$ **(red squares)** and $\boldsymbol{\sigma_{\text{stat}}}$ **(blue circles)** are plotted versus N_{iter} in data with $\alpha \in \{0, 0.5, 1\}$. **Black** vertical dashed lines indicate the lowest nonzero N_{iter} value ($N_{\text{iter}}^{\text{opt.}}$) where $\sigma_{\text{iter}} < \sigma_{\text{stat}}$ for all $N_{\text{iter}} > N_{\text{iter}}^{\text{opt.}}$ values. The **green** dotted lines indicate the value of $N_{\text{iter}}^{\text{opt.}}$ used in the analysis. These plots are analogous to the ones for the away-side shown in Fig. 6.31 in Sec. 6.6.

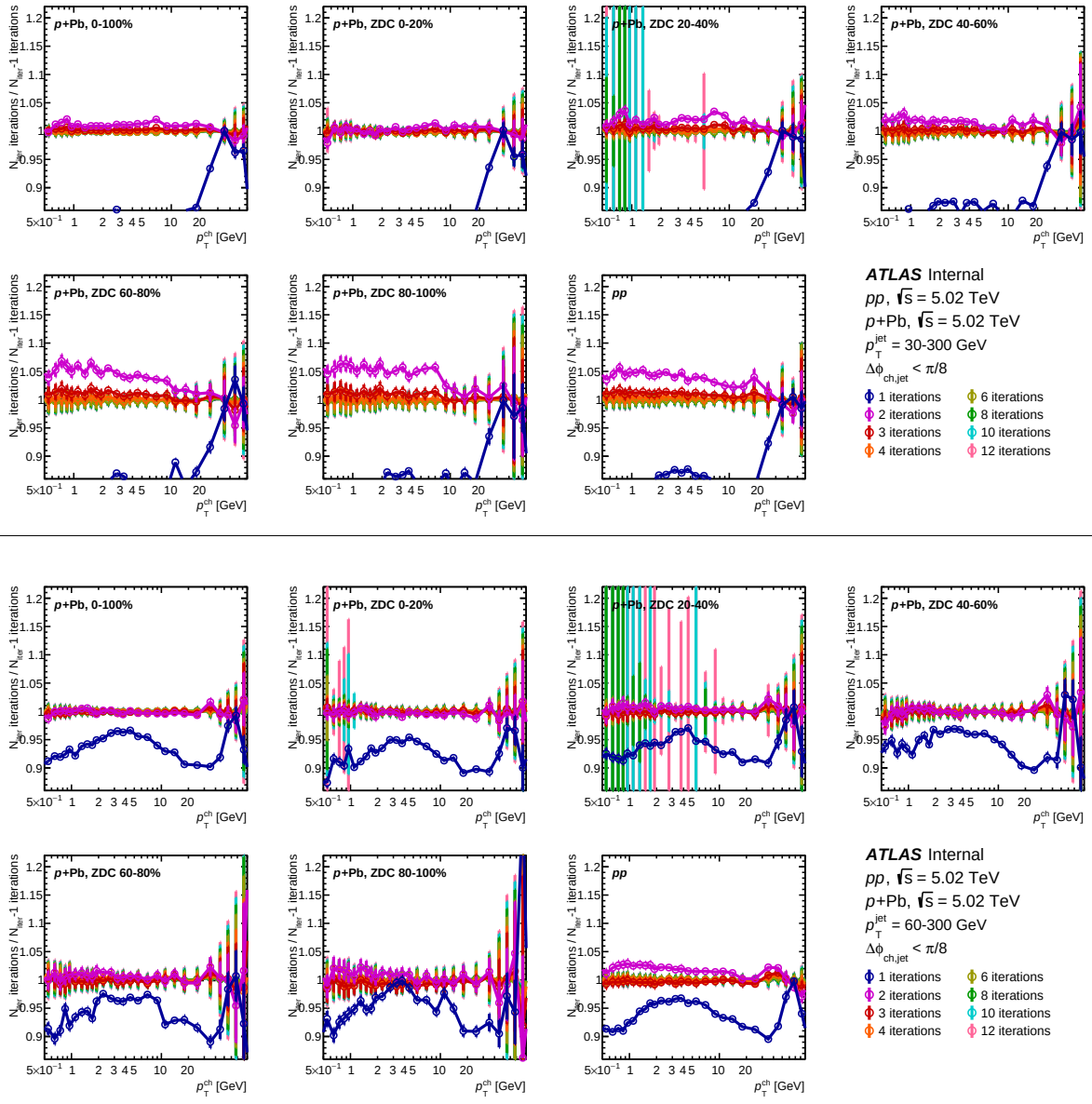


Figure B.7: The convergence ratio is studied as a function of $p_{\mathrm{T}}^{\mathrm{ch}}$ and the N_{iter}. Uncertainties represent solely the uncertainty on the numerator. Analogous plots for the away-side are shown in Fig. 6.32 in Sec. 6.6.

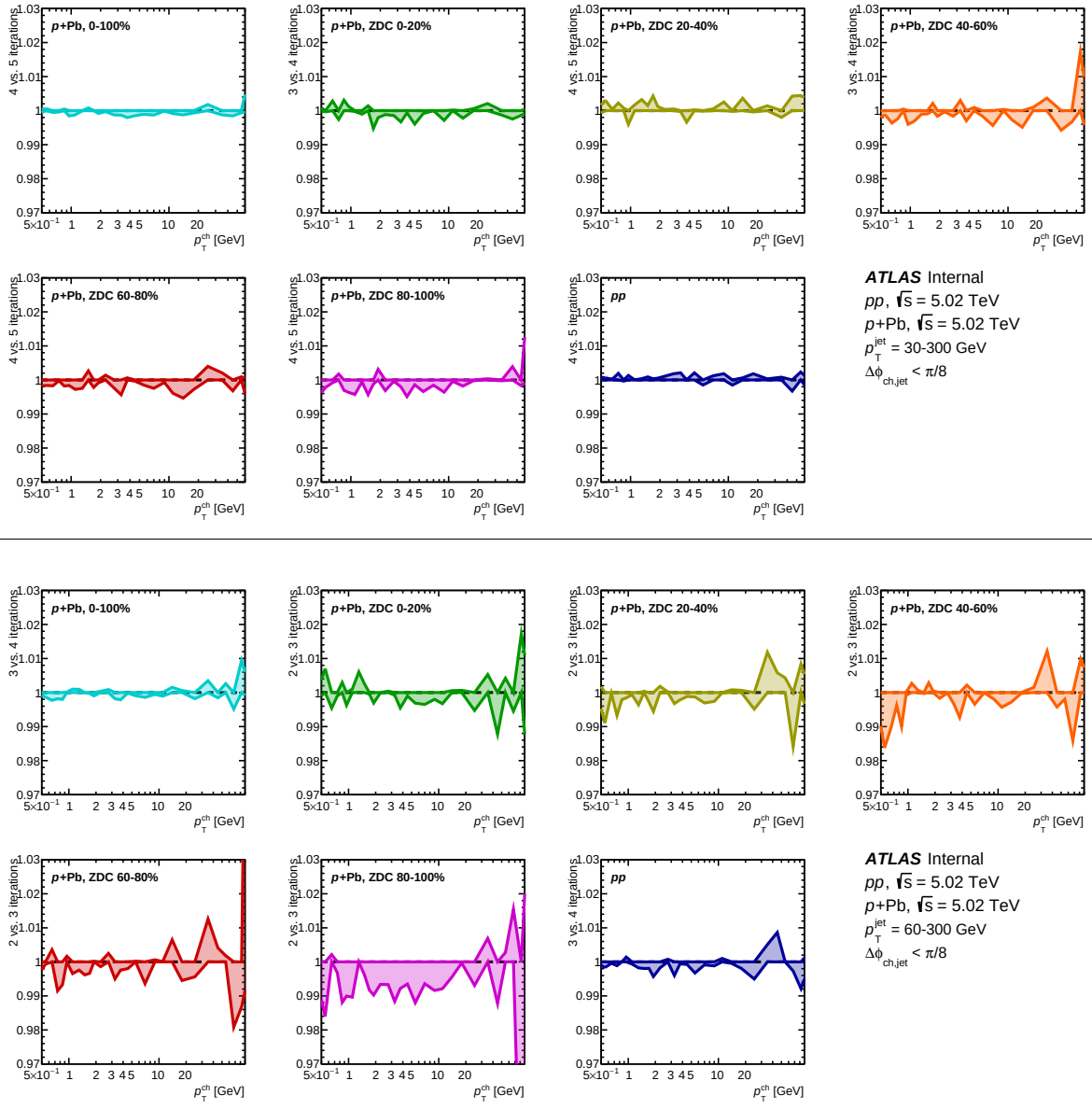


Figure B.8: The convergence ratio at $N_{\mathrm{iter}}^{\mathrm{opt.}}$ is studied as a function of $p_{\mathrm{T}}^{\mathrm{ch}}$. The uncertainty band shows the effect of the additional iteration. Analogous plots for the away-side are shown in Fig. 6.33 in Sec. 6.6.

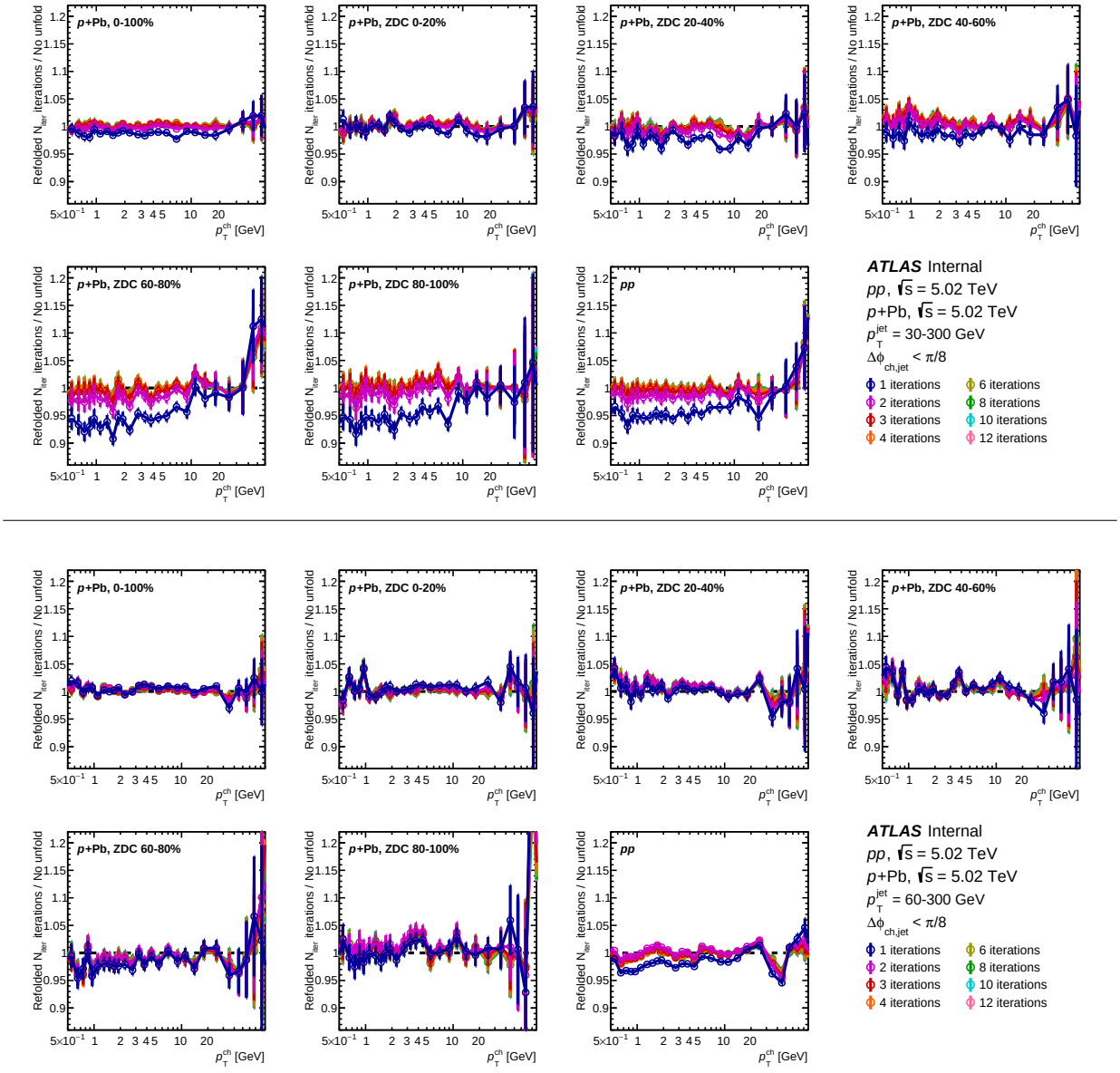


Figure B.9: The refolded distribution of charged particles is studied as a function of $p_{\mathrm{T}}^{\mathrm{ch}}$ and the number of iterations. The y-axis shows the ratio of the refolded distribution near-side charged particle yield $\hat{N}$, integrated over $p_{\mathrm{T}}^{\mathrm{jet}} = 30$–$300$ GeV (top) and $p_{\mathrm{T}}^{\mathrm{jet}} = 60$–$300$ GeV (bottom), at N_{iter} iterations to that prior to the unfolding (i.e. the "raw" distribution). Each panel corresponds to a different p+Pb centrality selection or pp in the lower right. The uncertainties represent solely the uncertainty on the numerator. Analogous plots for the away-side are shown in Fig. 6.37 in Sec. 6.6.

B.4 Monte Carlo Closure Studies

It is important to demonstrate that, when the analysis procedure is performed on simulated events from Monte Carlo, the distributions with reconstructed charged particles capture the distributions at the generator or truth level. This test is an important check against the accuracy of the analysis procedure. If the truth-level distributions are recovered with reconstructed-level objects, then the analysis is said to achieve *closure*. Significant deviations away from the truth-level distribution signify *non-closure* and can represent unaccounted-for sources of systematic uncertainty or potential bias.

In this section we study how well the analysis closes in MC. The yield at the reconstructed-level measured in these events consists of the generator signal plus the background from the uncorrelated data event. To remove this component, these events are matched in the same manner as the data distributions, as described in the previous section. One change is made to the mixing procedure, namely that the centrality matching is performed with the pure data $\Sigma E_{\mathrm{T}}^{\mathrm{FCal,Pb}}$ value rather than the MC + data overlay value. This is because the MC event can add to the sum and bias the centrality matching towards more central events. This tends to result in an oversubtraction of the background. The purpose of the MC closure check is to show that given a particular definition of the signal – the charged-hadron yield in Pythia simulated events – the average yield in matched events will converge to the correct background such that the unfolded result accurately represents the same truth-level quantity. So, we argue that this modification is warranted to demonstrate that the truth-level yield can be successfully recovered from the mixed event.

To ensure independent samples between filling the response matrices and checking analysis closure, we perform a half-closure test, which randomly assigns events to exclusively fill either the response matrix or the closure-check histograms. This is done by sending even entries in the TTree to the response matrix and odd entries to the histograms. We also perform a full-closure test, where all events fill both the response matrix as the closure histograms. We note that the response matrices in data use the result from all MC events since there is no issue with statistical

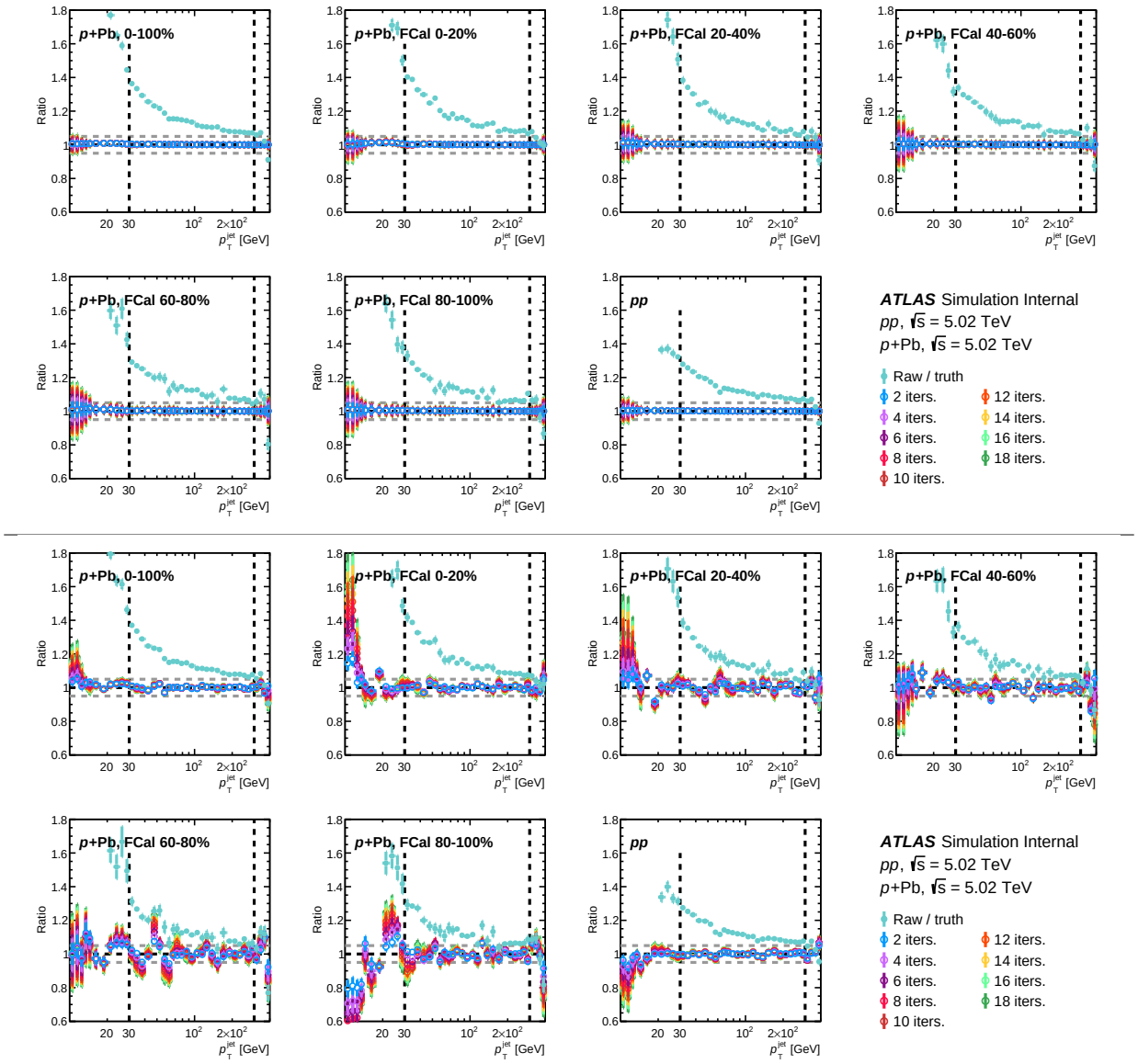


Figure B.10: The full closure (top) and half closure (bottom) of the jet p_{T} distributions is studied separately from the charged-hadron yields. Vertical dashed lines in **black** indicate the fiducial jet p_{T} selections used in data.

independence between data and MC.

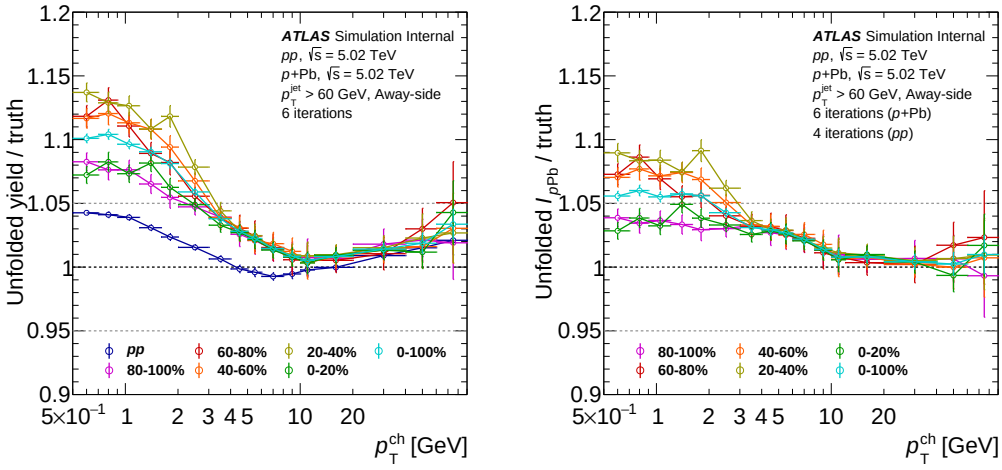
In Fig. B.10 the full and half closure tests are performed on the jet p_{T} distribution, for various numbers of iterations on the unfolding. We find that in both tests the unfolded distributions converge well onto the truth distribution within the fiducial region 30–300 GeV. Agreement is within 5% everywhere in this range and not visibly different from unity above about 60 GeV. Disagreement

in the underflow and overflow bins is expected and is observed, since jets with extremely low $p_{\mathrm{T}}^{\mathrm{jet}} \lesssim 15$ GeV are frequently ill-calibrated or not reconstructed, and the dijet p_{T} sampling terminates at 400 GeV. We also note that the half and full closure tests are compatible.

For the charged-particle distributions, we first perform a modified closure test where we restrict to primary charged particles. As a reminder, primary particles in the data overlay samples *must* come from the generated event, since overlay tracks have no truth-match. Therefore this restriction completely eliminates the underlying event background, and is a useful tool for cross-checking the combination of the tracking corrections and the unfolding. For this closure check, the primary fraction correction is not applied as all tracks are primary by construction. As the tracking corrections are already derived from the full MC sample, we only show the results from the full statistics here (no division of MC events is performed like in the half closure test). The main results are shown in Figs. B.12 and B.14. We see that, particularly for the $p_{\mathrm{T}}^{\mathrm{jet}} > 30$ GeV selection, the pre-unfolded (raw) distribution underestimates the truth value, as expected from the jet p_{T} migration effect. After unfolding with some number of iterations, the results reproduce the truth values with excellent accuracy, generally to within $\lesssim$ 2–3%, though high-$p_{\mathrm{T}}^{\mathrm{ch}}$ particles in the 30 GeVselection are slightly higher than truth by about $\sim$ 5% across each system & centrality. The closure is found to depend very little on the number of iterations across all selections. This study demonstrates that the tracking acceptance corrections and unfolding procedure are working acceptably well.

Following this study, we then look into the more complete closure study, where tracks are not restricted to primaries only and the UE must be subtracted. In this study we apply the full UE subtraction as described above. Since this check can also include non-primary particles we also correct by the primary fraction. We look at the full and half closure tests on the per-jet yield measurement, as well as the $I_{p\mathrm{Pb}}$ ratio. The idea is that effects common to both p+Pb and pp will cancel in the ratio, so looking at the closure on $I_{p\mathrm{Pb}}$ is useful for understanding the precision of the final measurement in data.

We see that the nominal closure study looks nearly identical to the only primary tracks



(a) Yield closure **(b)** $I_{p\mathrm{Pb}}$ closure

Figure B.11: A summary of the full closure test on the charged-hadron **(a)** yield measurement **(b)** and $I_{p\mathrm{Pb}}$ opposite ($\Delta\phi > 7\pi/8$) to a jet above 60 GeV is shown.

closure at high-$p_{\mathrm{T}}^{\mathrm{ch}}$, which is expected because the tracking purity is very high, and the signal-to-background is very high in this limit. At low $p_{\mathrm{T}}^{\mathrm{ch}}$, there is some tension in the closure study with a non-trivial centrality dependence. Both the central-most (0–20%) and peripheral-most (80–100%) bins have shapes which resemble the pp, indicating that the analysis is working as expected in these bins. The mid-central bins from 20–80% have the worst closure, which can as much as $\sim 15\%$. This is unexpected, as performance typically deteriorates uniformly from peripheral to central events.

Because the study with primary tracks only showed acceptable closure, we conclude that this non-closure is related to either including the primary tracks fraction correction or the underlying event estimate. We note that the sensitivity to the mixed event matching categories is taken as a systematic uncertainty – little sensitivity is observed to these. However, it is possible that there is some unobserved effect that is not accounted for with our definition of the mixed event.

For example, it is possible that, if the jet is correlated with event reaction plane (i.e., the jet is azimuthally correlated with the underlying event) then the UE subtraction in the HI jet reconstruction should allow nonzero v_n parameters, otherwise there will be a jet bias. This bias would cause the azimuthal (ϕ) distribution of particles in the UE of the trigger event to not match the matched event UE. Of course, in the MC, there is no correlation by construction between the jet

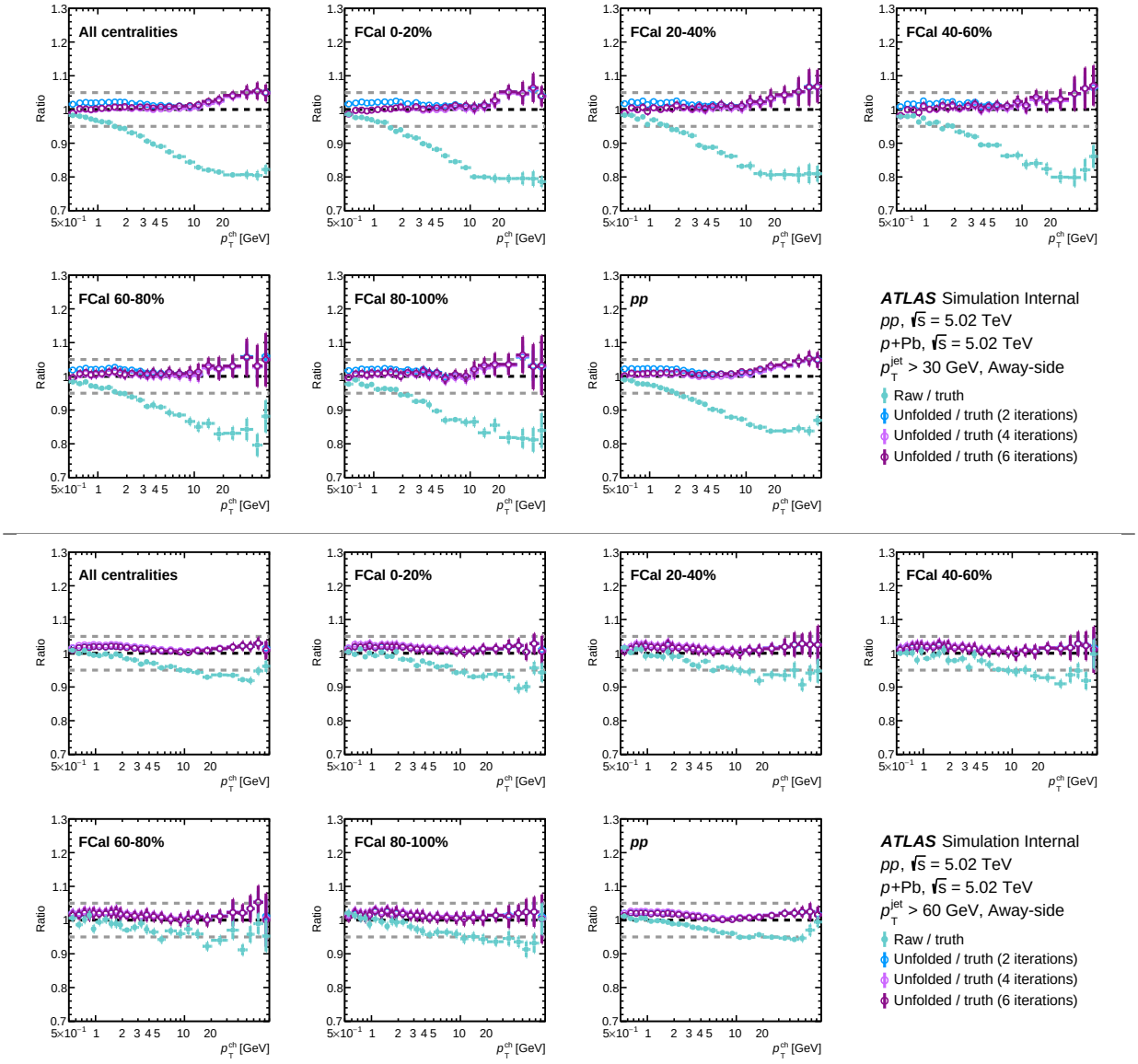


Figure B.12: The results of the closure test when restricting to only primary tracks is shown for particles opposite to ($\Delta\phi > 7\pi/8$) a jet between 30–300 GeV (top) or 60–300 GeV (bottom).

and the UE because they are taken from independent events (the jet represents a pure MC event while the UE is taken from data), so this could not explain the excess observed in the 20–80% centralities.

If the cause is the primary track fraction, we note that the fake is very low for all of the datasets and it is unlikely for the fake rate to be misestimated by 10%. However, we previously

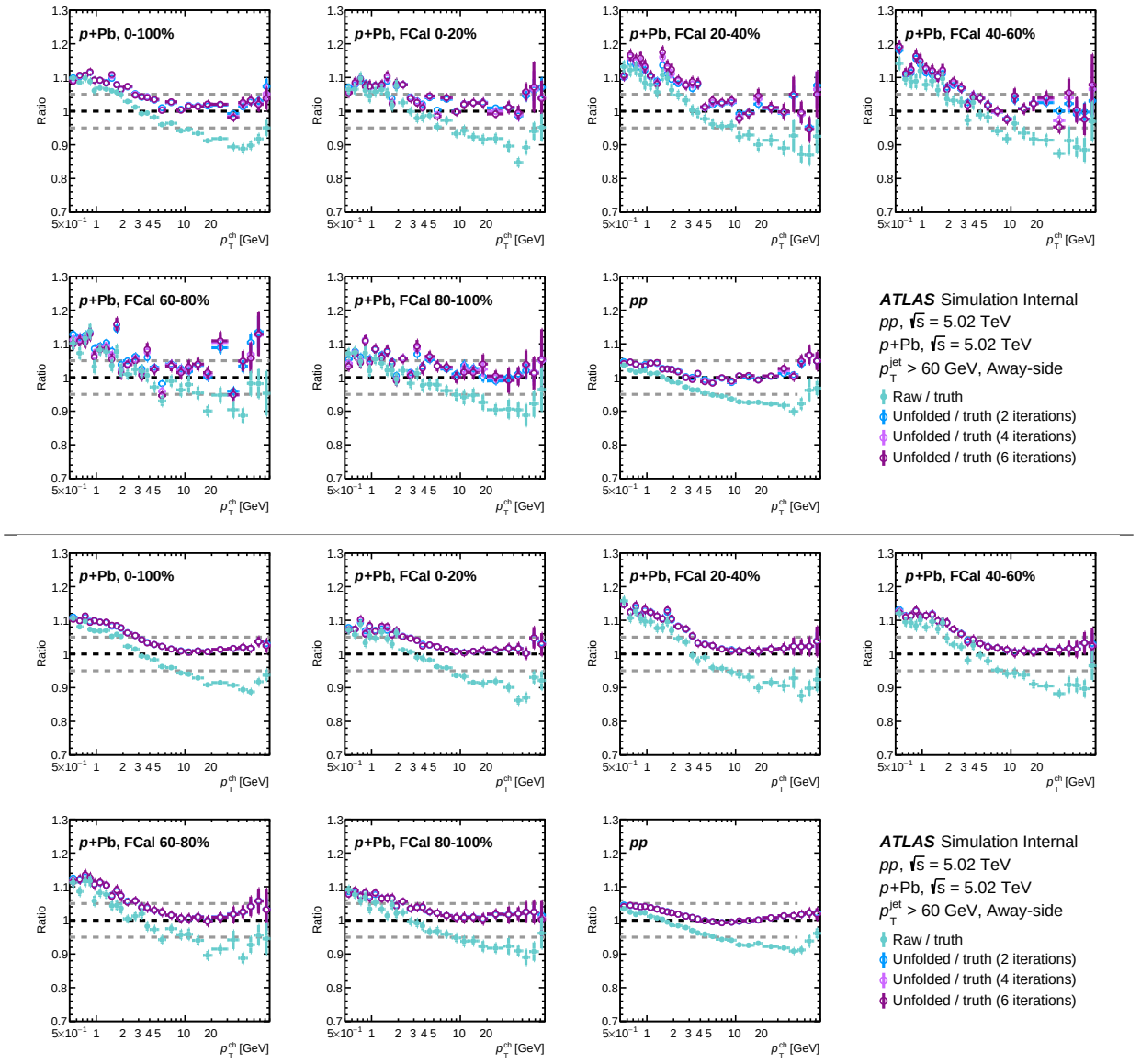


Figure B.13: The half (top) and full (bottom) closure tests are shown for particles opposite to ($\Delta\phi > 7\pi/8$) a jet between 60–300 GeV.

discussed how if the fake rate is different between jets and minimum bias events due to more fakes being reconstructed in the core of jets, then it is possible for a bias of $\mathcal{O}(10\%)$ to be observed on the final result. While this may be the cause, it is worth noting that (1) the bias would be most significant in the central bin, where the signal-to-background is lowest (which is not observed), and (2) a conservative systematic on the fake rate in jets already covers this effect by considering the

difference between the primary fraction derived from the Pythia dijets and the HIJING minimum bias.

Thus, we do not claim to understand the origin of this effect. However, we have investigated each potential source and find no evidence of a bias in the analysis methodology. Because (1) the closure ratios are only $> 5\%$ at low $p_{\mathrm{T}}^{\mathrm{ch}}$, where signal vs. background is more ambiguous and subjective to the particular UE definition, and (2) the possible sources of non-closure have been investigated, we propose to adopt the degree of non-closure as a source of systematic uncertainty. At high-$p_{\mathrm{T}}^{\mathrm{ch}}$, the non-closure pattern is nearly identical between p+Pb and pp, which indicates that both come from a common source. We would therefore allow the uncertainty to cancel between p+Pb and pp, so it would not lead to a significant impact in the precision region $\gtrsim 5$ GeV, but account for potential bias below this cut.

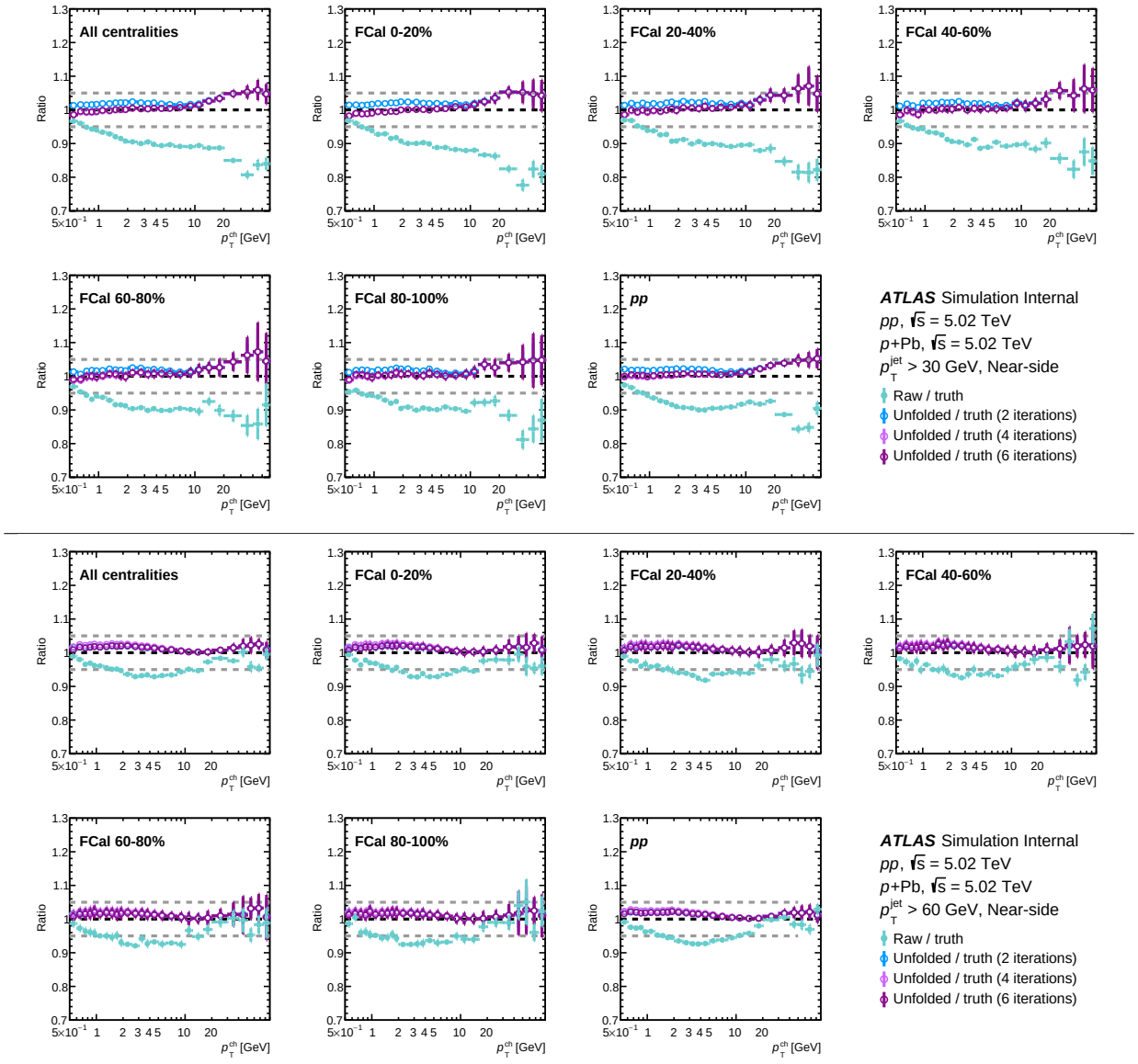


Figure B.14: The results of the closure test when restricting to only primary tracks is shown for particles nearby ($\Delta\phi < \pi/8$) a jet between 30–300 GeV (top) or 60–300 GeV (bottom).

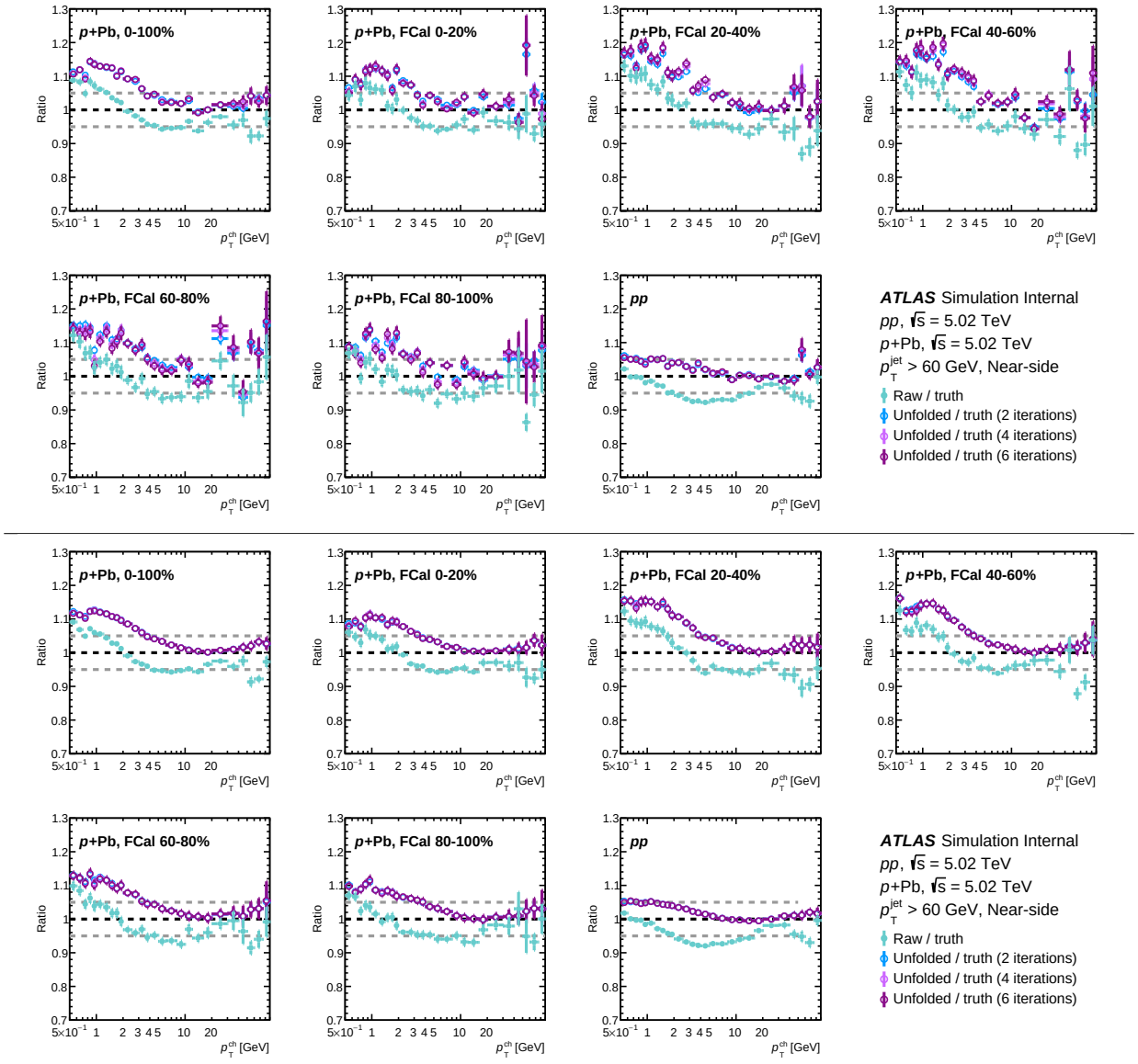


Figure B.15: The half (top) and full (bottom) closure tests are shown for particles nearby ($\Delta\phi < \pi/8$) a jet between 60–300 GeV.

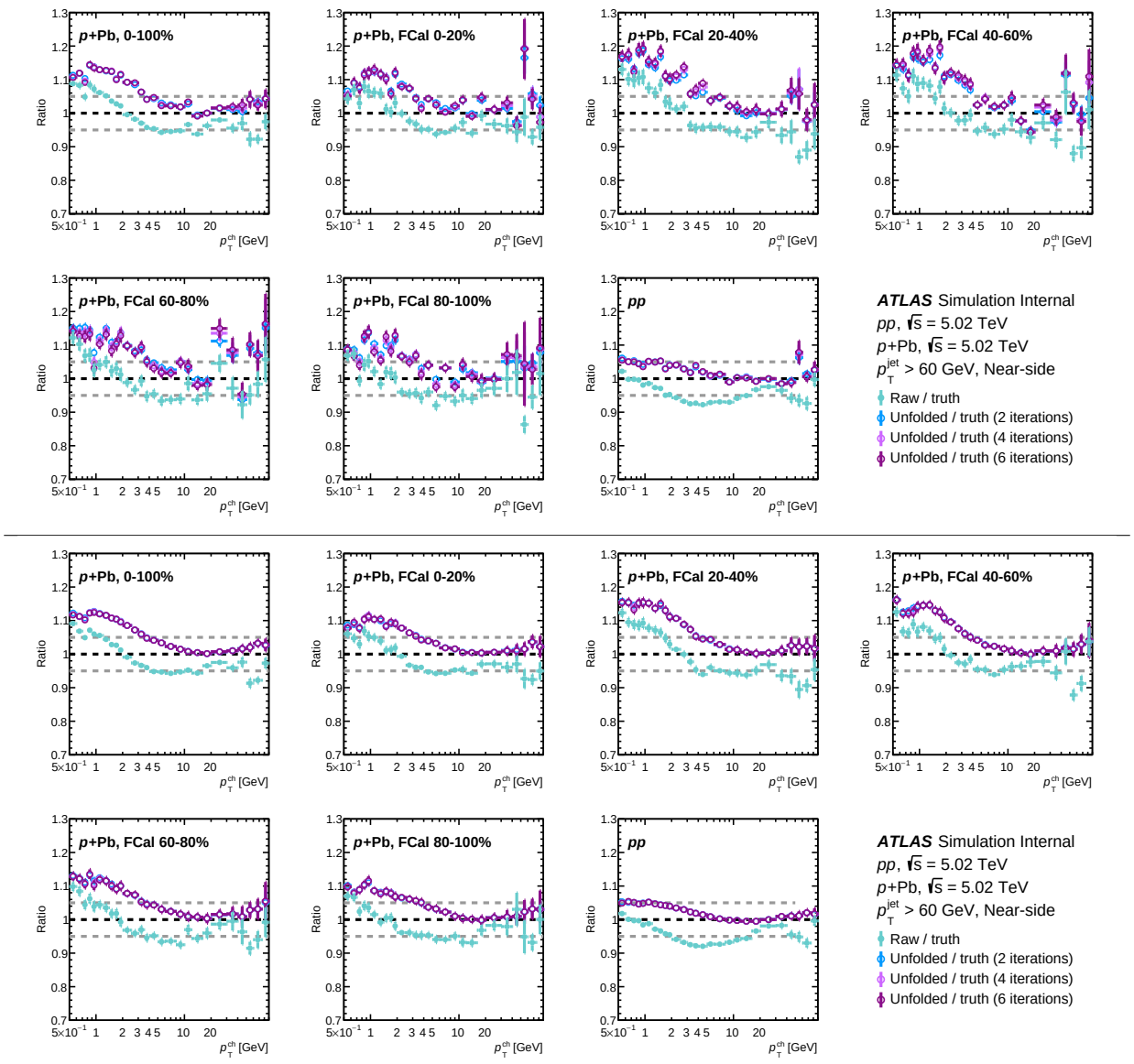


Figure B.16: The half (top) and full (bottom) closure tests are shown for particles opposite to ($\Delta\phi > 7\pi/8$) a jet between 30–300 GeV.

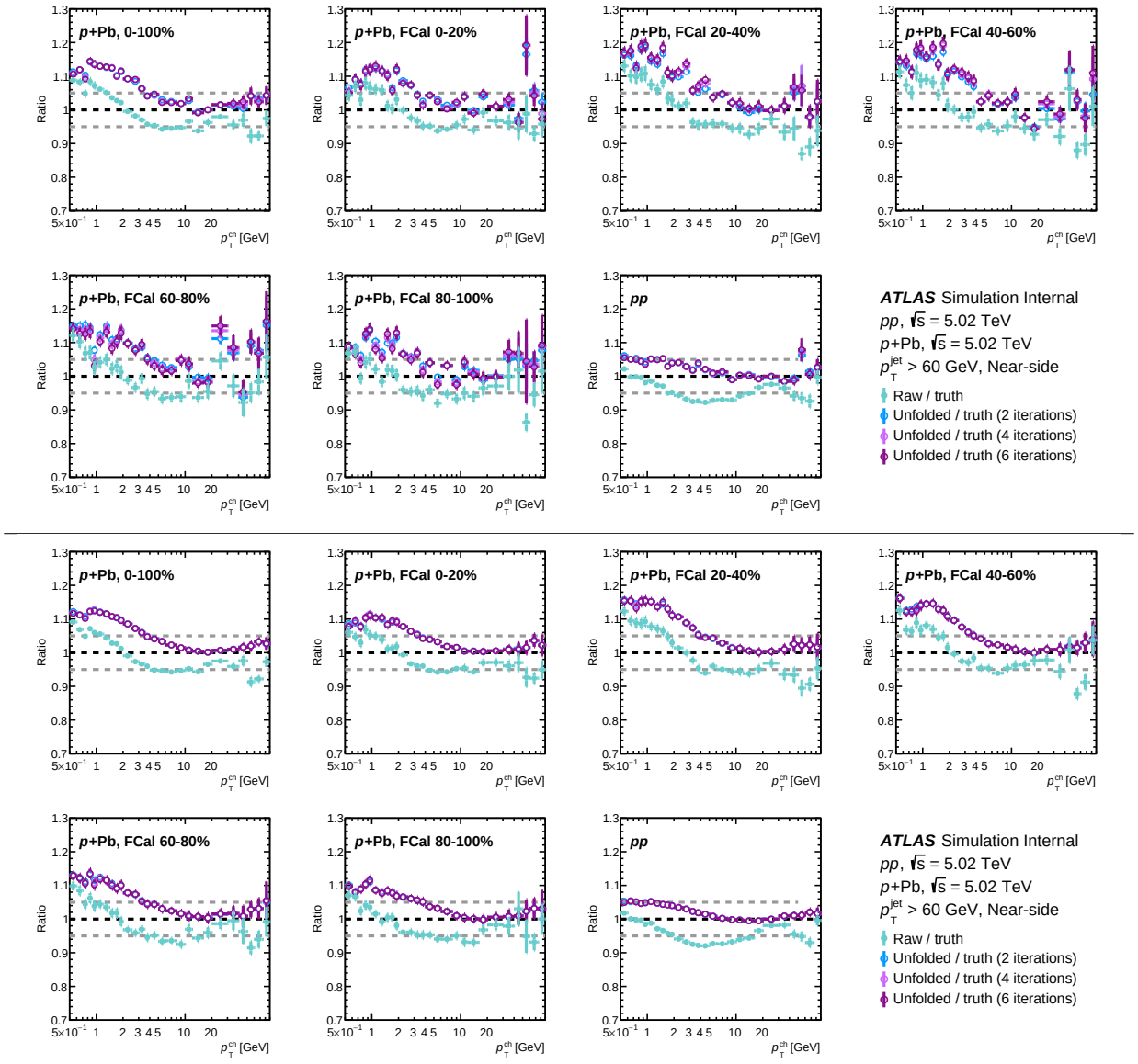
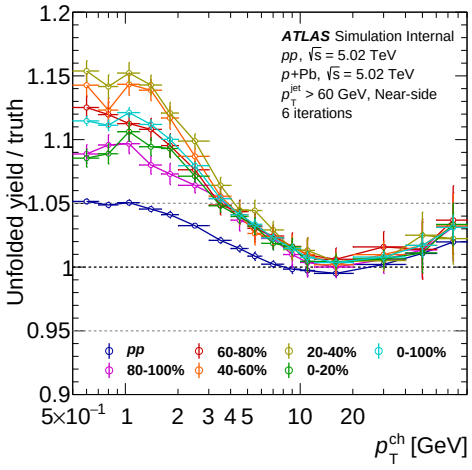
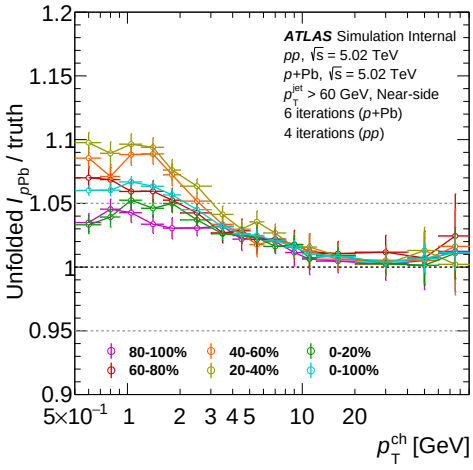


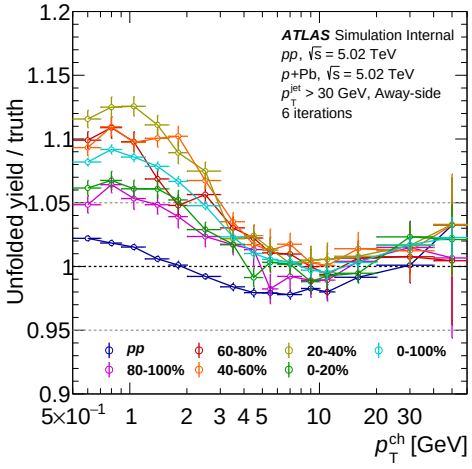
Figure B.17: The half (top) and full (bottom) closure tests are shown for particles nearby ($\Delta\phi < \pi/8$) a jet between 30–300 GeV.



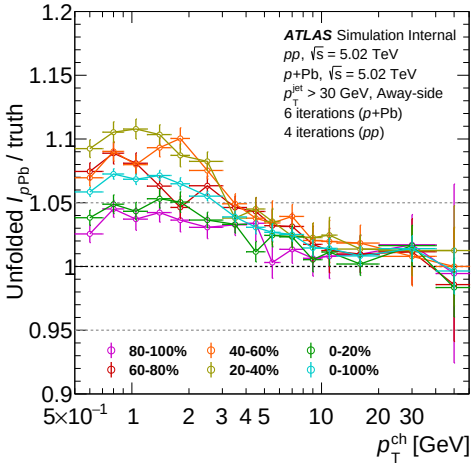
(a) Yield, $p_{\mathrm{T}}^{\mathrm{jet}} > 60$ GeV, near-side



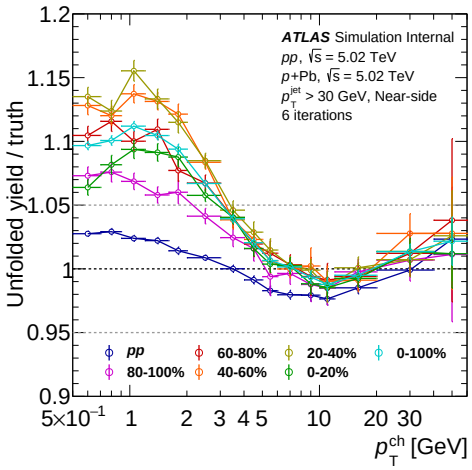
(b) $I_{p\mathrm{Pb}}$



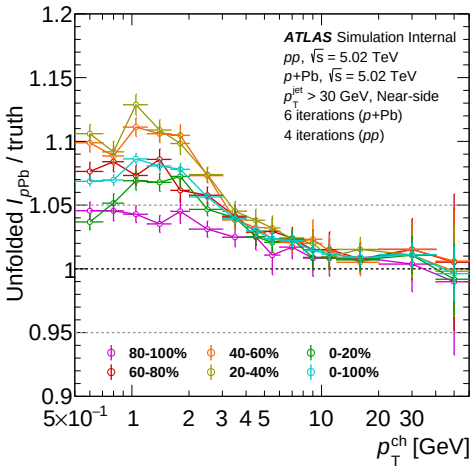
(c) Yield, $p_{\mathrm{T}}^{\mathrm{jet}} > 30$ GeV, away-side



(d) $I_{p\mathrm{Pb}}$



(e) Yield, $p_{\mathrm{T}}^{\mathrm{jet}} > 30$ GeV, near-side



(f) $I_{p\mathrm{Pb}}$

Figure B.18: A summary of the full closure tests for the charged-hadron **(a,c,e)** yield measurements and **(b,d,f)** $I_{p\mathrm{Pb}}$'s **(a,b)** nearby ($\Delta\phi < \pi/8$) a jet above 60 GeV, **(c,d)** opposite ($\Delta\phi > 7\pi/8$) to a jet above 30 GeV and **(e,f)** nearby ($\Delta\phi < \pi/8$) a jet above 30 GeV is shown.

B.5 Decomposition of All Systematic Uncertainties

In this Appendix, we document the systematic uncertainties in all bins reported in the analysis not shown in the main text, including additional centrality selections, the lower $p_{\mathrm{T}}^{\mathrm{jet}}$ selection, and all of the $I_{p\mathrm{Pb}}$ ratios. These figures include

- Figs. B.19 and B.23, which show uncertainties pertaining to the jet energy scale for charged hadrons correlated with a $p_{\mathrm{T}}^{\mathrm{jet}} > 60$ GeV or $p_{\mathrm{T}}^{\mathrm{jet}} > 30$ GeV jet,
- Figs. B.20 and B.24, which show uncertainties pertaining to the tracking for charged hadrons correlated with a $p_{\mathrm{T}}^{\mathrm{jet}} > 60$ GeV or $p_{\mathrm{T}}^{\mathrm{jet}} > 30$ GeV jet,
- Figs. B.21 and B.25, which show uncertainties pertaining to the mixed event & signal extraction for charged hadrons correlated with a $p_{\mathrm{T}}^{\mathrm{jet}} > 60$ GeV or $p_{\mathrm{T}}^{\mathrm{jet}} > 30$ GeV jet, and
- Fig. B.22, which shows a summary of all uncertainties for charged hadrons correlated with a $p_{\mathrm{T}}^{\mathrm{jet}} > 30$ GeV jet.

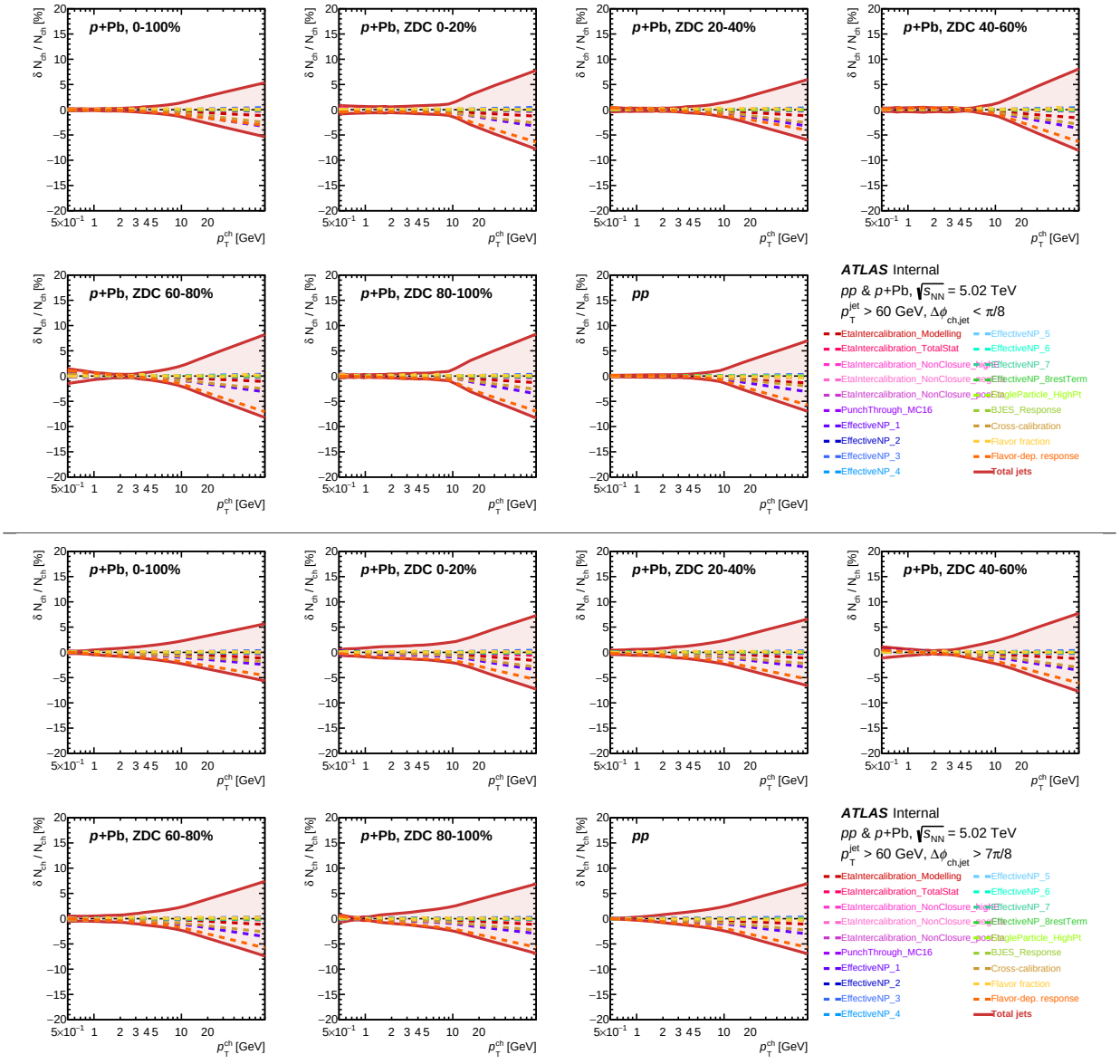


Figure B.19: Systematic uncertainties related to the jet energy scale are plotted versus $p_{\mathrm{T}}^{\mathrm{ch}}$ in the near-side ($\Delta\phi < \pi/8$; top rows) and the away-side ($\Delta\phi > 7\pi/8$; bottom rows) for events with a jet above 60 GeV.

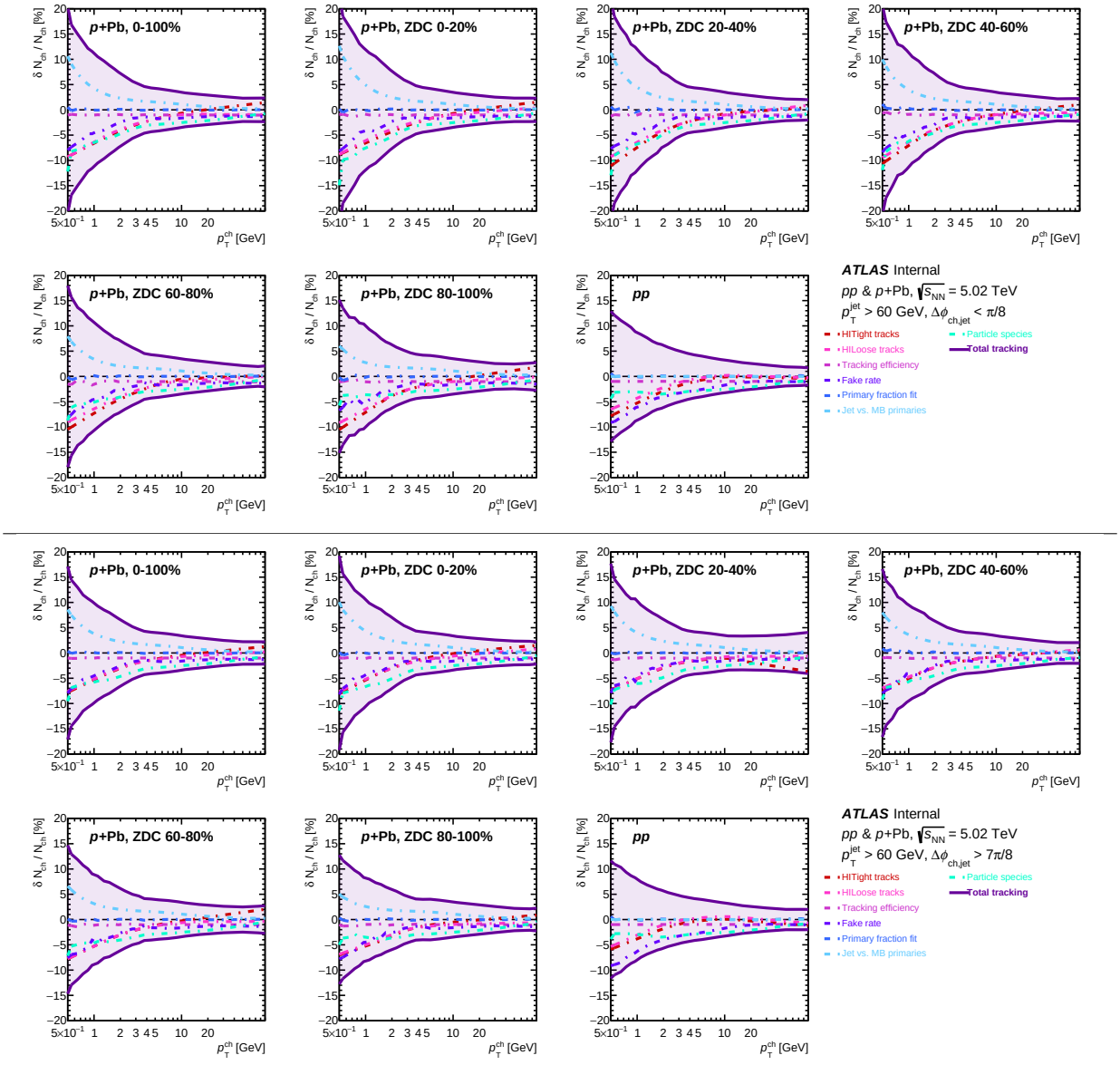


Figure B.20: Systematic uncertainties related to tracking are plotted versus $p_{\mathrm{T}}^{\mathrm{ch}}$ in the near-side ($\Delta\phi < \pi/8$; top rows) and the away-side ($\Delta\phi > 7\pi/8$; bottom rows) for events with a jet above 60 GeV.

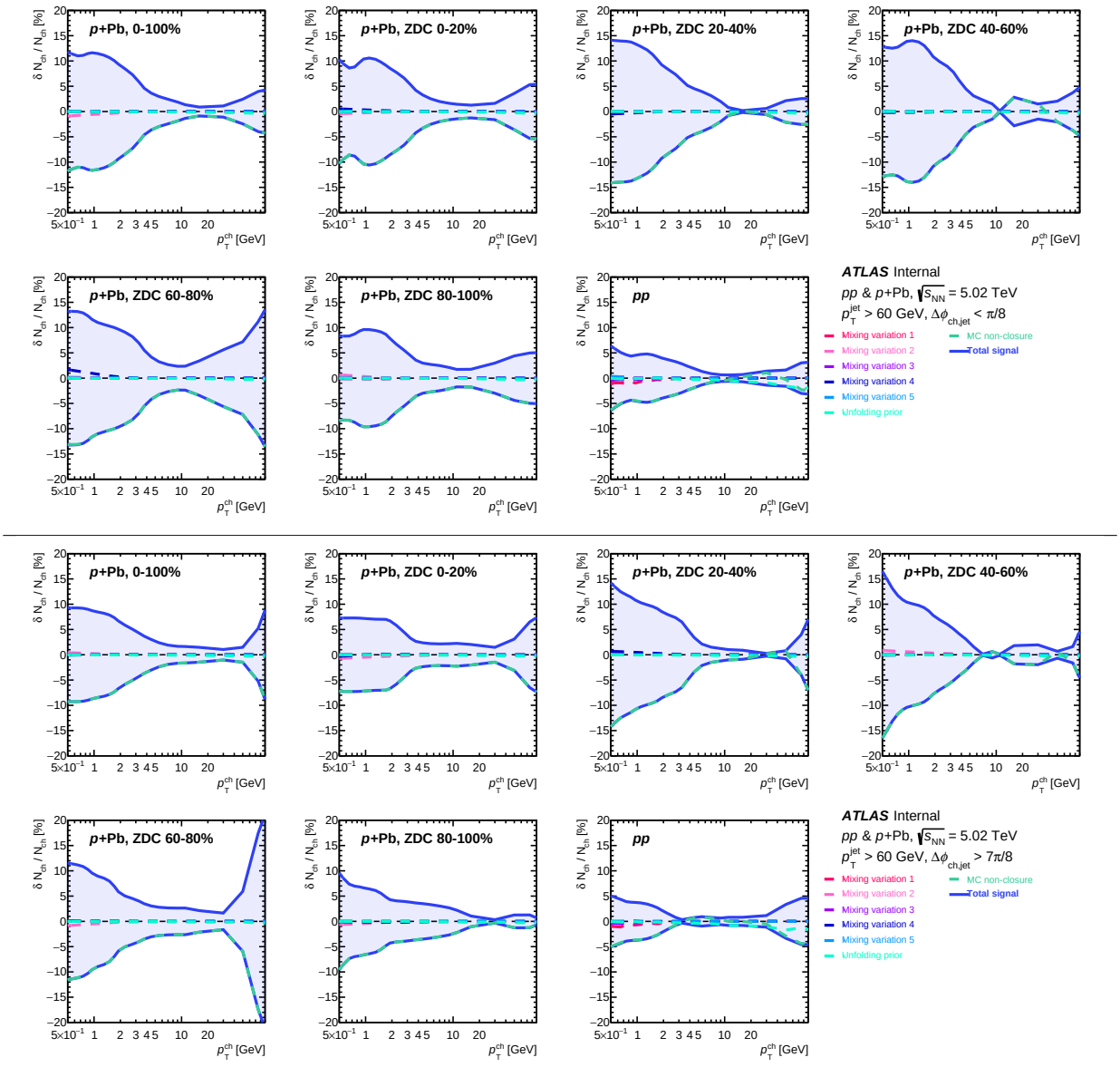


Figure B.21: Systematic uncertainties related to the mixed event & signal extraction are plotted versus $p_{\mathrm{T}}^{\mathrm{ch}}$ in the near-side ($\Delta\phi < \pi/8$; top rows) and the away-side ($\Delta\phi > 7\pi/8$; bottom rows) for events with a jet above 60 GeV.

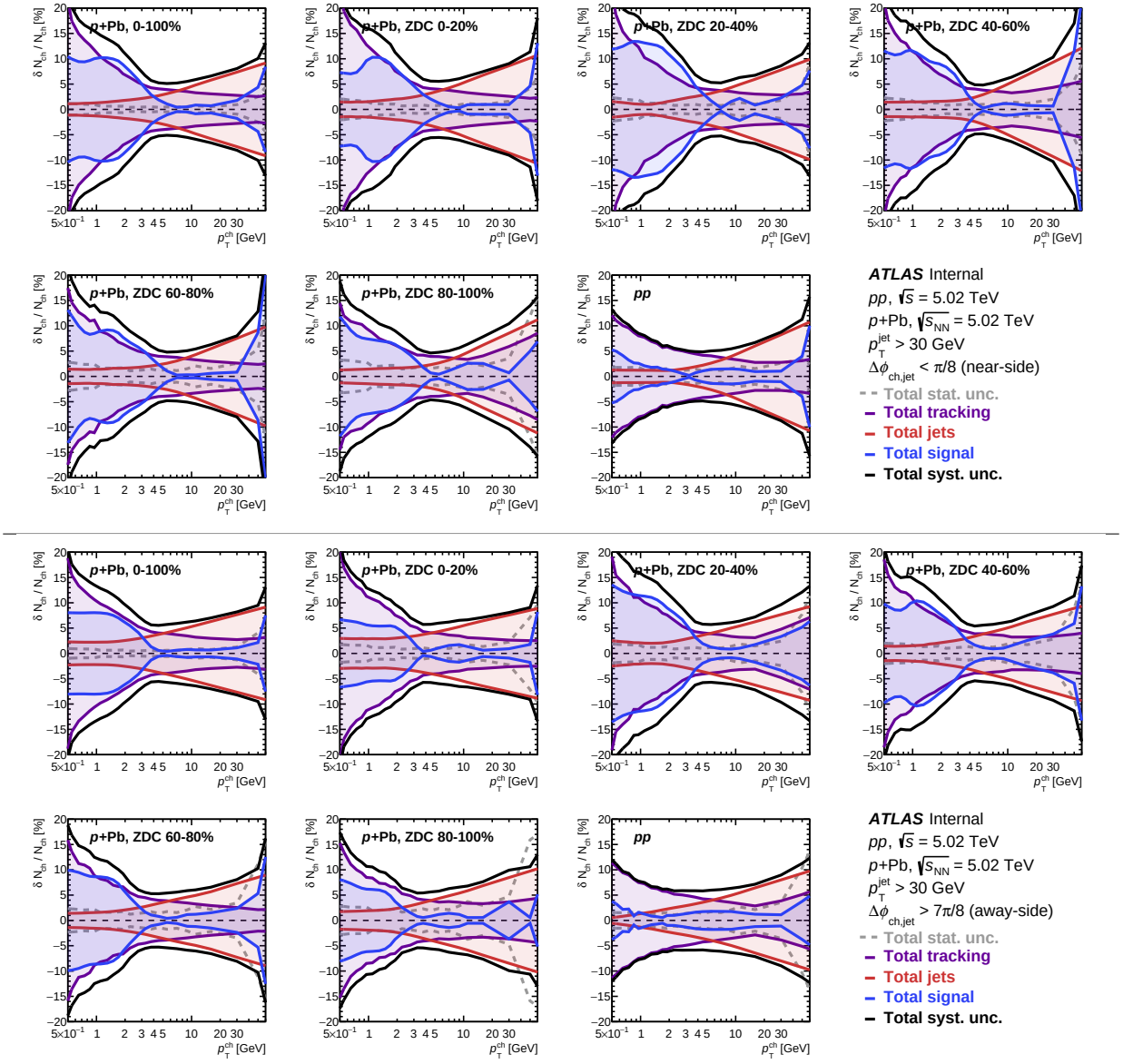


Figure B.22: Total systematic uncertainties for each source (**UE modeling & signal extraction; blue**, **charged-particle tracking; violet**, and **jet-tagging; maroon**) and the **total (black)** are plotted versus $p_{\mathrm{T}}^{\mathrm{ch}}$ in the near-side ($\Delta\phi < \pi/8$; top rows) and the away-side ($\Delta\phi > 7\pi/8$; bottom rows) for events with a jet above 30 GeV. The total statistical (**gray**) and total systematic uncertainty **(black)** are also shown.

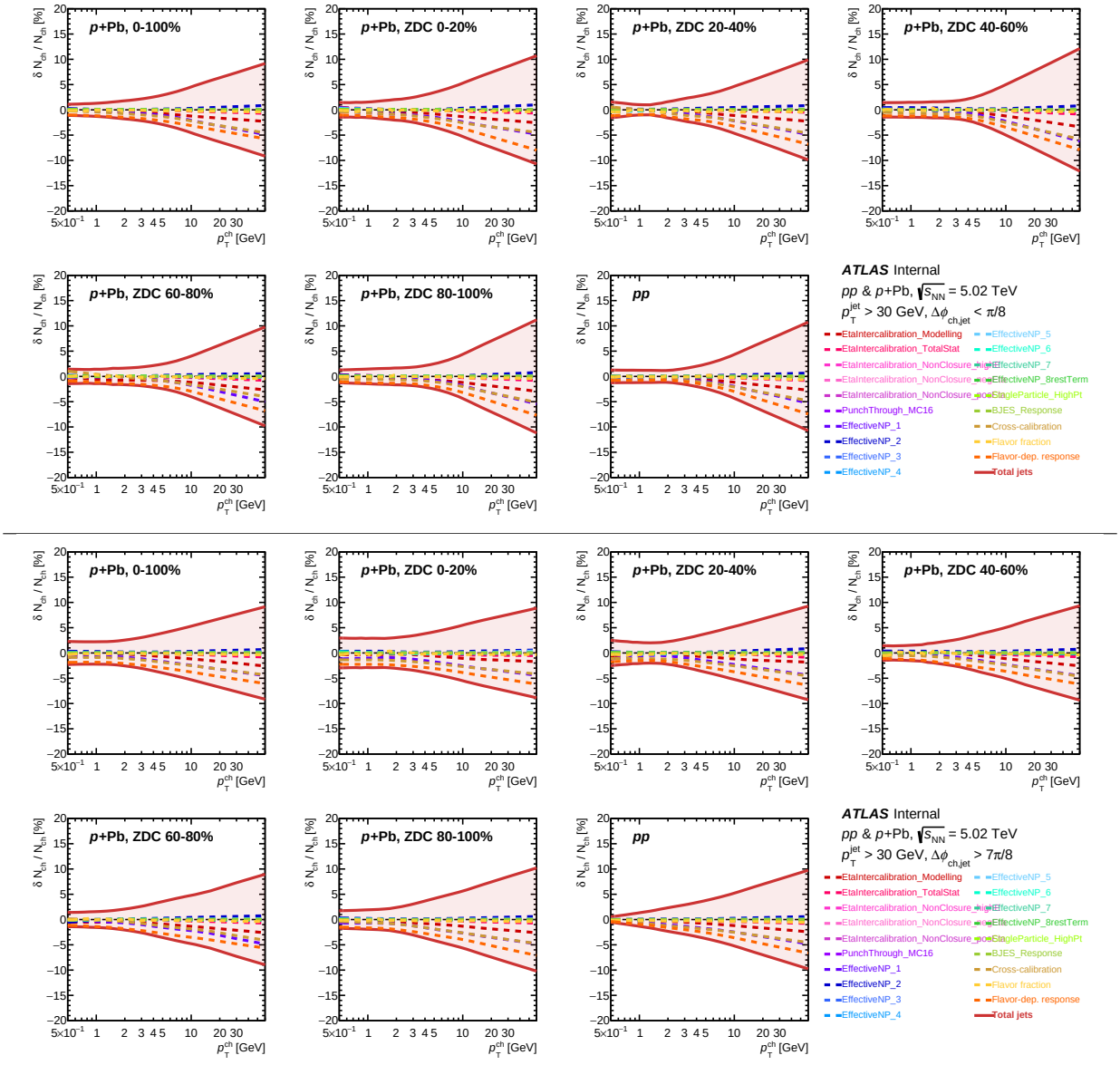


Figure B.23: Systematic uncertainties related to the jet energy scale are plotted versus $p_{\mathrm{T}}^{\mathrm{ch}}$ in the near-side ($\Delta\phi < \pi/8$; top rows) and the away-side ($\Delta\phi > 7\pi/8$; bottom rows) for events with a jet above 30 GeV.

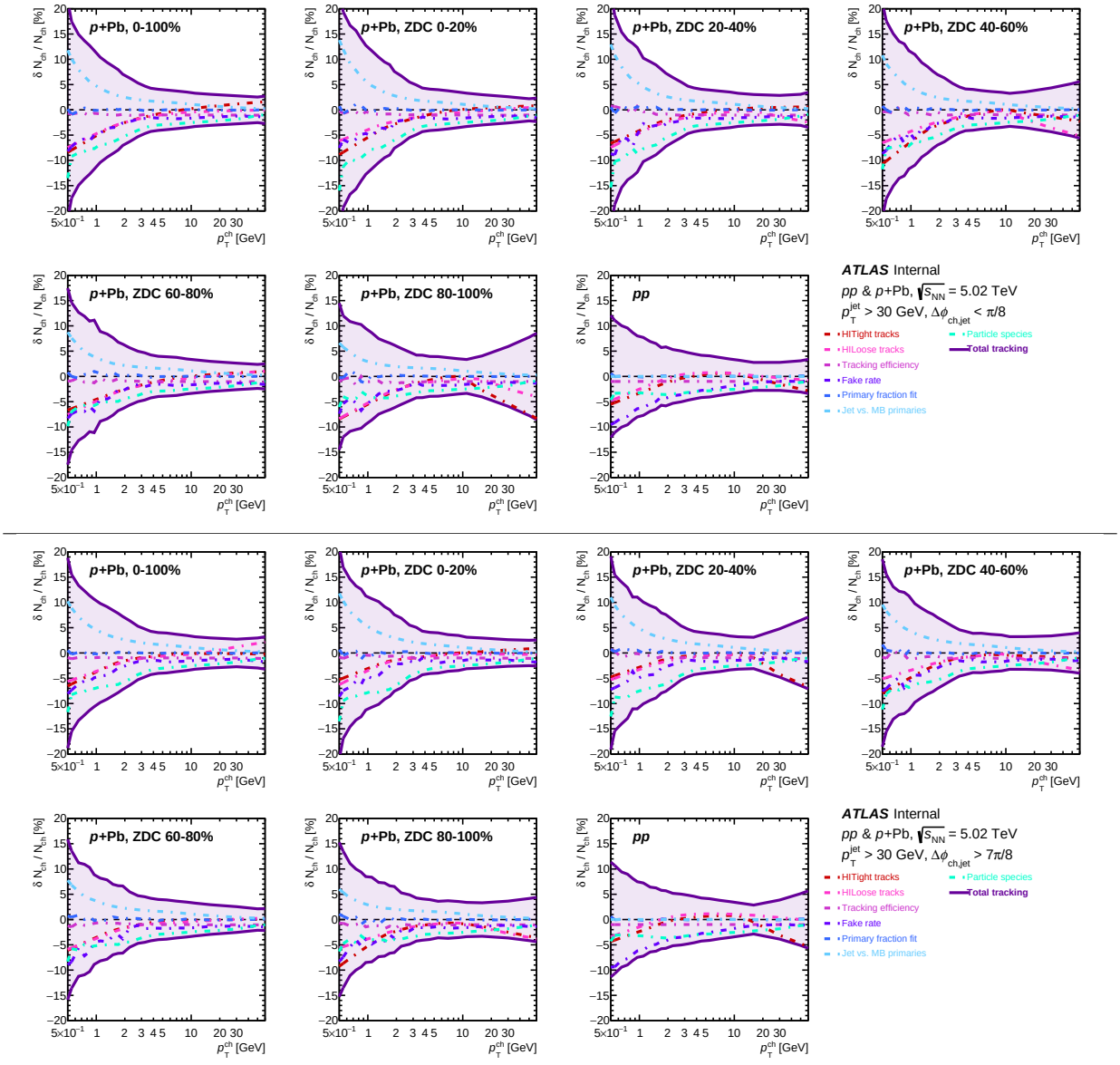


Figure B.24: Systematic uncertainties related to tracking are plotted versus $p_{\mathrm{T}}^{\mathrm{ch}}$ in the near-side ($\Delta\phi < \pi/8$; top rows) and the away-side ($\Delta\phi > 7\pi/8$; bottom rows) for events with a jet above 30 GeV.

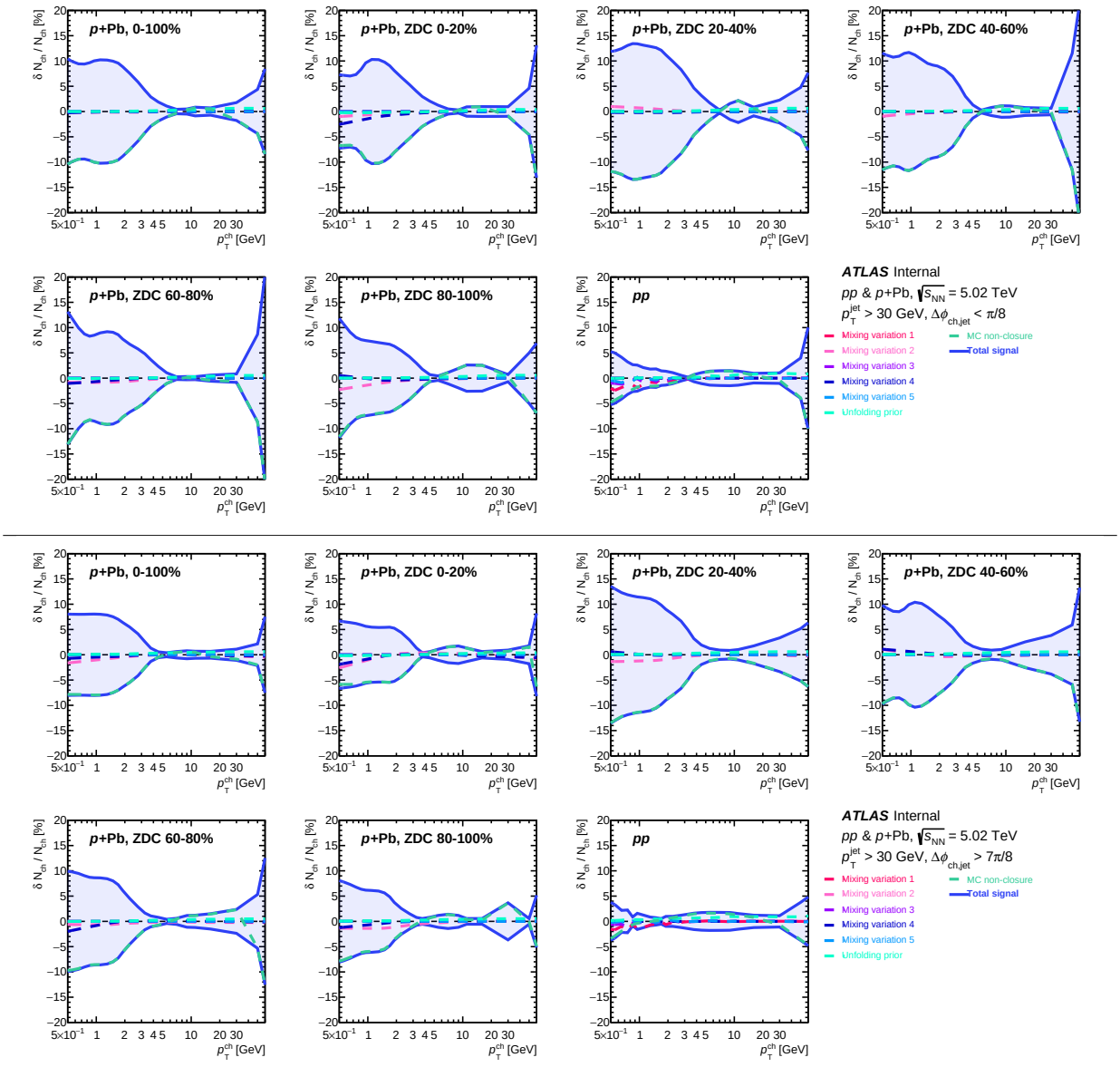
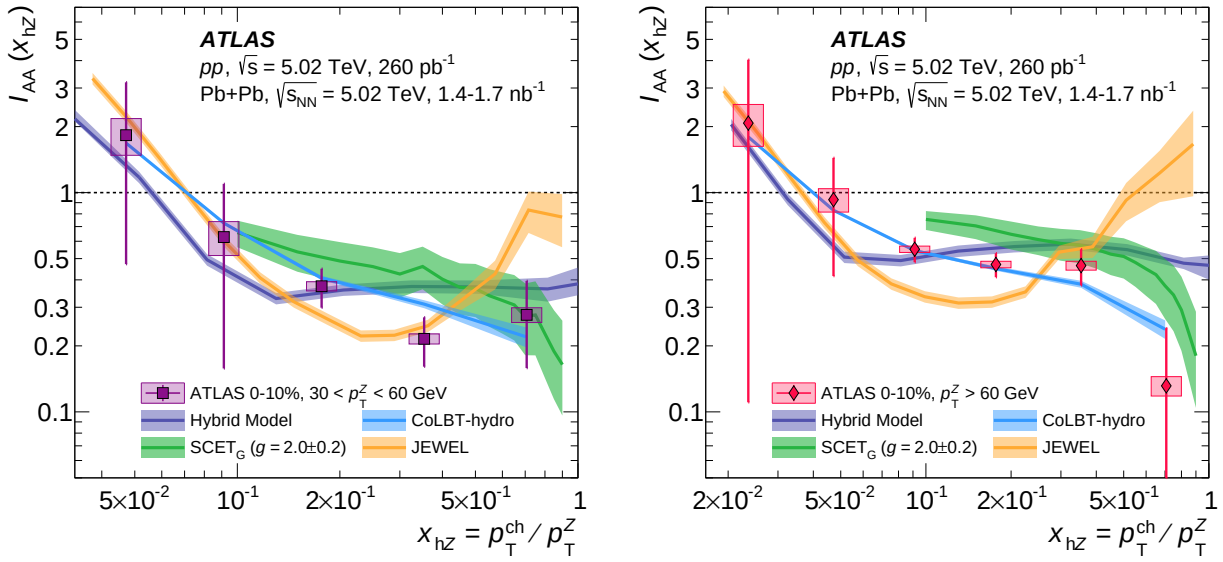


Figure B.25: Systematic uncertainties related to the mixed event & signal extraction are plotted versus $p_{\mathrm{T}}^{\mathrm{ch}}$ in the near-side ($\Delta\phi < \pi/8$; top rows) and the away-side ($\Delta\phi > 7\pi/8$; bottom rows) for events with a jet above 30 GeV.

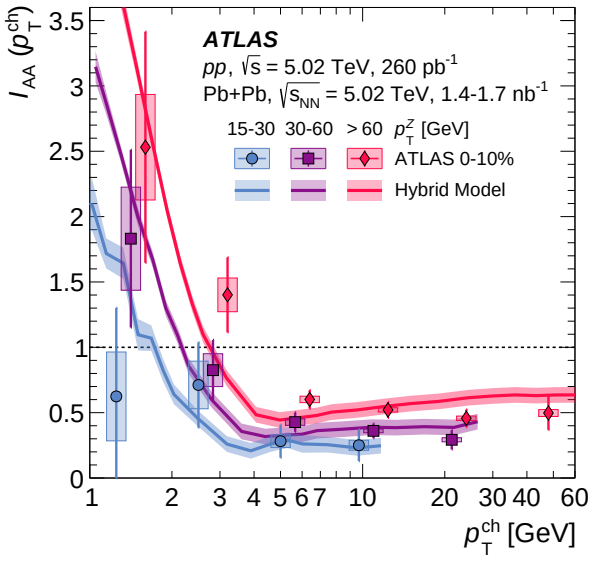
Appendix C

Auxiliary Results Figures

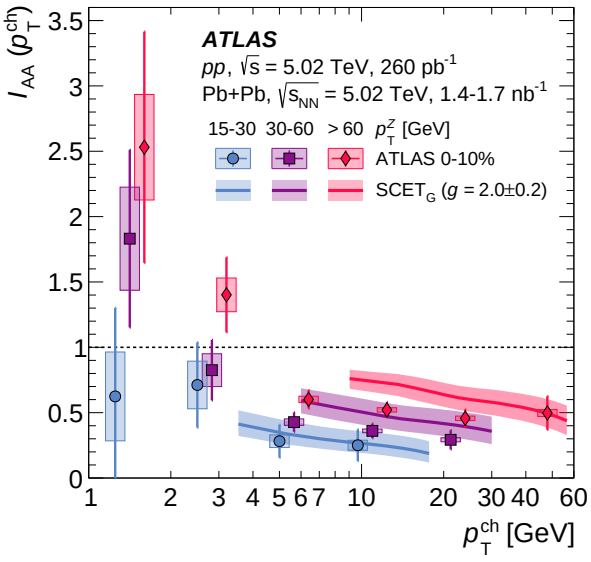


(a) $p_{\mathrm{T}}^{Z} = 30$–60 GeV **(b)** $p_{\mathrm{T}}^{Z} > 60$ GeV

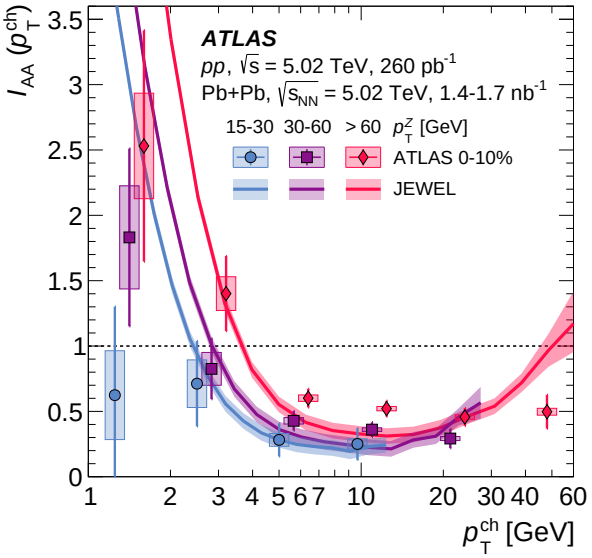
Figure C.1: Comparison of the Z-tagged charged-hadron I_{AA} versus x_{hZ} with jet quenching models, including the Hybrid strong/weak coupling model (with and without the jet wake) [163, 165, 181], a coupled Linear Boltzmann Transport and hydrodynamics model (CoLBT-hydro) [176, 302], calculations for the Z-tagged hadron invariant yields in soft collinear effective theory with Glauber gluons [152, 160, 303, 304], and the pQCD-based JEWEL model [148, 156, 157] with medium-recoils included. Model uncertainties are all statistical, except for the $\mathrm{SCET_G}$ prediction, which varies the jet-medium coupling by $\Delta g = \pm 0.2$. Each panel shows a different p_{T}^{Z} bin 0–10% Pb+Pb events (compared to the pp baseline): **(a)** $p_{\mathrm{T}}^{Z} = 30$–60 GeV, **(b)** $p_{\mathrm{T}}^{Z} > 60$ GeV.



(a) Hybrid model

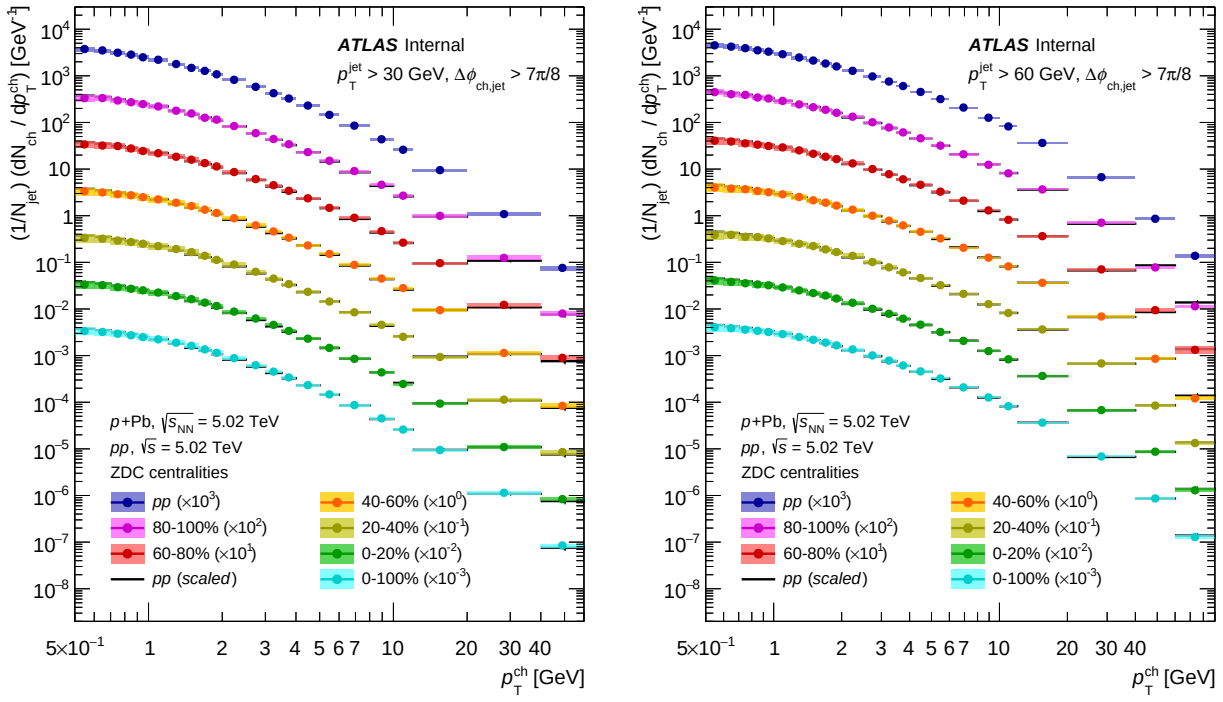


(b) $\mathrm{SCET_G}$



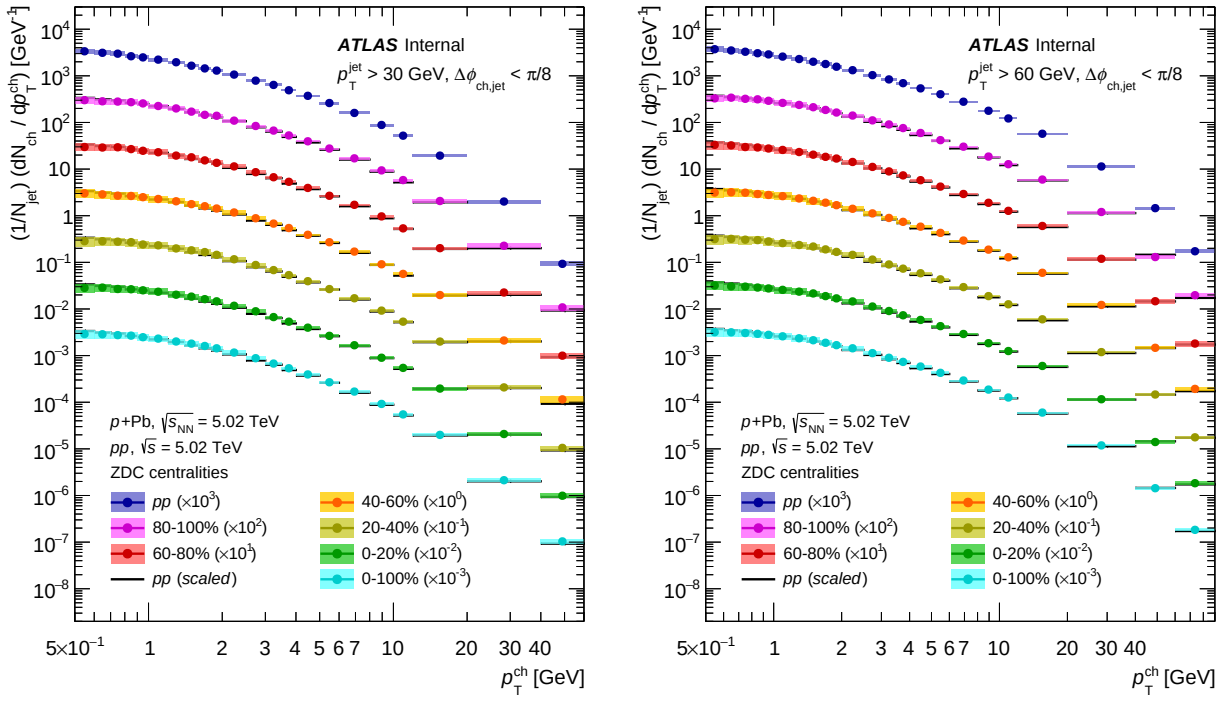
(c) Jewel

Figure C.2: Comparison of the Z-tagged charged-hadron I_{AA} versus $p_{\mathrm{T}}^{\mathrm{ch}}$ with jet quenching models, including **(a)** the Hybrid strong/weak coupling model (with and without the jet wake) [163, 165, 181], **(b)** calculations for the Z-tagged hadron invariant yields in soft collinear effective theory with Glauber gluons [152, 160, 303, 304], and **(c)** the pQCD-based Jewel model [148, 156, 157] with medium-recoils included. Model uncertainties are all statistical, except for the $\mathrm{SCET_G}$ prediction, which varies the jet-medium coupling by $\Delta g = \pm 0.2$. Each panel shows a different model comparison in 0–10% Pb+Pb events (compared to the pp baseline). Different colors and marker styles indicate different p_{T}^{Z} bins.



(a) $p_{\mathrm{T}}^{\mathrm{jet}} > 30$ GeV **(b)** $p_{\mathrm{T}}^{\mathrm{jet}} > 60$ GeV

Figure C.3: The per-jet yields of charged particles in the away-side ($\Delta\phi > 7\pi/8$) are plotted for pp and different ZDC p+Pb centrality selections as a function of charged-particle p_{T}. Particles are correlated with a jet above **(a)** 30 GeV or **(b)** above 60 GeV.



(a) $p_{\mathrm{T}}^{\mathrm{jet}} > 30$ GeV **(b)** $p_{\mathrm{T}}^{\mathrm{jet}} > 60$ GeV

Figure C.4: The per-jet yields of charged particles in the near-side ($\Delta\phi < \pi/8$) are plotted for pp and different ZDC p+Pb centrality selections as a function of charged-particle p_{T}. Particles are correlated with a jet above **(a)** 30 GeV or **(b)** above 60 GeV.

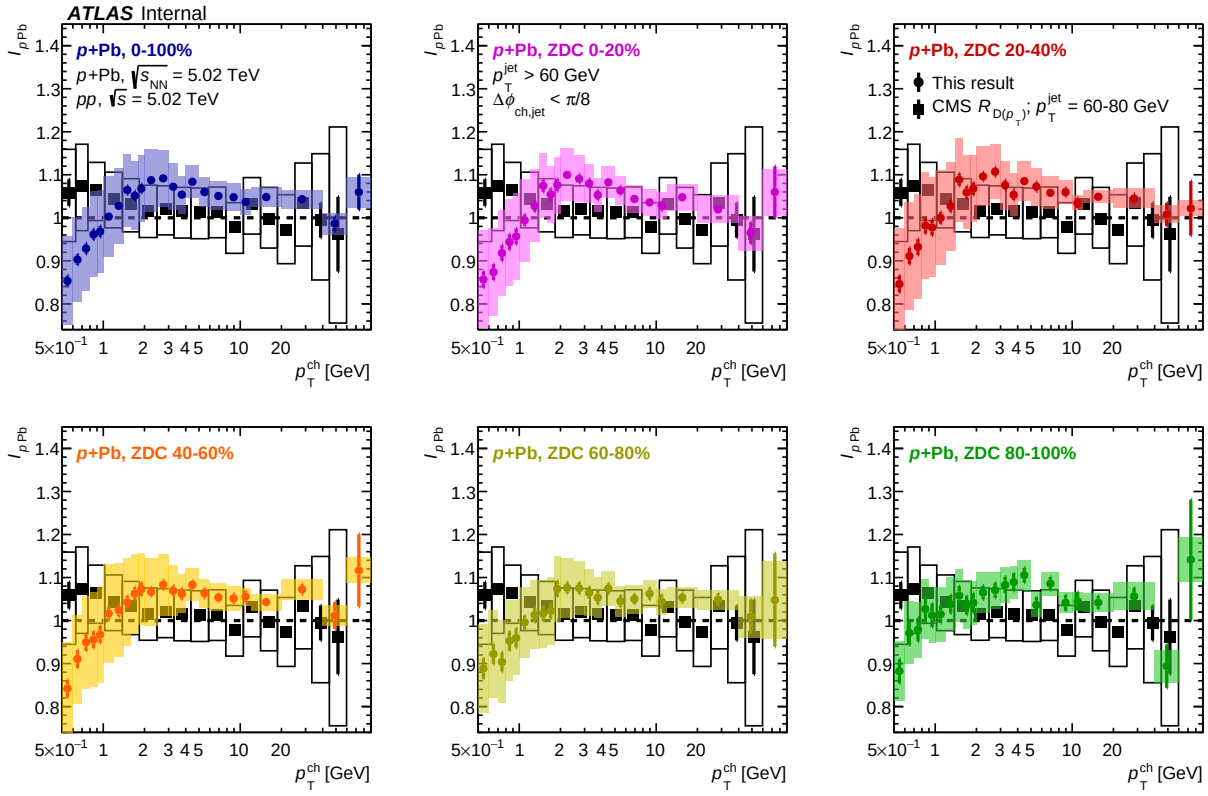


Figure C.5: Near-side ($\Delta\phi < \pi/8$) $I_{p\mathrm{Pb}}$ in each p+Pb ZDC-selected centrality are compared to preliminary jet fragmentation functions measured by CMS [309]. Particles are correlated with a jet above 60 GeV. The fragmentation function measurement corresponds to jets in the range $p_{\mathrm{T}}^{\mathrm{jet}} = 60$–$80$ GeV. The fragmentation function measurements are identical in each centrality selection.